ITALIAN PHYSICAL SOCIETY

PROCEEDINGS
OF THE
INTERNATIONAL SCHOOL OF PHYSICS
"ENRICO FERMI"

COURSE CLXXX

edited by M. ANSELMINO and H. AVAKIAN
Directors of the Course
and
D. HASCH and P. SCHWEITZER

VARENNA ON LAKE COMO
VILLA MONASTERO
28 June – 8 July 2011

Three-Dimensional Partonic Structure of the Nucleon

2012

IOS
Press

AMSTERDAM, OXFORD, TOKIO, WASHINGTON DC

Copyright © 2012 by Società Italiana di Fisica

All rights reserved. No part of this publication may be reproduced, stored in a retrieval system, or transmitted, in any form or any means, electronic, mechanical, photocopying, recording or otherwise, without the prior permission of the copyright owner.

ISSN 0074-784X (print)
ISSN 1879-8195 (online)

ISBN 978-1-61499-196-0 (print) (IOS Press)
ISBN 978-1-61499-197-7 (online) (IOS Press)
ISBN 978-88-7438-076-3 (SIF)

LCCN 2012955876

Production Manager
A. Oleandri

Copy Editor
M. Missiroli

jointly published and distributed by:

IOS PRESS
Nieuwe Hemweg 6B
1013 BG Amsterdam
The Netherlands
fax: +31 20 687 0019
`info@iospress.nl`

SOCIETÀ ITALIANA DI FISICA
Via Saragozza 12
40123 Bologna
Italy
fax: +39 051 581340
`order@sif.it`

Distributor in the USA and Canada
IOS Press, Inc.
4502 Rachael Manor Drive
Fairfax, VA 22032
USA
fax: +1 703 323 3668
`sales@iospress.com`

Proprietà Letteraria Riservata
Printed in Italy

Supported by

Istituto Nazionale di Fisica Nucleare (INFN)

Camera di Commercio di Lecco

Jefferson Science Associates, Newport News, VA (USA)

Jefferson Laboratory, Newport News, VA (USA)

Dipartimento di Fisica Teorica, Università di Torino

INFN, Sezione di Torino

Progetto Hadron Physics 2, INFN Frascati

Wolfram Research, Champaign, IL (USA)

This page intentionally left blank

INDICE

M. Anselmino, H. Avakian, D. Hasch and P. Schweitzer – Preface . . . pag. XIII

Gruppo fotografico dei partecipanti al Corso . . . . » XV

S. E. Kuhn – Experimental methods in polarized DIS and SIDIS . . . . » 1

1. Introduction . . . . » 1
2. Components of typical DIS and SIDIS experiments . . . . » 5
   - 2˙1. Polarized beams . . . . » 6
   - 2˙2. Polarized targets . . . . » 9
   - 2˙3. Detector elements . . . . » 13
     - 2˙3.1. Magnets . . . . » 13
     - 2˙3.2. Wire chambers . . . . » 14
     - 2˙3.3. Vertex trackers . . . . » 14
     - 2˙3.4. Scintillators . . . . » 15
     - 2˙3.5. Cherenkov counters and transition radiation detectors . . . . . . » 16
     - 2˙3.6. Electromagnetic calorimeters . . . . » 17
     - 2˙3.7. Hadronic calorimeters and other detector types . . . . » 18
   - 2˙4. Experimental facilities . . . . » 18
3. Methods and challenges in the analysis of DIS and SIDIS experiments . . . . » 20
   - 3˙1. Calibration . . . . » 20
   - 3˙2. Observables . . . . » 21
   - 3˙3. Raw asymmetries . . . . » 24
   - 3˙4. Dilution . . . . » 24
   - 3˙5. Beam and target polarization . . . . » 26
   - 3˙6. Backgrounds . . . . » 28
   - 3˙7. Corrections and model inputs . . . . » 29
   - 3˙8. Conclusion . . . . » 31

P. J. Mulders – Transverse momenta of partons in high-energy scattering processes . . . . » 33

1. Introduction . . . . » 33
2. Basics . . . . » 34
   - Quantum mechanics . . . . » 34
   - Momenta and phase space . . . . » 35
   - Quantum field theory . . . . » 37

3. Electroweak scattering processes .... pag. 38
4. Structure functions and cross-sections .... » 41
5. Virtual photon cross-sections .... » 44
6. Form factors .... » 45
7. Partons in QCD .... » 47
8. The diagrammatic approach .... » 49
Correlators, describing parton distributions .... » 49
The operator in coordinate space .... » 52
Interpretation as densities .... » 52
Relation to forward amplitudes .... » 52
9. Quark correlation functions in 1PI leptoproduction .... » 53
Structure functions and cross-sections .... » 54
The parton model approach .... » 55
10. Collinear parton distributions .... » 56
11. Bounds on the distribution functions .... » 57
12. Transverse-momentum–dependent correlation functions .... » 59
13. Fragmentation functions .... » 61
Examples of azimuthal asymmetries .... » 62
14. Inclusion of subleading contributions .... » 63
15. Color gauge invariance .... » 64
Gluonic pole matrix elements .... » 67
16. Gluon TMDs .... » 68
17. Concluding remarks .... » 71
Appendix A What information is in the form factors .... » 72
Appendix B Polarized leptoproduction .... » 73
Appendix C Polarized parton densities .... » 75
Appendix D Forms of quantization .... » 75
Appendix E Field quantization in front form .... » 76

M. Diehl – Generalized parton distributions .... » 81

1. Introduction .... » 81
2. Factorization in QCD .... » 82
  2˙1. Examples for factorization: DIS and DVCS .... » 82
    2˙1.1. Kinematics .... » 83
    2˙1.2. Dominant momentum regions .... » 84
    2˙1.3. Power counting .... » 84
    2˙1.4. Collinear expansion .... » 86
  2˙2. Parton distributions and hard-scattering kernels .... » 87
  2˙3. Loop corrections and evolution .... » 89
3. Properties and physics of GPDs .... » 90
  3˙1. Sum rules .... » 93
  3˙2. Impact parameter .... » 95
    3˙2.1. Transverse deformation and spin-orbit correlations .... » 96
  3˙3. Transverse momentum *vs.* transverse position of partons .... » 97
4. Studying GPDs in exclusive reactions .... » 99
  4˙1. From process amplitudes to GPDs .... » 101
  4˙2. A closer look at DVCS .... » 102

A. Bacchetta – TMDs at work .... pag. 107
1. Introduction .... » 107
2. Notation .... » 110
3. Inclusive DIS .... » 111
4. DIS in the parton model .... » 114
5. DIS beyond the parton model .... » 123
6. Semi-inclusive DIS .... » 127
7. Semi-inclusive DIS in the parton model .... » 131
8. The correlation functions .... » 134
9. Structure functions in the parton model .... » 141
10. Beyond the parton model .... » 143
11. Beyond the parton model: high transverse momentum .... » 145
12. Some phenomenology: unpolarized cross-sections .... » 149
13. Weighted asymmetries .... » 153

A. Prokudin – Phenomenology of transverse-momentum–dependent distributions .... » 157
1. Introduction .... » 157
2. Moments of TMDs and three-dimensional partonic structure .... » 160
The Hilbert space of state vectors .... » 161
Unitarity .... » 163
3. Hadron tensors and structure functions .... » 164
4. SIDIS cross-section .... » 171
5. Structure functions .... » 174
5˙1. $F_{UU,T}$ .... » 174
5˙2. $F_{UT,T}^{\sin(\phi_h-\phi_S)}$ .... » 175
5˙3. Sivers asymmetry .... » 178
5˙4. Phenomenological extractions and models of Sivers function .... » 179
5˙5. Wanzura-Wilczek approximation .... » 185
5˙6. A_{LL} asymmetry .... » 186
5˙7. $A_{LT}^{\cos(\phi_h-\phi_S)}$ asymmetry .... » 188
Appendix A .... » 192

B. Pasquini and C. Lorcé – Models for TMDs and numerical methods .... » 197
1. Introduction .... » 197
2. Transverse-momentum–dependent parton distributions .... » 200
2˙1. Definitions .... » 200
2˙2. Helicity and four-component bases .... » 202
3. Model relations .... » 207
4. Amplitude approach .... » 209
4˙1. Connection between light-cone helicity and canonical spin .... » 209
4˙2. TMDs in canonical-spin basis .... » 210
4˙3. Spherical symmetry .... » 212
5. Wave function approach .... » 213
5˙1. Overlap representation of the TMDs on the light cone .... » 213
5˙2. Overlap representation of the TMDs in the canonical-spin basis .... » 215

5˙3. Spherical symmetry . . . . pag. 216
5˙4. $SU(6)$ spin-flavour symmetry . . . . » 217
6. Quark models . . . . » 218
6˙1. Light-cone models . . . . » 219
6˙2. Covariant parton model . . . . » 220
6˙3. Mean-field models . . . . » 221
6˙4. Spectator models . . . . » 222
7. $SU(6)$-symmetry breaking in a light-cone constituent quark model . . . . » 224
7˙1. Light-cone constituent quark model . . . . » 225
7˙2. Results for TMDs . . . . » 227
7˙3. Observables . . . . » 229
8. Conclusions . . . . » 233
Appendix A Spinors and polarization four-vectors . . . . » 236
Appendix B Components of the 3Q LCWF in the light-cone and canonical polarization bases . . . . » 237
Appendix C Connection to a quark-diquark picture . . . . » 238
Appendix C.1 Scalar diquark . . . . » 238
Appendix C.2 Axial-vector diquark . . . . » 239

M. Guidal – Deep virtual Compton scattering: From data to generalized parton distributions (or Compton form factors) . . . . » 245

1. Introduction . . . . » 245
2. From GPDs to data . . . . » 248
3. The DVCS data . . . . » 251
4. From data to GPDs . . . . » 255
5. Conclusion . . . . » 258

A. A. Rostomyan – Analysis tools for azimuthal asymmetries . . . . » 261

1. Definition of azimuthal asymmetries . . . . » 261
2. Maximum-likelihood method . . . . » 262
2˙1. Graphical illustration of statistical uncertainties of parameters . . . . . » 264
2˙2. Advantages and disadvantages . . . . » 265
3. MINUIT . . . . » 266
4. Implementation of the maximum-likelihood method . . . . » 267
4˙1. Beam/target polarization balancing . . . . » 269
Conclusions . . . . » 270

G. K. Mallot – Spin physics at COMPASS: Present and future . . . . » 271

1. Introduction . . . . » 271
2. The COMPASS experiment at CERN . . . . » 273
3. Longitudinal spin structure results . . . . » 276
3˙1. Quarks . . . . » 276
3˙2. Gluons . . . . » 282
4. Transverse spin structure results . . . . » 285
4˙1. Transversity . . . . » 286

- 4˙2. Transverse-momentum dependent distributions ... pag. 288
- 5. COMPASS plans for the future ... » 289
  - 5˙1. GPD programme ... » 290
  - 5˙2. Drell-Yan programme ... » 296
- 6. Conclusions ... » 301

V. D. Burkert – The JLab 12 GeV upgrade and the initial science program » 303

- 1. Introduction ... » 303
- 2. The electron accelerator and the 12 GeV experimental equipment ... » 306
- 3. Generalized parton distributions and deeply virtual Compton scattering ... » 307
- 4. Semi-inclusive deeply inelastic scattering and TMDs ... » 311
- 5. Inclusive structure functions and moments ... » 315
  - 5˙1. Valence quark structure and flavor dependence at large x ... » 316
  - 5˙2. Spin structure functions and parton distributions ... » 317
  - 5˙3. Global analysis of polarized parton densities ... » 319
  - 5˙4. Moments of spin structure functions ... » 319
- 6. Electromagnetic form factors at short distances ... » 321
  - 6˙1. Nucleon elastic form factors ... » 321
  - 6˙2. Nucleon resonance transition form factors ... » 322
- 7. Gluonic excitations of hadrons. ... » 322
  - 7˙1. Hybrid mesons ... » 322
  - 7˙2. Hybrid baryons ... » 325
- 8. Quarks and hadrons in the nuclear medium ... » 326
  - 8˙1. Color transparency ... » 326
  - 8˙2. Quark propagation and hadron formation ... » 326
- 9. Search for new physics ... » 328
  - 9˙1. Search for physics beyond the Standard Model ... » 328
  - 9˙2. Heavy photon search ... » 329
- 10. Conclusions ... » 331

D. Hasch – The structure of the nucleon at an EIC ... » 333

- 1. Preface ... » 333
- 2. Introduction: The physics case of an EIC ... » 334
  - 2˙1. Spin and flavour structure of the proton ... » 335
  - 2˙2. Three-dimensional nucleon structure ... » 336
  - 2˙3. Some more exciting topics for an EIC ... » 338
- 3. EIC realisations: Introduction ... » 338
- 4. EIC realisations: Baseline designs at BNL and JLab ... » 340
  - 4˙1. eRHIC at BNL ... » 340
  - 4˙2. MEIC at JLab ... » 343
- 5. EIC realisations: Challenges and R&D ... » 345
  - 5˙1. Luminosity at a collider ... » 346
  - 5˙2. Energy recovering linacs ... » 346
  - 5˙3. Crab crossing ... » 347
  - 5˙4. Electron cooling ... » 348
  - 5˙5. Ring design ... » 349
- 6. EIC realisations: Kinematics and requirements ... » 349

6˙1. Kinematic range in x and Q^2 . . . . . . pag. 350
6˙2. Particle identification . . . . . . » 351
6˙3. Vertex detectors . . . . . . » 352
6˙4. The very forward (backward) region . . . . . . » 352
7. EIC realisations: Detector concepts . . . . . . » 353
8. Conclusions . . . . . . » 354

P. Schweitzer – Fermi problem . . . . . . » 357

1. Introduction . . . . . . » 357
2. The problem . . . . . . » 358
3. Analysis of the results . . . . . . » 359
Summary . . . . . . » 360

Elenco dei partecipanti . . . . . . » 361

Preface

The CLXXX Course, “Three-Dimensional Partonic Structure of the Nucleon”, of the “Enrico Fermi” School, held in Varenna from June 28 to July 8, 2011, was devoted to the study of the 3-dimensional structure of protons and neutrons (nucleons) and to the properties and motion of the nucleon internal constituents, quarks and gluons (partons).

This issue is central in many theoretical and experimental activities and has marked a real transition, in the last two decades, in our exploration of the ultimate structure of matter, addressing fundamental questions such as the orbital motion of quarks and gluons inside the nucleons, their spatial distribution and the correlation between spin and intrinsic motion. A real 3-dimensional imaging of the nucleon as a composite object, both in momentum and coordinate space, is slowly emerging.

Several dedicated experiments are either running (COMPASS, JLab and RHIC) or analyzing previously collected data (HERMES). Other experimental facilities are under construction (J-PARC and the upgrading of JLab) or being planned (PANDA, PAX, ENC, EIC). All these have a central focus in the study of the 3-dimensional nucleon structure.

Enormous theoretical progress has been achieved in the last years with the new concepts of Transverse Momentum Dependent (TMDs) and Generalized Parton Distributions (GPDs). These can be studied respectively in inclusive and exclusive processes at the above-mentioned facilities by looking at spin asymmetries and azimuthal distribution of final hadrons or leptons. The collection and interpretation of data, with theorists and experimentalists working together, is and will be one of the major activities in hadron physics; the international scientific community working in the field is constantly growing.

The proposed School had the ambitious goal of educating postgraduate students, so that they could end up becoming specialists in hard scattering and partonic azimuthal distributions analysis and could be able to join CLAS, COMPASS, RHIC, J-PARC, PAX, PANDA, EIC, ENC and any of the dedicated experiments; or they could perform theoretical and phenomenological studies of TMDs and GPDs.

The School was attended by 40 students and 3 observers from 13 different Countries. Basic introductory lectures were delivered by 7 lecturers and more specialized topics covered by 7 seminar speakers. All of them are among the world experts in their own field. Special attention was given to the interaction among lecturers and students and to favor active participation. Lectures and seminars were focused on the conceptual theoretical ideas, the experimental techniques and the phenomenological interpretation of data. Special lectures and tutorials were dedicated to data analysis and model building, with the active participation of students.

The main topics discussed can be summarized as follows:

- Partonic distributions, fragmentation functions and factorization in QCD (collinear case).
- Theory of Transverse Momentum Dependent partonic distributions (TMDs).
- Theory of Generalized Partonic Distributions (GPDs).
- Experimental methods in studies of hard scattering processes.
- Extraction of TMDs and GPDs from data.
- Analysis tools for azimuthal asymmetries.
- Models for TMDs and numerical methods.
- Future experiments.

In conclusion the organizers of the Course warmly thank the Jefferson Science Associates, the Jefferson Laboratory, and the HadronPhysics2 European Project of the FP7 framework for their generous financial support; the Wolfram Research for supporting the School with complimentary licenses of Mathematica for Students. Special thanks are due to Barbara Alzani, Monica Bonetti, Roberta Comastri and Ramona Brigatti for their precious, continuous and invaluable help both during the preparation of the Course and its organization at Villa Monastero.

M. ANSELMINO, H. AVAKIAN, D. HASCH and P. SCHWEITZER

This page intentionally left blank

Società Italiana di Fisica
SCUOLA INTERNAZIONALE DI FISICA «E. FERMI»
CLXXX CORSO - VARENNA SUL LAGO DI COMO
VILLA MONASTERO 28 Giugno - 8 Luglio 2011

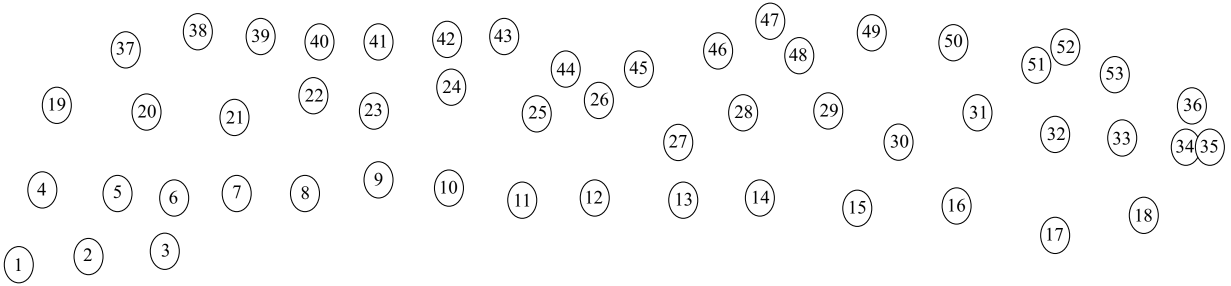

1) Brigatti Ramona
2) Hasch Delia
3) Alzani Barbara
4) Brodski Irina
5) Park Sanghwa
6) Petrosyan Anush
7) Ghandilyan Yeranuhi
8) Kvaltine Nicholas
9) Webb Grant
10) Du Fresne von Hohenesche Nicolas
11) Avakian Harut
12) Anselmino Mauro
13) Buffing Martinus
14) Joosten Sylvester
15) Guegan Baptiste
16) Gohn Wes
17) Guttman Julia
18) Key Aaron
19) Khachatryan Vardan
20) De Sanctis Enzo
21) Bowles Jennifer
22) Kuhn Sebastian
23) Mulders Piet
24) Johansson Tord
25) Diehl Markus
26) Xiong Xiaonu
27) Bertelli Susanna
28) Romanelli Giovanni
29) Pitonyak Daniel
30) Nocera Emanuele
31) Pauk Vladyslav
32) Beranek Tobias
33) Elia Carmine
34) Rinaldi Matteo
35) Schmidt Katharina
36) Aghasyan Mher
37) Movsisyan Aram
38) Stratmann Marco
39) Schweitzer Peter
40) Bacchetta Alessandro
41) Cepila Jan
42) Myska Miroslav
43) Osipenko Misha
44) Pasquini Barbara
45) Pisano Silvia
46) Pereira Anefalos Sergio
47) Sokhan Daria
48) Khandramai Viacheslav
49) Gabdrakhmanov Ilnur
50) Smith Gary
51) Golembiovskaya Mayya
52) Van Der Veken Frederik
53) Zagrebelny Vitaly

This page intentionally left blank

Proceedings of the International School of Physics "Enrico Fermi"
Course CLXXX "Three-Dimensional Partonic Structure of the Nucleon"
edited by M. Anselmino, H. Avakian, D. Hasch and P. Schweitzer
(IOS, Amsterdam; SIF, Bologna)
DOI 10.3254/978-1-61499-197-7-1

Experimental methods in polarized DIS and SIDIS

S. E. Kuhn

Old Dominion University - Norfolk, VA 23529, USA

Summary. — In these lecture notes, I describe typical experimental equipment and methods, as well as analysis procedures, for measurements of inclusive Deep Inelastic (DIS) and Semi-Inclusive Deep Inelastic Scattering (SIDIS) of (polarized) leptons off (polarized) targets. While some of the topics I discuss have broader applicability (for instance, for measurements of exclusive processes, or for hadron-hadron interactions), I concentrate on lepton scattering experiments, with particular emphasis on experiments already completed or planned at the Continuous Electron Beam Accelerator Facility (CEBAF) at Jefferson Lab.

1. – Introduction

The goal of these lecture notes is to provide an overview of the experimental methods and analysis procedures that have been used (and are likely to be used in some form in the future) to study the three-dimensional partonic structure of the nucleon, as expressed in transverse momentum-dependent (TMD) parton distribution functions and in generalized parton distributions (GPDs). These (relatively novel) concepts are building upon the well-known nucleon structure functions and form factors to describe not only the distribution of longitudinal momentum and helicity over the partonic constituents of the nucleon, but to yield additional information on the transverse position, momentum and spin of these partons.

© Società Italiana di Fisica

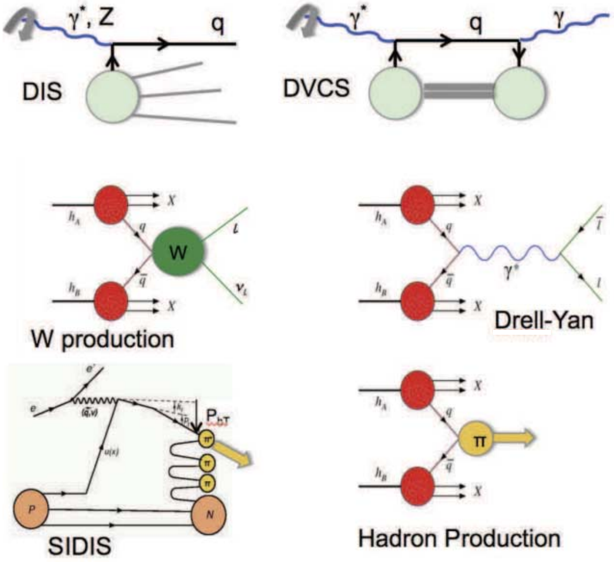

Fig. 1. – Different reaction mechanisms that can be used to probe the partonic structure of the nucleon. The first four mechanisms involve the electroweak probe, while the last one is purely hadronic, and the second to last one combines both probes. DIS, DVCS and SIDIS reactions are induced by (mostly) virtual photons (wiggly lines) emitted from scattered charged leptons (which can transfer some of their initial polarization to the virtual photon) on (up to now) stationary nucleon targets, while the other three reactions are initiated with hadron beams impinging on stationary or counter-circulating nucleons.

In fig. 1 I give a very generic overview of the kind of reactions that can be used to study GPDs and TMDs. In the following, I will focus in particular on the transverse momentum-dependent (TMD) structure functions which correlate intrinsic transverse momenta, $\vec{k}_\perp$, of quarks inside the nucleon with their spins, $\vec{s}$, and with that of the nucleon as a whole ($\vec{S}$). These TMDs can be most cleanly accessed by semi-inclusive deep inelastic scattering (SIDIS) experiments, and most of the experimental details given below refer to this case. This is not meant to distract from the importance of other observables, *e.g.*, Drell-Yan experiments and hadron-hadron collisions which are addressed elsewhere in this volume. Given the many experimental communalities and the greater simplicity, I will discuss inclusive scattering (DIS), as well.

Other lecture notes in this volume give a fundamental description of the theoretical foundations of both integrated and TMD structure functions. While I do not want to duplicate these more rigorous descriptions, I would like to begin by making a few general observations on the constraints on the information that is at least in principle accessible, based on simple symmetry considerations. I hope this may help to guide the intuition of "newcomers" to this field as to why certain mathematical correlations between spins and momenta are discussed most prominently.

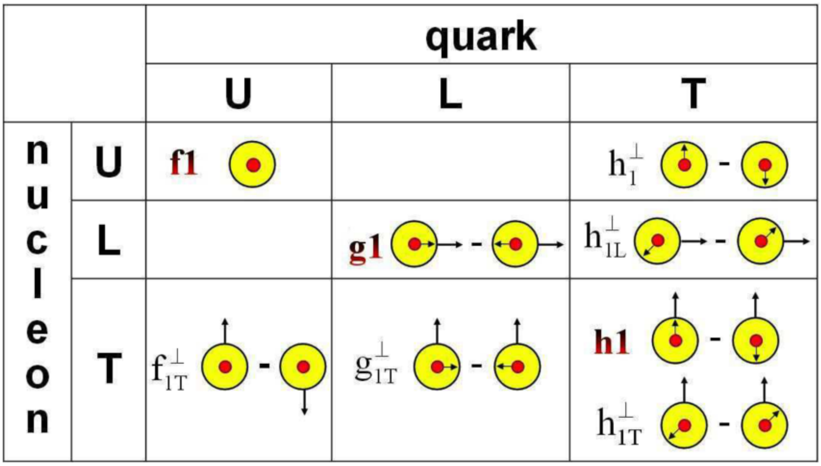

Fig. 2. – Usual arrangement of leading twist TMDs depending on both target and quark spin direction (U = unpolarized, L = longitudinally polarized, T = transversely polarized).

To start, we observe that because rotations and boosts do not commute in special relativity, we have to treat longitudinal degrees of freedom differently than transverse ones. Using the customary "infinite" (high) momentum frame, in which the nucleon moves with velocity $\approx c$ along the $\hat{z}$ direction, we can describe the former through the momentum fraction x and helicity h carried by a given quark, given the helicity H of the nucleon as a whole (H and h are the spin projections on $\hat{z}$). This information is complemented by the transverse momentum $\vec{k}_\perp$ and transverse spin $\vec{s}_\perp$ of the partons, and the transverse spin $\vec{S}_\perp$ of the nucleon. Since the components of the spin vector do not commute, we cannot expect to simultaneously specify h and $\vec{s}_\perp$ or H and $\vec{S}_\perp$.

Apart from this constraint, we therefore have two vectors ($\vec{k}_\perp$ and $\hat{z}$), two axial vectors ($\vec{s}_\perp$ and $\vec{S}_\perp$) and two pseudoscalars (h, H) to form any proper observable, which by necessity must be a scalar. In the following, we will list the possible combinations up to the second power in $\vec{k}_\perp$—surprisingly, there are not all that many. If we do not use $\vec{k}_\perp$ at all (meaning we integrate over all $\vec{k}_\perp$), only three possible combinations survive: The identity

$$\mathbb{1} \tag{1}$$

(which corresponds to the quark densities as a function of x, *i.e.* the structure function F_1 in the top left corner of the usual 3×3 matrix shown in fig. 2), the product

$$hH \tag{2}$$

(yielding the usual spin structure function g_1, in the center) and the product

$$\vec{s}_\perp \cdot \vec{S}_\perp \tag{3}$$

(the so-called transversity h_1, which resides in the bottom right corner and is as fundamental as the other two).

Adding one power of $\vec{k}_\perp$, we have two options to form a product of two pseudoscalars, namely

$$h\left(\vec{k}_\perp \cdot \vec{S}_\perp\right) \tag{4}$$

and

$$H\left(\vec{k}_\perp \cdot \vec{s}_\perp\right) \tag{5}$$

(the two "worm gear" functions at the ends of the middle row and the middle column). Alternatively, we can form two triple products which must by necessity involve the two vectors $\vec{k}_\perp$ and $\hat{z}$ and one of the two axial vectors:

$$\vec{S}_\perp \cdot \left(\vec{k}_\perp \times \hat{z}\right) \tag{6}$$

(the Sivers function, in the left bottom corner), and

$$\vec{s}_\perp \cdot \left(\vec{k}_\perp \times \hat{z}\right), \tag{7}$$

the Boer-Mulders function (top right corner). Including one more power of $\vec{k}_\perp$ yields four new TMDs, including the $\vec{k}_\perp^2$ moments of the three "diagonal" structure functions discussed first. The most interesting fourth possibility is the combination

$$\left(\vec{S}_\perp \cdot \vec{k}_\perp\right)\left(\vec{s}_\perp \cdot \vec{k}_\perp\right) - \frac{1}{2}\vec{k}_\perp^2\left(\vec{S}_\perp \cdot \vec{s}_\perp\right) \tag{8}$$

which corresponds to the "pretzelosity" function (lower right corner). Readers are encouraged to try other combinations—they will find that they either simplify to (combinations of) the structures already discussed, or are identical zero (*e.g.*, combinations like $\vec{k}_\perp \cdot \hat{z}$), or they do not transform like proper scalars under parity inversion(^{1}). Therefore, the 8 correlations discussed (plus $\vec{k}_\perp^2$ moments of the first three) form the complete set of information, in the context of the (leading twist) naïve parton model, one can even in principle expect to access up to terms quadratic in $\vec{k}_\perp$.

(^{1}) Initially, concerns were raised that the two combinations eqs. (6), (7) are "odd" under Time Reversal (TR). Indeed, reversing time reverses all three vectors in the triple products (including $\hat{z}$ since the nucleon will go "backwards"), yielding an overall minus sign. However, a full TR operation also requires interchanging initial and final state, which basically turns SIDIS into a Drell-Yan reaction. Sure enough, the prediction (so far untested) is that the Sivers and Boer-Mulders functions reverse sign in Drell-Yan.

Similar symmetry considerations can also constrain the *observables* in SIDIS. The quark momenta and spins, $\vec{s}_\perp$ and $\vec{k}_\perp$, are not directly accessible; instead, one has to use the transverse momentum of the outgoing hadron, $\vec{P}_{h\perp}$. One more vector, $\hat{x}$, is given by the direction of the outgoing lepton (perpendicular to the virtual photon, $\hat{q}$), and one can form the axial vector $\hat{y} = \hat{q} \times \hat{x}$. Finally, one has the helicity of the virtual photon, h_γ, which is determined by kinematics and the helicity of the scattering lepton. Once again, the simple-most scalar one can observe is the identity (the cross-section which relates to F_1), followed by $H \cdot h_\gamma$ (which accesses g_1). Beyond this, one can form products like $H(\vec{P}_{h\perp} \cdot \hat{y})$ and $h_\gamma(\vec{P}_{h\perp} \cdot \hat{y})$ which correspond to the $\sin(\phi_h)$ moments of the single target (A_{UL}) and beam (A_{LU}) asymmetries. Concentrating on transverse target spin, we have the combinations

$$(\vec{P}_{h\perp} \cdot \hat{x})(\vec{S}_\perp \cdot \hat{y}) = |P_{h\perp}||S_\perp| \cos(\phi_h) \sin(\phi_S) \tag{9}$$

(a product of two scalars) and

$$(\vec{P}_{h\perp} \cdot \hat{y})(\vec{S}_\perp \cdot \hat{x}) = |P_{h\perp}||S_\perp| \sin(\phi_h) \cos(\phi_S) \tag{10}$$

(a product of two pseudo-scalars). One can combine these two terms either as a difference, $\sin(\phi_h)\cos(\phi_S) - \cos(\phi_h)\sin(\phi_S) = \sin(\phi_h - \phi_S)$, which is the "Sivers moment", or as a sum, $\sin(\phi_h)\cos(\phi_S) + \cos(\phi_h)\sin(\phi_S) = \sin(\phi_h + \phi_S)$, which is the "Collins moment". Higher cos and sin moments can also be formed by an arbitrary number of scalars (analog to eq. (9)) and an even number of pseudo-scalars (analog to eq. (10)). Of course, the challenge is to tease out which information on the quark-level correlations (eqs. (1)–(8)) one can gain from the measurable scalars discussed here—this requires a theoretical understanding of both hard scattering and hadronization and is discussed in other contributions to this volume.

It is important to keep in mind the difference between the coordinate system used here, with $\hat{z}$ along the direction of the momentum transfer $\vec{q}$, and the beam coordinate system. In particular, if the target is polarized along or perpendicular to the beam, proper rotation of $\vec{S}$ is required before applying any of these relationships.

Having laid the foundations of what can be measured (and what kind of information about TMDs can be expected to be contained in these measurements), we now turn to a description of the actual experimental apparatus typically used (sect. **2**) and common analysis methods to extract the relevant observables. (sect. **3**).

2. – Components of typical DIS and SIDIS experiments

Practically all experiments that can access information on the internal quark-gluon structure of the nucleon have a few ingredients in common: A "target" of nucleons to be probed (often required to be polarized either in transverse or longitudinal direction), a beam of either leptons or hadrons to probe the target with (including electrons, positrons, muons, neutrinos, pions and nucleons as well as anti-nucleons), and a detector system to measure at least part of the final state (in the context of SIDIS and DVCS, at least one hadron and/or photon as well as the scattered lepton). Note that even for colliding beams, one can always treat one of the beams as “the target”—of course, for pp- and $p\bar{p}$-collider, the choice is arbitrary.

In the following, we will first discuss the production and acceleration of polarized beams (with emphasis on lepton beams), followed by an overview of typical polarized targets. We will then look at some common detector elements found, in some combination, in most high-energy experiments. Finally, we survey briefly some experimental facilities that have either contributed to our knowledge of nucleon structure (including GPDs and TMDs) in the past, are actively taking data now, or are on track to begin operation in the near future. Clearly, an exhaustive discussion would be impossible and of little value to most readers; instead, I will give some references to the literature.

2˙1. *Polarized beams.* – For a full exploration of the three-dimensional structure of the nucleon, we need polarized beams as probes. In particular, in SIDIS and DIS, polarized leptons are used to produce (partially) polarized real and virtual photons that couple to the quarks inside the nucleon and can probe their helicity (h). In DVCS, beam spin asymmetries can untangle the Compton Amplitude from its interference with Bethe-Heitler photon emission. There are basically three techniques that have been used to produce polarized leptons:

1) A polarized electron “gun” followed by acceleration (*e.g.*, linear traveling wave accelerators).

2) The “natural” polarization of muons from weak decays of pions.

3) The Sokolov-Ternov effect (“self-polarization” of a circulating lepton beam due to synchrotron radiation).

We now discuss each method in some more detail.

1) Let us examine as an example the polarized electron beam of the Jefferson Lab Continuous Beam Accelerator (CEBAF): The laser-driven source produces electron beams (polarized up to 85%) at currents up to $300\,\mu$A, using bandgap photoemission from a strained GaAs cathode coated with Cesium inside an ultra-high-vacuum system [1]. (The state of the art is using a “superlattice” of a thin GaAs layer on top of GaAsP bulk material—the mismatch between the lattice spacing “strains” the GaAs layer and removes a degeneracy of energy bands that limited electron polarization to less than 50% in earlier guns. These cathodes have become so efficient that even experiments that do not require electron polarization are now run in this configuration.) The polarized photons for this process [2] are supplied by MOPA (Master-Oscillator-Power-Amplifier) or Ti:sapphire lasers followed by a HV-driven bi-refringent Pockel cell that converts linear to circular polarization, allowing rapid reversal of the beam helicity at up to 60 Hz. As shown in fig. 3, a *half-wave plate* (HWP) can be inserted in the laser beam to change the polarization phase by 180°

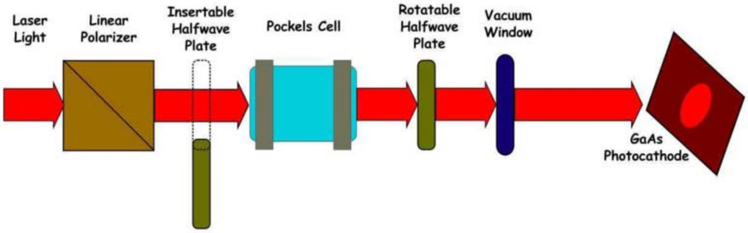

Fig. 3. – Polarized source. Graphic from K. Paschke.

(for suppression of systematic false asymmetries). The electrons are initially accelerated by the high electric potential of the source ($\approx 100\,\mathrm{kV}$) and then pass through a "Wien filter" with crossed electric and magnetic fields that keep them on axis while rotating their spins into any arbitrary desired direction. The 100 kV electrons enter the injector line [1,3], where their energies are boosted prior to their introduction into the main accelerating structure consisting of two superconducting linacs connected by recirculation arcs. Each linac segment contains a series of superconducting niobium RF cavities, driven by 5-kW klystrons [4]. Detailed descriptions of the accelerator can be found in refs. [4,1,5,6]. Figure 4 shows an overall diagram of the CEBAF accelerator. The electron spins keep precessing in the recirculating arcs, requiring careful tuning of both the accelerator energy and the Wien filter to accomplish high polarization (typically longitudinal) in the experimental halls.

To deliver beam to all 3 of the research halls (A, B and C), a $\frac{1}{3}$ harmonic RF separator system splits the interleaved bunches and delivers the beam to the appropriate experimental halls [4]. Electrons delivered to Halls A and C are bent through arcs with steering magnets while electrons continuing straight forward can then be delivered to Hall B. The currents in all three halls can be dialed independently and

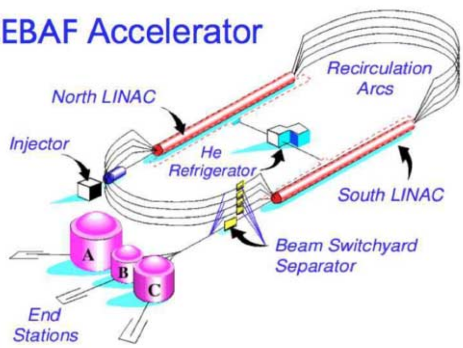

Fig. 4. – Layout of CEBAF.

can range from a few nA in Hall B to over 100 μA in the other two halls. Together with long targets (gases, solids and liquids), luminosities of 10^{34}–10^{37} cm^{-2} s^{-1} are achievable.

Polarimeters are employed at several stages along this process to precisely measure the beam polarization. For instance, before acceleration, spin-dependent electron scattering in the Coulomb field of nuclei ("Mott scattering") is used to get the initial polarization. In each of the experimental Halls, the workhorse polarimeters use the cross-section asymmetry of electron-electron ("Möller") scattering for electrons with parallel *vs.* antiparallel spin which can be precisely calculated in QED. The target electrons are provided by a magnetized ("Permandur") foil and the scattered electrons are bent outwards with a series of magnets (*e.g.*, quadrupoles) and detected in scintillators or calorimeters (see below), either as singles or in coincidence with the knocked-out target electrons. A more technically demanding method uses polarized laser light interacting with high energy electron ("Compton backscattering"), which has a well-known asymmetry (basically, only electrons with spin opposite to the photon helicity can absorb and reemit such a photon). This approach is not only more precise (to better than 1%) but also has the advantage that it is "non-destructive", allowing continuous monitoring of the beam polarization during actual data taking (while the target of a Möller polarimeter disrupts the beam, forcing these measurements to be done during special runs). On the other hand, very large photon fluxes are needed, which may require optical cavities and a complicated beam chicane to bring the beam into interaction with the stored photons.

2) Muon beams at CERN come from the weak decay $\pi^+ \rightarrow \mu^+\nu_\mu$. The pions are created when high-energy proton beams interact with massive stationary targets and are then energy-selected. By also controlling the muon energy, one can select muons from forward or backward decays in the pion rest frame. These muons are right-handed (being "anti-particles" created through the parity-violating weak charged current) which translates into a natural, well-known helicity in the lab frame. Since reversing this helicity requires a retuning of the beam line, it cannot be done as frequently as for electron beams.

3) The electrons and positrons used at HERA for the HERMES experiment are stored beams in a circular ring. Due to their centripetal acceleration, they emit synchrotron radiation (which requires a constant but modest supply of RF acceleration to re-supply the lost energy). This radiation has a slight dependence on the vertical (with respect to the ring plane) spin of the leptons, which leads over time to a build-up of transverse polarization of the stored beam (Sokolov-Ternov effect). This transversal polarization can be measured and turned into longitudinal polarization for experiments by using spin rotators (combinations of magnets that yield no net deflection of the beam but a 90 degree precession of the lepton spins).

Hadron beams can also be polarized; *e.g.*, at RHIC an atomic beam source selects hyperfine states of the hydrogen atom with the desired proton polarization which are then injected into a series of accelerators. Great care has to be taken to avoid depolarizing resonances during acceleration. In the end, the protons are injected into one of the two counter-rotating RHIC rings. An elaborate scheme of magnets ("Siberian snakes", spin rotators) turn the spins on each circular orbit to compensate for misalignments and to provide any desired polarization at the interaction point.

Even more ambitious schemes are being discussed for the polarization of anti-protons, including spin filters that utilize the preferential absorption (annihilation) of antiprotons on stationary, spin-polarized hydrogen.

2˙2. *Polarized targets.* – Apart from counter-rotating polarized beams (*e.g.*, at RHIC), stationary polarized targets come in three basic varieties:

1) Solid-state cryogenic targets employing proton- (or deuteron-) rich compounds.

2) Noble gas targets (in particular ^{3}He).

3) Atomic beam targets.

Again, we will discuss each type in turn.

1) High density polarized targets of protons and deuterons are usually made of compounds like ammonia (NH_3, ND_3) or alcohols that are rich in bound hydrogen atoms and that are solid at cryogenic temperatures [7, 8]. Another material that has been used is lithium deuteride (^{6}LiD), where the Li nucleus can be approximated to first order as a bound state of an alpha-particle and a second deuteron (which is also polarizable). In each case, the goal is to maximize the number of polarizable target nucleons with respect to the total target composition. A particular high ratio of polarizable nucleons to total target density has been achieved with frozen samples of hydrogen-deuteron molecules (HD-ice). A second consideration is that the target material must allow the introduction of paramagnetic centers (unpaired electrons—see below) and must be sufficiently "radiation-hard" (in particular if used in an intense electron beam).

Paramagnetic centers (which provide polarizable single electrons) are introduced through chemical doping or irradiation with photons or electrons. The target material is then cooled to about 1 K or below (using liquid-helium refrigerators at very low pressure or ^{3}He/^{4}He dilution refrigerators) and immersed in a very strong magnetic field (of order several Tesla). In these conditions, the free-electron spins approach a polarization of 100%. Irradiating the target material at a frequency near that of the electron spin resonance (typically in the microwave range—of order 100 GHz) induces transitions that flip the spin of both the electron and a neighboring nucleus. Due to their short relaxation time ($\sim 10^{-3}$ s), the electron spins quickly relax back to the lower energy state, and become again available for more spin-flip transitions, while the nuclear spins couple weakly to the lattice and take much longer ($\sim 10^3$ s) to relax. A continuous irradiation results in the transfer of unpaired electron polarization to the nuclei in their vicinity, which is then transmitted to the remote nuclei by the nuclear dipole-dipole interaction (spin diffusion) [9,10]. Proton polarizations of over 90% and deuteron polarizations of 40–60% have been achieved with this method. The combination of microwave frequency and target field (direction) determines the direction of the polarization, which can be reversed on typical time scales of hours. The target is either constantly repolarized with microwaves (Dynamic Nuclear Polarization—DNP [9]) during exposure to the beam (especially high-intensity beams) or is cooled to even lower temperatures where nucleon spin relaxation times become long enough for the duration of the experiment (frozen spin mode).

The target polarization is typically monitored continuously using an NMR system. RF radiation at the nucleon spin resonance frequency is coupled into the target and flips a small number of nucleon spins. These changing magnetic dipoles induce a signal in the pickup coil (which can be identical to the input coil) and the size of the signal is indicative of the total polarization and can be normalized to the well-known polarization of hydrogen nuclei in a thermalized sample. A typical example of such a target (which was used at SLAC and Jefferson Lab's Halls A and C) is shown in fig. 5; a similar target for Hall B is described in detail in ref. [11].

Some of the challenges of these solid-state targets come from their susceptibility to radiation damage from beam exposure. To mitigate this, the beam is typically rastered over the front face of the target (avoiding local depolarization), and the beam current must be limited to about 100 nA. Still, the radiation damage sustained by the target material from the electron beam must be repaired by an annealing process where the target material is heated to $\sim$ 80–90 K, which can require an interruption of the experiment for one hour or more on a regular basis (*e.g.*, daily). After a few annealing cycles, the target material must be exchanged with fresh material. Another challenge comes from the fact that a lot of different material is in the path of the electron beam, not only the desired polarized nucleons, but also other atoms in the compound used (*e.g.*, nitrogen) as well as liquid-helium coolant, entrance and exit windows, foils to hold the target material in place, super-insulation foils, etc. For this reason, only 15–25% of detected scattering events actually come from polarized nucleons (= "dilution factor"). Finally, turning the target polarization perpendicular to the beam direction (for transverse spin dependent asymmetries) leads to a large magnetic field bending the primary beam. This requires a system of compensating beam magnets ("chicane") and sufficient shielding of detector elements against the large background of low-energy electrons and photons spread out by this field. Compact frozen spin targets (including HD-Ice) may be able to mitigate this problem.

2) For measurements on the neutron, one can either compare asymmetries on the deuteron (approximately a proton and a neutron with equal polarization) to that on the proton, or use a target nucleus in which most of the polarization is carried

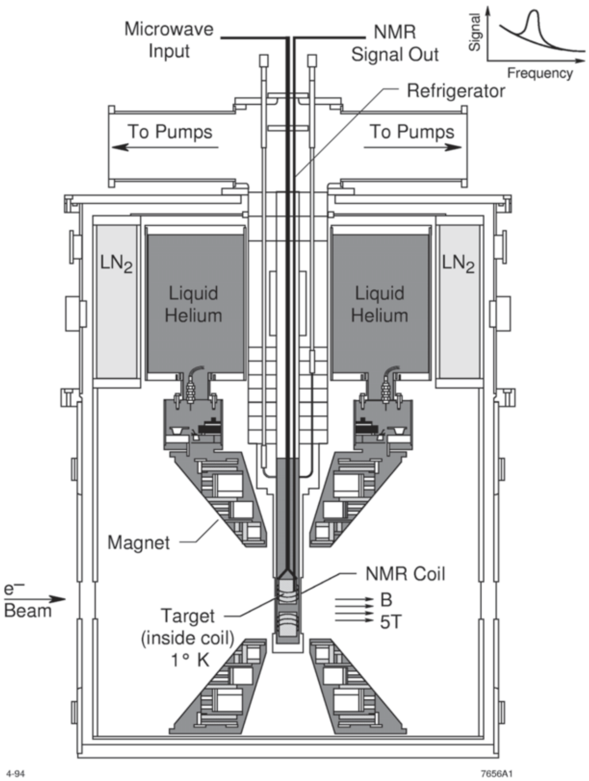

Fig. 5. – Typical cryogenic DNP target. The 5 Tesla magnetic field is supplied by a series of Helmholtz coils (superconductor immersed in 4 K liquid helium) while the target itself is cooled further to 1 K by pumping away helium gas from the target refrigerator and therefore lowering the pressure and consequently the boiling temperature of ^{4}He. Microwave radiation at about 140 GHz and 1 Watt, supplied by an Extended Interaction Oscillator—EIO—tube, induces the desired HF transitions that transfer polarization from the unpaired electrons to nucleons. The polarization of the latter is measured using an NMR system with a induction/pickup coil surrounding the target (a typical signal from this system is shown in the top right corner).

by the neutron, namely ^{3}He. Indeed, according to modern wave functions of this nucleus, the probability to "find" it in an s-state with zero proton polarization is about 87%. The correction due to residual proton polarization is only a few percent; other nuclear corrections (binding and coherent processes) have to be taken into account but are considered to be under control. The advantage of ^{3}He is that it is a gas at room temperature, making the target conceptionally simple and able to withstand large beam currents (up to 15 μA so far in Jefferson Lab's Hall A). The gas, with pressures of about 10 atm, can be held in a thin, long glass tube, yielding luminosities in excess of $10^{36}\,\mathrm{cm}^{-2}\,\mathrm{s}^{-1}$, at least an order of magnitude higher than for cryogenic solid state targets, and less susceptible to local depolarization (because of the high mobility of the helium atoms).

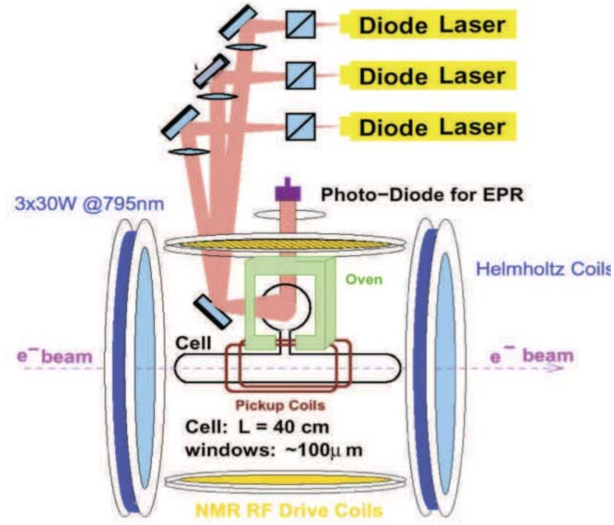

Fig. 6. – Polarized ^{3}He gas target as used in Jefferson Lab's Hall A. The upper half of the target cell is heated and contains the alkali vapor. The large Helmholtz coils provide the holding field that defines the quantization axis for the polarization.

The helium nuclei (with spin 1/2) are polarized through spin-exchange collisions with alkali atoms, which are suspended as a vapor by heating a spherical volume connected to the main target cylinder by a thin tube.The alkali atoms in turn are polarized through absorption of circularly polarized laser light, typically supplied by high-power diode lasers. Recent progress has come from using a hybrid alkali vapor, in which rubidium atoms absorb the laser light (tuned to their absorption frequency), then exchange their electron spins with potassium atoms which in turn polarize the helium nuclei. In-beam polarizations of 65% have been achieved with this technique, yielding the highest figure of merit for any polarized target. The polarization is again measured using NMR or, alternatively, electron paramagnetic resonance (EPR). A schematic for this type of target is shown in fig. 6.

3) Potentially the purest polarized target, with no background material at all, can be made if atomic hydrogen (or deuterium) is polarized and concentrated at high enough density for useful luminosity. The densities in question are very low (of order 10^{13} nucleons/cm^3) compared to solid or gaseous targets (because otherwise the atoms would recombine to H_2 or D_2 molecules and lose their polarization). Therefore, these targets are only practical for the immense beam currents (10–100 mA) present in lepton storage rings. This in turn requires the targets to be windowless. The solution is to use a very long, thin tube along the beam that is constantly fed with a beam of atomic, polarized hydrogen. Through a differential pumping system, the atoms "leaking out" at the ends can be removed. The incoming stream of atoms is provided by a atomic beam source (where hydrogen gas is dissociated

through RF power) followed by sextupole magnets to select electron spin states and RF transition units that induce hyperfine transitions to transfer the electron spin to the nuclear one. This scheme has been successfully used by the HERMES collaboration at the HERA lepton ring.

2·3. *Detector elements.* – Again, in this section we can only give a very superficial survey of some common detector elements used in high-energy physics. Readers that are working as experimentalists in this field will need much more in-depth information on the physical principles only touched upon here, and a much more detailed understanding of the *specific* detector elements used in "their" experiment. A good starting point is the book by Leo [12], which lays out both the Physics principles and some of the analysis methods used in Nuclear and High-Energy Physics experiments. Beyond this, hopefully there will be NIM articles, manuals, web pages and other sources of information (experts!) to consult.

2·3.1. Magnets. Most spectrometers contain magnetic fields that have two functions: Deflecting or "screening out" unwanted background (in particular low-energy electrons from Möller scattering and photons as well as their conversion products) and bending particle tracks to allow a measurement of their momenta. One can roughly distinguish two different spectrometer types:

1) High-resolution, high-luminosity spectrometers employ a series of quadrupoles (for focussing and thereby increasing the accepted phase space) and dipoles which bend the scattered particles (according to their momenta) by a substantial amount into a well-shielded "detector hut", where tracks can be measured precisely and extended backwards to the interaction vertex. These types of spectrometer typically can reach momentum resolution of 10^{-4} and, with well-defined (and modest) apertures, are well suited for absolute cross-section measurements. For coincidence experiments (like SIDIS and DVCS), these spectrometers must be augmented by additional detectors for secondary particles.

2) Large acceptance spectrometers are built to simultaneously collect scattered beam particles over a wide kinematic range, as well as other particles produced in the interaction. They are characterized by wide open geometry combined with large particle detectors. While there are some special cases of large acceptance detectors without magnetic fields (employing some other method of shielding and particle identification), most spectrometers of this type use large, open magnets. If the reaction products are distributed over a large angular range (*e.g.*, in the case of colliding beams), large solenoidal magnets (usually with iron return yokes) are employed. If scattered and produced particles are typically produced in the forward direction (fixed target experiments), large forward dipoles (*e.g.*, HERMES) can be used, perhaps augmented by large-angle recoil detectors. A third configuration (used by CLAS in Jefferson Lab's Hall B) employs a set of large "pancake" coils to create a toroidal field circling the beam, which itself is in a field-free region.

Such a toroid can produce large transverse fields in the forward direction (where high-momentum scattered particles tend to go) while extending to larger angles for lower-energy particles. The new CLAS12 detector for the energy upgraded beam in Hall B will combine both a toroidal field (in the forward direction) and a solenoidal field in the region of large angles.

2˙3.2. Wire chambers. There are several methods to measure the trajectories of charged particles (bent by a magnetic field) which are based on the principle of the wire chamber. The basic ingredients of this detector type include a gaseous volume in which the traversing particles create electron-ion pairs through collisions with gas atoms. An electric field is set up between an anode plane (at negative high voltage), which can be either a foil or a grid of wires, and a cathode wire. The latter is typically thin, yielding a very strong electric field (proportional to $1/r$ where r is the distance from the wire). The electrons drift to the cathode wire in this field and accelerate in its vicinity to high enough energy to knock out additional electrons, yielding an avalanche which amplifies the original signal by several orders of magnitude. In the simplest version of this device, the electronic readout of a given wire then signals the approximate location of the particle track.

This scheme can be augmented by measuring the arrival time of the electron avalanche at the cathode wire, provided a reliable "start time" can be calculated for the moment when the particle track ionizes the gas (see below). If the relationship between drift time and distance from the wire is known, the track can be localized to much better precision than the distance between wires. These drift chambers are usually made of several layers of "sense" (cathode) wires interspersed with foils or three-dimensional grids of anode wires. By combining the information from several layers and groups of layers (at various angles relative to each other) a full three-dimensional reconstruction of the track can be achieved. However, a very large number of wires and corresponding readout electronics may be needed for a large acceptance device. This can be circumvented by using instead a *time projection chamber* (TPC), where the anode plane is at one end of the ionization volume, very far from the cathode plane, and a complete "ionization image" of a track is drifted towards the cathode plane where a set of crossed wires or other devices can reconstruct the track in three dimensions (using drift time for the distance from the plane).

Recently, alternative methods have been developed for the amplification step in these ionization drift detectors, *e.g.*, thin foils with small holes punched into them and with a large voltage across the thickness of the foil (gaseous electron multipliers, GEMs) or fine wire meshes suspended a few mm above a readout plane (micro-mega's). Other related detector types include straw tubes (where each wire is surrounded by its own separate gas volume).

2˙3.3. Vertex trackers. In addition to gaseous ionization detectors, other detector types are used to reconstruct particle tracks. In particular for applications that require very high spatial resolution (*e.g.*, to differentiate between particles originating from the original interaction point along the beam line and secondary particles from decays of relatively long-lived reaction products, like strange mesons and baryons) silicon vertex trackers play a big role. Their operating principle is somewhat similar to that of a wire chamber, but instead of knocking electrons out of gas molecules, the initial "ionization" is provided by the creation of electron-hole pairs in a pn junction in a semiconductor, which is depleted from charge carriers by an applied high voltage. The advantage is that because of the much higher material density and the lower energy required (a few eV), a much higher number of charge carriers per track length can be generated. The signal can be read out directly by drifting the electrons and holes in the applied HV field to a grid of strip electrodes, yielding a 2-dimensional location for the track. Adding several layers (again with varying orientation) allows a 3-dimensional reconstruction. With a "pitch" on the order of $100\,\mu$m between strips, very high resolution in space can be achieved. In addition, the magnitude of the signal reflects the energy loss (and therefore the velocity) of the particles traversing the detector.

2˙3.4. Scintillators. Detectors that convert the collisional energy loss of traversing charged particles into scintillation light are the ideal complements to tracking devices like wire chambers. While their spatial resolution is modest, they often have excellent timing characteristics (allowing the determination of "arrival time" to within 100 ps uncertainty or less) and the ability to measure particle energy loss. Two basic categories of scintillating materials in use are doped organic (plastic) materials and crystals. Examples for the latter are NaI (sodium iodide), BaF_2, germanium oxides, etc. (the boundaries to electromagnetic calorimeters are not well defined in this case).

In organic scintillators, charged particles passing through transfer energy through collisions with atomic electrons that are then excited into a higher energy level. These electrons return to the ground state by emitting light. A small admixture of "foreign" atoms (dopants) is used to shift the frequency of this light to a lower value for which the scintillator is transparent. The light is transported through total internal reflection towards a photon detector (see below). This type of scintillator exists in both liquid and solid (plastic) form and can achieve extremely short response and relaxation times, making them ideal for demanding timing applications. For this reason, plastic scintillators are often used to measure the time of flight (ToF) for a particle over a known distance (using either two scintillators spaced some distance apart or some independent determination of the "start time" at the vertex). Such ToF measurements yield the velocity of the particle which, in conjunction with its momentum (measured with magnetic fields and tracking devices) reveals its mass and therefore its identity. They also supply the "start time" information to extract track position from drift time measurements in drift chambers. At the same time, the amount of light output is roughly proportional to the energy loss of the detected particle, which allows a second, direct measurement of its velocity v through the Bethe-Bloch formula for collisional energy loss (see, *e.g.*, the book by Leo [12]). In particular, one can distinguish between particles that move non-relativistically and lose energy at a rate approximately proportional to $1/v^2$ and moderately relativistic particles ($\gamma\beta \approx 1$) which have the smallest linear energy loss of approximately 2 MeV per material density of $1\,\text{g/cm}^2$ traversed ("minimum ionizing"). At even more relativistic energies, the energy loss rises again, but only slowly (logarithmically with $\gamma\beta$).

Crystalline detectors are typically used to completely convert the energy of incoming particles (in particular photons and electrons) into light output, by a combination of Compton scattering, pair production and photo-excitation of atoms. For this reason, high-Z and high density materials like NaI salt are preferred, as long as they are transparent to the produced scintillation light.

For both types of scintillating materials, photon detectors are needed to convert the light into an electric signal. This is most often accomplished by phototubes (PMT = photon multiplier tube), which can detect even single photons (with some efficiency). Incoming photons knock out electrons from an alkali electrode (*e.g.*, Cs). A sequence of HV acceleration gaps with secondary electrodes ("dynodes") multiply the number of electrons with each step, leading to an amplified signal for further electronic signal processing. Alternative readout schemes include avalanche photo diodes, Silicon Photomultipliers and several others.

2˙3.5. Cherenkov counters and transition radiation detectors. For particles moving very close to the speed of light, ToF measurements are no longer able to discriminate between different velocities (and therefore particle masses), and alternative methods to measure their velocity are needed. This is the domain of Cherenkov counters which are particularly well suited for speeds in this range. The basic principle of a Cherenkov counter is similar to the sound signal generated when an object exceeds the local speed of sound within a medium ("sonic boom"). Electromagnetic waves created from atoms disturbed by a passing charged particle add up coherently in a cone of opening angle α around the flight path, where $\cos\alpha = (c/n)/v_p$, with n being the index of refraction of the medium that the particle with velocity v_p is passing through. Implicit in this relationship is the fact that particles with $v_p < c/n$ do not emit any such Cherenkov light.

Accordingly, Cherenkov detectors can be operated in two different modes: As *threshold* Cherenkov counters or by measuring the angle α in some fashion. The former type is more simple to build and operate—all that is required is a vessel containing a medium (usually a gas) with index of refraction n chosen such that only one of two particle types that one wants to distinguish from each other will exceed the threshold velocity c/n. As an example, electrons with momentum $10\,\text{MeV}/c$ have a velocity already within 0.1% of c, yielding a signal in a gas with $n > 1.001$. On the other hand, a negatively charged pion (which otherwise may be hard to distinguish from such an electron) will have to have a momentum of $2.8\,\text{GeV}/c$ before reaching the same threshold, making such a threshold Cherenkov counter a very good discriminator between electrons and pions in medium-energy applications. The Cherenkov light produced by fast particles must be collected (using optical mirrors) and guided unto a photon detector, such as a phototube. Of course, one has to be careful choosing the proper gas, to avoid background from scintillation. Another background comes from material in the way of the outgoing particles (*e.g.*, previous detectors or the entrance windows to the gas volume itself), where passing charged particles (even if they are too slow to trigger the Cherenkov response) may knock out atomic electrons with enough speed to "masquerade" as a primary electron.

Detectors that can determine the cone angle α (within some precision) are much more versatile. While threshold Cherenkov counters have no discriminating power against particles once they reach the velocity threshold, such angle-sensitive detectors can distinguish several different particle types over a range of momenta and do not have to be fine-tuned to a specific "one-trick" job. The main method of measuring α in use today involves a complete "imaging" of the ring of photons produced along the cone—this detector type is called "Ring Imaging Cherenkov" (RICH). It typically involves a somewhat denser medium (in particular artificially produced materials like aerogel with indices of refraction n that can be tuned within a few % of 1) to guarantee a sufficient number of photons and a larger opening angle. The whole cone is than imaged onto an array of (possibly position sensitive) phototubes and the radius of the ring of photon signals determines α and therefore v_p. A somewhat simpler incarnation (called "DIRC") uses denser medium (large α) together with total internal reflection to bring the direction signal out of a tight detector package into an "expansion volume" where the angle can be measured, again by photodetectors.

Further approaches towards measuring very high velocities use the (modest) dependence of collisional energy loss on velocity of highly relativistic particles (Bethe-Bloch equation, see above) or the electromagnetic field produced when high-speed particles go from one medium into another one with different n (Transition Radiation Detector—TRD). This radiation stems from the requirement of matching the electromagnetic field on both sides of the boundary according to Maxwell's equations.

2˙3.6. Electromagnetic calorimeters. Another detector type that is particularly sensitive to light-mass particles as well as electromagnetic radiation (photons) is the electromagnetic shower calorimeter. This detector is also used to reconstruct neutral pions from their two decay photons and thus play an important role even for hadron identification.

An electromagnetic calorimeter makes use of the fact that fast, light particles being slowed down in the field of high-Z nuclei tend to give off bremsstrahlung photons (due to their high deceleration) while photons can pair-produce light particle-antiparticle pairs (in particular electron-positron). This leads to a chain or cascade of energy being transferred to an ever increasing number of photons, electrons and positrons (an electromagnetic shower), whose total energy can ultimately be measured by scintillation light generated through atomic collisions. (Additional mechanisms for this electromagnetic shower development include photoeffect and Compton scattering as well as positron annihilation.) By either collecting all of this collisional energy loss in form of photons (using high-Z transparent materials like CsI salt or lead glass) or by sampling the energy loss with scintillators interspersed with lead sheets, the total energy carried by the incoming primary particle (lepton or photon) can be reconstructed with some resolution (typically $\Delta E/E \propto \sqrt{1/E}$). On the other hand, (semi-)relativistic but heavier particles (like pions, muons, etc.) will lose only a fraction of their energy, primarily through collisional losses (which are smallest for minimum ionizing particles) and can therefore be discriminated from electrons and photons by their much smaller signals in the calorimeter (relative to their momenta). Some background may come from negative pions being absorbed by protons within atomic nuclei, leading to electromagnetic energy (*e.g.*, from π^0 decay), Further discrimination power can be achieved by looking both at the longitudinal and vertical profile of the electromagnetic shower. Photons and electrons will tend to loose most of their energies (and produce the largest signals) early on (within the first layers of the calorimeter), while particles losing energy primarily through collisions will deposit energy throughout the length of their path. Similarly, the electromagnetic shower will broaden with distance traveled, leading to a wider transverse profile than hadron-induced showers.

2˙3.7. Hadronic calorimeters and other detector types. While electromagnetic calorimeters maximize the number of *radiation lengths* of their active material (using high-Z elements), hadronic calorimeters instead rely on overall material (measured in terms of interaction lengths) in the path of outgoing particles to generate hadronic "showers". These showers consist of cascades of strongly interacting particles (pions, kaons and others) that are produced or knocked out when a high-energy hadron interacts with the detector material. By sampling the energy deposited by all these particles (through scintillators), the total energy of the hadron (or a jet of hadrons) can be inferred. This is also the preferred method to detect and identify neutrons, which do not interact with most of the detector types discussed so far. Electromagnetic calorimeters as well as simple scintillator detector usually have *some* efficiency for the detection of neutrons through the protons they can knock out of the detector material.

This cursory overview could not include all types of detectors presently in use or considered for experiments in high energy physics; there are many other, specialized types like muon counters, pad counters, and numerous others.

2˙4. *Experimental facilities.* – The history of measurements of the parton structure of the nucleon began with SLAC, which measured deep inelastic structure functions for unpolarized beam and target for the first time in the 60's of last century [13], and polarized structure functions beginning in the late 70's [14]. These pioneering efforts were later followed by a string of inclusive spin structure function experiments (E142-E155) during the 1990's. This program used high energy (10–50 GeV) polarized electrons scattering off polarized nucleon targets (^{3}He gas, solid ammonia and LiD) and has been completed for a while. The spectrometers used had relatively small acceptance, and the low duty factor (of order 10^{-4}) of the beam did not allow any coincidence measurements of SIDIS. However, the high luminosity available provided data with very good statistical precision.

A second set of measurements began in the 1980's at CERN and evolved over a sequence of experiments (EMC, NMC, SMC) to the COMPASS experiment, which is still actively taking data and has a promising future as COMPASS II. COMPASS uses "naturally polarized" decay muons from pions produced with the CERN high-energy proton beam and very large solid polarized targets to study inclusive and semi-inclusive DIS, including tagged structure functions and TMDs. In the future, DVCS and Drell-Yan measurements are also planned. Reaction products are detected with the 60 m long forward COMPASS spectrometer, which will be augmented for COMPASS II. A detailed description of the COMPASS program is given elsewhere in these proceedings.

The HERMES experiment at DESY used the 27 GeV internal circulating electron or positron beam in the HERA electron-proton collider (polarized through the Sokolov-Ternov effect and a combination of spin rotators) and a very thin internal target of atomic (polarized) hydrogen, deuterium and ^{3}He to measure DIS, SIDIS and DVCS under a large variety of target and beam configurations. A large acceptance spectrometer in the forward direction (augmented by a recoil detector) was used to detect and identify scattered leptons and produced hadrons like pions and kaons. HERMES is no longer taking data, but some results are still under analysis. Its program is again extensively discussed in these proceedings.

A very different approach to access partons in nucleons is employed by the PHENIX and STAR Collaborations, which use colliding polarized proton beams at the RHIC accelerator complex. Large acceptance detectors measure single hadrons (pions, etas, kaons), jets, and photons to gain information on the underlying hard interaction in the collision. The RHIC experiments have unique access to the polarized (integrated) gluon distribution, and, through W production, have also begun to probe the polarization of the quark sea, separated by flavor. Using transversely polarized protons, TMDs can by studied, as well, and in the future, Drell-Yan experiments are planned also (including a new experiment, AnDY, at RHIC). See elsewhere in these proceedings for a more comprehensive overview of the RHIC program.

At Jefferson Lab, first measurements of both DIS and SIDIS reactions have been completed using the existing 6 GeV highly polarized electron beam and fixed proton, deuteron and ^{3}He targets. In Hall B, scattered electrons and produced secondary particles are detected in the CEBAF Large Acceptance Spectrometer (CLAS) which surrounds the target with a nearly 4π acceptance. Experiments on both proton (NH_3) and deuteron (ND_3) targets have mapped out inclusive structure functions over a wide kinematic range, from very low to moderate momentum transfer ($0.01 \le Q^2 \le 5\,\mathrm{GeV}^2$) and from the nucleon resonance region into the DIS region. First results on SIDIS measurements have been published, and additional ones are under analysis. More data have been taken on NH_3 and ND_3 targets in Hall C, where both existing small-acceptance spectrometers (HMS, SOS) and dedicated devices (BETA) with larger acceptance have been used. The unique advantage of these experiments was the use of a transversely polarized hydrogen target (not yet available in Hall B). SIDIS results exist mostly for unpolarized targets. Experiments in Hall A concentrated on polarized ^{3}He targets, which are a good approximation to free polarized neutrons. Again, both the standard high-resolution spectrometers in that Hall and more dedicated, larger acceptance devices (Big Bite) were used. In addition to a wide range of polarized inclusive structure functions, Hall A has recently published the first direct measurement of Collins and Sivers asymmetries on the neutron. Hall A also has the world record for the highest luminosity polarized target. Both Halls A and B have also collected high precision data on DVCS.

The experimental program at Jefferson Lab will undergo a brief hiatus starting next year, when the facility and all three halls are upgraded for the future 11–12 GeV beam operation. The availability of nearly double the beam energy in all three halls will significantly expand the kinematic range accessible within DIS kinematics. All three halls will receive substantial upgrades: Hall C with a new Super-High Momentum Spectrometer (SHMS), Hall B with the largely new CLAS12 spectrometer (discussed elsewhere in these proceedings) and Hall A with Super Big Bite and SoLID (assuming funding will be made available). Correspondingly, a complete program of measurements in DIS, SIDIS and DVCS has been proposed and approved that will map all TMDs and GPDs over the kinematic region $0.1 < x < 0.8$ with unprecedented precision.

Looking further into the future, hadron facilities already online (JPARC, FNAL) and under construction (FAIR) will make important contributions, in particular by studying Drell-Yan processes. For a complete picture of the nucleon parton structure, down to very low x where gluons and sea quarks dominate, a polarized electron-ion collider is indispensable. Such a collider can reach much higher center-of-mass energies than existing fixed-target experiments. Plans for such a collider (EIC) are underway both at RHIC and at Jefferson Lab, as well as in other countries. The technical challenges of achieving high luminosity (combined with full-acceptance detector systems) are formidable, but possible solutions have been demonstrated. It is hoped that a decision for such an EIC will be made soon, which could allow the start of experiments in the mid 2020's.

3. – Methods and challenges in the analysis of DIS and SIDIS experiments

3˙1. *Calibration.* – All detector elements discussed in subsect. **2˙3** and making up a particular experimental apparatus have a few features in common: They convert a signal amplitude (*e.g.*, number of photo-electrons) or timing information into an electric signal and ultimately, via electronic devices like ADCs and TDCs, into numerical information. Part of the challenge in analyzing experimental data is to properly correlate these numbers to physical properties (like charge, energy, momentum, and velocity) of observed particles. This requires proper calibration of all detector elements (how does a given energy deposit in a scintillator or the distance of a particle track from the wire of a drift chamber translate into ADC and TDC values), as well as proper matching of tracks (which signals belong to each unique particle detected in the event, and what can we infer about that particle's properties) and event reconstruction (which particles belong to the same event, and what is the overall event structure).

These tasks often require a substantial commitment of time and expertise, and are handled somewhat differently by different experimental collaborations. Often, a full-blown simulation (using event generators like Pythia, Lepto, …and general-purpose simulation codes like GEANT4) is the first step to understanding the detector response to specific particle properties. Equally important are corrections of measured quantities for known effects (energy loss, radiation) and detector-specific properties (inefficiencies, acceptance limits). All of these tasks make up a major part of an experimental analysis, but there is little value in attempting a generic description at this place.

Instead, in the following we assume that both detector calibration and the first level of data reconstruction (conversion from "raw" numerical data to collections of events with identified particle tracks) has already been accomplished, and look at a few of the remaining steps one has to follow to extract meaningful physics results.

3·2. *Observables.* – Once we define what we call the "target" (either a solid piece of material, or a defined volume of liquid or gas, or, in the case of colliding beams, a bunch of particles in one of the counterrotating beams), we can talk about the probability $P(\Delta k_i)$ for a single beam particle traversing the target to initiate an "event" with a number of particles ending up in specified kinematic bins (designated by Δk_i). This number will in general depend on the conditions we require for counting an event within a specific signature (for example, "one scattered beam particle within limits $\Delta k_1 = E'_1 \ldots E'_2$ in final energy and angular range $\Delta k_2 = \theta'_1 \ldots \theta'_2$, $\Delta k_3 = \phi'_1 \ldots \phi'_2$"—inclusive scattering; or "3 final state particles together carrying the full initial-state four-momentum and within certain kinematic bins Δk_i each"—fully exclusive events). In any case, this probability will be directly proportional to the density n_T of the target (in number of target nucleons per unit volume) and to the target length L. Since the product $n_T L$ has dimension 1/area, it follows that the proportionality constant must have dimension area:

$$P(\Delta k_i) = n_T L \cdot \Delta\sigma(\Delta k_i). \tag{11}$$

(Note that $n_T = \rho(\mathrm{g/cm}^3) \cdot N_A(\mathrm{atoms/mol})/A(\mathrm{amu})$ for fixed targets of known mass density ρ.) An alternative (and maybe more familiar) way to define the cross-section $\Delta\sigma$ (implicitly) follows if you multiply eq. (11) with the rate of incoming beam particles $\dot{n}_{\mathrm{in}} = I_{\mathrm{beam}}/e$ (where e is the charge of each beam particle and I is the charge current). This yields the total event rate on the l.h.s., and the right-hand side becomes $\mathcal{L} \cdot \Delta\sigma$ with the luminosity $\mathcal{L} = n_T L \dot{n}_{\mathrm{in}}$. In the limit where the size of each kinematic bin Δk_i becomes infinitely small, we can define the differential cross-section as the asymptotic limit

$$\frac{\mathrm{d}\sigma}{\mathrm{d}k_1 \mathrm{d}k_2 \ldots \mathrm{d}k_n} = \lim \frac{\Delta\sigma(\Delta k_i)}{\Pi \Delta k_i}. \tag{12}$$

In practical experiments with relatively large acceptance and finite kinematic bins, one can only extract the mean cross-section averaged over a kinematic bin, or, if one assumes a certain kinematic dependence, an overall scale if one includes a parametrization of the acceptance of the detector:

$$N_{\mathrm{counts}} = \sigma_0 \int \mathcal{L}\mathrm{d}t \int \mathrm{d}k_1 \int \mathrm{d}k_2 \ldots \int \mathrm{d}k_n \frac{\mathrm{d}\sigma/\sigma_0}{\mathrm{d}k_1 \mathrm{d}k_2 \ldots \mathrm{d}k_n} \mathrm{Acc}(k_1, k_2, \ldots, k_n), \tag{13}$$

where σ_0 is the overall scale to be extracted from the data. Alternatively, if it is known that the cross-section is proportional to $\cos(\phi)$ or, more generally, the first few terms in a Fourier series, one can form moments with sine's and cosine's to extract the corresponding Fourier components.

In a typical inclusive DIS experiment, the kinematic variables used to describe the scattering of a lepton with incoming beam energy E off a target nucleon of mass M can be the final energy E' and direction θ_e, ϕ_e of the lepton in the lab, or, more useful for physics analysis, the four-vector momenta k^μ, k'^μ and P^μ of the incoming and scattered lepton

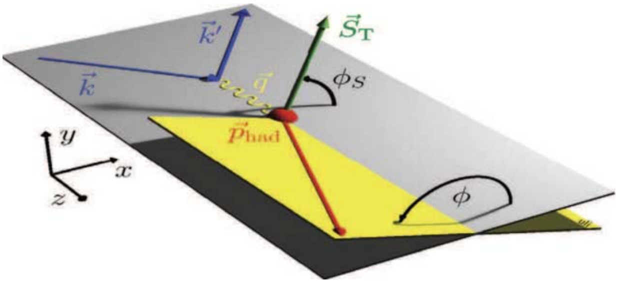

Fig. 7. – Definition of typical kinematical variables for SIDIS.

as well as the target nucleon before the scattering (with $P^\mu P_\mu = M^2$ and 4-momentum transfer $q^\mu = k^\mu - k'^\mu$). From these, the following relativistic invariants can be formed:

$$\begin{aligned}
\nu &= q^\mu P_\mu / M = E - E', \\
Q^2 &= q^\mu q_\mu \approx 4EE' \sin^2(\theta_e/2), \\
x &= \frac{Q^2}{2q^\mu P_\mu} = \frac{Q^2}{2M\nu}, \\
y &= \frac{q^\mu P_\mu}{k^\mu P_\mu} = \frac{\nu}{E}, \\
W &= \sqrt{(P^\mu + q^\mu)^2} = \sqrt{M^2 + 2M\nu - Q^2},
\end{aligned}$$

where the last expressions in the definitions of ν, Q^2 and y are the (approximate) formulae in the target rest frame. Converting the differential cross-section from one set of variables to another requires proper evaluation of the Jacobian describing the new variables in terms of the old ones.

Adding a final-state hadron with 4-momentum P_h^μ in the case of SIDIS, some typical variables used are the energy fraction $z = P_h^0/\nu$ (in the target rest frame), the transverse momentum $\vec{P}_{hT}$ or, equivalently, the Feynman variable $x_F = \hat{q} \cdot \vec{P}_h^{\rm cm}/P_h(\rm max)$ and the rapidity (often approximated with the pseudo-rapidity $\eta = -\log[\tan\theta_h/2]$). in either case, one also needs the angle Φ between the hadronic and leptonic plane, see fig. 7. Finally, in the case of a polarized target, one describes the quantization axis of the polarization by its direction angles θ_S, ϕ_S relative to the leptonic plane. In principle, the cross-section can be expressed as a function of any suitable combination of these variables.

Speaking about polarized targets (and beams), it is important to realize that the polarization $\vec{P}$ (for a spin-1/2 target) or the beam helicity h are statistical quantities describing a whole ensemble of particles, and are closely related to the concept of the density matrix in quantum mechanics. While the interpretation of $\vec{P}$ appears rather intuitive, one should keep the following in mind:

- A single spin-1/2 particle is "always 100% polarized" along *some* direction, but it makes little sense to talk about its polarization (since it is usually unmeasurable due to the uncertainty relation); on the other hand, it also makes no sense to say that the polarization is the "fraction of polarized target nucleons" or that accounting for the polarization is the same thing as "subtracting the unpolarized contribution".

- *Any* measurement on an ensemble of polarized spin-1/2 particles can be expressed in terms of the polarization vector $\vec{P}$ (with length $0 \leq |\vec{P}| \leq 1$)—there is no further information available. For instance, an ensemble of nucleons with totally random orientation of their spins in all possible directions has the same $\vec{P}$ as an ensemble where exactly 1/2 of all spins point in $+z$ direction and the other 1/2 in $-z$ direction (namely, zero)—and no conceivable measurement can distinguish these two cases. It is only for our convenience that we often describe the polarization along a preferred quantization axis (*e.g.*, the magnetic holding field of a polarized target) by the equation $P_z = (N^+ - N^-)/(N^+ + N^-)$, where N^+, N^- are the number of nucleons with spin "up" *vs.* "down".

- Any observable that depends on the target spin has to be proportional to $\vec{P}$; *e.g.*, the cross-section difference between two different target spin orientations can always be written as $\Delta\sigma_1 - \Delta\sigma_2 = \sigma_0 \vec{A} \cdot (\vec{P}_1 - \vec{P}_2)$. Here, σ_0 is an overall scale, and the *analyzing power* $\vec{A}$ contains the information on the spin dependence of the reaction. By using rotational invariance, once can also relate the analyzing power to azimuthal angles, yielding the familiar $\sin\phi$ dependence of most single-spin asymmetries.

- These properties of polarization and analyzing power can be generalized to both the case of higher spin (*e.g.*, the spin-1 deuteron nucleus can be described by a set of 5 more—tensor—polarization components) and to reactions involving more than one spin (*e.g.*, double-spin asymmetries). Interested readers are referred to the Madison convention [15] for additional details(2).

As an example, consider the double-spin asymmetry $A_{\|}$ typically measured in DIS polarized scattering. The cross-section in this case depends on both the helicity of the lepton beam and the target nucleon polarization. Since the helicity is a pseudo-scalar, only the component of the target polarization P_z along the z-direction and the sideways component P_x in the lepton scattering plane can combine with it to form a measurable scalar. The measured cross-section then becomes

---

(2) One should emphasize that the Madison convention needs to be modified somewhat to account for relativity; *e.g.*, the simple three-vector behavior of $\vec{A}$ and $\vec{P}$ has to be replaced by a separate treatment of longitudinal (high momentum) degrees of freedom (helicities h, H) and transverse ones (where the non-relativistic approximation works fine); see the Introduction. However, keeping the vector character of $\vec{A}$ and $\vec{P}$ in mind can be a great heuristic tool to derive the possible angle-dependence of single- and double-spin asymmetries, for example.

$$\mathrm{d}\sigma = \sigma_0 \left(1 + h \cdot \left[A_{\|} P_z + A_{\perp} P_x\right]\right). \tag{14}$$

The connection between the "analyzing powers" $A_{\|}, A_{\perp}$ and the physics quantities A_1, A_2 as well as the spin structure functions g_1, g_2 for DIS can be found in a recent comprehensive review of the longitudinal spin structure of the nucleon [16].

3˙3. *Raw asymmetries.* – The first step in any analysis of spin-dependent DIS or SIDIS is typically to form the raw asymmetry

$$A_{\mathrm{raw}} = \frac{n^+ - n^-}{n^+ + n^-}, \tag{15}$$

where n^+, n^- are the total number of counts for two different spin states, properly normalized to the time-integrated luminosity for each spin state. Typically, care must be taken to also take the data acquisition—DAQ—"life time" into account, *e.g.*, by integrating the luminosity $\mathcal{L}$ only over those time intervals where the DAQ is not "busy" after an event trigger, etc. At very high event rates, it is also important to properly treat nonlinearities due to event truncation, pile-up, etc. There are, of course, other avenues towards extracting physics results from spin-dependent measurements, *e.g.*, by directly extracting cross-section differences as in eq. (14), or properly weighted moments of such cross-section differences. The details depend a lot on the experimental details which may make one method more advantageous than another.

In the inclusive case, it is usually sufficient to reverse only one of the two spin degrees of freedom, either the beam helicity h or the target polarization (P_x, P_z)(3). The former is preferred for electron DIS experiments since the beam helicity can be "flipped" rapidly, yielding a strong suppression of any systematic changes of the target density or detector acceptance times efficiency. This is important to minimize false asymmetries due to such possible effects. For further reduction and to study such systematic errors, one can combine measurements with opposite target polarization (yielding opposite signs of the helicity asymmetry). In the case of the CEBAF electron beam, one can also insert the half-wave plate to reverse the correlation between true beam helicity and all possible beam fluctuations correlated with the laser polarization at the injector. In the case of single-target spin asymmetries, much more care must be taken to avoid false asymmetries—see below for a full discussion.

3˙4. *Dilution.* – The dilution factor (DF) for an asymmetry measurement is the ratio of counts from the target material one wants to study (*e.g.*, protons, deuterons or ^{3}He nuclei) divided by the total number of counts. It is typically defined for the case of no polarization. The necessity to determine this factor is the major drawback of the asymmetry method described here; if one measures cross-section differences directly, one does not need to account for DF, but instead has to reach a complete understanding of the (absolute!) target density, beam intensity, detector acceptance and efficiency of all detector elements (including the trigger). Needless to say, neither colliding beam experiments nor experiments like HERMES that use an open atomic beam source target have to worry (much) about dilution.

---

(3) To be precise, in that case one does get a contribution from parity-violating asymmetries due to the interference between weak and electromagnetic interaction. However, these asymmetries are usually much smaller than the sought-after parity-allowed spin asymmetries, at least for fixed-target experiments, and are further suppressed by the steps outlined below.

To determine the dilution factor (which of course depends on all kinematic variables of interest), one needs to know the dimensions and densities of any material traversed by the beam in the vicinity of the target (unless one can remove its contribution by using a vertex cut). This includes vacuum entrance and exit windows, heat shielding foils, liquid coolant, target foils and the actual target material (*e.g.*, NH_3) in the case of a cryogenic solid target, or quench gas admixtures (N_2) and entrance and exit windows for a gaseous (^3He) target. Even HD-Ice targets contain some "foreign" material in the form of windows and embedded Al wires to remove excess heat. However, typical solid state (*e.g.*, ammonia) targets tend to have the worst (smallest) dilution factors, because the "carrier atoms" (*e.g.*, the nitrogen in the ammonia molecule) contain many more nucleons than the polarizable hydrogen or deuterium.

If all necessary information can be obtained with sufficient precision, and a reliable model describing the (radiated) cross-section from all target components exists, one can simply calculate DF directly. However, often there are quantities that are not easy to determine by direct measurements. One example is the total density and length of ammonia in the target cell for NH_3/ND_3 targets, the so-called packing fraction PF. This quantity is usually quite uncertain, both because the frozen ammonia "beads" making up the target are quite irregular in shape, size and packing, and because it is very difficult to make reliable measurements of dimensions and densities at a few Kelvin temperature. Such quantities are therefore typically extracted from auxiliary measurements, *e.g.*, by comparing the rate from the ammonia target with that from a dedicated carbon slab (in an otherwise identical environment) with well-known thickness. Again, the cross-section model (where it exists) can then be used to determine DF. For an example of dilution factors extracted with this method, see fig. 8 and ref. [17].

While the model-based approach is clearly preferred (it yields smooth DFs without being limited by statistics and systematics of auxiliary measurements), it may not always be possible to come up with a realistic enough model for the unpolarized cross-sections needed. This is in particular true at present for SIDIS, where one needs such cross-sections (including radiative effects) for a 5-dimensional grid of kinematic bins (*e.g.*, Q^2, x, z, P_{hT}, and perhaps even Φ). In the nuclear case, such cross-sections must account not only for EMC–effect-like suppression at very large and very small x, but also for attenuation and P_{hT}-broadening of all different types of hadrons that are produced inside the nucleus. While data on these effects are slowly becoming available, there are not yet reliable parametrizations for all kinematics of interest. In this (and similar) case(s), one has to instead rely on the auxiliary measurements alone, maybe together

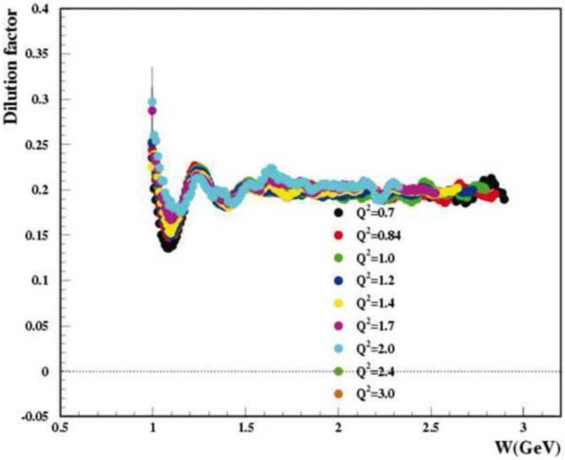

Fig. 8. – Example for the dilution factor of a typical polarized deuterium (ND_3) target.

with a parametrization of cross-section ratios as a function of the relevant variables. For example, one can use measured rates from carbon and "empty" (liquid helium only) targets to model the rates from similar nuclei like nitrogen in ammonia. It becomes then extremely important to plan for (and execute) a sufficient number of such auxiliary measurements, interspersed evenly throughout the experiment to minimize systematic drifts in detector performance.

In either case, one has to divide the measured raw asymmetry introduced in the previous section by the dilution factor for each kinematic bin to get the desired "nucleon asymmetry". This works well for double-spin asymmetries, but potentially becomes more difficult in the case of single target spin asymmetry measurements where the dilution factor may vary significantly over the time span between two opposite target polarizations.

A final complication comes form the fact that some of the unwanted target material (*e.g.*, nitrogen atoms) can themselves be slightly polarized, leading to a contribution to not only the denominator but also the numerator of the asymmetry. This can be even an intended effect, *e.g.*, in the case of cryogenic ^{6}LiD as a deuteron target, where the Li atom can be considered to be an effective polarized deuteron target with an inert ^{4}He core in some approximation. In this case, the Li polarization and its contribution to the asymmetry must be carefully evaluated; in most other cases, some relatively simple and small correction suffices (for instance, assuming "equal spin temperature" for the nuclear and nucleon spins, combined with a simple shell-model evaluation of the bound nucleon spin in terms of the nuclear one).

3˙5. *Beam and target polarization.* – Our previous discussion has clearly shown the importance of correctly measuring the polarization of both beam and target to extract spin asymmetries. With experiments collecting larger and larger amounts of data (thereby beating down the statistical error on the measured asymmetry, which goes roughly like

$1/\sqrt{N_{\text{tot}}}$), the uncertainty on the knowledge of these quantities can become an important and perhaps limiting factor on the ultimate precision achievable. We have already discussed in sect. **2** some methods used to determine beam and target polarization directly (in conjunction with the discussion of various types of polarized beams and targets). Often, these methods will suffice when pushed to the highest possible precision; on the other hand, secondary methods can lead to even smaller errors or serve as important systematic checks.

One such method frequently employed at lower-energy accelerators involves the measurement of elastic or quasi-elastic asymmetries, in particular double-spin asymmetries. These asymmetries are often very well known, since they only depend (weakly!) on the ratio G_E/G_M of elastic electromagnetic form factors of the nucleon. By detecting the scattered lepton and the recoil nucleon in coincidence, one can reduce backgrounds (dilution) to very low and manageable levels. In particular when the data can be accumulated simultaneously with the main experiment (in the case of large acceptance devices, like CLAS), systematic errors are minimized and statistical ones can become reasonably small. This leads to a superior determination of, at the least, the product $h \cdot P_{\text{Target}}$, from which even P_{Target} alone can be extracted if the beam helicity h is measured well.

Once h and P_{Target} are in hand, one again simply divides the measured double-spin asymmetry by their product in the case of DIS or DSAs in SIDIS. However, to disentangle both single- and double-spin asymmetries in SIDIS, taking possible long-term changes of $\mathcal{L}$, detector acceptance and efficiency, and DF into account, a more complicated equation needs to be employed. In the most general case, one gets (assuming rapid reversal of beam helicity) for the example of a longitudinally polarized target:

$$A_{LL} = -\frac{1}{\left|P_b^+P_t^+\right|\left|P_b^-\right| + \left|P_b^-P_t^-\right|\left|P_b^+\right|}\left(\frac{\left|P_t^-\right|}{DF^+} + \frac{\left|P_t^+\right|}{DF^-}\right)\frac{\left|P_b^-\right|\left(n^{++} - n^{-+}\right) + \frac{d^+}{d^-}\left|P_b^+\right|\left(n^{--} - n^{+-}\right)}{\left|P_t^-\right|\left(n^{++} + n^{-+}\right) + \left|P_t^+\right|\frac{d^+}{d^-}\left(n^{--} + n^{+-}\right)}$$

$$\approx -\frac{1}{\langle DF\rangle}\frac{\left|P_b^-\right|\left(n^{++} - n^{-+}\right) + \frac{d^+}{d^-}\left|P_b^+\right|\left(n^{--} - n^{+-}\right)}{\left|P_b^+\right|\left|P_b^-P_t^-\right|\left(n^{++} + n^{-+}\right) + \left|P_b^-\right|\left|P_b^+P_t^+\right|\frac{d^+}{d^-}\left(n^{--} + n^{+-}\right)}$$

$$A_{UL} = \frac{\left(\frac{\left|P_t^-\right|}{DF^+} + \frac{\left|P_t^+\right|}{DF^-}\right)}{\left(\left|P_t^+\right| + \left|P_t^-\right|\right)}\frac{n^{++} + n^{-+} - \frac{d^+}{d^-}\left(n^{--} - n^{+-}\right)}{\left|P_t^-\right|\left(n^{++} + n^{-+}\right) + \left|P_t^+\right|\frac{d^+}{d^-}\left(n^{--} + n^{+-}\right)} \approx \frac{1}{\langle DF\rangle}\frac{n^{++} + n^{-+} - \frac{d^+}{d^-}\left(n^{--} - n^{+-}\right)}{\left|P_t^-\right|\left(n^{++} + n^{-+}\right) + \left|P_t^+\right|\frac{d^+}{d^-}\left(n^{--} + n^{+-}\right)}$$

where P_b is the beam polarization (helicity), P_t the target polarization in z-direction, and d refers to common factors entering the luminosity, *i.e.* total target density times length, detector acceptance and efficiency, etc.; single indices $+, -$ refer to the two possible orientations (signs) of the target polarization, while double indices refer to the beam helicity sign first and the target polarization sign second. The second expression for each asymmetry assumes that the dilution factor does not vary for the two different target polarizations. For experiments where the target polarization can be flipped more quickly (ABS and gaseous targets) or where two or more different targets with opposite polarization compensate for the slow reversal rate of both polarizations (SMC/COMPASS), modified but similar equations can be developed to minimize any false asymmetries from long-term changes.

3˙6. *Backgrounds.* – So far, we have assumed that all registered counts for either polarization (combination) come only from the particles and event types we are interested in, namely scattered leptons and coincident hadrons of a given type (π, K, etc.). In practice, there are several sources of contamination that one has to correct for. The potential for falsely identified particles and for unwanted events contributing to the measured counts depends strongly on the quantity measured and the experimental facility/set up, and requires in-depth investigation for each experiment. Here, I only give a few examples for typical backgrounds for DIS and SIDIS with electron (positron) beams. Note that I do not treat background from unpolarized target material here, since this has been dealt with in the section on dilution factor. We also mentioned already the background asymmetry coming from slightly polarized target nuclei.

The first type of background comes from particles (typically hadrons) that are misidentified as electrons. This background is most severe for inclusive measurements, where no cross checks on event type can be applied. In our discussion of Cherenkov counters and electromagnetic (shower) calorimeters (sect. **2**) we already pointed out a few possible sources of such misidentifications. Typically, Cherenkov detectors (especially of the threshold type) become less and less efficient suppressing light hadron signals (*e.g.*, from π^-) as momentum increases (and totally inefficient above their threshold). In addition, single-photon noise in the phototubes, knock-on electrons, direct hits on optical elements and the like can create false positives (electron ID when no electron was present). Conversely, shower counters become more efficient at higher energies (where their relative energy resolution gets better and the total energy deposited by an electromagnetic shower is much larger than that of a minimum ionizing particle). Still, there is some finite probability for an incoming hadron generating a hadronic or even electromagnetic shower that can lead to false positives. Therefore, one usually needs to combine both particle detector types (plus additional ones, like time-of-flight, transition radiation or even several Cherenkov layers) and study the efficiency as well as background suppression of each one in detail, to arrive at an overall electron ID efficiency. For instance, one can require a very high energy deposit in a shower counter (which would usually lead to lower electron efficiency) to select a more pure electron sample, for which the reaction of the corresponding Cherenkov counter can be studied as a function of kinematic variables.

In the case of SIDS, of course one also has to worry about misidentifying one hadron type for another one (*e.g.*, pions or protons for kaons). Similar considerations as for electrons apply—one has to study all aspects of particle ID very carefully to minimize and properly characterize such backgrounds.

Another challenge is to account for event topologies that result in the same final states but are not of the desired type. For instance, properly identified electrons can nevertheless be from a source other than scattering of beam particles. The most important source of this background is the conversion of photons into e^+e^- pairs in material making up the target or detector, where the photons are either from hadron decay or produced as part of the electromagnetic background. Another source is the Dalitz decay $\pi^0 \to \gamma e^+ e^-$ of neutral pions (and other hadrons). Fortunately, all of these sources yield positrons as well as electrons in equal numbers and kinematic distribution ("charge-symmetric background"), which allows subtraction from the electron sample by carefully measuring or parametrizing the rates and asymmetries of the positrons.

Similarly, pions and other hadrons can come from exclusive production of vector mesons, etc. that then decay into these particles. It can be argued whether this is a true background or part of the signal, but it clearly will lead to different rates and asymmetries than purely SIDIS events. Of course, any coincident measurements (like SIDIS) also have to account for accidental coincidences where the electron and the hadron come from two different interactions occurring close in time to each other. These backgrounds can be subtracted by studying the distribution in relative timing between the two particles and using far-out-of-time events as a representative background sample.

3˙7. *Corrections and model inputs.* – Corrections that need to be applied to the data are of two different varieties: In the first case, one has to account for known and possibly unknown deviations of the detector from an ideal one, *e.g.*, by correcting measured particle momenta for physical effects like collisional energy loss and multiple scattering as well as imperfect knowledge of magnetic fields, detector geometry and response. These effects are often parametrized and the parameters determined by a fit to well-constrained reactions like elastic scattering. Under the same heading one can also subsume corrections for the finite acceptance and efficiency of the various detector elements, and the cuts and hardware (trigger) logic that have to be met for proper event identification. Usually, these corrections (and some of the others already mentioned) require a detailed simulation of the whole experimental apparatus, for instance with a general-purpose code like GEANT.

The second type of corrections are needed to convert measured quantities (asymmetries, cross section differences) into physics observables that can be directly compared to theoretical predictions and models. At a minimum, this usually requires corrections for higher-order QED processes involving diagrams beyond the simple one-photon exchange (Born) diagram. While these corrections could be properly considered the responsibility of model builders and theorists, they typically require intimate knowledge of the experimental apparatus (the materials in the beam that degrade its energy through bremsstrahlung photon emission and the detector properties like resolution that determine what final states with photon emission still contribute to the measurement). Therefore, they are typically considered part of the experimentalists job, although the rather complicated QED equations needed are often provided by or co-developed with theorists. In addition to the QED aspect, one also needs to have a model of the hadronic reaction over a much wider kinematic range than measured, since events at different kinematics but with radiated extra photons can feed into a kinematic bin of interest. In fig. 9 we show an example of a measurement of the inclusive double-spin asymmetry (open blue circles)

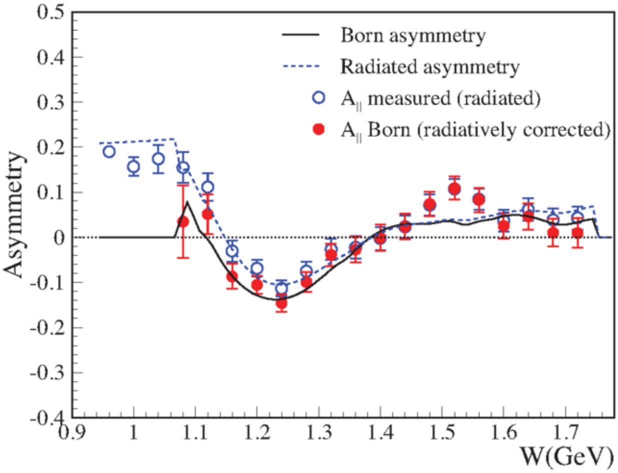

Fig. 9. – (Colour on-line) Radiative corrections for a measurement of the inclusive double-spin asymmetry $A_{\|}$. See text for explanations.

that was corrected for radiative QED effects (resulting in the full, red circles for the final data points). As one can see, a model for this asymmetry (solid line) was needed as input to these corrections, with the dashed line indicating the calculated radiated asymmetry. The corrections become large both close to the elastic peak ($W = 0.94\,\text{GeV}$) and at large W (low E') due to the dominance of emission of a single high-energy photon (suppressed only like $1/E_\gamma$) followed by elastic scattering with low energy and momentum transfer (and correspondingly large cross-section). These extreme kinematic regions are therefore usually removed (through a cut on y) from DIS analyses. Fortunately, radiative corrections for SIDIS are usually smaller since the presence of a hadron carrying some fraction of the photon energy suppresses elastic tails. On the other hand, the event topology is much more complicated, making the necessary QED calculations and radiative codes even more involved.

At the last step of analysis, one often needs to convert the measured quantity into a physics observable of interest by accounting for small, unwanted contributions (like the term $A_\perp P_x$ in eq. (14)) or by converting asymmetries into spin structure functions. This typically requires models of unmeasured quantities, like unpolarized cross-sections or structure functions (F_1 and R for DIS) and asymmetries like A_2. If one wants to evaluate moments of (spin) structure functions, one may also have to use models to account for any unmeasured kinematic range (*e.g.*, high ν or an angular range not covered by the detector). These models have to be developed and readjusted in successive iterations to yield the best description of all available data (from the present and other experiments), and the systematic uncertainty of the final results coming from model uncertainties has to be determined.

3˙8. *Conclusion.* – At the end of this long and arduous process, from building and commissioning apparatus, planning, executing and monitoring a measurement (often over several months), to calibrations, corrections and final results, fame and glory surely awaits the experimenter who has gained new or improved information on the still-mysterious inner structure of the nucleon and goes forth to publish and represent her results at conferences held at exotic and beautiful locales. . . like Varenna!

* * *

This work is supported by a research grant from the US Department of Energy. I would like to thank my collaborators at the Thomas Jefferson National Accelerator Facility for their inspiring work and for freely sharing their knowledge and wisdom.

REFERENCES

[1] Sinclair C. *et al.*, *Phys. Rev. ST Accel. Beams*, **10** (2007) 023501.
[2] Schultz D., *Proceedings of the 3rd European Particle Accelerator Conference, Berlin, Germany* (1992).
[3] Liu H., *Nucl. Instrum. Methods A*, **400** (1997) 213.
[4] Leeman C. *et al.*, *Annu. Rev. Nucl. Part. Sci.*, **51** (2001) 413.
[5] Kazimi R. *et al. Proceedings of the 9th European Particle Accelerator Conference 2004* EPAC-2004-TUPLT164, JLAB-ACO-04-251.
[6] Stutzman M. *et al.*, *Nucl. Instrum. Methods A*, **574** (2007) 213.
[7] Meyer W., *Nucl. Instrum. Methods A*, **526** (2004) 12.
[8] Crabb D. and Meyer W., *Annu. Rev. Nucl. Part. Sci.*, **47** (1997) 67.
[9] de Boer W., *CERN Journal 74-11* (1974).
[10] Borghini M., *CERN Journal 68-32* (1968).
[11] Keith C., Anghinolfi M., Battaglieri M., Bosted P. E., Branford D. *et al.*, *Nucl. Instrum. Methods A*, **501** (2003) 327.
[12] Leo W., *Techniques for Nuclear and Particle Physics Experiments* (Springer Verlag, New York) 1994.
[13] Bloom E. D. *et al.*, *Phys. Rev. Lett.*, **23** (1969) 930.
[14] Alguard M. J. *et al.*, *Phys. Rev. Lett.*, **37** (1976) 1261.
[15] Barschall H. and Haeberli W. (Editors), *Polarization Phenomena in Nuclear Reactions* (University of Wisconsin Press) 1970.
[16] Kuhn S. E., Chen J. P. and Leader E., *Prog. Part. Nucl. Phys.*, **63** (2009) 1.
[17] Fersch R. *et al.*, in preparation.

This page intentionally left blank

Proceedings of the International School of Physics "Enrico Fermi"
Course CLXXX "Three-Dimensional Partonic Structure of the Nucleon"
edited by M. Anselmino, H. Avakian, D. Hasch and P. Schweitzer
(IOS, Amsterdam; SIF, Bologna)
DOI 10.3254/978-1-61499-197-7-33

Transverse momenta of partons in high-energy scattering processes

P. J. Mulders

Nikhef and Department of Physics and Astronomy, VU University Amsterdam
De Boelelaan 1081, NL-1081 HV Amsterdam, The Netherlands

Summary. — In these lectures we study how properties of hadrons like charge densities and parton distributions can be described within the framework of quantum chromodynamics and how they appear in high-energy scattering cross-sections. For the parton distributions, we specifically look at the role of transverse momenta of partons.

1. – Introduction

The central topic of these lectures is the proton. We want to grasp its structure. On the one hand, as part of our quest to understand the heart of the matter, at least the visible matter, in our universe. On the other hand, because protons besides electrons are basic tools in experiments that probe the fundamental forces in nature. Therefore we want to use their properties, global ones like energy, momentum and spin, but also other indirect degrees of freedom. The latter is of interest in particular for the proton, which is a composite state. Although a number of global variables can be used in the characterization of the quantum state,

$$|\mathrm{proton}\rangle = |M, S; \boldsymbol{P}, M_s; \ldots\rangle,$$

© Società Italiana di Fisica

the full quantum state of a proton is much more complex than the corresponding electron state,

$$|m_e, s; \boldsymbol{p}, m_s; \dots\rangle = b_e^\dagger(\boldsymbol{p}, m_s)|0\rangle,$$

which is created from the vacuum by a creation operator, satisfying elementary (anti-commutation) relations. The only properties remaining in the $\dots$ for the electron are charges determining the coupling of the electron to electroweak gauge bosons. Creation and annihilation operators appear in the free-field expansion of the electron field. They are multiplied with plane-wave solutions including a spinor structure in Dirac space. Using these fields a nice description of electrons and their interactions through the coupling to photons is achieved within the framework of the $U(1)$ gauge theory of quantum electrodynamics and its embedding in the larger framework of the Standard Model of particle physics.

Within the Standard Model the strong interactions are described by an $SU(3)$ color gauge theory, Quantum Chromodynamics (QCD). A basic problem is that the constituents in this theory, quarks and gluons, do not appear as asymptotic states, so the starting point in scattering experiments, be it as the objects of study or as the tools, are hadrons, the bound states of QCD.

In these lectures, for which background material can also be found in refs. [1,2], I want to discuss a variety of aspects in the study of hadronic structure and focus on the physical meaning of form factors, and quark momentum distributions. Focus is on extending the concept of collinear quark distributions to transverse-momentum–dependent (TMD) parton distribution functions (PDFs), for which we also refer to reviews in refs. [3, 4].

2. – Basics

Quantum mechanics. – When looking at the structure of a quantum-mechanical state in coordinate or momentum space, it is important to realize that these are conjugate, making things quite different from classical phase space in which one can consider coordinates and momenta as independent degrees of freedom. For purpose of illustration consider a state described with a one-dimensional spatial wave function $\varphi(x) = \langle x|\varphi\rangle$ or the corresponding momentum space representation $\tilde{\varphi}(p) = \langle p|\varphi\rangle$, linked through $\langle x|p\rangle = e^{ipx}$,

$$\varphi(x) = \int \frac{\mathrm{d}p}{2\pi}\, e^{ipx}\, \tilde{\varphi}(p) \quad \text{and} \quad \tilde{\varphi}(p) = \int \mathrm{d}x\; e^{-ipx}\, \varphi(x). \tag{1}$$

In many applications a momentum q is transferred to the system and absorbed, described by a (charge) operator

$$\hat{Q}(q) = \int \frac{\mathrm{d}p}{2\pi} \left| p + \frac{1}{2}q \right\rangle \left\langle p - \frac{1}{2}q \right| = \int \mathrm{d}x\; |x\rangle\, e^{iqx}\, \langle x|. \tag{2}$$

One measures an elastic response $\sigma(q) \propto |F(q)|^2$, where $F(q)$ is the expectation value of the operator $\hat{Q}(q)$, known as the *form factor*

$$(3)\qquad F(q) = \langle\varphi|\hat{Q}(q)|\varphi\rangle = \int \frac{\mathrm{d}p}{2\pi}\,\tilde{\varphi}^*\left(p+\frac{1}{2}q\right)\tilde{\varphi}\left(p-\frac{1}{2}q\right) = \int \mathrm{d}x\; e^{iqx}\,|\varphi(x)|^2,$$

which is the Fourier transform of the charge density $\rho(x) = |\varphi(x)|^2$. The form factor at $q = 0$ is just a number, in this case the normalization of the wave function. In other applications one knocks out a particle from the system, producing a plane-wave final state $|q\rangle$. The inelastic response is now $\sigma(q) \propto W(q)$, which reflects the momentum distribution $f(p)$, in the simplest case at $q = p$. Interchanging the roles of x and p in the above equation, this momentum distribution can be written as

$$(4)\qquad f(p) = |\tilde{\varphi}(p)|^2 = \int \mathrm{d}x\,\mathrm{d}y\; e^{ipy}\,\varphi^*\left(x-\frac{1}{2}y\right)\varphi\left(x+\frac{1}{2}y\right).$$

It is important to note that the form factors are non-local in momentum space, the momentum distribution is non-local in coordinate space.

A convenient way to incorporate both is the concept of quantum phase-space (Wigner) distributions. For a nice introduction in the field of hadron physics we refer to ref. [5]. The Wigner functions in quantum mechanics are defined as

$$(5)\qquad W(x,p) = \int \mathrm{d}y\; e^{ipy}\,\varphi^*\left(x-\frac{1}{2}y\right)\varphi\left(x+\frac{1}{2}y\right)$$

$$(6)\qquad = \int \frac{\mathrm{d}q}{2\pi}\; e^{-iqx}\,\tilde{\varphi}^*\left(p+\frac{1}{2}q\right)\tilde{\varphi}\left(p-\frac{1}{2}q\right).$$

The densities are obtained after integration over positions or momenta, respectively

$$(7)\qquad f(p) = \tilde{\varphi}^*(p)\,\tilde{\varphi}(p) = \int \mathrm{d}x\; W(x,p),$$

$$(8)\qquad \rho(x) = \varphi^*(x)\,\varphi(x) = \int \frac{\mathrm{d}p}{2\pi}\; W(x,p).$$

The Wigner distributions, generalized to appropriate 3-dimensional variables, are useful tools in analyzing the 3-dimensional structure of nucleons.

Momenta and phase space. – In more dimensions and in relativistic situations we will use momentum four vectors with components p^μ, either expressed as time- and space-like components $p = (p^0, \boldsymbol{p})$ or light-cone components $p = [p^-, p^+, p_T]$, with $p^\pm = (p^0 \pm p^3)/\sqrt{2}$. We will often use tetrads of vectors n_α to formalize components. The components of n_α are $n_\alpha^\mu = g_\alpha^\mu$. In particular, we may look in a covariant treatment for a time-like and space-like set of vectors $n_0^\mu = \hat{t}^\mu$ and $n_3^\mu = \hat{z}^\mu$ to give a covariant meaning to $p^0 \equiv p \cdot n_0$. For light-cone components one needs two light-like vectors $n_\pm^\mu$ satisfying

$n_+ \cdot n_- = 1$ and one has $p^\pm = p \cdot n_\mp$. In the transverse directions one works with the tensors

$$g_T^{\mu\nu} = g^{\mu\nu} - \hat{n}_+^{\{\mu}\hat{n}_-^{\nu\}} = g^{\mu\nu} + n_3^\mu n_3^\nu - n_0^\mu n_0^\nu, \tag{9}$$

$$\epsilon_T^{\mu\nu} = \epsilon^{-+\mu\nu} = \epsilon^{03\mu\nu}, \tag{10}$$

where we use $\epsilon^{0123} = \epsilon^{-+12} = 1$. For light-cone components the scaling of plus-component with α and minus-component with $1/\alpha$ just corresponds to a boost. The well-known measure or phase space for momentum states (with $p^2 = m^2$) and positive energy ($p^0 > 0$ or $p^+ > 0$) is given by

$$\begin{aligned} \int \mathrm{d}\tilde{p} &= \int \frac{\mathrm{d}4p}{(2\pi)^4}\,(2\pi)\,\delta(p^2 - m^2)\,\theta(p^0) \\ &= \int \frac{\mathrm{d}^3p}{(2\pi)^3\,2p^0} = \int \frac{\mathrm{d}p^0\,\mathrm{d}^2p_T}{(2\pi)^3\,2p^3} = \int \frac{\mathrm{d}p^+\,\mathrm{d}^2p_T}{(2\pi)^3\,2p^+} = \int \frac{\mathrm{d}p^-\,\mathrm{d}^2p_T}{(2\pi)^3\,2p^-}. \end{aligned} \tag{11}$$

Exercise: Show that for on-shell momenta $p^2 = m^2$ one has

$$p = p^+ n_+ + p^- n_- + \boldsymbol{p}_T \quad \text{with} \quad p^- = (m^2 + \boldsymbol{p}_T^2)/2p^+, \tag{12}$$

$$p = p^0 n_0 + \boldsymbol{p} \quad \text{with} \quad p^0 = \pm\sqrt{\boldsymbol{p}^2 + m^2}. \tag{13}$$

Show that for an off-shell momentum $p = P - P_R$ with $P^2 = M^2$ and $P_R^2 = M_R^2$ one can write in terms of light-cone components

$$P = P^+ n_+ + (M^2/2P^+) n_- \quad \text{and} \quad p = xP^+ n_+ + \sigma\, n_- + \boldsymbol{p}_T$$

(x is the light-cone momentum fraction) with

$$2P^+\sigma = 2\,p \cdot P - x\,M^2 = p^2 - M_R^2 + (1-x)M^2, \tag{14}$$

$$(1-x)p^2 = x(1-x)\,M^2 - x\,M_R^2 - \boldsymbol{p}_T^2, \tag{15}$$

which is useful for applications to quarks in nucleons. In terms of the usual four vector components one can write

$$P = Mn_0 \quad \text{and} \quad p = En_0 + \boldsymbol{p}$$

with

$$M\,E = p{\cdot}P = (M^2 + m^2 - M_R^2)/2 \approx Mm - M_R B \tag{16}$$

$$p^2 = (M^2 + M_R^2) - 2M\sqrt{\boldsymbol{p}^2 + M_R^2} \approx m^2 - 2mB - (M/M_R)\,\boldsymbol{p}^2, \tag{17}$$

where we have shown the results also for small binding energies, *i.e.* for $M_R = M - m + B$ with $B \ll \{m, M, M_R\}$, *e.g.*, applicable to electrons in atoms or nucleons in nuclei.

Quantum field theory. – In quantum field theory space-time dependence is treated in a different way, as only momentum operators as generator of space-time translations and the corresponding momentum eigenstates remain useful concepts. The fields $\phi(x)$ act as operators in Hilbert space with wave functions showing up as modes in the description of the space-time dependence multiplied with creation or annihilation operators for these modes, which in the standard free-field expansions create or annihilate momentum eigenstates. Composite operators like the current for fermions, $J^\mu(x) = \overline{\psi}(x)\,\gamma^\mu\psi(x)$, become important because they describe the coupling to photons or electromagnetic fields.

Simplifying our treatment one has operators $O(x)$ which having in them creation and annihilation operators have in essence the same structure as the operator $\hat{Q}(q)$ in our quantum-mechanical discussion. The field operator allows transitions between momentum eigenstates, $\langle P'|O(x)|P\rangle$. In the situation that the operator involves different degrees of freedom (say quarks) than the states (say hadrons), these states are like the states $|\varphi\rangle$ in the quantum-mechanical case. One expresses the matrix element as

$$\langle P'|O(x)|P\rangle = e^{iq\cdot x}\left[G_1(q^2) - i\,q_\mu\,G_2^\mu(q^2)\right], \tag{18}$$

where translation invariance now is used and all unknowns are in the *form factors* depending on the relevant invariants which is $t = q^2$ with $q = P' - P$. Realize, actually, how much info there is in the vectors. If we use $n_0 \sim P + P'$ (orthogonal to the spacelike direction $q = \boldsymbol{q}$). Thus also G_2^μ is spacelike (orthogonal to n_0). We note the relation of form factors at $q^2 = 0$ to forward matrix elements,

$$G_1(0) = \langle P|O(x)|P\rangle \quad \text{and} \quad G_2^\mu(0) = \langle P|x^\mu\,O(x)|P\rangle. \tag{19}$$

This provides covariant definitions of vector or axial charges as well as magnetic moments and masses in quantum field theory. See Appendix A for the nucleon form factor.

Extending our analysis to non-local field combinations, we can look at off-forward expectation values of non-local correlators, in essence Wigner functions

$$\langle P'|O\left(x - \frac{1}{2}y, x + \frac{1}{2}y\right)|P\rangle = e^{i\Delta\cdot x}\,\langle P'|O\left(-\frac{1}{2}y, \frac{1}{2}y\right)|P\rangle, \tag{20}$$

where $\Delta = P' - P$. These types of matrix elements, both off-forward ($\Delta \neq 0$), as well as non-local ($y \neq 0$) are the topic of *generalized parton distribution functions.* We limit ourselves to forward matrix elements and look at the specific example that the non-local combination involves a "square" combination of two fields $\phi(x)$, *i.e.* $O(x_1, x_2) = \phi^\dagger(x_1)\,\phi(x_2)$. In that case, one can easily see that the forward matrix element is a momentum density given by

$$\begin{aligned} f(p) &= \int \mathrm{d}^4y\; e^{ip\cdot y}\langle P|\phi^\dagger\left(-\frac{1}{2}y\right)\,\phi\left(\frac{1}{2}y\right)|P\rangle = \int \mathrm{d}^4y\; e^{ip\cdot y}\,\langle P|\phi^\dagger(0)\,\phi(y)|P\rangle \\ &= \sum_X \int \frac{\mathrm{d}^4P_X}{(2\pi)^4}\;(2\pi)^4\,\delta^4(P_X - P + p)\left|\langle P_X|\phi(0)|P\rangle\right|^2 \end{aligned} \tag{21}$$

which represents the momentum distribution of ϕ-particles in the target, summed over all final states that remain after removing or adding a ϕ-particle.

3. – Electroweak scattering processes

Electroweak scattering processes are in a sense ideal to study properties of hadrons. Only one specific process, namely lepton-hadron scattering will be dealt with in detail. A signal for an electroweak process is the presence of leptons which do not feel strong interactions. Characteristic processes are the following three types, the *annihilation* process, $\ell\bar{\ell} \to X$, the *lepton-hadron* scattering process, $\ell H \to \ell' X$, and the *lepton-pair production* process, $AB \to \ell\bar{\ell}X$ (Drell-Yan process). All of these processes involve electroweak currents, coupling to the leptons in a known way. The advantage of electromagnetic processes further lies in the fact that the process is accurately described in terms of the exchange of one photon, as the coupling, $\alpha = e^2/4\pi \approx 1/137$ is weak. The same is true for the weak vector bosons. On the hadronic side, the coupling to the quarks is known, but the structure of hadrons in terms of quarks and gluons is the unknown part. The fact that the coupling to the quarks is known, however, enables the study of quarks and (indirectly) gluons.

First let us consider the variables that are used to describe these scattering processes.
1) *Electron-positron annihilation:* $\ell\bar{\ell} \to X$ *or* $\ell\bar{\ell} \to h(P_h)X$

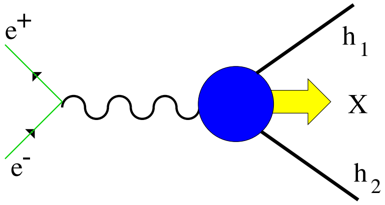

$$q^2 = (\ell + \ell')^2 \equiv Q^2 \geq 0, \tag{22}$$
$$2P_{h_i} \cdot q \equiv z_i\, Q^2, \tag{23}$$
$$2P_1 \cdot \ell \equiv y\, P_1 \cdot q. \tag{24}$$

In the case of production of hadrons with a timelike (virtual) photon one can consider the rest-frame of the virtual photon, in which case it is clear that Q is a measure of the excitation energy.
2) *Lepton-hadron scattering:* $\ell H(P) \to \ell' X$ *or* $\ell H(P) \to \ell' h(P_h)X$

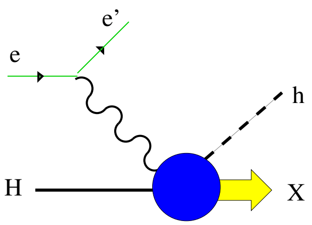

$$q^2 = (\ell - \ell')^2 \equiv -Q^2 \leq 0, \tag{25}$$
$$2P \cdot q \equiv 2M\,\nu \equiv \frac{Q^2}{x_{\rm B}}, \tag{26}$$
$$2P_h \cdot q \equiv -z_h\, Q^2, \tag{27}$$
$$P \cdot \ell \equiv \frac{P \cdot q}{y} = \frac{Q^2}{2x_{\rm B}y}. \tag{28}$$

The variable $x_{\rm B}$ is the Bjorken scaling variable. In this scattering process a hadron is probed with a spacelike (virtual) photon, for which one can consider a frame in which the momentum only has a spatial component, from which it is clear that the resolving power of the probing photon is of the order $\lambda \approx 1/Q$. Roughly speaking one probes a nucleus (1-10 fm) with $Q \approx$ 10-100 MeV, baryon or meson structure (with sizes in the order of 1 fm) with $Q \approx$ 0.1-1 MeV and one probes deep into the nucleon (< 0.1 fm) with $Q > 2\,\mathrm{GeV}$.

Exercise: Rewrite the invariant mass squared of the hadronic final state, W^2, in terms of invariants and use that $W^2 \geq M^2$ to show that $0 \leq x_{\mathrm{B}} \leq 1$, with $x_{\mathrm{B}} = 1$ corresponding to elastic scattering.
3) *Lepton-pair production or Drell-Yan scattering:* $A(P_A)B(P_B) \to \ell\bar{\ell}X$

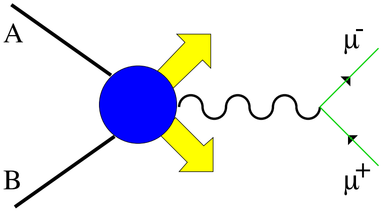

$$q^2 = (\ell + \ell')^2 \equiv Q^2 \geq 0, \tag{29}$$

$$2P_A \cdot q \equiv \frac{Q^2}{x_{\mathrm{A}}}, \tag{30}$$

$$2P_B \cdot q \equiv \frac{Q^2}{x_{\mathrm{B}}}, \tag{31}$$

$$2\ell \cdot q \equiv \frac{P_A \cdot q}{y}. \tag{32}$$

In Drell-Yan scattering one already has two hadrons to start with. Here Q^2 is the invariant mass of the lepton pair. The above processes are characteristic for a large number of other processes involving particles for which the interactions are fully known on the one side and hadrons on the other side.

Taking inclusive lepton-hadron scattering as an example, the cross-section is given by

$$E' \frac{\mathrm{d}\sigma}{\mathrm{d}^3\ell'} = \frac{1}{s - M^2}\, \frac{\alpha^2}{Q^4}\, L_{\mu\nu}\, 2MW^{\mu\nu}, \tag{33}$$

where $L_{\mu\nu}$ is the lepton tensor,

$$L_{\mu\nu}(\ell, \ell'; \lambda_e) = 2\ell_\mu \ell'_\nu + 2\ell_\nu \ell'_\mu - Q^2 g_{\mu\nu} + 2i\lambda_e\, \epsilon_{\mu\nu\rho\sigma} q^\rho \ell^\sigma \tag{34}$$

and $W_{\mu\nu}$ is the hadron tensor, which depends on exchanged momentum q and target momentum P. It contains the information on the hadronic part of the scattering process,

$$\begin{aligned} &2MW_{\mu\nu}(P, q) = \\ &\frac{1}{2\pi} \sum_n \int \frac{\mathrm{d}^3 P_n}{(2\pi)^3\, 2E_n} \langle P|J_\mu^\dagger(0)|P_n\rangle \langle P_n|J_\nu(0)|P\rangle (2\pi)^4 \delta^4(P + q - P_n). \end{aligned} \tag{35}$$

Exercise: Show, using $\delta^4(P + q - P_n) = \int \mathrm{d}^4x\ \exp[iP \cdot x + iq \cdot x - iP_n \cdot x]$, shifting the argument of the current, $J_\mu(x) = \exp[iP_{op} \cdot x] J_\mu(0) \exp[-iP_{op} \cdot x]$ and using completeness for the intermediate states that the hadron tensor can be written as the expectation value of the product of currents $J_\mu(x) J_\nu(0)$. Then, adding a second term $\propto J_\nu(0) J_\mu^\dagger(0) \delta^4(P -$

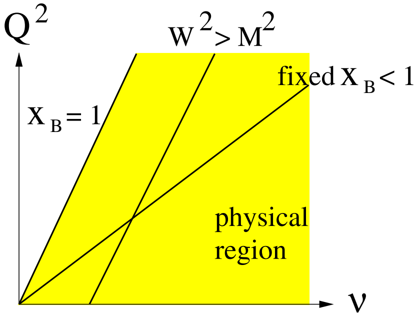

Fig. 1. – The physical region in deep inelastic scattering in the Q^2-ν plane. The variable $\nu = P \cdot q/M$ is the photon energy in the target (momentum P) rest frame. Indicated are lines of constant invariant mass squared for the hadronic system, $W^2 = (P+q)^2$. The elastic limit $W^2 = M^2$ corresponds with $\nu = Q^2/2M$ or $x_\mathrm{B} = 1$.

$q - P_n$), which in the physical region ($\nu > 0$) is zero because of the spectral conditions of the intermediate states n ($P_n^0 > M$) one can after a similar procedure combine the terms to

$$2M\,W_{\mu\nu} = \frac{1}{2\pi}\int \mathrm{d}^4x\; e^{i\,q\cdot x}\,\langle P|[J_\mu^\dagger(x), J_\nu(0)]|P\rangle, \tag{36}$$

where summation and averaging over spins is understood.

In the leptoproduction $e + H \to e' + X$ the (unobserved) final state X can be the target (elastic scattering) or an excitation thereof. In fig. 1 a plot of the two independent variables ν and Q^2 is given as well as lines for fixed W^2 or fixed x_B. Elastic scattering corresponds to $W^2 = M^2$ or $x_\mathrm{B} = 1$. For an elementary fermion that cannot be broken up or excited, this line relates ν and Q^2. For nucleons the elastic scattering cross-section (on top of the $1/Q^4$ of the Mott cross-section) is proportional to a form factor squared, measuring the expectation value of the electromagnetic current $\langle P'|J^\mu(x)|P\rangle$. It is also possible to excite the system. This gives rise to inelastic contributions in the cross-section at $\nu > Q^2/2M$, starting at the threshold $W = M + M_\pi$. When Q^2 and the energy transfer ν are high enough the cross-section will reflect elastic scattering off the pointlike constituents of the nucleon and the cross-section will become equal to an incoherent sum of the electron-quark cross-section. This is known as the deep inelastic scattering region, in which one finds Bjorken scaling. The cross-section, more precisely the structure functions, become functions of one (kinematic) variable x_B, which is identified with the momentum fraction of the struck quark in the nucleon, enabling measurement of quark distributions. In zeroth-order the cross-section thus becomes constant along lines of fixed x_B (scaling).

It is also possible to consider in more detail the space-time correlations that are probed. As already indicated q is space-like. But from the kinematics of deep inelastic scattering one can see that the process probes the light-cone. Sitting in the nucleon rest-frame we note that both $q^0 = \nu$ and $q^3 = \sqrt{Q^2+\nu^2}$ go to infinity but working at finite x_B one sees that taking the sum and the difference only one of them goes to infinity. Choosing $\boldsymbol{q}$ along the negative z-axis one has $q^- = (\nu + |\boldsymbol{q}|)/\sqrt{2} \to \infty$ and $q^+ = (\nu - |\boldsymbol{q}|)/\sqrt{2} \approx -M_N x_B/\sqrt{2}$. This corresponds in the hadronic tensor which involves a Fourier transform of the product of currents to $|x^+| \approx 1/q^- \to 0$ and $|x^-| \approx 1/|q^+| \to 1/Mx_B$ or $|\boldsymbol{x}| \approx |t| \approx 1/Mx_B$. Thus, depending on the value of x_B the distances and times not necessarily are small, but one has $x^2 = x^+x^- - \boldsymbol{x}_\perp^2 \approx -\boldsymbol{x}_\perp^2 \le 0$, while, on the other hand, causality requires that $x^2 \ge 0$. Therefore, one sees that deep inelastic scattering probes the light-cone, $x^2 \approx 0$.

4. – Structure functions and cross-sections

The simplest thing one can do with the hadron tensor is to express it in standard tensors and functions depending on the invariants, the *structure functions*. Instead of the traditional choice using tensors, $g_{\mu\nu}$, $P_\mu P_\nu$ and $\epsilon_{\mu\nu\rho\sigma}\, q^\rho P^\sigma$ multiplying structure functions W_1, W_2 and W_3 depending on ν and Q^2, we immediately go to a dimensionless representation. First we define a Cartesian basis of vectors [6], starting with the natural space-like momentum (defined by q). Using the target hadron momentum P^μ one can construct an orthogonal four vector $\tilde{P}^\mu = P^\mu - (P\cdot q/q^2)\, q^\mu$, which is timelike with length $\tilde{P}^2 = \kappa\, P\cdot q$ with

$$\kappa = 1 + \frac{M^2\, Q^2}{(P\cdot q)^2} = 1 + \frac{4\, M^2 x_\mathrm{B}^2}{Q^2}. \tag{37}$$

The quantity κ takes into account mass corrections $\propto M^2/Q^2$ which will vanish for large Q^2 $(\kappa \to 1)$. Thus we define

$$Z^\mu \equiv -q^\mu, \tag{38}$$

$$T^\mu \equiv -\frac{q^2}{P\cdot q}\, \tilde{P}^\mu = q^\mu + 2x_\mathrm{B}\, P^\mu. \tag{39}$$

For these vectors we have $Z^2 = -Q^2$ and $T^2 = \kappa\, Q^2$ and we will often use the normalized vectors $\hat{z}^\mu = -\hat{q}^\mu = Z^\mu/Q$ and $\hat{t}^\mu = T^\mu/Q\sqrt{\kappa}$. With respect to these vectors one can use the transverse tensors, $g_\perp^{\mu\nu} \equiv g^{\mu\nu} + \hat{q}^\mu\hat{q}^\nu - \hat{t}^\mu\hat{t}^\nu$ and $\epsilon_\perp^{\mu\nu} \equiv \epsilon^{\mu\nu\rho\sigma}\hat{t}_\rho\hat{q}_\sigma$. To get the parametrization of hadronic tensors, such as the one in eq. (36), including for generality also an (axial) spin vector S (see Appendix B), we use the general symmetry property,

$$W_{\mu\nu}(q,P,S) = W_{\nu\mu}(-q,P,S) \tag{40}$$

as well as properties following from hermiticity, parity and time-reversal invariance,

$$W^*_{\mu\nu}(q,P,S) = W_{\nu\mu}(q,P,S), \tag{41}$$

$$W_{\mu\nu}(q,P,S) = \overline{W}_{\nu\mu}(\bar{q},\bar{P},-\bar{S}) \qquad \text{(parity)}, \tag{42}$$

$$W^*_{\mu\nu}(q,P,S) = \overline{W}_{\mu\nu}(\bar{q},\bar{P},\bar{S}) \qquad \text{(time reversal)}, \tag{43}$$

where $\bar{p} = (p^0, -\boldsymbol{p})$. Finally we use current conservation implying $q^\mu W_{\mu\nu} = W_{\mu\nu} q^\nu = 0$. Note that depending on the situation not all constraints can be applied. For inclusive unpolarized leptoproduction one obtains as the most general form for the symmetric tensor,

$$\begin{aligned} M\, W^{\mu\nu\,(S)}(P,q) &= \left(\frac{q^\mu q^\nu}{q^2} - g^{\mu\nu}\right) F_1(x_{\rm B},Q^2) + \frac{\tilde{P}^\mu \tilde{P}^\nu}{P\cdot q}\, F_2(x_{\rm B},Q^2) \\ &= -g_\perp^{\mu\nu}\, \underbrace{F_1(x_{\rm B},Q^2)}_{F_T} + \hat{t}^\mu \hat{t}^\nu\, \underbrace{\left(-F_1 + \frac{\kappa}{2x_{\rm B}}\, F_2\right)}_{F_L}, \end{aligned} \tag{44}$$

where the structure functions F_1, F_2 or the transverse and longitudinal structure functions, $F_T = F_1$ and F_L, depend only on the for the hadron part relevant invariants Q^2 and $x_{\rm B}$. This is the structure for the electromagnic (photon exchange) part of the electroweak interaction. For the weak (W- or Z-exchange) part both vector and axial vector currents with different parity behavior come in. In that case also the following antisymmetric tensor is allowed,

$$M\, W^{\mu\nu\,(A)}(q,P) = \frac{i\epsilon^{\mu\nu\rho\sigma} P_\rho q_\sigma}{(P\cdot q)}\, F_3(x_{\rm B},Q^2) = i\,\kappa\,\epsilon_\perp^{\mu\nu}\, F_3(x_{\rm B},Q^2). \tag{45}$$

It appears in the part of the tensor in which one of the currents in the product is a vector current and the other an axial vector current.

The cross-section is obtained from the contraction of lepton and hadron tensors. It is convenient to expand also the lepton momenta ℓ and $\ell' = \ell - q$ in other vectors. Examples using ℓ and P (and the scaling variables for leptoproduction) are

$$\ell' = x_{\rm B} y\, P + (1-y)\,\ell + Q\sqrt{1-y}\,\hat{\ell}_{\perp(\ell,P)}, \tag{46}$$

or using P and q (or linear combinations like P and n or $\hat{t}$ and $\hat{z}$)

$$\begin{aligned} \ell' &= \frac{x_{\rm B}}{y}\, P + \frac{1-y}{y}\, \frac{Q^2}{2x_{\rm B}}\, n + \frac{Q\sqrt{1-y}}{y}\, \hat{\ell}_{\perp(q,P)} \\ &= \frac{(2-y)Q}{2y}\, \hat{t}^\mu + \frac{Q}{2}\, \hat{q}^\mu + \frac{Q\sqrt{1-y}}{y}\, \hat{\ell}_{\perp(q,P)}, \end{aligned} \tag{47}$$

where $n = (q + x_{\rm B} P)/P{\cdot}q = (\hat{t} + \hat{z})/\sqrt{2}$, which is the (approximately) light-like vector $n^2 \approx 0$, conjugate to P, $P{\cdot}n = 1$. The unit vectors $\hat{\ell}_\perp$ define the transverse directions with between brackets following the $\perp$ the momenta with respect to which the perpendicular directions are being considered. We note that in particular when one considers azimuthal

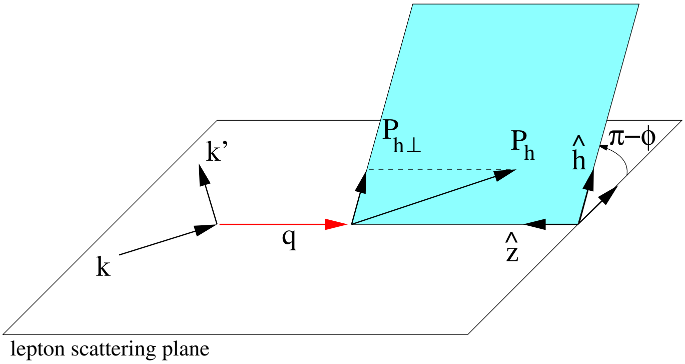

Fig. 2. – Kinematics for lepton-hadron scattering. Transverse directions indicated with a $\perp$ index are orthogonal to P and q, *e.g.*, the orthogonal component of the momentum of a produced hadron has been indicated as example. Similarly one can consider the orthogonal component of the spin vector of the target.

asymmetries one should be careful with the phase space,

$$\text{(48)}\qquad \mathrm{d}\tilde{\ell}' = \frac{\mathrm{d}(\ell'\cdot P)\,\mathrm{d}|\ell_{\perp(\ell,P)}|^2\,\mathrm{d}\varphi_{\ell P}}{(2\pi)^3\,2(\ell'\cdot P)} = \frac{y\,s}{8\pi^2}\,\mathrm{d}x_\mathrm{B}\,\mathrm{d}y\,\frac{\mathrm{d}\varphi_{\ell P}}{2\pi}$$

$$\text{(49)}\qquad = \frac{\mathrm{d}(\ell'\cdot n)\,\mathrm{d}|\ell_{\perp(q,P)}|^2\,\mathrm{d}\varphi_{qP}}{(2\pi)^3\,2(\ell'\cdot n)} = \frac{s}{8\pi^2\,y}\,\mathrm{d}x_\mathrm{B}\,\mathrm{d}y\,\frac{\mathrm{d}\varphi_{qP}}{2\pi}.$$

The kinematics in the frame where virtual photon and target are collinear (including target rest frame) is illustrated in fig. 2. With the definition of $\hat{\ell}_\perp$, we obtain neglecting mass corrections ($\kappa = 1$) for unpolarized leptons the symmetric leptonic tensor

$$\text{(50)}\qquad L^{\mu\nu\,(S)} = \frac{Q^2}{y^2}\Bigg[-2\left(1-y+\frac{1}{2}\,y^2\right)g_\perp^{\mu\nu} + 4(1-y)\hat{t}^\mu\hat{t}^\nu$$
$$+4(1-y)\left(\hat{\ell}_\perp^\mu\,\hat{\ell}_\perp^\nu + \frac{1}{2}\,g_\perp^{\mu\nu}\right) + 2(2-y)\sqrt{1-y}\;\hat{t}^{\{\mu}\hat{\ell}_\perp^{\nu\}}\Bigg].$$

We will need this form when we look at explicit production of particles h in the final state. The explicit contraction of lepton and hadron tensors for inclusive scattering gives for electromagnetic scattering (only symmetric tensor and $\kappa = 1$) the result

$$\text{(51)}\qquad \frac{\mathrm{d}\sigma^{ep}}{\mathrm{d}x_\mathrm{B}\mathrm{d}y} = \frac{4\pi\,\alpha^2\,x_\mathrm{B}\,s}{Q^4}\left[\left(1-y+\frac{1}{2}\,y^2\right)F_T(x_\mathrm{B},Q^2) + (1-y)\,F_L(x_\mathrm{B},Q^2)\right]$$
$$= \frac{2\pi\,\alpha^2\,s}{Q^4}\left[(1-y)\,F_2(x_\mathrm{B},Q^2) + x_\mathrm{B}\,y^2\,F_1(x_\mathrm{B},Q^2)\right].$$

We have now used the known photon coupling to the lepton and parametrized our ignorance for what happened with the hadron in a hadronic tensor. The fact that we know how the photon interacts with the (quark) constituents of the hadrons will be used later to relate the structure functions to quark properties. In the same way one also knows for the weak interaction processes leading to antisymmetric part containing F_3 in the tensor for unpolarized hadrons, how the Z^0 and W couple to quarks. To describe weak interactions also the antisymmetric part of the lepton tensor is needed, which is also encountered when one looks at polarization (see Appendix B).

5. – Virtual photon cross-sections

Dressing the hadronic tensor $W_{\mu\nu}$ with photon polarization vectors one obtains the total cross-section for $\gamma^* H \to$ everything, where γ^* indicates a virtual photon. For a given virtuality Q^2 of the photon this cross-section depends on only one variable, $W^2 = (P+q)^2$, or equivalently on the variable $\nu = P \cdot q/M$,

$$\sigma^{\gamma^* H}(\nu) = \frac{4\pi^2\alpha}{K}\, \epsilon^{\mu *} W_{\mu\nu} \epsilon^{\nu}, \tag{52}$$

where $4M\,K$ is the photon flux factor. This flux factor only is physical for real photons ($Q^2 = 0$). One convention is to take $4M\,K = 4\sqrt{(P\cdot q)^2 - P^2 q^2}$, *i.e.* $K = \sqrt{\nu^2 + Q^2}$. Other possibilities are to take the real photon result $4M\,K = 4\,P\cdot q$ or $K = \nu$ (Hand convention). Another convention that has been used is to equate the final-state invariant mass squared $W^2 = (P+q)^2$, *i.e.* take the result $4M\,K = 2(W^2 - M^2)$ for a massless photon and equate W^2 to the invariant mass in the case of a virtual photon, $W^2 = 2\,P\cdot q + M^2 - Q^2$ or $K = \nu - Q^2/2M$.

Being a (total) cross-section for (virtual) photoabsorption, the hadronic tensor is related to the forward (virtual) Compton amplitude through the optical theorem,

$$W_{\mu\nu} = \frac{1}{\pi} \mathrm{Im}\, T_{\mu\nu}, \tag{53}$$

where

$$2M\,T_{\mu\nu}(P,q) = i \int \mathrm{d}^4x\; e^{iq\cdot x} \langle P | \mathcal{T} J_\mu(x) J_\nu(0) | P\rangle. \tag{54}$$

For a virtual photon we need three polarization vectors ϵ^μ_α, where α indicates the polarization directions (perpendicular to q^μ),

$$\epsilon^\mu_\pm = \frac{1}{\sqrt{2}}\,(0, \mp 1, -i, 0) = \mp \frac{1}{\sqrt{2}} (\epsilon_x \pm i\,\epsilon_y) \quad \text{and} \quad \epsilon^\mu_L = \frac{1}{\sqrt{Q^2}}\,(q^3, 0, 0, q^0). \tag{55}$$

One gets two transverse structure functions and one longitudinal structure function, $F_\alpha = \epsilon^{\mu *}_\alpha\, M W_{\mu\nu} \epsilon^\nu_\alpha$. Because of the fact that they are cross-sections for (virtual) photons, the structure functions, F_+, F_- and F_L are positive. We have (as already indicated)

$$F_T = \frac{1}{2}\,(F_+ + F_-) = F_1, \quad F_L = \frac{F_2}{2x_{\mathrm{B}}} - F_1, \quad \text{and} \quad F_3 = F_+ - F_-. \tag{56}$$

6. – Form factors

In the structure functions the currents $J_\mu(x)$ enter that describe for instance coupling to photons or other electroweak bosons. Even if in that case the currents are known to be quark-currents(^{1}),

$$
\begin{aligned}
&(57) \qquad J_\mu^{(\gamma)} = :\overline{\psi}(x)\, Q\, \gamma_\mu \psi(x):,\\
&(58) \qquad J_\mu^{(Z)} = :\overline{\psi}(x)\,(I_W^3 - Q\sin^2\theta_W)\,\gamma_{\mu L}\,\psi(x): - :\overline{\psi}(x)\, Q\sin^2\theta_W\, \gamma_{\mu R}\,\psi(x):\\
&\qquad\qquad\;\; = :\overline{\psi}(x)\,(I_W^3 - 2\,Q\sin^2\theta_W)\,\gamma_\mu\,\psi(x): - :\overline{\psi}(x)\, I_W^3\,\gamma_\mu\gamma_5\,\psi(x):,\\
&(59) \qquad J_\mu^{(W)} = :\overline{\psi}(x)\, I_W^{\pm}\,\gamma_{\mu L}\psi(x):,
\end{aligned}
$$

where $\gamma_{\mu R/L} = \gamma_\mu(1 \pm \gamma_5)$. Although one has known currents of which even the flavor decomposition is known, their expectation values are not known.

In the special case in which the final state is identical to the initial state (elastic scattering, which is part of the inclusive scattering) $P' = P + q$ and is fixed to be $(P+q)^2 = M^2$, *i.e.* $x_\mathrm{B} = 1$. We can still use the formalism developed so far, but the hadronic tensor becomes becomes

$$
2M\, W_{\mu\nu}(q,P) = \underbrace{\langle P|J_\mu(0)|P'\rangle\langle P'|J_\nu(0)|P\rangle}_{H_{\mu\nu}(P;P')}\,\frac{1}{Q^2}\,\delta(1-x_\mathrm{B}). \qquad (60)
$$

One needs the hadronic current matrix elements, instead of those of the commutator or the time-ordered product. The current matrix elements are expressed in form factors, which are Fourier transforms of charge and current distributions. We will consider in more detail the vector and axial vector currents, V_μ and A_μ. For composite systems the expectation values of these currents are in general unknown. One can however write down a most general form and use translation invariance. The most general form consistent with the requirements of Poincaré invariance, gauge invariance and invariance under parity and time reversal yields for a spin 0 system (*e.g.*, a pion or a ^{12}C nucleus) the form

$$
\langle P', S'|V_\mu(x)|P,S\rangle = (P_\mu + P'_\mu)\,F(Q^2)e^{i(P'-P)\cdot x}, \qquad (61)
$$

involving one invariant function (*form factor*) depending on the (only) invariant, $q^2 \equiv -Q^2$, where $q = P' - P$. For spin-(1/2) systems (such as a nucleon, ^{3}H or ^{3}He) the most general expression for the expectation value of the current can be written using

---

(^{1}) Note that the factors $e\,, e/2\,\sin\theta_W\,\cos\theta_W$ and $e/2\sqrt{2}\,\sin\,\theta_W$ that would be expected for the $\gamma\,, Z^0$ and W-couplings to the quarks are omitted here. In writing cross-sections, they will be needed (like the e^2 in previous section) and are conventionally included in the fine structure constant α and the Fermi coupling $G_F/\sqrt{2} = e^2/8M_W^2\sin^2\theta_W$.

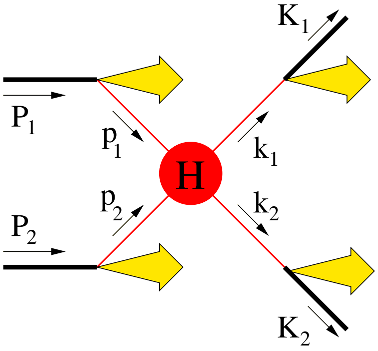

Fig. 3. – Schematic illustration of the contribution of a hard subprocess, parton (p_1)+ parton (p_2) $\to$ parton (k_1)+ parton (k_2), to the (2-particle inclusive) scattering process hadron (P_1)+ hadron (P_2) $\to$ hadron (K_1)+ hadron (K_2) + X, at the level of the amplitude. The process being hard implies for the hadronic momenta $P_1 \cdot P_2 \sim P_1 \cdot K_1 \sim Q^2$, etc.

free Dirac spinors $U(P,S)$,

$$\langle P', S'|V_\mu(0)|P,S\rangle = \overline{U}(P',S')\left[\gamma_\mu\, F_1(Q^2) + \frac{i\sigma_{\mu\nu}q^\nu}{2M}\, F_2(Q^2)\right] U(P,S), \tag{62}$$

with $\sigma_{\mu\nu} = \frac{i}{2}[\gamma_\mu,\gamma_\nu]$. The functions F_1 and F_2 are the Dirac and Pauli form factors.

The elastic cross-section then is found by inserting the parametrizations, for instance in the case of electromagnetic scattering one obtains the tensor $H_{\mu\nu}$

$$\begin{aligned} H_{\mu\nu}(P,P') &= \frac{1}{2}\sum_{S,S'}\langle P,S|J_\mu(0)|P',S'\rangle\langle P',S'|J_\nu(0)|P,S\rangle \\ &= \frac{1}{2}\mathrm{Tr}\,\left[\Gamma_\mu(\not{P}'+M)\Gamma_\nu(\not{P}+M)\right] \\ &= \left(\frac{q_\mu q_\nu}{q^2} - g_{\mu\nu}\right) Q^2(F_1+F_2)^2 + 4\,\tilde{P}_\mu\tilde{P}_\nu\left(F_1^2 + \frac{Q^2}{4M^2}\,F_2^2\right) \\ &= -g_{\perp\,\mu\nu}\,Q^2G_M^2 + \hat{t}_\mu\hat{t}_\nu\,4M^2\,G_E^2. \end{aligned} \tag{63}$$

One thus sees the following *elastic* contribution in the transverse and longitudinal structure functions:

$$F_T(x_\mathrm{B},Q^2) = G_M^2(Q^2)\,\delta(1-x_\mathrm{B}), \tag{64}$$

$$F_L(x_\mathrm{B},Q^2) = \frac{4M^2}{Q^2}\,G_E^2(Q^2)\,\delta(1-x_\mathrm{B}). \tag{65}$$

In Appendix A, we have given some basic background information on the nucleon form factors.

7. – Partons in QCD

The most intuitive way to discuss hard scattering processes is the parton model. One assumes a momentum distribution of quarks in the nucleon and folds it with the cross-section of a hard process, schematically shown in fig. 3. In the case of deep inelatic scattering one needs the γ^*-quark cross-section, given by

$$\begin{aligned}\hat{\sigma}(\gamma^* q) &= \frac{4\pi^2\alpha}{2p\cdot q}\,\epsilon^*_\mu \widehat{W}^{\mu\nu}\epsilon_\nu\\ 2M\,\widehat{W}_{\mu\nu}(p,q) &= \left[\left(\frac{q_\mu q_\nu}{q^2} - g_{\mu\nu}\right)Q^2 + 4\,\tilde{p}_\mu\tilde{p}_\nu\right]\delta(2\,p\cdot q + q^2)\end{aligned}$$

(note that there are in principle ambiguities here because of the flux factor for virtual photons). One finds

$$\hat{\sigma}_T(\gamma^* q) = 4\pi^2\alpha\; e_q^2\;\delta(2p\cdot q - Q^2), \tag{66}$$

$$\hat{\sigma}_L(\gamma^* q) = 4\pi^2\alpha\; e_q^2\;\frac{4m^2}{Q^2}\,\delta(2p\cdot q - Q^2) \ll \hat{\sigma}_T. \tag{67}$$

These partonic cross-sections are folded with a probability function for finding partons in the target. It is convenient to use here light-cone components

$$p = xP + p_T + (p\cdot P - xM^2)n,$$

where n is a (at present) arbitrary light-like vector satisfying $P\cdot n = 1$. This vector plays the role of $n = n_-$, while in that case $n_+ = P - \frac{1}{2}M^2\,n$. Within the hard scattering process the dominant contraction of P with other vectors are much larger than M^2, so the second term in n_+ is irrelevant or in other words P can be considered a light-like vector itself. This Sudakov decomposition of the parton model is useful since it separates the components of p into a "large" one $p \approx xP$ with $x = p\cdot n/P\cdot n = p^+/P^+$ being a momentum fraction, a "normal-sized" component p_T and a small component involving the light-cone energy $p^- = p\cdot P - \frac{1}{2}xM^2$. For the leading-order results one can integrate over p^- and usually also over p_T and look at the momentum distribution $f_i(x)$ for parton i. Although most results are independent of n one can construct it from other vectors in the problem, in the case of inclusive deep inelastic scattering the vector $n = (q+xP)/P\cdot q$ satisfies the requirements.

Exercise: Derive the light-cone expansion for the (external) vectors P and q,

$$\left.\begin{array}{l} q^2 = -Q^2\\ P^2 = M^2\\ 2\,P\cdot q = \frac{Q^2}{x_{\rm B}}\end{array}\right\}\longleftrightarrow\left\{\begin{array}{l} q = \ \frac{Q}{\sqrt{2}}\,n_- \ - \ \frac{Q}{\sqrt{2}}\,n_+\\ \\ P = \frac{x_{\rm B}M^2}{Q\sqrt{2}}\,n_- + \frac{Q}{x_{\rm B}\sqrt{2}}\,n_+\end{array}\right. ,$$

or in light-cone components ($n_+ \equiv [0, A, 0_\perp]$ and $n_- \equiv [1/A, 0, 0_\perp]$)

$$q = \left[\frac{Q^2}{A\sqrt{2}}, -\frac{A}{\sqrt{2}}, \mathbf{0}_\perp\right], \quad \text{and} \quad P = \left[\frac{x_\mathrm{B} M^2}{A\sqrt{2}}, \frac{A}{x_\mathrm{B}\sqrt{2}}, \mathbf{0}_\perp\right] \approx \left[0, \frac{A}{x_\mathrm{B}\sqrt{2}}, \mathbf{0}_\perp\right].$$

What is the effect of a boost? What is A in the nucleon rest-frame. $A \to \infty$ is referred to as the *infinite momentum frame.* In particular the first representation with light-like vectors shows that when Q^2 becomes large, the nucleon momentum is on the scale Q in essence light-like. While the hard momentum has both components proportional to Q, this is not the case for P and one has $P^- \ll q^-$. In deep-inelastic scattering the plus components are of the same order with ratio being the scaling variable $x_\mathrm{B} = -q^+/P^+$. Under the assumption that all invariants $p \cdot P \sim M_R^2 \sim p^2 \sim P^2 = M^2 \ll Q^2$ one sees that for the expansion in terms of $n_\pm$ one has for a quark in a hadron (as one would have for an on-shell quark) that $p^+ \sim P^+ \sim Q$, while $p^- \sim M^2/Q$ and $p_T^2 \sim M^2$ (see eqs. (14) and (15). This is sufficient to derive the parton model results.

Using the cross-section for $\gamma^* q$ (elastic scattering) given above,

$$\hat{\sigma}_T = \frac{4\pi^2\alpha}{Q^2}\,\delta(1 - x_p). \tag{68}$$

where $x_p = -q^+/p^+$ and introducing probabilities $f_i(x)$ for finding partons carrying momentum fraction $x = p^+/P^+ = x_\mathrm{B}/x_p$ of the target light-cone momentum, leads to(^{2})

$$\sigma_T = \sum_i e_i^2 \int \mathrm{d}x\, f_i(x)\, \frac{4\pi^2\alpha}{Q^2}\,\delta\left(1 - \frac{x_\mathrm{B}}{x}\right) = \frac{4\pi^2\alpha}{Q^2} \sum_i e_i^2\, x_\mathrm{B}\, f_i(x_\mathrm{B}). \tag{69}$$

Comparing with

$$\sigma_T = \frac{8\pi^2\alpha}{Q^2}\, x_\mathrm{B}\, F_1, \tag{70}$$

we get

$$F_1(x_\mathrm{B}) = \frac{1}{2}\sum_i e_i^2\, f_i(x_\mathrm{B}). \tag{71}$$

As $\hat{\sigma}_L \propto 1/Q^2 \to 0$ one obtains $F_L = 0$ or the Callan-Gross relation,

$$F_2(x_\mathrm{B}) = 2x_\mathrm{B}\, F_1(x_\mathrm{B}). \tag{72}$$

(^{2}) We note that the probability involves in fact $f_i(x)\,\mathrm{d}x/x$, but we need to fold conting rates which requires that we need the cross-section multiplied by flux factors. The ratio of the flux factors for quarks and hadrons is $p \cdot q/P \cdot q \approx p^+/P^+ = x$. Hence we need to weigh the cross-section with $f_i(x)\,\mathrm{d}x$.

8. – The diagrammatic approach

The diagrammatic approach has a different starting point. It realizes the absence of wave functions for the quarks and gluons. The situation thus differs from that of QED with physical electrons and photons. In the latter case one knows how in the calculation of an S-matrix element contraction of annihilation and creation operator in the field and particle state lead to the spinor wave function. For positive times $\xi^0 = t > 0$ one has

$$(73)\qquad \langle 0|\psi_i(\xi)|p,s\rangle = \langle 0|\psi_i(\xi)\, b^\dagger(\boldsymbol{p},s)|0\rangle = \langle 0|\psi_i(0)|p,s\rangle\, e^{-i\,p\cdot\xi} = u_i(\boldsymbol{p},s)\, e^{-i\,p\cdot\xi},$$

with $p^0 = +E_p = +\sqrt{\boldsymbol{p}^2+m^2}$. Such a matrix element is "untruncated" as seen, *e.g.*, from

$$(74)\ \langle 0|\psi_i(\xi)|p,s\rangle\,\theta(t) = \theta(t)\int \frac{d^4k}{(2\pi)^4}\, e^{-ik\cdot\xi}\, \frac{i(\not k+m)}{k^2-m^2+i\epsilon}\, \frac{u_i(\boldsymbol{p},s)}{2m}\,(2\pi)^3\, 2E_p\, \delta^3(\boldsymbol{k}-\boldsymbol{p}).$$

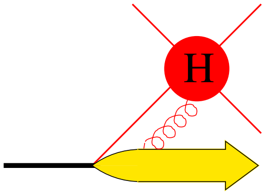

In a process involving composite hadronic states $|P\rangle$, like in fig. 3 contractions with one or several of the quark and gluon operators may be involved, leading to nonzero matrix elements for a quark between the hadron state and a remainder, but also for nonzero matrix elements involving multi-parton field combinations,

$$\langle X|\psi_i(\xi)|P\rangle,\ \langle X|A^\mu(\eta)\,\psi(\xi)|P\rangle,\ldots.$$

Correlators, describing parton distributions. – For a particular hadron and a parton field combination, one may collect those operators that involve hadron $|P\rangle$ into (distribution) correlators

$$(75)\qquad \Phi_{ij}(p;P) = \sum_X \int \frac{d^3P_X}{(2\pi)^3\, 2E_X}\, \langle P|\overline{\psi}_j(0)|X\rangle\,\langle X|\psi_i(0)|P\rangle\,\delta^4(p+P_X-P)$$
$$= \frac{1}{(2\pi)^4}\int d^4\xi\; e^{i\,p\cdot\xi}\,\langle P|\overline{\psi}_j(0)\,\psi_i(\xi)|P\rangle,$$

where a summation over color indices is understood. It is often convenient to use momentum space fields, $\psi(p) \equiv \int d^4x\; e^{i\,p\cdot x}\,\psi(x)$, for a free-field expansion leading to

$$(76)\qquad \psi_i(\boldsymbol{p},t) = \sum_s\left(u_i(\boldsymbol{p},s)\, b(\boldsymbol{p},s)\frac{e^{-iE_pt}}{2E_p} + v_i(-\boldsymbol{p},s)\, d^\dagger(-\boldsymbol{p},s)\frac{e^{iE_pt}}{2E_p}\right),$$

$$(77)\qquad \psi_i(p) = \sum_s\Big(u_i(\boldsymbol{p},s)\, b(\boldsymbol{p},s)\,(2\pi)\delta(p^2-m^2)\,\theta(p^0)$$
$$+v_i(-\boldsymbol{p},s)\, d^\dagger(-\boldsymbol{p},s)\,(2\pi)\delta(p^2-m^2)\,\theta(-p^0)\Big).$$

For the correlator we have

$$(2\pi)^4\delta^4(p-p')\,\Phi_{ij}(p;P) = \frac{1}{(2\pi)^4}\,\langle P|\overline{\psi}_j(p')\,\psi_i(p)|P\rangle. \tag{78}$$

This latter form is convenient for interpretation of the nature of the correlators because for a free-field we have

$$\begin{aligned}\langle X|\psi_i(p)|P\rangle = {}&\langle P_X|b(\boldsymbol{p},s)|P\rangle\,u_i(\boldsymbol{p},s)\,(2\pi)\delta(p^2-m^2)\,\theta(p^0)\\ &+\langle P_X|d^\dagger(-\boldsymbol{p},s)|P\rangle\,v_i(-\boldsymbol{p},s)\,(2\pi)\delta(p^2-m^2)\,\theta(-p^0).\end{aligned}$$

One also encounters correlators involving matrix elements including gluon fields, of the form

$$\Phi^\mu_{A\,ij}(p,p_1;P) = \frac{1}{(2\pi)^8}\int \mathrm{d}^4\xi\,\mathrm{d}^4\eta\; e^{i\,(p-p_1)\cdot\xi}\;e^{i\,p_1\cdot\eta}\;\langle P|\overline{\psi}_j(0)\,A^\mu(\eta)\,\psi_i(\xi)|P\rangle, \tag{79}$$

or with momentum space operators (for gluons $A_\mu(p) \equiv \int \mathrm{d}^4x\; e^{i\,p\cdot x}\,A_\mu(x)$) one has

$$(2\pi)^4\delta^4(p-p')\,\Phi^\mu_{A\,ij}(p,p_1;P) = \frac{1}{(2\pi)^8}\,\langle P|\overline{\psi}_j(p')\,A^\mu(p_1)\,\psi_i(p-p_1)|P\rangle. \tag{80}$$

Pictorially one has for the correlators,

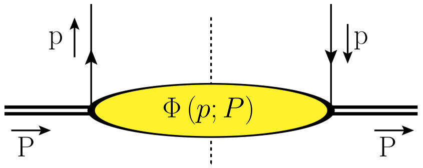

or

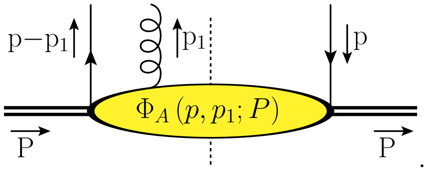

.

We will not attempt to calculate these, but leave them as the soft parts, requiring nonperturbative QCD methods to calculate them. In particular, although being "untruncated" in the quark legs, they will no longer exhibit poles corresponding to free quarks. These are fully unintegrated parton correlators for initial state hadrons, in general quite problematic quantities. For example, they are by themselves not even color gauge-invariant, an issue to be discussed below. We will later also discuss similar correlators for final state hadrons. When more hadrons are involved, one needs to consider two-hadron correlators, involving two-hadron states (or correlators involving hadronic states in initial and final state), etc. If the hadrons are well separated in momentum phase-space with $P_i\cdot P_j \sim Q^2$, one expects on dimensional grounds that incoherent contributions are suppressed by $1/(P_i-P_j)^2 \sim 1/Q^2$. Such a separation in momentum space requires a hard inclusive scattering process ($Q^2 \sim s$), which then at high energy and/or for large momentum transfer still can be factorized into forward correlators. The inclusive character is needed to assure that partons originate from *one* hadron, leaving a (target) jet. In turn, partons decay into a jet in which we limit ourselves to the consideration of an identified hadronic state (which could in principle also be a multi-particle, *e.g.*, two-pion, state). In all of the hadronic states mentioned before one can also consider polarized hadronic states (see Appendices B and C). The spin of quarks is contained in Dirac structure and that of gluons in the Lorentz structure of correlators.

The basic idea in the diagrammatic approach is to realize that the correlator involves hadronic states and quark and gluon operators. The correlators can be studied independent of the hard process, provided we have dealt with the issue of color gauge invariance. The correlator is the Fourier transform in the space-time arguments of the quark and gluon fields. In the correlators, all momenta of hadrons *and* quarks and gluons (partons) inside the hadrons are soft which means that $p^2 \sim p \cdot P \sim P^2 = M_N^2 \ll Q^2 \sim s$. The *off-shellness* being of hadronic order implies that in the hard process partons are in essence *on-shell.* Consistency of this may be checked by using QCD interactions to give partons a large off-shellness of $\mathscr{O}(Q)$ and check the behavior as a function of the momenta. In these considerations one must also realize that beyond tree-level one has to distinguish bare and renormalized fields.

The simplest expression that is needed in scattering a photon from the target, is the correlator and the scattering of the photon from a quark. Restricting us to the quark part is

$$
\begin{aligned}
(81)\quad 2MW^{\mu\nu}(P,q) &= \sum_q e_q^2 \int \mathrm{d}p^- \mathrm{d}p^+ \mathrm{d}^2\boldsymbol{p}_\perp \mathrm{Tr}\left(\Phi(p)\gamma^\mu(\not p + \not q + m)\gamma^\nu\right)\delta((p+q)^2 - m^2)\\
&\approx \sum_q e_q^2 \int \mathrm{d}p^- \mathrm{d}p^+ \mathrm{d}^2\boldsymbol{p}_\perp \mathrm{Tr}\left(\Phi(p)\gamma^\mu \frac{\not q}{2q^-}\gamma^\nu\right)\delta(p^+ + q^+)\\
&\approx -g_\perp^{\mu\nu}\frac{1}{2}\int \mathrm{d}p^- \mathrm{d}^2\boldsymbol{p}_\perp \mathrm{Tr}\left(\gamma^+\Phi(p)\right)\Big|_{p^+ = x_{\mathrm{B}}\,P^+} + \dots,
\end{aligned}
$$

where $\Phi(p)$ is the correlator discussed above. The relevant soft part then is a particular Dirac trace of the quantity

$$
(82)\quad \Phi_{ij}(x) = \int \mathrm{d}p^-\, \mathrm{d}^2p_T\; \Phi_{ij}(p,P,S) = \int \frac{\mathrm{d}\xi^-}{2\pi}\; e^{ip\cdot\xi}\langle P,S|\overline{\psi}_j(0)\psi_i(\xi)|P,S\rangle\Big|_{\xi^+ = \xi_T = 0},
$$

depending on the light-cone fraction $x = p^+/P^+$.

Comparing with the general form of the hadronic tensor, we read off (including now also the antiquark part)

$$
(83)\qquad 2\,F_1(x_{\mathrm{B}}) = 2M\,W_1(x_{\mathrm{B}},Q^2) = \sum_q e_q^2\,\left[f_1^q(x_{\mathrm{B}}) + \bar{f}_1^q(x_{\mathrm{B}})\right],
$$

with

$$
(84)\qquad f_1^q(x) = \int \frac{\mathrm{d}\xi\cdot P}{4\pi}\; e^{ip\cdot\xi}\,\langle P,S|\overline{\psi}(0)\not n\psi(\xi)|P,S\rangle\Big|_{\xi\cdot n = \xi_\perp = 0} = \frac{1}{2}\,\mathrm{Tr}\left(\Phi(x)\not n\right),
$$

$$
(85)\qquad \bar{f}_1^q(x) = \int \frac{\mathrm{d}\xi\cdot P}{4\pi}\; e^{-ip\cdot\xi}\langle P,S|\overline{\psi}(0)\not n\psi(\xi)|P,S\rangle\Big|_{\xi\cdot n = \xi_\perp = 0},
$$

often simply denoted as $q(x) = f_1^q(x)$, satisfying $\overline{q}(x) = -q(-x)$ (Exercise!). The result is (as expected) a light-cone correlation function of quark fields.

The operator in coordinate space. – The parton result for the structure functions can also be derived by inserting free currents in the hadronic tensor for the current commutator and using the expression for the free-field commutator.

Exercise: Use the anticommutation relations for free quark fields, $\{\psi(\xi), \overline{\psi}(0)\} = \frac{1}{2\pi}\,\not{\partial}\,\delta(\xi^2)\,\epsilon(\xi^0)$ to derive for the $g_{\mu\nu}$ contribution in the current-current commutator for quarks

$$
\begin{aligned}
(86)\qquad [J_\mu(\xi), J_\nu(0)] &= [:\overline{\psi}(\xi)\gamma_\mu\psi(\xi):, :\overline{\psi}(0)\gamma_\nu\psi(0):] \\
&= \frac{-g_{\mu\nu}}{2\pi}\left[\partial_\rho\,\delta(\xi^2)\,\epsilon(\xi^0)\right] :\overline{\psi}(\xi)\gamma^\rho\psi(0) - \overline{\psi}(0)\gamma^\rho\psi(\xi): \;.
\end{aligned}
$$

An important feature, evident in the free-current commutator, is the light-cone dominance. By sandwiching the commutator between physical states and taking the Fourier transform, it is a straightforward calculation to obtain again the hadron tensor and the same result as in the diagrammatic approach above. Details can be found in ref. [7].

Interpretation as densities. – To convince oneself that the above expressions for $f_1(x)$ and $bar f_1(x)$ actually can be interpreted as quark momentum density one needs to realize that $\overline{\psi}(\xi)\gamma^+\psi(0) = \sqrt{2}\,\psi_+^\dagger(\xi)\psi_+(0)$ where $\psi_\pm = P_\pm\,\psi$ are projections obtained with projection operators $P_\pm = \frac{1}{2}\gamma^\mp\gamma^\pm$. One then can insert a complete set of states and obtain

$$
\begin{aligned}
(87)\qquad f_1(x) &= \int \frac{d\xi^-}{2\pi\sqrt{2}}\, e^{ip\cdot\xi}\,\langle P,S|\psi_+^\dagger(0)\psi_+(\xi)|P,S\rangle\Big|_{\xi^+=\xi_T=0} \\
&= \frac{1}{\sqrt{2}}\sum_n |\langle P_n|\psi_+|P\rangle|^2\,\delta\left(P_n^+ - (1-x)P^+\right),
\end{aligned}
$$

which represents the probability that a quark is annihilated from $|P\rangle$ giving a state $|n\rangle$ with $P_n^+ = (1-x)P^+$. As a further note, we mention that ψ_+ fields are actually the good fields of the light-cone quantized field theory, so the expansion in plane wave states with specified p^+ and p_T components makes sense even in the interacting theory (see Appendices D and quantum forms).

Relation to forward amplitudes. – The full hadronic tensor as a squared amplitude is also the imaginary part of a forward amplitude (optical theorem). The same relation holds for the hard (QCD) amplitude. A similar property also holds for the soft part after integration over the light-cone momentum $p^- = p\cdot P$. All operators in the correlator now are evaluated at light-cone time $\xi^+ = \xi\cdot n = 0$. This implies that time-ordering has become automatic. Thus not only the full hadronic tensor, but also the correlators $\Phi(x, p_T)$ and $\Phi(x)$, besides being densities, can be seen as time-ordered products of

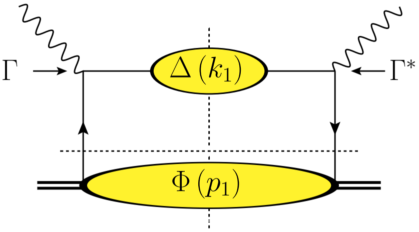

Fig. 4. – The simplest (parton-level) diagrams for semi-inclusive scattering, of which we consider one-particle inclusive leptoproduction. Note that also the diagram with opposite fermion flow has to be added.

fields, which means related to the forward antiquark-hadron scattering amplitudes [8, 9]. This is important because amplitudes in a field-theoretical setting have various analytic properties, *e.g.*, related to unitarity. That the time-ordering is only evident in light-cone time is not a problem, because the ordering as such is covariant.

9. – Quark correlation functions in 1PI leptoproduction

We now consider the case in which one particle is detected in coincidence with the scattered lepton, *one-particle-inclusive* or 1PI leptoproduction. The kinematics of this process is already in the picture given before (fig. 2). With a target hadron (momentum P) and a detected hadron h in the final state (momentum P_h) one has a situation in which two hadrons are involved and the operator product expansion cannot be used. Within the framework of QCD and knowing that the photon or Z^0 current couples to the quarks, it is possible to write down a diagrammatic expansion for leptoproduction, with in the deep inelastic limit ($Q^2 \to \infty$) as relevant diagrams only the ones given in fig. 4 for 1-particle inclusive scattering.

In analogy with the case of inclusive scattering, we also in 1-particle inclusive scattering parametrize the momenta with the help of two lightlike vectors, which are chosen now along the hadron momenta,

$$\left.\begin{array}{l} q^2 = -Q^2 \\ P^2 = M^2 \\ P_h^2 = M_h^2 \\ 2\,P\cdot q = \frac{Q^2}{x_{\mathrm{B}}} \\ 2\,P_h\cdot q = -z_h\,Q^2 \end{array}\right\} \longleftrightarrow \left\{\begin{array}{l} P_h = \frac{z_h\,Q}{\sqrt{2}}\,n_- + \frac{M_h^2}{z_h\,Q\sqrt{2}}\,n_+ \\[2ex] q = \frac{Q}{\sqrt{2}}\,n_- \;-\; \frac{Q}{\sqrt{2}}\,n_+ \;+\; q_T \\[2ex] P = \frac{x_{\mathrm{B}}M^2}{Q\sqrt{2}}\,n_- + \frac{Q}{x_{\mathrm{B}}\sqrt{2}}\,n_+ \end{array}\right.$$

An additional invariant z_h comes in. Note that the expansion is appropriate for the so-called current fragmentation, in which case the produced hadron is *hard* with respect to the target momentum, *i.e.* $P\cdot P_h \sim Q^2$. The minus component p^- is irrelevant in the lower soft part, while the plus component k^+ is irrelevant in the upper soft part. Note that after the choice of P and P_h one can no longer omit a transverse component in the other vector, in the consideration above put in the momentum transfer q. One sees that one has (up to mass effects) the relation

$$q_T^\mu = q^\mu + x_\mathrm{B}\,P^\mu - \frac{P_h^\mu}{z_h} \equiv -Q_T\,\hat{h}^\mu. \tag{88}$$

This relation allows the experimental determination of the "transverse momentum" effect from the external vectors q, P and P_h which are in general not collinear. The vector $\hat{h}$ defines the orientation of the hadronic plane in fig. 2.

An important consequence in the theoretical approach (fig. 4) is that one can no longer simply integrate over the transverse components of the quark momenta.

Structure functions and cross-sections. – For an unpolarized (or spin-0) hadron in the final state the symmetric part of the tensor is given by

$$\begin{aligned} M\mathcal{W}_S^{\mu\nu}(q,P,P_h) = {} & -g_\perp^{\mu\nu}\,\mathcal{H}_T + \hat{t}^\mu\hat{t}^\nu\,\mathcal{H}_L \\ & + \hat{t}^{\,\{\mu}\hat{h}^{\nu\}}\,\mathcal{H}_{LT} + \left(2\,\hat{h}^\mu\hat{h}^\nu + g_\perp^{\mu\nu}\right)\mathcal{H}_{TT}. \end{aligned} \tag{89}$$

Noteworthy is that also an antisymmetric term in the tensor is allowed,

$$M\mathcal{W}_A^{\mu\nu}(q,P,P_h) = -i\hat{t}^{\,[\mu}\hat{h}^{\nu]}\,\mathcal{H}'_{LT}. \tag{90}$$

Clearly the lepton tensor in eq. (50) or (B.3) is able to distinguish all the structures in the semi-inclusive hadron tensor.

The symmetric part gives the cross-section for unpolarized leptons,

$$\begin{aligned} \frac{\mathrm{d}\sigma_{OO}}{\mathrm{d}x_\mathrm{B}\mathrm{d}y\,\mathrm{d}z_h\mathrm{d}^2q_T} = \frac{4\pi\,\alpha^2\,s}{Q^4}\,x_\mathrm{B}z_h\Biggl\{ & \left(1-y+\frac{1}{2}\,y^2\right)\mathcal{H}_T + (1-y)\,\mathcal{H}_L \\ & - (2-y)\sqrt{1-y}\,\cos\phi_h^\ell\;\mathcal{H}_{LT} \\ & + (1-y)\,\cos 2\phi_h^\ell\;\mathcal{H}_{TT}\Biggr\}, \end{aligned} \tag{91}$$

while the antisymmetric part gives the cross-section for a polarized lepton (note the target is not polarized!)

$$\frac{\mathrm{d}\sigma_{LO}}{\mathrm{d}x_\mathrm{B}\mathrm{d}y\,\mathrm{d}z_h\mathrm{d}^2q_T} = \lambda_e\,\frac{4\pi\,\alpha^2}{Q^2}\,z_h\,\sqrt{1-y}\,\sin\phi_h^\ell\;\mathcal{H}'_{LT}. \tag{92}$$

Of course many more structure functions appear for polarized targets or if one considers polarimetry in the final state. In this case the (theoretically) most convenient way to describe the spin vector of the target is via an expansion of the form

$$S^\mu = -S_L\,\frac{Mx_\mathrm{B}}{Q\sqrt{2}}\,n_- + S_L\,\frac{Q}{Mx_\mathrm{B}\sqrt{2}}\,n_+ + S_T. \tag{93}$$

One has up to $\mathcal{O}(1/Q^2)$ corrections $S_L \approx M\,(S\cdot q)/(P\cdot q)$ and $S_T \approx S_\perp$, where the subscript $\perp$ still refers to perpendicular to q and P. For a pure state one has $S_L^2 + \boldsymbol{S}_T^2 = 1$, in general this quantity being less or equal than one.

The parton model approach. – The expression for $\mathcal{W}_{\mu\nu}$ can be rewritten as a nonlocal product of currents and it is a straightforward exercise to show by inserting the currents $j_\mu(x) =: \overline{\psi}(x)\gamma_\mu\psi(x) :$ that for 1-particle inclusive scattering one obtains in tree approximation

$$
\begin{aligned}
(94)\qquad & 2M\mathcal{W}_{\mu\nu}(q;PS;P_hS_h)\\
&= \frac{1}{(2\pi)^4}\int \mathrm{d}^4x\; e^{iq\cdot x}\,\langle PS|:\overline{\psi}_j(x)(\gamma_\mu)_{jk}\psi_k(x):\sum_X |X;P_hS_h\rangle\\
&\qquad\qquad\times\langle X;P_hS_h|:\overline{\psi}_l(0)(\gamma_\nu)_{li}\psi_i(0):|PS\rangle\\
&= \frac{1}{(2\pi)^4}\int \mathrm{d}^4x\; e^{iq\cdot x}\,\langle PS|\overline{\psi}_j(x)\psi_i(0)|PS\rangle(\gamma_\mu)_{jk}\\
&\qquad\times\langle 0|\psi_k(x)\sum_X |X;P_hS_h\rangle\langle X;P_hS_h|\overline{\psi}_l(0)|0\rangle(\gamma_\nu)_{li}\\
&\quad + \frac{1}{(2\pi)^4}\int \mathrm{d}^4x\; e^{iq\cdot x}\,\langle PS|\psi_k(x)\overline{\psi}_l(0)|PS\rangle(\gamma_\nu)_{li}\\
&\qquad\times\langle 0|\overline{\psi}_j(x)\sum_X |X;P_hS_h\rangle\langle X;P_hS_h|\psi_i(0)|0\rangle(\gamma_\mu)_{jk}+\dots\\
&= \int \mathrm{d}^4p\,\mathrm{d}^4k\,\delta^4(p+q-k)\;\mathrm{Tr}\left(\Phi(p)\gamma_\mu\Delta(k)\gamma_\nu\right) + \left\{\begin{array}{c} q\leftrightarrow -q\\ \mu\leftrightarrow\nu\end{array}\right\},
\end{aligned}
$$

where we encounter not only a correlator describing quark distributions but also a correlator describing the fragmentation process,

$$
(95)\qquad \Phi_{ij}(p) = \frac{1}{(2\pi)^4}\int \mathrm{d}^4\xi\; e^{ip\cdot\xi}\,\langle PS|\overline{\psi}_j(0)\psi_i(\xi)|PS\rangle,
$$

$$
(96)\qquad \Delta_{kl}(k) = \frac{1}{(2\pi)^4}\int \mathrm{d}^4\xi\; e^{ik\cdot\xi}\,\langle 0|\psi_k(\xi)\sum_X |X;P_hS_h\rangle\langle X;P_hS_h|\overline{\psi}_l(0)|0\rangle.
$$

Note that in Φ (quark production) a summation over colors is assumed, while in Δ (quark decay) an averaging over colors is assumed. The quantities Φ and Δ correspond to the blobs in fig. 4 and parametrize the soft physics, leading to the definitions of distribution and fragmentation functions [10-12]. Soft refers to all invariants of momenta being small as compared to the hard scale, *i.e.* for $\Phi(p)$ one has $p^2 \sim p\cdot P \sim P^2 = M^2 \ll Q^2$.

The fact that $p{\cdot}P$ and $k{\cdot}P_h$ are soft, allows rewriting of

$$
\begin{aligned}
\delta^4(p+q-k) &= P{\cdot}P_h\delta(p{\cdot}P_h + q{\cdot}P_h)\,\delta(P{\cdot}q - k{\cdot}P)\,\delta^2(p_T+q_T-k_T)\\
&= P{\cdot}P_h\,\delta(x-x_{\mathrm{B}})\,\delta(1/z_h - z^{-1})\,\delta^2(p_T+q_T-k_T),
\end{aligned}
$$

where we used that $x_{\text{B}} \equiv Q^2/2P{\cdot}q \approx -q{\cdot}P_h/P{\cdot}P_h$ and $z_h = -2P_h{\cdot}q/Q^2 = P{\cdot}P_h/P{\cdot}q$. Thus the semi-inclusive tensor becomes

$$(97)\quad 2M\mathcal{W}_{\mu\nu}(q;PS;P_hS_h) = \int \mathrm{d}^2p_T\,\mathrm{d}^2k_T\,\delta^2(p_T+q_T-k_T)\;\mathrm{Tr}\left(\Phi(x,p_T)\gamma_\mu\Delta(z,k_T)\gamma_\nu\right),$$

with convoluted transverse momentum dependent (TMD) correlators for distributions and fragmentation [12],

$$(98)\quad \Phi_{ij}(x,p_T;n) = \int \frac{\mathrm{d}(\xi^-)\,\mathrm{d}^2\xi_T}{(2\pi)^3}\;e^{i\,p\cdot\xi}\;\langle P|\overline{\psi}_j(0)\,\psi_i(\xi)|P\rangle\Big|_{\xi^+=0},$$

$$(99)\quad \Delta_{ij}(z,k_T;n) = \sum_X \int \frac{\mathrm{d}\xi^+\mathrm{d}^2\xi_T}{(2\pi)^3}\;e^{ik\cdot\xi}\;\mathrm{Tr}\langle 0|\psi_i(\xi)|P_h,X\rangle\langle P_h,X|\overline{\psi}_j(0)|0\rangle\Big|_{\xi^-=0},$$

where we have suppressed the hadron momenta.

In general many more diagrams have to be considered in evaluating the hadron tensors, but in the deep inelastic limit they can be neglected or considered as corrections to the soft blobs. We return to this later. One situation we want to mention here are target fragmentation parts involving matrix elements of the form $\langle PS|\psi_j(x)\sum_X|X;P_hS_h\rangle\;\langle X;P_hS_h|\psi_i(0)|PS\rangle$, known as *fracture functions.* They are relevant in the situation where $P\cdot P_h \sim M^2$ (target fragmentation region), which can be distinguished experimentally from the region we are interested in, $P\cdot P_h \sim Q^2$ (current fragmentation region).

10. – Collinear parton distributions

The form of Φ is constrained by hermiticity, parity and time-reversal invariance. The quantity depends besides the quark momentum p on the target momentum P and the spin vector S and one must have

$$(100)\qquad \text{(hermiticity)} \;\;\Rightarrow\;\; \Phi^\dagger(p,P,S) = \gamma_0\,\Phi(p,P,S)\,\gamma_0,$$

$$(101)\qquad \text{(parity)} \;\;\Rightarrow\;\; \Phi(p,P,S) = \gamma_0\,\Phi(\bar{p},\bar{P},-\bar{S})\,\gamma_0,$$

$$(102)\qquad \text{(time reversal)} \;\;\Rightarrow\;\; \Phi^*(p,P,S) = (-i\gamma_5C)\,\Phi(\bar{p},\bar{P},\bar{S})\,(-i\gamma_5C),$$

where $C = i\gamma^2\gamma_0$, $-i\gamma_5C = i\gamma^1\gamma^3$ and $\bar{p} = (p^0,-\boldsymbol{p})$.

To obtain the leading contribution in inclusive deep inelastic scattering one can integrate over the component p^- and the transverse momenta (see discussion in the section where the parton model has been derived). This integration restricts the nonlocality in $\Phi(p)$. When one wants to calculate the leading order in $1/Q$ for a hard process, one looks for leading parts in M/P^+ because $P^+ \propto Q$. The leading contribution [13] in the integrated part turns out to be proportional to $(M/P^+)^0$, given by

$$(103)\qquad \Phi(x) = \frac{1}{2}\left\{f_1(x)\,\not{n}_+ + S_L\,g_1(x)\,\gamma_5\,\not{n}_+ + h_1(x)\,\frac{\gamma_5\,[\not{S}_\perp,\not{n}_+]}{2}\right\}.$$

The precise expression of the functions $f_1(x)$, etc. as integrals over the amplitudes can be easily written down after tracing with the appropriate Dirac matrix,

$$f_1(x) = \int \frac{d\xi^-}{4\pi}\, e^{ip\cdot\xi}\, \langle P,S|\overline{\psi}(0)\gamma^+\psi(\xi)|P,S\rangle\Big|_{\xi^+=\xi_T=0}, \tag{104}$$

$$S_L\, g_1(x) = \int \frac{d\xi^-}{4\pi}\, e^{ip\cdot\xi}\, \langle P,S|\overline{\psi}(0)\gamma^+\gamma_5\psi(\xi)|P,S\rangle\Big|_{\xi^+=\xi_T=0}, \tag{105}$$

$$S_T^i\, h_1(x) = \int \frac{d\xi^-}{4\pi}\, e^{ip\cdot\xi}\, \langle P,S|\overline{\psi}(0)\, i\sigma^{i+}\gamma_5\, \psi(\xi)|P,S\rangle\Big|_{\xi^+=\xi_T=0}. \tag{106}$$

Including flavor indices, the functions $f_1^q(x) = q(x)$ and $g_1^q(x) = \Delta q(x)$ are precisely the functions that we encountered before.

The third function in the above parametrization is known as *transversity* or *transverse spin distribution* [14, 15]. Including flavor indices one also denotes $h_1^q(x) = \delta q(x)$. In the same way as we have seen for $f_1(x)$ and $g_1(x)$, the function h_1 can be interpreted as a density, but one needs instead of the projectors on quark chirality states, $P_{R/L} = \frac{1}{2}(1 \pm \gamma_5)$, those on quark transverse spin states, $P_{\uparrow/\downarrow} = \frac{1}{2}(1 \pm \gamma^i\gamma_5)$. One has

$$f_1(x) = f_{1R}(x) + f_{1L}(x) = f_{1\uparrow}(x) + f_{1\downarrow}(x), \tag{107}$$

$$g_1(x) = f_{1R}(x) - f_{1L}(x), \tag{108}$$

$$h_1(x) = f_{1\uparrow}(x) - f_{1\downarrow}(x). \tag{109}$$

This results in some trivial bounds such as $f_1(x) \geq 0$ and $|g_1(x)| \leq f_1(x)$. We already did discuss the support and charge conjugation properties of $f_1(x)$. The analysis for all these functions shows that the support is in all cases $-1 \leq x \leq 1$, while the charge conjugation properties of the functions are $\overline{f}(x) = -f(-x)$ (C-even) for f_1 and h_1 and $\overline{f}(x) = +f(-x)$ (C-odd) for g_1.

Exercise: Show that the Dirac structure for h_1 in terms of chirality states is $\overline{\psi}_R\psi_L$ and $\overline{\psi}_L\psi_R$. Such functions are called *chiral-odd*. Explain why chiral-odd functions cannot be measured in inclusive deep inelastic scattering.

11. – Bounds on the distribution functions

The trivial bounds on the distribution functions ($|h_1(x)| \leq f_1(x)$ and $|g_1(x)| \leq f_1(x)$) can be sharpened. For instance one can look explicitly at the structure in Dirac space of the correlation function Φ_{ij}. Actually, we will look at the correlation functions $(\Phi\,\gamma_0)_{ij}$, which involves at leading-order matrix elements $\psi_{+j}^\dagger(0)\psi_{+i}(\xi)$. One has in Weyl representation ($\gamma^0 = \rho^1$, $\gamma^i = -i\rho^2\sigma^i$, $\gamma_5 = i\gamma^0\gamma^1\gamma^2\gamma^3 = \rho^3$) the matrices

$$P_+ = \begin{pmatrix} 1 & 0 & 0 & 0 \\ 0 & 0 & 0 & 0 \\ 0 & 0 & 0 & 0 \\ 0 & 0 & 0 & 1 \end{pmatrix},$$

$$P_+\gamma_5 = \begin{pmatrix} 1 & 0 & 0 & 0 \\ 0 & 0 & 0 & 0 \\ 0 & 0 & 0 & 0 \\ 0 & 0 & 0 & -1 \end{pmatrix}, \qquad P_+\gamma^1\gamma_5 = \begin{pmatrix} 0 & 0 & 0 & 1 \\ 0 & 0 & 0 & 0 \\ 0 & 0 & 0 & 0 \\ 1 & 0 & 0 & 0 \end{pmatrix}.$$

The good projector only leaves two (independent) Dirac spinors, one right handed (R), one left handed (L). On this basis of good R and L spinors the for hard scattering processes relevant matrix $(\Phi\not{n}_-)$ is given by

$$(\Phi\,\not{n}_-)_{ij}(x) = \begin{pmatrix} f_1 + S_L\,g_1 & (S_T^1 + i\,S_T^2)\,h_1 \\ (S_T^1 - i\,S_T^2)\,h_1 & f_1 - S_L\,g_1 \end{pmatrix}. \tag{110}$$

One can also turn the S-dependent correlation function Φ into a matrix in the nucleon spin space via the standard spin-(1/2) density matrix $\rho(P,S)$. The relation is $\Phi(x;P,S) = \mathrm{Tr}\,[\Phi(x;P)\,\rho(P,S)]$. Writing

$$\Phi(x;P,S) = \Phi_O + S_L\,\Phi_L + S_T^1\,\Phi_T^1 + S_T^2\,\Phi_T^2, \tag{111}$$

one has on the basis of spin-(1/2) target states with $S_L = +1$ and $S_L = -1$, respectively,

$$\Phi_{ss'}(x) = \begin{pmatrix} \Phi_O + \Phi_L & \Phi_T^1 - i\,\Phi_T^2 \\ \Phi_T^1 + i\,\Phi_T^2 & \Phi_O - \Phi_L \end{pmatrix} \tag{112}$$

Exercise: Show by generalizing $\Phi(p)$ to a matrix elements between states $\langle P,s|$ and $|P,s'\rangle$ that for the matrix $M = (\Phi\not{n}_-)^T$ (transposed in Dirac space) one has $v^\dagger M v \geq 0$ for any direction v in Dirac space.

On the basis $+R$, $-R$, $+L$ and $-L$ the matrix in quark $\otimes$ nucleon spin-space becomes

$$(\Phi(x)\,\not{n}_-)^T = \begin{array}{cc} \left(\begin{array}{cccc} f_1 + g_1 & 0 & 0 & 2\,h_1 \\ 0 & f_1 - g_1 & 0 & 0 \\ 0 & 0 & f_1 - g_1 & 0 \\ 2\,h_1 & 0 & 0 & f_1 + g_1 \end{array}\right) & \begin{array}{c} \textcircled{R}\rightarrow \\ \leftarrow\textcircled{R} \\ \textcircled{L}\rightarrow \\ \leftarrow\textcircled{L} \end{array} \\ \begin{array}{cccc} \textcircled{R}\rightarrow & \leftarrow\textcircled{R} & \textcircled{L}\rightarrow & \leftarrow\textcircled{L} \end{array} & \end{array} \tag{113}$$

Of this matrix any diagonal matrix element must always be positive, hence the eigenvalues must be positive, which gives a bound on the distribution functions stronger than the trivial bounds, namely

$$|h_1(x)| \leq \frac{1}{2}\,(f_1(x) + g_1(x)) \tag{114}$$

known as the Soffer bound [16].

Exercise: Show that a change to the transverse quark spin basis gives the quark production matrix

$$(\Phi(x)\,\not{n}_-)^T = \begin{pmatrix} f_1 + h_1 & 0 & 0 & g_1 + h_1 \\ 0 & f_1 - h_1 & g_1 - h_1 & 0 \\ 0 & g_1 - h_1 & f_1 - h_1 & 0 \\ g_1 + h_1 & 0 & 0 & f_1 + h_1 \end{pmatrix} \tag{115}$$

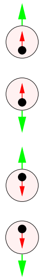

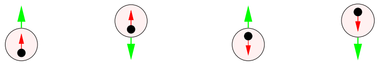

12. – Transverse-momentum–dependent correlation functions

For the TMD correlators for distributions in eq. (98) one can write down parametrizations which for the parts involving unpolarized targets (O), longitudinally polarized targets (L) and transversely polarized targets (T) up to parts proportional to M/P^+ take the form [17, 18]

$$\Phi_O(x, \boldsymbol{p}_T) = \frac{1}{2}\left\{ f_1(x, \boldsymbol{p}_T)\,\not{n}_+ + h_1^\perp(x, \boldsymbol{p}_T)\,\frac{i\,[\not{p}_T, \not{n}_+]}{2M} \right\}, \tag{116}$$

$$\Phi_L(x, \boldsymbol{p}_T) = \frac{1}{2}\left\{ S_L\, g_{1L}(x, \boldsymbol{p}_T)\,\gamma_5\,\not{n}_+ + S_L\, h_{1L}^\perp(x, \boldsymbol{p}_T)\,\frac{\gamma_5\,[\not{p}_T, \not{n}_+]}{2M} \right\}, \tag{117}$$

$$\begin{aligned} \Phi_T(x, \boldsymbol{p}_T) = \frac{1}{2}\Bigg\{ & f_{1T}^\perp(x, \boldsymbol{p}_T)\,\frac{\epsilon_{\mu\nu\rho\sigma}\gamma^\mu n_+^\nu p_T^\rho S_T^\sigma}{M}, \\ & + \frac{\boldsymbol{p}_T \cdot \boldsymbol{S}_T}{M}\, g_{1T}(x, \boldsymbol{p}_T)\,\gamma_5\,\not{n}_+ + h_{1T}(x, \boldsymbol{p}_T)\,\frac{\gamma_5\,[\not{S}_T, \not{n}_+]}{2} \\ & + \frac{\boldsymbol{p}_T \cdot \boldsymbol{S}_T}{M}\, h_{1T}^\perp(x, \boldsymbol{p}_T)\,\frac{\gamma_5\,[\not{p}_T, \not{n}_+]}{2M} \Bigg\}. \end{aligned} \tag{118}$$

All functions appearing here have a natural interpretation as densities. This is seen as discussed before for the $\boldsymbol{p}_T$-integrated functions. Now it includes densities such as the density of longitudinally polarized quarks in a transversely polarized nucleon (g_{1T}) and the density of transversely polarized quarks in a longitudinally polarized nucleon ($h_{1L}^\perp$).

Upon integration over p_T not all functions survive. We are then left with the collinear correlator in eq. (103) with $f_1(x) = \int \mathrm{d}^2p_T\ f_1(x,p_T)$, $g_1(x) = \int \mathrm{d}^2p_T\ g_{1L}(x,p_T)$ and $h_1(x) = \int \mathrm{d}^2p_T[h_{1T}(x) + \frac{\boldsymbol{p}_T^2}{2M^2}\, h_{1T}^\perp(x,p_T)]$. The explicit treatment of transverse momenta also provides also a way to include the evolution of quark distribution and fragmentation functions. The assumption that soft parts vanish sufficiently fast as a function of the invariants $p\cdot P$ and p^2, which at constant x implies a sufficiently fast vanishing as a function of $\boldsymbol{p}_T^2$, simply turns out not to be true. Assuming that the result for $\boldsymbol{p}_T^2 \geq \mu^2$ is given by the emission of an additional gluon one finds that the extra distribution written in terms of p_T becomes

$$f_1(x,\boldsymbol{p}_T^2) \overset{\boldsymbol{p}_T^2\geq\mu^2}{\Longrightarrow} \frac{1}{\pi\,\boldsymbol{p}_T^2}\,\frac{\alpha_s(\mu^2)}{2\pi}\int_x^1 \frac{\mathrm{d}y}{y}\,P_{qq}\left(\frac{x}{y}\right)\,f_1(y;\mu^2), \tag{119}$$

which gives $f_1(x;\mu^2) \equiv \pi\int_0^{\mu^2} \mathrm{d}\boldsymbol{p}_T^2\ f_1(x,\boldsymbol{p}_T^2)$ a logarithmic-scale dependence. A more detailed discussion of problems in matching small and large p_T is given in ref. [19].

Actually we find that different functions survive when one integrates over $\boldsymbol{p}_T$ weighting with p_T^α, *e.g.*,

$$\begin{aligned}\Phi_\partial^\alpha(x) &\equiv \int \mathrm{d}^2p_T\,\frac{p_T^\alpha}{M}\,\Phi(x,\boldsymbol{p}_T)\\ &= \frac{1}{2}\Bigg\{-g_{1T}^{(1)}(x)\,S_T^\alpha\,\not{n}_+\gamma_5 - S_L\,h_{1L}^{\perp(1)}(x)\,\frac{[\gamma^\alpha,\not{n}_+]\gamma_5}{2}\\ &\qquad - f_{1T}^{\perp(1)}\,\epsilon^\alpha{}_{\mu\nu\rho}\gamma^\mu n_-^\nu S_T^\rho - h_1^{\perp(1)}\,\frac{i[\gamma^\alpha,\not{n}_+]}{2}\Bigg\},\end{aligned} \tag{120}$$

involving *transverse moments* defined as

$$g_{1T}^{(1)}(x) = \int \mathrm{d}^2p_T\,\frac{\boldsymbol{p}_T^2}{2M^2}\,g_{1T}(x,\boldsymbol{p}_T), \tag{121}$$

and similarly for the other functions. The functions $h_1^\perp$ and $f_{1T}^\perp$ are *T-odd*. As we will explain in the section on color gauge invariance they do not to vanish because time reversal invariance cannot be used for the transverse moments. Also for fragmentation functions they will not vanish. The T-odd functions correspond to unpolarized quarks in a transversely polarized nucleon ($f_{1T}^\perp$) or transversely polarized quarks in an unpolarized hadron ($h_1^\perp$). The easiest way to interpret the functions is by considering their place in the quark production matrix $(\Phi(x, p_T)\, \not{n}_-)^T$, which becomes [20]

$$\begin{array}{cccc}
\text{R}\rightarrow & \leftarrow\text{R} & \text{L}\rightarrow & \leftarrow\text{L} \\
\left(\begin{array}{cccc}
f_1 + g_{1L} & \frac{|p_T|}{M}\, e^{i\phi}\, g_{1T} & \frac{|p_T|}{M}\, e^{-i\phi}\, h_{1L}^{\perp} & 2\, h_1 \\
\frac{|p_T|}{M}\, e^{-i\phi}\, g_{1T}^{*} & f_1 - g_{1L} & \frac{|p_T|^2}{M^2}\, e^{-2i\phi}\, h_{1T}^{\perp} & -\frac{|p_T|}{M}\, e^{-i\phi}\, h_{1L}^{\perp *} \\
\frac{|p_T|}{M}\, e^{i\phi}\, h_{1L}^{\perp *} & \frac{|p_T|^2}{M^2}\, e^{2i\phi}\, h_{1T}^{\perp} & f_1 - g_{1L} & -\frac{|p_T|}{M}\, e^{i\phi}\, g_{1T}^{*} \\
2\, h_1 & -\frac{|p_T|}{M}\, e^{i\phi}\, h_{1L}^{\perp} & -\frac{|p_T|}{M}\, e^{-i\phi}\, g_{1T} & f_1 + g_{1L}
\end{array}\right)
\end{array}.$$

In this representation T-odd functions can be incorporated as imaginary parts, $f_{1T}^{\perp} = -\mathrm{Im}\, g_{1T}$ and $h_1^{\perp} = \mathrm{Im}\, h_{1L}^{\perp}$.

13. – Fragmentation functions

Just as for the distribution functions one can perform an analysis of the soft part describing the quark fragmentation in eq. (99). For the production of unpolarized (or spin 0) hadrons h in hard processes one needs to leading order in $1/Q$ the $(M_h/P_h^-)^0$ part of the correlation function,

$$\Delta_O(z, \boldsymbol{k}_T) = z\, D_1(z, \boldsymbol{k}'_T)\, \not{n}_- + z\, H_1^{\perp}(z, \boldsymbol{k}'_T)\, \frac{i\, [\not{k}_T, \not{n}_-]}{2M_h}. \tag{122}$$

The arguments of the fragmentation functions D_1 and $H_1^{\perp}$ are $z = P_h^-/k^-$ and $\boldsymbol{k}'_T = -z\boldsymbol{k}_T$. The first is the (lightcone) momentum fraction of the produced hadron, the second is the transverse momentum of the produced hadron with respect to the quark. The fragmentation function D_1 is the equivalent of the distribution function f_1. It can be interpreted as a quark decay function, giving the probability of finding a hadron h in a quark. The quantity $n_h = \int \mathrm{d}z\ D_1(z)$ is the number of hadrons.

Exercise: Show that the normalization of the fragmentation functions is given by $\sum_h \int \mathrm{d}z\ z\, D_1^{q\to h}(z)$ by relating this quantity to a local operator. One needs to eliminate the hadrons in the intermediate state via the momentum operator

$$P^{\mu} = \sum_{h,X} |P_h, X\rangle\, P_h^{\mu}\, \langle P_h, X|.$$

The function $H_1^{\perp}$, interpretable as the difference between the numbers of unpolarized hadrons produced from a transversely polarized quark depending on the hadron's transverse momentum, is allowed because of the non-applicability of time reversal invariance [21]. This is natural for the fragmentation functions [22, 23] because of the appearance of out-states $|P_h, X\rangle$ in the definition of Δ, in contrast to the plane wave states appearing in Φ. The function $H_1^\perp$ is of interest because it is chiral odd. This means that it can be used to probe the chiral-odd quark distribution function h_1, which can be achieved, *e.g.*, by measuring a particular azimuthal asymmetry of produced pions in the current fragmentation region.

The spin structure of fragmentation functions is also conveniently summarized by explicitly giving it on a R and L chiral quark basis, for which we find for decay into spin-zero hadrons,

$$(\Delta(z,k_T)\not{n}_+)^T = \begin{array}{cc} \left(\begin{array}{cc} D_1 & i\,\frac{|k_T|\,e^{-i\phi}}{M_h}\,H_1^\perp \\ -i\,\frac{|k_T|\,e^{+i\phi}}{M_h}\,H_1^\perp & D_1 \end{array}\right) & \begin{array}{c} \textcircled{R} \\ \textcircled{L} \end{array} \\ \begin{array}{cc} \textcircled{R} & \textcircled{L} \end{array} & \end{array} \tag{123}$$

Examples of azimuthal asymmetries. – Transverse-momentum dependence shows up in the azimuthal dependence in the SIDIS cross-section (via $\hat{h}$ or transverse spin vectors), in most cases requiring polarization of beam and/or target or requiring polarimetry [24, 25, 3]. Examples of leading azimuthal asymmetries, appearing for polarized leptoproduction are

$$\left\langle \frac{Q_T}{M}\,\sin(\phi_h^\ell - \phi_S^\ell)\right\rangle_{OT} = \frac{2\pi\alpha^2\,s}{Q^4}\,|\boldsymbol{S}_T|\left(1 - y + \frac{1}{2}\,y^2\right)\sum_{a,\bar{a}} e_a^2\,x_{\rm B}\,f_{1T}^{\perp(1)a}(x_{\rm B})D_1^a(z_h). \tag{124}$$

$$\left\langle \frac{Q_T}{M_h}\,\sin(\phi_h^\ell + \phi_S^\ell)\right\rangle_{OT} = \frac{4\pi\alpha^2\,s}{Q^4}\,|\boldsymbol{S}_T|\,(1-y)\sum_{a,\bar{a}} e_a^2\,x_{\rm B}\,h_1^a(x_{\rm B})H_1^{\perp(1)a}(z_h). \tag{125}$$

The notation $\langle W\rangle$ is the q_T-integrated cross-section including a weight W. The factor Q_T is included, because it together with the direction $\hat{h}$ combines to q_T, allowing a defolding of the cross-section in distribution and fragmentation parts (one of them weighted with transverse momentum). Note that both of these asymmetries involve T-odd functions, which can only appear in single spin asymmetries. The latter can easily be checked from the conditions on the hadronic tensor, which are the same as those in eq. (41) to (43). They require an odd number of spins vectors entering in the symmetric part and an even number of spins entering in the antisymmetric part of the hadron tensor. The results of single spin asymmetries in SIDIS measurements on a transversely polarized target from HERMES [26] are shown in fig. 5. An extended review of transverse-momentum-dependent functions and transversity can be found in refs. [27, 4].

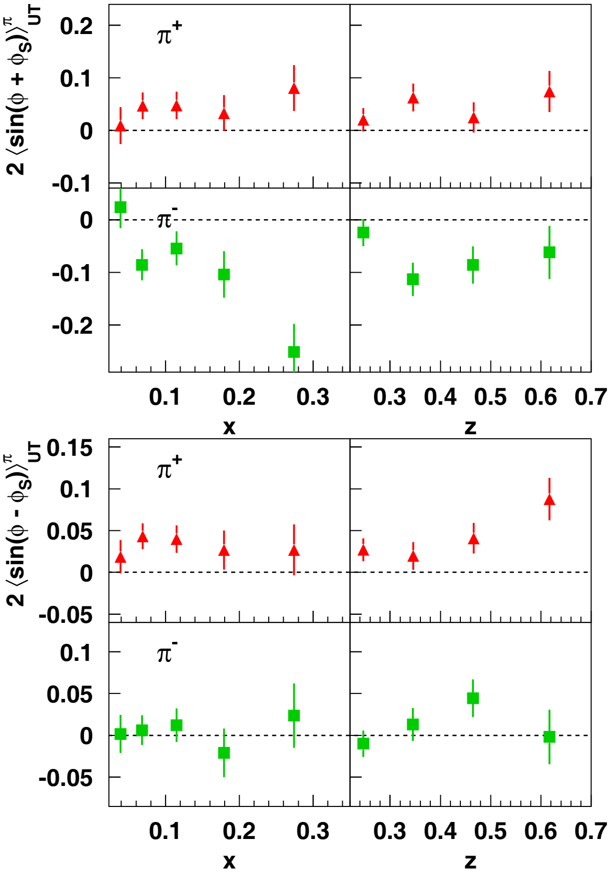

Fig. 5. – Weighted asymmetries for the Collins and Sivers angles (see eqs. (124) and (125)) obtained in semi-inclusive single spin asymmetries measured on a transversely polarized hydrogen target by the HERMES Collaboration at DESY [26]. The error bars represent the statistical uncertainties.

14. – Inclusion of subleading contributions

If one proceeds up to order $1/Q$ one also needs terms in the parametrization of the soft part proportional to M/P^+. Limiting ourselves to the $\boldsymbol{p}_T$-integrated correlations one needs [13]

$$\Phi(x) = \frac{1}{2}\left\{ f_1(x)\,\not{n}_+ + S_L\, g_1(x)\,\gamma_5\,\not{n}_+ + h_1(x)\,\frac{\gamma_5\,[\not{S}_T,\not{n}_+]}{2}\right\} + \frac{M}{2P^+}\left\{ e(x) + g_T(x)\,\gamma_5\,\not{S}_T + S_L\,h_L(x)\,\frac{\gamma_5\,[\not{n}_+,\not{n}_-]}{2}\right\}. \tag{126}$$

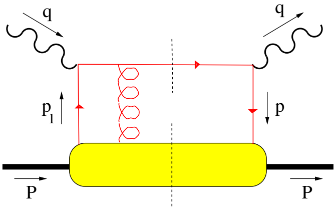

Fig. 6. – Example of a contribution involving a quark-gluon matrix element that must be included at subleading order in lepton hadron inclusive scattering.

We will use inclusive scattering off a transversely polarized nucleon ($|\boldsymbol{S}_\perp| = 1$) as an example to show how higher twist effects can be incorporated in the cross-section. The hadronic tensor for a transversely polarized nucleon is zero in leading order in $1/Q$. At order $1/Q$ one obtains a contribution from the handbag diagram, which turns out to involve the transverse moments in Φ^α_∂ in eq. (120). There is a second contribution at order $1/Q$, however, coming from diagrams as the one shown in fig. 6. For these gluon diagrams one needs bilocal matrix elements containing $1/Q$ one only needs the matrix element of the bilocal combinations $\overline{\psi}(0)\,gA^\alpha_T(\xi)\,\psi(\xi)$ and $\overline{\psi}(0)\,gA^\alpha_T(0)\,\psi(\xi)$. The $\Phi^\alpha_A(x)$ and $\Phi^\alpha_\partial(x)$ contributions sum to $\Phi^\alpha_D(x)$ involving matrix elements of bilocal combinations $\overline{\psi}(0)\,iD^\alpha_T\,\psi(\xi)$ for which one can Use the QCD equations of motion to relate them to the functions appearing in Φ [13, 28],

$$\Phi^\alpha_D(x) = \frac{M}{2}\left\{-\left(x\,g_T - \frac{m}{M}\,h_1\right) S^\alpha_T\,\not{n}_+\gamma_5 - S_L\left(x\,h_L - \frac{m}{M}\,g_1\right)\frac{[\gamma^\alpha,\not{n}_+]\gamma_5}{2}\right\}. \tag{127}$$

The distribution function g_T, *e.g.*, shows up in the corresponding structure function of polarized inclusive deep inelastic scattering

$$2M\,W^{\mu\nu}_A(q,P,S_T) = i\,\frac{2Mx_{\mathrm{B}}}{Q}\,\hat{t}^{[\mu}\epsilon_\perp^{\nu]\rho}S_{\perp\rho}\,g_T(x_{\mathrm{B}}), \tag{128}$$

leading for the structure function $g_T(x_{\mathrm{B}},Q^2)$ defined in eq. (B.9) to the result

$$g_T(x_{\mathrm{B}},Q^2) = \frac{1}{2}\sum_q e_q^2\left(g^q_T(x_{\mathrm{B}}) + g^{\bar{q}}_T(x_{\mathrm{B}})\right). \tag{129}$$

15. – Color gauge invariance

We have sofar disregarded two issues. The first issue is that the correlation function Φ discussed in previous sections involve two quark fields at different space-time points and hence are not color gauge invariant. The second issue are the gluonic diagrams similar as the ones we have discussed in the previous section (see fig. 6), among which

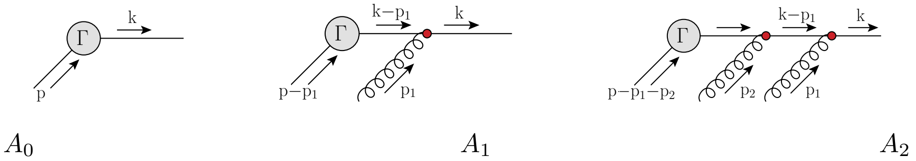

Fig. 7. – Inclusion of collinear gluons from $\Phi_{A\ldots A}(p - p_1 \ldots - p_N, p_1, \ldots, p_N)$ coupling to an outgoing (colored) quark line with momentum k results in a Wilson line running from the point ξ in field $\psi(\xi)$ to the point where $\xi^- = \infty$.

also correlation functions appear involving matrix elements with longitudinal (A^+) gluon fields,

$$\overline{\psi}_j(0)\, gA^+(\eta)\, \psi_i(\xi).$$

These do not lead to any suppression. The reason is that because of the +-index in the gluon field the matrix element is proportional to P^+, p^+ or $M\,S^+$ rather than the proportionality to $M\,S_T^\alpha$ or p_T^α that one gets for a gluonic matrix element with transverse gluons.

A straightforward calculation, however, shows that the gluonic diagrams with one or more longitudinal gluons involve matrix elements (soft parts) of operators $\overline{\psi}\psi$, $\overline{\psi}\,A^+\,\psi$, $\overline{\psi}\,A^+A^+\,\psi$, etc. (see fig. 7) can be resummed into a correlation function

$$\Phi_{ij}(x) = \int \frac{d\xi^-}{2\pi}\; e^{ip\cdot\xi}\, \langle P,S|\overline{\psi}_j(0)\, U_{[0,\xi]}\, \psi_i(\xi)|P,S\rangle\bigg|_{\xi^+=\xi_T=0}, \tag{130}$$

where U is a gauge link operator [29, 28, 30-32]

$$U_{[0,\xi]} = \mathcal{P}\exp\left[-i\int_0^{\xi^-} d\zeta^-\, A^+(\zeta)\right] \tag{131}$$

(path-ordered exponential with path along the "minus" direction). *Et voilà*, the unsuppressed gluonic diagrams combine into a color gauge-invariant correlation function [33, 34]. We note that at the level of operators, one expands

$$\overline{\psi}(0)\psi(\xi) = \sum_n \frac{\xi^{\mu_1}\ldots\xi^{\mu_n}}{n!}\,\overline{\psi}(0)\partial_{\mu_1}\ldots\partial_{\mu_n}\psi(0), \tag{132}$$

in a set of local operators, but only the expansion of the non-local combination with a gauge link

$$\overline{\psi}(0)\, U_{[0,\xi]}\, \psi(\xi) = \sum_n \frac{\xi^{\mu_1}\ldots\xi^{\mu_n}}{n!}\,\overline{\psi}(0)D_{\mu_1}\ldots D_{\mu_n}\psi(0), \tag{133}$$

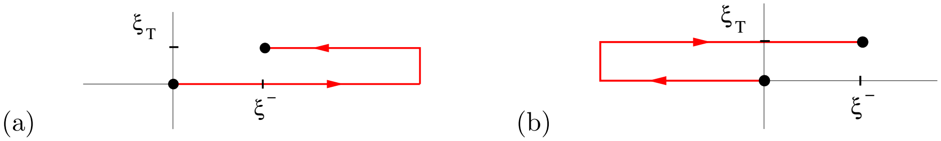

Fig. 8. – The gauge link structure in the quark-quark correlator Φ in SIDIS (a) and DY (b), respectively.

is an expansion in terms of local gauge invariant operators. The latter operators are precisely the local (quark) operators that appear in the operator product expansion applied to inclusive deep inelastic scattering.

For the p_T-dependent functions, one finds that inclusion of A^+ gluonic diagrams leads to a color gauge-invariant matrix element with links running via $\xi^= = \pm\infty$ [35,36] where the direction depends on the coupling of the gluons to a final-state or initial-state color line. For instance in lepton-hadron scattering one has a situation like the one in fig. 7 and one finds

$$\Phi^{[+]}(x, \boldsymbol{p}_T) = \int \frac{d\xi^- d^2\boldsymbol{\xi}_T}{(2\pi)^3}\, e^{ip\cdot\xi}\, \langle P,S|\overline{\psi}(0)\, U^{[+]}_{[0,\xi]}\, \psi(\xi)|P,S\rangle\Big|_{\xi^+=0}\,, \tag{134}$$

where the link $U^{[+]}$ is shown in fig. 8a. In contrast, for Drell-Yan scattering one finds a gauge link that runs via minus infinity, involving the link in fig. 8b. We note that the gauge link involves transverse gluons [29,28] showing that one in processes involving more hadrons the effects of transverse gluons are not necessarily suppressed, as has also been shown in explicit model calculations [37]. Integration over transverse momenta implies in the correlator, which is a Fourier transform that $\xi_T = 0_T$, in which case the $U^{[+]}$ and $U^{[-]}$ links reduce to a unique collinear link connecting 0 and ξ^-.

The transverse-momentum–dependent distribution functions, however, do depend on the gauge link structure, which is still tractable in simple processes like DIS or DY with a simple color flow, but the color structure of various correlators become entangled if the color flow is more complicated [30-32].

Even if the color flow is simple, like SIDIS or DY, there are effects. Most notable is a sign change in single spin asymmetries going from SIDIS to DY. To understand this sign change, one notes that TMDs are no longer constrained by time reversal, as the time reversal operation interchanges the $U^{[+]}$ and $U^{[-]}$ links, leading to the appearance of T-odd functions in eqs. (116)-(118) and also occurring in eq. (120). One has, *e.g.*,

$$\Phi_O^{[\pm]}(x, \boldsymbol{p}_T) = \frac{1}{2}\left\{ f_1(x, \boldsymbol{p}_T)\, \not{n}_+ \pm h_1^\perp(x, \boldsymbol{p}_T)\, \frac{i\,[\not{p}_T, \not{n}_+]}{2M} \right\}. \tag{135}$$

Looking back at our example of an azimuthal asymmetry, we have seen the $\sin(\phi_h^\ell - \phi_S^\ell)$ asymmetry proportional to $f_{1T}^\perp D_1$. The corresponding asymmetry in Drell-Yan proportional to $f_{1T}^\perp \overline{f}_1$ would get an additional minus sign. Actually for the fragmentation correlator, such as Δ_O in eq. (122) there is no such dependence on the gauge link [38-40]. The function $H_1^\perp$, however, is nonzero because the states $|P_h, X\rangle$ in the case of fragmentation are out-states and time reversal (changing out- into in-states) simply cannot be used as a constraint. The asymmetry in eq. (125) thus will not change sign going from SIDIS to the corresponding DY asymmetry. In general situations in which one has a convolution of TMD distribution functions of two hadrons in the initial state, factorization is, already at tree-level hampered by the entanglement of Wilson lines [41, 42]. At the level of the weighted asymmetries, it implies more complicated factors than just a sign change in the appearance of the weighted functions.

Gluonic pole matrix elements. – The inclusion of gauge links also allows us to study in some more detail the operator structure of the T-odd parts in the correlators. Given the full operator structure for a TMD correlator including a gauge links $U^{[\pm]}$ one can explicitly calculate the transverse moments $\Phi_\partial^\alpha(x)$ of which we have given the parametrization in eq. (120). One finds that they, depending on the gauge links, can be related to color gauge invariant quark-quark-gluon matrix elements Φ_G^α and Φ_D^α,

$$\begin{aligned}\left(\Phi_\partial^{[\pm]\alpha}\right)_{ij}(x) &= \int \mathrm{d}^2p_T \int \frac{\mathrm{d}\xi^-\mathrm{d}^2\boldsymbol{\xi}_\perp}{(2\pi)^3}\; e^{i\,p\cdot\xi}\,\langle P,S|\overline{\psi}_j(0)\,U^-_{[0,\pm\infty]}U^T_{[0_T,\pm\infty_T]}\\ &\qquad\qquad \times i\partial_\xi^\alpha\, U^T_{[\pm\infty_T,\xi_T]}U^-_{[\pm\infty,\xi]}\,\psi_i(\xi)|P,S\rangle\Big|_{\xi^+=0}\\ &= \int \frac{\mathrm{d}\xi^-}{(2\pi)}\; e^{ip\cdot\xi}\Big\{\langle P,S|\overline{\psi}_j(0)\,U^-_{[0,\xi]}\,iD_T^\alpha\psi_i(\xi)|P,S\rangle\Big|_{\mathrm{LC}}\\ &\quad - \langle P,S|\overline{\psi}_j(0)\,U^-_{[0,\pm\infty]}\int_{\pm\infty}^{\xi^-}\mathrm{d}\eta^-\;U^-_{[\pm\infty,\eta]}\,g\,G^{+\alpha}(\eta)\,U^-_{[\eta,\xi]}\,\psi_i(\xi)|P,S\rangle\Big|_{\mathrm{LC}}\Big\},\end{aligned}$$

or

$$\Phi_\partial^{[\pm]\,\alpha}(x) = \Phi_D^\alpha(x) - \int_{-\infty}^{\infty}\mathrm{d}p_1^+\;\frac{i}{p_1^+\mp i\epsilon}\,\Phi_G^\alpha(p^+,p^+-p_1^+), \tag{136}$$

where

$$\Phi^\alpha_{D\,ij}(x) = \int\frac{\mathrm{d}\xi^-}{2\pi}\; e^{i\,p\cdot\xi}\langle P,S|\overline{\psi}_j(0)\,U^-_{[0,\xi]}\,iD^\alpha(\xi)\psi_i(\xi)|P,S\rangle\Big|_{\mathrm{LC}}. \tag{137}$$

The difference between correlation functions with links running to ±∞, respectively, is related to a collinear quark-gluon correlator,

$$\Phi_\partial^{[+]\alpha}(x) - \Phi_\partial^{[-]\alpha}(x) = 2\pi\,\Phi_G^\alpha(x,x), \tag{138}$$

the latter being given the name *gluonic-pole* matrix element since it corresponds to the soft-gluon point $p_1^+ = 0$. It is a collinear matrix element which has been extensively studied [43-50] as a collinear mechanism to generate single spin asymmetries. With the definition

$$\Phi_A^\alpha(x) = \mathrm{PV}\int_{-\infty}^{\infty} \mathrm{d}p_1^+ \, \frac{i}{p_1^+} \, \Phi_G^\alpha(p^+, p^+ - p_1^+), \tag{139}$$

one gets a separation

$$\Phi_\partial^{[\pm]\,\alpha}(x) = \underbrace{\Phi_D^\alpha(x) - \Phi_A^\alpha(x)}_{\widetilde{\Phi}_\partial^\alpha} \pm \pi \, \Phi_G^\alpha(x,x), \tag{140}$$

into T-even and T-odd parts.

16. – Gluon TMDs

Except in higher twist matrix elements and in gauge links, gluon fields also appear in the gluon distribution functions. To better understand the treatment of gluon fields, we also make for gluon fiels $A^\mu(\eta)$ a Sudakov expansion,

$$A^\mu(\eta) = A^n(\eta)\, P^\mu + A_T^\mu(\eta) + \big(A^P(\eta) - A^n(\eta)\, M^2\big)\, n^\mu. \tag{141}$$

A similar expansion can be written down for $A^\mu(p)$. It will be convenient to look at the (collinear) gluon field component along parton momentum p^μ, hence we write

$$\begin{aligned} A^\mu(p) &= \int \mathrm{d}^4\eta \; e^{i\,p\cdot\eta}\, A^\mu(\eta) \\ &= \int \mathrm{d}^4\eta \; e^{ip\cdot\eta} \left[\frac{A^n(\eta)}{p{\cdot}n}\, p^\mu + \frac{(p{\cdot}n)\, A_T^\mu(\eta) - p_T^\mu\, A^n(\eta)}{p{\cdot}n} \right. \\ &\qquad \left. + \frac{(p{\cdot}n)\, A^P(\eta) - (p{\cdot}P)\, A^n(\eta)}{p{\cdot}n}\, n^\mu \right]. \end{aligned} \tag{142}$$

In the correlator the momentum $p^\mu \longrightarrow i\partial^\mu(\eta)$, so

$$A^\mu(p) = \frac{1}{p{\cdot}n} \int \mathrm{d}^4\eta \; e^{i\,p\cdot\eta} \Big[A^n(\eta)\, p^\mu + i\partial^n(\eta)\, A_T^\mu(\eta) - i\partial_T^\mu(\eta)\, A^n(\eta) + \big(i\partial^n(\eta) A^P(\eta) - i\partial^P(\eta) A^n(\eta)\big)\, n^\mu \Big] \tag{143}$$

$$= \frac{1}{p{\cdot}n} \left[A^n(p)\, p^\mu + i\, G_T^{n\mu}(p) + i\, G^{nP}(p)\, n^\mu \right]. \tag{144}$$

Although the latter appears to be only true for the Abelian case, we will find the same result in the non-Abelian case, but to complete that proof, we first need to incorporate

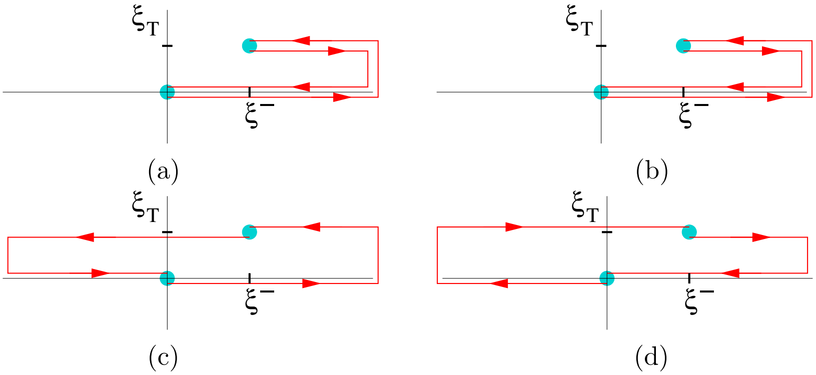

(a) (b)

(c) (d)

Fig. 9. – The gauge links for gluon TMDs.

the collinear gluons into the matrix elements as gauge links. For that we need the $A^n(p)$ gluons and actually also some boundary terms (shown very explicitly in ref. [42]). Using the expansion in eq. (144) rather than the one in eq. (141) streamlines the inclusion of collinear gluons, because one can immediately make use of Ward identities. It circumvents the explicit treatment of transverse-momentum–dependent parts (as done in ref. [28]). The results are of course identical.

Rather than transverse gluon fields one thus encounters $G^{n\alpha}$ field strengths in the matrix elements, as we saw explicitly already in the previous section. Transverse-momentum–dependent gluon distribution functions are projections of the TMD correlator Γ (often also referred to as Φ^g)

$$\Gamma^{[U,U']\,\mu\nu}(x,p_T) = \frac{1}{(p{\cdot}n)^2}\int \frac{\mathrm{d}(\xi{\cdot}P)\,\mathrm{d}^2\xi_T}{(2\pi)^3}\,e^{ip\cdot\xi} \times \mathrm{Tr}\,\langle P,S|\,F^{n\mu}(0)\,U_{[0,\xi]}\,F^{n\nu}(\xi)\,U'_{[\xi,0]}\,|P,S\rangle\,\big\rfloor_{\mathrm{LF}}. \tag{145}$$

Here the field-operators are written in the color-triplet representation requires the inclusion of *two* Wilson lines $U_{[0,\xi]}$ and $U'_{[\xi,0]}$. They again arise from the resummation of gluon initial- and final-state interactions. In general this will lead to two unrelated Wilson lines U and U'. In the particular case that $U' = U^\dagger$, the gluon correlator can also be written as the product of two gluon fields with the Wilson line U in the adjoint representation of $SU(N)$. This is for instance the case for the gluon correlators which acquire gaugelinks as in figs. 9a and b, but not for the gluon correlators in figs. 9c and d.

In the p_T-integrated correlator on the lightcone the process dependence of the TMD gluon correlator disappears,

$$\begin{aligned}\Gamma^{\mu\nu}(x) &= \int \mathrm{d}^2p_T\Gamma^{[U,U']\,\mu\nu}(x,p_T)\\ &= \frac{1}{(p{\cdot}n)^2}\int \frac{\mathrm{d}(\xi{\cdot}P)}{2\pi}e^{ix(\xi\cdot P)}\,\mathrm{Tr}\langle P,S|F^{n\mu}(0)U^n_{[0,\xi]}F^{n\nu}(\xi)U^n_{[\xi,0]}|P,S\rangle\big\rfloor_{\mathrm{LC}}.\end{aligned} \tag{146}$$

However, as for the quark correlator, a subprocess-dependence due to the Wilson lines in the TMD gluon correlators remains in the transverse moments. The analogue of the process-dependent decomposition in the case of the gluon correlator is (with for each diagrammatic contribution d a TMD correlator $\Gamma^{[\mathcal{U},\mathcal{U}']}(x{,}p_T) = \Gamma^{[\mathcal{U}(D),\mathcal{U}'(D)]}(x{,}p_T) \equiv \Gamma^{[D]}(x{,}p_T)$ and omitting the gluon field indices μ and ν) [51],

$$\Gamma_{\partial}^{[D]\,\alpha}(x) = \widetilde{\Gamma}_{\partial}^{\alpha}(x) + C_G^{(f)\,[D]}\,\pi\Gamma_{G_f}^{\alpha}(x{,}x) + C_G^{(d)\,[D]}\,\pi\Gamma_{G_d}^{\alpha}(x{,}x). \tag{147}$$

The matrix elements Γ_{G_f} and Γ_{G_d} are the two gluonic pole matrix elements that correspond to the two possible ways to construct color-singlets from three gluon fields [52,51]. They involve the antisymmetric f and symmetric d structure constants of $SU(3)$, respectively. The only process dependence coming from the Wilson lines in the TMD correlators is contained in the gluonic pole strengths $C_G^{(f/d)\,[D]} \equiv C_G^{(f/d)\,[\mathcal{U}(D),\mathcal{U}'(D)]}$. The collinear correlators are

$$\begin{aligned}
\Gamma_D^{\mu\nu;\alpha}(x) &= \frac{1}{(p{\cdot}n)^2}\int\frac{\mathrm{d}(\xi{\cdot}P)}{2\pi}\;e^{ix(\xi\cdot P)} \\
&\qquad\times \mathrm{Tr}\,\langle P{,}S|\,F^{n\mu}(0)\,U_{[0;\xi]}^{n}\,\big[iD^{\alpha}(\xi),F^{n\nu}(\xi)\big]\,U_{[\xi;0]}^{n}\,|P{,}S\rangle\,\big\rfloor_{\mathrm{LC}}, \\
\Gamma_{G_f}^{\mu\nu;\alpha}(x,x{-}x') &= \frac{1}{(p{\cdot}n)^2}\int\frac{\mathrm{d}(\xi{\cdot}P)}{2\pi}\frac{\mathrm{d}(\eta{\cdot}P)}{2\pi}\;e^{ix'(\eta\cdot P)}e^{i(x-x')(\xi\cdot P)} \\
&\qquad\times \mathrm{Tr}\,\langle P{,}S|\,F^{n\mu}(0)\,\big[U_{[0,\eta]}^{n}gF^{n\alpha}(\eta)U_{[\eta,0]}^{n},U_{[0,\xi]}^{n}F^{n\nu}(\xi)U_{[\xi,0]}^{n}\big]\,|P{,}S\rangle\,\big\rfloor_{\mathrm{LC}}, \\
\Gamma_{G_d}^{\mu\nu;\alpha}(x,x{-}x') &= \frac{1}{(p{\cdot}n)^2}\int\frac{\mathrm{d}(\xi{\cdot}P)}{2\pi}\frac{\mathrm{d}(\eta{\cdot}P)}{2\pi}\;e^{ix'(\eta\cdot P)}e^{i(x-x')(\xi\cdot P)} \\
&\qquad\times \mathrm{Tr}\,\langle P{,}S|\,F^{n\mu}(0)\,\big\{U_{[0,\eta]}^{n}gF^{n\alpha}(\eta)U_{[\eta,0]}^{n},U_{[0,\xi]}^{n}F^{n\nu}(\xi)U_{[\xi,0]}^{n}\big\}\,|P{,}S\rangle\,\big\rfloor_{\mathrm{LC}},
\end{aligned}$$

and

$$\widetilde{\Gamma}_{\partial}^{\alpha}(x) = \Gamma_D^{\alpha}(x) - \int \mathrm{d}x'\;P\frac{i}{x'}\;\Gamma_{G_f}^{\alpha}(x,x{-}x'). \tag{148}$$

For gluon distribution functions we follow the naming convention discussed in ref. [53] and use the parameterizations of the TMD gluon correlators in ref. [54]

$$\begin{aligned}
\Gamma^{(T\text{-even})\,\mu\nu}(x{,}p_T) &= \frac{1}{2x}\bigg\{-g_T^{\mu\nu}\,f_1^g(x{,}p_T^2) + \left(\frac{p_T^{\mu}p_T^{\nu}}{M^2} + g_T^{\mu\nu}\frac{\boldsymbol{p}_T^2}{2M^2}\right)h_1^{\perp g}(x{,}p_T^2) \\
&\qquad + i\epsilon_T^{\mu\nu}S_L\;g_{1L}^g(x{,}p_T^2) + i\epsilon_T^{\mu\nu}\,\frac{\boldsymbol{p}_T{\cdot}\boldsymbol{S}_T}{M}\;g_{1T}^g(x{,}p_T^2)\bigg\}, \\
\Gamma_{(f/d)}^{(T\text{-odd})\,\mu\nu}(x{,}p_T) &= \frac{1}{2x}\bigg\{g_T^{\mu\nu}\frac{\epsilon_T^{p_TS_T}}{M}\;f_{1T}^{\perp g\,(f/d)}(x{,}p_T^2) - \frac{\epsilon_T^{p_T\{\mu}S_T^{\nu\}}+\epsilon_T^{S_T\{\mu}p_T^{\nu\}}}{4M}\;h_{1T}^{g\,(f/d)}(x{,}p_T^2) \\
&\qquad - \frac{\epsilon_T^{p_T\{\mu}p_T^{\nu\}}}{2M^2}S_L\;h_{1L}^{\perp g\,(f/d)}(x{,}p_T^2) - \frac{\epsilon_T^{p_T\{\mu}p_T^{\nu\}}}{2M^2}\frac{\boldsymbol{p}_T{\cdot}\boldsymbol{S}_T}{M}\;h_{1T}^{\perp g\,(f/d)}(x{,}p_T^2)\bigg\}.
\end{aligned}$$

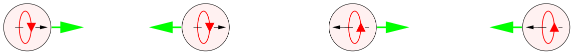

$$\left(\begin{array}{cccc}
f_1 + g_{1L} & \frac{p_T e^{-i\phi}}{M}\, g_{1T}^* & e^{-2i\phi}\, h_1^{\perp\,\prime} & i\frac{k_T e^{-3i\phi}}{M} h_{1T}^{\perp(1)} \\
\frac{k_T e^{+i\phi}}{M}\, g_{1T} & f_1 - g_{1L} & \frac{ik_T e^{-i\phi}}{M}\, h_1 & e^{-2i\phi}\, h_1^{\perp(1)\,*} \\
e^{+2i\phi}\, h_1^{\perp(1)\,*} & \frac{-ik_T e^{+i\phi}}{M}\, h_1 & f_1 - g_{1L} & \frac{k_T e^{-i\phi}}{M}\, g_{1T}^* \\
-i\frac{k_T e^{+3i\phi}}{M} h_{1T}^{\perp(1)} & e^{+2i\phi}\, h_1^{\perp(1)} & \frac{k_T e^{+i\phi}}{M}\, g_{1T} & f_1 + g_{1L}
\end{array}\right)$$

Fig. 10. – Illustration of the rich structure when one includes spin and transverse-momentum dependence for gluon distribution (or fragmentation) functions. Given are matrix elements involving gluonic fields with different helicities (two possibilities) between proton states with different helicities (two possibilities). On top the basis entities are given, with inside the circle the gluon helicity. In this representation T-odd functions appear as imaginary entries, which are only allowed in off-diagonal elements, in particular $f_{1T}^{\perp} = -\mathrm{Im} g_{1T}$ and $h_{1L}^{\perp} = -\mathrm{Im} h_1^{\perp}$. All functions depend on longitudinal momentum fraction (x) and absolute value of transverse momentum (k_T). The angle ϕ is the azimuthal angle of the transverse momentum vector. The notation $h_1^{\perp(1)}(x,k_T^2) \equiv (k_T^2/2M^2)\, h_1^{\perp}(x,k_T^2)$ is used and $h_1 \equiv h_{1T} + h_{1T}^{\perp(1)}$. A gluon index ($g$) used in the text is omitted from all functions. The functions $f_{1..}$ and $g_{1..}$ are sum and difference of matrix elements of gluon fields with different circular polarization, while the functions $h_{1..}$ involve gluon fields with different polarizations (becoming diagonal elements if one uses linear polarization). Finally the subscripts L and T indicate the polarization of the nucleon states between which the gluon field operators are evaluated. On the chosen helicity basis matrix elements between transversely polarized nucleons are off-diagonal.

Its spin structure is also illustrated in fig. 10. We note that one has two distinct gluon-Sivers distribution functions $f_{1T}^{\perp\,g\,(f)}(x,p_T^2)$ and $f_{1T}^{\perp\,g\,(d)}(x,p_T^2)$ corresponding to the two ways to construct T-odd gluon correlators.

17. – Concluding remarks

The material in these lectures is just a selection from the work that is going on in the field of TMDs. We have tried to focus on some basics, which is the structure of the matrix elements. We have not addressed the rich phenomenology of azimuthal asymmetries [24, 25, 3, 4]. Neither have we addressed aspects going beyond tree-level, which is important to get to the full field theoretical treatment of TMDs including evolution [55, 56].

* * *

This work is part of research programs of the foundation for Fundamental Research of Matter (FOM) and the National Organization for Scientific Research (NWO) as well as the FP 7 EU-program Hadron Physics (No. 227431). Most figures were made using Jaxodraw [57, 58].

Appendix A.

What information is in the form factors

We look here specifically at the space-like form factors discussed above, with $q = P' - P$ and $q^2 = -Q^2$. We have already introduced the time-like vector $\hat{t}^\mu$, which in this case is proportional to $T^\mu = P^\mu + P'^\mu$, thus $q \cdot \hat{t} = 0$. Any four-vector can be expanded as $a = (a \cdot \hat{t})\,\hat{+}\boldsymbol{a}$ and one has specifically $q = \boldsymbol{q}$. A further specification of the spacelike direction (z-direction or transverse) is at this stage not needed, but may for specific applications be useful. The frame in which $\hat{t} = (1, 0, 0, 0)$ is known as the Breit frame or the Brick-Wall frame.

Working out the current expression for the nucleon with the above definition of zero and space-like components (or if one likes in the Breit frame) with $P'^0 = P^0$, $\boldsymbol{P} = -\boldsymbol{q}/2$, $\boldsymbol{P}' = +\boldsymbol{q}/2$, gives

$$\text{(A.1)} \qquad \langle P', S' | J_0^{\text{em}}(0) | P, S \rangle = 2M \left[F_1 - \frac{Q^2}{4M^2}\, F_2 \right] \equiv 2M\, G_E(Q^2),$$

$$\text{(A.2)} \qquad \langle P', S' | \boldsymbol{J}^{\text{em}}(0) | P, S \rangle = [F_1 + F_2]\ (i\boldsymbol{\sigma}_N \times \boldsymbol{q}) \equiv G_M(Q^2)\, (i\boldsymbol{\sigma}_N \times \boldsymbol{q}),$$

where $\chi_{S'}^\dagger\, \boldsymbol{\sigma}\, \chi_S \ \equiv\ \boldsymbol{\sigma}_N$. These expressions show the relevance of the Sachs form factors G_E and G_M. The quantity $e\, G_E(0)$ is the charge Q of the nucleon, $e\, G_M(0)/M$ is the magnetic moment of the nucleon. The quantity $\kappa = G_M(0) - Q = G_M(0) - G_E(0)$ is the anomalous magnetic moment. Following eqs. (19) one has the forward matrix elements

$$\text{(A.3)} \qquad \langle P, S' | J_0^{\text{em}}(0) | P, S \rangle = 2M\, F_1(0) = 2M\, G_E(0),$$

$$\text{(A.4)} \qquad \langle P, S' | (\boldsymbol{r} \times \boldsymbol{J}^{\text{em}})(0) | P, S \rangle = [F_1(0) + F_2(0)]\ \boldsymbol{\sigma}_N = G_M(0)\, \boldsymbol{\sigma}_N.$$

For an elementary fermion one has $F_1(Q^2) = 1$ and $F_2(Q^2) = 0$. For the nucleon one has for the proton $F_1^p(0) = Q_p = 1$ and $F_2^p(0) = \kappa_p = 1.793$ and for the neutron $F_1^n(0) = Q_n = 1$ and $F_2^n(0) = \kappa_n = -1.913$. Roughly one has for nucleons the dipole-like behavior

$$\text{(A.5)} \qquad G_E^p(Q^2) \approx \frac{G_M^p}{\mu_p} \approx \frac{G_M^n}{\mu_n} \approx \frac{1}{(1 + Q^2/\Lambda^2)^2}\,,$$

with $\Lambda^2 \ \approx 0.71\,\text{GeV}^2$ and $\mu_N = G_M^N(0) = Q_N + \kappa_N$ is the nucleon magnetic moment.

We note that for the (diagonal) vector currents for the quarks, $V_\mu^q = \overline{\psi}^q \gamma_\mu \psi^q$, the quantities $F_1^q(0)$ are (by definition) the quark numbers $F_1^q(0) = n_q$. The matrix element of the electromagnetic current J_μ^{em} in eq. (57) then indeed satisfying $F_1^{em}(0) = Q$ (the charge of the hadron state).

Appendix B.

Polarized leptoproduction

For spin-polarized leptons in the initial state we have

$$\text{(B.1)}\qquad \begin{aligned} L^{(s)}_{\mu\nu} &= \mathrm{Tr}\left[\gamma_\mu(\not k' + m)\gamma_\nu(\not k + m)\,\frac{1 \pm \gamma_5\,\not s)}{2}\right] \\ &= 2\,k_\mu k'_\nu + 2\,k'_\mu k_\nu - Q^2\,g_{\mu\nu} \pm 2i\,m\,\epsilon_{\mu\nu\rho\sigma}q^\rho s^\sigma . \end{aligned}$$

Note that for light particles or particles at high energies helicity states ($\hat{s} = \hat{\boldsymbol{k}}$) become chirality eigenstates. For $L_{\mu\nu}$ the equivalence is easily seen because for $s^\mu = (|\boldsymbol{k}|/m, E\hat{\boldsymbol{k}}/m)$ ($s^2 = -1$ and $s \cdot p = 0$) one obtains in the limit $E \approx |\boldsymbol{k}|$ the result $m\,s^\mu \approx k^\mu$. Then the leptonic tensor for helicity states ($\lambda_e = \pm$) becomes

$$\text{(B.2)}\qquad L^{(\lambda_e = \pm 1/2)}_{\mu\nu} \approx L^{(R/L)}_{\mu\nu} = L^{(S)}_{\mu\nu} + \lambda_e\,L^{(A)}_{\mu\nu},$$

where the antisymmetric lepton tensor is given by

$$\text{(B.3)}\qquad L^{(A)}_{\mu\nu}(k,k') = \mathrm{Tr}\,\left[\gamma_\mu\gamma_5\not k'\gamma_\nu\not k\right] = 2i\,\epsilon_{\mu\nu\rho\sigma}q^\rho k^\sigma .$$

Expanding in the Cartesian set $\hat{t}, \hat{z}$ and the vector $\hat{\ell}$ in the same way as for the symmetric part, we have for the antisymmetric part of the leptonic tensor(³) the result

$$\text{(B.4)}\qquad L^{\mu\nu\,(A)} = \frac{Q^2}{y^2}\left[-i\,y(2-y)\,\epsilon_\perp^{\mu\nu} - 2i\,y\sqrt{1-y}\;\hat{t}^{\,[\mu}\epsilon_\perp^{\nu]\rho}\hat{\ell}_\rho\right].$$

One can use polarized leptons in deep inelastic $\vec{e}p \to X$ to probe the antisymmetric tensor for unpolarized hadrons, containing the F_3 structure function. This contribution comes in via the interference between the γ and Z interference term.

In the situation where the target is polarized, one has several more structure functions as compared to the case of an unpolarized target. For a spin-(1/2) particle the initial state is described by a 2-dimensional spin density matrix $\rho = \sum_\alpha |\alpha\rangle p_\alpha \langle\alpha|$ describing the probabilities p_α for a variety of spin possibilities. This density matrix is Hermitean

---

(³) A useful relation is

$$\epsilon_{\mu\nu\rho\sigma}\,g_{\alpha\beta} = \epsilon_{\alpha\nu\rho\sigma}\,g_{\mu\beta} + \epsilon_{\mu\alpha\rho\sigma}\,g_{\nu\beta} + \epsilon_{\mu\nu\alpha\sigma}\,g_{\rho\beta} + \epsilon_{\mu\nu\rho\alpha}\,g_{\sigma\beta}$$

or for a vector $a_\perp$ orthogonal to $\hat{t}$ and $\hat{q}$,

$$\begin{aligned} \epsilon^{\mu\nu\rho\sigma}\hat{z}_\rho a_{\perp\sigma} &= \hat{t}^{\,[\mu}\epsilon_\perp^{\nu]\rho}a_{\perp\rho}, \\ \epsilon^{\mu\nu\rho\sigma}\hat{t}_\rho a_{\perp\sigma} &= -\hat{z}^{\,[\mu}\epsilon_\perp^{\nu]\rho}a_{\perp\rho}. \end{aligned}$$

with $\mathrm{Tr}\,\rho = 1$. It can in the target rest frame be expanded in terms of the unit matrix and the Pauli matrices,

$$\rho_{ss'} = \frac{1}{2}\left(1 + \boldsymbol{S}\cdot\boldsymbol{\sigma}_{ss'}\right), \tag{B.5}$$

where $\boldsymbol{S}$ is the spin vector. When $|\boldsymbol{S}| = 1$ one has a pure state (only one state $|\alpha\rangle$ and $\rho^2 = \rho$), when $|\boldsymbol{S}| \le 1$ one has an ensemble of states. For the case $|\boldsymbol{S}| = 0$ one has simply an averaging over spins, corresponding to an unpolarized ensemble. To include spin one could generalize the hadron tensor to a matrix in spin space, $\tilde{W}^{\mu\nu}_{s's}(q,P) \propto \langle P, s'|J^\mu|X\rangle\langle X|J^\nu|P, s>$ depending only on the momenta or one can look at the tensor $\sum_\alpha p_\alpha \tilde{W}^{\mu\nu}_{\alpha\alpha}(q,P)$. The latter is given by

$$W^{\mu\nu}(q,P,S) = \mathrm{Tr}\left(\rho(P,S)\tilde{W}^{\mu\nu}(q,P)\right), \tag{B.6}$$

with the spacelike spin vector S appearing *linearly* and in an arbitrary frame satisfying $P\cdot S = 0$. It has invariant length $-1 \le S^2 \le 0$. It is convenient to write

$$S^\mu = \frac{S_L}{M}\left(P^\mu - \frac{M^2}{P\cdot q}\,q^\mu\right) + S^\mu_\perp, \tag{B.7}$$

with

$$S_L \equiv \frac{M\,(S\cdot q)}{(P\cdot q)}. \tag{B.8}$$

For a pure state one has $S_L^2 + \boldsymbol{S}_\perp^2 = 1$. Parity requires that the polarized part of the tensor, *i.e.* the part containing the spin vector, enters in an antisymmetric tensor of the form

$$\begin{aligned} M\,W^{\mu\nu\,(A)}(q,P,S) &= S_L\,\frac{i\epsilon^{\mu\nu\rho\sigma}q_\rho P_\sigma}{(P\cdot q)}\,g_1 + \frac{M}{P\cdot q}\,i\epsilon^{\mu\nu\rho\sigma}q_\rho S_{\perp\sigma}\,(g_1+g_2) \\ &= -iS_L\,\epsilon_\perp^{\mu\nu}\,g_1 - i\,\frac{2M}{Q}\,\hat{t}^{\,[\mu}\epsilon_\perp^{\nu]\rho}S_{\perp\rho}\,x_{\mathrm{B}}(g_1+g_2). \end{aligned} \tag{B.9}$$

It contains two structure functions $g_1(x_{\mathrm{B}},Q^2)$ and $g_2(x_{\mathrm{B}},Q^2)$. One also uses $g_T \equiv g_1 + g_2$. The resulting cross-section is

$$\frac{\mathrm{d}\Delta\sigma_{LL}}{\mathrm{d}x_{\mathrm{B}}\,\mathrm{d}y} = \frac{4\pi\,\alpha^2}{Q^2}\,\lambda_e\left[S_L\,(2-y)\,g_1 - |\boldsymbol{S}_\perp|\,\cos\phi_S^\ell\,\frac{2M}{Q}\,\sqrt{1-y}\,x_{\mathrm{B}}(g_1+g_2)\right]. \tag{B.10}$$

(Note that in all of the above formulas mass corrections proportional to M^2/Q^2 have been neglected.)

Appendix C.

Polarized parton densities

Analogously to the unpolarized structure functions one can obtain for the polarized structure functions

$$2\,g_1(x_{\mathrm{B}}) = \sum_q e_q^2\,[g_1^q(x_{\mathrm{B}}) + \bar{g}_1^q(x_{\mathrm{B}})], \tag{C.1}$$

where

$$S_L g_1^q(x) = \frac{1}{4\pi}\int \mathrm{d}\xi^-\; e^{ixP^+\xi^-}\,\langle P,S|\overline{\psi}(0)\gamma^+\gamma_5\psi(\xi)|P,S\rangle\Big|_{\xi^+=\xi_\perp=0}, \tag{C.2}$$

often denoted as $\Delta q(x) = g_1^q(x)$. This correlation exists in a hadron with the light-cone component of the spin vector $S_L \neq 0$. It represents the difference of chiral even and odd quarks (in infinite momentum frame quarks parallel or antiparallel to proton spin). The corresponding quark fields are projected out by

$$P_{R/L} = \frac{1}{2}(1 \pm \gamma_5), \tag{C.3}$$

which commute with the projectors $P_\pm$. In this way one obtains distributions $q_R(x)$ and $q_L(x)$ for which $q(x) = q_R(x) + q_L(x)$ and $\Delta q(x) = q_R(x) - q_L(x)$.

Exercise: Show that the antiquark distributions are given by $\bar{q}(x) = -q(-x)$ and $\Delta\bar{q}(x) = \Delta q(-x)$. To do this start with the "proper" definition of antiquark distributions,

$$\Phi_{ij}^c(p) = \frac{1}{(2\pi)^4}\int \mathrm{d}^4\xi\; e^{ip\cdot\xi}\,\langle PS|\overline{\psi}_j^c(0)\psi_i^c(\xi)|PS\rangle, \tag{C.4}$$

with $\psi^c(\xi) = C\overline{\psi}^T(\tilde{\xi})$. Show that one finds $\overline{\Phi}(p) = -C(\Phi^c)^T C^\dagger$. One also needs to use the anticommutation relations for fermions, to obtain $\overline{\Phi}_{ij}(p) = -\Phi_{ij}(-p)$, which leads to the crossing relations for quark and antiquark distributions.

Appendix D.

Forms of quantization

As discussed by Dirac in his seminal paper (P.A.M. Dirac, *Forms of Relativistic Dynamics, Rev. Mod. Phys.*, **21** (1949) 392) there are more *forms* of quantization. One can for instance start on a hypersurface $x^0 = \text{const.}$, known as *instant form* or on a hypersurface $x^+ = (x^0 + x^3)/\sqrt{2} = \text{const.}$, known as *front form*. Depending on the choice, there are different sets of *dynamical generators* out of the ten Poincaré generators that leave the hypersurface invariant. These so-called kinematical generators can be chosen to be free of interactions.

In *instant form* there are six kinematical generators, three translations P^i and three rotations $J^i = \frac{1}{2}\,\epsilon_{ijk}\,M^{jk}$. Quantization in instant form starts with (interaction independent) canonical commutation relations $[x^i, p^j] = i\,\delta^{ij}$ and $[s^i, s^j] = i\,\epsilon^{ijk}\,s^k$, with on the $x^0 = t$ hypersurface the kinematical generators given by

(D.1) $$\boldsymbol{P} = \boldsymbol{p},$$

(D.2) $$\boldsymbol{J} = \boldsymbol{r} \times \boldsymbol{p} + \boldsymbol{s}.$$

In *front form* there are seven kinematical generators, three translations P^+ and P_T^i, and furthermore $J^3 = M^{12}$, M^{-+}, M^{1+}, M^{2+}. Quantization in front form starts with (interaction-independent) canonical commutation relations $[x^+, p^-] = i$, $[x^i, p^j] = i\,\delta_T^{ij}$ ($i = 1$,2), with on the $x^+ = \tau$ hypersurface the (simple) kinematical generators given by

(D.3) $$P^+ = p^+,$$

(D.4) $$\boldsymbol{P}_T = \boldsymbol{p}_T,$$

(D.5) $$J^3 = M^{12} = x^1 p^2 - x^2 p^1 + \lambda,$$

(D.6) $$M^{-+} = x^- p^+ - \tau p^-,$$

(D.7) $$M^{i+} = x^i p^+ - \tau p^i \qquad (i = 1, 2).$$

Spin $\boldsymbol{s}$ and light-cone helicity λ are allowed extensions with vanishing commutators with the x and p operators.

Exercise: Check that the kinematical operators satisfy the commutation relations of the Poincaré group,

(D.8) $$[P^\mu, P^\nu] = 0,$$

(D.9) $$[M^{\mu\nu}, P^\rho] = -i\left(g^{\mu\rho} P^\nu - g^{\nu\rho} P^\mu\right),$$

(D.10) $$[M^{\mu\nu}, M^{\rho\sigma}] = -i\left(g^{\mu\rho} M^{\nu\sigma} - g^{\nu\rho} M^{\mu\sigma}\right) - i\left(g^{\mu\sigma} M^{\rho\nu} - g^{\nu\sigma} M^{\rho\mu}\right).$$

Appendix E.

Field quantization in front form

In order to discuss the quantization of the QCD field-theoretical Lagrangian we need the "momenta"

(E.1) $$\overline{\Pi}_\psi^\mu = \frac{\delta \mathcal{L}}{\delta\,\partial_\mu \psi} = \frac{i}{2}\,\overline{\psi}\gamma^\mu,$$

(E.2) $$\Pi_\psi^\mu = \frac{\delta \mathcal{L}}{\delta\,\partial_\mu \overline{\psi}} = -\frac{i}{2}\,\gamma^\mu \psi,$$

(E.3) $$\Pi_{A_\nu}^\mu = \frac{\delta \mathcal{L}}{\delta\,\partial_\mu A_\nu} = -F^{\mu\nu}.$$

In *instant form* fields are quantized by imposing equal time commutation relations with the conjugate momenta. These momenta can be obtained from the above general momenta. We find for the fermion field $\overline{\Pi}_\psi = \delta\mathcal{L}/\delta\,\partial_0\psi = \frac{i}{2}\,\psi^\dagger$. The canonical momentum of the A^μ fields and the remaining components of the field tensor are given by

$$F^{0i} = -E^i = \dot{A}^i + \partial_i A^0 - i\,g\,[A^0, A^i] = \dot{A}^i + D_i A^0, \tag{E.4}$$

$$F^{ij} = -\partial_i\,A^j + \partial_j\,A^i - i\,g\,[A^i, A^j] = -\epsilon^{ijk}\,B^k, \tag{E.5}$$

where $\dot{A}^\mu = \partial_0 A^\mu$. The absence of a canonical momentum for A^0 implies a constraint

$$\frac{\delta\mathcal{L}}{\delta\,A^0} = -D_i E^i + j^0 = 0, \tag{E.6}$$

where $D_i E^i = [D_i, E^i] = \partial_i E^i + ig\,[A^i, E^i]$ and $j^0 = \psi^\dagger\psi$. This equation is the non-abelian Gauss' law. The other equations of motion are

$$\big(i\,\gamma^0 D_0 + i\,\gamma^i D_i - m\big)\,\psi = 0, \tag{E.7}$$

$$D_0 F^{0i} + D_j F^{ji} = j^i. \tag{E.8}$$

Rewriting slightly, we have as equations of motion

$$i\,D_0\psi = -\gamma_0\,\big(i\,\gamma^j D_j - m\big)\,\psi = \big(i\,\gamma^j D_j + m\big)\,\gamma_0\,\psi, \tag{E.9}$$

$$D_0 E^i = \epsilon^{ikl} D_k B^l - j^i, \tag{E.10}$$

$$D_j E^j = j^0. \tag{E.11}$$

Note that the last of these equations is just the constraint implied by the absence of a canonical momentum for A^0. The constraint involves interactions, in this case through $\dot{A}^i$ in E^i. To proceed, one still can make a gauge choice. We just want to mention that the (obvious) choice $A^0 = 0$ in combination with $\partial_\mu\,A^\mu = 0$ has problems (Gribov ambiguity).
(The classical reference on constraints in quantum mechanics is P.A.M. Dirac, *Lectures on Quantum Mechanics*, (Belfer graduate school of Science), 1964.)

In *front form quantization*, fields are quatized by imposing equal time commutation relations with the conjugate momenta using the light-cone time x^+, *i.e.* $\dot{\psi} = \partial_+\psi = \partial^-\psi$, etc. In terms of the light-cone coordinates one has for the fermion field $\overline{\Pi}_\psi = \delta\mathcal{L}/\delta\,\partial_+\psi = \frac{i}{\sqrt{2}}\,\psi_+^\dagger$, where the *good/bad* fields $\psi_\pm = P_\pm\psi$ are introduced with the projectors $P_\pm \equiv \frac{1}{2}\gamma^\mp\gamma^\pm$. We note that there is no canonical momentum for the bad field ψ_-. For the gluon fields one has (using $i, j, \dots$ for transverse indices!)

$$F^{-+} = \dot{A}^+ - \partial_- A^- + ig\,[A^+, A^-] = \dot{A}^+ - D_- A^-, \tag{E.12}$$

$$F^{-i} = \dot{A}^i + \partial_i A^- + ig\,[A_T^i, A^-] = \dot{A}_T^i + D_{Ti} A^- \equiv -E_T^i, \tag{E.13}$$

$$F^{+i} = \partial_- A^i + \partial_i A^+ - ig\,[A_T^i, A^+] = \partial_- A_T^i + D_i A^+ \equiv B_T^i, \tag{E.14}$$

$$F^{ij} = \partial_j A_T^i - \partial_i A_T^j - ig\,[A_T^i, A_T^j] \equiv -\epsilon_T^{ij}\,B, \tag{E.15}$$

the first two being canonical momenta. Note that there is no canonical momentum for A^-. We can simplify by going to the light-cone gauge $A^+ = 0$. In that case the first and third expressions simplify

$$F^{-+} = -\partial_- A^-, \tag{E.16}$$

$$F^{+i} = B_T^i = \partial_- A_T^i. \tag{E.17}$$

These equations actually also indicate that choosing $A^+ = 0$ not removes all gauge freedom. Inverting the equations shows that one also needs to specify a boundary condition at infinity. To be precise one needs a prescription for $(\partial_-)^{-1}$, for which we use

$$(\partial_-)^{-1} f(x^-) = \frac{1}{2}\int dy^- \epsilon(x^- - y^-) f(y^-), \tag{E.18}$$

i.e. one imposes an antisymmetric boundary condition $f(-\infty) = -f(\infty)$. The equations of motion made explicit in light-cone coordinates and using the gauge $A^+ = 0$ are

$$\begin{aligned}
&\big(i\gamma^+ D_+ + i\gamma^- D_- + i\gamma^i D_i - m\big)\,\psi = 0,\\
&D_- F^{-+} + D_i F^{i+} = \partial_- F^{-+} + \partial_i F^{i+} + ig\,[A_T^i, F^{i+}] = j^+,\\
&D_+ F^{+-} + D_i F^{i-} = \dot{F}^{+-} - ig\,[A^-, F^{+-}] + \partial_i F^{i-} + ig\,[A_T^i, F^{i-}] = j^-,\\
&D_+ F^{+i} + D_- F^{-i} + D_j F^{ji} = \dot{F}^{+i} - ig\,[A^-, F^{+i}] + \partial_- F^{-i} + \partial_j F^{ji} + ig\,[A_T^j, F^{ji}] = j^i.
\end{aligned}$$

Using the fields $\psi_\pm$, the equations of motion become

$$2i\, D_+ \psi_+ = \big(i\,\not{D}_T + m\big)\,(\gamma^-\,\psi_-), \tag{E.19}$$

$$i\,\partial_-(\gamma^-\psi_-) = \big(i\,\not{D}_T - m\big)\,\psi_+, \tag{E.20}$$

$$-(\partial_-)^2 A^- - D_T\cdot B_T = j^+ = g\sqrt{2}\,\psi_+^\dagger\psi^+, \tag{E.21}$$

$$D_+(\partial_- A^-) + D_T\cdot E_T = j^- = \frac{g}{\sqrt{2}}\,(\gamma^-\psi_-)^\dagger(\gamma^-\psi_-), \tag{E.22}$$

$$D_+ B_T^i - \partial_- E_T^i + \epsilon_T^{ij} D_j\, B = j^i = \frac{g}{\sqrt{2}}\left[(\gamma^-\psi_-)^\dagger\gamma^i\psi_+ + \psi_+^\dagger\gamma^i(\gamma^-\psi_-)\right]. \tag{E.23}$$

The second equation is a constraint not involving interactions, which can be solved as $\psi_-[A_T, \psi_+]$, since there are no time-derivatives involved. The same is true for the third equation, which can be solved as $A^-[A_T, \psi_+]$. To be precise

$$(\gamma^-\psi_-) = (i\partial_-)^{-1}(i\not{D}_T - m)\,\psi_+, \tag{E.24}$$

$$A^- = (i\partial_-)^{-2}\left[g\,\psi_+^\dagger\psi_+ + D_T\cdot B_T\right]. \tag{E.25}$$

One is left with two (independent) equations governing the time dependence of a minimal set of fields, ψ_+ and A_T^i. For these (dynamical) fields canonical commutation relations can be imposed independent of the interactions (J.B. Kogut and D.E. Soper, *Quantum* *electrodynamics in the infinite-momentum frame, Phys. Rev. D*, **1** (1970) 2901). The lagrangian left after gauge fixing can also be written as

$$\text{(E.26)}\qquad \begin{aligned}\mathcal{L}_G &= -\frac{1}{2}\,F^{+-}F^{-+} + \frac{1}{2}\,F^{+i}F^{-i} - \frac{1}{2}\,B^2\\ &= \frac{1}{2}\left(\partial_- A^-\right)^2 - \frac{1}{2}\,E_{\scriptscriptstyle T}\cdot B_{\scriptscriptstyle T} - \frac{1}{2}\,B^2.\end{aligned}$$

The fermionic part (including the quark-gluon interaction terms) is

$$\text{(E.27)}\ \begin{aligned}\mathcal{L}_F = {}&\frac{i}{\sqrt{2}}\left(\psi_+^\dagger\dot{\psi}_+ - \dot{\psi}_+^\dagger\psi_+\right) + g\sqrt{2}\,\psi_+^\dagger A^-\psi_+ + \frac{1}{2\sqrt{2}}\left(\gamma^-\psi_-\right)^\dagger \overleftrightarrow{\partial}_-\left(\gamma^-\psi_-\right)\\ &+ \frac{1}{\sqrt{2}}\left[\left(\gamma^-\psi_-\right)^\dagger\left(i\not{D}_{\scriptscriptstyle T} - m\right)\psi_+ + \psi_+^\dagger\left(i\not{D}_{\scriptscriptstyle T} + m\right)\left(\gamma^-\psi_-\right)\right].\end{aligned}$$

The nice thing of the front form quantization is the fact that the fields ψ_+ and $A_{\scriptscriptstyle T}$ are dynamical fields, for which canonical equal (light-cone) time commutation relations can be imposed, of which the right-hand side is interaction independent. That means that a free-field expansion for ψ_+ is a sensible thing, even if the quanta are confined. This is the basis behind the successful parton model in deep inelastic scattering.

REFERENCES

[1] CLOSE, FRANK E., DONNACHIE, SANDY E. and SHAW, GRAHAM E., *Electromagnetic interactions and hadronic structure* (Cambridge University Press) 2007.
[2] MULDERS P., *Prog. Part. Nucl. Phys.*, **55** (2005) 243.
[3] BACCHETTA A., DIEHL M., GOEKE K., METZ A. and MULDERS P. J., *JHEP*, **0702** (2007) 093.
[4] BARONE V., BRADAMANTE F. and MARTIN A., *Prog. Part. Nucl. Phys.*, **65** (2010) 267.
[5] BELITSKY A. V., JI X.-D. and YUAN F., *Phys. Rev. D*, **69** (2004) 074014.
[6] MENG R.-B., OLNESS F. I. and SOPER D. E., *Nucl. Phys. B*, **371** (1992) 79.
[7] JAFFE R. L., *Relativistic Dynamics and Quark Nuclear Physics*, edited by JOHNSON M. B. and PICKLESHEIMER A. (Wiley, New York) 1986.
[8] JAFFE R. L., *Nucl. Phys. B*, **229** (1983) 205.
[9] DIEHL M. and GOUSSET T., *Phys. Lett. B*, **428** (1998) 359.
[10] SOPER D. E., *Phys. Rev. D*, **15** (1977) 1141.
[11] SOPER D. E., *Phys. Rev. Lett.*, **43** (1979) 1847.
[12] COLLINS J. C. and SOPER D. E., *Nucl. Phys. B*, **194** (1982) 445.
[13] JAFFE R. L. and JI X.-D., *Nucl. Phys. B*, **375** (1992) 527.
[14] ARTRU X. and MEKHFI M., *Z. Phys. C*, **45** (1990) 669.
[15] CORTES J., PIRE B. and RALSTON J., *Z. Phys. C*, **55** (1992) 409.
[16] SOFFER J., *Phys. Rev. Lett.*, **74** (1995) 1292.
[17] RALSTON J. P. and SOPER D. E., *Nucl. Phys. B*, **152** (1979) 109.
[18] TANGERMAN R. D. and MULDERS P. J., *Phys. Rev. D*, **51** (1995) 3357.
[19] BACCHETTA A., BOER D., DIEHL M. and MULDERS P. J., *JHEP*, **0808** (2008) 023.
[20] BACCHETTA A., BOGLIONE M., HENNEMAN A. and MULDERS P. J., *Phys. Rev. Lett.*, **85** (2000) 712.

[21] Collins J. C., *Nucl. Phys. B*, **396** (1993) 161.
[22] Hagiwara K., Hikasa K.-i. and Kai N., *Phys. Rev. D*, **27** (1983) 84.
[23] Jaffe R. L. and Ji X.-D., *Phys. Rev. Lett.*, **71** (1993) 2547.
[24] Mulders P. J. and Tangerman R. D., *Nucl. Phys. B*, **461** (1996) 197.
[25] Boer D. and Mulders P. J., *Phys. Rev. D*, **57** (1998) 5780.
[26] Airapetian A. *et al.*, *Phys. Rev. Lett.*, **94** (2005) 012002.
[27] Barone V., Drago A. and Ratcliffe P. G., *Phys. Rep.*, **359** (2002) 1.
[28] Boer D., Mulders P. J. and Pijlman F., *Nucl.Phys. B*, **667** (2003) 201.
[29] Belitsky A. V., Ji X. and Yuan F., *Nucl. Phys. B*, **656** (2003) 165.
[30] Bomhof C. J., Mulders P. J. and Pijlman F., *Phys. Lett. B*, **596** (2004) 277.
[31] Bomhof C. J., Mulders P. J. and Pijlman F., *Eur. Phys. J. C*, **47** (2006) 147.
[32] Bomhof C. J. and Mulders P. J., *Nucl. Phys. B*, **795** (2008) 409.
[33] Efremov A. V. and Radyushkin A. V., *Theor. Math. Phys.*, **44** (1980) 573.
[34] Efremov A. V. and Radyushkin A. V., *Theor. Math. Phys.*, **44** (1981) 664.
[35] Boer D. and Mulders P. J., *Nucl. Phys. B*, **569** (2000) 505.
[36] Collins J. C., *Phys. Lett. B*, **536** (2002) 43.
[37] Brodsky S. J., Hwang D. S. and Schmidt I., *Phys. Lett. B*, **530** (2002) 99.
[38] Gamberg L. P., Mukherjee A. and Mulders P. J., *Phys. Rev. D*, **77** (2008) 114026.
[39] Meissner S. and Metz A., *Phys. Rev. Lett.*, **102** (2009) 172003.
[40] Gamberg L. P., Mukherjee A. and Mulders P. J., *Phys. Rev. D*, **83** (2011) 071503.
[41] Rogers T. C. and Mulders P. J., *Phys. Rev. D*, **81** (2010) 094006.
[42] Buffing M. and Mulders P., *JHEP*, **1107** (2011) 065.
[43] Efremov A. V. and Teryaev O. V., *Sov. J. Nucl. Phys.*, **36** (1982) 140.
[44] Efremov A. V. and Teryaev O. V., *Phys. Lett. B*, **150** (1985) 383.
[45] Qiu J.-W. and Sterman G., *Phys. Rev. Lett.*, **67** (1991) 2264.
[46] Qiu J.-W. and Sterman G., *Nucl. Phys. B*, **378** (1992) 52.
[47] Qiu J.-W. and Sterman G., *Phys. Rev. D*, **59** (1999) 014004.
[48] Kanazawa Y. and Koike Y., *Phys. Lett. B*, **478** (2000) 121.
[49] Eguchi H., Koike Y. and Tanaka K., *Nucl. Phys. B*, **763** (2007) 198.
[50] Koike Y. and Tanaka K., *Phys. Lett. B*, **646** (2007) 232.
[51] Bomhof C. J. and Mulders P. J., *JHEP*, **0702** (2007) 029.
[52] Ji X.-D., *Phys. Lett. B*, **289** (1992) 137.
[53] Meissner S., Metz A. and Goeke K., *Phys. Rev. D*, **76** (2007) 034002.
[54] Mulders P. J. and Rodrigues J., *Phys. Rev. D*, **63** (2001) 094021.
[55] Collins J. C., *Foundations of perturbative QCD* (Cambridge University Press) 2011.
[56] Aybat S. and Rogers T. C., *Phys. Rev. D*, **83** (2011) 114042.
[57] Binosi D. and Theussl L., *Comput. Phys. Commun.*, **161** (2004) 76.
[58] Binosi D., Collins J., Kaufhold C. and Theussl L., *Comput. Phys. Commun.*, **180** (2009) 1709.

Proceedings of the International School of Physics "Enrico Fermi"
Course CLXXX "Three-Dimensional Partonic Structure of the Nucleon"
edited by M. Anselmino, H. Avakian, D. Hasch and P. Schweitzer
(IOS, Amsterdam; SIF, Bologna)
DOI 10.3254/978-1-61499-197-7-81

Generalized parton distributions

M. Diehl

Deutsches Elektronen-Synchroton DESY - 22603 Hamburg, Germany

Summary. — These lectures give an introduction to the theory of generalized parton distributions, starting from the underlying concepts, highlighting their physical interest, and discussing the possibilities to study them experimentally.

1. – Introduction

These lectures give an introduction to the theory of generalized parton distributions (GPDs). We first review the general ideas of factorization, highlighting the similarities and differences between generalized and usual parton distributions. We then discuss which specific information about hadron structure is contained in GPDs, focusing on the nucleon spin structure and on spatial imaging of partons. We explain the relation between GPDs and transverse-momentum dependent distributions (TMDs). Finally, we give some information about the exclusive scattering processes that allow us to study GPDs in experiments. One of the attractive features of GPDs is that they are related with many other aspects of QCD. This also means that it is impossible to give a full account of the field in these lectures. We will mostly focus on basics.

The literature on GPDs is vast, and we will only occasionally cite the original papers that have brought the field forward over the last one and a half decade. Instead, we point the reader to several reviews [1-5] that provide a fairly comprehensive overview, each giving slightly different emphasis to the many facets of the field.

© Società Italiana di Fisica

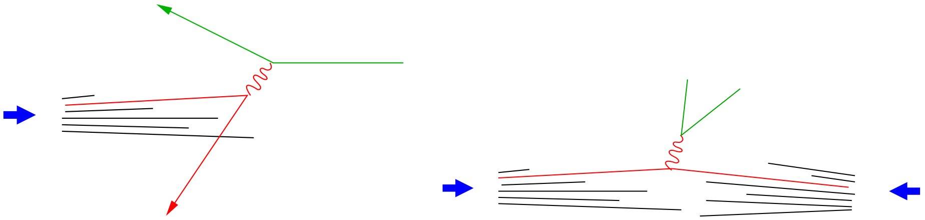

Fig. 1. – (Colour on-line) Representation of deep inelastic scattering (left) and of the Drell-Yan process (right) in the parton model. The blue arrows represent the incoming protons.

2. – Factorization in QCD

The way we think about quarks and gluons is strongly shaped by the parton model, which states that in a high-energy collision a fast-moving proton behaves like a set of free partons with low transverse momenta. The cross-section of a collision is then calculated from the cross-section of a parton-level process (*e.g.*, $\ell q \to \ell q$ or $\ell \bar{q} \to \ell \bar{q}$ in deep inelastic scattering, or $q\bar{q} \to \ell^+\ell^-$ in the Drell-Yan process) times the distribution function(s) to find the corresponding parton(s) in the hadron(s). The underlying physical picture is sketched in fig. 1.

The concept of factorization implements the ideas of the parton model (which is a *model*) into QCD (which is the *quantum field theory* of strong interactions) and corrects these ideas when necessary:

- it specifies the conditions (process, kinematics, observables) under which a description in terms of parton-level cross-sections and parton distributions is valid;
- it provides a systematic procedure for calculating corrections to the parton-model assumption that partons are free, using the perturbative expansion in α_s for the interactions between partons;
- it provides a definition of parton densities that allows one to study their properties in a systematic way and, in principle, to compute them using non-perturbative methods in QCD.

2˙1. *Examples for factorization: DIS and DVCS.* – In this subsection we sketch the main steps in establishing a factorized description of a process. We will gloss over many technical details and refer the reader to [6-8] for a more careful treatment. The discussion will proceed in parallel for two example processes:

1) deep inelastic scattering (DIS), *i.e.* $\gamma^*(q) + p(p) \to X$, where q and p denote four-momenta. This is a fully inclusive process, to be summed over all hadronic systems X. According to the optical theorem, the cross-section for this process is proportional to the imaginary part of the amplitude for Compton scattering, $\gamma^*(q) + p(p) \to \gamma^*(q) + p(p)$. We will discuss this amplitude and only convert it into a total inclusive cross-section at the very end.

2) Deeply virtual Compton scattering (DVCS), *i.e.* $\gamma^*(q)+p(p)\to\gamma(q')+p(p')$. This is a fully exclusive process with two specified particles in the final state, and we need to calculate its amplitude. Note that in this case we have a momentum transfer between the incoming and the outgoing proton in the Compton amplitude. For DIS this transfer is zero, according to the prescription of the optical theorem.

In both cases, we are concentrating on the strong-interaction part of the physical process and have taken away the QED part, which is the radiation of a virtual photon $\gamma^*(q)$ from a lepton.

2·1.1. Kinematics. Factorization can be established for a specified kinematical limit, which is called the Bjorken limit in DIS: $Q^2=-q^2\to\infty$ at fixed Bjorken scaling variable $x_B=Q^2/(2pq)=Q^2/(Q^2+W^2-m^2)$, where $W^2=(p+q)^2$ is the square of the hadronic center-of-mass energy and m denotes the proton mass. For DVCS we extend this limit by specifying that $t=(p-p')^2$ should remain finite as $Q^2\to\infty$; this is understood when we refer to the Bjorken limit in the following. In an experiment Q^2 is of course not infinite, and the above limit translates into the requirements that Q^2 and W^2 should be large compared with all other relevant scales (including the scale of non-perturbative QCD dynamics, which may be represented by the proton mass), and that for DVCS they should in particular be large compared with $|t|$.

To derive factorization it is convenient to work with light-cone coordinates. For any given four-vector v these are given by

$$v^+=(v^0+v^3)/\sqrt{2}\,,\qquad\qquad v^-=(v^0-v^3)/\sqrt{2}\,,\tag{1}$$

and the transverse components are collected in a two-dimensional vector $\boldsymbol{v}=(v^1,v^2)$. It is easy to show(¹) that under a boost along the z axis v^+ is multiplied by a number and v^- by the inverse of that number. In particular, the ratio w^+/v^+ of two plus-components is invariant under such a boost. It is also easy to derive the rules of calculation

$$vw=v^+w^-+v^-w^+-\boldsymbol{v}\boldsymbol{w}\,,\qquad\qquad \mathrm{d}^4v=\mathrm{d}v^+\,\mathrm{d}v^-\,\mathrm{d}^2\boldsymbol{v}\,.\tag{2}$$

Returning to our two processes, we now choose a reference frame in which the incoming proton moves fast to the right, so that p^+ is large (of order Q), p^- is very small (of order m^2/Q) and $\boldsymbol{p}=\boldsymbol{0}$. We also require that q^- and q^+ are of order Q and that $\boldsymbol{q}=\boldsymbol{0}$. One reason why such a frame is useful is that in later stages it will allow us to neglect small momentum components compared with large ones. (A frame in which a hadron moves fast is also convenient for making contact with the physical picture of the parton model.) It is easy to see that the γ^*p center of mass is an example of such a frame if the z-axis is chosen along the proton momentum p. With a little more work, one also finds that the

---

(¹) Whenever we state that something is easy, the reader is encouraged to check the corresponding statement as an exercise.

requirement of small t for DVCS translates into $p'^+ \sim q'^- \sim Q$, $p'^- \sim q'^+ \sim m^2/Q$ and $|\boldsymbol{p}'| = |\boldsymbol{q}'| \sim m$, *i.e.* the outgoing proton moves fast to the right and the produced real photon fast to the left.

2·1.2. Dominant momentum regions. The next step is to consider all possible graphs for the process under study, *i.e.* for Compton scattering in our case. For simplicity we restrict ourselves to the light quarks (u, d, s) in the following; the inclusion of heavy quarks into the factorization formalism is possible but involves a number of complications. According to a general analysis by Libby and Sterman [9], which uses rather advanced methods of quantum field theory, the dominant contribution to any graph in the kinematic limit we are taking comes from a limited set of regions for the loop momenta:

1) *hard* momenta with $k^+ \sim k^- \sim |\boldsymbol{k}| \sim Q$, which are far off shell, $|k^2| \sim Q^2$,

2) momenta that are approximately *collinear* to one of the external hadrons and are weakly off shell, $|k^2| \sim m^2$. In DIS this means that the corresponding lines move fast to the right, $k^+ \sim Q$, $k^- \sim m^2/Q$ and $|\boldsymbol{k}| \sim m$. For DVCS there is an additional complication: since the final-state photon is real it can split into almost collinear partons (thus acting quite like a hadron), so that loop momenta may also correspond to particles moving fast to the left.

3) Momenta that are *soft*, having momentum components k^+, k^- and $|\boldsymbol{k}|$ much smaller than Q. How small exactly these components are requires more discussion, and we shall gloss over this issue here.

According to these criteria, one can organize any graph into hard, collinear and soft subgraphs in the region where it gives the dominant contribution to the amplitude we want to calculate. Note that for a given graph there may be several possibilities to organize it into subgraphs, corresponding to distinct regions of the loop momenta. Some examples for this are shown in fig. 2.

2·1.3. Power counting. Not all of the graphs selected by the Libby-Sterman criterion actually give dominant contributions to the amplitude, and a further selection is possible using power counting. This means that one determines how a given graph scales with m and Q, which can be done in a very general manner.

1) By construction, a hard subgraph involves only the large scale Q and not the small scale m. It therefore behaves like Q raised to a power that is given by the mass dimension of the subgraph. Note the elegance of this argument: it allows us to make a statement about an infinite number of subgraphs with specified external lines (which is enough to fix the mass dimension) without calculating them, and the actual mass dimension can be determined by choosing a conveniently simple graph. Figure 3 shows a few examples.

2) A somewhat more involved (but still very general) argument allows one to determine the power behavior of collinear subgraphs. One finds that for each external quark

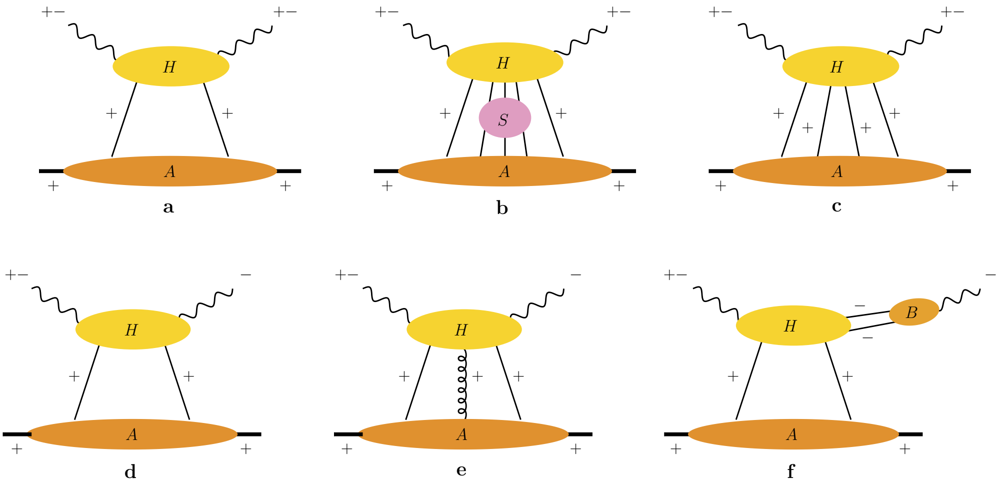

Fig. 2. – Examples of graphs that can give leading contributions to DIS (top row) and to DVCS (bottom row) according to the Libby-Sterman analysis. A + (−) next to a line indicates that it has a plus (minus) momentum of order Q. Hard subgraphs are denoted by H, soft subgraphs by S, and subgraphs collinear to the proton by A. In the case of DVCS one can also have a subgraph B collinear to the outgoing photon.

or antiquark a collinear subgraph can give at most a power $Q^{1/2}$. For each right-moving external gluon one gets a power Q if the gluon polarization vector points in the plus-direction, no power of Q if the gluon polarization is transverse, and a power of $1/Q$ if it points in the minus-direction. For left-moving gluons one has an analogous statement.

3) The integration measure for a collinear line is easily found to scale as $\mathrm{d}^4k = \mathrm{d}k^+\,\mathrm{d}k^-\,\mathrm{d}^2\boldsymbol{k} \sim m^4$.

4) The scaling behavior of soft subgraphs and of their integration measure can also be determined. It depends on the exact scaling of the soft momentum components but can never give a positive power of Q.

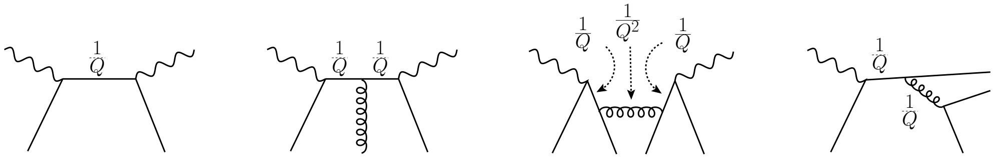
$\frac{1}{Q}$
$\frac{1}{Q}$ $\frac{1}{Q}$
$\frac{1}{Q}$ $\frac{1}{Q^2}$ $\frac{1}{Q}$
$\frac{1}{Q}$
$\frac{1}{Q}$

Fig. 3. – Examples of hard subgraphs (corresponding to those in fig. 2) and their power behavior in Q. The $1/Q$ and $1/Q^2$ factors correspond to the different mass dimensions of fermion and boson propagators. Note that propagators for external lines are not included in a hard graph.

From points 1) and 2) we can deduce the important rule that the dominant graphs are those that have the smallest possible number of external partons in the hard subgraph: additional external partons lead to a suppression from more hard propagators that cannot be counterbalanced by the extra powers of Q from the collinear subgraphs. In fig. 2 this selection leaves us with graphs a and d.

The only exception to the rule just stated is that one can add an arbitrary number of right-moving gluons with polarization in the plus-direction (and of left-moving gluons with polarization in the minus-direction if the process involves a left-moving hadron). To have such an infinity of graphs sounds like disaster for practical calculations. Luckily, a Ward identity (which reflects the gauge invariance of QCD) allows one to cast all those graphs into a form with no extra gluons in the hard subgraph and a Wilson line operator multiplying the collinear subgraph. In these lectures I will not further discuss this issue (which is of much greater importance for TMDs than for GPDs).

The leading graphs for Compton scattering do not involve any soft subgraphs. Let me mention that soft subgraphs can appear in the leading result for processes with more than one hadron in either the initial or the final state, such as semi-inclusive DIS (SIDIS) or Drell-Yan lepton pair production. The treatment of soft subgraphs in such situations is quite nontrivial and often constitutes the most difficult part in establishing a factorization formula for the process.

2˙1.4. Collinear expansion. We have achieved a significant simplification by identifying a relatively small subset of graphs that are relevant in the kinematic limit we are interested in. For DIS and DVCS these are respectively graphs a and d in fig. 2, plus corresponding graphs where gluons instead of quarks are exchanged between the collinear and hard subgraphs. We can simplify even more by neglecting small momentum components compared with large ones when evaluating the hard subgraph $H(k)$, where k denotes the momentum of one of the incoming partons (the other one being fixed by momentum conservation). More precisely, we make a Taylor expansion

$$H(k^+, k^-, \boldsymbol{k}) = H(k^+, 0, \boldsymbol{0}) + \boldsymbol{k} \left[\frac{\partial}{\partial \boldsymbol{k}} H(k^+, 0, \boldsymbol{k}) \right]_{\boldsymbol{k}=\boldsymbol{0}} + \mathcal{O}(m^2)\,. \tag{3}$$

From the discussion in the previous subsection we can deduce that the first term in this expansion is dominant, whereas the second one comes with a relative suppression by $|\boldsymbol{k}|/Q \sim m/Q$. Retaining only the leading term, the loop integral for the complete amplitude can be simplified as

$$\int \mathrm{d}^4 k\, H(k) A(k) \approx \int \mathrm{d}k^+\, H(k^+ 0, \boldsymbol{0}) \left[\int \mathrm{d}k^-\, \mathrm{d}^2\boldsymbol{k}\, A(k) \right]. \tag{4}$$

We also neglect the light quark masses in $H(k)$. In words, the hard subgraph is now evaluated in approximate kinematics, with the incoming and outgoing partons being on shell and strictly collinear to the proton. One therefore also speaks of the "collinear approximation". By contrast, the collinear subgraph $A(k)$ is integrated over the small minus and transverse components of the parton momentum; the corresponding integral is described by "collinear" or "integrated" parton distributions. It is very important to note that in the parton distributions we do *not* put the partons on shell and do *not* set their transverse momentum to zero. In the hard scattering, these quantities are small compared with the scale Q and can be neglected, but in the collinear factor they are as large as other relevant scales (in particular the scale of nonperturbative interactions) and are integrated over rather than set to zero.

Keeping the second term in the Taylor expansion (3), one can also calculate the $1/Q$ corrections to the amplitude, *i.e.* terms that vanish in the Bjorken limit. In the selection described in subsubsect. **2**˙1.3 one then needs to keep more graphs, in particular graph e in fig. 2 with a transversely polarized gluon. For reasons explained in [10], the leading contribution in the $1/Q$ expansion is referred to as "twist two", the first subleading one as "twist three" and the $1/Q^2$ suppressed one as "twist four". Yet higher corrections are hardly ever discussed.

2˙2. *Parton distributions and hard-scattering kernels.* – The discussion so far was done in terms of Feynman graphs, which are the graphical representation for the rules of perturbation theory. For the hard subgraphs this is fine: they describe dynamics at a high scale Q, where the running coupling $\alpha_s(Q)$ is small and allows computation in successive orders of perturbation theory. However, the collinear subgraph is dominated by virtualities of order m^2 and describes nonperturbative dynamics. We therefore need a definition for the collinear subgraph that makes sense beyond perturbation theory. This is achieved by writing $\int \mathrm{d}k^- \,\mathrm{d}^2\boldsymbol{k}\, A(k)$ as a matrix element of quark or gluon field operators sandwiched between proton states. Since fields live in position rather than momentum space, it is useful to introduce the Fourier transform $\tilde{A}(z)$ of $A(k)$. We then have

$$(5)\qquad \begin{aligned}\int \mathrm{d}k^- \,\mathrm{d}^2\boldsymbol{k}\, A(k) &= \int \mathrm{d}k^- \,\mathrm{d}^2\boldsymbol{k} \int \frac{\mathrm{d}^4 z}{(2\pi)^4}\, e^{ikz}\, \tilde{A}(z)\\ &= \int \frac{\mathrm{d}z^-}{2\pi}\, e^{ik^+z^-}\, \tilde{A}(z)\Big|_{z^+=0,\boldsymbol{z}=\boldsymbol{0}} .\end{aligned}$$

An explicit example for an operator definition is

$$(6)\qquad \begin{aligned} f_1(x) &= \frac{1}{2}\int \frac{\mathrm{d}z^-}{2\pi}\, e^{ixp^+z^-}\, \langle p|\bar{q}\left(-\frac{1}{2}z\right)\gamma^+ W\left[-\frac{1}{2}z, \frac{1}{2}z\right]\, q(\frac{1}{2}z)|p\rangle\Big|_{z^+=0,\boldsymbol{z}=\boldsymbol{0}}\\ &= \begin{cases} q(x), & \text{for } x>0,\\ -\bar{q}(-x), & \text{for } x<0.\end{cases}\end{aligned}$$

Remember that a quark field operator q contains the annihilation operator b for a quark and the creation operator $d^\dagger$ for an antiquark. The quark density $q(x)$ thus corresponds to the term $b^\dagger b$ in the product $\bar{q}\ldots q$ of fields, whereas the antiquark density $\bar{q}(-x)$ comes from the term $dd^\dagger = -d^\dagger d$, with an overall minus sign reflecting that fermion

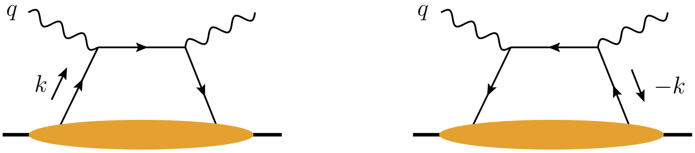

Fig. 4. – Handbag graphs for DIS and DVCS.

fields anticommute. W is the Wilson line operator announced in subsubsect. **2**˙1.3 and will not be further discussed here.

A generalized parton distribution is defined in the same way as in (6), with the only difference that the proton states in the bra and the ket are not identical and have different momenta (and possibly different spin orientations).

Consider now the hard subgraphs for DIS and DVCS at leading order in the strong coupling. The Compton amplitude is then given by the so-called "handbag diagrams" shown in fig. 4. Let me not calculate these graphs in detail but rather give the answer and discuss some of its most important features.

For both DIS and DVCS the expression of the hard-scattering graph is, up to global factors, given by the propagator of the horizontal quark or antiquark line in the figure. For the graph on the left, the denominator of this propagator is $(k+q)^2 + i\epsilon$, where $i\epsilon$ is Feynman's prescription for treating the propagator pole. Using the collinear approximation (4) we have $(k+q)^2 + i\epsilon \approx 2(k^+ + q^+)q^- + i\epsilon$. One easily finds that $q^+/p^+ = -x_B$ in the Bjorken limit. Defining the plus-momentum fraction $x = k^+/p^+$ of the quark line, we obtain a hard-scattering kernel proportional to

$$\frac{1}{x - x_B + i\varepsilon} = \mathrm{PV}\,\frac{1}{x - x_B} - i\pi\delta(x - x_B) \tag{7}$$

for the graph on the left in fig. 4, where PV denotes Cauchy's principal value prescription. Putting together all global factors, we obtain the DIS cross-section

$$\sigma_{\mathrm{tot}}(\gamma^* p \to X) \propto \mathrm{Im}\,\mathcal{A}(\gamma^* p \to \gamma^* p) = \pi \sum_q (ee_q)^2 \big[q(x_B) + \bar{q}(x_B)\big]\,, \tag{8}$$

where e is the positron charge and ee_q the charge of the quark. The term with $q(x_B)$ comes from the graph on the left and the term with $\bar{q}(x_B)$ from the graph on the right in fig. 4. For DVCS we are interested in both the real and imaginary part of the amplitude and schematically have

$$\mathcal{A}(\gamma^* p \to \gamma p) = \sum_q (ee_q)^2 \left[\mathrm{PV}\!\int \mathrm{d}x\, \frac{\mathrm{GPD}(x, x_B, t)}{x_B - x} + i\pi\, \mathrm{GPD}(x_B, x_B, t)\right] + \dots\,, \tag{9}$$

where the contribution from the graph on the right is denoted by an ellipsis. Note that we have glossed over the spin degrees of freedom in (8) and (9). For DVCS this will be

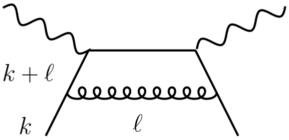

Fig. 5. – A higher-order graph for the hard scattering subprocess in DIS and DVCS.

repaired in subsect. **4˙2**. For DIS on an unpolarized proton (8) is the complete answer at leading order in α_s.

2˙3. *Loop corrections and evolution.* – When one calculates hard subgraphs at higher order in α_s, a complication arises which we will briefly discuss now. Take the graph in fig. 5 as an example. When the momentum ℓ becomes collinear to k the transverse part of the loop integral diverges like $\int \mathrm{d}\boldsymbol{\ell}^2/\boldsymbol{\ell}^2$ at its lower end. A naive calculation of the hard subgraph would thus give an infinite result. But at this point we should realize that the hard subgraph is not meant to include the momentum configuration where ℓ (and hence $k+\ell$) is collinear to k: this configuration should be part of the collinear subgraph and not of the hard one.

To obtain a proper factorization formula, we must thus associate the graph at the top of fig. 6 with two different configurations: if the gluon with momentum ℓ is collinear to k, then it belongs into the collinear subgraph, otherwise it goes into the hard subgraph. To implement this, one needs a so-called factorization scale μ, which is used to separate the two regions. One could then calculate the hard subgraph with $\boldsymbol{\ell}^2 > \mu^2$ (avoiding the collinear divergence mentioned above) and, at the same time, require that in the collinear subgraph this gluon should have $\boldsymbol{\ell}^2 < \mu^2$ (which avoids an ultraviolet divergence that would otherwise appear). In this way, both the hard-scattering amplitude and the

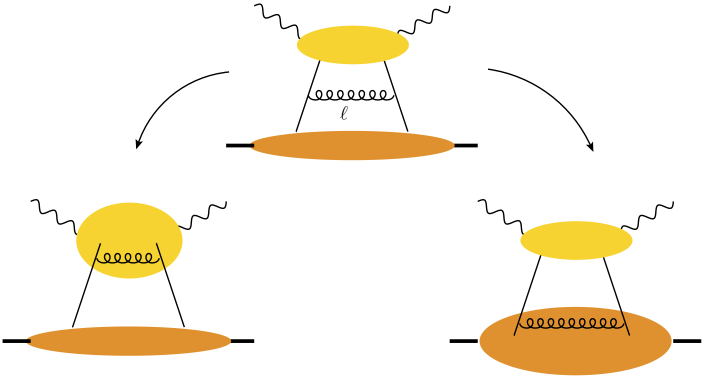

Fig. 6. – Factorization at higher order for DIS or DVCS. Depending on its momentum, the gluon in the top graph belongs either to the hard subgraph (bottom left) or to the collinear one (bottom right).

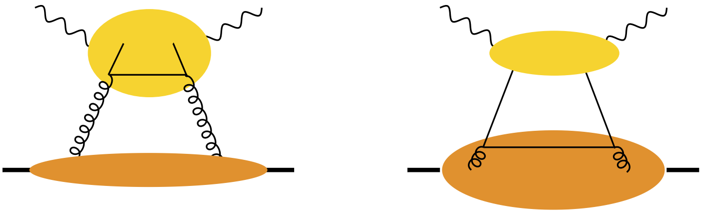

Fig. 7. – Graphs showing the interplay of quark and gluon distributions under scale evolution.

parton distribution become μ dependent. In practice one does not calculate with a cutoff, which has undesirable properties such as breaking Lorentz and gauge invariance, resorting instead to a mathematical trick called dimensional regularization, which we will not further explain here. In physical terms, one may say that we use the scale μ to separate the "structure" of the proton in terms of partons (described by the parton distribution) and the "interaction" of a parton (described by the hard scattering). One can also think of $1/\mu$ as the scale in transverse configuration space at which the target structure is resolved by the hard-scattering process.

The μ dependence of the parton distribution can be described by a differential equation, which goes under the name of DGLAP evolution equation for the case of ordinary parton distributions. In the overall cross-section, the dependence on the arbitrary separation scale μ should cancel, and indeed it would if one could compute the hard scattering to all orders in α_s. This one can unfortunately not do, and one finds that when the perturbative series for the hard scattering is calculated to some order α_s^n one retains a residual μ dependence in the physical cross-section of order α_s^{n+1}, *i.e.* at an order that is beyond the accuracy of the calculation. One often uses this effect and varies μ by some factor, say between $1/2$ and 2, to estimate the size of uncalculated higher-order corrections. Within such a factor, μ should be taken of order Q; otherwise the perturbative expansion of the hard scattering has a poor convergence due to large logarithms of μ/Q. From a physics point of view this is not surprising: a hard scattering process at momentum scale Q is able to resolve the proton structure with a spatial resolution of order $1/\mu \sim 1/Q$.

Figure 6 describes the radiation of a gluon from a quark that subsequently undergoes a hard scattering. Similarly, a gluon can split into a $q\bar{q}$ pair as shown in fig. 7. This implies that as one changes the scale μ, quark and gluon distributions communicate with each other; one says that they "mix" under evolution.

3. – Properties and physics of GPDs

We have seen how generalized parton distributions arise in the description of hard exclusive scattering processes on the proton. Let us now take a closer look at these distributions themselves. In close analogy to the forward matrix element (6), which

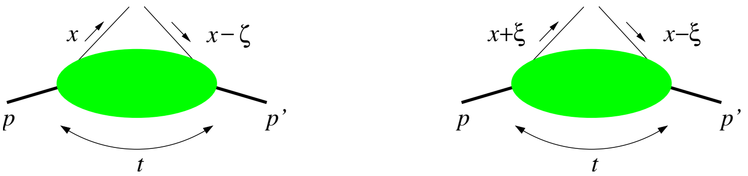

Fig. 8. – Kinematical variables describing a GPD. In the left graph plus-momentum fractions refer to p and in the right graph they refer to $P = \frac{1}{2}(p + p')$. In DVCS one has $\zeta = x_B$ and $\xi = x_B/(2 - x_B)$ in terms of the Bjorken variable.

describes the usual quark and antiquark densities, we have

$$
\begin{aligned}
(10)\quad F^q &= \frac{1}{2} \int \frac{\mathrm{d}z^-}{2\pi}\, e^{ixP^+z^-} \left\langle p', s' \middle| \bar{q}\left(-\frac{1}{2}z\right) \gamma^+ W\left[-\frac{1}{2}z, \frac{1}{2}z\right] q\left(\frac{1}{2}z\right) \middle| p, s \right\rangle \Big|_{z^+=0,\boldsymbol{z}=\boldsymbol{0}} \\
&= H^q(x,\xi,t)\, \frac{\bar{u}(p',s')\,\gamma^+ u(p,s)}{2P^+} + E^q(x,\xi,t)\, \frac{i}{2m}\, \bar{u}(p',s')\, \frac{\sigma^{+\alpha}\Delta_\alpha}{2P^+}\, u(p,s)\,,
\end{aligned}
$$

where $\Delta = p' - p$ is the momentum transfer to the proton.

Note that there are two common choices of kinematical variables for GPDs in the literature, as shown in fig. 8. The one on the left-hand side (going back to Radyushkin [11]) defines plus-momentum fractions w.r.t. the incoming proton and is the one we used in subsect. **2**·2. The one on the right (due to Ji [1]) is used in (10) and treats the two protons and the two quark lines in a symmetric way: x is the average plus-momentum of the two quark lines with respect to the average proton momentum $P = \frac{1}{2}(p + p')$, and the so-called skewness variable $\xi = (p - p')^+/(p + p')^+$ quantifies the plus-momentum loss of the proton. In both parameterizations one has the squared invariant momentum transfer $t = \Delta^2$ as a third variable. Note that the GPDs H^q and E^q additionally depend on the factorization scale μ as discussed in the previous section; this dependence will not be explicitly written in the following.

We have already seen that the forward matrix element (6) describes either a quark or an antiquark distribution, depending on the sign of x, which determines the relevant combination of creation and annihilation operators of the field product $\bar{q} \dots q$. Repeating the same argument for (10) one finds that there are three distinct regions, as illustrated in fig. 9. The regions $\xi < x < 1$ and $-1 < x < -\xi$ are the respective analogs to the regions of positive and negative x for the parton densities. They are also called DGLAP regions, because the evolution equation for the μ dependence in these regions is very similar to the usual DGLAP evolution equation for parton densities. The central region $-\xi < x < \xi$ has no analog in parton densities and describes the coherent emission of a $q\bar{q}$ pair. It has been baptized ERBL region, since the evolution equation in this case is a generalization of the ERBL evolution equation, which describes the scale dependence of a meson distribution amplitude (*i.e.* of the amplitude for a meson to fluctuate into a $q\bar{q}$ pair and nothing else). The realization that the apparently so different DGLAP and ERBL equations are closely connected was one of several aspects that led to the discovery of the GPD concept [12].

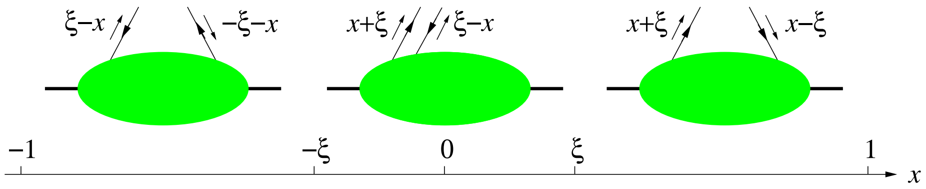

Fig. 9. – Partonic interpretation of a GPD in different regions of x. For $|x| > 1$ the matrix element in (10) is zero.

It is instructive to represent the GPDs in terms of the wave functions for the two proton states $\langle p'|$ and $|p\rangle$. In the DGLAP region with $x > \xi$ one then obtains a product $\psi^*_{x+\xi}\,\psi_{x-\xi}$ of wave functions for different momentum fractions $x+\xi$ and $x-\xi$ of the quark, which may be regarded as an interference term between different parton configurations of the proton. In the usual parton densities one has instead a squared wave function $|\psi_x|^2$ and can hence interpret the distribution as the probability density to find a quark with momentum fraction x.

Given the finite momentum transfer to the proton (and thus also to the parton) GPDs depend on more kinematic variables than usual parton densities. They also have a richer spin structure, because the spin orientations s' and s of the two proton states in (10) need not be the same, which reflects that in an exclusive scattering process the polarization of the outgoing proton may differ from the one of the incoming proton. In (10) the spin dependence of the matrix element is parameterized by two GPDs H^q and E^q, which are multiplied by suitable products involving the proton spinors $\bar{u}(p', s')$ and $u(p, s)$.

It is easy to see that if we set $p = p'$ in (10), then the factor multiplying H^q reduces to unity, whereas E^q is multiplied by zero. This means that H^q becomes equal to $f_1(x)$ for $\xi = 0$ and $t = 0$, so that the usual quark and antiquark densities are boundary values of the GPD H^q. By contrast, no information on E^q can be obtained from usual parton densities. Evaluating the spinor products in (10) for nonzero ξ and t and for definite helicities $\lambda, \lambda' = \pm 1$ of the proton states, one obtains

$$(11) \qquad F^q_{\lambda=\lambda'} \propto H^q - \frac{\xi^2}{1-\xi^2}\, E^q\,, \qquad\qquad F^q_{\lambda\neq\lambda'} \propto e^{\lambda i\varphi}\, \frac{|\mathbf{\Delta}|}{2m}\, E^q\,,$$

where φ is the azimuthal angle of the transverse momentum transfer $\mathbf{\Delta}$. From ordinary quantum mechanics we recall that the operator for orbital angular momentum L^z along the z-axis is $-i\partial/\partial\varphi$. The exponential $e^{\lambda i\varphi}$ thus indicates that the proton helicity flip matrix element $F^q_{\lambda\neq\lambda'}$ involves one unit of orbital angular momentum, as is necessary for conserving the total angular momentum J^z along z. More explicitly, one can write this matrix element as the interference of wave functions with different orbital angular momentum [13]. This one of several ways to see that E^q is intimately related with orbital angular momentum.

The operator $\bar{q}(-\frac{1}{2}z)\,\gamma^+ q(\frac{1}{2}z)$ in (10) projects onto unpolarized quarks. For longitudinal quark polarization one defines

$$(12)\quad \tilde{F}^q = \frac{1}{2}\int \frac{\mathrm{d}z^-}{2\pi}\, e^{ixP^+z^-}\, \langle p',s'|\bar{q}\left(-\frac{1}{2}z\right)\gamma^+\gamma_5 W\left[-\frac{1}{2}z,\frac{1}{2}z\right] q\left(\frac{1}{2}z\right)|p,s\rangle\Big|_{z^+=0,\boldsymbol{z}=\mathbf{0}}$$
$$= \tilde{H}^q(x,\xi,t)\,\frac{\bar{u}(p',s')\,\gamma^+\gamma_5\,u(p,s)}{2P^+} + \tilde{E}^q(x,\xi,t)\,\frac{1}{2m}\,\bar{u}(p',s')\,\frac{\gamma_5\Delta^+}{2P^+}\,u(p,s)\,.$$

For $p = p'$ the distribution $\tilde{H}^q$ reduces to the distribution $\Delta q(x)$ of polarized quarks if $x > 0$ and to the distribution $\Delta\bar{q}(-x)$ of polarized antiquarks if $x < 0$. Since $\tilde{E}^q$ is multiplied by $\Delta^+/(2P^+) = -\xi$ in (12), it becomes invisible in the forward limit, just as E^q. Similar matrix elements and GPDs can be written down for transversely polarized quarks, and for unpolarized or polarized gluons.

3˙1. *Sum rules.* – We have emphasized several times the close connection between GPDs and ordinary parton densities. Let us now investigate another important connection: the one between GPDs and form factors. We easily see that, if we integrate the matrix element in (10) over x, the exponential turns into a δ function, $\int \mathrm{d}x\, e^{ixP^+z^-} \propto \delta(z^-)$. This means that we go from the nonlocal operator $\bar{q}(-\frac{1}{2}z)\,\gamma^+ W[-\frac{1}{2}z,\frac{1}{2}z]\,q(\frac{1}{2}z)$ to a *local* operator $\bar{q}(0)\,\gamma^+ q(0)$, which gives the plus-component of the electromagnetic current when multiplied by the quark charge and summed over flavors. The proton matrix element of this current is parameterized by the Dirac and Pauli form factors $F_1(t)$ and $F_2(t)$, and we can thus identify

$$(13)\qquad \sum_q e_q \int_{-1}^{1} \mathrm{d}x\, H^q(x,\xi,t) = F_1(t)\,, \qquad \sum_q e_q \int_{-1}^{1} \mathrm{d}x\, E^q(x,\xi,t) = F_2(t)\,.$$

The transition from a nonlocal to a local operator in the matrix elements corresponds to different ways in which the proton is probed in DVCS and in elastic scattering, as sketched in fig. 10.

Something remarkable has happened in (13): after integration over x, the dependence on ξ has disappeared. This is a consequence of Lorentz invariance and can be shown in a little calculation, which I will however not give here. Roughly speaking, by integrating over x we have removed the dependence of the matrix element on the particular space-time direction that was used when we defined plus and minus components in (1). The result can then no longer depend on ξ, whose definition refers to the plus-direction; only a dependence on the Lorentz invariant t is allowed.

If we take Mellin moments, *i.e.* integrate the matrix element in (10) over x with a weight x^n, then the exponential factor $e^{ixP^+z^-}$ turns into the n-th derivative of a δ-function. Letting this act on $q(-\frac{1}{2}z)\ldots W[-\frac{1}{2}z,\frac{1}{2}z]\,q(\frac{1}{2}z)$ gives local operators with covariant derivatives $\partial^+ + igA^+(0)$ between the quark fields $\bar{q}(0)$ and $q(0)$. For the derivative part ∂^+ this is easy to see, and with a bit more work one finds that the gluon potential part comes from taking the derivative of the Wilson line operator $W[-\frac{1}{2}z,\frac{1}{2}z]$.

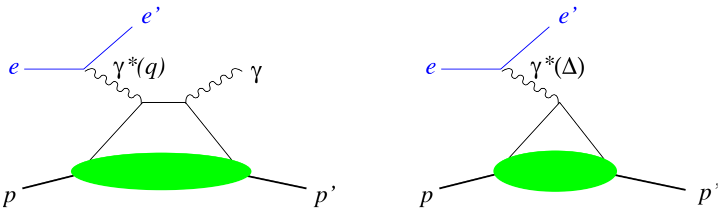

Fig. 10. – DVCS (left) probes the proton with a preferred direction, given by the γ^* momentum in the $\gamma^* p$ center-of-mass. In elastic scattering (right) the photon with its pointlike coupling to quarks is a local probe that does not single out any space-time direction.

One also finds that Lorentz invariance restricts the possible dependence on ξ of the result to be a polynomial of a specific order,

$$\begin{aligned} &\int_{-1}^{1} \mathrm{d}x\, x^{n-1} H^q(x,\xi,t) = \sum_{k=0}^{n} (2\xi)^k\, A^q_{n,k}(t)\,, \\ &\int_{-1}^{1} \mathrm{d}x\, x^{n-1} E^q(x,\xi,t) = \sum_{k=0}^{n} (2\xi)^k\, B^q_{n,k}(t)\,, \end{aligned} \tag{14}$$

where k is even because the GPDs are even functions of ξ due to time reversal invariance. The constraint in (14) is called *polynomiality*, and the absence of ξ dependence in (13) is a special case of it (with polynomials of degree zero). Note that this property requires a delicate interplay between the DGLAP and ERBL regions under the integral: although the physical interpretation of these regions is very different, Lorentz invariance ties them together in a way that is not easy to grasp for our intuition. On a more practical side, ensuring polynomiality (and hence Lorenz invariance) is an important criterion to fulfill when one writes down models for GPDs. Two of the most widely used approaches satisfy this criterion by construction, namely the ansatz using double distributions described in [14, 2] and the ansatz using conformal moments in [15, 16].

The Mellin moments with $n = 2$ in (14) play a particular role. The are matrix elements of the quark part of the energy-momentum tensor. For the sum $H^q + E^q$ one finds the celebrated sum rule of Ji [17]:

$$\frac{1}{2}\int_{-1}^{1} \mathrm{d}x\, x\big[H^q(x,\xi,t) + E^q(x,\xi,t)\big] = \frac{1}{2}\big[A^q_{2,0}(t) + B^q_{2,0}(t)\big] = J^q(t)\,, \tag{15}$$

where $J^q(0)$ gives the *total* angular momentum carried by quarks and antiquarks of flavor q in the proton, including both their helicity and their orbital motion. Whereas a wealth of inclusive processes with polarized targets allows us to measure the helicity of partons, probing their orbital angular momentum is much more difficult, and Ji's sum rule offers a rare chance to do this. A relation analogous to (15) exists for gluon GPDs and $J^g(t)$. The attentive reader will have noticed that there is no term going with ξ^2 in (15), unlike in the general formula (14). The reason is that for the highest coefficients there one has $A^q_{n,n}(t) + B^q_{n,n}(t) = 0$.

Notice finally that matrix elements of local operators are suitable for evaluation in Euclidean space-time. For n up to 2 the form factors in (14) have been calculated on the lattice, which provides a valuable opportunity to study aspects of GPDs in a fully nonperturbative fashion. More details on this can be found in Philipp Hägler's lectures at this school, and in the review [18].

3˙2. *Impact parameter.* – Among the most interesting aspects of GPDs is that they contain information about the spatial distribution of partons inside the proton. To quantify where the partons are, we first need to localize the proton. We do this by forming wave packets

$$|p^+, \boldsymbol{b}\rangle = \int \frac{\mathrm{d}^2\boldsymbol{p}}{(2\pi)^2}\, e^{-i\boldsymbol{b}\boldsymbol{p}}\, |p^+, \boldsymbol{p}\rangle \tag{16}$$

centered at position $\boldsymbol{b}$ in the transverse plane, while keeping the plus-momentum of the state fixed. This allows us to discuss the localization of partons while keeping information about their longitudinal momentum. This can in particular be done in a frame where the proton moves fast, so that we can keep a parton model picture. Remarkably, the localization in two dimensions is possible even in a relativistic theory, where an object cannot be localized in all three space dimensions with an accuracy better than its Compton wavelength.

The proton is an extended object itself, and closer analysis shows that the position $\boldsymbol{b}$ of the state (16) can be understood as the *center of plus-momentum* of the proton constituents,

$$\boldsymbol{b} = \frac{\sum_i p_i^+\, \boldsymbol{b}_i}{\sum_i p_i^+}\,, \tag{17}$$

where the i quarks or gluons have plus-momenta p_i^+ and positions $\boldsymbol{b}_i$. This may be seen as a relativistic analog of the center of mass in nonrelativistic physics, where the weights are given by the masses m_i instead of the plus-momenta of the constituents.

Let us now consider the operator

$$\mathcal{O} = \frac{1}{2} \int \frac{\mathrm{d}z^-}{2\pi}\, e^{ixP^+z^-}\, \bar{q}\left(-\frac{1}{2}z\right) \gamma^+ W\left[-\frac{1}{2}z, \frac{1}{2}z\right] q\left(\frac{1}{2}z\right) \Bigg|_{z^+=0,\boldsymbol{z}=\boldsymbol{0}} \tag{18}$$

in (10), which describes partons localized at transverse position $\boldsymbol{z} = \boldsymbol{0}$, and take its matrix element between localized proton states, setting $p'^+ = p^+$ for simplicity. We have

$$\begin{aligned} \langle p^+, -\boldsymbol{b}'|\mathcal{O}|p^+, -\boldsymbol{b}\rangle &= \int \frac{\mathrm{d}^2\boldsymbol{p}'}{(2\pi)^2}\, \frac{\mathrm{d}^2\boldsymbol{p}}{(2\pi)^2}\, e^{-i(\boldsymbol{b}'\boldsymbol{p}'-\boldsymbol{b}\boldsymbol{p})}\, \langle p^+, \boldsymbol{p}'|\mathcal{O}|p^+, \boldsymbol{p}\rangle \\ &= \int \frac{\mathrm{d}^2\boldsymbol{P}}{(2\pi)^2}\, \frac{\mathrm{d}^2\boldsymbol{\Delta}}{(2\pi)^2}\, e^{-i(\boldsymbol{b}'-\boldsymbol{b})\boldsymbol{P}-i(\boldsymbol{b}'+\boldsymbol{b})\boldsymbol{\Delta}/2}\, \langle p^+, \boldsymbol{p}'|\mathcal{O}|p^+, \boldsymbol{p}\rangle\,, \end{aligned} \tag{19}$$

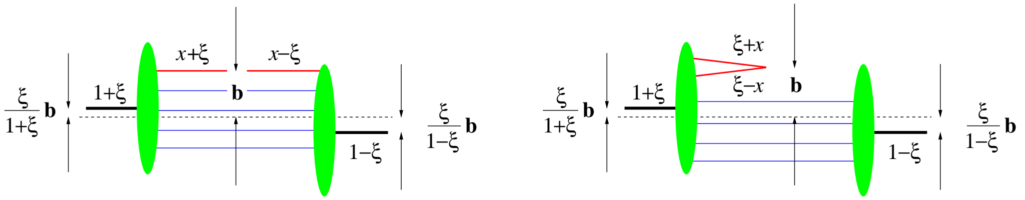

Fig. 11. – Impact parameter interpretation of a GPD in the DGLAP region (left) and in the ERBL region (right).

where in the last step we have changed variables from $\boldsymbol{p}', \boldsymbol{p}$ to $\boldsymbol{P} = \frac{1}{2}(\boldsymbol{p}+\boldsymbol{p}')$, $\boldsymbol{\Delta} = \boldsymbol{p}' - \boldsymbol{p}$. On the r.h.s. we recognize the matrix element that appears in the definition (10) of GPDs. Using Lorentz invariance one can show that this matrix element depends on the difference $\boldsymbol{\Delta}$ of transverse momenta of two proton states but not on their average. We can hence carry out the integration over $\boldsymbol{P}$ and get

$$\langle p^+, -\boldsymbol{b}' | \mathcal{O} | p^+, -\boldsymbol{b} \rangle = \delta^{(2)}(\boldsymbol{b}' - \boldsymbol{b}) \int \frac{\mathrm{d}^2\boldsymbol{\Delta}}{(2\pi)^2}\, e^{-i\boldsymbol{b}\boldsymbol{\Delta}} \, \langle p^+, \boldsymbol{p}' | \mathcal{O} | p^+, \boldsymbol{p} \rangle \,. \tag{20}$$

Taking equal helicities for the proton states in (20) and using (10) we can identify

$$q(x, \boldsymbol{b}^2) = \int \frac{\mathrm{d}^2\boldsymbol{\Delta}}{(2\pi)^2}\, e^{-i\boldsymbol{b}\boldsymbol{\Delta}} \, H^q(x, \xi = 0, t = -\boldsymbol{\Delta}^2) \tag{21}$$

as the probability density to find a quark with momentum fraction x at a transverse distance $\boldsymbol{b}$ from the center of the proton [19]. One easily finds that integrating (21) over $\boldsymbol{b}$ gives back the usual quark density $q(x)$.

For nonzero skewness ξ the picture is slightly more complicated since we have no probability interpretation. Nevertheless, one finds that the Fourier transform of the GPD w.r.t. $\boldsymbol{\Delta}$ gives information about the position of the parton in the transverse plane [20]. This is shown in fig. 11. The transverse shift of the proton position is a consequence of the finite plus-momentum transfer, which changes the center of plus-momentum. Since in an exclusive process $\boldsymbol{\Delta}$ is a observable quantity, we can rather directly obtain spatial information from experiment.

3·2.1. Transverse deformation and spin-orbit correlations. We will now see what happens with the localization of partons in the proton in the presence of polarization. For simplicity we set $\xi = 0$ again; but a similar discussion can be given for nonzero ξ. As we see in (11), the distribution E^q describes proton helicity flip. We may change basis from helicity eigenstates $|{\uparrow}\rangle$, $|{\downarrow}\rangle$ to states $|\pm\rangle_X = \big(|{\uparrow}\rangle \pm |{\downarrow}\rangle\big)/\sqrt{2}$, which correspond to definite spin along the positive or negative x direction. We then easily find that the helicity-flip matrix elements correspond to a polarization difference in the transverse plane:

$${}_X\langle + | \mathcal{O} | + \rangle_X \; - \; {}_X\langle - | \mathcal{O} | - \rangle_X = \langle {\uparrow} | \mathcal{O} | {\downarrow} \rangle + \langle {\downarrow} | \mathcal{O} | {\uparrow} \rangle \tag{22}$$

for any operator $\mathcal{O}$. Using this for the helicity-flip matrix element in (11) and taking the Fourier transform w.r.t. $\boldsymbol{\Delta}$, we find that the density of quarks in a proton polarized along the positive x direction is

$$q_X(x,\boldsymbol{b}) = q(x,\boldsymbol{b}^2) - \frac{b^y}{m}\,\frac{\partial}{\partial \boldsymbol{b}^2}\, e^q(x,\boldsymbol{b}^2)\,, \tag{23}$$

where the Fourier transform $e^q(x,\boldsymbol{b}^2)$ of $E^q(x,\xi=0,t=-\boldsymbol{\Delta}^2)$ is defined in analogy to (21). The transverse distribution of partons is hence shifted sideways if the proton has transverse polarization. This shift is described by E^q, which thus quantifies a particular spin-orbit correlation in the proton. We know that this correlation must be sizeable at least for *some* values of x because the first moment of E^q is related with the Pauli form factor, which is known experimentally. For $t=0$ one finds

$$\int_{-1}^{1} \mathrm{d}x\, E^u(x,\xi,0) \approx 1.67\,, \qquad \int_{-1}^{1} \mathrm{d}x\, E^d(x,\xi,0) \approx -2.03\,. \tag{24}$$

How big the corresponding effects are for sea quarks and for gluons is an intriguing question and currently unknown. Let me remark that an analogous transverse shift in the spatial distribution is also obtained if the quark instead of the proton carries transverse polarization. This is quantified by transversity GPDs, which are not discussed in these lectures for reasons of space.

3˙3. *Transverse momentum vs. transverse position of partons.* – We have seen that GPDs describe the partonic structure of hadrons in transverse configuration space. Quite different information is contained in transverse-momentum–dependent parton distributions (TMDs), which can be measured in semi-inclusive DIS or in Drell-Yan production. Let us take a closer look at the relation between these two types of distributions.

From ordinary quantum mechanics we are accustomed to the fact that transverse position and transverse momentum are Fourier conjugate variables. This remains true in quantum field theory, as we have already used when constructing a spatially localized proton state in (16). Likewise, we can write down a quark field operator associated with partons of definite transverse momentum. Namely,

$$q(\boldsymbol{k},z^-,z^+=0) = \int \mathrm{d}^2\boldsymbol{z}\, e^{-i\boldsymbol{z}\boldsymbol{k}}\, q(\boldsymbol{z},z^-,z^+=0) \tag{25}$$

annihilates quarks with transverse momentum $\boldsymbol{k}$ and creates antiquarks with transverse momentum $-\boldsymbol{k}$. In the matrix elements defining GPDs (as well as in those defining TMDs) we have bilinear operators. Simple algebra gives

$$\begin{aligned} \bar{q}(\boldsymbol{k}')\, q(\boldsymbol{k}) &= \int \mathrm{d}^2\boldsymbol{z}'\, \mathrm{d}^2\boldsymbol{z}\, e^{i(\boldsymbol{z}'\boldsymbol{k}'-\boldsymbol{z}\boldsymbol{k})}\, \bar{q}(\boldsymbol{z}')\, q(\boldsymbol{z})\,, \\ \boldsymbol{z}'\boldsymbol{k}' - \boldsymbol{z}\boldsymbol{k} &= (\boldsymbol{z}'-\boldsymbol{z})\,\frac{\boldsymbol{k}'+\boldsymbol{k}}{2} + \frac{\boldsymbol{z}'+\boldsymbol{z}}{2}\,(\boldsymbol{k}'-\boldsymbol{k})\,, \end{aligned} \tag{26}$$

where we have omitted the arguments for plus- and minus-components. We thus see that

- the average transverse momentum is Fourier conjugate to the transverse position difference and
- the transverse momentum difference is Fourier conjugate to the average transverse momentum,

where the "average" and "difference" refer to the two operators, and hence to the two parton legs in the corresponding matrix elements. Note that the average transverse momentum and position are independent variables and *not* related by a Fourier transform.

After this little exercise we can contrast the impact parameter distributions discussed in the previous subsections with TMDs. For simplicity we set $\xi = 0$ in the following and do not display longitudinal variables in the field operators and proton states. Furthermore, we use fields depending on transverse position and proton states with definite transverse momentum. In an impact parameter distribution

$$q(x, \boldsymbol{b}) \propto \int \mathrm{d}^2\boldsymbol{\Delta}\, e^{-i\boldsymbol{b}\boldsymbol{\Delta}} \left\langle \frac{1}{2}\boldsymbol{\Delta} \middle| \bar{q}(\boldsymbol{0}) \ldots q(\boldsymbol{0}) \middle| -\frac{1}{2}\boldsymbol{\Delta} \right\rangle \tag{27}$$

we have quarks at position $\boldsymbol{0}$ and proton states at position $-\boldsymbol{b}$ (so that $\boldsymbol{b}$ is the distance of the quarks from the proton center). For a TMD we have instead quarks with transverse momentum $\boldsymbol{k}$ in a proton with transverse momentum $\boldsymbol{0}$,

$$q(x, \boldsymbol{k}) \propto \int \mathrm{d}^2\boldsymbol{z}\, e^{-i\boldsymbol{z}\boldsymbol{k}} \langle \boldsymbol{0} | \bar{q}\left(-\frac{1}{2}\boldsymbol{z}\right) \ldots q\left(\frac{1}{2}\boldsymbol{z}\right) | \boldsymbol{0} \rangle . \tag{28}$$

The two functions carry different information about the proton and cannot be obtained from each other. We can however introduce GPDs that are not integrated over transverse momentum:

$$H(x, \boldsymbol{k}, \boldsymbol{\Delta}) \propto \int \mathrm{d}^2\boldsymbol{z}\, e^{-i\boldsymbol{z}\boldsymbol{k}} \left\langle \frac{1}{2}\boldsymbol{\Delta} \middle| \bar{q}\left(-\frac{1}{2}\boldsymbol{z}\right) \ldots q\left(\frac{1}{2}\boldsymbol{z}\right) \middle| -\frac{1}{2}\boldsymbol{\Delta} \right\rangle , \tag{29}$$

still keeping $\xi = 0$ for simplicity. At $x > 0$ these distributions correspond to a quark leaving the proton with transverse momentum $\boldsymbol{k} - \frac{1}{2}\boldsymbol{\Delta}$ and returning with transverse momentum $\boldsymbol{k} + \frac{1}{2}\boldsymbol{\Delta}$. Fourier transforming this w.r.t. $\boldsymbol{\Delta}$ as we did with transverse-momentum integrated GPDs, we obtain a distribution

$$W(x, \boldsymbol{k}, \boldsymbol{b}) \propto \int \mathrm{d}^2\boldsymbol{\Delta}\, \mathrm{d}^2\boldsymbol{z}\, e^{-i\boldsymbol{b}\boldsymbol{\Delta} - i\boldsymbol{z}\boldsymbol{k}} \left\langle \frac{1}{2}\boldsymbol{\Delta} \middle| \bar{q}\left(-\frac{1}{2}\boldsymbol{z}\right) \ldots q\left(\frac{1}{2}\boldsymbol{z}\right) \middle| -\frac{1}{2}\boldsymbol{\Delta} \right\rangle \tag{30}$$

associated with transverse momentum $\boldsymbol{k}$ and transverse position $\boldsymbol{b}$ of the quark, where we must now keep in mind that both quantities are averaged over the quark legs that leave the proton and return to it. Distributions with this structure are well known in other parts of physics and go under the name of Wigner distributions. They contain at the

$$\begin{tikzcd}
H(x,\boldsymbol{z},\boldsymbol{\Delta}) \arrow[r, leftrightarrow, "\text{FT } \boldsymbol{z}\leftrightarrow\boldsymbol{k}"'] & H(x,\boldsymbol{k},\boldsymbol{\Delta}) \arrow[r, leftrightarrow, "\text{FT } \boldsymbol{\Delta}\leftrightarrow\boldsymbol{b}"] \arrow[d, "\boldsymbol{\Delta}=\boldsymbol{0}"'] \arrow[dr, "\int d^2\boldsymbol{k}"] & W(x,\boldsymbol{k},\boldsymbol{b}) \arrow[dl, "\int d^2\boldsymbol{b}"] \arrow[dr, "\int d^2\boldsymbol{k}"] & \\
q(x,\boldsymbol{z}) \arrow[r, leftrightarrow, "\text{FT } \boldsymbol{z}\leftrightarrow\boldsymbol{k}"'] & q(x,\boldsymbol{k}) \arrow[dr, "\int d^2\boldsymbol{k}"] & H(x,\boldsymbol{\Delta}) \arrow[r, leftrightarrow, "\text{FT } \boldsymbol{\Delta}\leftrightarrow\boldsymbol{b}"'] \arrow[d, "\boldsymbol{\Delta}=\boldsymbol{0}"'] \arrow[dr, "\int dx\, x^{n-1}"] & q(x,\boldsymbol{b}) \arrow[dl, "\int d^2\boldsymbol{b}"'] \\
 & & q(x) & F_n(\boldsymbol{\Delta})
\end{tikzcd}$$

Fig. 12. – Different types of distributions and their connection with each other. GPDs and related quantities are all taken at $\xi = 0$. The form factor F_n corresponds to $A_{n,0}$ in (14).

same time the information of impact parameter distributions and of TMDs. They can, *e.g.*, be calculated in quark models, but unfortunately we do not know how to determine them from an observable process in a model independent way.

Figure 12 gives an overview of the different types of distributions and form factors we have seen. Let me mention that the distributions on the very left depend on the relative transverse position between the two quark fields in the operator definition and are for instance useful for the resummation of Sudakov logarithms; an aspect I will not discuss here.

4. – Studying GPDs in exclusive reactions

In sect. **2** we have used the process of deeply virtual Compton scattering, $\gamma^* p \to \gamma p$, to introduce the concept of GPDs. There are, however, more processes where the same distributions can be measured. As a "mirror process" of DVCS one may regard timelike Compton scattering (TCS), $\gamma p \to \gamma^* p$, where the initial photon is real and the final one has a timelike virtuality, whereas in DVCS the final photon is real and the initial one has a spacelike virtuality. The timelike photon in TCS decays into a lepton pair (just as in the Drell-Yan process) and the physically observed process is $\gamma p \to \ell^+ \ell^- p$. It turns out that at leading order in α_s DVCS and TCS involve exactly the same integrals over GPDs, whereas at higher orders the integrals differ [21]. Already different integrals at lowest order are involved in the description of double DVCS, $\gamma^* p \to \gamma^* p$, where the initial photon has a spacelike and the final photon a timelike virtuality. In the following we collectively refer to DVCS, TCS and double DVCS as "Compton scattering".

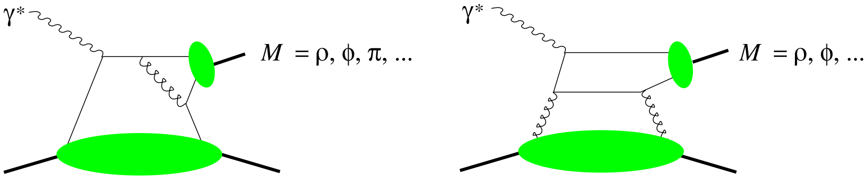

Fig. 13. – Example graphs for hard exclusive meson production, involving quark GPDs (left) or, for vector mesons, gluon GPDs (right).

A large class of processes involving GPDs is the exclusive production of mesons from a virtual photon, $\gamma^* p \to Mp$, where M can be a light meson such as a pion, kaon, ρ, ϕ etc. If the produced meson is made from two heavy quarks, such as a J/Ψ or an Υ, the quark mass provides a hard scale and the initial photon may also be real. Figure 13 shows example graphs for these processes. If the meson has negative charge conjugation parity $C = -1$, as is the case of vector mesons, both quark and gluon GPDs appear at lowest order in the strong coupling. These channels are therefore particularly sensitive to gluons in the proton, whereas in Compton scattering gluon GPDs only appear at the level of α_s corrections and through the scale evolution of the quark GPDs (in the same way in which the ordinary gluon distribution appears in DIS). Especially good "gluon filters" are J/Ψ and Υ production, since GPDs for heavy quarks only become relevant at very high virtualities Q of the photon (much higher than the heavy quark mass).

Using parity invariance of the hard-scattering subprocess one can show that (in the Bjorken limit) vector meson production involves the distributions H^q, E^q, H^g, E^g for unpolarized partons, whereas the production of pseudoscalar mesons is sensitive to longitudinal quark polarization in the form of $\tilde{H}^q, \tilde{E}^q$ (gluons do not contribute in this case because pseudoscalar mesons have $C = +1$). By contrast, one finds that Compton scattering involves $H^q, E^q, \tilde{H}^q, \tilde{E}^q$ at tree level and additionally the corresponding gluon GPDs at higher order. Furthermore, Compton scattering and the different meson production channels involve different linear combinations of GPDs for the various quark flavors. It is thus the combination of many processes that will ultimately be necessary to disentangle the many GPDs, a situation well-known from the study of ordinary parton distributions.

The theory description of meson production is, however, more complicated than the one for Compton scattering. The most obvious complication is that meson production involves two types of collinear subgraphs, one for the proton and one for the meson, and correspondingly depends on two types of nonperturbative functions: GPDs for the proton and the distribution amplitude of the produced meson. Moreover, various studies find that meson production is more sensitive to corrections, both to higher orders in α_s and to power corrections in $1/Q$, see, *e.g.*, [22] and [23,24]. A reliable theory description therefore requires larger values of Q for meson production; how large depends on the channel and is often subject of debate among theorists.

Another important difference between Compton scattering and meson production is the selection of helicities in the hard-scattering subprocess. One finds that the leading amplitude for DVCS and TCS is Q independent at fixed ξ (up to logarithmic scaling violation effects) and involves transverse photon polarization. (For double DVCS one has an additional leading amplitude with longitudinal photons, starting however only at order α_s.) By contrast, the leading amplitude for light meson production at given ξ scales like $1/Q$ up to logarithms and involves longitudinal photon and meson production. Only for J/Ψ and Υ electroproduction with Q comparable to the meson mass do we have amplitudes of similar magnitude for transverse and for longitudinal polarization of the photon and the meson.

4˙1. *From process amplitudes to GPDs.* – In subsect. **2**˙2 we have already seen that the amplitude for DVCS is given by an integral over GPDs times a factor describing the hard-scattering process (commonly called a hard-scattering kernel). We will now take a closer look at this. Let us first take a closer look at the spin structure. For the leading amplitudes of DVCS one can write a general decomposition

$$\begin{aligned}(31)\qquad e^{-2}\mathcal{A}(\gamma^* p \to \gamma p) = {} & \mathcal{H}\,\frac{\bar{u}(p',s')\,\gamma^+ u(p,s)}{2P^+} + \mathcal{E}\,\frac{i}{2m}\,\bar{u}(p',s')\,\frac{\sigma^{+\alpha}\Delta_\alpha}{2P^+}\,u(p,s) \\ & + \mu\left[\tilde{\mathcal{H}}\,\frac{\bar{u}(p',s')\,\gamma^+\gamma_5\,u(p,s)}{2P^+} - \xi\tilde{\mathcal{E}}\,\frac{1}{2m}\,\bar{u}(p',s')\,\gamma_5\,u(p,s)\right],\end{aligned}$$

where $\mu = \pm 1$ is the helicity of the initial and final state photon. $\mathcal{H}$, $\mathcal{E}$, $\tilde{\mathcal{H}}$ and $\tilde{\mathcal{E}}$ depend on ξ, t, Q^2 and are called Compton form factors. The prefactors and proton spinor products in (31) have been chosen to match the GPD definitions (10) and (12). To leading order in α_s one has

$$(32)\qquad \mathcal{H}(\xi,t,Q^2) = \sum_q e_q^2 \int_{-1}^{1} \mathrm{d}x\,\frac{H^q(x,\xi,t;Q^2) - H^q(-x,\xi,t;Q^2)}{\xi - x - i\varepsilon}\,,$$

where the last argument of H^q is the factorization scale, set equal to Q^2 here. Analogous relations hold for the other three GPDs. Note that the decomposition (31) remains valid at higher orders in α_s. Furthermore, one can write down similar decompositions for exclusive meson production. Using the relation (7) with x_B replaced by ξ, we see that at leading order in α_s the imaginary parts of the Compton form factors are given by GPDs at the points $x = \xi$ and $x = -\xi$, *i.e.* at the boundaries between the DGLAP and ERBL regions. The real parts of the form factors are given by principal value integrals over the full x interval from -1 to 1 and thus seem to depend on more details of the GPDs. However, one can prove a dispersion relation, which at leading order in α_s reads [25]

$$\begin{aligned}(33)\qquad \mathrm{Re}\,\mathcal{H}(\xi,t,Q^2) &= \mathrm{PV}\!\int_{-1}^{1} \mathrm{d}x\,\frac{H^q(x,\xi,t;Q^2) - H^q(-x,\xi,t;Q^2)}{\xi - x} \\ &= \mathrm{PV}\!\int_{-1}^{1} \mathrm{d}x\,\frac{H^q(x,x,t;Q^2) - H^q(-x,x,t;Q^2)}{\xi - x} + \mathcal{C}(t;Q^2)\end{aligned}$$

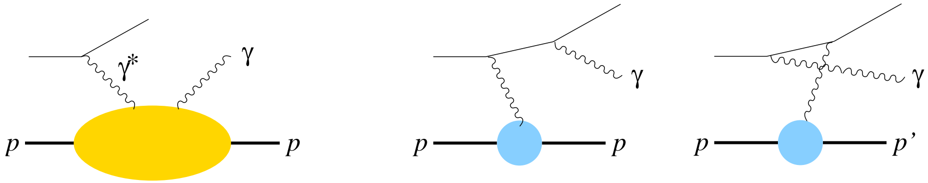

Fig. 14. – The two subprocesses contributing to the process $\ell p \to \ell \gamma p$: virtual Compton scattering (left) and the Bethe-Heitler process (right).

where $\mathcal{C}(t; Q^2)$ is independent of ξ and can be computed in terms of $H^q(x, \xi, t; Q^2)$. More precisely, $\mathcal{C}(t; Q^2)$ is an integral over the so-called D term first introduced in [26]. A relation analogous to (33) holds for $\mathcal{E}$ and involves $-\mathcal{C}(t; Q^2)$ instead of $\mathcal{C}(t; Q^2)$ on the r.h.s., and analogous relations for $\tilde{\mathcal{H}}$ and $\tilde{\mathcal{E}}$ do not have such a term at all [27]. Up to the quantity $\mathcal{C}(t; Q^2)$ the Compton form factors thus involve only GPDs at $x = \pm\xi$.

An important consequence of this is that a leading order analysis of Compton scattering (and likewise of any meson production channel) cannot reconstruct the full x dependence of GPDs at given ξ. Only the effects incorporated in Q^2 evolution and in the explicit higher-order corrections contain information about the GPDs away from $x = \pm\xi$. To which extent a reconstruction of the full x dependence using such effects can be achieved in realistic situations is currently not clear.

4˙2. *A closer look at DVCS.* – There is another aspect that singles out Compton scattering compared with meson production. In the following we concentrate on the DVCS process; a similar discussion can be given for TCS and for double DVCS.

Recall that DVCS is observed in elastic lepton-proton scattering, $\ell p \to \ell \gamma p$. The same reaction can take place by emitting the photon from the lepton line, as shown in fig. 14. This is the Bethe-Heitler process, where the scattering on the proton is mediated by a single photon of momentum Δ. The necessary information on the proton structure is hence described by the electromagnetic form factors $F_1(t)$ and $F_2(t)$ we already encountered in (13); since these are well measured at low t one can calculate the Bethe-Heitler process to good precision.

The relative importance of DVCS and the Bethe-Heitler process strongly depends on kinematics, with their relative strength roughly going like

$$\text{(34)} \qquad \frac{\mathrm{d}\sigma^{C}}{\mathrm{d}x_B\, \mathrm{d}Q^2\, \mathrm{d}t\, \mathrm{d}\phi} : \frac{\mathrm{d}\sigma^{BH}}{\mathrm{d}x_B\, \mathrm{d}Q^2\, \mathrm{d}t\, \mathrm{d}\phi} \sim \frac{1}{y^2} \frac{1}{Q^2} : \frac{1}{|t|}\,,$$

where the superscripts C and BH respectively stand for Compton and Bethe-Heitler. $y = Q^2/(x_B\, s_{\ell p})$ is the usual inelasticity variable in lepton-proton scattering, with $s_{\ell p}$ being the squared ℓp center-of-mass energy, and ϕ is the azimuthal angle between the plane determined by the leptons and the plane determined by the hadrons in the proton rest frame (see [28] for a precise definition). The factors $1/Q^2$ and $1/t$ in (34) respectively come from the propagators of the virtual photons in DVCS and the Bethe-Heitler process, and the factor $1/y^2$ comes from the lepton-photon vertex in DVCS. The two subprocesses interfere at the amplitude level, and the size of their interference term $\mathrm{d}\sigma^I/(\mathrm{d}x_B\,\mathrm{d}Q^2\,\mathrm{d}t\,\mathrm{d}\phi)$ is typically in-between the two contributions in (34).

Since the validity of factorization for DVCS requires $|t|$ to be small compared with Q^2, the Bethe-Heitler process is typically more important, except for small y. However, even if y is not small, one can extract information about Compton scattering from the DVCS-Bethe-Heitler interference. This actually provides a unique chance: since the Bethe-Heitler process amplitude can be computed, the interference term allows one to measure not only size of the DVCS amplitude but also its *phase*. In other words, it gives separate information about the real and imaginary parts of the Compton form factors.

To "filter out" the interference term in the ℓp cross-section one can make use of several asymmetries. As is evident from fig. 14 the DVCS contribution to the ℓp amplitude contains a single lepton-photon vertex and thus changes sign if one switches from a negative to a positive lepton beam. By contrast, the Bethe-Heitler amplitude contains two lepton-photon vertices and is independent of the lepton charge $e_\ell = \pm 1$. The interference term is therefore linear in e_ℓ and can be separated by measuring the beam charge asymmetry.

A different way of separating the different contributions makes use of the polarization of the initial lepton or the initial proton. Using the invariance of strong and electromagnetic interactions under parity and time reversal, one can show that a single-spin asymmetry (either w.r.t. the lepton or to the proton) does not receive any contribution from the Bethe-Heitler process by itself, leaving one with the interference term and the pure DVCS contribution. In full glory one has

$$
\begin{aligned}
(35)\qquad \mathrm{d}\sigma(\ell p \to \ell\gamma p) \sim\ & \mathrm{d}\sigma^{BH}_{UU} && + e_\ell\,\mathrm{d}\sigma^{I}_{UU} && + \mathrm{d}\sigma^{C}_{UU} \\
& + P_\ell S_L\,\mathrm{d}\sigma^{BH}_{LL} && + e_\ell P_\ell S_L\,\mathrm{d}\sigma^{I}_{LL} && + P_\ell S_L\,\mathrm{d}\sigma^{C}_{LL} \\
& + P_\ell S_T\,\mathrm{d}\sigma^{BH}_{LT} && + e_\ell P_\ell S_T\,\mathrm{d}\sigma^{I}_{LT} && + P_\ell S_T\,\mathrm{d}\sigma^{C}_{LT} \\
& && + e_\ell P_\ell\,\mathrm{d}\sigma^{I}_{LU} && + P_\ell\,\mathrm{d}\sigma^{C}_{LU} \\
& && + e_\ell S_L\,\mathrm{d}\sigma^{I}_{UL} && + S_L\,\mathrm{d}\sigma^{C}_{UL} \\
& && + e_\ell S_T\,\mathrm{d}\sigma^{I}_{UT} && + S_T\,\mathrm{d}\sigma^{C}_{UT}\,,
\end{aligned}
$$

where the first subscript U, L in $\mathrm{d}\sigma$ indicates an unpolarized or longitudinally polarized lepton beam and the second subscript U, L, T an unpolarized, longitudinally or transversely polarized proton target. P_ℓ is the lepton beam polarization, and S_L, S_T denote the longitudinal and transverse proton polarizations. For a transversely polarized proton, one has in addition a dependence on the azimuthal angle ϕ_S between the lepton plane and the target spin in the proton rest frame (see [28]). As announced, there is no Bethe-Heitler contribution to the single spin terms LU, UL and UT in (35). Using parity invariance, one can further show that the single spin terms are odd under the simultaneous replacement $\phi \to -\phi$ and $\phi_S \to -\phi_S$, whereas the unpolarized or double spin terms UU, LL and LT are even under that replacement.

TABLE I. – *Linear combinations of Compton form factors in the DVCS-Bethe-Heitler interference terms. The electromagnetic form factors* F_1 *and* F_2 *are to be evaluated at momentum transfer* t. *An ellipsis indicates terms that come with one or more powers of* ξ *and thus are suppressed in a wide range of kinematics. Complete expressions can be found in* [29,30].

Target polarization	GPD combination
Unpolarized	$F_1\mathcal{H} + \xi(F_1+F_2)\tilde{\mathcal{H}} - \frac{t}{4m^2}F_2\,\mathcal{E}$
Longitudinal	$F_1\tilde{\mathcal{H}} + \xi(F_1+F_2)\mathcal{H} - \big[\frac{\xi}{1+\xi}F_1 + \frac{t}{4m^2}F_2\big]\xi\tilde{\mathcal{E}} + \dots$
Transverse $\propto \sin(\phi-\phi_S)$	$F_2\mathcal{H} - F_1\,\mathcal{E} + \dots$
Transverse $\propto \cos(\phi-\phi_S)$	$F_2\tilde{\mathcal{H}} - F_1\;\xi\tilde{\mathcal{E}} + \dots$

TABLE II. – *Combinations of meson production form factors for the leading terms in the cross-section at large* Q^2.

Meson	Target polarization	GPD combination
Vector	Unpolarized	$\lvert\mathcal{H}_M\rvert^2 - \frac{t}{4m^2}\lvert\mathcal{E}_M\rvert^2 - \xi^2\,\lvert\mathcal{H}_M+\mathcal{E}_M\rvert^2$
	Transverse $\propto \sin(\phi-\phi_S)$	$\mathrm{Im}(\mathcal{E}_M^*\mathcal{H}_M)$
Pseudoscalar	Unpolarized	$(1-\xi^2)\,\lvert\tilde{\mathcal{H}}_M\rvert^2 - \frac{t}{4m^2}\,\lvert\xi\tilde{\mathcal{E}}_M\rvert^2 - 2\xi\,\mathrm{Re}(\xi\tilde{\mathcal{E}}^*_M\tilde{\mathcal{H}}_M)$
	Transverse $\propto \sin(\phi-\phi_S)$	$\mathrm{Im}(\xi\tilde{\mathcal{E}}^*_M\tilde{\mathcal{H}}_M)$

The interference terms contain information about the phase of the Compton amplitude in a very simple manner: the single-spin terms $\mathrm{d}\sigma^I_{UT}$, $\mathrm{d}\sigma^I_{UL}$ and $\mathrm{d}\sigma^I_{UT}$ are linear in the imaginary parts of the Compton form factors, *i.e.* to $\mathrm{Im}\,\mathcal{H}$, $\mathrm{Im}\,\mathcal{E}$, $\mathrm{Im}\,\tilde{\mathcal{H}}$ and $\mathrm{Im}\,\tilde{\mathcal{E}}$, whereas the unpolarized or double-spin terms $\mathrm{d}\sigma^I_{UU}$, $\mathrm{d}\sigma^I_{LL}$ and $\mathrm{d}\sigma^I_{LT}$ are linear in their real parts. Even better, one finds that in the interference terms one has *four* independent observables that allow one to separate the four Compton form factors. This is because for transverse polarization one can separate two terms that depend either on $\sin(\phi-\phi_S)$ or on $\cos(\phi-\phi_S)$, which, respectively, are maximal when the target spin is perpendicular to the hadron plane or in this plane. The different linear combinations are shown in table I.

We see that DVCS contains a multitude of observables that permit rather detailed access to the different GPDs. For meson production, the number of observables that can be computed in the Bjorken limit using collinear factorization is more limited: in fact one only has the unpolarized $\gamma^* p$ cross-section and the single-spin asymmetry for transverse proton polarization. Table II shows the corresponding bilinear combinations of meson production form factors, which are integrals over GPDs defined in a similar way as for Compton scattering [30]. Note that the relevant phase between form factors is important here: the term $\mathrm{Im}(\mathcal{E}^*_M\mathcal{H}_M)$ is for instance small if $\mathcal{E}^*_M$ and $\mathcal{H}_M$ are individually large but have nearly equal complex phases.

* * *

It is a pleasure to thank the students of the school for the many good questions they asked, and M. Anselmino and his team for organizing such a wonderful school.

REFERENCES

[1] Ji X.-D., *J. Phys. G*, **24** (1998) 1181 [hep-ph/9807358].

[2] Goeke K., Polyakov M. V. and Vanderhaeghen M., *Prog. Part. Nucl. Phys.*, **47** (2001) 401 [hep-ph/0106012].

[3] Diehl M., *Phys. Rep.*, **388** (2003) 41 [hep-ph/0307382].

[4] Belitsky A. V. and Radyushkin A. V., *Phys. Rep.*, **418** (2005) 1 [hep-ph/0504030].

[5] Boffi S. and Pasquini B., *Riv. Nuovo Cimento*, **30** (2007) 387 [arXiv:0711.2625].

[6] Collins J. C., Frankfurt L. and Strikman M., *Phys. Rev. D*, **56** (1997) 2982 [hep-ph/9611433].

[7] Collins J. C., hep-ph/9907513.

[8] Collins J. C., *Foundations of perturbative QCD* (CUP, Cambridge) 2011.

[9] Libby S. B. and Sterman G. F., *Phys. Rev. D*, **18** (1978) 4737.

[10] Jaffe R. L., hep-ph/9602236.

[11] Radyushkin A. V., *Phys. Rev. D*, **56** (1997) 5524 [hep-ph/9704207].

[12] Müller D. *et al.*, *Fortsch. Phys.*, **42** (1994) 101 [hep-ph/9812448].

[13] Burkardt M. and Schnell G., *Phys. Rev. D*, **74** (2006) 013002 [hep-ph/0510249].

[14] Musatov I. V. and Radyushkin A. V., *Phys. Rev. D*, **61** (2000) 074027 [hep-ph/9905376].

[15] Kumerički K., Müller D. and Passek-Kumerički K., *Nucl. Phys. B*, **794** (2008) 244 [hep-ph/0703179].

[16] Kumerički K. and Müller D., arXiv:1008.2762.

[17] Ji X.-D., *Phys. Rev. Lett.*, **78** (1997) 610 [hep-ph/9603249].

[18] Hägler Ph., *Phys. Rep.*, **490** (2010) 49 [arXiv:0912.5483].

[19] Burkardt M., *Int. J. Mod. Phys. A*, **18** (2003) 173 [hep-ph/0207047].

[20] Diehl M., *Eur. Phys. J. C*, **25** (2002) 223; **31** (2003) 277 [hep-ph/0205208](Erratum).

[21] Pire B., Szymanowski L. and Wagner J., *Phys. Rev. D*, **83** (2011) 034009 [arXiv:1101.0555].

[22] Diehl M. and Kugler W., *Eur. Phys. J. C*, **52** (2007) 933 [arXiv:0708.1121].

[23] Vanderhaeghen M., Guichon. P. A. M. and Guidal M., *Phys. Rev. D*, **60** (1999) 094017 [hep-ph/9905372].

[24] Goloskokov S. V. and Kroll P., *Eur. Phys. J. C*, **53** (2008) 367 [arXiv:0708.3569].

[25] Anikin I. V. and Teryaev O. V., *Phys. Rev. D*, **76** (2007) 056007 [arXiv:0704.2185].

[26] Polyakov M. V. and Weiss C., *Phys. Rev. D*, **60** (1999) 114017 [hep-ph/9902451].

[27] Diehl M. and Ivanov D. Yu., *Eur. Phys. J. C*, **52** (2007) 919 [arXiv:0707.0351].

[28] Bacchetta A., D'Alesio U., Diehl M. and Miller C. A., *Phys. Rev. D*, **70** (2004) 117504 [hep-ph/0410050].

[29] Belitsky A. V., Müller D. and Kirchner A., *Nucl. Phys. B*, **629** (2002) 323 [hep-ph/0112108].

[30] Diehl M. and Sapeta S., *Eur. Phys. J. C*, **41** (2005) 515 [hep-ph/0503023].

This page intentionally left blank

Proceedings of the International School of Physics “Enrico Fermi”
Course CLXXX “Three-Dimensional Partonic Structure of the Nucleon”
edited by M. Anselmino, H. Avakian, D. Hasch and P. Schweitzer
(IOS, Amsterdam; SIF, Bologna)
DOI 10.3254/978-1-61499-197-7-107

TMDs at work

A. Bacchetta

Dipartimento di Fisica, Università di Pavia, and INFN, Sezione di Pavia
via Bassi 6, Pavia, Italy

Summary. — The following lecture notes are an introduction to some aspects of transverse-momentum–dependent parton distribution functions (TMDs). Some parts of the present notes were not actually covered during the school, but are given here for reference.

1. – Introduction

We are still profoundly far from fully understanding QCD and nucleons. If we take a look at the list of nucleons properties in the Particle Data Group tables, we can read what is the nucleons mass, spin, quark content, charge, magnetic moment, charge radius... It is fair to say that, with the partial exception of the mass, we cannot explain any single one of these quantities from first principles. The fundamental reason is that we are unable to explain confinement (see, *e.g.*, [1]).

One of the ways we can follow to better understand QCD and confinement is to study the inner structure of the nucleon in higher and higher details. In these years, thanks to the contributions of HERMES, COMPASS and the JLab experiments, we are reaching the opportunity to reconstruct multi-dimensional pictures of the nucleon. The knowledge of the multi-dimensional structure allows the analysis of properties otherwise inaccessible: quark-gluon correlations, effects of final-state interactions, spin-orbit and

© Società Italiana di Fisica

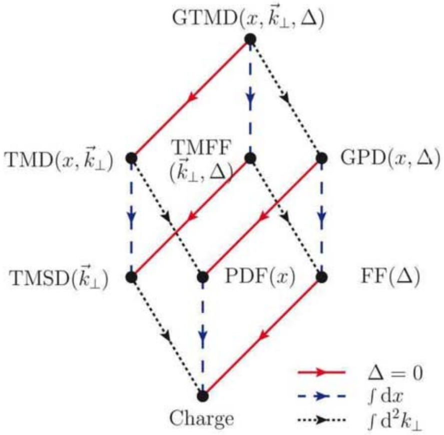

Fig. 1. – Representation of the projections of the GTMDs into parton distributions and form factors (picture from ref. [4]).

spin-spin correlations, and much more. The situation may be compared to protein studies: our present knowledge of the proton structure is limited to one dimension and can be compared to knowing the sequence of amino acids of proteins. It is an extremely important piece of information, but insufficient to understand them. Starting from the 1960s, it has become possible to reconstruct their 3D structure. These advances literally revolutionized our understanding of protein chemistry. Hopefully, we can expect to do the same in hadronic physics.

Partons inside the proton can have a specific momentum and a specific position (with respect to some definition of the center of the proton). Their state can be described by Wigner distributions in six-dimensions (three position and three momentum coordinates) [2, 3]. Wigner distributions are the quantum-mechanical constructions that are closest to a classical probability density in phase-space. Strictly speaking, due to the Heisenberg uncertainty principle, they cannot be considered as probability densities and are not positive definite. For this reason, they are often defined as quasi-probability distributions. However, they can be used to compute the expectation value of any physical observable. In this sense, they represent the maximal knowledge of the partonic structure. They are equivalent to knowing the complete wave function of partons inside the nucleon.

Projections of Wigner distributions on some of the available dimensions do have a probabilistic interpretation (see fig. 1). Of these, we will take into consideration in these lectures only Transverse-Momentum–dependent parton distribution functions (TMDs). In order to be able to define them, we need to distinguish a longitudinal direction from two transverse directions. To observe the internal structure of the proton we need a hard probe (*i.e.* with high four-momentum). This requirement allows us to define a longitudinal direction: it could be defined as the direction of the probe in the rest-frame of the nucleon, or the direction of the nucleon in the center-of-mass frame of nucleon and probe (or in any other frame where proton and probe are collinear). The transverse plane is the one orthogonal to the longitudinal direction.

If we integrate over all coordinates and the two transverse components of momentum we obtain a projection of the Wigner distributions on the longitudinal momentum only. These projections are well studied and have a name: they correspond to the standard Parton Distribution Functions (PDFs). They represent the probability of finding a parton inside a nucleon with a given fraction of the nucleons longitudinal momentum. In this sense, they are pictures of the partonic structure of the nucleon in only one dimension in momentum space. At this point, it is worthwhile remarking that this interpretation is valid at the parton-model level, *i.e.* when the nucleon constituents can be treated approximately as free for the purpose of calculating the interaction with the probe. In the formal QCD treatment, this interpretation is modified and corresponds to the parton-model concept only in the lowest order of perturbation theory [5, 6]. In this sense, we can say that parton distributions are approximate images of the partonic structure.

If we integrate Wigner distributions over all coordinates, we obtain the so-called transverse-momentum distributions (TMDs). They represent pictures of three-dimensional densities in momentum space.

In these lectures I will discuss some aspects related to the theory and phenomenology of TMDs. Historically, partonic transverse momentum has been discussed as early as in the Seventies (see, *e.g.*, [7,8]), few years after the birth of the parton model [9,10]. Transverse momentum can be generated also by the radiation of gluons: the first analysis of this contribution was done in 1979 [11], few years after the birth of QCD. The first study that put together the nonperturbative and perturbative components of TMDs in a formally solid way was an article of Collins and Soper in 1981 [12]: we could probably identify the birth of TMDs in this work. We started using the name TMDs only very recently. For a while we have been talking about transverse-momentum–dependent parton distribution functions (TMD PDFs), then simplified it to TMDs (see, *e.g.*, ref. [13]). Especially in the field of low-x physics, the name "unintegrated parton distribution functions" is also commonly used (see, *e.g.*, [14]).

In spite of this relatively long history, TMDs represent still a largely unexplored field. There are many nontrivial questions that do not have an answer yet. For instance, we still do not have a clear understanding of the detailed shape of the proton (in momentum space). At present, we know that experimental data are consistent with a Gaussian distribution with a width (*i.e.* an average transverse momentum) of about 0.6 GeV at an energy scale of 2 GeV. Roughly speaking, half of it is coming from the primordial transverse momentum of the quark and half is acquired through perturbative gluon radiation. There are indications that the transverse-momentum distribution becomes larger at lower longitudinal momentum. We also do not know if there is a difference in the distribution of partons with different flavors: is one flavor more concentrated in the center and the other in the sides? Or are the flavors uniformly mixed? There are first feeble indications from experimental measurements and from lattice-QCD computations that the down quark distribution is larger than the up [15, 16].

The above considerations apply when we average over the nucleons spin direction. There is even more fun when spin is taken into account. For instance, suppose the spin of the nucleon is moving toward us and its spin is pointing upwards: it turns out that we

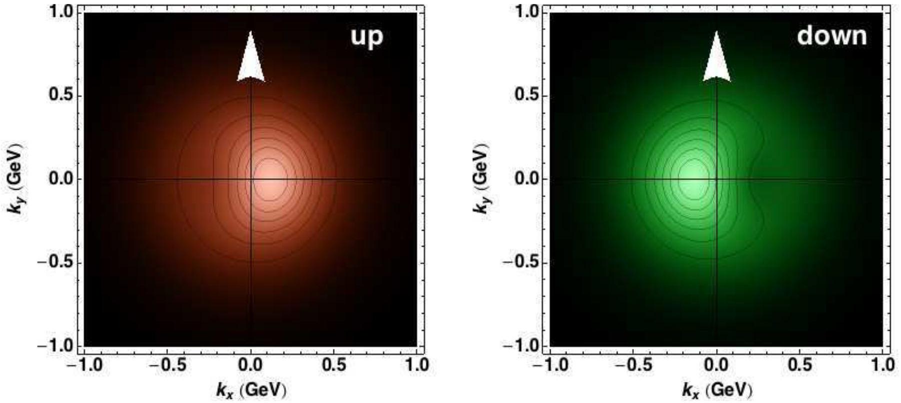

Fig. 2. – The up- and down-quark density distortion in transverse-momentum space, obtained by studies of the Sivers function [17].

see up quarks moving preferentially to the right and down quarks to the left. In terms of images in momentum space, the distributions are not cylindrically symmetric anymore, but distorted in opposite ways for up and down quarks (see fig. 2).

It is worthwhile describing the progress made in understanding this kind of effect. It was first proposed by Sivers in 1990 as a way to explain large left-right asymmetries observed in pion-nucleus collisions [18]. For this reason we nowadays normally speak about the Sivers effect, and the Sivers function describes the left-right distortion in the distribution of partons. For more than a decade, this effect was thought to vanish due to time-reversal symmetry. Starting from a model calculation in 2002, theory studies made clear that the Sivers function could be nonzero [19]. In 2004, the first experimental evidence of a nonzero Sivers effect was reported by the HERMES Collaboration [20], recently confirmed by the COMPASS Collaboration [21]. These breakthroughs forced a profound revision of the QCD treatment of transverse-momentum distributions, still partially underway [6]. For instance, one of the consequences is that the Sivers function in deep inelastic scattering (where an electron strikes a quark inside the nucleon) has an opposite sign compared to the Sivers function in Drell-Yan processes (where an antiquark annihilates a quark inside the nucleon). In other words, an antiquark probe should see a distortion exactly opposite to fig. 5. This striking prediction, due to John Collins [22], should be confirmed (of falsified!) in the next few years by planned experiments (*e.g.*, COMPASS at CERN, AnDY at Brookhaven National Lab).

In order to study all these interesting issues, we need first of all to get acquinted with the underlying formalism.

2. – Notation

These notes are written using the so-called "Amsterdam notation," as done in Piet Mulders's lectures. In the recent paper [23] a slightly different notation was adopted.

Notation differences are a common source of headaches, but it would be too difficult in these lecture notes to abandon the Amsterdam notation. Here, however, a correspondence table is provided:

Amsterdam	[23]	Description
p	k	momentum of parton in distribution function
$\boldsymbol{p}_T$	$\boldsymbol{k}_\perp$	parton transverse momentum in distribution function
k	p	momentum of fragmenting parton
$\boldsymbol{k}_T$	$\boldsymbol{p}_\perp$	trans. momentum of fragmenting parton w.r.t. final hadron
$\boldsymbol{K}_T$	$\boldsymbol{P}_\perp$	trans. momentum of final hadron w.r.t. fragmenting parton
$\boldsymbol{P}_{h\perp}$	$\boldsymbol{P}_{hT}$	transverse momentum of final hadron w.r.t. virtual photon

3. – Inclusive DIS

Inclusive DIS has been discussed in depth in the lectures of Piet Mulders. I will not repeat here all the discussion and summarize only some of the relevant results, adding some details here and there.

We consider the process

$$\ell(l) + N(P) \to \ell(l') + X, \tag{1}$$

where ℓ denotes the beam lepton, N the nucleon target, and where four-momenta are given in parentheses. We neglect the lepton mass. We denote by M the mass of the nucleon. As usual we define $q = l - l'$ and $Q^2 = -q^2$ and introduce the variables

$$x_B = \frac{Q^2}{2\,P\cdot q}\,, \qquad\qquad y = \frac{P\cdot q}{P\cdot l}\,. \tag{2}$$

In these lectures, we will systematically neglect all correction of order M/Q, unless otherwise specified.

The spin vector of the target is denoted by S. Our definition of the azimuthal angle ϕ_S of the outgoing hadron and the target spin is shown in fig. 7 and consistent with the Trento conventions [24]. The helicity of the lepton beam is denoted by λ_e. $S_\perp$ is the transverse parts of S with respect to the photon momentum. $S_\parallel$ is the component of S in the negative z-direction in fig. 7, *i.e.* positive $S_\parallel$ corresponds to the target spin pointing against the virtual photon.

The cross-section for polarized electron-nucleon scattering can be written in a general way as the contraction between a leptonic and a hadronic tensor

$$\frac{\mathrm{d}^3\sigma}{\mathrm{d}x_B\,\mathrm{d}y\,\mathrm{d}\phi_S} = \frac{\alpha^2}{2\,s\,x_B\,Q^2}\,L_{\mu\nu}(l,l',\lambda_e)\;2MW^{\mu\nu}(q,P,S), \tag{3}$$

where $\alpha = e^2/4\pi$. The formula above is valid in the so-called "single-photon exchange approximation." Some QED radiative corrections can be included without modifying this formula [25], but effects such as double-photon exchange are left out [26].

Considering the lepton to be longitudinally polarized, in the massless limit the leptonic tensor is given by

$$\begin{aligned} L_{\mu\nu} &= \sum_{\lambda_e'} \Big(\bar{u}(l',\lambda_e')\,\gamma_\mu\,u(l,\lambda_e)\Big)^* \,\Big(\bar{u}(l',\lambda_e')\,\gamma_\nu\,u(l,\lambda_e)\Big) \\ &= -Q^2 g_{\mu\nu} + 2\left(l_\mu l'_\nu + l'_\mu l_\nu\right) + 2\mathrm{i}\,\lambda_e\,\epsilon_{\mu\nu\rho\sigma}\,l^\rho l'^\sigma . \end{aligned} \tag{4}$$

Ex. 1

Compute the leptonic tensor using Mathematica and the FeynCalc package (www.feyncalc.org). The most important instructions are

```
<< HighEnergyPhysics‘FeynCalc‘

ScalarProduct[l, lp] = Q^2/2;

Amp0 = Contract[
Spinor[l].(-I e GA[\[Mu]]).((1 + GA[5] \[Lambda])/2).Spinor[lp]]

Amp0bar = ComplexConjugate[Amp0] /. \[Mu] -> \[Nu]

FermionSpinSum[Amp0 Amp0bar]

Lept = FermionSpinSum[Amp0 Amp0bar]
/. {DiracTrace -> Tr} /. {\[Lambda]^2 -> 1}
```

The leptonic tensor contains all the information on the leptonic probe, which can be described by means of perturbative QED, while the information on the hadronic target is contained in the hadronic tensor

$$2MW^{\mu\nu}(q,P,S) = \frac{1}{2\pi}\sum_{\mathcal{X}}\int \frac{\mathrm{d}^3\boldsymbol{P}_{\mathcal{X}}}{(2\pi)^3\,2P^0_{\mathcal{X}}}\,(2\pi)^4\,\delta^{(4)}\Big(q+P-P_{\mathcal{X}}\Big)\,H^{\mu\nu}(P,S,P_{\mathcal{X}}), \tag{5}$$

$$H^{\mu\nu}(P,S,P_{\mathcal{X}}) = \big\langle P,S\big|\,J^\mu(0)\,\big|\mathcal{X}\big\rangle\big\langle\mathcal{X}\big|\,J^\nu(0)\,\big|P,S\big\rangle. \tag{6}$$

The state $\mathcal{X}$ symbolizes any final state, with total momentum $P_{\mathcal{X}}$. It is integrated over since in inclusive processes the final state goes undetected.

In general, the structure of the hadronic tensor can be parametrized in terms of *structure functions*. In the case of inclusive DIS, given the constraints of hermiticity and elm gauge invariance, we can introduce four structure functions. There are multiple definitions of the structure functions. A possible one is

$$2MW^{\mu\nu}(q,P,S) = \frac{1}{x_B}\biggl[-g_\perp^{\mu\nu}F_T(x_B,Q^2) + \hat{t}^\mu\hat{t}^\nu F_L(x_B,Q^2) \\ + \mathrm{i}S_L\epsilon_\perp^{\mu\nu}2x_B\,(g_1(x_B,Q^2) - \gamma^2 g_2(x_B,Q^2)) \\ + \mathrm{i}\hat{t}^{[\mu}\epsilon_\perp^{\nu]\rho}S_\rho 2x_B\gamma\,(g_1(x_B,Q^2) + g_2(x_B,Q^2))\biggr], \tag{7}$$

where the involved vectors and tensors are defined in the same way as in Piet Mulders's notes. The connection with the standard unpolarized structure functions is

$$F_T(x_B,Q^2) = 2x_B F_1(x_B,Q^2), \tag{8}$$

$$F_L(x_B,Q^2) = (1+\gamma^2)F_2(x_B,Q^2) - 2x_B F_1(x_B,Q^2). \tag{9}$$

The contraction of the leptonic and hadronic tensors leads to the following expression for the inclusive DIS cross-section:

$$\frac{\mathrm{d}\sigma}{\mathrm{d}x_B\,\mathrm{d}y\,\mathrm{d}\phi_S} = \frac{2\alpha^2}{x_B y Q^2}\,\frac{y^2}{2\,(1-\varepsilon)}\biggl\{F_T + \varepsilon F_L + S_\parallel\lambda_e\sqrt{1-\varepsilon^2}\;2x_B\,(g_1 - \gamma^2 g_2) \\ - |\boldsymbol{S}_\perp|\lambda_e\sqrt{2\,\varepsilon(1-\varepsilon)}\,\cos\phi_S\,2x_B\gamma\,(g_1+g_2)\biggr\}, \tag{10}$$

where the structure functions on the r.h.s. depend on x_B and Q^2 (*i.e.* $P\cdot Q$ and q^2). We also introduced the ratio ε of longitudinal and transverse photon flux in

$$\varepsilon = \frac{1-y}{1-y+\frac{1}{2}y^2}, \qquad \text{and} \qquad \gamma = \frac{2Mx_B}{Q}. \tag{11}$$

It is often necessary, especially for experimental reasons, to distinguish also the component of S parallel or orthogonal to the lepton beam instead of the virtual photon. However, the difference between the two quantities is M/Q suppressed. A thorough discussion about this point has been presented, *e.g.*, in ref. [27].

Ex. 2

Equation (10) does not yet look as the standard results in the literature, *e.g.*, eq. (2.7) in [28]. Check the correspondence by expressing the results with respect to the lepton beam direction, making use of the following relations

$$S_\parallel^\gamma = \cos\theta\,S_\parallel^e + \sin\theta\,|\boldsymbol{S}_\perp^e|\cos\psi,$$

$$|\boldsymbol{S}_\perp^\gamma|\cos\phi_S = \cos\theta\,|\boldsymbol{S}_\perp^e|\cos\psi - \sin\theta\,S_\parallel^e$$

and

$$\cos\theta = \frac{1+\gamma^2 y/2}{\sqrt{1+\gamma^2}} = \frac{1-(1-y)\varepsilon}{\sqrt{1-\varepsilon^2}}\,,$$

$$\sin\theta = \gamma\sqrt{\frac{1-y-\gamma^2y^2/4}{1+\gamma^2}} = \frac{\varepsilon y}{\sqrt{2\,\varepsilon(1-\varepsilon)}}\,.$$

4. – DIS in the parton model

For the treatment of inclusive DIS, it is convenient to choose a frame where the proton and photon momenta have no transverse components. In terms of light-cone vectors, it means

(12) $$P^\mu = P^+ n_+^\mu + \frac{M^2}{2P^+}\, n_-^\mu\,,$$

(13) $$q^\mu = -x_B P^+ n_+^\mu + \frac{Q^2}{2x_B P^+}\, n_-^\mu\,.$$

The spin vector of the target can then be decomposed as

(14) $$S^\mu = S_L\, \frac{(P\cdot n_-)\, n_+^\mu - (P\cdot n_+)\, n_-^\mu}{M} + S_T^\mu\,.$$

It is particularly convenient to work in a reference frame where

(15) $$xP^+ = Q/\sqrt{2}.$$

Ex. 3

Derive the following expressions of the involved momenta in the frame we are using

(16a) $$P^\mu = \left[\frac{x_B M^2}{Q\sqrt{2}},\ \frac{Q}{x_B\sqrt{2}},\ \mathbf{0}\right]$$

(16b) $$q^\mu = \left[\frac{Q}{\sqrt{2}},\ -\frac{Q}{\sqrt{2}},\ \mathbf{0}_T\right]$$

(16c) $$l^\mu = \left[\frac{Q}{y\sqrt{2}},\ \frac{(1-y)Q}{y\sqrt{2}},\ \frac{Q\sqrt{1-y}}{y},\ 0\right],$$

(16d) $$l'^\mu = \left[\frac{(1-y)Q}{y\sqrt{2}},\ \frac{Q}{y\sqrt{2}},\ \frac{Q\sqrt{1-y}}{y},\ 0\right].$$

The phenomenology of DIS taught us that at sufficiently high Q^2 we can assume that the scattering of the electron takes place off a quark of mass m inside the nucleon. The final state $\mathcal{X}$ can be split in a quark with momentum k plus a state X with momentum P_X. Considering the electron-quark interaction at tree level only, the hadronic tensor can be written as

$$(17)\quad \begin{aligned} 2MW^{\mu\nu}(q,P,S) = {} & \frac{1}{2\pi}\sum_q e_q^2 \sum_X \int \frac{\mathrm{d}^3\boldsymbol{P}_X}{(2\pi)^3\, 2P_X^0} \int \frac{\mathrm{d}^3\boldsymbol{k}}{(2\pi)^3\, 2k^0}\, (2\pi)^4\, \delta^{(4)}\Big(P+q-k-P_X\Big) \\ & \times \big\langle P,S\big|\, \overline{\psi}_i(0)\,\big|X\big\rangle\big\langle X\big|\,\psi_j(0)\,\big|P,S\big\rangle\, \gamma^\mu_{ik}\, (\not{k}+m)_{kl}\, \gamma^\nu_{lj}, \end{aligned}$$

where k is the momentum of the struck quark, the index q denotes the quark flavor and e_q is the fractional charge of the quark. Note that, for simplicity, we omitted the flavor indices on the quark fields. The integration over the phase space of the final-state quark can be replaced by a four-dimensional integral with an on-shell condition,

$$(18)\qquad \int \frac{\mathrm{d}^3\boldsymbol{k}}{2k^0} \longrightarrow \int \mathrm{d}^4k\; \delta\left(k^2-m^2\right)\, \theta\left(k^0-m\right),$$

so that the hadronic tensor can be rewritten as

$$(19)\quad \begin{aligned} 2MW^{\mu\nu}(q,P,S) = {} & \sum_q e_q^2 \sum_X \int \frac{\mathrm{d}^3\boldsymbol{P}_X}{(2\pi)^3\, 2P_X^0} \int \mathrm{d}^4k\; \delta\left(k^2-m^2\right)\, \theta\left(k^0-m\right) \\ & \times \delta^{(4)}\Big(P+q-k-P_X\Big)\, \big\langle P,S\big|\, \overline{\psi}_i(0)\,\big|X\big\rangle\big\langle X\big|\,\psi_j(0)\,\big|P,S\big\rangle\, \gamma^\mu_{ik}\, (\not{k}+m)_{kl}\, \gamma^\nu_{lj}. \end{aligned}$$

Next, we Fourier transform the Dirac delta function according to

$$(20)\qquad \delta^{(4)}\Big(P+q-k-P_X\Big) \longrightarrow \int \frac{\mathrm{d}^4\xi}{(2\pi)^4}\; \mathrm{e}^{\mathrm{i}\,(P+q-k-P_X)\cdot\xi}$$

and we introduce the momentum $p = k - q$ to obtain

$$(21)\quad \begin{aligned} 2MW^{\mu\nu}(q,P,S) = {} & \sum_q e_q^2 \sum_X \int \frac{\mathrm{d}^3\boldsymbol{P}_X}{(2\pi)^3\, 2P_X^0} \int \mathrm{d}^4p\; \delta\Big(\big(p+q\big)^2-m^2\Big)\, \theta\left(p^0+q^0-m\right) \\ & \times \int \frac{\mathrm{d}^4\xi}{(2\pi)^4}\; \mathrm{e}^{\mathrm{i}\,(P-p-P_X)\cdot\xi}\, \big\langle P,S\big|\, \overline{\psi}_i(0)\,\big|X\big\rangle\big\langle X\big|\,\psi_j(0)\,\big|P,S\big\rangle\, \gamma^\mu_{ik}\, (\not{p}+\not{q}+m)_{kl}\, \gamma^\nu_{lj}. \end{aligned}$$

Finally, we use part of the exponential to perform a translation of the field operators and we use completeness to eliminate the unobserved X states, so that

$$(22)\quad \begin{aligned} 2MW^{\mu\nu}(q,P,S) = {} & \sum_q e_q^2 \int \mathrm{d}^4p\; \delta\Big(\big(p+q\big)^2-m^2\Big)\, \theta\left(p^0+q^0-m\right) \int \frac{\mathrm{d}^4\xi}{(2\pi)^4}\; \mathrm{e}^{-\mathrm{i}p\cdot\xi} \\ & \times \Big(\big\langle P,S\big|\, \overline{\psi}_i(\xi)\; \psi_j(0)\,\big|P,S\big\rangle\, \gamma^\mu_{ik}\, (\not{p}+\not{q}+m)_{kl}\, \gamma^\nu_{lj}\Big). \end{aligned}$$

Three-Dimensional Partonic Structure of the Nucleon, edited by M. Anselmino, et al., IOS Press, 2013. ProQuest Ebook Central,
http://ebookcentral.proquest.com/lib/bibliotecaupves-ebooks/detail.action?docID=1137463.

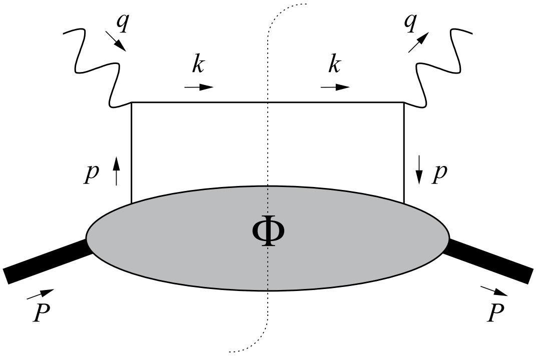

Fig. 3. – The handbag diagram, describing the hadronic tensor for inclusive DIS at Born level.

The hadronic tensor can be written in a more compact way by introducing the quark-quark correlation function Φ

$$2MW^{\mu\nu}(q,P,S) = \sum_q e_q^2 \int \mathrm{d}^4p\, \delta\left(\left(p+q\right)^2 - m^2\right)\, \theta\left(p^0+q^0-m\right) \times \mathrm{Tr}\left[\Phi(p,P,S)\gamma^\mu\left(\not{p}+\not{q}+m\right)\gamma^\nu\right], \tag{23}$$

where

$$\begin{aligned}\Phi_{ji}(p,P,S) &= \frac{1}{(2\pi)^4}\int \mathrm{d}^4\xi\ \mathrm{e}^{-\mathrm{i}p\cdot\xi}\langle P,S|\,\bar{\psi}_i(\xi)\ \psi_j(0)\,|P,S\rangle \\ &= \sum_X \int \frac{\mathrm{d}^3\boldsymbol{P}_X}{(2\pi)^3\,2P_X^0}\ \langle P,S|\,\bar{\psi}_i(0)\,|X\rangle\langle X|\,\psi_j(0)\,|P,S\rangle\ \delta^{(4)}\Big(P-p-P_X\Big).\end{aligned} \tag{24}$$

As the quark fields should carry a flavor index that we omitted, also the correlation functions are flavor dependent and they should be indicated more appropriately as Φ^q. A graphical representation of the hadronic tensor at tree level in the parton model is given by the so-called *handbag diagram*, depicted in fig. 3.

We parametrize the quark momentum p in the following way:

$$p^\mu = \left[\frac{p^2+|\boldsymbol{p}_T|^2}{2xP^+},\ xP^+,\ \boldsymbol{p}_T\right]. \tag{25}$$

In our approach, we assume that neither the virtuality of the quark, p^2, nor its transverse momentum squared, $|\boldsymbol{p}_T|^2$, can be large in comparison with the hard scale Q^2. Under these conditions, the quark momentum is soft with respect to the hadron momentum and its relevant component is xP^+. In eq. (23), neglecting terms which are $1/Q$ suppressed, we can use an approximate expression for the delta function

$$\delta\left(\left(p+q\right)^2 - m^2\right) \approx \delta(p^+ + q^+) \approx P^+\,\delta(x-x_B) \tag{26}$$

and replace

$$\mathrm{d}^4 p = \mathrm{d}^2 \boldsymbol{p}_T \, \mathrm{d}p^- \, P^+ \, \mathrm{d}x \tag{27}$$

and obtain

$$\begin{aligned} 2MW^{\mu\nu}(q,P,S) &\approx \sum_q e_q^2 \int \mathrm{d}^2\boldsymbol{p}_T \, \mathrm{d}p^- \, \mathrm{d}x \, \frac{P^+}{2P\cdot q} \, \delta\,(x - x_B) \\ &\quad \times \mathrm{Tr}\left[\Phi^q(p,P,S)\,\gamma^\mu\,(\not{p} + \not{q} + m)\,\gamma^\nu\right] \\ &= \sum_q e_q^2 \, \frac{1}{2}\mathrm{Tr}\left[\Phi^q(x_B,S)\,\gamma^\mu \frac{P^+}{P\cdot q}\,(\not{p} + \not{q} + m)\,\gamma^\nu\right], \end{aligned} \tag{28}$$

where we introduced the integrated correlation function

$$\begin{aligned} \Phi^q_{ji}(x,S) &= \int \mathrm{d}^2\boldsymbol{p}_T \, \mathrm{d}p^- \; \Phi^q_{ji}(p,P,S)\Big|_{p^+ = xP^+} \\ &= \int \frac{\mathrm{d}\xi^-}{2\pi} \; \mathrm{e}^{-\mathrm{i}p\cdot\xi} \langle P,S|\,\bar{\psi}^q_i(\xi)\;\psi^q_j(0)\,|P,S\rangle\Big|_{\xi^+ = \boldsymbol{\xi}_T = 0} . \end{aligned} \tag{29}$$

Here, the subscript and superscript q stands for the quark flavor.

Finally, from the outgoing quark momentum, $p + q$, we can select only the minus component and obtain the final form for the hadronic tensor at leading twist

$$2MW^{\mu\nu}(q,P,S) \approx \sum_q e_q^2 \, \frac{1}{2}\mathrm{Tr}\left[\Phi^q(x_B,S)\,\gamma^\mu\gamma^+\gamma^\nu\right]. \tag{30}$$

A few words to justify the last approximation are in order. The dominance of the minus component is most easily seen in the infinite momentum frame, where $p^- + q^-$ is of the order of Q, while $p^+ + q^+ = 0$, and $\boldsymbol{p}_T$ and m are of the order of 1. However, if we perform a $1/Q$ expansion of the full expression, including the correlation function Φ^q (starting from eq. (38)), we would be able to check that in any collinear frame the dominant terms arise only from the combination of plus component in the correlation function and minus components in the outgoing quark momentum.

At this point, we need to analyze the structure of the correlation function Φ^q (in the following, we will omit the flavor superscript q).

To get more insight into the information contained in the correlation function, which is a Dirac matrix, we can decompose it in a general way on a basis of Dirac structures. Each term of the decomposition can be a combination of the Lorentz vectors p and P, the Lorentz pseudovector S (in case of spin-half hadrons) and the Dirac structures

$$\mathbf{1},\ \gamma_5,\ \gamma^\mu,\ \gamma^\mu\gamma_5,\ \mathrm{i}\sigma^{\mu\nu}\gamma_5,$$

where $\sigma^{\mu\nu} = \mathrm{i}[\gamma^\mu, \gamma^\nu]/2$. The spin vector can only appear linearly in the decomposition. Moreover, each term of the full expression has to satisfy the conditions of Hermiticity and parity invariance

$$\text{(31a)} \qquad \text{Hermiticity:} \qquad \Phi(p, P, S) = \gamma^0\, \Phi^\dagger(p, P, S)\, \gamma^0,$$

$$\text{(31b)} \qquad \text{parity:} \qquad \Phi(p, P, S) = \gamma^0\, \Phi(\tilde{p}, \tilde{P}, -\tilde{S})\, \gamma^0$$

where $\tilde{p}^\nu = \delta^{\nu\mu} p_\mu$ and so forth for the other vectors.

To simplify the discussion, let us first consider an unpolarized target. The most general decomposition is

$$\Phi(p, P) = M\, A_1\, \mathbf{1} + A_2\, \not{P} + A_3\, \not{p} + \frac{A_4}{M}\, \sigma_{\mu\nu} P^\mu p^\nu, \tag{32}$$

where the amplitudes A_i are real scalar functions $A_i = A_i(p \cdot P, p^2)$ with dimension $1/[m]^4$. The above expression is what we could call the "doubly unintegrated correlation function" (see, *e.g.*, ref. [29]).

In reality, the above expression is incomplete, because on top of the vectors p, P we should also take into account the vector n_- which is related to the direction of the gauge link (see sect. **10** and Piet Mulder's notes). Because of this, new structures appear in the decomposition of eq. (38) [30]. The full decomposition for a nucleon target has been studied in ref. [31]. For an unpolarized target we obtain [32]

$$\begin{aligned} \Phi(p, P|n_-) = {} & M\, A_1\, \mathbf{1} + A_2\, \not{P} + A_3\, \not{p} + \frac{A_4}{M}\, \sigma_{\mu\nu} P^\mu p^\nu \\ & + \frac{M^2}{P \cdot n_-} \not{n}_-\, B_1 + \frac{iM}{2P \cdot n_-} [\not{P}, \not{n}_-]\, B_2 + \frac{iM}{2P \cdot n_-} [\not{p}, \not{n}_-]\, B_3 \\ & + \frac{1}{P \cdot n_-} \varepsilon^{\mu\nu\rho\sigma} \gamma_\mu \gamma_5 P_\nu p_\rho n_{-\sigma}\, B_4, \end{aligned} \tag{33}$$

where

$$\epsilon^{0123} = +1. \tag{34}$$

If we keep only the leading terms in $1/P^+$ (which in the end will turn out to appear in the cross-section with a leading power in $1/Q$, *i.e.* leading twist), we obtain

$$\Phi(p, P) \approx P^+ \left(A_2 + x A_3\right) \not{n}_+ + P^+ \frac{\mathrm{i}}{2M} \left[\not{n}_+, \not{p}_T\right] A_4. \tag{35}$$

For our purposes, we are interested in the calculation of the object entering the expression of the hadronic tensor, what we called the integrated correlation function, eq. (29). In the unpolarized case it is very simple (now reintroducing also the flavor index q):

$$\Phi^q(x) = f_1^q(x) \not{n}_+/2, \tag{36}$$

where we introduced the integrated parton distribution function

$$f_1^q(x) = \int \mathrm{d}^2\, \boldsymbol{p}_T\, \mathrm{d}p^2\, \mathrm{d}(2p\cdot P)\; \delta\left(\boldsymbol{p}_T^2 + x^2M^2 + p^2 - 2xp\cdot P\right) \left[A_2^q + xA_3^q\right]. \tag{37}$$

The function $f_1^q(x)$ is usually referred to as the unpolarized parton distribution, and it is often denoted also as simply $q(x)$ (where q stands for the quark flavor).

If we now extend the analysis to the polarized case, the most general decomposition of the correlation function Φ imposing Hermiticity and parity invariance is [33, 34]

$$\begin{aligned}\Phi(p,P,S) = {}& M\,A_1\,\mathbf{1} + A_2\,\not{P} + A_3\,\not{p} + \frac{A_4}{M}\,\sigma_{\mu\nu}P^\mu p^\nu + \mathrm{i}A_5\; p\cdot S\,\gamma_5\\ &+ M\,A_6\,\not{S}\,\gamma_5 + A_7\,\frac{p\cdot S}{M}\,\not{P}\,\gamma_5 + A_8\,\frac{p\cdot S}{M}\,\not{p}\,\gamma_5 + \mathrm{i}A_9\,\sigma_{\mu\nu}\gamma_5 S^\mu P^\nu\\ &+ \mathrm{i}A_{10}\,\sigma_{\mu\nu}\gamma_5 S^\mu p^\nu + \mathrm{i}A_{11}\,\frac{p\cdot S}{M^2}\,\sigma_{\mu\nu}\gamma_5 P^\mu p^\nu + A_{12}\,\frac{\epsilon_{\mu\nu\rho\sigma}\gamma^\mu P^\nu p^\rho S^\sigma}{M}\,,\end{aligned} \tag{38}$$

where the amplitudes A_i real scalar functions $A_i = A_i(p\cdot P, p^2)$ with dimension $1/[m]^4$. We do not give here the full expression when considering also the vector n_-, which can be found in ref. [31].

The general expression of the integrated correlation function becomes

$$\Phi(x,S) = \frac{1}{2}\left\{f_1\not{n}_+ + S_L\,g_{1L}\gamma_5\not{n}_+ + h_1\,\frac{[\not{S}_T, \not{n}_+]\gamma_5}{2}\right\}, \tag{39}$$

where we introduced the integrated parton distribution functions

$$f_1(x) = \int \mathrm{d}^2\boldsymbol{p}_T\, \mathrm{d}p^2\, \mathrm{d}(2p\cdot P)\; \delta\left(\boldsymbol{p}_T^2 + x^2M^2 + p^2 - 2xp\cdot P\right) \left[A_2 + xA_3\right], \tag{40a}$$

$$\begin{aligned}g_{1L}(x) = {}& \int \mathrm{d}^2\boldsymbol{p}_T\, \mathrm{d}p^2\, \mathrm{d}(2p\cdot P)\; \delta\left(\boldsymbol{p}_T^2 + x^2M^2 + p^2 - 2xp\cdot P\right)\\ &\times \left[-A_6 - \left(\frac{p\cdot P}{M^2} - x\right)(A_7 + xA_8)\right],\end{aligned} \tag{40b}$$

$$\begin{aligned}h_1(x) = {}& \int \mathrm{d}^2\boldsymbol{p}_T\, \mathrm{d}p^2\, \mathrm{d}(2p\cdot P)\; \delta\left(\boldsymbol{p}_T^2 + x^2M^2 + p^2 - 2xp\cdot P\right)\\ &\times \left[-A_9 - xA_{10} + \frac{\boldsymbol{p}_T^2}{2M^2}A_{11}\right].\end{aligned} \tag{40c}$$

The function g_{1L}^q (after reinserting the quark flavor superscript) is the helicity distribution of parton q and it can be denoted also as Δq(1). The function h_1 is known as the parton transversity distribution; in the literature it is sometimes denoted as δq, $\Delta_T q$, although in the original paper of Ralston and Soper [33] it was called h_T.

---

(1) In the Amsterdam literature this function is usually denoted as g_1. Here, however, we prefer to name it g_{1L} to clearly distinguish it from the structure function defined in eq. (7).

The individual distribution functions can be isolated by means of the projection

$$\Phi^{[\Gamma]} \equiv \frac{1}{2}\mathrm{Tr}\,(\Phi\Gamma)\,, \tag{41}$$

where Γ stands for a specific Dirac structure. In particular, we see that

$$f_1(x) = \Phi^{[\gamma^+]}(x), \tag{42a}$$

$$g_{1L}(x) = \Phi^{[\gamma^+\gamma^5]}(x), \tag{42b}$$

$$h_1(x) = \Phi^{[\mathrm{i}\sigma^{i+}\gamma^5]}(x). \tag{42c}$$

Once we have determined the general decomposition of the correlation function, we can compute the cross-section using eqs. (30) and (3).

Ex. 4

Using the leptonic tensor calculated in Ex. 1, compute the cross-section for polarized inclusive DIS in the parton model with Mathematica. The relevant instructions are

```
GAp = GS[Momentum[nm]];
GAm = GS[Momentum[np]];
GA5 = DiracGamma[5];

ScalarProduct[nm, np] = 1;
ScalarProduct[l, np] = 1/Sqrt[2] (((2 - y) Q)/(2 y) - Q/2);
ScalarProduct[l, nm] = 1/Sqrt[2] (((2 - y) Q)/(2 y) + Q/2);
ScalarProduct[lp, np] = 1/Sqrt[2] (((2 - y) Q)/(2 y) + Q/2);
ScalarProduct[lp, nm] = 1/Sqrt[2] (((2 - y) Q)/(2 y) - Q/2);

Phi = (f1 + Sl g1 GA5 + h1 GA5 .GS[Momentum[St]]).(GAm/2)

MW = 1/2 1/2 (Tr[Phi.GA[\[Mu]].GAp .GA[\[Nu]]]) //
Collect[#, {f1 D1, h1perp H1perp}, Simplify] &

(\[Alpha]^2 y)/(2 Q^4) Contract[Lept 2 MW] // Simplify
```

The final result of the cross-section can be obtained from the expressions of the structure functions, which is summarized in the following relations:

$$F_1 = \frac{1}{2} \sum_q e_q^2 \, f_1^q(x_B), \tag{43}$$

$$F_L = 0, \tag{44}$$

$$g_1 = \frac{1}{2} \sum_q e_q^2 \, g_{1L}^q(x_B), \tag{45}$$

$$g_1 + g_2 = 0. \tag{46}$$

A few remarks about the above results. First of all, we see that the transversity distribution does not occur in any of the above structure functions. This is due to the specific Dirac structure of the transversity term in the correlation function, eq. (39): that term contains two Dirac matrices, and it enters a trace with three more Dirac matrices in eq. (30). Therefore, the term disappears. Another interesting observation is that the structure-function combination $g_1 + g_2$ vanishes. We mention that the function becomes nonzero when going to the subleading-twist level in the analysis of the correlation function. Finally, the longitudinal structure function F_L vanishes, and it remains zero also at the next-to-leading-twist (NLT) level. To obtain a nonzero function we have to consider QCD corrections of order α_S (set to zero at the parton-model level) or go to the NNLT level.

In Piet Mulders's lecture notes quite a lot of attention has been devoted to analyzing the correlation functions and their probabilistic interpretation. Therefore, I will just repeat some crucial results here. The leading-twist part of the correlator Φ can be projected out using the projector

$$\mathcal{P}_+ = \frac{1}{2} \, \gamma^- \gamma^+. \tag{47}$$

Before the interaction with the virtual photon, the relevant components of the quark fields are the plus components, $\psi_+ = \mathcal{P}_+ \, \psi$. They are usually referred to as the *good components*.

The matrix

$$F(x, S) = \Big(\mathcal{P}_+ \Phi(x, S) \gamma^+\Big)^T \tag{48}$$

describes a probability to find a (good projection of a) quark with a certain chirality in a target with a certain spin vector S. The dependence on S can be replaced by expressing F as a matrix in the target helicity space. This matrix must be positive semidefinite since it describes a probability density matrix.

The correlation function is a 4×4 Dirac matrix. However, due to the presence of the projector on the good components of the quark fields, the leading-twist part spans only a 2×2 Dirac subspace. This is evident if we express the Dirac structures of eq. (101) in the chiral or Weyl representation (see also the discussion around eq. (105)).

The resulting matrix is [35, 36]

$$(49)\qquad F(x)^{\Lambda_1'\Lambda_1}_{\chi_1\chi_1'} = \left(\begin{array}{cc|cc} f_1(x)+g_{1L}(x) & 0 & 0 & 2h_1(x) \\ 0 & f_1(x)-g_{1L}(x) & 0 & 0 \\ \hline 0 & 0 & f_1(x)-g_{1L}(x) & 0 \\ 2h_1(x) & 0 & 0 & f_1(x)+g_{1L}(x) \end{array}\right).$$

where the inner blocks are in the hadron helicity space (indices $\Lambda_1'\Lambda_1$), while the outer matrix is in the quark chirality space (indices $\chi_1'\chi_1$). Note that because of the inversion of the quark indices, the lower left block has $\chi_1' = R$, $\chi_1 = L$ and vice versa for the upper right block. Since this matrix must be positive semidefinite, we can readily obtain the positivity conditions

$$(50a)\qquad f_1(x) \geq 0,$$

$$(50b)\qquad |g_{1L}(x)| \leq f_1(x),$$

$$(50c)\qquad |h_1(x)| \leq \frac{1}{2}\big(f_1(x) + g_{1L}(x)\big).$$

The last relation is known as the *Soffer bound* [37].

The probabilistic interpretation of the functions f_1 and g_{1L} is manifest, since they occupy the diagonal elements of the matrix and they are therefore connected to squares of probability amplitudes

$$(51)\qquad f_1(x) = \frac{1}{2}\left(F(x)^{\frac{1}{2}\,\frac{1}{2}}_{R\,R} + F(x)^{\frac{1}{2}\,\frac{1}{2}}_{L\,L}\right), \qquad g_{1L}(x) = \frac{1}{2}\left(F(x)^{\frac{1}{2}\,\frac{1}{2}}_{R\,R} - F(x)^{\frac{1}{2}\,\frac{1}{2}}_{L\,L}\right).$$

On the other hand, the transversity distribution is off-diagonal in the chirality basis. This should make clear that it is *chiral odd* and that it does not describe the square of a probability amplitude, but rather the interference between two different amplitudes

$$(52)\qquad h_1(x) = \frac{1}{2} F(x)^{\frac{1}{2}\,-\frac{1}{2}}_{R\,L}.$$

The transversity distribution recovers a probability interpretation if we choose the so-called *transversity basis*, instead of the helicity basis, for both quark and hadron [38, 39]. The transversity basis is formed by the "transversity up" and "transversity down" states. They can be expressed in terms of chirality eigenstates

$$(53)\qquad u_\uparrow = \frac{1}{\sqrt{2}}\left(u_R + u_L\right), \qquad u_\downarrow = \frac{1}{\sqrt{2}}\left(u_R - u_L\right).$$

The same relation holds between the hadron transversity and helicity states.

In the new basis, the scattering matrix takes the form

$$(54)\qquad F(x)^{\Lambda_1'\Lambda_1}_{\chi_1\chi_1'} =$$

$$\left(\begin{array}{cc|cc} f_1(x)+h_1(x) & 0 & 0 & g_{1L}(x)+h_1(x) \\ 0 & f_1(x)-h_1(x) & g_{1L}(x)-h_1(x) & 0 \\ \hline 0 & g_{1L}(x)-h_1(x) & f_1(x)-h_1(x) & 0 \\ g_{1L}(x)+h_1(x) & 0 & 0 & f_1(x)+h_1(x) \end{array}\right),$$

and clearly the transversity distribution function can be defined as

$$(55)\qquad h_1(x) = \frac{1}{2}\left(F(x)^{\uparrow\uparrow}_{\uparrow\uparrow} - F(x)^{\uparrow\uparrow}_{\downarrow\downarrow}\right).$$

5. – DIS beyond the parton model

In these short lectures, we did not have time to study much of the QCD corrections to the parton-model picture. For what concerns inclusive DIS and collinear PDFs, I refer to the excellent lectures of Marco Stratmann. The most recent and authoritative reference on this issue is the book by John Collins [6].

In very concise and qualitative terms, let me just mention that the inclusion of QCD corrections to the parton model leads to the important results of *factorization* and *evolution*, the second being almost a direct consequence of the first. QCD factorization theorems are central to understanding high energy hadronic scattering cross-sections in terms of the fundamentals of perturbative QCD. In addition to providing a practical prescription for order-by-order calculations, derivations of factorization provide a solid theoretical foundation for concepts like PDFs.

The parton-model approach relies on the assumption that we can separate a hard scattering (in DIS, the scattering of an electron off a quark) from a nonperturbative part of the process. When dealing with the hard-scattering side, we can consider the parton as being approximately free and on-shell (the parton is in reality off-shell, but its off-shellness is small compared to the hard scale involved in the scattering, such as the Q^2 of the photon). This situation allows us to compute the hard scattering using purely perturbative QED and QCD. The success of this approach gives a heuristic proof of the validity of the assumptions.

However, using the theoretical framework offered by QCD it is possible to give proofs of the approximate validity of the parton model approach and improve it. Explicit examples are usually given at the so-called “one-loop” level. In DIS, this requires taking into consideration the diagrams shown in fig. 4.

These diagrams contain all sorts of divergences: ultraviolet and infrared (both collinear and soft). Ultraviolet divergences can be taken care of using renormalization. This requires the use of a regularization scheme (*e.g.*, dimensional regularization) and implies the introduction of a renormalization scale μ_R. Divergences are then “hidden”

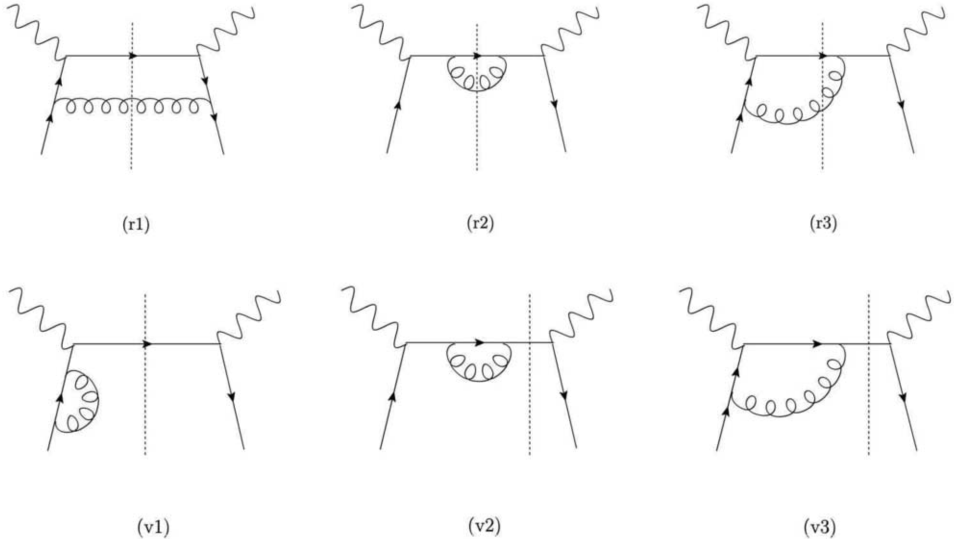
(r1) (r2) (r3)

(v1) (v2) (v3)

Fig. 4. – Cut diagrams representing real and virtual corrections to the $\gamma^* q \to q$ process. Some Hermitean conjugate diagrams are not shown.

inside the values of the parameters of the theory, which are fixed by experimental measurements. Physical observables cannot depend on the renormalization scale, leading to renormalization-group equations and, *e.g.*, the running of the coupling constant.

Infrared divergences are of two types: collinear (when the gluon is emitted collinear to the quark) and soft (when the gluon carries vanishing momentum). For DIS, soft divergences cancel in the sum of virtual and real diagrams. Collinear divergences require the use of a regularization scheme (*e.g.*, dimensional regularization or mass regularization) and the introduction of a factorization scale μ_F (often chosen for convenience to be equal to μ_R). Divergences are then hidden inside nonperturbative objects involved in the process (*e.g.*, collinear parton distribution functions). Physical observables cannot depend on the factorization scale, leading to evolution equations of the PDFs.

Factorization theorems show that the above procedure can be explicitly followed and generalized to an arbitrary number of gluon insertions. Eventually, they demonstrate that, order by order, the cross-section for, *e.g.*, DIS might be written schematically as

$$d\sigma \sim |\mathcal{H}|^2 \otimes \Phi(x). \tag{56}$$

The precise field-theoretic definitions of the correlation function $\Phi(x)$ emerges naturally from factorization. In the hard part $|\mathcal{H}|^2$, all propagators must be off-shell by order the hard scale Q so that asymptotic freedom applies, and small-coupling perturbation theory is valid, with non-factorizing contributions suppressed by powers of Q.

Such theorems have been worked out in detail only for a few processes (DIS, Drell-Yan processes, e^+e^- annihilation). For instance, there exhist no complete factorization proof for hadron-hadron collisions into hadrons (see sect. 14.7 in the book of Collins [6]).

Finally, already at the level of DIS and collinear PDFs there is the question of the gauge invariance of parton distribution functions.

So far we used the following definition for the correlation function:

$$\Phi_{ij}(p, P, S) = \frac{1}{(2\pi)^4} \int \mathrm{d}^4\xi \; \mathrm{e}^{\mathrm{i}p\cdot\xi} \big\langle P, S \big| \, \overline{\psi}_j(0) \; \psi_i(\xi) \, \big| P, S \big\rangle, \tag{57}$$

or, alternatively,

$$\Phi_{ij}(x, S) = \int \frac{\mathrm{d}\xi^-}{2\pi} \; \mathrm{e}^{-\mathrm{i}p\cdot\xi} \big\langle P, S \big| \, \overline{\psi}_i^q(\xi) \; \psi_j^q(0) \, \big| P, S \big\rangle \Big|_{\xi^+=\boldsymbol{\xi}_T=0}. \tag{58}$$

with $p^+ = xP^+$.

It turns out that something is missing. The reason can be easily understood: the correlator as defined above is not gauge invariant, because the two quark field operators are at two different positions. If we perform a local (Abelian for now) gauge transformation on the fields

$$\psi(\xi) \to \mathrm{e}^{\mathrm{i}\alpha(\xi)} \, \psi(\xi) \tag{59}$$

the correlator evidently changes. This is something to worry about because the parton distribution functions composing the correlator can be extracted from experimental measurements and they should be gauge invariant.

To fix the problem, we have to insert a gauge link or Wilson line in between the quark fields, with the following gauge transformation properties:

$$\mathcal{L}(\xi_1, \xi_2) \to \mathrm{e}^{\mathrm{i}\alpha(\xi_1)} \, \mathcal{L}(\xi_1, \xi_2) \, \mathrm{e}^{-\mathrm{i}\alpha(\xi_2)}. \tag{60}$$

In principle, any gauge link (*i.e.* running along any path) can make the definition of the correlator gauge-invariant. However, in QCD different gauge links give rise to physically different correlators (because a closed QCD gauge link is not equal to unity). From the appropriate calculations (which are partially covered in Piet Mulders's notes) it turns out that the proper gauge-invariant definition of the quark-quark correlator is

$$\Phi_{ij}(x, S) = \int \frac{\mathrm{d}\xi^-}{2\pi} \; \mathrm{e}^{-\mathrm{i}p\cdot\xi} \langle P, S | \bar{\psi}_j(0) \, \mathcal{L}^{n_-}_{(0,+\infty)} \, \mathcal{L}^{n_-}_{(+\infty,\xi)} \, \psi_i(\xi) | P, S \rangle \Big|_{\xi^+=0}, \tag{61}$$

where the gauge links (Wilson lines) are defined as

$$\mathcal{L}^{n_-}_{(0,+\infty)} \quad = \mathcal{P}\exp\left[-\mathrm{i}g \int_{\infty^-}^{\xi^-} \mathrm{d}\eta^- A^+(\eta^-, 0, \mathbf{0}_T)\right] \approx 1 - ig \int_{\infty^-}^{\xi^-} \mathrm{d}\eta^- A^+(\eta^-, 0, \mathbf{0}_T) \tag{62}$$

The graphical representation of the gauge link involved in DIS is given in fig. 5.

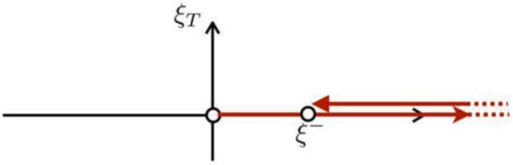

Fig. 5. – The path of the gague link in inclusive DIS. It could be viewed as formed by two infinitely long straight links, which however cancel to give the net result of a finite, straight link along the minus light-cone direction.

The gauge link can be derived by calculating the leading-twist contributions of diagrams of the type shown in fig. 6 and their Hermitean conjugates. If we stop at the single-gluon level, the situation may be understood already at the level of the diagrams in fig. 4. We know that only the sum of all diagrams is gauge invariant. Some diagrams vanish in certain gauges. In light-cone gauges, for instance, only the first diagrams on the left give a nonzero contribution. The gluon polarization sum in that gauge is

$$d^{\mu\nu}(l;n_-) = -g^{\mu\nu} + \frac{l^\mu n_-^\nu + l^\nu n_-^\mu}{l^+} \,. \tag{63}$$

In this gauge, it is easy to operate a kind of separation as the one shown in fig. 6, since the starting diagrams are already of the desired form and the other diagrams do not contribute. In Feynman gauge, the polarization sum includes only the first term on the r.h.s. of eq. (63). However, the contributions corresponding to the second term are recovered in the calculation of the other diagrams in fig. 4.

One final comment at this point: already when considering single-gluon corrections, another class of divergences appear, the so-called light-cone or rapidity divergences. It is beyond the scope of these lectures to give a detailed explanation of these divergences. Let me just say that, when performing the calculation in the light-cone gauge, these divergences arise from the second term on the r.h.s. of eq. (63), containing $1/l^+$. In

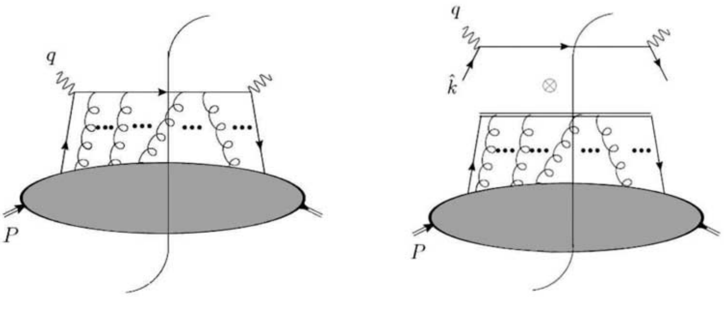

Fig. 6. – (a) Example of higher-order diagrams that can give rise to the gauge link. (b) Factorization into gauge-link contributions.

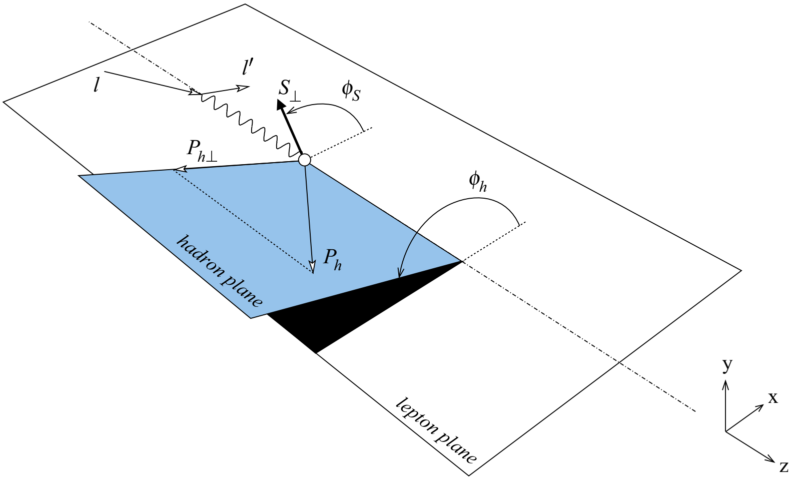

Fig. 7. – Definition of azimuthal angles for semi-inclusive deep inelastic scattering in the target rest frame. $P_{h\perp}$ and $S_\perp$ are the transverse parts of P_h and S with respect to the photon momentum [24].

different gauges, these divergences appear in other diagrams. Similarly to soft infrared divergences, these divergences exist already when one defines collinear PDFs in inclusive DIS. However, they cancel when summing the contributions corresponding to real and virtual diagrams. Graphically, these divergences can be connected to the presence of infinitely long gauge links. However, in the case of collinear PDFs the two gauge links $\mathcal{L}^{n-}_{(0,+\infty)}$ and $\mathcal{L}^{n-}_{(+\infty,\xi)}$ cancel each other, with the net effect of reducing to a finite link $\mathcal{L}^{n-}_{(0,\xi)}$, as depicted in fig. 5.

6. – Semi-inclusive DIS

We consider now the process

$$\ell(l) + N(P) \rightarrow \ell(l') + h(P_h) + X, \tag{64}$$

where ℓ denotes the beam lepton, N the nucleon target, and h the produced hadron, and where four-momenta are given in parentheses. We neglect the lepton mass. We denote by M and M_h respective masses of the nucleon and of the hadron h. As usual we define $q = l - l'$ and $Q^2 = -q^2$ and introduce the variables

$$x_B = \frac{Q^2}{2\,P\cdot q}\,, \qquad y = \frac{P\cdot q}{P\cdot l}\,, \qquad z_h = \frac{P\cdot P_h}{P\cdot q}\,. \tag{65}$$

We consider the case where the detected hadron h has spin zero or where its polarization is not measured. $P_{h\perp}$ is the transverse parts P_h with respect to the photon momentum. The vectors and angles involved are depicted in fig. 7.

The cross-section for one-particle inclusive electron-nucleon scattering can be written as

$$\frac{2E_h\,\mathrm{d}^6\sigma}{\mathrm{d}^3\boldsymbol{P}_h\,\mathrm{d}x_B\,\mathrm{d}y\,\mathrm{d}\phi_S} = \frac{\alpha^2}{2sx_BQ^2}\,L_{\mu\nu}(l,l',\lambda_e)\,2MW^{\mu\nu}(q,P,S,P_h), \tag{66}$$

or, equivalently, as

$$\frac{\mathrm{d}^6\sigma}{\mathrm{d}x_B\,\mathrm{d}y\,\mathrm{d}z_h\,\mathrm{d}\phi_S\,\mathrm{d}^2\boldsymbol{P}_{h\perp}} = \frac{\alpha^2}{4z_hsx_BQ^2}\,L_{\mu\nu}(l,l',\lambda_e)\;2MW^{\mu\nu}(q,P,S,P_h). \tag{67}$$

To obtain the previous formula, we made use of the relation $\mathrm{d}^3P_h/2E_h \approx \mathrm{d}z_h\,\mathrm{d}^2\boldsymbol{P}_{h\perp}/2z_h$.

The hadronic tensor for one-particle inclusive scattering is defined as

$$\begin{aligned}2MW^{\mu\nu}(q,P,S,P_h) &= \frac{1}{(2\pi)^4}\sum_{\mathcal{X}'}\int\frac{\mathrm{d}^3\boldsymbol{P}_{\mathcal{X}'}}{2P^0_{\mathcal{X}'}}\,2\pi\,\delta^{(4)}\Big(q+P-P_{\mathcal{X}'}-P_h\Big)\\ &\quad\times H^{\mu\nu}(P,S,P_{\mathcal{X}'},P_h),\end{aligned} \tag{68}$$

$$H^{\mu\nu}(P,S,P_{\mathcal{X}'},P_h) = \big\langle P,S\big|\,J^\mu(0)\,\big|P_h,\mathcal{X}'\big\rangle\big\langle P_h,\mathcal{X}'\big|\,J^\nu(0)\,\big|P,S\big\rangle. \tag{69}$$

In semi-inclusive DIS, the hadronic tensor can be parametrized in terms of 18 structure functions [40]. We do not give here the explicit formula of the hadronic tensor but only give the resulting cross-section after contraction with the leptonic tensor:

$$\begin{aligned}&\frac{\mathrm{d}\sigma}{\mathrm{d}x_B\,\mathrm{d}y\,\mathrm{d}\phi_S\,\mathrm{d}z\,\mathrm{d}\phi_h\,\mathrm{d}P_{h\perp}^2}\,\frac{\alpha^2}{x_By\,Q^2}\,\frac{y^2}{2\,(1-\varepsilon)}\\ &\quad\times\Bigg\{F_{UU,T}+\varepsilon F_{UU,L}+\sqrt{2\,\varepsilon(1+\varepsilon)}\,\cos\phi_h\,F_{UU}^{\cos\phi_h}\\ &\quad+\varepsilon\cos(2\phi_h)\,F_{UU}^{\cos 2\phi_h}+\lambda_e\,\sqrt{2\,\varepsilon(1-\varepsilon)}\,\sin\phi_h\,F_{LU}^{\sin\phi_h}\\ &\quad+S_\parallel\left[\sqrt{2\,\varepsilon(1+\varepsilon)}\,\sin\phi_h\,F_{UL}^{\sin\phi_h}+\varepsilon\sin(2\phi_h)\,F_{UL}^{\sin 2\phi_h}\right]\\ &\quad+S_\parallel\,\lambda_e\left[\sqrt{1-\varepsilon^2}\,F_{LL}+\sqrt{2\,\varepsilon(1-\varepsilon)}\,\cos\phi_h\,F_{LL}^{\cos\phi_h}\right]\\ &\quad+|\boldsymbol{S}_\perp|\Bigg[\sin(\phi_h-\phi_S)\,\Big(F_{UT,T}^{\sin(\phi_h-\phi_S)}+\varepsilon\,F_{UT,L}^{\sin(\phi_h-\phi_S)}\Big)\\ &\qquad+\varepsilon\,\sin(\phi_h+\phi_S)\,F_{UT}^{\sin(\phi_h+\phi_S)}+\varepsilon\,\sin(3\phi_h-\phi_S)\,F_{UT}^{\sin(3\phi_h-\phi_S)}\\ &\qquad+\sqrt{2\,\varepsilon(1+\varepsilon)}\,\sin\phi_S\,F_{UT}^{\sin\phi_S}+\sqrt{2\,\varepsilon(1+\varepsilon)}\,\sin(2\phi_h-\phi_S)\,F_{UT}^{\sin(2\phi_h-\phi_S)}\Bigg]\end{aligned} \tag{70}$$

$$+ |\boldsymbol{S}_\perp|\lambda_e \Bigg[\sqrt{1-\varepsilon^2}\,\cos(\phi_h-\phi_S)\,F_{LT}^{\cos(\phi_h-\phi_S)} + \sqrt{2\,\varepsilon(1-\varepsilon)}\,\cos\phi_S\,F_{LT}^{\cos\phi_S}$$
$$+ \sqrt{2\,\varepsilon(1-\varepsilon)}\,\cos(2\phi_h-\phi_S)\,F_{LT}^{\cos(2\phi_h-\phi_S)}\Bigg]\Bigg\}.$$

The first and second subscript of the above structure functions indicate the respective polarization of beam and target, whereas the third subscript in $F_{UU,T}$ and $F_{UU,L}$ specifies the polarization of the virtual photon. Using definition (11), the depolarization factors can be written in terms of the y variable as

$$\frac{y^2}{2\,(1-\varepsilon)} = \left(1-y+y^2/2\right), \tag{71}$$

$$\frac{y^2}{2\,(1-\varepsilon)}\,\varepsilon = (1-y), \tag{72}$$

$$\frac{y^2}{2\,(1-\varepsilon)}\,\sqrt{1-\varepsilon^2} = y\,(1-y/2)\,, \tag{73}$$

$$\frac{y^2}{2\,(1-\varepsilon)}\,\sqrt{2\,\varepsilon(1+\varepsilon)} = (2-y)\,\sqrt{1-y}, \tag{74}$$

$$\frac{y^2}{2\,(1-\varepsilon)}\,\sqrt{2\,\varepsilon(1-\varepsilon)} = y\,\sqrt{1-y}. \tag{75}$$

Integration of eq. (70) over the transverse momentum $\boldsymbol{P}_{h\perp}$ of the outgoing hadron gives the semi-inclusive deep inelastic scattering cross-section

$$\frac{\mathrm{d}\sigma}{\mathrm{d}x_B\,\mathrm{d}y\,\mathrm{d}\phi_S\,\mathrm{d}z} = \frac{2\alpha^2}{x_B y Q^2}\,\frac{y^2}{2\,(1-\varepsilon)}\Big\{F_{UU,T} + \varepsilon F_{UU,L} + S_\parallel\lambda_e\,\sqrt{1-\varepsilon^2}\,F_{LL}$$
$$+ |\boldsymbol{S}_\perp|\,\sqrt{2\,\varepsilon(1+\varepsilon)}\,\sin\phi_S\,F_{UT}^{\sin\phi_S} + |\boldsymbol{S}_\perp|\lambda_e\,\sqrt{2\,\varepsilon(1-\varepsilon)}\,\cos\phi_S\,F_{LT}^{\cos\phi_S}\Big\}, \tag{76}$$

where now the structure functions on the r.h.s. are integrated versions of the previous ones, *i.e.*

$$F_{UU,T}(x_B,z_h,Q^2) = \int \mathrm{d}^2\boldsymbol{P}_{h\perp}\,F_{UU,T}(x_B,z_h,P_{h\perp}^2,Q^2) \tag{77}$$

and similarly for the other functions.

Finally, the connection the result for totally inclusive DIS can be obtained by

$$\frac{\mathrm{d}\sigma(\ell p\to\ell X)}{\mathrm{d}x_B\,\mathrm{d}y\,\mathrm{d}\phi_S} = \sum_h\int \mathrm{d}z_h\,z_h\,\frac{\mathrm{d}\sigma(\ell p\to\ell hX)}{\mathrm{d}z\,\mathrm{d}x_B\,\mathrm{d}y\,\mathrm{d}\phi_S}\,, \tag{78}$$

where we have summed over all hadrons in the final state. This leads to the result already given in eq. (10), once we identify

$$\sum_h \int \mathrm{d}z_h\, z_h\, F_{UU,T}(x_B, z_h, Q^2) = F_T(x_B, Q^2), \tag{79}$$

$$\sum_h \int \mathrm{d}z_h\, z_h\, F_{UU,L}(x_B, z_h, Q^2) = F_L(x_B, Q^2), \tag{80}$$

$$\sum_h \int \mathrm{d}z_h\, z_h\, F_{LL}(x_B, z_h, Q^2) = 2x_B\, \big(g_1(x_B, Q^2) - \gamma^2 g_2(x_B, Q^2)\big), \tag{81}$$

$$\sum_h \int \mathrm{d}z_h\, z_h\, F_{LT}^{\cos\phi_S}(x_B, z_h, Q^2) = -2x_B\gamma\, \big(g_1(x_B, Q^2) + g_2(x_B, Q^2)\big). \tag{82}$$

Time-reversal invariance requires (see, *e.g.*, ref. [27])

$$\sum_h \int \mathrm{d}z_h\, z_h\, F_{UT}^{\sin\phi_S}(x_B, z_h, Q^2) = 0. \tag{83}$$

The choice of a convenient frame to deal with semi-inclusive DIS is less straightforward than for inclusive DIS, due to the presence of P_h. We have two choices:

- FRAME 1: Keep the photon and proton to be collinear, give a transverse component to P_h. This means to keep the parametrization of the vectors as given in eq. (16) and simply adding

$$P_h^\mu = \left[\frac{z_h Q}{\sqrt{2}},\ \frac{M_h^2 + |\boldsymbol{P}_{h\perp}|^2}{z_h Q\sqrt{2}},\ \boldsymbol{P}_{h\perp}\right]. \tag{84}$$

- FRAME 2: Keep the proton and outgoing hadron to be collinear, give a transverse component to q. In terms of light-cone vectors this means choosing

$$P^\mu = P^+ n_+^\mu + \frac{M^2}{2P^+}\, n_-^\mu\,, \tag{85}$$

$$P_h^\mu = P_h^- n_-^\mu + \frac{M_h^2}{2P_h^-}\, n_+^\mu\,. \tag{86}$$

In this frame, the photon momentum has a transverse component. If we further fix

$$xP^+ = P_h^-/z = Q/\sqrt{2}, \tag{87}$$

we can explicitly write the vectors involved as follows:

$$P^\mu = \left[\frac{x_B M^2}{Q\sqrt{2}},\, \frac{Q}{x_B\sqrt{2}},\, \mathbf{0}\right], \tag{88a}$$

$$P_h^\mu = \left[\frac{z_h Q}{\sqrt{2}},\, \frac{M_h^2}{z_h Q\sqrt{2}},\, \mathbf{0}\right], \tag{88b}$$

$$q^\mu = \left[\frac{Q}{\sqrt{2}},\, -\frac{\left(Q^2-|\boldsymbol{q}_T|^2\right)}{Q\sqrt{2}},\, \boldsymbol{q}_T\right] \approx \left[\frac{Q}{\sqrt{2}},\, -\frac{Q}{\sqrt{2}},\, \boldsymbol{q}_T\right]. \tag{88c}$$

The first choice seems to be the most simple one, but in reality from the theoretical point of view it is better to stick to the second option, in order to preserve a symmetry between P and P_h.

In any case, it turns out that if we neglect subleading twist corrections, all vectors in the two frames are approximately the same, the only difference is the presence of $\boldsymbol{P}_\perp$ in FRAME 1 and the presence of $\boldsymbol{q}_T$ in FRAME 2, and the two are simply connected by

$$\boldsymbol{q}_T = -z\boldsymbol{P}_{h\perp}. \tag{89}$$

Therefore, in this section we are not going to care very much about distinguishing the two frames, and every time we have $\boldsymbol{q}_T$ we can replace it with $-z\boldsymbol{P}_{h\perp}$ or vice versa, at our convenience.

In this section, we will also use without distinguishing them $S_\perp \leftrightarrow S_T$ and $S_\parallel \leftrightarrow S_L$.

7. – Semi-inclusive DIS in the parton model

In the spirit of the parton model, the virtual photon strikes a quark inside the nucleon. In the case of current fragmentation, the tagged final state hadron comes from the fragmentation of the struck quark. The scattering process can then be factorized in two soft hadronic parts connected by a hard scattering part, as shown in fig. 8.

Considering only the Born-level contribution to the hard scattering, the hadronic tensor can be written as

$$\begin{aligned} 2MW^{\mu\nu}(q,P,S,P_h) = \sum_q e_q^2 \int \mathrm{d}^4p\,\mathrm{d}^4k\;\delta^{(4)}\left(p+q-k\right) \\ \times \mathrm{Tr}\left(\Phi(p,P,S)\,\gamma^\mu\,\Delta(k,P_h)\,\gamma^\nu\right), \end{aligned} \tag{90}$$

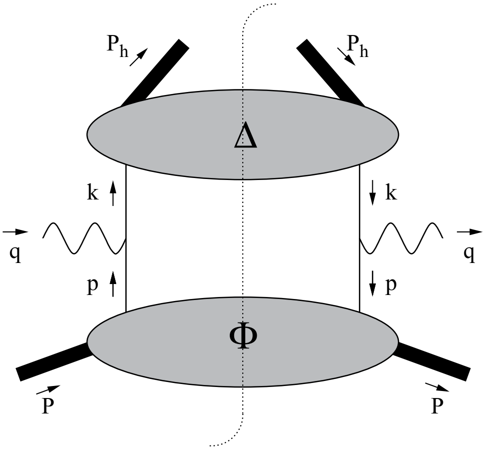

Fig. 8. – The bull diagram, describing the hadronic tensor at tree level.

where Φ and Δ are so-called quark-quark correlation functions and are defined as

$$\begin{aligned}\Phi_{ji}(p,P,S) &= \frac{1}{(2\pi)^4}\int \mathrm{d}^4\xi\; \mathrm{e}^{\mathrm{i}p\cdot\xi}\big\langle P,S\big|\,\overline{\psi}_i(0)\;\psi_j(\xi)\,\big|P,S\big\rangle \\ &= \sum_X \int \frac{\mathrm{d}^3\boldsymbol{P}_X}{(2\pi)^3\,2P_X^0}\;\big\langle P,S\big|\,\overline{\psi}_i(0)\,\big|X\big\rangle\big\langle X\big|\,\psi_j(0)\,\big|P,S\big\rangle\;\delta^{(4)}\Big(P-p-P_X\Big),\end{aligned} \tag{91}$$

$$\begin{aligned}\Delta_{kl}(k,P_h) &= \frac{1}{(2\pi)^4}\int \mathrm{d}^4\xi\; \mathrm{e}^{\mathrm{i}k\cdot\xi}\,\big\langle 0\big|\,\psi_k(\xi)\,\big|P_h\big\rangle\big\langle P_h\big|\,\overline{\psi}_l(0)\,\big|0\big\rangle \\ &= \sum_Y \int \frac{\mathrm{d}^3\boldsymbol{P}_Y}{(2\pi)^3\,2P_Y^0}\;\big\langle 0\big|\,\psi_k(0)\,\big|P_h,Y\big\rangle\big\langle P_h,Y\big|\,\overline{\psi}_l(0)\,\big|0\big\rangle\;\delta^{(4)}\Big(k-P_h-P_Y\Big).\end{aligned} \tag{92}$$

We need to introduce a parametrization for the vectors

$$p^\mu = \left[\frac{p^2+|\boldsymbol{p}_T|^2}{2xP^+},\; xP^+,\; \boldsymbol{p}_T\right], \tag{93a}$$

$$k^\mu = \left[\frac{P_h^-}{z},\; \frac{z\left(k^2+|\boldsymbol{k}_T|^2\right)}{2P_h^-},\; \boldsymbol{k}_T\right]. \tag{93b}$$

Neglecting terms which are $1/Q$ suppressed, we can write

$$\begin{aligned}\delta^{(4)}\left(p+q-k\right) &\approx \delta(p^+ + q^+)\,\delta(q^- - k^-)\,\delta^{(2)}\Big(\boldsymbol{p}_T+\boldsymbol{q}_T-\boldsymbol{k}_T\Big) \\ &\approx \frac{1}{P^+\,P_h^-}\,\delta(x-x_B)\,\delta(1/z-1/z_h)\,\delta^{(2)}\Big(\boldsymbol{p}_T+\boldsymbol{q}_T-\boldsymbol{k}_T\Big)\end{aligned} \tag{94}$$

and replacing

$$\mathrm{d}^4 k = \mathrm{d}^2 \boldsymbol{k}_T \, \mathrm{d}k^+ \, P_h^- \, \frac{\mathrm{d}\, z}{z^2} \tag{95}$$

we obtain the compact expression

$$2MW^{\mu\nu}(q, P, S, P_h) = 2z_h \, \mathcal{I}\Big[\mathrm{Tr}(\Phi(x_B, \boldsymbol{p}_T, S)\, \gamma^\mu \, \Delta(z_h, \boldsymbol{k}_T)\, \gamma^\nu)\Big], \tag{96}$$

where, as we shall do very often, we used the shorthand notation

$$\begin{aligned} \mathcal{I}\Big[\cdots\Big] &\equiv \int \mathrm{d}^2\boldsymbol{p}_T \, \mathrm{d}^2\boldsymbol{k}_T \, \delta^{(2)}\Big(\boldsymbol{p}_T + \boldsymbol{q}_T - \boldsymbol{k}_T\Big) \, \Big[\cdots\Big] \\ &= \int \mathrm{d}^2\boldsymbol{p}_T \, \mathrm{d}^2\boldsymbol{k}_T \, \delta^{(2)}\Big(\boldsymbol{p}_T - \frac{\boldsymbol{P}_{h\perp}}{z} - \boldsymbol{k}_T\Big) \, \Big[\cdots\Big], \end{aligned} \tag{97}$$

and where we introduced the "unintegrated" or "transverse-momentum–dependent" correlation functions

$$\Phi(x, \boldsymbol{p}_T, S) \equiv \int \mathrm{d}p^- \Phi(p, P, S)\Big|_{p^+ = xP^+}, \tag{98a}$$

$$\Delta(z, \boldsymbol{k}_T) \equiv \frac{1}{2z} \int \mathrm{d}k^+ \Delta(k, P_h)\Big|_{k^- = P_h^-/z}. \tag{98b}$$

While the distribution correlation function Φ describes the *confinement* of partons inside hadrons, the fragmentation correlation function Δ describes the way a virtual parton "decays" into a hadron plus something else, *i.e.* $q^* \to hY$. This process is referred to as *hadronization*. It is a clear manifestation of color confinement: the asymptotic physical states detected in experiment must be color neutral, so that quarks have to evolve into hadrons(^{2}).

Integrating the cross-section over $\boldsymbol{P}_{h\perp}$ we get

$$\frac{\mathrm{d}^4\sigma}{\mathrm{d}x_B \, \mathrm{d}y \, \mathrm{d}z_h \, \mathrm{d}\phi_S} = \frac{\alpha^2}{4z_h s x_B \, Q^2} \, L_{\mu\nu}(l, l', \lambda_e) \, 2MW^{\mu\nu}(q, P, S), \tag{99}$$

where

$$2MW^{\mu\nu}(q, P, S) = 2z_h \, \mathrm{Tr}(\Phi(x_B, S)\, \gamma^\mu \, \Delta(z_h)\, \gamma^\nu), \tag{100a}$$

$$\Phi(x, S) \equiv \int \mathrm{d}p^- \, \mathrm{d}^2\boldsymbol{p}_T \, \Phi(p, P, S)\Big|_{p^+ = xP^+}, \tag{100b}$$

$$\Delta(z) \equiv \frac{z}{2} \int \mathrm{d}k^+ \, \mathrm{d}^2\boldsymbol{k}_T \, \Delta(k, P_h)\Big|_{k^- = P_h^-/z}. \tag{100c}$$

(^{2}) Note that on the way to the final state hadrons, the color carried by the initial quark can be neutralized without breaking factorization, for instance via soft gluon contributions.

8. – The correlation functions

As we did for inclusive DIS, we need now to consider the general decomposition of the correlation function. Neglecting the contribution coming from the light-cone vector n_-, we can start from the decompositions of eq. (38). To simplify the discussion, let us start from the unpolarized case, eq. (32).

The big difference from the inclusive DIS calculation is that we now need the transverse-momentum–dependent correlation function defined in eq. (98a). Following analogous steps as done for the inclusive DIS case and keeping only the leading-twist terms, we obtain

$$\Phi(x,\boldsymbol{p}_T)_{\mathrm{T}w-2} = \left\{ f_1(x,\boldsymbol{p}_T^2) + \mathrm{i} h_1^{\perp}(x,\boldsymbol{p}_T^2)\frac{\not{p}_T}{M} \right\} \not{n}_+/2. \tag{101}$$

Here we introduced the parton distribution functions

$$f_1(x,p_T^2) = 2P^+ \int \mathrm{d}p^-\,(A_2 + xA_3)\,, \qquad h_1^{\perp}(x,p_T^2) = 2P^+ \int \mathrm{d}p^-\,(-A_4)\,. \tag{102}$$

The function $f_1(x,\boldsymbol{p}_T^2)$ is the unpolarized transverse-momentum–dependent PDF (unpolarized TMD). The function $h_1^{\perp}(x,\boldsymbol{p}_T^2)$ is the so-called Boer-Mulders TMD [41].

We can do the same exercise also for the fragmentation correlation function defined in eq. (98b), with very few changes. I do not go through all the analysis here, and just quote the final result

$$\Delta(z,\boldsymbol{k}_T)_{\mathrm{T}w-2} = \left(D_1(z,\boldsymbol{k}_T^2) + i\,H_1^{\perp}(z,\boldsymbol{k}_T^2)\,\frac{\not{k}_T}{M_h} \right) \not{n}_-/2. \tag{103}$$

The function $D_1(z,\boldsymbol{k}_T^2)$ is the unpolarized transverse-momentum–dependent fragmentation function (unpolarized TMD FF). The function $H_1^{\perp}(z,\boldsymbol{k}_T^2)$ is the so-called Collins function [42].

The Boer-Mulders and Collins functions are particularly relevant because they give rise to nontrivial transverse-momentum dependences of cross-sections already at the level of unpolarized processes (*e.g.*, SIDIS experiments such as ZEUS and H1 at DESY, e^+e^- annihilation experiments, and in principle even at the LHC).

Another important property of the Boer-Mulders and Collins functions is that they are T-odd (or naive time-reversal odd), according to the definition

$$\Phi^*_{\text{T-even}}(p,P,S) = \mathrm{i}\gamma^1\gamma^3\,\Phi_{\text{T-even}}(\tilde{p},\tilde{P},\tilde{S})\,\mathrm{i}\gamma^1\gamma^3, \tag{104a}$$

$$\Phi^*_{\text{T-odd}}(p,P,S) = -\mathrm{i}\gamma^1\gamma^3\,\Phi_{\text{T-odd}}(\tilde{p},\tilde{P},\tilde{S})\,\mathrm{i}\gamma^1\gamma^3. \tag{104b}$$

The above definition does not fully correspond to time-reversal invariance and T-odd functions do not violate time-reversal invariance. They give rise to observables to observables that change sign when inverting momenta and angular momenta (*e.g.*, single-spin asymmetries).

As mentioned already for inclusive DIS, the correlation function is a 4 × 4 Dirac matrix. However, its leading-twist part spans only a 2 × 2 Dirac subspace. Using the chiral or Weyl representation, the correlation function reads

$$\left(\mathcal{P}_+\,\Phi(x,\boldsymbol{p}_T)\gamma^+\right)_{ji} = \begin{pmatrix} f_1 & 0 & 0 & \mathrm{i}e^{\mathrm{i}\phi_p}\,\dfrac{|\boldsymbol{p}_T|}{M}\,h_1^\perp \\ 0 & 0 & 0 & 0 \\ 0 & 0 & 0 & 0 \\ -\mathrm{i}e^{-\mathrm{i}\phi_p}\,\dfrac{|\boldsymbol{p}_T|}{M}\,h_1^\perp & 0 & 0 & f_1 \end{pmatrix}. \tag{105}$$

As shown by this explicit form, the four-dimensional Dirac space can be reduced to a two-dimensional space, retaining only the nonzero part of the correlation function. The relevant part of the Dirac space is the one corresponding to good quark fields. The correlation matrix in the good quark chirality space is then simply

$$\left(\mathcal{P}_+\,\Phi\gamma^+\right)_{\chi_1'\chi_1} = \begin{pmatrix} f_1 & \mathrm{i}e^{\mathrm{i}\phi_p}\,\dfrac{|\boldsymbol{p}_T|}{M}\,h_1^\perp \\ -\mathrm{i}e^{-\mathrm{i}\phi_p}\,\dfrac{|\boldsymbol{p}_T|}{M}\,h_1^\perp & f_1 \end{pmatrix}. \tag{106}$$

From the matrix representation in the chirality space it should be clear why the function $h_1^\perp$ is defined to be *chiral odd.*

The distribution matrix is clearly Hermitean. When an exponential $e^{\mathrm{i}l'\phi_p}$ appears in the matrix, we have to take into account l' units of angular momentum in the final state. The condition of angular-momentum conservation then requires $\chi_1' + l' = \chi_1$. The condition parity conservation is

$$F(x,\boldsymbol{p}_T)_{\chi_1\chi_1'} = (-1)^{l'}\,F(x,\boldsymbol{p}_T)_{-\chi_1\,-\chi_1'}\Big|_{l'\to -l'}. \tag{107}$$

The fact that the matrix has to be positive definite allows us to derive the positivity bound

$$\frac{|\boldsymbol{p}_T|}{M}\,|h_1^\perp(x,\boldsymbol{p}_T^2)| \le f_1(x,\boldsymbol{p}_T^2). \tag{108}$$

When including also target polarization, starting from the general decomposition presented in eq. (38), the leading order part of the transverse-momentum–dependent correlation function becomes

$$\Phi(x,p_T) = \frac{1}{2}\left\{ f_1\not{n}_+ + f_{1T}^\perp\,\frac{\epsilon_T^{\rho\sigma}S_{T\rho}p_{T\sigma}}{M}\,\not{n}_+ + g_{1s}\gamma_5\not{n}_+ \right.$$
$$\left. + h_{1T}\,\frac{[\not{S}_T,\not{n}_+]\gamma_5}{2} + h_{1s}^\perp\,\frac{[\not{p}_T,\not{n}_+]\gamma_5}{2M} + \mathrm{i}\,h_1^\perp\,\frac{[\not{p}_T,\not{n}_+]}{2M} \right\}.$$

Here we introduced

$$\epsilon_T^{\alpha\beta} = \epsilon^{\alpha\beta\rho\sigma}\, n_{+\rho} n_{-\sigma}. \tag{109}$$

The distribution functions on the r.h.s. depend on x and p_T^2, except for the functions with subscript s, where we use the shorthand notation [34]

$$g_{1s}(x, p_T) = S_L\, g_{1L}(x, p_T^2) - \frac{S_T \cdot p_T}{M}\, g_{1T}(x, p_T^2) \tag{110}$$

and so forth for the other functions. It is also useful to introduce the function

$$h_1(x, \boldsymbol{p}_T^2) \equiv h_{1T}(x, \boldsymbol{p}_T^2) + h_{1T}^{\perp(1)}(x, \boldsymbol{p}_T^2). \tag{111}$$

The definition of the parton distribution functions in terms of the amplitudes A_i, introduced in eq. (38), can be found elsewhere [43-45].

The two functions $f_{1T}^{\perp}$ (Sivers function) and $h_1^{\perp}$ (Boer-Mulders function) are T-odd [31,41]. The notation for the distribution functions follows closely that of ref. [34], sometimes referred to as "Amsterdam notation." We remark that a number of other notations exist for some of the distribution functions, see *e.g.* refs. [33,46,47]. In particular, transverse-momentum–dependent functions at leading twist have been widely discussed by Anselmino *et al.* [48-50]. The connection between the notation in these papers and the one used here is discussed in App. C of ref. [50]. The following names are in common use for the TMDs:

- f_1: unpolarized TMD;
- g_{1L}: helicity TMD;
- h_1: transversity TMD;
- $f_{1T}^{\perp}$: Sivers TMD;
- $h_1^{\perp}$: Boer-Mulders TMD;
- $g_{1T}^{\perp}$: worm-gear TMD, or transversal helicity TMD;
- $h_{1L}^{\perp}$: worm-gear TMD, or Kotzinian-Mulders TMD, or longitudinal transversity TMD;
- $h_{1T}^{\perp}$: pretzelosity TMD or quadrupole TMD.

The table in fig. 9 lists the TMDs with their connection to quark and target polarizations.

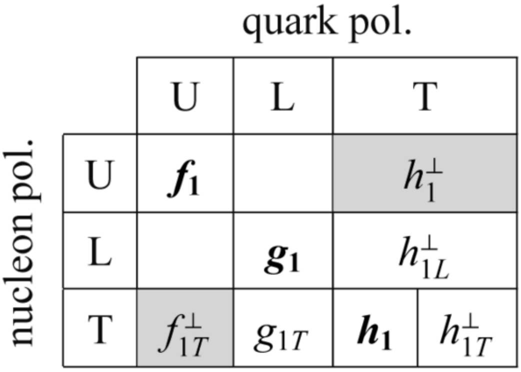
quark pol.
nucleon pol.

nucleon pol. \ quark pol.	U	L	T	
U	$\boldsymbol{f_1}$		$h_1^\perp$	
L		$\boldsymbol{g_1}$	$h_{1L}^\perp$	
T	$f_{1T}^\perp$	g_{1T}	$\boldsymbol{h_1}$	$h_{1T}^\perp$

Fig. 9. – Twist-2 transverse-momentum–dependent distribution functions. The U,L,T correspond to unpolarized, longitudinally polarized and transversely polarized nucleons (rows) and quarks (columns). Functions in boldface survive transverse-momentum integration. Functions in gray cells are T-odd.

Useful relations are

$$\Phi^{[\gamma^+]} = f_1(x,p_T^2) - \frac{\epsilon_T^{\rho\sigma}\, p_{T\rho} S_{T\sigma}}{M}\, f_{1T}^\perp(x,p_T^2)\,, \tag{112}$$

$$\Phi^{[\gamma^+\gamma_5]} = S_L\, g_{1L}(x,p_T^2) - \frac{p_T\cdot S_T}{M}\, g_{1T}(x,p_T^2)\,, \tag{113}$$

$$\begin{aligned}\Phi^{[\mathrm{i}\sigma^{\alpha+}\gamma_5]} &= S_T^\alpha\, h_1(x,p_T^2) + S_L\,\frac{p_T^\alpha}{M}\, h_{1L}^\perp(x,p_T^2)\\ &\quad - S_{T\rho}\frac{p_T^\alpha p_T^\rho - \frac{1}{2}\,p_T^2\, g_T^{\alpha\rho}}{M^2}\, h_{1T}^\perp(x,p_T^2) - \frac{\epsilon_T^{\alpha\rho} p_{T\rho}}{M}\, h_1^\perp(x,p_T^2)\,.\end{aligned} \tag{114}$$

Transverse-momentum–dependent parton distributions of leading twist can be interpreted as number densities (see *e.g.*, refs. [46,51,52]). To connect with this interpretation, we take the example of the distribution of unpolarized quarks in a polarized proton, which is given by [24]

$$\begin{aligned} f_{q/p^\uparrow}(x,p_T) &= \Phi^{[\not{n}_-]}\\ &= f_1^q(x,p_T^2) - f_{1T}^{\perp q}(x,p_T^2)\,\frac{\epsilon^{\mu\nu\rho\sigma} P_\mu p_\nu S_\rho (n_-)_\sigma}{M\,(P\cdot n_-)}\\ &= f_1^q(x,p_T^2) - f_{1T}^{\perp q}(x,p_T^2)\,\frac{(\hat{\boldsymbol{P}}\times \boldsymbol{p}_T)\cdot \boldsymbol{S}}{M}\,. \end{aligned} \tag{115}$$

The second expression in (115) holds in any frame where $\boldsymbol{n}$ and the direction $\hat{\boldsymbol{P}}$ of the proton momentum point in opposite directions. Therefore $f_{1T}^{\perp q} > 0$ corresponds to a preference of the quark to move to the left if the proton is moving towards the observer and the proton spin is pointing upwards.

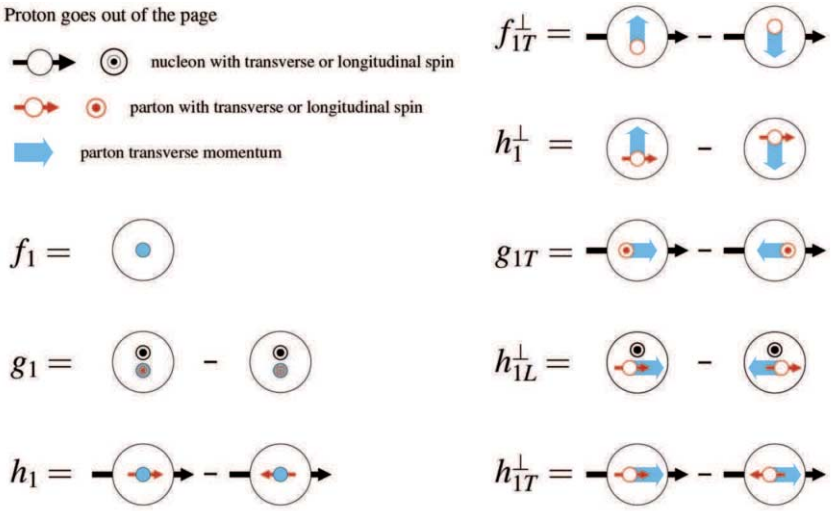
Proton goes out of the page
nucleon with transverse or longitudinal spin
parton with transverse or longitudinal spin
parton transverse momentum
$f_{1T}^{\perp} =$
-
$h_1^{\perp} =$
-
$f_1 =$
$g_{1T} =$
-
$g_1 =$
-
$h_{1L}^{\perp} =$
-
$h_1 =$
-
$h_{1T}^{\perp} =$
-

Fig. 10. – Probabilistic interpretation of twist-2 transverse-momentum–dependent distribution functions. To avoid ambiguities, it is necessary to indicate the directions of quark's transverse momentum, target spin and quark spin, and specify that the proton is moving out of the page, or alternatively the photon is moving into the page.

Let us give the corresponding relation for the Boer-Mulders function. The distribution of transversely polarized quarks in an unpolarized proton is (see eq. (11) and (12) of [53])

$$
\begin{aligned}
f_{q^{\uparrow}/p}(x, p_T) &= \Phi(S=0)^{[\not{n}_-]} + \Phi(S=0)^{[i\sigma_{\mu\nu}\gamma_5\, n_-^{\mu}\, S_q^{\nu}]} \\
&= \frac{1}{2}\left(f_1^q(x, p_T^2) - h_1^{\perp q}(x, p_T^2)\, \frac{\epsilon^{\mu\nu\rho\sigma} P_\mu p_\nu S_{q\rho} (n_-)_\sigma}{M\ (P \cdot n_-)} \right) \\
&= \frac{1}{2}\left(f_1^q(x, p_T^2) - h_1^{\perp q}(x, p_T^2)\, \frac{(\hat{\boldsymbol{P}} \times \boldsymbol{p}_T) \cdot \boldsymbol{S}_q}{M} \right),
\end{aligned}
\tag{116}
$$

where S_q is the covariant spin vector of the quark. Therefore, $h_1^{\perp q} > 0$ corresponds to a preference of the quark to move to the left if the proton is moving towards the observer and the quark spin is pointing upwards.

The probabilistic interpretation of TMDs is summarized in fig. 10.

For any transverse-momentum dependent distribution function, it will turn out to be convenient to define the notation

$$
f^{(1/2)}(x, \boldsymbol{p}_T^2) \equiv \frac{|\boldsymbol{p}_T|}{2M}\, f(x, \boldsymbol{p}_T^2), \tag{117a}
$$

$$
f^{(n)}(x, \boldsymbol{p}_T^2) \equiv \left(\frac{\boldsymbol{p}_T^2}{2M^2} \right)^{n} f(x, \boldsymbol{p}_T^2), \tag{117b}
$$

for n integer.

As done in the previous section, we can express the transverse-momentum–dependent correlation function as a matrix in the parton chirality space $\otimes$ target helicity space. To simplify the formulae, it is useful to identify the T-odd functions as imaginary parts of some of the T-even functions, which become then complex scalar functions. The following redefinitions are required(³):

$$g_{1T} + \mathrm{i} f_{1T}^{\perp} \to g_{1T}, \qquad h_{1L}^{\perp} + \mathrm{i} h_{1}^{\perp} \to h_{1L}^{\perp}. \tag{118}$$

The resulting correlation matrix is [35, 36]

$$F(x,\boldsymbol{p}_T)^{\Lambda_1'\Lambda_1}_{\chi_1\chi_1'} = \tag{119}$$
$$\left(\begin{array}{cc|cc}
f_1 + g_{1L} & \frac{|\boldsymbol{p}_T|}{M}\,\mathrm{e}^{-\mathrm{i}\phi_p}\,g_{1T} & \frac{|\boldsymbol{p}_T|}{M}\,\mathrm{e}^{\mathrm{i}\phi_p}\,h_{1L}^{\perp *} & 2\,h_1 \\
\frac{|\boldsymbol{p}_T|}{M}\,\mathrm{e}^{\mathrm{i}\phi_p}\,g_{1T}^{*} & f_1 - g_{1L} & \frac{|\boldsymbol{p}_T|^2}{M^2}\mathrm{e}^{2\mathrm{i}\phi_p}\,h_{1T}^{\perp} & -\frac{|\boldsymbol{p}_T|}{M}\,\mathrm{e}^{\mathrm{i}\phi_p}\,h_{1L}^{\perp} \\
\hline
\frac{|\boldsymbol{p}_T|}{M}\,\mathrm{e}^{-\mathrm{i}\phi_p}\,h_{1L}^{\perp} & \frac{|\boldsymbol{p}_T|^2}{M^2}\mathrm{e}^{-2\mathrm{i}\phi_p}\,h_{1T}^{\perp} & f_1 - g_{1L} & -\frac{|\boldsymbol{p}_T|}{M}\,\mathrm{e}^{-\mathrm{i}\phi_p}\,g_{1T}^{*} \\
2\,h_1 & -\frac{|\boldsymbol{p}_T|}{M}\,\mathrm{e}^{-\mathrm{i}\phi_p}\,h_{1L}^{\perp *} & -\frac{|\boldsymbol{p}_T|}{M}\,\mathrm{e}^{\mathrm{i}\phi_p}\,g_{1T} & f_1 + g_{1L}
\end{array}\right),$$

where for sake of brevity we did not explicitly indicate the x and $\boldsymbol{p}_T^2$ dependence of the distribution functions and where ϕ_p is the azimuthal angle of the transverse-momentum vector.

The distribution matrix is clearly Hermitean. The condition of angular-momentum conservation becomes $\Lambda_1' + \chi_1' + l' = \Lambda_1 + \chi_1$. The condition of parity invariance becomes

$$F(x,\boldsymbol{p}_T)^{\Lambda_1'\Lambda_1}_{\chi_1\chi_1'} = (-1)^{l'}\, F(x,\boldsymbol{p}_T)^{-\Lambda_1'\,-\Lambda_1}_{-\chi_1\,-\chi_1'}\Big|_{l'\to -l'}. \tag{120}$$

Bounds to insure positivity of any matrix element can be obtained by looking at the one-dimensional and two-dimensional subspaces and at the eigenvalues of the full matrix. The one-dimensional subspaces give the trivial bounds

$$f_1(x,\boldsymbol{p}_T^2) \geq 0\,, \qquad \left|g_{1L}(x,\boldsymbol{p}_T^2)\right| \leq f_1(x,\boldsymbol{p}_T^2)\,. \tag{121}$$

(³) From a rigorous point of view, it would be better to introduce new functions, *e.g.*, $\tilde{g}_{1T}$ and $\tilde{h}_{1L}^{\perp}$, but this would overload the notation.

From the two-dimensional subspaces we get

$$|h_1| \le \frac{1}{2}(f_1 + g_{1L}) \le f_1, \tag{122a}$$

$$\left|h_{1T}^{\perp(1)}\right| \le \frac{1}{2}(f_1 - g_{1L}) \le f_1, \tag{122b}$$

$$\left|g_{1T}^{(1)}\right|^2 + \left|f_{1T}^{\perp(1)}\right|^2 \le \frac{\boldsymbol{p}_T^2}{4M^2}(f_1 + g_{1L})(f_1 - g_{1L}) \le \left(f_1^{(1/2)}\right)^2, \tag{122c}$$

$$\left|h_{1L}^{\perp(1)}\right|^2 + \left|h_1^{\perp(1)}\right|^2 \le \frac{\boldsymbol{p}_T^2}{4M^2}(f_1 + g_{1L})(f_1 - g_{1L}) \le \left(f_1^{(1/2)}\right)^2, \tag{122d}$$

where, once again, we did not explicitly indicate the x and $\boldsymbol{p}_T^2$ dependence to avoid too heavy a notation. Besides the Soffer bound of eq. (122a), now extended to include the transverse-momentum dependence, new bounds for the distribution functions are found. These bounds can be very useful for phenomenological applications.

The positivity bounds can be sharpened even further by imposing the positivity of the eigenvalues of the correlation matrix. The complete analysis has been accomplished in ref. [35] (see also ref. [36]).

The connection with the integrated distribution functions defined in eq. (40) is

$$f_1(x) = \int \mathrm{d}^2\boldsymbol{p}_T\, f_1(x, \boldsymbol{p}_T^2), \tag{123a}$$

$$g_{1L}(x) = \int \mathrm{d}^2\boldsymbol{p}_T\, g_{1L}(x, \boldsymbol{p}_T^2), \tag{123b}$$

$$h_1(x) = \int \mathrm{d}^2\boldsymbol{p}_T\, h_1(x, \boldsymbol{p}_T^2). \tag{123c}$$

The above identification is however a dangerous step. At parton-model level, it is not a big problem if we assume that TMDs fall-off sufficently fast (*i.e.*, they are integrable and their total integral is approximately equal to their integral in the region $\boldsymbol{p}_T^2 \ll Q^2$). We may have in mind that partons have some "intrinsic" transverse momentum of order $\boldsymbol{p}_T^2 \sim M^2$ or $\boldsymbol{p}_T^2 \sim \Lambda_{\mathrm{QCD}}^2$. This is however *not* the case when we take into consideration QCD corrections. In this case, partons acquire transverse momentum also through gluon radiation. First of all, this has the consequence that TMDs in QCD are *not* integrable, so we must give up the above relations in general. Secondly, it becomes impossible—or a matter of conventions—to distinguish an intrinsic part of transverse momentum from a perturbative part. TMDs contain both.

Another way to state the problem is the following: the steps we took to analyze SIDIS were based on the assumption that $\boldsymbol{P}_{h\perp}^2 \ll Q^2$. We never needed this approximation for inclusive DIS, where we introduced collinear PDFs. Collinear PDFs are obtained from an integration over $\boldsymbol{P}_{h\perp}^2$ up to a limit of the order of Q^2. They contain therefore also contributions that are outside the reach of the TMD formalism. Therefore, we should not expect in general that the integral of TMDs gives back collinear PDFs: something must be missing.

Is there then no relation between TMDs and collinear PDFs? The full QCD formalism tells us that there is a relation, but it is between PDFs and the high-transverse-momentum tail of TMDs.

9. – Structure functions in the parton model

Inserting the parameterizations of the different correlators in expression (96) of the hadronic tensor and contracting it with the leptonic tensor, one can calculate the leptoproduction cross-section for semi-inclusive DIS and project out the different structure functions appearing in eq. (70). To have a compact notation for the results, we introduce the notation

$$\begin{aligned}\mathcal{C}\big[wfD\big] = x_B \sum_q e_q^2 \int \mathrm{d}^2\boldsymbol{p}_T\, \mathrm{d}^2\boldsymbol{k}_T\, \delta^{(2)}\big(\boldsymbol{p}_T - \boldsymbol{k}_T - \boldsymbol{P}_{h\perp}/z\big) \\ \times w(\boldsymbol{p}_T, \boldsymbol{k}_T)\, f^q(x_B, p_T^2)\, D^q(z, k_T^2),\end{aligned} \tag{124}$$

with the unit vector $\hat{\boldsymbol{h}} = \boldsymbol{P}_{h\perp}/|\boldsymbol{P}_{h\perp}|$, where $w(\boldsymbol{p}_T, \boldsymbol{k}_T)$ is an arbitrary function.

These are the expressions for the structure functions appearing in eq. (70)

$$F_{UU,T} = \mathcal{C}\big[f_1 D_1\big], \tag{125}$$

$$F_{UU,L} = 0, \tag{126}$$

$$F_{UU}^{\cos\phi_h} = 0 \tag{127}$$

$$F_{UU}^{\cos 2\phi_h} = \mathcal{C}\left[-\frac{2\,\big(\hat{\boldsymbol{h}}\cdot\boldsymbol{k}_T\big)\,\big(\hat{\boldsymbol{h}}\cdot\boldsymbol{p}_T\big) - \boldsymbol{k}_T\cdot\boldsymbol{p}_T}{M M_h} h_1^\perp H_1^\perp\right], \tag{128}$$

$$F_{LU}^{\sin\phi_h} = 0, \tag{129}$$

$$F_{UL}^{\sin\phi_h} = 0, \tag{130}$$

$$F_{UL}^{\sin 2\phi_h} = \mathcal{C}\left[-\frac{2\,\big(\hat{\boldsymbol{h}}\cdot\boldsymbol{k}_T\big)\,\big(\hat{\boldsymbol{h}}\cdot\boldsymbol{p}_T\big) - \boldsymbol{k}_T\cdot\boldsymbol{p}_T}{M M_h} h_{1L}^\perp H_1^\perp\right], \tag{131}$$

$$F_{LL} = \mathcal{C}\big[g_{1L} D_1\big], \tag{132}$$

$$F_{LL}^{\cos\phi_h} = 0, \tag{133}$$

$$F_{UT,T}^{\sin(\phi_h-\phi_S)} = \mathcal{C}\left[-\frac{\hat{\boldsymbol{P}}_{h\perp}\cdot\boldsymbol{p}_T}{M} f_{1T}^\perp D_1\right], \tag{134}$$

$$F_{UT,L}^{\sin(\phi_h-\phi_S)} = 0, \tag{135}$$

$$F_{UT}^{\sin(\phi_h+\phi_S)} = \mathcal{C}\left[-\frac{\hat{\boldsymbol{P}}_{h\perp}\cdot\boldsymbol{k}_T}{M_h} h_1 H_1^\perp\right], \tag{136}$$

$$\begin{aligned}&F_{UT}^{\sin(3\phi_h-\phi_S)}\\&\quad=\mathcal{C}\biggl[\frac{2\,\bigl(\hat{\boldsymbol{P}}_{h\perp}\cdot\boldsymbol{p}_T\bigr)\,\bigl(\boldsymbol{p}_T\cdot\boldsymbol{k}_T\bigr)+\boldsymbol{p}_T^2\,\bigl(\hat{\boldsymbol{P}}_{h\perp}\cdot\boldsymbol{k}_T\bigr)-4\,(\hat{\boldsymbol{P}}_{h\perp}\cdot\boldsymbol{p}_T)^2\,(\hat{\boldsymbol{P}}_{h\perp}\cdot\boldsymbol{k}_T)}{2M^2M_h}h_{1T}^{\perp}H_1^{\perp}\biggr],\end{aligned}\tag{137}$$

$$F_{UT}^{\sin\phi_S}=0,\tag{138}$$

$$F_{UT}^{\sin(2\phi_h-\phi_S)}=0,\tag{139}$$

$$F_{LT}^{\cos(\phi_h-\phi_S)}=\mathcal{C}\biggl[\frac{\hat{\boldsymbol{P}}_{h\perp}\cdot\boldsymbol{p}_T}{M}g_{1T}D_1\biggr],\tag{140}$$

$$F_{LT}^{\cos\phi_S}=0,\tag{141}$$

$$F_{LT}^{\cos(2\phi_h-\phi_S)}=0,\tag{142}$$

It has to be stressed that in much of the past literature a different definition of the azimuthal angles has been used, whereas in the present work we adhere to the Trento conventions [24].

Ex. 5

Compute some of the structure functions above using Mathematica and Feyncalc. For convenince, you can use the following definitions:

```
eta= {{0, 1, 0, 0}, {1, 0, 0, 0}, {0, 0, -1, 0}, {0, 0, 0, -1}}

GAp = GS[Momentum[nm]];
GAm = GS[Momentum[np]];
GA5 = DiracGamma[5];
```

And you have to introduce the following scalar products (the first two instructions are just a convenient way to write all scalar products of light-cone vectors):

```
Unit = {nm, np, ni, nj};
Table[ScalarProduct[Unit[[i]], Unit[[j]]] = eta[[i, j]], {i, 1,
4}, {j, 1, 4}];

ScalarProduct[pt, np] = 0;
ScalarProduct[pt, nm] = 0;
ScalarProduct[kt, np] = 0;
ScalarProduct[kt, nm] = 0;

ScalarProduct[St, nm] = 0;
ScalarProduct[St, np] = 0;
```

Now you can introduce the decompositions of the correlation functions. In this first example, we take into consideration only three of the eight terms in eq. (109)

```
Phi = (f1 - g1T Pair[Momentum[pt], Momentum[St]]/M GA5 -
f1Tperp Pair[Momentum[pt], Momentum[epsT[St]]]/M).(GAm/2)

Delta = (D1 + I H1perp 1/Mh GS[Momentum[kt]]).(GAp/2)
```

Build a first version of the hadronic tensor, according to eq. (96). Note that for convenience we can avoid introducing explicitly the convolution in eq. (97). We need to remember to include it in the final result.

```
MW0 = 1/2 2 z (Tr[Phi.GA[\[Mu]].Delta .GA[\[Nu]]]) //
Collect[#, {f1 D1, f1Tperp D1, D1 g1T}, Simplify] &
```

Apply the following crucial replacements and cast the tensor in a convenient form

```
HadTensSimpl = {Pair[Momentum[pt], Momentum[St]] ->
SSt Cos[-\[Phi] + \[Phi]St] Pair[Momentum[pt], Momentum[h]],
Pair[Momentum[pt], Momentum[epsT[St]]] ->
SSt Sin[-\[Phi] + \[Phi]St] Pair[Momentum[pt], Momentum[h]]}

MW = MW0 /. HadTensSimpl // Simplify
```

Finally, contract with the leptonic tensor (obtained in Ex. 1)

```
crosssection1 = (\[Alpha]^2 y)/(2 z Q^4)
Contract[Lept 2 MW]// Expand //
Collect[#, {f1 D1, f1Tperp D1, h1 H1perp, D1 g1T}, Simplify] &
```

By comparing the result with eq. (70) and after fixing all small mistakes in the above, you should be able to identify the structure functions corresponding to eqs. (125), (134), and (140).

10. – Beyond the parton model

A first important difference between TMDs and PDFs when we also start taking gluons into account is in the shape of the gauge link. The proper gauge-invariant definition of the quark-quark correlator is

$$\Phi_{ij}(x,p_T) = \int \frac{\mathrm{d}\xi^-\,\mathrm{d}^2\xi_T}{(2\pi)^3}\, e^{\mathrm{i}p\cdot\xi}\, \langle P|\bar{\psi}_j(0)\,\mathcal{U}^{n_-}_{(0,+\infty)}\,\mathcal{U}^{n_-}_{(+\infty,\xi)}\,\psi_i(\xi)|P\rangle\Big|_{\xi^+=0}, \tag{143}$$

where the gauge links (Wilson lines) are defined as

$$\mathcal{U}^{n_-}_{(0,+\infty)} = \mathcal{U}^{n_-}(0^-,\infty^-;\mathbf{0}_T)\,\mathcal{U}^{T}(\mathbf{0}_T,\boldsymbol{\infty}_T;\infty^-), \tag{144}$$

$$\mathcal{U}^{n_-}_{(+\infty,\xi)} = \mathcal{U}^{T}(\boldsymbol{\infty}_T,\boldsymbol{\xi}_T;\infty^-)\,\mathcal{U}^{n_-}(\infty^-,\xi^-,\boldsymbol{\xi}_T). \tag{145}$$

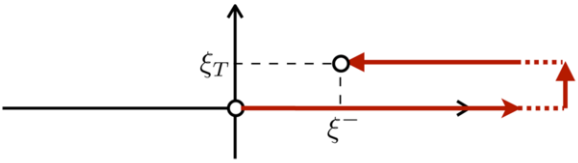

Fig. 11. – Path of the gauge link for semi-inclusive DIS.

Here $\mathcal{U}^{n_-}(a^-,b^-;\boldsymbol{c}_T)$ indicates a Wilson line running along the minus direction from $[a^-,0,\boldsymbol{c}_T]$ to $[b^-,0,\boldsymbol{c}_T]$, while $\mathcal{U}^{T}(\boldsymbol{a}_T,\boldsymbol{b}_T;c^-)$ indicates a Wilson line running in the transverse direction from $[c^-,0,\boldsymbol{a}_T]$ to $[c^-,0,\boldsymbol{b}_T]$, *i.e.*

$$\mathcal{U}^{n_-}(a^-,b^-;\boldsymbol{c}_T)=\mathcal{P}\exp\left[-\mathrm{i}g\int_{a^-}^{b^-}\mathrm{d}\eta^-A^+(\eta^-,0,\boldsymbol{c}_T)\right], \tag{146}$$

$$\mathcal{U}^{T}(\boldsymbol{a}_T,\boldsymbol{b}_T;c^-)=\mathcal{P}\exp\left[-\mathrm{i}g\int_{\boldsymbol{a}_T}^{\boldsymbol{b}_T}\mathrm{d}\eta_T\cdot A_T(c^-,0,\boldsymbol{\eta}_T)\right]. \tag{147}$$

In particular

$$\begin{aligned}\mathcal{U}^{n_-}(\infty^-,\xi^-,\boldsymbol{\xi}_T)&=\mathcal{P}\exp\left[-\mathrm{i}g\int_{\infty^-}^{\xi^-}\mathrm{d}\eta^-A^+(\eta^-,0,\boldsymbol{\xi}_T)\right]\\&\approx 1-ig\int_{\infty^-}^{\xi^-}\mathrm{d}\eta^-A^+(\eta^-,0,\boldsymbol{\xi}_T),\end{aligned} \tag{148}$$

$$\begin{aligned}\mathcal{U}^{T}(\boldsymbol{\infty}_T,\boldsymbol{\xi}_T;\infty^-)&=\mathcal{P}\exp\left[-\mathrm{i}g\int_{\boldsymbol{\infty}_T}^{\boldsymbol{\xi}_T}\mathrm{d}\eta_T\cdot A_T(\infty^-,0,\boldsymbol{\eta}_T)\right]\\&\approx 1-ig\int_{\boldsymbol{\infty}_T}^{\boldsymbol{\xi}_T}\mathrm{d}\eta_T\cdot A_T(\infty^-,0,\boldsymbol{\eta}_T).\end{aligned} \tag{149}$$

The correlator in eq. (143) is the one appearing in semi-inclusive DIS. Its path is pictorially shown in fig. 11.

A remarkable property of TMDs is that the detailed shape of the Wilson line is process dependent. This immediately leads to the conclusion that TMDs are not universal. However, for transverse-momentum–dependent fragmentation functions, the shape of the Wilson line appears to have no influence on physical observables [54-57]. In SIDIS and Drell-Yan, the difference between the Wilson line consists in a simple direction reversal and leads to calculable effects, namely a simple sign reversal of all T-odd TMDs [22].

In more complex processes, such as proton-proton collisions into hadrons, it was initially proposed to introduce more intricate gauge links [58-60], but it seems now that it becomes even impossible to disentangle them [61].

Similarly to standard collinear PDFs, it is essential to define TMDs in a formally clear way, through the proof of factorization theorems. TMDs appear when factorizing semi-inclusive processes. For instance, while totally inclusive DIS can be described introducing collinear PDFs, TMDs appear in semi-inclusive DIS if the transverse momentum of one outgoing hadron, $P_{h\perp}$, is measured.

Dealing with semi-inclusive processes pushes the difficulty of proving factorization theorems to a higher level of complications. TMD factorization is in fact a challenging arena where many of the simplifications used in collinear factorization cannot be applied. Nevertheless, factorization for semi-inclusive DIS has been worked out explicitly at leading twist (twist 2) and one-loop order [6, 12, 62, 63]. For instance, the structure function $F_{UU,T}$ in the region $P_{h\perp}^2 \ll Q^2$ can be expressed as

$$\begin{aligned} F_{UU,T} = {}& \big|H\big(x\zeta^{1/2}, z^{-1}\zeta_h^{1/2}, \mu_F\big)\big|^2 \sum_a x\, e_a^2 \int \mathrm{d}^2\boldsymbol{p}_T\, \mathrm{d}^2\boldsymbol{k}_T \\ & \times \delta^{(2)}\big(\boldsymbol{p}_T - \boldsymbol{k}_T - \boldsymbol{P}_{h\perp}/z\big)\, f_1^a(x, p_T^2; \zeta, \mu_F)\, D_1^a(z, k_T^2; \zeta_h, \mu_F). \end{aligned} \tag{150}$$

The formula contains the (calculable) hard scattering factor H and the transverse-momentum-dependent PDFs and fragmentation functions. Following refs. [6, 63], there is no "soft factor" in the above formula. The soft factor can be introduced to absorb infrared soft divergences. In this alternative definition, these divergences are absorbed already in the TMDs.

According to TMD factorization, TMDs depend also on a cutoff ζ. This cutoff is used to regulate light-cone or rapidity divergences. As we mentioned in the DIS discussion, these divergences cancel in inclusive DIS thanks to the summation of virtual and real diagrams and the integration over transverse momentum, similarly to soft divergences. In semi-inclusive DIS, they do not cancel. Various ways to deal with these divergences have been proposed [5, 12, 62, 64].

TMD evolution is different from that of standard PDFs and takes into account how TMD shape is influenced by the radiation of infinitely many gluons (transverse-momentum resummation) [65]. What needs to be obtained from data is the nonperturbative part of the functions (*i.e.* what cannot be computed with perturbative QCD). Figure 12 (from [63]) shows the effect of TMD evolution on the distribution of up quarks (the nonperturbative part is taken from [66] and [67]). The effect of gluon radiation is a broadening of the TMD.

In general and in simplified terms, the study of TMD factorization requires a deeper understanding of what happens when a quark is hit inside a nucleon, with a particular attention to the infinitely many gluons that surround the quark, beyond the simple case when its transverse momentum is integrated over.

11. – Beyond the parton model: high transverse momentum

Three scales are involved in semi-inclusive DIS: the scale of nonperturbative QCD dynamics, which we represent by the nucleon mass M, the transverse momentum $P_{h\perp}$, and the photon virtuality Q, which we require to be large compared with M. For the considerations of this section, it is convenient to consider the transverse momentum $q_T^2 \approx P_{h\perp}^2/z^2$.

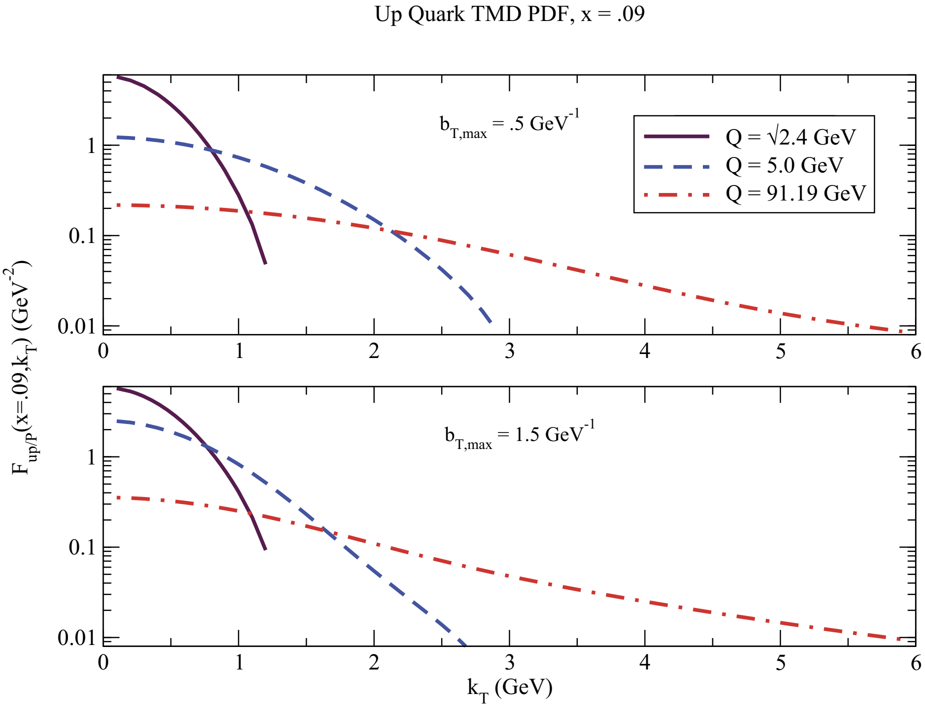

Fig. 12. – The up-quark TMD for $Q = \sqrt{2.4}, 5.0$ and 91.19 GeV and $x = 0.09$ from ref. [63]. The upper and lower plot refer to two different choices for the parameter $b_{\max}$ needed in the full TMD formula.

At high q_T ($q_T \gg M$) the structure functions can be described using collinear factorization, *i.e.* in terms of collinear distribution and fragmentation functions together with perturbative radiation. At low q_T ($q_T \ll Q$) the structure functions can be described using TMD factorization [12, 62], *i.e.* in terms transverse-momentum–dependent (TMD) parton distribution and fragmentation functions. The low- and high-q_T domains overlap for $M \ll q_T \ll Q$ (intermediate transverse momentum), where both descriptions can hence be applied. This important property is what allows us to establish a connection between collinear PDFs and the tail of TMDs.

Ideally, we would like to have an expression for the polarized SIDIS cross-section that describes in a smooth way the physics from low to high transverse momentum. This issue becomes crucial at collider experiments, where the possibility to reach high values of Q leaves room to meaningfully distinguish between high, intermediate, and low transverse momentum.

In order to address the problem two steps are needed: i) identify the structure functions for which a matching is possible, ii) work out a formula that describes the structure function at any transverse momentum. In the following I will briefly discuss some crucial results.

To study the power behavior of the structure functions, it is important to realize that the power expansions are done in two different ways in the two descriptions. At low q_T, first we expand in $(q_T/Q)^{n-2}$ and neglect terms with n bigger than a certain value (so far, analyses have been carried out only up to $n=3$, *i.e.* twist-3). To study the behavior at intermediate q_T we further expand in $(M/q_T)^k$. Vice versa, at high q_T we first expand in $(M/q_T)^n$ (also in this case, analyses are available up to $n=3$, *i.e.* twist-3). To study the intermediate-q_T region, we further expand in $(q_T/Q)^{k-2}$. We can encounter two different situations:

– Type-I observables, where the leading terms at high and low transverse momentum have the same behavior. For instance,

$$F(q_T,Q) = A\left[\frac{q_T}{Q}\right]^0\left[\frac{M}{q_T}\right]^2 + B\left[\frac{q_T}{Q}\right]^2\left[\frac{M}{q_T}\right]^2 + \dots\,, \tag{151}$$

where the term A is leading in both the low- and high-q_T calculations. In this case, the calculations at high and low transverse momentum must yield exactly the same result at intermediate transverse momentum [65, 68]. If a mismatch occurs, it means that one of the calculations is incorrect or incomplete.

– Type-II observables, where the leading terms at high and low transverse momentum have different behavior. For instance,

$$F(q_T,Q) = A'\left[\frac{q_T}{Q}\right]^0\left[\frac{M}{q_T}\right]^4 + B'\left[\frac{q_T}{Q}\right]^2\left[\frac{M}{q_T}\right]^2 + \dots\,, \tag{152}$$

where the first term is leading and the second term subleading in the low-q_T calculation, whereas the reverse holds in the high-q_T calculation. In this case, if the calculations at high and low transverse momentum are performed at their respective leading order, they describe two different mechanisms and will not lead to the same result at intermediate transverse momentum. In order to "match", the calculations should be carried out in both regimes up to the sub-subleading order. We could call this situation an "expected mismatch", since it is simply due to the difference between the two expansions.

In table I we list the power behavior of the structure functions at intermediate transverse momentum, as obtained from the limits of the low-q_T and high-q_T calculation. For details of the calculation, we refer to [69].

In the last column of the table we identify type-II structure functions, fow which the low-q_T and high-q_T calculations at leading order pick up two different components of the full structure function. They therefore describe two different mechanisms and do not match.

TABLE I. – *Behavior of SIDIS structure functions in the region $M \ll q_T \ll Q$, as deduced from the low-q_T calculation based on TMD factorization and the high-q_T calculation based on collinear factorization. Empty fields indicate that no calculation is available. The last column indicates whether the expressions match exactly, do not match exactly, or should not be expected to match. In parentheses: expected answers based on analogy, rather than actual calculation.*

Structure function	low-q_T power	high-q_T power	exact match
$F_{UU,T}$	$1/q_T^2$	$1/q_T^2$	yes
$F_{UU,L}$		$1/Q^2$	
$F_{UU}^{\cos\phi_h}$	$1/(Q\,q_T)$	$1/(Q\,q_T)$	no
$F_{UU}^{\cos 2\phi_h}$	$1/q_T^4$	$1/Q^2$	type II
$F_{LU}^{\sin\phi_h}$	$1/(Q\,q_T)$	$1/(Q\,q_T)$	(no)
$F_{UL}^{\sin\phi_h}$	$1/(Q\,q_T)$		(no)
$F_{UL}^{\sin 2\phi_h}$	$1/q_T^4$		(type II)
F_{LL}	$1/q_T^2$	$1/q_T^2$	yes
$F_{LL}^{\cos\phi_h}$	$1/(Q\,q_T)$	$1/(Q\,q_T)$	no
$F_{UT,T}^{\sin(\phi_h-\phi_S)}$	$1/q_T^3$	$1/q_T^3$	yes
$F_{UT,L}^{\sin(\phi_h-\phi_S)}$		$1/(Q^2\,q_T)$	
$F_{UT}^{\sin(\phi_h+\phi_S)}$	$1/q_T^3$	$1/q_T^3$	yes
$F_{UT}^{\sin(3\phi_h-\phi_S)}$	$1/q_T^3$	$1/(Q^2\,q_T)$	type II
$F_{UT}^{\sin\phi_S}$	$1/(Q\,q_T^2)$	$1/(Q\,q_T^2)$	(no)
$F_{UT}^{\sin(2\phi_h-\phi_S)}$	$1/(Q\,q_T^2)$	$1/(Q\,q_T^2)$	(no)
$F_{LT}^{\cos(\phi_h-\phi_S)}$	$1/q_T^3$		(yes)
$F_{LT}^{\cos\phi_S}$	$1/(Q\,q_T^2)$		(no)
$F_{LT}^{\cos(2\phi_h-\phi_S)}$	$1/(Q\,q_T^2)$		(no)

For type-II observables, if one aims at studying the leading-twist contribution from transverse momentum distributions, some considerations have to be kept in mind:

- the leading contribution from the high-q_T calculation (often referred to as a pQCD or radiative correction) is a competing effect that has to be taken into account [70-72];
- q_T-weighted asymmetries enhance the high-q_T mechanism and thus are not appropriate to extract TMDs;

- it is at present impossible to construct an expression that extends the high-q_T calculation to $q_T \approx M$, since this requires a smooth merging into unknown twist-4 contributions, which most probably cannot be factorized (see also ref. [73]);
- it may be useful to build observables that are least sensitive to the effect of radiative corrections.

We stress that the above considerations apply not only to semi-inclusive DIS, but also to Drell-Yan and e^+e^- annihilation [74], which have been already used to extract the Boer-Mulders and Collins functions [72, 75].

The structure functions with a "yes" or "no" in the last column of table I are type-I observables, where on the basis of power counting we know that two calculations describe the same physics and should therefore exactly match. In these cases, the high-q_T calculation describes the perturbative tail of the low-q_T effect. The two mechanisms need not be distinguished. Using resummation it should be possible to construct expressions for these observables that are valid at any q_T.

Six of these structure functions have been calculated explicitly. The following structure functions all involve twist-2 TMDs and indeed present an exact matching: $F_{UU,T}$, F_{LL} [76], $F_{UT,T}^{\sin(\phi_h-\phi_S)}$ (Sivers structure function) [77] (see also the additions in ref. [78]) and $F_{UT}^{\sin(\phi_h+\phi_S)}$ (Collins structure function) [79]. We expect also $F_{LT}^{\cos(\phi_h-\phi_S)}$ to match exactly, since it has been shown explicitly for a similar structure function in the Drell-Yan case [80].

The structure functions $F_{UU}^{\cos\phi_h}$ and $F_{LL}^{\cos\phi_h}$ do not match [69]. In analogy to these results, we expect that also all the others will not match, since they are twist-3 in the low-q_T regime, and the TMD factorization formalism is probably complete only at twist 2.

In summary, at the moment there is the hope to build descriptions of the structure functions that go from low to high transverse momentum for the five structure functions with a "yes" in the last column of table I.

12. – Some phenomenology: unpolarized cross-sections

In this section, I briefly outline the steps that are necessary to interpret unpolarized cross-section data in terms of TMDs.

The unpolarized cross-sections for SIDIS integrated over the azimuthal angle, but not on the absolute value of $P_{h\perp}$ read

$$\frac{\mathrm{d}\sigma}{\mathrm{d}x\,\mathrm{d}y\,\mathrm{d}z\,\mathrm{d}P_{h\perp}^2} = \frac{4\pi^2\alpha^2}{xQ^2}\,\frac{y}{2\,(1-\varepsilon)}\Big(F_{UU,T}(x,z,P_{h\perp}^2,Q^2) + \varepsilon F_{UU,L}(x,z,P_{h\perp}^2,Q^2)\Big). \tag{153}$$

To have a compact notation for the results, we introduce the notation

$$f\otimes D = x_B\int \mathrm{d}^2\boldsymbol{p}_T\,\mathrm{d}^2\boldsymbol{k}_T\,\delta^{(2)}\big(\boldsymbol{p}_T-\boldsymbol{k}_T-\boldsymbol{P}_{h\perp}/z\big)\,f^a(x_B,p_T^2)\,D^a(z,k_T^2). \tag{154}$$

We obtain

$$F_{UU,T} = \sum_a e_a^2 f_1^a \otimes D_1^a, \qquad F_{UU,L} = \mathcal{O}\left(\frac{M^2}{Q^2}, \frac{P_{h\perp}^2}{Q^2}\right), \tag{155}$$

Since the longitudinal structure function is suppressed as $1/Q^2$ in the low transverse momentum region, we will neglect it.

To introduce some simplification, we resort to tsospin and charge-conjugation relations, which imply for "favored" functions

$$D_1^{u\to\pi^+} = D_1^{\bar{d}\to\pi^+} = D_1^{d\to\pi^-} = D_1^{\bar{u}\to\pi^-}, \equiv D_1^{\mathrm{f}} \tag{156}$$

$$D_1^{u\to K^+} = D_1^{\bar{u}\to K^-}, \equiv D_1^{\mathrm{fd}} \tag{157}$$

$$D_1^{\bar{s}\to K^+} = D_1^{s\to K^-} \equiv D_1^{\mathrm{f}'} \tag{158}$$

for the "unfavored" functions

$$D_1^{\bar{u}\to\pi^+} = D_1^{d\to\pi^+} = D_1^{\bar{d}\to\pi^-} = D_1^{u\to\pi^-} \equiv D_1^{\mathrm{d}}, \tag{159}$$

$$D_1^{s\to\pi^+} = D_1^{\bar{s}\to\pi^+} = D_1^{s\to\pi^-} = D_1^{\bar{s}\to\pi^-} \equiv D_1^{\mathrm{df}}, \tag{160}$$

$$D_1^{\bar{u}\to K^+} = D_1^{\bar{d}\to K^+} = D_1^{d\to K^+} = D_1^{\bar{d}\to K^-} = D_1^{d\to K^-} = D_1^{u\to K^-} \equiv D_1^{\mathrm{dd}}, \tag{161}$$

$$D_1^{s\to K^+} = D_1^{\bar{s}\to K^-} \equiv D_1^{\mathrm{d}'}. \tag{162}$$

There are in principle seven independent functions. If needed, a further assumption could be to set $D_1^{\mathrm{f}'} = D_1^{\mathrm{f}}$ and $D_1^{\mathrm{d}'} = D_1^{\mathrm{d}}$, leaving five independent functions.

In general, the convolution cannot be disentangled. Only if the functions have a specific functional form we can obtain a simple expression.

To study the flavor structure of TMDs, it is necessary to use different targets and detect different final-state hadrons. The structure functions for the different combinations of target and outgoing hadron read then

$$9F_{UU,T}^{p/\pi^+}(x,z,P_{h\perp}^2) = \left(4\,f_1^u + f_1^{\bar{d}}\right)\otimes D_1^{\mathrm{f}} + \left(4\,f_1^{\bar{u}} + f_1^d\right)\otimes D_1^{\mathrm{d}} + \left(f_1^s + f_1^{\bar{s}}\right)\otimes D_1^{\mathrm{df}}, \tag{163}$$

$$9F_{UU,T}^{p/\pi^-}(x,z,P_{h\perp}^2) = \left(4\,f_1^{\bar{u}} + f_1^d\right)\otimes D_1^{\mathrm{f}} + \left(4\,f_1^u + f_1^{\bar{d}}\right)\otimes D_1^{\mathrm{d}} + \left(f_1^s + f_1^{\bar{s}}\right)\otimes D_1^{\mathrm{df}}, \tag{164}$$

$$9F_{UU,T}^{n/\pi^+}(x,z,P_{h\perp}^2) = \left(4\,f_1^d + f_1^{\bar{u}}\right)\otimes D_1^{\mathrm{f}} + \left(4\,f_1^{\bar{d}} + f_1^u\right)\otimes D_1^{\mathrm{d}} + \left(f_1^s + f_1^{\bar{s}}\right)\otimes D_1^{\mathrm{df}} \tag{165}$$

$$9F_{UU,T}^{n/\pi^-}(x,z,P_{h\perp}^2) = \left(4\,f_1^{\bar{d}} + f_1^u\right)\otimes D_1^{\mathrm{f}} + \left(4\,f_1^d + f_1^{\bar{u}}\right)\otimes D_1^{\mathrm{d}} + \left(f_1^s + f_1^{\bar{s}}\right)\otimes D_1^{\mathrm{df}}, \tag{166}$$

$$9F_{UU,T}^{p/K^+}(x,z,P_{h\perp}^2) = 4\,f_1^u\otimes D_1^{\mathrm{fd}} + \left(4\,f_1^{\bar{u}} + f_1^d + f_1^{\bar{d}}\right)\otimes D_1^{\mathrm{dd}} + f_1^{\bar{s}}\otimes D_1^{\mathrm{f}'} + f_1^s\otimes D_1^{\mathrm{d}'}, \tag{167}$$

$$9F_{UU,T}^{p/K^-}(x,z,P_{h\perp}^2) = 4\,f_1^{\bar{u}}\otimes D_1^{\mathrm{fd}} + \left(4\,f_1^u + f_1^d + f_1^{\bar{d}}\right)\otimes D_1^{\mathrm{dd}} + f_1^s\otimes D_1^{\mathrm{f}'} + f_1^{\bar{s}}\otimes D_1^{\mathrm{d}'}, \tag{168}$$

$$(169)\qquad 9F_{UU,T}^{n/K^+}(x,z,P_{h\perp}^2) = 4\,f_1^d\otimes D_1^{\mathrm{fd}} + \left(4\,f_1^{\bar d}+f_1^u+f_1^{\bar u}\right)\otimes D_1^{\mathrm{dd}} + f_1^{\bar s}\otimes D_1^{\mathrm{f}'} + f_1^s\otimes D_1^{\mathrm{d}'},$$

$$(170)\qquad 9F_{UU,T}^{n/K^-}(x,z,P_{h\perp}^2) = 4\,f_1^{\bar d}\otimes D_1^{\mathrm{fd}} + \left(4\,f_1^{d}+f_1^u+f_1^{\bar u}\right)\otimes D_1^{\mathrm{dd}} + f_1^{s}\otimes D_1^{\mathrm{f}'} + f_1^{\bar s}\otimes D_1^{\mathrm{d}'}$$

Were there no difference in the transverse-momentum distribution for different flavors and/or for different fragmentation functions, all the above structure functions would display the same $P_{h\perp}$ behavior. Therefore, a non-flat $P_{h\perp}$ dependence of any ratio of them would expose these differences.

For illustration purposes, let us neglect the sea-quark contributions and focus only on the pions. We obtain

$$(171)\qquad 9F_{UU,T}^{p/\pi^+}(x,z,P_{h\perp}^2) = 4\,f_1^u\otimes D_1^{\mathrm{f}} + f_1^d\otimes D_1^{\mathrm{d}},$$

$$(172)\qquad 9F_{UU,T}^{p/\pi^-}(x,z,P_{h\perp}^2) = f_1^d\otimes D_1^{\mathrm{f}} + 4\,f_1^u\otimes D_1^{\mathrm{d}},$$

$$(173)\qquad 9F_{UU,T}^{n/\pi^+}(x,z,P_{h\perp}^2) = 4\,f_1^d\otimes D_1^{\mathrm{f}} + f_1^u\otimes D_1^{\mathrm{d}},$$

$$(174)\qquad 9F_{UU,T}^{n/\pi^-}(x,z,P_{h\perp}^2) = f_1^u\otimes D_1^{\mathrm{f}} + 4\,f_1^d\otimes D_1^{\mathrm{d}}.$$

Let us assume Gaussians distribution of transverse momentum, both for the distribution and fragmentation function, *i.e.*

$$(175)\qquad f_1^a(x,p_T^2) = \frac{f_1^a(x)}{\pi\rho_a^2}e^{-\boldsymbol{p}_T^2/\rho_a^2}, \qquad\qquad D_1^a(z,k_T^2) = \frac{D_1^a(z)}{\pi\sigma_a^2}e^{-z^2\boldsymbol{k}_T^2/\sigma_a^2}.$$

The convolution turns out to be in this case

$$(176)\qquad f_1^a\otimes D_1^a = f_1^a(x)D_1^a(z)\frac{1}{\pi(z^2\rho_a^2+\sigma_a^2)}\,e^{-\boldsymbol{P}_{h\perp}^2/(z^2\rho_a^2+\sigma_a^2)}.$$

Let us assume that the favored and unfavored fragmentation functions have the same transverse-momentum width

$$(177)\qquad \sigma_{\mathrm{f}}^2 = \sigma_{\mathrm{d}}^2 = 0.3\,\mathrm{GeV}^2$$

and let us further assume that at the average x and z we have $f_1^u/f_1^d \approx 0.25$ and $D_1^{\mathrm{f}}/D_1^{\mathrm{f}} \approx 0.40$. A simple calculation yields the plot in fig. 13 for two different choices of the u and d transverse-momentum widths.

The transverse-momentum dependence of the partonic functions is usually assumed to be a flavor-independent Gaussian [67,81]. The tree-level approximation and the Gaussian assumption are known to be inadequate at $P_{h\perp}^2 \gg M^2$, but they could effectively describe the physics at $P_{h\perp}^2 \approx M^2$. Especially for low-energy experiments, this is where the bulk of the data is.

There is an extensive literature where the analysis is carried out to a higher level of complication, but only for the specific case of unpolarized observables integrated over the azimuthal angle of the measured transverse momentum. The analysis is usually

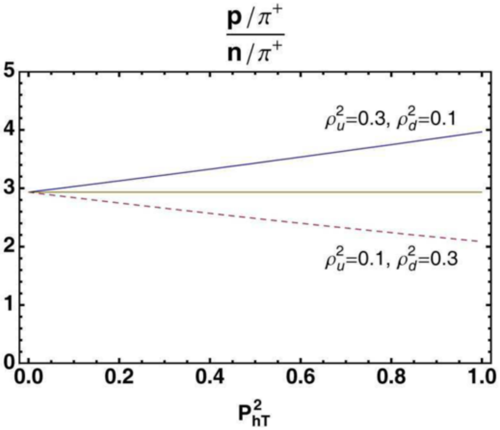

Fig. 13. – Ratio $F_{UU,T}^{p/\pi^+}/F_{UU,T}^{n/\pi^+}$ at typical average kinematics as a function of $P_{h\perp}^2$, with two different assumptions on the average transverse momentum squared of u and d quarks (the flat line corresponds to assuming them to be the same).

performed in the space of the Fourier-conjugate to $P_{h\perp}$ (b-space) in the Collins-Soper-Sterman (CSS) framework [65]. The relation with the TMD formalism has been explicitly shown in ref. [63]. The most recent study along these lines is presented in ref. [82]. The region of $P_{h\perp}^2 \gg M^2$, or $b^2 \ll 1/M^2$, can be calculated perturbatively, but when $P_{h\perp}^2 \approx M^2$ a nonperturbative component has to be introduced and its parameters must be fitted to experimental data. This component is usually assumed to be a flavor-independent Gaussian. The most advanced extraction of the nonperturbative contributions is presented in ref. [66]. A slightly different approach for the extraction has been followed in ref. [83].

At present, we can make the conservative statement that unpolarized quark TMDs seems to be well described by flavor-independent Gaussians with $\sqrt{\langle p_T^2 \rangle} \approx 0.4$–$0.8\,\text{GeV}$, depending on the kinematics.

The knowledge of the details of the unpolarized TMDs has an impact also on high-energy physics. In fig. 14b, the cross-section for Z boson production at the Tevatron is plotted [84]. The difference between the curves originates from different models and fits of the nonperturbative component of the TMDs. Apart from the details, the plot shows that the knowledge of TMDs is essential for precision studies at the Tevatron. Even the determination of a fundamental parameter of the Standard Model, the mass of the W boson, is affected by the uncertainties of the knowledge of unpolarized TMDs. In ref. [85], the CDF collaboration discussed several ways to fit the W mass. According to the analysis, TMDs uncertainties generate an error of 3.9 MeV on the W mass determination (the total systematic error is about 34 MeV).

More information is needed to study in detail the flavor structure of TMDs. Interesting are coming out from JLab, COMPASS and HERMES and it is an exciting time for this kind of studies [16, 86-88].

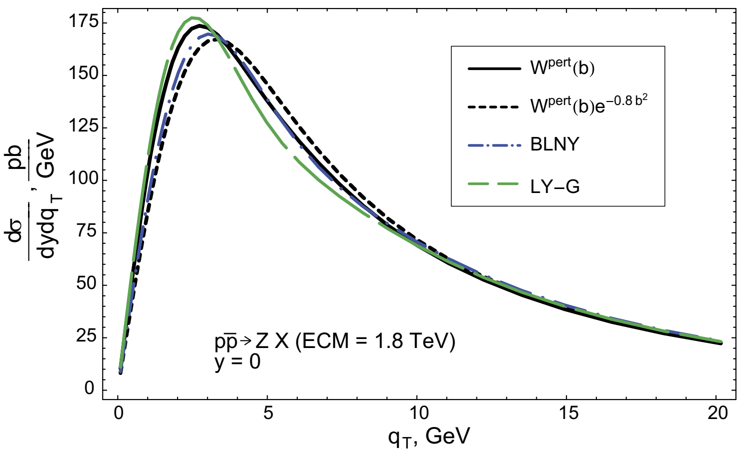

Fig. 14. – The cross-sections of Z boson production at the Tevatron, computed in the CSS formalism. The difference between the curves shows the impact of choosing different nonperturbative components for the TMDs. See ref. [84] for details.

13. – Weighted asymmetries

In the structure functions we have expressions such as

$$\mathcal{C}\left[-\frac{\hat{\boldsymbol{P}}_{h\perp}\cdot\boldsymbol{p}_T}{M}f_{1T}^{\perp}D_1\right], \tag{178}$$

where the two functions appear in a convolution. The general way to split the convolution is to use transverse-momentum-weighted asymmetries. For instance

$$W=\int \mathrm{d}^2\boldsymbol{P}_{h\perp}\,\frac{|\boldsymbol{P}_{h\perp}|}{M}\,\mathcal{C}\left[-\frac{\hat{\boldsymbol{P}}_{h\perp}\cdot\boldsymbol{p}_T}{M}f_{1T}^{\perp}D_1\right], \tag{179}$$

in fact

$$\begin{aligned}
W &= -x_B\sum_q e_q^2\int \mathrm{d}^2\boldsymbol{P}_{h\perp}\,\mathrm{d}^2\boldsymbol{p}_T\,\mathrm{d}^2\boldsymbol{k}_T\,\delta^{(2)}\big(\boldsymbol{p}_T-\boldsymbol{k}_T-\boldsymbol{P}_{h\perp}/z_h\big)\,\frac{\boldsymbol{P}_{h\perp}\cdot\boldsymbol{p}_T}{M}f_{1T}^{\perp q}D_1^q,\\
&= -x_B\,z_h^2\sum_q e_q^2\int \mathrm{d}^2\boldsymbol{p}_T\,\mathrm{d}^2\boldsymbol{k}_T\,\frac{(\boldsymbol{p}_T-\boldsymbol{k}_T)\cdot\boldsymbol{p}_T}{M^2}f_{1T}^{\perp q}D_1^q,\\
&= -x_B\sum_q e_q^2\int \mathrm{d}^2\boldsymbol{p}_T\,\frac{|\boldsymbol{p}_T|^2}{M^2}\,f_{1T}^{\perp q}\;z_h^2\!\int \mathrm{d}^2\boldsymbol{k}_T\,D_1^q\\
&= -x_B\sum_q e_q^2\,2f_{1T}^{\perp(1)q}(x_B)\,D_1(z_h).
\end{aligned} \tag{180}$$

Why weighted asymmetries are important? From a phenomenological side, they allow us to separately study transverse moments of TMDs and fragmentation functions, as simple products instead of convolutions. From the theoretical point of view, after the weighted integral is performed we can deal with collinear objects again and some of the complications entailed in TMD factorization may drop.

The above expression is again a parton-model level expression. If we want a QCD expression, the minimal requirement is that the involved transverse-momentum integrals could be treated in a similar way as the functions f_1 and D_1. To this purpose, table I can be useful. You can see that the structure function containing the Sivers function, (134), in table I is indicated as a type-I observable with exact matching. Moreover, the structure function falls as $1/q_T^3$, which means that if we weigh it with a power of q_T it acquires the same power behavior as the "standard" unpolarized structure function. This may indicate that we can analyze weighted asymmetries with similar techniques as collinear structure functions.

REFERENCES

[1] Sivers D., `arXiv:1109.2521`.
[2] Ji X., *Phys. Rev. Lett.*, **91** (2003) 062001.
[3] Belitsky A. V., Ji X. and Yuan F., *Phys. Rev. D*, **69** (2004) 074014.
[4] Lorce C., Pasquini B. and Vanderhaeghen M., *JHEP*, **1105** (2011) 041.
[5] Collins J. C., *Acta Phys. Polon. B*, **34** (2003) 3103.
[6] Collins J., *Foundations of Perturbative QCD*, Cambridge Monographs on Particle Physics, Nuclear Physics and Cosmology (Cambridge University Press) 2011. URL `http://books.google.it/books?id=0xGi1KW9vykC`
[7] Soper D. E., *Phys. Rev. Lett.*, **38** (1977) 461.
[8] Close F., Halzen F. and Scott D., *Phys. Lett. B*, **68** (1977) 447.
[9] Feynman R. P., *Phys. Rev. Lett.*, **23** (1969) 1415.
[10] Bjorken J. D. and Paschos E. A., *Phys. Rev.*, **185** (1969) 1975.
[11] Parisi G. and Petronzio R., *Nucl. Phys. B*, **154** (1979) 427.
[12] Collins J. C. and Soper D. E., *Nucl. Phys. B*, **193** (1981) 381.
[13] Bacchetta A., Conti F. and Radici M., *Phys. Rev. D*, **78** (2008) 074010.
[14] Jung H., `arXiv:hep-ph/0411287`.
[15] Musch B. U., Hagler P., Negele J. W. and Schafer A., *Phys. Rev. D*, **83** (2011) 094507.
[16] Mkrtchyan H. *et al.*, *Phys. Lett. B*, **665** (2008) 20.
[17] Bacchetta A. and Radici M., *Phys. Rev. Lett.*, **107** (2011) 212001.
[18] Sivers D. W., *Phys. Rev. D*, **41** (1990) 83.
[19] Brodsky S. J., Hwang D. S. and Schmidt I., *Phys. Lett. B*, **530** (2002) 99.
[20] Airapetian A. *et al.*, *Phys. Rev. Lett.*, **94** (2005) 012002.
[21] Alekseev M. *et al.*, *Phys. Lett. B*, **692** (2010) 240.
[22] Collins J. C., *Phys. Lett. B*, **536** (2002) 43.
[23] Boer D., Diehl M., Milner R., Venugopalan R., Vogelsang W. *et al.*, `arXiv:1108.1713`.
[24] Bacchetta A., D'Alesio U., Diehl M. and Miller C. A., *Phys. Rev. D*, **70** (2004) 117504.

[25] Akushevich I., Shumeiko N. and Soroko A., *Eur. Phys. J. C*, **10** (1999) 681.
[26] Schlegel M. and Metz A., *AIP Conf. Proc.*, **1149** (2009) 543.
[27] Diehl M. and Sapeta S., *Eur. Phys. J. C*, **41** (2005) 515.
[28] Lampe B. and Reya E., *Phys. Rep.*, **332** (2000) 1.
[29] Collins J. C., Rogers T. C. and Stasto A. M., *Phys. Rev. D*, **77** (2008) 085009.
[30] Goeke K., Metz A., Pobylitsa P. V. and Polyakov M. V., *Phys. Lett. B*, **567** (2003) 27.
[31] Goeke K., Metz A. and Schlegel M., *Phys. Lett. B*, **618** (2005) 90.
[32] Bacchetta A., Mulders P. J. and Pijlman F., *Phys. Lett. B*, **595** (2004) 309.
[33] Ralston J. P. and Soper D. E., *Nucl. Phys. B*, **152** (1979) 109.
[34] Mulders P. J. and Tangerman R. D., *Nucl. Phys. B*, **461** (1996) 197; **484** (1996) 538(Erratum).
[35] Bacchetta A., Boglione M., Henneman A. and Mulders P. J., *Phys. Rev. Lett.*, **85** (2000) 712.
[36] Bacchetta A., Boglione M., Henneman A. and Mulders P. J., `arXiv:hep-ph/0005140`, *Proceedings of the Workshop on Nucleon Structure in the High x-Bjorken Region (HiX 2000), Philadelphia, PA, USA, 30 Mar - 1 Apr 2000*.
[37] Soffer J., *Phys. Rev. Lett.*, **74** (1995) 1292.
[38] Jaffe R. L., `arXiv:hep-ph/9602236`.
[39] Jaffe R. L., `arXiv:hep-ph/9710465`.
[40] Bacchetta A., Diehl M., Goeke K., Metz A., Mulders P. J. and Schlegel M., *JHEP*, **02** (2007) 093.
[41] Boer D. and Mulders P. J., *Phys. Rev. D*, **57** (1998) 5780.
[42] Collins J. C., *Nucl. Phys. B*, **396** (1993) 161.
[43] Levelt J., *Deep inelastic semi-inclusive processes*, Ph.D. thesis, Vrije Universiteit Amsterdam (1993).
[44] Tangerman R. D., *Higher-twist correlations in polarized hadrons*, Ph.D. thesis, Vrije Universiteit Amsterdam (1996).
[45] Jakob R., Mulders P. J. and Rodrigues J., *Nucl. Phys. A*, **626** (1997) 937.
[46] Barone V., Drago A. and Ratcliffe P. G., *Phys. Rep.*, **359** (2002) 1.
[47] Idilbi A., Ji X., Ma J.-P. and Yuan F., *Phys. Rev. D*, **70** (2004) 074021.
[48] Anselmino M., Boglione M., Hansson J. and Murgia F., *Phys. Rev. D*, **54** (1996) 828.
[49] Anselmino M., Leader E. and Murgia F., *Phys. Rev. D*, **56** (1997) 6021.
[50] Anselmino M. *et al.*, *Phys. Rev. D*, **73** (2006) 014020.
[51] Anselmino M., Boglione M. and Murgia F., *Phys. Lett. B*, **362** (1995) 164.
[52] Anselmino M., Boglione M. and Murgia F., *Phys. Rev. D*, **60** (1999) 054027.
[53] Boglione M. and Mulders P. J., *Phys. Rev. D*, **60** (1999) 054007.
[54] Collins J. C. and Metz A., *Phys. Rev. Lett.*, **93** (2004) 252001.
[55] Yuan F., *Phys. Rev. D*, **77** (2008) 074019.
[56] Gamberg L. P., Mukherjee A. and Mulders P. J., *Phys. Rev. D*, **77** (2008) 114026.
[57] Meissner S. and Metz A., *Phys. Rev. Lett.*, **102** (2009) 172003.
[58] Bomhof C. J., Mulders P. J. and Pijlman F., *Phys. Lett. B*, **596** (2004) 277.
[59] Bacchetta A., Bomhof C. J., Mulders P. J. and Pijlman F., *Phys. Rev. D*, **72** (2005) 034030.
[60] Bomhof C. J., Mulders P. J. and Pijlman F., *Eur. Phys. J. C*, **47** (2006) 147.
[61] Rogers T. C. and Mulders P. J., *Phys. Rev. D*, **81** (2010) 094006.
[62] Ji X., Ma J.-P. and Yuan F., *Phys. Rev. D*, **71** (2005) 034005.
[63] Aybat S. and Rogers T. C., *Phys. Rev. D*, **83** (2011) 114042.
[64] Cherednikov I. O. and Stefanis N. G., *Phys. Rev. D*, **80** (2009) 054008.

[65] Collins J. C., Soper D. E. and Sterman G., *Nucl. Phys. B*, **250** (1985) 199.

[66] Landry F., Brock R., Nadolsky P. M. and Yuan C. P., *Phys. Rev. D*, **67** (2003) 073016.

[67] Schweitzer P., Teckentrup T. and Metz A., *Phys. Rev. D*, **81** (2010) 094019.

[68] Ji X., Qiu J.-W., Vogelsang W. and Yuan F., *Phys. Rev. Lett.*, **97** (2006) 082002.

[69] Bacchetta A., Boer D., Diehl M. and Mulders P. J., *JHEP*, **08** (2008) 023.

[70] Oganesian K., Avakian H., Bianchi N. and Di Nezza P., *Eur. Phys. J. C*, **5** (1998) 681.

[71] Barone V., Prokudin A. and Ma B.-Q., `arXiv:0804.3024`.

[72] Barone V., Melis S. and Prokudin A., *Phys. Rev. D*, **81** (2010) 114026.

[73] Berger E. L., Qiu J.-W. and Rodriguez-Pedraza R. A., *Phys. Rev. D*, **76** (2007) 074006.

[74] Boer D., *Nucl. Phys. B*, **806** (2009) 23.

[75] Lu Z. and Schmidt I., *Phys. Rev. D*, **81** (2010) 034023.

[76] Koike Y., Nagashima J. and Vogelsang W., *Nucl. Phys. B*, **744** (2006) 59.

[77] Ji X., Qiu J.-W., Vogelsang W. and Yuan F., *Phys. Lett. B*, **638** (2006) 178.

[78] Koike Y., Vogelsang W. and Yuan F., *Phys. Lett. B*, **659** (2008) 878.

[79] Yuan F. and Zhou J., *Phys. Rev. Lett.*, **103** (2009) 052001.

[80] Zhou J., Yuan F. and Liang Z.-T., *Phys. Rev. D*, **81** (2010) 054008.

[81] D'Alesio U. and Murgia F., *Phys. Rev. D*, **70** (2004) 074009.

[82] Bozzi G., Catani S., Ferrera G., de Florian D. and Grazzini M., *Phys. Lett. B*, **696** (2011) 207.

[83] Qiu J.-w. and Zhang X.-f., *Phys. Rev. D*, **63** (2001) 114011.

[84] Nadolsky P. M., *AIP Conf. Proc.*, **753** (2005) 158.

[85] Aaltonen T. *et al.*, *Phys. Rev. D*, **77** (2008) 112001.

[86] Rajotte J.-F., `arXiv:1008.5125`.

[87] Rajotte J.-F., Ph.D. thesis, München U. (2010).

[88] Joosten S., to appear in *Proceedings of the 19th International Workshop on Deep Inelastic Scattering (DIS 2008), Newport News, VA, USA, 11-15 April 2011.*

Proceedings of the International School of Physics "Enrico Fermi"
Course CLXXX "Three-Dimensional Partonic Structure of the Nucleon"
edited by M. Anselmino, H. Avakian, D. Hasch and P. Schweitzer
(IOS, Amsterdam; SIF, Bologna)
DOI 10.3254/978-1-61499-197-7-157

Phenomenology of transverse-momentum–dependent distributions

A. Prokudin

Thomas Jefferson National Accelerator Facility - Newport News, VA 23606, USA

Summary. — Transverse-momentum–dependent distributions reveal three-dimensional partonic structure of the nucleon. In these lectures I am going to discuss the phenomenology of TMDs and give some examples of calculations.

1. – Introduction

Inclusive and Semi-Inclusive Deep Inelastic Scatterings (DIS and SIDIS) are important tools to understand the structure of nucleons and nuclei. Spin asymmetries of polarized SIDIS are directly related to Transverse-Momentum–Dependent parton distribution (TMD) and fragmentation functions, and are the subjects of intense theoretical and experimental studies. Usual collinear parton distribution functions depend on the fraction of hadron momentum carried by the parton, x, and on virtuality of the probe, Q^2. TMDs additionally depend on the intrinsic transverse momentum of the parton, $\mathbf{p}_T$. This allows the study of a three-dimensional parton picture of the nucleon in momentum

© Società Italiana di Fisica

space. Such a picture could not be studied in great detail so far, and this is why SIDIS experiments at Electron Ion Collider are of extreme importance.

Three-dimensional parton picture of the nucleon is one of the main goals of nuclear physics in future and such a three-dimensional distribution in momentum space can be mapped by studying transverse-momentum–dependent distribution functions.

At leading twist, the spin structure of a spin-(1/2) hadron can be described by 8 TMDs. Each TMD represents a particular physics aspect of spin-orbit correlations at the parton level. The dependence of the SIDIS cross-section on the azimuthal angle of the electro-produced hadron with respect to the lepton scattering plane and polarization vector angle of the spin of the nucleon allows for separation of different contributions to the measured spin asymmetries. Unpolarized SIDIS cross-section can be used to study unpolarized TMD distribution for partons and unpolarized TMD fragmentation that encodes probe intrinsic dynamics of partons, in particular the so-called Boer-Mulders effect gives rise to $\cos(2\Phi_h)$ modulation of the cross-section. Polarized SIDIS experiments allow us to explore other TMDs, such as those related to the Sivers function, the Collins fragmentation function and transversity, helicity distributions and other distributions, the so-called Worm-Gear functions and pretzelosity.

Transverse-Momentum–Dependent distribution functions (TMDs) depend on two independent variables: fraction of hadron momentum carried by parton, x, and intrinsic transverse momentum of the parton, $\mathbf{p}_T$.

The quark-quark distribution correlation function is defined as [1-3]

$$(1)\qquad \Phi_{ij}(x,\mathbf{p}_T) = \int \frac{\mathrm{d}\xi^-\mathrm{d}^2\boldsymbol{\xi}_T}{(2\pi)^3}\, e^{ip\cdot\xi}\, \langle P,S_P|\bar{\psi}_j(0)\,\mathcal{U}^{n_-}_{(0,+\infty)}\,\mathcal{U}^{n_-}_{(+\infty,\xi)}\,\psi_i(\xi)|P,S_P\rangle\Big|_{\xi^+=0}$$

with $p^+ = xP^+$, $P^+ = (P^0+P^3)/\sqrt{2}$ is the big component of proton's momentum. $\mathcal{U}$ is the gauge link (Wilson line) that assures color gauge invariance of the correlator Φ_{ij}. It depends on position of the quark field in coordinate space and on light-cone vector n_- that defines the direction of gauge link.

Corresponding distribution functions can be obtained by projecting the correlator onto the full basis of γ matrices $\Phi^{[\Gamma]} = \frac{1}{2}\,\mathrm{Tr}[\Phi\,\Gamma]$. At leading twist (expansion in P^+) the spin structure of the proton can be described by 8 TMDs (see [3] and references therein):

$$(2)\qquad \Phi^{[\gamma^+]}(x,p_T) = f_1(x,p_T^2) - \frac{\epsilon_T^{\rho\sigma}\,p_{T\rho}S_{T\sigma}}{M}\,f_{1T}^{\perp}(x,p_T^2)\,,$$

$$(3)\qquad \Phi^{[\gamma^+\gamma_5]}(x,p_T) = S_L\,g_{1L}(x,p_T^2) - \frac{p_T\cdot S_T}{M}\,g_{1T}(x,p_T^2)\,,$$

$$(4)\qquad \Phi^{[i\sigma^{\alpha+}\gamma_5]}(x,p_T) = S_T^{\alpha}\,h_1(x,p_T^2) + S_L\,\frac{p_T^{\alpha}}{M}\,h_{1L}^{\perp}(x,p_T^2) \\ -\frac{p_T^{\alpha}p_T^{\rho} - \frac{1}{2}\,p_T^2\,g_T^{\alpha\rho}}{M^2}\,S_{T\rho}h_{1T}^{\perp}(x,p_T^2) - \frac{\epsilon_T^{\alpha\rho}\,p_{T\rho}}{M}h_1^{\perp}(x,p_T^2),$$

here the projections are done with respect to the quark's polarization, $\Phi^{[\gamma^+]}$ is the distribution of unpolarized quarks, $\Phi^{[\gamma^+\gamma_5]}$ is the distribution of longitudinally polarized quarks and $\Phi^{[i\sigma^{\alpha+}\gamma_5]}(x, p_T^2)$ is the distribution of transversely polarized quarks.

A powerful tool to study the spin structure is the measurement of spin asymmetries in the SIDIS process $\ell P(S_P) \to \ell' hX$. A number of structures can be measured in DIS process $\ell P(S_P) \to \ell' X$ or in SIDIS with two detected hadrons $\ell P(S_P) \to \ell' h_1 h_2 X$.

In addition, experimental data are available from fixed-target SIDIS $\ell P(S_P) \to \ell' hX$(1) polarized experiments HERMES with transversely polarized proton, COMPASS with transversely polarized proton and deuteron and JLab E06-010 with polarized ^{3}He(2). Meanwhile, BELLE has data on $e^+e^- \to h_1 h_2 X$ annihilation and RHIC provides data on spin asymmetries in hadron production $P(S_P)P \to hX$. Furthermore, the upcoming 12 GeV energy upgrade of JLab opens a unique opportunity in providing high-precision mapping of the transverse single spin asymmetries of neutron in 4D (x, Q^2, $z\, P_{h\perp}$) phase space in the valence quark region at relative low Q^2.

In principle all eight functions can be measured experimentally using spin asymmetries. An interesting question arises if there are some relations among TMDs. Positivity constrains of TMDs were derived in ref. [4].

Analysis of cross-sections in terms of partonic distributions is based on the so-called QCD factorization theorems in which perturbative physics of hard scattering of partons is separated from non-perturbative physics of underlying distributions. Non-perturbative distributions are then extracted from experimental data and their Q^2 dependence is governed by QCD evolution equations. Collinear factorization theorem [5,6] requires large momentum scales: both virtuality and hadron transverse momentum of the produced hadron to be large $P_{h\perp} \sim Q \gg \Lambda_{\rm QCD}$. In this case the transverse momentum of the produced hadron is mainly generated by QCD gluon radiation and it is not sensitive to the intrinsic motion of partons inside the parent hadron. TMD factorization theorems [7] are more restrictive, their require two very different momentum scales: $Q \gg P_{h\perp} \sim \Lambda_{\rm QCD}$, large Q is needed for perturbative treatment of underlying partonic subprocess and small-scale $P_{h\perp}$ ensures that observables are sensitive to intrinsic parton motion.

Spin-dependent observables are then described in different ways, either via TMD distributions, such as Sivers function, of via the so-called twist-3 three-parton correlation functions [8, 9, 6, 10]: quantum interference of two scattering amplitudes, one with one acting parton and the other with two acting partons, usually a quark and a gluon.

TMD approach is consistent [11-14] with collinear (twist-3) approach in the region where both of them are valid. Thus two formalisms are connected, it was shown [15] that Sivers function that describes production of low transverse momentum hadron is related to the twist-3 matrix element that is responsible for high transverse momentum hadron production. This makes it extremely important to study experimentally the region where both formalisms are valid. Future Electron Ion Collider is the ideal place for it, interplay

---

(1) $P(S_P)$ stands for momentum and polarization vector of the hadron.

(2) Polarized ^{3}He is an effective polarized neutron target.

of TMD [7] and collinear [5, 6] factorization schemes can be studied as EIC will cover both low $P_{h\perp} \sim \Lambda_{\text{QCD}}$ and high $P_{h\perp} \sim Q$ ranges.

2. – Moments of TMDs and three-dimensional partonic structure

How do moments of TMDs occur and what is their meaning? Let us consider γ^+ projected spin density from eq. (2):

$$\Phi^{[\gamma^+]}(x, p_T^2) = f_1(x, p_T^2) - \frac{\epsilon_T^{\rho\sigma} p_{T\rho} S_{T\sigma}}{M} f_{1T}^\perp(x, p_T^2), \tag{5}$$

the density is not axial symmetric any more due to the presence of the term proportional to $\epsilon_T^{\rho\sigma} p_{T\rho} S_{T\sigma}$. The center of the distribution will be shifted from the origin. How could we quantify this shift?

Let us suppose that the spin of the proton is along $\hat{Y}$ direction, $S_T = (0, 1)$, then we have

$$\Phi^{[\gamma^+]}(x, p_T) = f_1(x, p_T^2) - \frac{p_{Tx}}{M} f_{1T}^\perp(x, p_T^2), \tag{6}$$

the shift then can be quantified if we integrate the distribution with the weight p_{Tx}, *i.e.* $\langle p_{Tx} \rangle = \int d^2 p_T p_{Tx} \Phi^{[\gamma^+]}(x, p_T^2)$ and we obtain

$$\begin{aligned} \langle p_{Tx} \rangle &= \int d^2 p_T \frac{p_{Tx}^2}{M} f_{1T}^\perp(x, p_T^2) \\ &= \frac{1}{2} \int d^2 p_T \frac{p_{Tx}^2 + p_{Ty}^2}{M} f_{1T}^\perp(x, p_T^2) \\ &= \int d^2 p_T \frac{p_T^2}{2M} f_{1T}^\perp(x, p_T^2), \end{aligned} \tag{7}$$

as far as $f_{1T}^\perp$ depends only on p_T^2.

Such an object is then called “first moment of Sivers function”,

$$f_{1T}^{\perp(1)} \equiv \int d^2 p_T \frac{p_T^2}{2M^2} f_{1T}^\perp(x, p_T^2), \tag{8}$$

and, as we can see, it has a particular interpretation as an average shift of the distribution from the origin:

$$M f_{1T}^{\perp(1)} = \langle p_{Tx} \rangle. \tag{9}$$

In fig. 1 we plot the Sivers function as a 3D distribution $f_1(x, p_T^2) - \frac{p_{Tx}}{M} f_{1T}^\perp(x, p_T^2)$ extracted [16] from the experimental data from HERMES [17] and COMPASS [18] Collaborations, we show a three-dimensional parton distribution at $x = 0.2$; as can be seen from fig. 1 the distribution of partons in a transversely polarized hadron is not rotational

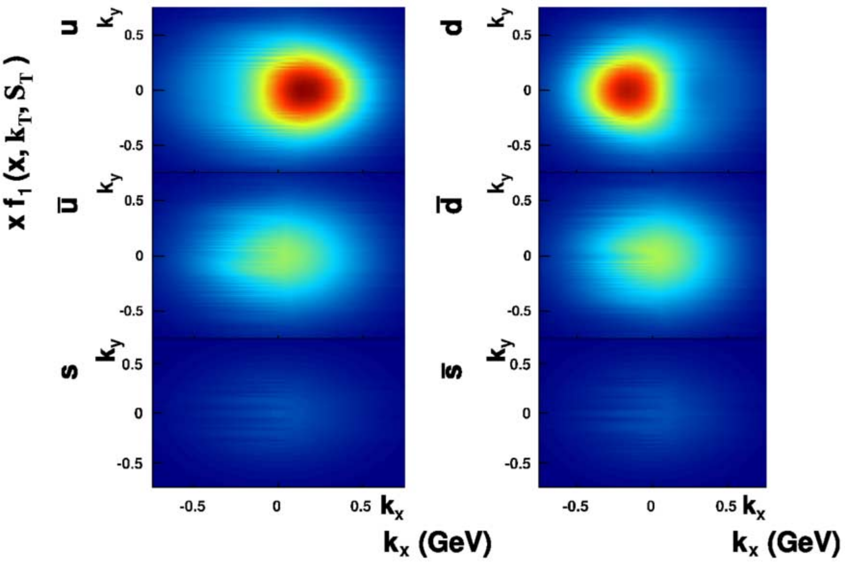

Fig. 1. – Extraction of Sivers function [16] shown as a three-dimensional parton distribution.

symmetric, the distributions have dipole deformation with respect to the "center" of the hadron.

The Hilbert space of state vectors. – Read ref. [19] for more mathematical introduction to axiomatic scattering theory.

The states of a single spinless particle are labeled by wave functions $\psi(\mathbf{x})$ that satisfy

$$\int \mathrm{d}^3x\, |\psi(\mathbf{x})|^2 < \infty. \tag{10}$$

Each wave function can be retarded as specifying the coordinates of an infinite-dimensional state vector $|\psi\rangle$. With any two of these vectors $|\psi\rangle$ and $|\phi\rangle$ one can form linear combinations $a\,|\psi\rangle + b\,|\phi\rangle$ and the scalar product $\langle\psi|\phi\rangle = \int \mathrm{d}^3x\, \psi(\mathbf{x})^*\phi(\mathbf{x})$. The norm, or length, of a vector is defined as $||\psi|| = +\sqrt{\langle\psi|\psi\rangle}$.

With these definitions the set of all vectors of a single particle forms a linear vector space known as the Hilbert space, $\mathcal{H}$. The Hilbert space appropriate for single spinless particle is $\mathcal{H} = \mathcal{L}^2(R^3)$, the space of square integrable functions $\psi(\mathbf{x})$ in real three-dimensional space R^3. For a system of N distinct spinless particles it is $\mathcal{L}^2(R^{3N})$, the space of square integrable functions $\psi(\mathbf{x_1}, \mathbf{x_2}, \ldots, \mathbf{x_N})$. For a single particle of spin s it is the $(2s+1)$-dimensional Hilbert space of all $(2s+1)$-component spinors.

An important property of any quantum-mechanical Hilbert space is that it has a countable orthonormal basis, there exists a set of vectors $|1\rangle\,, |2\rangle\,, \ldots$ in $\mathcal{H}$ such that

$$\langle n'|n\rangle = \delta_{n'n} \tag{11}$$

and every state vector $|\psi\rangle$ can be expanded as

$$(12) \qquad |\psi\rangle = \sum_n \psi_n \, |n\rangle \, .$$

The expansion coefficients ψ_n can be regarded as coordinates of $|\psi\rangle$ of the coordinate system, or representation, defined by $|1\rangle \, , |2\rangle \, , \ldots$ and given by

$$(13) \qquad \psi_n = \langle n|\psi\rangle.$$

The observables of the quantum-mechanical system are given by Hermitian operators whose eigenvectors are bases of $\mathcal{H}$. Note that most observables such as one-particle position and momentum $\mathbf{X}$ and $\mathbf{P}$ and the free Hamiltonian $H^0 = \mathbf{P}^2/2M$ have no "proper" eigenvectors at all. However for the purposes of quantum mechanics a generalization of the basis of eigenvectors is sufficient for the case of self-adjoint operators, that is why self-adjoint operators correspond to observables in quantum mechanics. Self-adjoint operator A is such that $A^\dagger = A$, there † means Hermitian conjugate. It follows then

$$(14) \qquad \langle\psi| \, A \, |\psi\rangle^* = \langle\psi| \, A^\dagger \, |\psi\rangle = \langle\psi| \, A \, |\psi\rangle \, ,$$

observables are real.

We could introduce, for example, the following "eigenvectors" $|\mathbf{x}\rangle$ for $\mathbf{X}$: $\mathbf{X} \, |\mathbf{x}\rangle = \mathbf{x} \, |\mathbf{x}\rangle$. Note the $|\mathbf{x}\rangle$ does not belong to $\mathcal{H}$ as far as $||\mathbf{x}|| = \infty$. However we will generalize the notion of orthonormal basis by the following normalization condition:

$$(15) \qquad \langle\mathbf{x}'|\mathbf{x}\rangle = \delta^{(3)}(\mathbf{x}' - \mathbf{x})$$

and define the expansion of any proper vector $|\psi\rangle$ by

$$(16) \qquad |\psi\rangle = \int \mathrm{d}^3x \, \psi(\mathbf{x}) \, |\mathbf{x}\rangle \, .$$

The expansion coefficient $\psi(\mathbf{x})$ is just the familiar spatial wave function and is given, according to eq. (15), by

$$(17) \qquad \psi(\mathbf{x}) = \langle\mathbf{x}|\psi\rangle,$$

this clarifies our previous claim that $\psi(\mathbf{x})$ can be regarded as the coordinate of $|\psi\rangle$ in a particular coordinate system in $\mathcal{H}$.

Similarly we will introduce momentum eigenvectors $|\mathbf{p}\rangle$ which we normalize so that

$$(18) \qquad \langle\mathbf{p}'|\mathbf{p}\rangle = (2\pi)^3\delta^{(3)}(\mathbf{p}' - \mathbf{p}).$$

For any $|\psi\rangle$ the quantity $\langle\mathbf{p}|\psi\rangle$ is the momentum space wave function $\tilde{\psi}(\mathbf{p})$ of $|\psi\rangle$.

With our normalization the spatial wave function of $|\mathbf{p}\rangle$ is

$$\langle \mathbf{x}|\mathbf{p}\rangle = e^{i\,\mathbf{p}\cdot\mathbf{x}}. \tag{19}$$

In the following we will make use of the following four-dimensional Fourier transforms (compare to eq. (1)):

$$\tilde{\phi}(p) = \int \frac{\mathrm{d}^4 x}{(2\pi)^4}\, e^{ix\cdot p}\phi(x), \tag{20}$$

$$\phi(x) = \int \mathrm{d}^4 p\, e^{-ix\cdot p}\tilde{\phi}(p) \tag{21}$$

and the two-dimensional Fourier transforms for transverse vectors $\mathbf{p} = (p_1, p_2)$:

$$\tilde{\phi}(\mathbf{p}) = \int \frac{\mathrm{d}^2 \mathbf{x}}{(2\pi)^2}\, e^{-i\mathbf{x}\cdot\mathbf{p}}\phi(\mathbf{x}), \tag{22}$$

$$\phi(\mathbf{x}) = \int \mathrm{d}^2\mathbf{p}\, e^{i\mathbf{x}\cdot\mathbf{p}}\tilde{\phi}(\mathbf{p}). \tag{23}$$

Time dependence of state vectors are governed by the Schroedinger equation

$$i\frac{\mathrm{d}}{\mathrm{d}t}\,|\psi_t\rangle = H\,|\psi_t\rangle\,, \tag{24}$$

here the state vector $|\psi_t\rangle$ is time dependent. The solution is

$$|\psi_t\rangle = e^{-iHt}\,|\psi\rangle \tag{25}$$

the operator $e^{-iHt} = U(t)$ is also called time evolution operator. As far as H is self-adjoint, $H^\dagger = H$, it follows that $U(t)$ is a unitary operator:

$$U(t)^\dagger U(t) = U(t)U(t)^\dagger = 1. \tag{26}$$

Unitarity. – We will discuss probabilities and matrix elements, the operator S is such that a system in state $|\Phi\rangle$ goes into state $|\chi\rangle$ is equal to

$$w(\chi \leftarrow \Phi) = |\,\langle\chi|\,S\,|\Phi\rangle\,|^2. \tag{27}$$

We will need to calculate squares of amplitudes in order to obtain cross-sections. A useful method of doing it is employing unitarity of S matrix:

$$SS^\dagger = S^\dagger S = 1. \tag{28}$$

Suppose that we are interested in state a going to state b, the element of S matrix is then

$$S_{ab} = \delta_{ab} + i(2\pi)^4\delta^{(4)}(p_a - p_b)T_{ab}; \tag{29}$$

the first term δ_{ab} implies that in case of $a = b$ this sets goes into itself, while for other cases an amplitude T_{ab} will define probability of a to go into b.

Using eq. (28) in the form $\sum_c S_{ac}S^*_{bc} = \delta_{ab}$, where c are all possible states in which a and b can go, we obtain

$$\operatorname{Im} T_{ab} = \frac{1}{2}\sum_c T_{ac}T^*_{bc}(2\pi)^4\delta^{(4)}(p_a - p_c). \tag{30}$$

In terms of braket notations it can be written as

$$\operatorname{Im} \langle\chi| T |\Phi\rangle = \frac{1}{2}\sum_X \langle\chi| T |X\rangle \langle X| T^\dagger |\Phi\rangle (2\pi)^4\delta^{(4)}(P_\Phi - P_X). \tag{31}$$

3. – Hadron tensors and structure functions

Let us consider Deep Inelastic Scattering (DIS) process $\ell P \to \ell' X$. In one-photon approximation (which holds rather well, as far as many photon exchanges are suppressed by electromagnetic coupling constant $\alpha \simeq 1/137$) we can define the following variables:

$$\begin{aligned} s &= (P + l)^2 = M_p^2 + 2P\cdot l \quad \text{energy of the } ep \text{ system},\\ W^2 &= (P+q)^2 \quad \text{energy of the } \gamma^* p \text{ system},\\ Q^2 &= -q^2 > 0 \quad \text{photon's virtuality.} \end{aligned} \tag{32}$$

Other useful variables:

$$\begin{aligned} \nu &= P\cdot q \quad \text{neglecting the proton mass,} \quad W^2 = 2\nu - Q^2 = Q^2\frac{1-x}{x},\\ y &= \frac{P\cdot q}{P\cdot l} = \frac{W^2 + Q^2}{s} = \frac{2\nu}{s},\\ x &= \frac{Q^2}{2\,P\cdot q} = \frac{Q^2}{2\nu} \Rightarrow Q^2 = sxy. \end{aligned}$$

The cross-section is

$$\mathrm{d}^3\sigma^{\ell+P\to\ell'+X} = \frac{1}{4P\cdot l}\left(\frac{4\pi\alpha}{Q^2}\right)^2 |\mathcal{M}|^2(2\pi)^4\frac{\mathrm{d}^3 l'}{(2\pi)^3 2E'}. \tag{33}$$

where

$$|\mathcal{M}|^2 = L_{\mu\nu}W^{\mu\nu}. \tag{34}$$

Here the leptonic tensor is given by

$$L_{\mu\nu} = \langle l|J^\mu(0)|l'\rangle\langle l'|J^\nu(0)|l\rangle, \tag{35}$$

where J^μ is the electromagnetic current operator and $|l\rangle$ is the electron state.

It can be calculated in perturbative QED. Electron state is $|l\rangle \equiv b^\dagger(l)|0\rangle$ one-particle state of an elementary Dirac fermion. Using plane-wave expansion for free fermions the electron wave function can be written as

$$|l\rangle \equiv \Psi(x,l) = u(l,\lambda)e^{-il\cdot x}, \tag{36}$$

where u is a spinor satisfying the Dirac equation

$$(\not{l} - m_e)u(l,\lambda) = 0, \tag{37}$$

where m_e is the electron mass.

The matrix element in eq. (35) can be written as

$$\langle l'|J^\mu(0)|l\rangle = \bar{u}(l',\lambda')\gamma^\mu u(l,\lambda). \tag{38}$$

We obtain

$$L_{\mu\nu} = \mathrm{Tr}(\not{l}\gamma_\mu\ \not{l}'\gamma_\nu) = 4(l_\mu l'_\nu + l_\nu l'_\mu - (l\cdot l')g_{\mu\nu} + im_l\epsilon_{\mu\nu\alpha\beta}s_l^\alpha q^\beta). \tag{39}$$

In case of longitudinal polarization the spin vector is

$$s_l^\alpha = \lambda\frac{l^\alpha}{m_l}\ \lambda = \pm1; \tag{40}$$

thus the lepton mass cancels and we get

$$L_{\mu\nu} = \mathrm{Tr}(\not{l}\gamma_\mu\ \not{l}'\gamma_\nu) = 4(l_\mu l'_\nu + l_\nu l'_\mu - (l\cdot l')g_{\mu\nu} + i\lambda\epsilon_{\mu\nu\alpha\beta}l^\alpha q^\beta), \tag{41}$$

note that in case of transverse polarization of the incoming electron no such cancellation occurs and the process is suppressed by a factor m_l/E. That is why transverse polarization of electrons is not interesting in this case.

The hadronic tensor is defined by

$$W_{\mu\nu}(q,P) = \frac{1}{2}\sum_X\int\prod_{i\in X}\frac{\mathrm{d}^3P_i}{(2\pi)^3 2E_i}\langle P,S_P|J_\mu^\dagger(0)|X\rangle\langle X|J_\nu(0)|P,S_P\rangle\delta^{(4)}(P+q-P_X), \tag{42}$$

we can use the following representation of the delta-function:

$$\delta^{(4)}(P+q-P_X) = \int\frac{\mathrm{d}^4\xi}{(2\pi)^4}e^{-i(P+q-P_X)\cdot\xi} \tag{43}$$

and using translation invariance we can rewrite this definition (using completeness of states) as

$$
\begin{aligned}
(44)\quad W_{\mu\nu}(q,P) =& \frac{1}{2}\sum_X \int \frac{\mathrm{d}^4\xi}{(2\pi)^4} \int \prod_{i\in X} \frac{\mathrm{d}^3 P_i}{(2\pi)^3 2E_i} e^{-i(P+q-P_X)\cdot\xi} \\
&\times \langle P, S_P | J^\dagger_\mu(0) | X\rangle \langle X | J_\nu(0) | P, S_P\rangle \\
=& \frac{1}{2}\sum_X \int \frac{\mathrm{d}^4\xi}{(2\pi)^4} \int \prod_{i\in X} \frac{\mathrm{d}^3 P_i}{(2\pi)^3 2E_i} e^{-iq\cdot\xi} \\
&\times \langle P, S_P | J^\dagger_\mu(0) | X\rangle \langle X | e^{iP_X\cdot\xi} J_\nu(0) e^{-iP\cdot\xi} | P, S_P\rangle \\
=& \frac{1}{2}\sum_X \int \frac{\mathrm{d}^4\xi}{(2\pi)^4} \int \prod_{i\in X} \frac{\mathrm{d}^3 P_i}{(2\pi)^3 2E_i} e^{-iq\cdot\xi} \\
&\times \langle P, S_P | J^\dagger_\mu(0) | X\rangle \langle X | e^{i\hat{P}\cdot\xi} J_\nu(0) e^{-i\hat{P}\cdot\xi} | P, S_P\rangle \\
=& \frac{1}{2}\sum_X \int \frac{\mathrm{d}^4\xi}{(2\pi)^4} \int \prod_{i\in X} \frac{\mathrm{d}^3 P_i}{(2\pi)^3 2E_i} e^{-iq\cdot\xi} \langle P, S_P | J^\dagger_\mu(0) | X\rangle \langle X | J_\nu(\xi) | P, S_P\rangle \\
=& \frac{1}{2}\sum_X \int \frac{\mathrm{d}^4\xi}{(2\pi)^4} e^{-iq\cdot\xi} \langle P, S_P | J^\dagger_\mu(0) J_\nu(\xi) | P, S_P\rangle .
\end{aligned}
$$

In the following we will also use notation of the so-called light-cone kinematics. Before we do it let us observe that deep inelastic limit $Q^2, \nu \to \infty$ and $x = Q^2/2M\nu$ probe light-cone dynamics of the current commutator.

The scalar product in the exponential eq. (44) can be written as

$$
(45)\qquad q\cdot\xi = \frac{(q^0+q^3)}{\sqrt{2}}\frac{(\xi^0-\xi^3)}{\sqrt{2}} + \frac{(q^0-q^3)}{\sqrt{2}}\frac{(\xi^0+\xi^3)}{\sqrt{2}} - \mathbf{q}_T\cdot\xi_T,
$$

in the rest frame of the nucleon the momenta are given by

$$
(46)\qquad P^\mu = (M,0,0,0),\ q^\mu = (\nu,0,0\sqrt{\nu^2+Q^2});
$$

in deep inelastic limit we observe that

$$
(47)\qquad q^0+q^3 \sim 2\nu,\ q^0-q^3 \sim \frac{Q^2}{2\nu}.
$$

We expect that the dominant contribution of the integral from eq. (44) comes from regions with less rapid oscillations $q\cdot\xi = \mathcal{O}(1)$, hence

$$
(48)\qquad \xi^0+\xi^3 \sim \mathcal{O}(1/\nu),\ \xi^0-\xi^3 \sim \mathcal{O}(1/xM).
$$

Thus

$$
(49)\qquad (\xi^0)^2-(\xi^3)^2 \sim \mathcal{O}(1/Q^2),
$$

and $\xi^2 = (\xi^0)^2 - (\xi^3)^2 - \xi_T^2 \le (\xi^0)^2 - (\xi^3)^2 \sim \mathcal{O}(1/Q^2)$ vanishes, then $Q^2 \to \infty$. This means that deep inelastic kinematics probes the light-cone behavior of the current product.

We note that $W^*_{\mu\nu} = W_{\nu\mu}$. Thus we can divide $W^{\mu\nu}$ into $\mu \leftrightarrow \nu$ symmetric and anti-symmetric parts and denote

$$W^{\mu\nu} = W^{S,\mu\nu} + iW^{A,\mu\nu}. \tag{50}$$

Here we are interested in reactions with unpolarized leptons, the corresponding part of $L_{\mu\nu}$ is symmetric and thus the anti-symmetric part of $W^{\mu\nu}$ does not contribute.

In general $W^{S,\mu\nu}$ can be parametrized as

$$W^{S,\mu\nu}(q,P) = ag^{\mu\nu} + bP^\mu P^\nu + cP^\mu q^\nu + dP^\nu q^\mu + eq^\mu q^\nu \tag{51}$$

with coefficients a, b, c, d, e which are called structure functions and depend on q, P or x, Q^2.

From electromagnetic current conservation $\partial_\mu j^\mu(x) = 0$ we obtain $q_\mu W^{S,\mu\nu} = q_\nu W^{S,\mu\nu} = 0$. This allow us to write

$$W^{S,\mu\nu}(q,P) = \left(-g^{\mu\nu} + \frac{q^\mu q^\nu}{Q^2}\right) W_1(x,Q^2) + \left(P^\mu + \frac{q^\mu}{2x}\right)\left(P^\nu + \frac{q^\nu}{2x}\right) W_2(x,Q^2). \tag{52}$$

Home work: Derive eq. (52). (See appendix A for solution.)

Home work: Derive expression for the anti-symmetric part of the hadron tensor.

$$\begin{aligned} W^{A,\mu\nu}(q,P) = {} & i\epsilon^{\mu\nu\rho\sigma} q_\rho S_\sigma M^2 G_1(x,Q^2) \\ & + i\epsilon^{\mu\nu\rho\sigma} q_\rho \left((P\cdot q)S_\sigma - (S\cdot q)P_\sigma\right) G_2(x,Q^2). \end{aligned} \tag{53}$$

Instead of $W_{1,2}$ one usually introduces

$$\begin{aligned} F_1 &\equiv W_1, \\ F_2 &\equiv \nu W_2, \\ F_L &\equiv F_2 - 2xF_1. \end{aligned} \tag{54}$$

(55)

We will use usual Sudakov decomposition for four-vectors:

$$v^\mu = v^+ n_+^\mu + v^- n_-^\mu + v_\perp^\mu, \tag{56}$$

where light-cone vectors n_+^μ and n_-^μ are

$$n_+^\mu = \frac{1}{\sqrt{2}}(1,0,0,1), \qquad n_-^\mu = \frac{1}{\sqrt{2}}(1,0,0,-1), \tag{57}$$

$$n_+ \cdot n_- = 1, \qquad n_+^2 = n_-^2 = 0. \tag{58}$$

Using light-cone coordinates $a^{\pm} = 1/\sqrt{2}(a^0 \pm a^3)$, and notations $v^\mu = [v^-, v^+, \mathbf{v}_\perp]$ we can rewrite these vectors as

$$n_+^\mu = \left[0^-, 1^+, \mathbf{0}_\perp\right], \qquad n_-^\mu = \left[1^-, 0^+, \mathbf{0}_\perp\right]. \tag{59}$$

The product of two four-vectors is then

$$v \cdot w = v^+ w^- + v^- w^+ - \mathbf{v}_\perp \cdot \mathbf{w}_\perp. \tag{60}$$

Note that $v_\perp^\mu \cdot v_{\perp\mu} = -\mathbf{v}_\perp^2$ and $n_\pm \cdot v_\perp = 0$.

Let us define four-vectors for the proton, the virtual photon and the struck quark:

$$\begin{aligned} P^\mu &= P^+ n_+^\mu + \frac{M^2}{2P^+} n_-^\mu, \\ q^\mu &= -\xi n_+^\mu + \frac{Q^2}{2\xi} n_-^\mu, \\ k^\mu &= x P^+ n_+^\mu + \frac{k^2 + {\mathbf{k}_\perp}^2}{2xP^+} n_-^\mu + k_\perp^\mu, \end{aligned} \tag{61}$$

where Sudakov vectors n_+, n_- are defined above, $x = k^+/P^+$ is the quark light-cone momentum fraction and $\mathbf{k}_\perp$ is the quark intrinsic transverse momentum, note that we have P^+ as the "big" component of the proton's momentum.

There exists another set of Sudakov vectors commonly used in the literature. We go to a frame where the proton is highly boosted (infinite energy frame $P \to \infty$) and define the following vectors (compare with eq. (57)):

$$P^\mu = (P, \mathbf{0}_\perp, P), \tag{62}$$

$$n^\mu = \left(\frac{1}{2P}, \mathbf{0}_\perp, -\frac{1}{2P}\right), \tag{63}$$

such as $n \cdot P = 1, n^2 = P^2 = 0$ and

$$q^\mu \equiv q_\perp^\mu + \nu n^\mu,\ n \cdot q = 0, P \cdot q = \nu, \tag{64}$$

$$q^2 = q_\perp^\mu q_{\perp\mu} = -\mathbf{q}_\perp^2 = -Q^2. \tag{65}$$

The following *projections* are then important for theoretical considerations:

$$P^\mu P^\nu W_{\mu\nu} = -\frac{\nu^2}{Q^2} W_1 + \frac{\nu^2}{4x^2} W_2 = \frac{\nu}{4x^2} F_L, \tag{66}$$

$$n^\mu n^\nu W_{\mu\nu} = W_2 = \frac{1}{\nu} F_2, \tag{67}$$

thus

$$F_2 = \nu n^\mu n^\nu W_{\mu\nu}, \tag{68}$$

$$F_L = \frac{4x^2}{\nu} P^\mu P^\nu W_{\mu\nu}. \tag{69}$$

The photon scatters on a quark inside the proton

$$W^{\mu\nu} = e_q^2 \int \frac{\mathrm{d}^4 p}{(2\pi)^2} Tr(\gamma^\mu (\not{p} + \not{q})\gamma^\nu \Phi(P,p))\delta((p+q)^2), \tag{70}$$

we can rewrite quark momentum as

$$p^\mu = \xi P^\mu + \frac{p^2 + \mathbf{k}_\perp^2}{2\xi} n^\mu + k_\perp^\mu, \tag{71}$$

thus

$$\delta((p+q)^2) = \delta(p^2 - Q^2 + 2\xi\nu - 2\mathbf{k}_\perp \cdot \mathbf{q}_\perp) \approx \delta(2\nu\xi - Q^2) = \frac{1}{2\nu}\delta(\xi - x), \tag{72}$$

thus *the photon scatters on a quark carrying a longitudinal fraction x of the proton momentum.*

Let us calculate F_2:

$$F_2 = \nu n^\mu n^\nu W_{\mu\nu} = \frac{1}{2} e_q^2 \int \frac{\mathrm{d}^4 p}{(2\pi)^2} Tr(\not{n}\ \not{p}\ \not{n}\Phi(P,p))\delta(\xi - x), \tag{73}$$

we use $\not{p}\ \not{n} = -\ \not{n}\ \not{p} + 2n\cdot p$,

$$F_2 = e_q^2 \int \frac{\mathrm{d}^4 p}{(2\pi)^4} \xi Tr(\not{n}\Phi(P,p))\delta(\xi - x); \tag{74}$$

now we introduce quark density, parton distribution function,

$$q(x) \equiv \int \frac{\mathrm{d}^4 p}{(2\pi)^2} Tr(\not{n}\Phi(P,p))\delta(\xi - x), \tag{75}$$

we have

$$F_2(x) = e_q^2 x q(x), \tag{76}$$

or summing over flavors and antiquarks

$$F_2(x) = \sum_q e_q^2 x (q(x) + \bar{q}(x)). \tag{77}$$

Let us calculate F_L:

$$F_L = \frac{4x^2}{\nu} P^\mu P^\nu W_{\mu\nu} = \frac{2x^2}{\nu^2} e_q^2 \int \frac{\mathrm{d}^4 p}{(2\pi)^4} Tr(\not{P}(\not{p}+\not{q})\not{P}\Phi(P,p))\delta(\xi - x); \tag{78}$$

we use $(\not{p}+\not{q})\not{P} = -\not{P}(\not{p}+\not{q}) + 2P\cdot(p+q)$, $P\cdot(p+q) = \frac{p^2+p_\perp^2}{\xi} + 2\nu$, thus

$$F_L = \frac{4x^2}{\nu} e_q^2 \int \frac{\mathrm{d}^4 p}{(2\pi)^4} \mathrm{Tr}(\not{P}\Phi(P,p))\delta(\xi - x), \tag{79}$$

it is suppressed at large Q^2, thus

$$F_2 = 2xF_1, \tag{80}$$

the so called Callan-Gross relation.

Home work: Callan-Gross relation implies that quarks are spin-(1/2) fermions. Why?

Experimentally there are 2 degrees of freedom (the lepton azimuthal angle ϕ is integrated over).

$$\mathrm{d}^3\sigma^{\ell+P\to\ell'+X} = \frac{1}{4P\cdot l}\left(\frac{4\pi\alpha}{Q^2}\right)^2 |\mathcal{M}|^2 (2\pi)^4 \frac{E'^2\mathrm{d}E'\sin\theta\mathrm{d}\theta\mathrm{d}\phi}{(2\pi)^3 2E'}, \tag{81}$$

where $l' = (E', E'\sin\theta, 0, E'\cos\theta)$.

$$\begin{aligned} \mathrm{d}^2\sigma^{\ell+P\to\ell'+X} &= \int \mathrm{d}\phi \mathrm{d}^3\sigma^{\ell+P\to\ell'+X} \\ &= 2\pi\frac{1}{4P\cdot l}\left(\frac{4\pi\alpha}{Q^2}\right)^2 |\mathcal{M}|^2 (2\pi)^4 \frac{E'^2\mathrm{d}E'\sin\theta\mathrm{d}\theta}{(2\pi)^3 2E'}, \end{aligned} \tag{82}$$

finally

$$\mathrm{d}^2\sigma^{\ell+P\to\ell'+X} = \frac{\pi^2}{s}\left(\frac{4\pi\alpha}{Q^2}\right)^2 |\mathcal{M}|^2 E'\mathrm{d}E'\sin\theta\mathrm{d}\theta. \tag{83}$$

At large Q^2 the photon acts as a microscope revealing proton structure at small distances $\sim 1/Q$.

Bjorken limit: large Q^2, fixed x. Equivalently large Q^2 and ν, thus $x = \frac{Q^2}{2\nu} \to$ const.

4. – SIDIS cross-section

Semi-inclusive deep inelastic scattering is the following process: $\ell + P \to \ell' + h + X$. It differs from usual DIS by the fact that a single hadron h is observed and an unobserved state X that comprises remains of the proton still exists.

The cross-section is the function of the following arguments:

$$\mathrm{d}^6\sigma^{\ell+P\to\ell'+h+X} = \frac{1}{4P\cdot l}\left(\frac{4\pi\alpha}{Q^2}\right)^2 |\mathcal{M}|^2(2\pi)^4 \frac{\mathrm{d}^3 l'}{(2\pi)^3 2E'}\frac{\mathrm{d}^3 P_h}{(2\pi)^3 2E_h}, \tag{84}$$

where

$$|\mathcal{M}|^2 = L_{\mu\nu}W^{\mu\nu}. \tag{85}$$

The hadronic tensor in this case is defined by

$$\begin{aligned} W_{\mu\nu}(q,P,P_h) = \frac{1}{2}\sum_X \int \prod_{i\in X} \frac{\mathrm{d}^3 P_i}{(2\pi)^3 2E_i} &\langle P, S_P|J_\mu^\dagger(0)|P_h, X\rangle \\ &\times \langle P_h, X|J_\nu(0)|P, S_P\rangle \delta^{(4)}(P+q-P_h-P_X). \end{aligned} \tag{86}$$

Other useful variables are

$$x = \frac{Q^2}{2\,P\cdot q}, \quad y = \frac{P\cdot q}{P\cdot l}, \quad z = \frac{P\cdot P_h}{P\cdot q}, \quad \gamma = \frac{2Mx}{Q}, \quad \varepsilon = \frac{1-y-\frac{1}{4}\gamma^2 y^2}{1-y+\frac{1}{2}y^2+\frac{1}{4}\gamma^2 y^2}\,. \tag{87}$$

Let us report SIDIS cross-section as parametrized in ref. [1, 3]:

$$\begin{aligned} &\frac{\mathrm{d}\sigma}{\mathrm{d}x\mathrm{d}y\mathrm{d}\psi\mathrm{d}z\mathrm{d}\phi_h\mathrm{d}P_{h\perp}^2} = \\ &\frac{\alpha^2}{xyQ^2}\frac{y^2}{2(1-\varepsilon)}\left(1+\frac{\gamma^2}{2x}\right)\Big\{F_{UU,T} + \varepsilon F_{UU,L} + \sqrt{2\,\varepsilon(1+\varepsilon)}\cos\phi_h\, F_{UU}^{\cos\phi_h} \\ &\quad +\varepsilon\cos(2\phi_h)F_{UU}^{\cos 2\phi_h} + \lambda_e\sqrt{2\varepsilon(1-\varepsilon)}\sin\phi_h F_{LU}^{\sin\phi_h} \\ &\quad +S_\parallel\Big[\sqrt{2\varepsilon(1+\varepsilon)}\sin\phi_h F_{UL}^{\sin\phi_h} + \varepsilon\sin(2\phi_h)F_{UL}^{\sin 2\phi_h}\Big] \\ &\quad +S_\parallel\lambda_e\Big[\sqrt{1-\varepsilon^2}F_{LL} + \sqrt{2\varepsilon(1-\varepsilon)}\cos\phi_h F_{LL}^{\cos\phi_h}\Big] \\ &\quad +|\mathbf{S}_\perp|\Big[\sin(\phi_h-\phi_S)\Big(F_{UT,T}^{\sin(\phi_h-\phi_S)} + \varepsilon F_{UT,L}^{\sin(\phi_h-\phi_S)}\Big) \\ &\quad +\varepsilon\sin(\phi_h+\phi_S)F_{UT}^{\sin(\phi_h+\phi_S)} + \varepsilon\sin(3\phi_h-\phi_S)F_{UT}^{\sin(3\phi_h-\phi_S)} \\ &\quad +\sqrt{2\varepsilon(1+\varepsilon)}\sin\phi_S F_{UT}^{\sin\phi_S} + \sqrt{2\varepsilon(1+\varepsilon)}\sin(2\phi_h-\phi_S)F_{UT}^{\sin(2\phi_h-\phi_S)}\Big] \\ &\quad +|\mathbf{S}_\perp|\lambda_e\Big[\sqrt{1-\varepsilon^2}\cos(\phi_h-\phi_S)F_{LT}^{\cos(\phi_h-\phi_S)} + \sqrt{2\varepsilon(1-\varepsilon)}\cos\phi_S F_{LT}^{\cos\phi_S} \\ &\quad +\sqrt{2\varepsilon(1-\varepsilon)}\cos(2\phi_h-\phi_S)F_{LT}^{\cos(2\phi_h-\phi_S)}\Big]\Big\}, \end{aligned} \tag{88}$$

where α is the fine-structure constant and the structure functions on the r.h.s. depend on x, Q^2, z and $P_{h\perp}^2$. The angle ψ is the azimuthal angle of ℓ' around the lepton beam axis with respect to an arbitrary fixed direction, which in case of a transversely polarized target we choose to be the direction of S. The corresponding relation between ψ and ϕ_S is given in ref. [20]; in deep inelastic kinematics one has $\mathrm{d}\psi \approx \mathrm{d}\phi_S$. The first and second subscript of the above structure functions indicate the respective polarization of beam and target, whereas the third subscript in $F_{UU,T}$, $F_{UU,L}$ and $F_{UT,T}^{\sin(\phi_h-\phi_S)}$, $F_{UT,L}^{\sin(\phi_h-\phi_S)}$ specifies the polarization of the virtual photon. Note that longitudinal or transverse target polarization refer to the photon direction here. The conversion to the experimentally relevant longitudinal or transverse polarization w.r.t. the lepton beam direction is straightforward and given in [20]. The ratio ε of longitudinal and transverse photon flux in (88) is given by

$$\varepsilon = \frac{1-y-\frac{1}{4}\gamma^2 y^2}{1-y+\frac{1}{2}y^2+\frac{1}{4}\gamma^2 y^2}, \tag{89}$$

so that the depolarization factors can be written as

$$\frac{y^2}{2\,(1-\varepsilon)} = \frac{1}{1+\gamma^2}\left(1-y+\frac{1}{2}y^2+\frac{1}{4}\gamma^2 y^2\right) \approx \left(1-y+\frac{1}{2}y^2\right), \tag{90}$$

$$\frac{y^2}{2\,(1-\varepsilon)}\varepsilon = \frac{1}{1+\gamma^2}\left(1-y-\frac{1}{4}\gamma^2 y^2\right) \approx (1-y), \tag{91}$$

$$\frac{y^2}{2\,(1-\varepsilon)}\sqrt{2\,\varepsilon(1+\varepsilon)} = \frac{1}{1+\gamma^2}\,(2-y)\sqrt{1-y-\frac{1}{4}\gamma^2 y^2} \approx (2-y)\,\sqrt{1-y}, \tag{92}$$

$$\frac{y^2}{2\,(1-\varepsilon)}\sqrt{2\,\varepsilon(1-\varepsilon)} = \frac{1}{\sqrt{1+\gamma^2}}y\sqrt{1-y-\frac{1}{4}\gamma^2 y^2} \approx y\,\sqrt{1-y}, \tag{93}$$

$$\frac{y^2}{2\,(1-\varepsilon)}\sqrt{1-\varepsilon^2} = \frac{1}{\sqrt{1+\gamma^2}}y\left(1-\frac{1}{2}y\right) \approx y\left(1-\frac{1}{2}y\right). \tag{94}$$

We will also employ the following cross-section:

$$\frac{\mathrm{d}\sigma}{\mathrm{d}x\,\mathrm{d}y\,\mathrm{d}\phi_S\,\mathrm{d}z\,\mathrm{d}\phi_h\,\mathrm{d}P_{h\perp}^2} = \frac{\mathrm{d}\sigma}{\mathrm{d}x\,\mathrm{d}y\,\mathrm{d}\phi_S\,\mathrm{d}z\,\mathrm{d}\phi_h\,2P_{h\perp}\mathrm{d}P_{h\perp}}, \tag{95}$$

so that if we denote

$$\frac{\mathrm{d}\sigma}{\mathrm{d}x\,\mathrm{d}y\,\mathrm{d}\phi_S\,\mathrm{d}z\,\mathrm{d}\phi_h\,\mathrm{d}P_{h\perp}^2} \equiv \mathrm{d}\sigma^{\uparrow}, \tag{96}$$

then the experimentally observable cross-section is

$$\frac{\mathrm{d}\sigma}{\mathrm{d}x\,\mathrm{d}y\,\mathrm{d}\phi_S\,\mathrm{d}z\,\mathrm{d}\phi_h\,\mathrm{d}P_{h\perp}} = 2P_{h\perp}\mathrm{d}\sigma^{\uparrow}. \tag{97}$$

We will use the following formula integrating the angular dependence:

$$\int_0^{2\pi} \cos^2(m\,\phi_h + n\,\phi_S)\mathrm{d}\phi_S = \int_0^{2\pi} \sin^2(m\,\phi_h + n\,\phi_S)\mathrm{d}\phi_S = \pi, \tag{98}$$

for integers n and m.

Moments of TMDs are defined accordingly as

$$f^{(n)}(x) = \int \mathrm{d}^2\mathbf{p}_T \left(\frac{p_T^2}{2M^2}\right)^n f(x, p_T^2), \tag{99}$$

$$D^{(n)}(z) = z^2 \int \mathrm{d}^2\mathbf{k}_T \left(\frac{k_T^2}{2M_h^2}\right)^n D(z, z^2k_T^2). \tag{100}$$

Partonic interpretation of structure functions can be obtained as the convolution of distribution and fragmentation functions [1,3]

$$F_{AB} = \mathcal{C}\big[w\,f\,D\big], \tag{101}$$

where $\mathcal{C}[\ldots]$ is defined as

$$\begin{aligned} C\big[w\,f\,D\big] = x\sum_a e_a^2 \int \mathrm{d}^2\mathbf{p}_T\mathrm{d}^2\mathbf{k}_T\delta^(2)\big(\mathbf{p}_T - \mathbf{k}_T \\ -\mathbf{P}_{h\perp}/z\big)\, w(\mathbf{p}_T, \mathbf{k}_T) f^a(x, p_T^2) D^a(z, z^2k_T^2), \end{aligned} \tag{102}$$

where $\hat{\mathbf{h}} = \mathbf{P}_{h\perp}/|\mathbf{P}_{h\perp}|$.

Fragmentation function have probabilistic interpretation with respect to the vector

$$\mathbf{K}_T = -\frac{\mathbf{k}_T}{z}, \tag{103}$$

so that

$$D_{1q}^h(z) \equiv \int \mathrm{d}^2\mathbf{K}_T D_1(z, K_T^2) = z^2 \int \mathrm{d}^2\mathbf{k}_T D_{1q}^h(z, z^2k_T^2). \tag{104}$$

Now we can rewrite eq.(102) using the “physical” vector $\mathbf{K}_T$:

$$\begin{aligned} \mathcal{C}\big[w\,f\,D\big] = x\sum_a e_a^2 \int \mathrm{d}^2\mathbf{p}_T\mathrm{d}^2\mathbf{K}_T\delta^{(2)}\big(z\mathbf{p}_T + \mathbf{K}_T - \mathbf{P}_{h\perp}\big)w \\ \times \left(\mathbf{p}_T, -\frac{\mathbf{K}_T}{z}\right) f^a(x, p_T^2) D^a(z, K_T^2), \end{aligned} \tag{105}$$

integrating δ function we obtain

$$(106)\quad \mathcal{C}\big[w f D\big] = x\sum_a e_a^2 \int \mathrm{d}^2\mathbf{p}_T w\left(\mathbf{p}_T, -\frac{(\mathbf{P}_{h\perp} - z\mathbf{p}_T)}{z}\right) f^a(x, p_T^2) D^a\left(z, (\mathbf{P}_{h\perp} - z\mathbf{p}_T)^2\right).$$

Moments of TMDs can be defined now with respect to physical vectors as

$$(107)\quad f^{(n)}(x) = \int \mathrm{d}^2\mathbf{p}_T \left(\frac{p_T^2}{2M^2}\right)^n f(x, p_T^2),$$

$$(108)\quad D^{(n)}(z) = \int \mathrm{d}^2\mathbf{K}_T \left(\frac{K_T^2}{2z^2M_h^2}\right)^n D(z, K_T^2).$$

5. – Structure functions

Let us give partonic interprateation to structure functions in eq. (88).

5·1. $F_{UU,T}$. – Probably the most simple one corresponds to unpolarised cross-section. The partonic interpretation of $F_{UU,T}$ is the following [3]:

$$(109)\quad F_{UU} = \mathcal{C}[f_1 D_1],$$

so that

$$(110)\quad F_{UU} = x\sum_a e_a^2 \int \mathrm{d}^2\mathbf{p}_T f_1^a(x, p_T^2) D_{1a}\left(z, (\mathbf{P}_{h\perp} - z\mathbf{p}_T)^2\right).$$

We assume Gaussian form for $f_1^a(x, p_T^2)$ and $D_1^a(z, K_T^2)$:

$$(111)\quad f_1^a(x, p_T^2) = f_1^a(x)\frac{1}{\pi\langle p_T^2\rangle_a}\exp\left[-\frac{\mathbf{p}_T^2}{\langle p_T^2\rangle_a}\right],$$

$$D_{1a}(x, K_T^2) = D_{1a}(z)\,\frac{1}{\pi\langle K_T^2\rangle_a}\,\exp\left[-\frac{\mathbf{K}_T^2}{\langle K_T^2\rangle_a}\right].$$

So that we have

$$(112)\quad F_{UU,T}(x, z, y, P_{hT}) = \sum_q \frac{1}{\pi(\langle K_T^2\rangle_q + \langle p_T^2\rangle_q z^2)}\exp\left(-\frac{P_{hT}^2}{\langle K_T^2\rangle_q + \langle p_T^2\rangle_q z^2}\right) e_q^2\, f_1^q(x)\, D_q^h(z).$$

We can finally derive the formula for $F_{UU,T}$ as a function of x, y, z:

$$(113)\quad F_{UU,T}(x, y, z) = \int \mathrm{d}^2 P_{hT} F_{UU,T} = x\sum_q e_q^2\, f_1^q(x)\, D_q^h(z).$$

However, as was pointed out by several authors, the probabilistic interpretation of parton densities should be assigned to the corresponding densities of some fixed spin configurations rather than to the spin-averaged ones. Following these arguments we could write

$$
\begin{aligned}
f_1^a(x, p_T^2, +S) &\propto \frac{1}{\pi \langle p_T^2 \rangle_a^+} \exp\left[-\frac{\mathbf{p}_T^2}{\langle p_T^2 \rangle_a^+}\right], \\
f_1^a(x, p_T^2, -S) &\propto \frac{1}{\pi \langle p_T^2 \rangle_a^-} \exp\left[-\frac{\mathbf{p}_T^2}{\langle p_T^2 \rangle_a^-}\right],
\end{aligned}
\tag{114}
$$

the same for fragmentation functions for fragmentation into spin-(1/2) hadron.

$$
\begin{aligned}
D_{1a}(z, p_T^2, +Sh) &\propto \frac{1}{\pi \langle K_T^2 \rangle_a^+} \exp\left[-\frac{\mathbf{K}_T^2}{\langle K_T^2 \rangle_a^+}\right], \\
D_{1a}(z, p_T^2, -Sh) &\propto \frac{1}{\pi \langle K_T^2 \rangle_a^-} \exp\left[-\frac{\mathbf{K}_T^2}{\langle K_T^2 \rangle_a^-}\right];
\end{aligned}
\tag{115}
$$

so that for spin-averaged distributions and fragmentations we will obtain

$$
\begin{aligned}
f_1^a(x, p_T^2) &= \frac{1}{2}\left(f_1^a(x, p_T^2, +S) + f_1^a(x, p_T^2, -S)\right) \\
&= \frac{f_1^a(x)}{2}\left(\frac{1}{\pi \langle p_T^2 \rangle_a^+} \exp\left[-\frac{\mathbf{p}_T^2}{\langle p_T^2 \rangle_a^+}\right] + \frac{1}{\pi \langle p_T^2 \rangle_a^-} \exp\left[-\frac{\mathbf{p}_T^2}{\langle p_T^2 \rangle_a^-}\right]\right), \\
D_{1a}(x, K_T^2) &= \frac{1}{2}\left(D_{1a}(z, p_T^2, +Sh) + D_{1a}(z, p_T^2, -Sh)\right) \\
&= \frac{D_{1a}(z)}{2}\left(\frac{1}{\pi \langle K_T^2 \rangle_a^+} \exp\left[-\frac{\mathbf{K}_T^2}{\langle K_T^2 \rangle_a^+}\right] + \frac{1}{\pi \langle K_T^2 \rangle_a^-} \exp\left[-\frac{\mathbf{K}_T^2}{\langle K_T^2 \rangle_a^-}\right]\right).
\end{aligned}
\tag{116}
$$

We will see advantages of these parameterizations once we start considering polarized distributions. If $\langle p_T^2 \rangle_a^+ = \langle p_T^2 \rangle_a^-$ and $\langle K_T^2 \rangle_a^+ = \langle K_T^2 \rangle_a^-$, then eq. (116) are the same as eq. (111).

With definitions of eq. (116) the formula for $F_{UT,T}$ becomes a little more complicated:

$$
\begin{aligned}
F_{UU,T}(x, z, y, P_{hT}) = x \sum_q \sum_{s1=+,-}^{s2=+,-} &\frac{1}{4} \frac{1}{\pi(\langle K_T^2 \rangle_q^{s2} + \langle p_T^2 \rangle_q^{s1} z^2)} \\
&\times \exp\left[-\frac{P_{hT}^2}{\langle K_T^2 \rangle_q^{s2} + \langle p_T^2 \rangle_q^{s1} z^2}\right] e_q^2 f_1^q(x) D_q^h(z).
\end{aligned}
\tag{117}
$$

Note that, integrated over P_{hT}, the formula remains the same as in eq. (113).

5˙2. $F_{UT,T}^{\sin(\phi_h - \phi_S)}$. – Distribution of unpolarized quarks inside a transversely polarized nucleon can be also written as

$$
f_{q/p^\uparrow}(x, \mathbf{p_T}, \mathbf{S}) = f_1(x, p_T^2) - f_{1T}^\perp(x, p_T^2) \frac{\mathbf{S} \cdot (\hat{\mathbf{h}} \times \mathbf{p_T})}{M},
\tag{118}
$$

here $\hat{\mathbf{h}} \equiv \frac{\mathbf{P}}{|\mathbf{P}|}$ and $\mathbf{S} \cdot (\hat{\mathbf{h}} \times \mathbf{p_T})$ is the correlation between the quark motion and the spin of the nucleon.

Sivers effect, probably, is one of the most important ones in TMD formalism. Sivers function is T-odd and vanishes without final state interactions. There are other reasons why it is extremely important:

- It allows three-dimensional mapping of partons inside the nucleon in the momentum space. Indeed, if we suppose that $\hat{\mathbf{h}} = (0, 0, -1)$ and the spin of the proton is along $\mathbf{y}$ direction, so that $\mathbf{S} = (0, 1, 0)$ and the transverse momentum of the quark is $\mathbf{p_T} = (p_{Tx}, p_{Ty}, 0)$, we obtain from eq. (118)

$$f_{q/p^\uparrow}(x, \mathbf{p_T}, \mathbf{S}) = f_1(x, p_T^2) + f_{1T}^\perp(x, p_T^2)\frac{p_{Tx}}{M}, \tag{119}$$

  the typical "dipole" modulation of the distribution. This shows that quark distributions is not symmetric with respect to p_{Tx}, quark distributions are shifted depending on the sign of the Sivers function.

- It is related to spin-orbit correlations. There are qualitative suggestions on relation of TMDs and parton orbital angular momentum, for example model calculations indicate such relations [21-23], however we still do not have a rigorous way to construct such a relation. An intuitive classical picture of rotating partons in the hadron and thus generating $\mathbf{L} \cdot \mathbf{S}$ correlations are very appealing and more rigorous QFT description is still lacking.

- It requires non-zero orbital angular momentum (OAM) of partons. Sivers functions require spin flip of the proton $f_{q/p^\uparrow}(x, \mathbf{p_T}, \mathbf{S}) - f_{q/p^\uparrow}(x, \mathbf{p_T}, -\mathbf{S}) \propto f_{1T}^\perp(x, p_T^2)$. This implies interference of wave functions with 1 unit of OAM difference. Model calculations will help to shed light on this issue, though not in a rigorous way.

- It represents non-trivial color dynamics of QCD. Colored objects are surrounded by gluons, profound consequence of gauge invariance technically implemented by Wilson lines—gauge links. The Sivers function has opposite sign when gluons couple after quark scatters (SIDIS) or before quark annihilates (DY) [24]

$$f_{1T}^\perp(x, p_T^2)^{\mathrm{SIDIS}} = -f_{1T}^\perp(x, p_T^2)^{\mathrm{DY}}, \tag{120}$$

  the prediction of change of sign based on color gauge symmetry and parity and time reversal invariance $\mathcal{P}, \mathcal{T}$ of strong interactions. Experimental test of this relation is a critical test of the TMD factorization.

- QCD evolution. The Sivers function depends on the large-scale Q and the evolution equation still remains a theoretical challenge. Investigation of Q^2 dependence is not only a theoretical, but also an important experimental issue.

For $F_{UT,T}^{\sin(\phi_h-\phi_S)}$ we have [1,3]

$$\begin{aligned}F_{UT,T}^{\sin(\phi_h-\phi_S)} &= \mathcal{C}\Big[-\frac{\hat{\mathbf{h}}\cdot\mathbf{p}_T}{M}f_{1T}^{\perp}D_1\Big]\\ &= -x\sum_a e_a^2\int \mathrm{d}^2\mathbf{p}_T\,\frac{\hat{\mathbf{h}}\cdot\mathbf{p}_T}{M}f_{1T}^{\perp a}(x,p_T^2)D_{1a}^h\left(z,(\mathbf{P}_{h\perp}-z\mathbf{p}_T)^2\right).\end{aligned}\tag{121}$$

The Sivers function is parameterized in terms of the unpolarized distribution function, as in refs. [25,16], in the following factorized form:

$$f_{1T}^{\perp q}(x,p_T^2) = -\mathcal{N}_q(x)\,\tilde{h}(p_T)\,f_1^q(x,p_T^2),\tag{122}$$

with

$$\mathcal{N}_q(x) = N_q\,x^{\alpha_q}(1-x)^{\beta_q}\,\frac{(\alpha_q+\beta_q)^{(\alpha_q+\beta_q)}}{\alpha_q^{\alpha_q}\,\beta_q^{\beta_q}},\tag{123}$$

$$\tilde{h}(p_T) = \sqrt{2e}\,\frac{M}{M_1}\,e^{-p_T^2/M_1^2},\tag{124}$$

where N_q, α_q, β_q and M_1 (GeV/c) are free parameters to be determined by fitting the experimental data.

Using this definition we obtain the following result:

$$\begin{aligned}F_{UT,T}^{\sin(\phi_h-\phi_S)} &= xzP_{hT}\sum_a e_a^2 f_1^a(x)D_{1a}(z)\frac{\sqrt{2e}M_1^3\langle p_T^2\rangle_q}{\pi(\langle K_T^2\rangle_q(M_1^2+\langle p_T^2\rangle_q)+\langle p_T^2\rangle_q M_1^2 z^2)^2}\cdot\\ &\quad\cdot\exp\left[-\frac{P_{hT}^2(M_1^2+\langle p_T^2\rangle_q)}{(\langle K_T^2\rangle_q(M_1^2+\langle p_T^2\rangle_q)+\langle p_T^2\rangle_q M_1^2 z^2)}\right].\end{aligned}\tag{125}$$

We can also rewrite this result in the following form:

$$\begin{aligned}F_{UT,T}^{\sin(\phi_h-\phi_S)} &= xzP_{hT}\sum_a e_a^2 f_1^a(x)D_{1a}(z)\frac{\sqrt{2e}\langle \tilde{p}_{TS}^2\rangle_q^2}{\pi M_1\langle p_T^2\rangle_q(\langle K_T^2\rangle_q+\langle \tilde{p}_{TS}^2\rangle_q z^2)^2}\cdot\\ &\quad\cdot\exp\left[-\frac{P_{hT}^2}{\langle K_T^2\rangle_q+\langle \tilde{p}_{TS}^2\rangle_q z^2}\right],\end{aligned}\tag{126}$$

where

$$\langle \tilde{p}_{TS}^2\rangle_q \equiv \frac{\langle p_T^2\rangle_q M_1^2}{M_1^2+\langle p_T^2\rangle_q}.\tag{127}$$

The first moment of the Sivers function defined in eq. (146) is then

$$f_{1T}^{\perp(1)q}(x) = -\sqrt{\frac{e}{2}}\,\frac{\mathcal{N}_q(x)\,f_1^q(x)\,M_1^3}{M\,(M_1^2+\langle p_T^2\rangle_q)}.\tag{128}$$

One could parametrize the Sivers function in such a way that the first moment of the Sivers function is present in the definition

$$f_{1T}^{\perp}(x,p_T^2) = \frac{2M^2}{\pi \langle p_{TS}^2\rangle} \exp\left[-\frac{p_T^2}{\langle p_{TS}^2\rangle^2}\right] f_{1T}^{\perp(1)q}(x), \tag{129}$$

indeed with such a definition we find

$$\int \mathrm{d}^2 p_T \frac{p_T^2}{2M^2} \frac{2M^2}{\pi \langle p_{TS}^2\rangle^2} \exp\left[-\frac{p_T^2}{\langle p_{TS}^2\rangle}\right] f_{1T}^{\perp(1)q}(x) = f_{1T}^{\perp(1)q}(x). \tag{130}$$

This allows us to extract directly the first moment of the Sivers The result for the structure function is

$$\begin{aligned} F_{UT,T}^{\sin(\phi_h-\phi_S)} &= -xzP_{hT}\sum_a e_a^2 f_{1T}^{\perp(1)a}(x) D_{1a}(z) \frac{2M}{\pi(\langle K_T^2\rangle_q + \langle p_{TS}^2\rangle_q z^2)^2}\, \cdot \\ &\quad \cdot \exp\left[-\frac{P_{hT}^2}{\langle K_T^2\rangle_q + \langle p_{TS}^2\rangle_q z^2}\right]. \end{aligned} \tag{131}$$

The first moment could be parametrized in an obvious way:

$$f_{1T}^{\perp(1)q}(x) = N_q\, x^{\alpha_q}(1-x)^{\beta_q}\, f_1^q(x), \tag{132}$$

note that implementation of positivity constraints become more complicated. The parametrization of eq. (146) is chosen in such a way that positivity bound [4] for the Sivers function

$$\frac{p_T^2}{M^2}\left((g_{1T}^q(x,p_T^2))^2 + (f_{1T}^{\perp q}(x,p_T^2))^2\right) \le (f_1^q(x,p_T^2))^2 \tag{133}$$

is automatically fulfilled(³). For eq. (129) such an easy implementation is not quite clear.

5˙3. *Sivers asymmetry.* – Let us discuss the asymmetry associated with the Sivers effect. The relevant part of the lepton-proton cross-section reads [3]

$$\begin{aligned} \frac{\mathrm{d}\sigma}{\mathrm{d}x\mathrm{d}y\mathrm{d}\phi_S\mathrm{d}z\mathrm{d}\phi_h P_{h\perp}\mathrm{d}P_{h\perp}} &= \frac{\alpha^2}{xyQ^2}\left(1+(1-y)^2\right) \\ &\quad \times\left\{F_{UU,T} + |\mathbf{S}_\perp|\sin(\phi_h-\phi_S) F_{UT,T}^{\sin(\phi_h-\phi_S)}\right\}, \end{aligned} \tag{134}$$

where α is the fine-structure constant and the structure functions on the r.h.s. depend on x, Q^2, z and $P_{h\perp}^2$.

(³) Smallness of $g_{1T}^q(x,p_T^2)$ is assumed. The trivial positivity bound from eq. (118) is $\frac{p_T}{M}|f_{1T}^{\perp q} \times (x,p_T^2)| \le f_1^q(x,p_T^2)$ and is also fulfilled.

Asymmetry is defined in the following way:

$$(135)\qquad \begin{aligned} A_{UT}^{\sin(\phi_h-\phi_S)} &\equiv 2\langle \sin(\phi_h-\phi_S)\rangle \\ &= 2\frac{\int \mathrm{d}\phi_h \mathrm{d}\phi_S \sin(\phi_h-\phi_S)\left(\mathrm{d}\sigma(\phi_h,\phi_S)-\mathrm{d}\sigma(\phi_h,\phi_S+\pi)\right)}{\int \mathrm{d}\phi_h \mathrm{d}\phi_S \left(\mathrm{d}\sigma(\phi_h,\phi_S)+\mathrm{d}\sigma(\phi_h,\phi_S+\pi)\right)}, \end{aligned}$$

where U stands for the unpolarized lepton beam, T for the transverse polarization of the target nucleon.

Numerator and denominator of eq. (135) can be written as

$$(136)\qquad \begin{aligned} \mathrm{d}\sigma(\phi_h,\phi_S)-\mathrm{d}\sigma(\phi_h,\phi_S+\pi) &= \frac{2\alpha^2}{sx^2y^2}\left(1+(1-y)^2\right)\sin(\phi_h-\phi_S)F_{UT,T}^{\sin(\phi_h-\phi_S)}, \\ \mathrm{d}\sigma(\phi_h,\phi_S)+\mathrm{d}\sigma(\phi_h,\phi_S+\pi) &= \frac{2\alpha^2}{sx^2y^2}\left(1+(1-y)^2\right)F_{UU,T}. \end{aligned}$$

And we have

$$(137)\qquad \begin{aligned} &\int \mathrm{d}\phi_h \mathrm{d}\phi_S \sin(\phi_h-\phi_S)(\mathrm{d}\sigma(\phi_h,\phi_S)-\mathrm{d}\sigma(\phi_h,\phi_S+\pi)) = \\ &\int \mathrm{d}\phi_h \mathrm{d}\phi_S \sin^2(\phi_h-\phi_S)\frac{2\alpha^2}{sx^2y^2}\left(1+(1-y)^2\right)F_{UT,T}^{\sin(\phi_h-\phi_S)} = \\ &\pi(2\pi)\frac{2\alpha^2}{sx^2y^2}\left(1+(1-y)^2\right)F_{UT,T}^{\sin(\phi_h-\phi_S)} \\ &\times\int \mathrm{d}\phi_h \mathrm{d}\phi_S \left(\mathrm{d}\sigma(\phi_h,\phi_S)+\mathrm{d}\sigma(\phi_h,\phi_S+\pi)\right) = \\ &\int \mathrm{d}\phi_h \mathrm{d}\phi_S \frac{2\alpha^2}{sx^2y^2}\left(1+(1-y)^2\right)F_{UU,T} = (2\pi)^2\frac{2\alpha^2}{sx^2y^2}\left(1+(1-y)^2\right)F_{UU,T}, \end{aligned}$$

thus the asymmetry can be written as

$$(138)\qquad A_{UT}^{\sin(\phi_h-\phi_S)}(x,z,P_{h\perp}) = \frac{\frac{2\alpha^2}{sx^2y^2}\left(1+(1-y)^2\right)}{\frac{2\alpha^2}{sx^2y^2}\left(1+(1-y)^2\right)}\frac{F_{UT,T}^{\sin(\phi_h-\phi_S)}}{F_{UU,T}}.$$

5˙4. *Phenomenological extractions and models of Sivers function.* – Phenomenological extractions of Sivers functions from experimental data were initiated by analysis of A_N in $PP^\uparrow \to \pi X$, done in refs. [26, 27]. However TMD factorization was proven for the case of SIDIS and DY [7, 28] and was not proven for this case, some counterexamples exist [29], and we will limit ourselves to analysis of SIDIS data.

SIDIS data were first analyzed in ref. [30], and the "1/2-moments" of the Sivers functions were then introduced in ref. [31] in the fit to the experimental data:

$$(139)\qquad q_T^{(1/2)}(x) \equiv 2f_{1T}^{\perp q(1/2)}(x,\mathbf{p}_T^2).$$

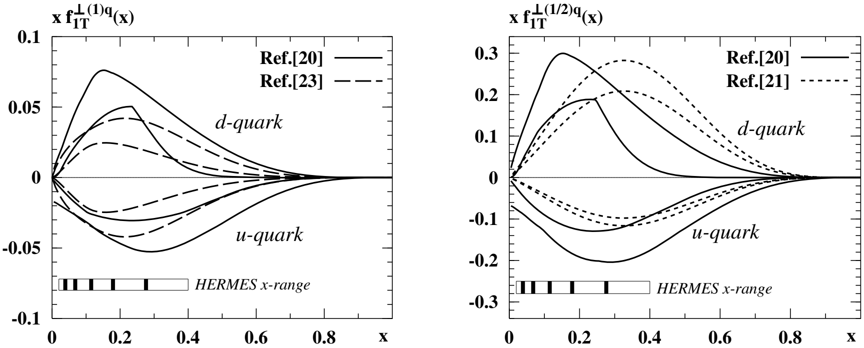

Fig. 2. – Ref. [35]: The first and 1/2-transverse moments of the Sivers quark distribution functions as extracted in refs. [25, 31-33]. The curves indicate the 1-σ regions of the various parameterizations.

In refs. [32, 33] the distributions of transverse parton momenta in f_1^a, $f_{1T}^{\perp a}$ and D_1^a were assumed to be Gaussian. In order to reduce the number of fit parameters, the prediction [34] from the limit of a large number of colors N_c was imposed. First moments of Sivers functions were extracted.

The results of refs. [25, 31-33] were compared in ref. [35], see fig. 2, and it was shown that extractions agree with each other very well.

A new set of fragmentation functions DSS [36] was adopted in ref. [16] where analysis of new HERMES data [37] on kaon production was made. Reference [36] shows that Kretzer fragmentation functions fail to reproduce charged kaon SIDIS multiplicities, and might not be adequate to reconstruct transverse single-spin asymmetries corresponding to kaon production.

Reference [16] stated that usage of DSS [36] was the key ingredient to resolve the so-called kaon puzzle: HERMES data [37] showed that K^+ Sivers asymmetries are larger than π^+ asymmetries and thus one of the explanations would be the enhancement due to sea quark TMD contributions. However careful analysis of fragmentation functions and usage of DSS [36] set allows to explain K^+ Sivers asymmetries with moderate sea quark contributions. The same conclusion was confirmed in ref. [38]. Future experimental data will shed light on sea quark Sivers contributions.

A 11-parameter fit to pion and kaon production at HERMES [37] and COMPASS [39] resulted in a good description of the data with χ^2/d.o.f. $\simeq$ 1.00.

The quality of results of ref. [16] is shown in figs. 3 and 4 where our best fit to the SSA is compared with the experimental data from refs. [37] and [39]: the SSAs are plotted as a function of one variable at a time, either x or z or P_T, while an integration over the other variables has been performed consistently with the cuts of the corresponding experiment.

In ref. [16], an extraction of the Sivers distribution functions was presented based on a fit of SIDIS experimental data from the HERMES and COMPASS Collaborations.

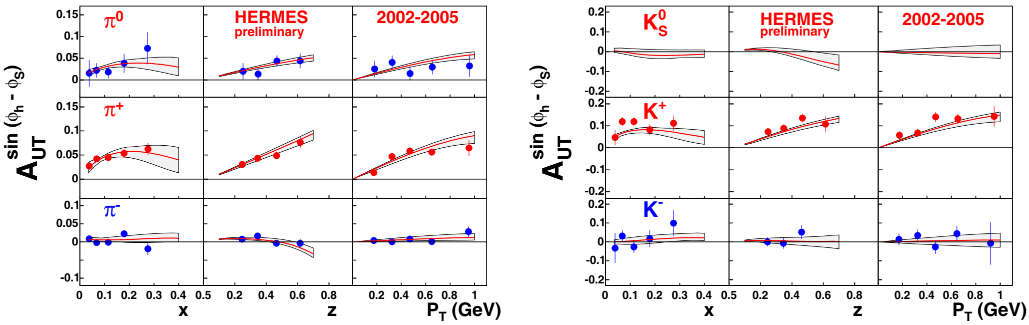

Fig. 3. – The results obtained from our simultaneous fit of the SIDIS $A_{UT}^{\sin(\phi_h-\phi_S)}$ Sivers asymmetries (solid lines) ref. [16], are compared with HERMES experimental data [37] for pion and kaon production (left and right panel, respectively). The shaded area corresponds to the statistical uncertainty of the parameters.

At that time, the only direct evidence of a non-zero Sivers effect came from HERMES experimental data on the azimuthal moment $A_{UT}^{\sin(\phi_h-\phi_S)}$, measured for pion and kaon production off a proton target [37]; the COMPASS Collaboration, instead, found a Sivers effect compatible with zero for SIDIS off a deuteron target [18]. The extraction of the Sivers functions was made even more challenging by the fact that the $A_{UT}^{\sin(\phi_h-\phi_S)}$ measured by HERMES for K^+ was surprisingly large, about twice as much as the analogous asymmetry for π^+ production, which hinted at a possible important role of the sea quarks [16].

Since then, new experimental results have become available: COMPASS have released new data on SIDIS production of spinless hadrons off a proton target, showing a clear Sivers asymmetry [40]; a new HERMES data analysis, based on a much larger statistics,

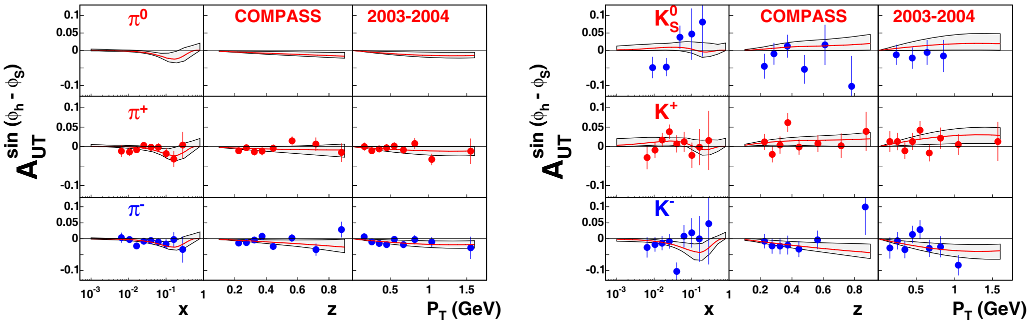

Fig. 4. – The results obtained from our fit (solid lines) are compared with the COMPASS measurements of $A_{UT}^{\sin(\phi_h-\phi_S)}$ for pion (left panel) ref. [16] and kaon (right panel) production [39] off a deuteron target. The shaded area corresponds to the statistical uncertainty of the parameters.

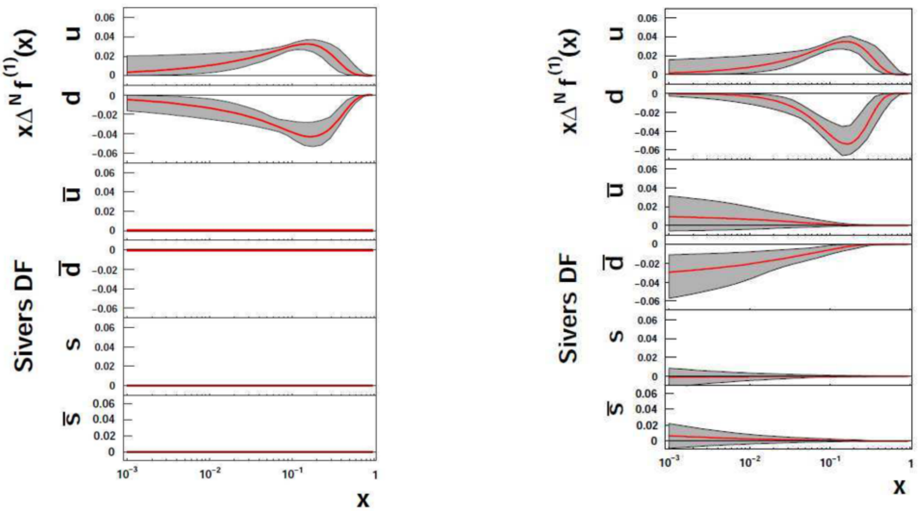

Fig. 5. – First $\mathbf{p}_T$-moment of the Sivers distribution function, $x\Delta^N f^{(1)}_{q/p^\uparrow}(x)$, ref. [42], as a function of x as obtained by fitting SIDIS experimental data from HERMES and COMPASS. The left (right) panel shows the results obtained from a fit which includes only valence (valence plus sea) quark contributions.

while confirming the previous pion data, softens the enhanced peak in the K^+ Sivers azimuthal moment [41].

A new extraction [42] of the Sivers function from the HERMES proton [41] and COMPASS deuteron data [18] was performed. COMPASS proton data [40] were excluded due to the presence of some experimental scale uncertainty which is difficult to account for in the analysis. The new forthcoming data from COMPASS on a proton target will become very useful in the future. New data will become available from JLab 6 and JLab 12 in the future.

In order to evaluate the significance of the sea-quark Sivers contributions first a fit of the SIDIS data was performed including only Sivers functions for u and d quarks. The results obtained are rather satisfactory, with a total $\chi^2_{\text{d.o.f}}$ of about 1.05.

Then a second fit was attempted, in which $\bar{u}$, $\bar{d}$, s, $\bar{s}$ sea contributions to the Sivers function were allowed, the total $\chi^2_{\text{d.o.f}}$ improves to about 0.9.

This can be considered as an indication of the presence of sea Sivers functions, see fig. 5.

Further experimental measurements from present and future facilities are strongly needed to reach a better knowledge on the important Sivers distribution functions, in particular in the large and small x regions where they are presently largely unconstrained. Electron Ion Collider will contribute to exploration of the Sivers function at small x. In the following sections we will analyze impact future experimental data from EIC on extraction of Sivers functions.

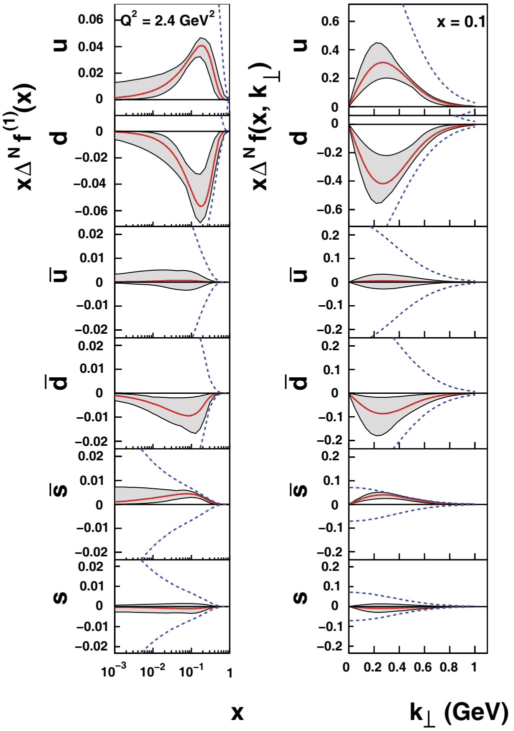

Fig. 6. – Sivers distribution functions for u, d and s flavors, at the scale $Q^2 = 2.4\,(\mathrm{GeV}/c)^2$, ref. [16], as determined by our simultaneous fit of HERMES and COMPASS data (see text for details). On the left panel, the first moment $x\,\Delta^N f^{(1)}(x)$, eq. (140), is shown as a function of x for each flavor, as indicated. Similarly, on the right panel, the Sivers distribution $x\,\Delta^N f(x, \mathbf{k}_\perp)$ is shown as a function of $\mathbf{k}_\perp$ at a fixed value of x for each flavor, as indicated. The highest and lowest dashed lines show the positivity limits $|\Delta^N f| = 2f$.

The Sivers functions of ref. [16] are presented, at the scale $Q^2 = 2.4\,(\mathrm{GeV}/c)^2$, in fig. 6, where we plot, on the left panel, the first $\mathbf{k}_\perp$ moment defined as

$$\Delta^N f^{(1)}_{q/p^\uparrow}(x) \equiv \int \mathrm{d}^2\mathbf{k}_\perp\, \frac{\mathbf{k}_\perp}{4M}\,\Delta^N f_{q/p^\uparrow}(x, \mathbf{k}_\perp) = -f_{1T}^{\perp(1)q}(x), \tag{140}$$

and, on the right panel, the $\mathbf{k}_\perp$ dependence of $\Delta^N f_{q/p^\uparrow}$ at a fixed value of $x = 0.1$. The highest and lowest dashed lines show the positivity limits $|\Delta^N f| = 2f$. Large-N_C prediction $f_{1T}^{\perp u} = -f_{1T}^{\perp d}$ is approximately satisfied, see eq. (141), as can be seen from fig. 6 such a prediction is confirmed by experimental data.

A model calculation with inclusion of final state interactions was done in refs. [43, 44] and non-zero Sivers asymmetry was shown for the first time. There exist a number of model calculations of Sivers functions. Light-cone quark model [23], diquark models [45, 46], MIT bag model [47, 21]. The model results compare well with the extracted Sivers function, as can be seen in fig. 7.

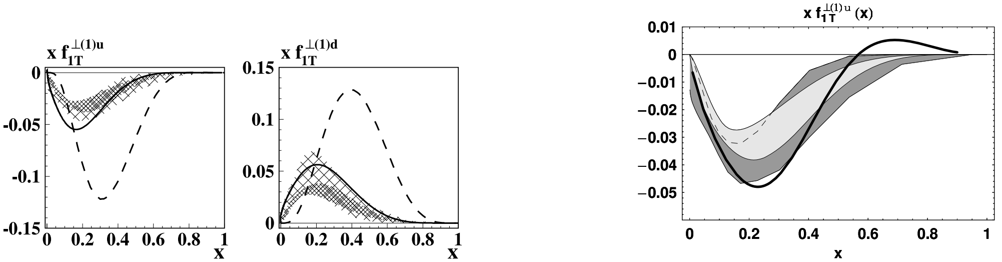

Fig. 7. – Right panel: results of model calculations of ref. [23] solid line, compared to results of ref. [16] extracted from experimental data. Left panels: results of model calculations of ref. [45] solid line, compared to results of ref. [16].

The u and d Sivers functions are also predicted to be opposite in the large N_c limit [34] and in chiral models [48]:

$$f_{1T}^{\perp u} = -f_{1T}^{\perp d}, \tag{141}$$

as can be seen from figs. 7 this is true in model calculations.

TMDs and in particular Sivers functions could be also studied in framework lattice QCD and the first results are already available.

In order to extract Sivers function from the data we need information on unpolarized SIDIS cross-section. An analysis of unpolarized SIDIS cross-section was performed in ref. [49]. The following Gaussian form of transverse momenta dependence was chosen:

$$\begin{aligned} f_1^q(x, p_T^2) &= f_1^q(x) \frac{1}{\pi \langle p_T^2 \rangle} \exp\left[-\frac{\mathbf{p}_T^2}{\langle p_T^2 \rangle}\right], \\ D_{1q}^h(z, K_T^2) &= D_{1q}^h(z) \frac{1}{\pi \langle K_T^2 \rangle} \exp\left[-\frac{\mathbf{K}_T^2}{\langle K_T^2 \rangle}\right], \end{aligned} \tag{142}$$

and the following values for the widths were obtained:

$$\langle p_T^2 \rangle = 0.25\ (\mathrm{GeV}^2), \qquad \langle K_T^2 \rangle = 0.2\ (\mathrm{GeV}^2) \tag{143}$$

These values are in a good accordance with recent phenomenological studies of ref. [50].

The parametrization chosen in eqs. (142) is such as

$$\int \mathrm{d}^2 p_T\ f_1^q(x, p_T^2) = f_1^q(x), \tag{144}$$

$$\int \mathrm{d}^2 K_T\ D_{1q}^h(z, K_T^2) = D_{1q}^h(z), \tag{145}$$

where $f_1^q(x)$ and $D_{1q}^h(z)$ are usual collinear PDF and FF, the analysis of ref. [25]: GRV98LO PDF [51] and Kretzer fragmentation functions of ref. [52]. The result of eqs. (145) is an assumption and, in this particular case, Gaussian parametrization allows us to have this exact match of TMD and collinear parton distributions. Some of TMD schemes satisfy the exact relation of eqs. (145), for example ref. [53].

The Sivers function is parameterized in terms of the unpolarized distribution function, as in refs. [25, 16], in the following factorized form:

$$f_{1T}^{\perp}(x,p_T^2) = -\mathcal{N}_q(x)\,\tilde{h}(p_T)\,f_1^q(x,p_T^2), \tag{146}$$

with

$$\mathcal{N}_q(x) = N_q\,x^{\alpha_q}(1-x)^{\beta_q}\,\frac{(\alpha_q+\beta_q)^{(\alpha_q+\beta_q)}}{\alpha_q^{\alpha_q}\,\beta_q^{\beta_q}}, \tag{147}$$

$$\tilde{h}(p_T) = \sqrt{2e}\,\frac{M}{M_1}\,e^{-p_T^2/M_1^2}, \tag{148}$$

where N_q, α_q, β_q and M_1 (GeV/c) are free parameters to be determined by fitting the experimental data.

The parametrization of eq. (146) is chosen in such a way that positivity bound [4] for the Sivers function

$$\frac{p_T^2}{M^2}\left((g_{1T}^q(x,p_T^2))^2 + (f_{1T}^{\perp q}(x,p_T^2))^2\right) \le (f_1^q(x,p_T^2))^2\,, \tag{149}$$

is automatically fulfilled(4).

5·5. *Wanzura-Wilczek approximation.* – A possibility to connect different TMDs is the so-called Wanzura-Wilczek approximation [54]. In this approximation one systematically neglects quark-gluon-quark correlations and derive certain relations among distribution functions. The most known one is the relation between structure functions g_1 and g_2:

$$\begin{aligned} g_1(x) &= \frac{1}{2}\sum_a e_a^2\,g_{1L}(x), \\ g_2(x) &= -g_1(x) + \frac{1}{2}\sum_a e_a^2\,g_T(x), \end{aligned} \tag{150}$$

where

$$\begin{aligned} g_{1L}(x) &= \int \mathrm{d}^2\,\mathbf{p}_T\,g_{1L}(x,p_T^2), \\ g_T^{a\,\mathrm{WW}}(x) &\approx \int_x^1 \frac{\mathrm{d}y}{y}\,g_1^a(y). \end{aligned} \tag{151}$$

---

(4) Smallness of $g_{1T}^q(x,p_T^2)$ is assumed. Trivial positivity bound from eq. (118) is $\frac{p_T}{M}|f_{1T}^{\perp q}\times (x,p_T^2)| \le f_1^q(x,p_T^2)$ and is also fulfilled.

Thus twist-three distribution function g_2 is related to g_1 and remarkably the experimental data [55, 56] indicate that this relation holds at a very good accuracy and might be violated by approximately 40% as discussed in ref. [57].

The key papers, where Wanzura-Wilczek approximation was applied to Transverse-Momentum–Dependent distributions (TMDs) in historical order, are refs. [58-62, 57].

An immediate application (or test) for the WW relations is provided by the following single/double spin asymmetries in SIDIS [60, 61], which could be measured at Jefferson Lab (in principle, also HERMES and COMPASS)

$$A_{UL}^{\sin 2\phi} \propto \sum_a e_a^2\, h_{1L}^{\perp(1)a}\, H_1^{\perp a}\,, \tag{152}$$

$$A_{LT}^{\cos(\phi-\phi_S)} \propto \sum_a e_a^2\, g_{1T}^{(1)a}\, D_1^a\,, \tag{153}$$

5·6. *A_{LL} asymmetry.* – In the following sections we will need to have information on k_T widths of TMD distributions. One of the sources of such information is experimental data. The widths of unpolarised distribution functions $f_1(x, p_T^2)$ and fragmentation functions $D_1(x, k_T^2)$ were derived in ref. [49] from the data to be $\langle p_T^2\rangle = 0.25\,\mathrm{GeV}^2$ and $\langle k_T^2\rangle = 0.2\,\mathrm{GeV}^2$.

Another source of information is lattice QCD and recent results of ref. [63] for the width of unpolarised distribution functions $f_1(x, p_T)$ $\langle p_T^2\rangle_u = (0.3741)^2$, $\langle p_T^2\rangle_d = (0.3839)^2\,\mathrm{GeV}^2$ are close to the phenomenological result of ref. [49].

Concerning $g_{1T}^{(1)a}$ and $h_{1L}^{\perp(1)a}$ no experimental data are available for extraction of widths. We would use the lattice QCD results of ref. [63].

In order to test the precision of lattice QCD results, let us consider an example $P_{h\perp}$ dependence of A_{LL} asymmetry. A_{LL} asymmetry was discussed in ref. [64], the authors used three different k_T widths of helicity distribution g_1. The experimental data of CLAS Collaboration [65] suggest that the width of g_1 is smaller than of f_1. The lattice QCD results of ref. [63] are $\langle p_T^2\rangle_u^{g_1} = (0.327)^2$, $\langle p_T^2\rangle_d^{g_1} = (0.385)^2$ confirming phenomenological and experimental findings.

The relevant part of the lepton-proton cross-section reads

$$\frac{\mathrm{d}\sigma}{\mathrm{d}x\mathrm{d}y\mathrm{d}\phi_S\mathrm{d}z\mathrm{d}\phi_h 2P_{h\perp}\mathrm{d}P_{h\perp}} = \frac{\alpha^2}{xyQ^2}\frac{y^2}{2(1-\varepsilon)}\left(1+\frac{\gamma^2}{2x}\right)\left\{F_{UU,T} + S_\parallel \lambda_e \sqrt{1-\varepsilon^2} F_{LL}\right\}, \tag{154}$$

depolarization factors can be approximated as

$$\frac{y^2}{2\,(1-\varepsilon)} = \frac{1}{1+\gamma^2}\left(1-y+\frac{1}{2}y^2+\frac{1}{4}\gamma^2 y^2\right) \approx \left(1-y+\frac{1}{2}y^2\right), \tag{155}$$

$$\frac{y^2}{2\,(1-\varepsilon)}\sqrt{1-\varepsilon^2} \approx y(1-\frac{1}{2}y).$$

We can rewrite cross-section as

$$(156)\qquad \frac{\mathrm{d}\sigma}{\mathrm{d}x\mathrm{d}y\mathrm{d}\phi_S\mathrm{d}z\mathrm{d}\phi_h\mathrm{d}P_{h\perp}} = 2P_{h\perp}\frac{\alpha^2}{2xyQ^2}\left\{\left(1+(1-y)^2\right)F_{UU,T} + S_{\parallel}\lambda_e y(2-y)F_{LL}\right\},$$

Single Spin Asymmetry is defined in the following way:

$$(157)\qquad A_{LL} = \frac{\int \mathrm{d}\phi_h\mathrm{d}\phi_S\left(\mathrm{d}\sigma^{\uparrow} - \mathrm{d}\sigma^{\downarrow}\right)}{\int \mathrm{d}\phi_h\mathrm{d}\phi_S\left(\mathrm{d}\sigma^{\uparrow} + \mathrm{d}\sigma^{\downarrow}\right)},$$

where ↑ (↓) denote the transverse polarization of the target nucleon, LL stands for the longitudinal polarization of the lepton beam and the target nucleon. Numerator and denominator of eq. (157) using $Q^2 = sxy$ can be written as

$$(158)\qquad \int \mathrm{d}\phi_h\mathrm{d}\phi_S(\mathrm{d}\sigma^{\uparrow} - \mathrm{d}\sigma^{\downarrow}) = 2P_{h\perp}(2\pi)^2\frac{\alpha^2}{sx^2y}\,(2-y)\,F_{LL},$$
$$\int \mathrm{d}\phi_h\mathrm{d}\phi_S(\mathrm{d}\sigma^{\uparrow} + \mathrm{d}\sigma^{\downarrow}) = 2P_{h\perp}(2\pi)^2\frac{\alpha^2}{sx^2y^2}\left(1+(1-y)^2\right)F_{UU,T}.$$

The partonic interpretation of F_{LL} is the following [3]:

$$(159)\qquad F_{LL} = \mathcal{C}[g_{1L}D_1],$$

so that

$$(160)\qquad F_{LL} = x\sum_a e_a^2\int \mathrm{d}^2\mathbf{p}_T\, g_{1L}^a(x,p_T^2)\, D_{1a}\left(z,(\mathbf{P}_{h\perp} - z\mathbf{p}_T)^2\right).$$

We assume Gaussian form for $g_{1L}^a(x,p_T^2)$ and $f_1^a(x,p_T^2)$:

$$(161)\qquad g_{1L}^a(x,p_T^2) = g_{1L}^a(x)\,\frac{1}{\pi\mu_{0a}^2}\exp\left[-\frac{\mathbf{p}_T^2}{\mu_{0a}^2}\right],$$
$$f_1^a(x,p_T^2) = f_1^a(x)\,\frac{1}{\pi\langle p_T^2\rangle_a}\exp\left[-\frac{\mathbf{p}_T^2}{\langle p_T^2\rangle_a}\right],$$

The values for the widths of $g_{1L}^a(x,p_T^2)$ and $f_1^a(x,p_T^2)$ are taken from ref. [63], $\mu_{0u}^2 = (0.327)^2$, $\mu_{0d}^2 = (0.385)^2\,\mathrm{GeV}^2$ and $\langle p_T^2\rangle_u = (0.3741)^2$, $\langle p_T^2\rangle_d = (0.3839)^2\,\mathrm{GeV}^2$.

We can finally derive the formula for A_{LL} asymmetry as a function of x, y, z:

$$(162)\qquad A_{LL}(x,y,z) = \frac{\int P_{hT}\mathrm{d}P_{hT}\int_0^{2\pi}\mathrm{d}\phi_h\mathrm{d}\phi_S(\mathrm{d}\sigma^{\uparrow} - \mathrm{d}\sigma^{\downarrow})}{\int P_{hT}\mathrm{d}P_{hT}\int_0^{2\pi}\mathrm{d}\phi_h\mathrm{d}\phi_S(\mathrm{d}\sigma^{\uparrow} + \mathrm{d}\sigma^{\downarrow})}$$
$$= \frac{\frac{2-y}{x^2y}\int \mathrm{d}^2P_{hT}F_{LL}}{\frac{1+(1-y)^2}{x^2y^2}\int \mathrm{d}^2P_{hT}F_{UU}} = \frac{\frac{2-y}{xy}\sum_q e_q^2 g_{1L}^q(x)D_q^h(z)}{\frac{1+(1-y)^2}{xy^2}\sum_q e_q^2 f_1^q(x)D_q^h(z)}.$$

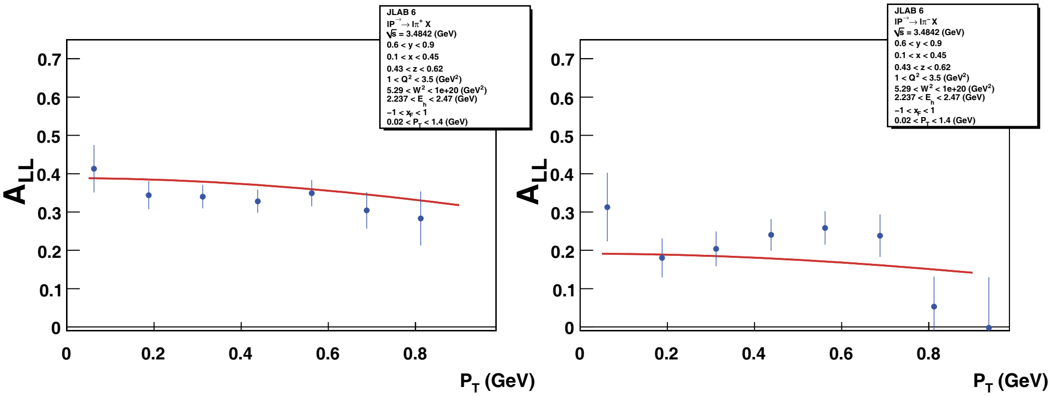

Fig. 8. – A_{LL} asymmetry compared with JLAB experimental results [65] for π^+ (left panel) and π^- (right panel).

For the asymmetry as a function of P_{hT} the formula is the following:

$$(163)\quad A_{LL}(P_{hT}) = \frac{\int \mathrm{d}x\mathrm{d}y\mathrm{d}z \int_0^{2\pi} \mathrm{d}\phi_h \mathrm{d}\phi_S (\mathrm{d}\sigma^{\uparrow} - \mathrm{d}\sigma^{\downarrow})}{\int \mathrm{d}x\mathrm{d}y\mathrm{d}z \int_0^{2\pi} \mathrm{d}\phi_h \mathrm{d}\phi_S (\mathrm{d}\sigma^{\uparrow} + \mathrm{d}\sigma^{\downarrow})} =$$

$$\frac{\int \mathrm{d}x\mathrm{d}y\mathrm{d}z \frac{2-y}{xy} \sum_q \frac{1}{\pi\left(\langle K_T^2\rangle + \mu_{0q}^2 z^2\right)^2} \exp\left[-P_{hT}^2/(\langle K_T^2\rangle + \mu_{0q}^2 z^2)\right] e_q^2 g_{1L}^q(x) D_q^h(z)}{\int \mathrm{d}x\mathrm{d}y\mathrm{d}z \frac{1+(1-y)^2}{xy^2} \sum_q \frac{1}{\pi(\langle K_T^2\rangle + \langle p_T^2\rangle_q z^2)} \exp\left(-P_{hT}^2/(\langle K_T^2\rangle + \langle p_T^2\rangle_q z^2)\right) e_q^2 f_1^q(x) D_q^h(z)}.$$

The results and comparison to JLAB experimental results ref. [65] are presented in fig. 8. We conclude that lattice QCD results give appropriate description of the experimental data and we will use results of ref. [63] for $g_{1T}^{(1)a}$ and $h_{1L}^{\perp(1)a}$ widths in the following sections.

5˙7. $A_{LT}^{\cos(\phi_h-\phi_S)}$ *asymmetry.* – The lepton-hadron cross-section can be expressed in a model-independent way by a set of structure functions, we write here only the part corresponding to $\cos(\phi_h - \phi_S)$ modulation (see ref. [3]):

$$\frac{\mathrm{d}\sigma}{\mathrm{d}x\mathrm{d}y\mathrm{d}\psi\mathrm{d}z\mathrm{d}\phi_h\mathrm{d}P_{h\perp}^2} =$$
$$\frac{\alpha^2}{xyQ^2}\frac{y^2}{2(1-\varepsilon)}\left(1+\frac{\gamma^2}{2x}\right)\left\{F_{UU,T} + |\mathbf{S}_\perp|\lambda_e\sqrt{1-\varepsilon^2}\cos(\phi_h-\phi_S)F_{LT}^{\cos(\phi_h-\phi_S)}\right\},$$

Neglecting the proton mass, the depolarization factors in eq. (164) can be rewritten as [3]

$$\begin{aligned}(164)\qquad &\frac{y^2}{2(1-\varepsilon)}=\frac{1}{1+\gamma^2}\left(1-y+\frac{1}{2}y^2+\frac{1}{4}\gamma^2y^2\right)\approx\left(1-y+\frac{1}{2}y^2\right),\\ &\frac{y^2}{2(1-\varepsilon)}\sqrt{1-\varepsilon^2}=\frac{1}{\sqrt{1+\gamma^2}}y\left(1-\frac{1}{2}y\right)\approx y\left(1-\frac{1}{2}y\right).\end{aligned}$$

In DIS kinematics $\mathrm{d}\psi\approx\mathrm{d}\phi_S$ and we obtain

$$\begin{aligned}(165)\quad &\frac{\mathrm{d}\sigma}{\mathrm{d}x\mathrm{d}y\mathrm{d}\phi_S\mathrm{d}z\mathrm{d}\phi_h\mathrm{d}P_{h\perp}^2}=\\ &\frac{\alpha^2}{2xyQ^2}\left\{\left(1+(1-y)^2\right)F_{UU,T}+|\mathbf{S}_\perp|\lambda_e y\,(2-y)\cos(\phi_h-\phi_S)F_{LT}^{\cos(\phi_h-\phi_S)}\right\}.\end{aligned}$$

Asymmetry is defined in the following way:

$$(166)\qquad A_{LT}^{\cos(\phi_h-\phi_S)}=2\frac{\int\mathrm{d}\phi_h\mathrm{d}\phi_S\cos(\phi_h-\phi_S)\left(\mathrm{d}\sigma^\uparrow-\mathrm{d}\sigma^\downarrow\right)}{\int\mathrm{d}\phi_h\mathrm{d}\phi_S\left(\mathrm{d}\sigma^\uparrow+\mathrm{d}\sigma^\downarrow\right)},$$

where ↑ (↓) denote the transverse polarization of the target nucleon, L stands for longitudinal polarization of lepton beam, T for the transverse polarization of the target nucleon. Numerator and denominator of eq. (166) using $Q^2=sxy$ can be written as

$$\begin{aligned}(167)\qquad \mathrm{d}\sigma^\uparrow-\mathrm{d}\sigma^\downarrow&=\frac{\alpha^2}{sx^2y^2}y\,(2-y)\cos(\phi_h-\phi_S)\,F_{LT}^{\cos(\phi_h-\phi_S)},\\ \mathrm{d}\sigma^\uparrow+\mathrm{d}\sigma^\downarrow&=\frac{\alpha^2}{sx^2y^2}\left(1+(1-y)^2\right)F_{UU,T}.\end{aligned}$$

And we have

$$\begin{aligned}(168)\quad &\int\mathrm{d}\phi_h\mathrm{d}\phi_S\cos(\phi_h-\phi_S)(\mathrm{d}\sigma^\uparrow-\mathrm{d}\sigma^\downarrow)=\\ &\int\mathrm{d}\phi_h\mathrm{d}\phi_S\cos(\phi_h-\phi_S)\frac{\alpha^2}{sx^2y^2}y\,(2-y)\cos(\phi_h-\phi_S)F_{LT}^{\cos(\phi_h-\phi_S)},\\ &=2P_{h\perp}\pi(2\pi)\frac{\alpha^2}{sx^2y^2}y\,(2-y)\\ &F_{LT}^{\cos(\phi_h-\phi_S)}\int\mathrm{d}\phi_h\mathrm{d}\phi_S\left(\mathrm{d}\sigma^\uparrow+\mathrm{d}\sigma^\downarrow\right)=\int\mathrm{d}\phi_h\mathrm{d}\phi_S\frac{\alpha^2}{sx^2y^2}\left(1+(1-y)^2\right)F_{UU,T}\\ &=2P_{h\perp}(2\pi)^2\frac{\alpha^2}{sx^2y^2}\left(1+(1-y)^2\right)F_{UU,T}.\end{aligned}$$

Weighted asymmetry is defined as [66]

$$(169)\qquad A_{LT}^{\frac{P_{hT}}{zM}\cos(\phi_h-\phi_S)}=2\frac{\int P_{hT}\mathrm{d}P_{hT}\mathrm{d}\phi_h\mathrm{d}\phi_S\frac{P_{hT}}{zM}\cos(\phi_h-\phi_S)\left(\mathrm{d}\sigma^\uparrow-\mathrm{d}\sigma^\downarrow\right)}{\int P_{hT}\mathrm{d}P_{hT}\mathrm{d}\phi_h\left(\mathrm{d}\sigma^\uparrow+\mathrm{d}\sigma^\downarrow\right)}.$$

We have [3]

$$F_{LT}^{\cos(\phi_h-\phi_S)} = \mathcal{C}\left[\frac{\hat{\mathbf{h}}\cdot\mathbf{p}_T}{M} g_{1T} D_1\right], \tag{170}$$

and thus using eq. (106)

$$F_{LT}^{\cos(\phi_h-\phi_S)} = x\sum_a e_a^2 \int \mathrm{d}^2\mathbf{p}_T\, \frac{\hat{\mathbf{h}}\cdot\mathbf{p}_T}{M} g_{1T}^a(x,p_T^2)\, D_{1a}^h\left(z,(\mathbf{P_{h\perp}}-\mathbf{zp_T})^\mathbf{2}\right). \tag{171}$$

Following refs. [49, 60] let us assume that transverse-momentum dependences of DFs and FFs are given by factorized Gaussian form:

$$\begin{aligned} f_1^q(x,p_T^2) &= f_1^q(x)\frac{1}{\pi\langle p_T^2\rangle}\exp\left[-\frac{\mathbf{p}_T^2}{\langle p_T^2\rangle}\right], \\ D_{1q}^h(z,K_T^2) &= D_{1q}^h(z)\frac{1}{\pi\langle K_T^2\rangle}\exp\left[-\frac{\mathbf{K}_T^2}{\langle K_T^2\rangle}\right], \\ g_{1T}^q(x,p_T^2) &= g_{1T}^q(x)\, N\exp\left[-\frac{\mathbf{p}_T^2}{\mu_1^2}\right], \end{aligned} \tag{172}$$

where we take values of $\langle p_T^2\rangle$ and $\langle K_T^2\rangle$ from ref. [49]: $\langle p_T^2\rangle = 0.25\,(\mathrm{GeV}^2)$, $\langle K_T^2\rangle = 0.2\,(\mathrm{GeV}^2)$.

We will use WW approximation [54] for calculations, so that

$$g_{1T}^{(1)q}(x) \approx\ x\int_x^1 \frac{\mathrm{d}y}{y}\, g_1^q(y). \tag{173}$$

We can use eq. (100) to calculate the first moment of $g_{1T}^q(x,k_T^2)$ of eq. (142) and obtain

$$g_{1T}^{(1)q}(x) = g_{1T}^q(x)\frac{\pi\mu_1^4 N}{2M^2}, \tag{174}$$

thus

$$g_{1T}^q(x,p_T^2) = g_{1T}^{(1)q}(x)\,\frac{2M^2}{\pi\mu_1^4}\exp\left[-\frac{\mathbf{p}_T^2}{\mu_1^2}\right]. \tag{175}$$

Let us remind that g_{1T}^q enters in the positivity bound [4] for the Sivers function $f_{1T}^{\perp q}$ [67, 68]

$$\frac{\mathbf{p_T^2}}{M^2}\left((g_{1T}^q(x,p_T^2))^2 + (f_{1T}^{\perp q}(x,p_T^2))^2\right) \le (f_1^q(x,p_T^2))^2, \tag{176}$$

so that it becomes important to measure g_{1T}^q in order to refine bounds for the Sivers function.

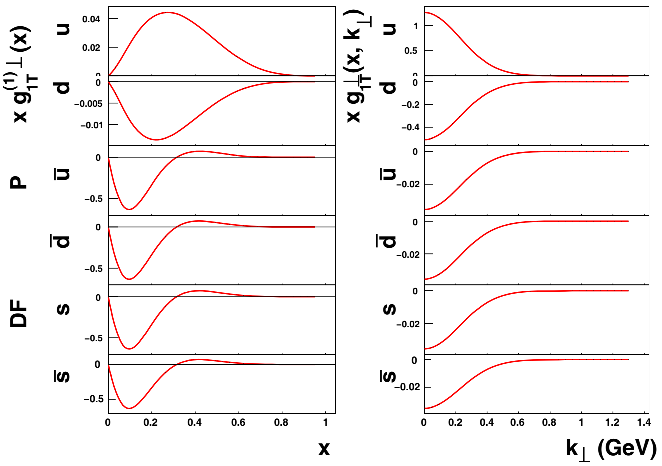

Fig. 9. – g_{1T}^q distributions.

We can finally derive the formula for $\cos(\phi_h - \phi_S)$ asymmetry as a function of x, y, z using eqs. (166), (136), (106), (142), (175), (171):

$$(177)\quad A_{LT}^{\cos(\phi_h-\phi_S)}(x,y,z) = 2\frac{\int P_{hT}\mathrm{d}P_{hT}\int_0^{2\pi}\mathrm{d}\phi_h\mathrm{d}\phi_S(\mathrm{d}\sigma^\uparrow-\mathrm{d}\sigma^\downarrow)\cos(\phi_h-\phi_S)}{\int P_{hT}\mathrm{d}P_{hT}\int_0^{2\pi}\mathrm{d}\phi_h\mathrm{d}\phi_S(\mathrm{d}\sigma^\uparrow+\mathrm{d}\sigma^\downarrow)} =$$

$$\frac{\frac{2-y}{x^2y}\int \mathrm{d}^2P_{hT}F_{LT}^{\cos(\phi_h-\phi_S)}}{\frac{1+(1-y)^2}{x^2y^2}\int \mathrm{d}^2P_{hT}F_{UU}} = \frac{\frac{2-y}{xy}\,\frac{Mz\sqrt{\pi}}{\sqrt{\langle K_T^2\rangle+\mu_1^2z^2}}\sum_q e_q^2 g_{1T}^{q(1)}(x)D_q^h(z)}{\frac{1+(1-y)^2}{xy^2}\sum_q e_q^2 f_1^q(x)\, D_q^h(z)}.$$

If one calculates the asymmetry as a function of P_{hT}, then the formula is the following:

$$(178)\quad A_{LT}^{\cos(\phi_h-\phi_S)}(P_{hT}) = 2\frac{\int \mathrm{d}x\mathrm{d}y\mathrm{d}z\int_0^{2\pi}\mathrm{d}\phi_h\mathrm{d}\phi_S(\mathrm{d}\sigma^\uparrow-\mathrm{d}\sigma^\downarrow)\cos(\phi_h-\phi_S)}{\int \mathrm{d}x\mathrm{d}y\mathrm{d}z\int_0^{2\pi}\mathrm{d}\phi_h\mathrm{d}\phi_S(\mathrm{d}\sigma^\uparrow+\mathrm{d}\sigma^\downarrow)} =$$

$$\frac{\int \mathrm{d}x\mathrm{d}y\mathrm{d}z\frac{2-y}{xy}\,\frac{2MzP_{hT}}{\pi\left(\langle K_T^2\rangle+\mu_1^2z^2\right)^2}\exp\left(-P_{hT}^2/(\langle K_T^2\rangle+\mu_1^2z^2)\right)\sum_q e_q^2 g_{1T}^{q(1)}(x)D_q^h(z)}{\int \mathrm{d}x\mathrm{d}y\mathrm{d}z\frac{1+(1-y)^2}{xy^2}\,\frac{1}{\pi(\langle K_T^2\rangle+\langle p_T^2\rangle z^2)}\exp\left(-P_{hT}^2/(\langle K_T^2\rangle+\langle p_T^2\rangle z^2)\right)\sum_q e_q^2 f_1^q(x)D_q^h(z)},$$

For weighted asymmetry (169) we have

$$(179)\quad A_{LT}^{\frac{P_{hT}}{zM}\cos(\phi_h-\phi_S)}(x,y,z) = 2\frac{\int \mathrm{d}P_{hT}^2\int_0^{2\pi}\mathrm{d}\phi_h\mathrm{d}\phi_S(\mathrm{d}\sigma^\uparrow-\mathrm{d}\sigma^\downarrow)\frac{P_{hT}}{zM}\cos(\phi_h-\phi_S)}{\int \mathrm{d}P_{hT}^2\int_0^{2\pi}\mathrm{d}\phi_h\mathrm{d}\phi_S(\mathrm{d}\sigma^\uparrow+\mathrm{d}\sigma^\downarrow)}$$

$$= \frac{2\frac{2-y}{xy}\sum_q e_q^2 g_{1T}^{q(1)}(x)D_q^h(z)}{\frac{1+(1-y)^2}{xy^2}\sum_q e_q^2 f_1^q(x)D_q^h(z)};$$

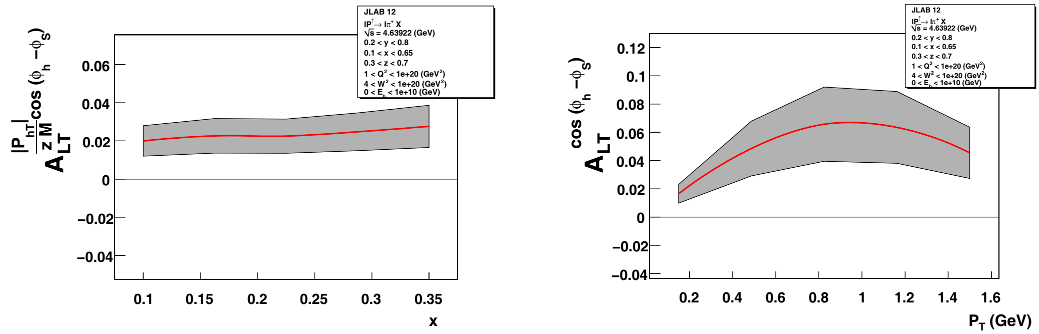

Fig. 10. – Left panel: $A_{LT}^{\frac{P_{hT}}{zM} \cos(\phi_h - \phi_S)}$ as a function of x, right panel: $A_{LT}^{\cos(\phi_h - \phi_S)}$ as a function of P_{hT} for JLab 12 GeV.

In order to make estimates for the asymmetries we need to fix the width of the distribution μ_1^2, we will use $\mu_1^2 = 0.1\,\text{GeV}^2$ for our estimates. The helicity distributions $g_1(x)$ are taken from ref. [69]. Integrated parton distribution and fragmentation functions, $f_{q/p}(x)$ and $D_{h/q}(z)$, are available in the literature; in particular, we use the GRV98LO PDF set [51] and the DSS fragmentation function set [36].

Resulting distributions g_{1T}^q are plotted in fig. 9.

Weighted and unweighted asymmetries $A_{LT}^{\frac{P_{hT}}{zM} \cos(\phi_h - \phi_S)}$, $A_{LT}^{\cos(\phi_h - \phi_S)}$ for JLab 12 GeV are plotted in fig. 10.

* * *

Authored by a Jefferson Science Associate, LLC under US DOE Contract No. DE-AC05-06OR23177. The US Government retains a non-exclusive, paid-up, irrevocable, world-wide license to publish or reproduce this manuscript for US Government purposes.

APPENDIX A.

In general $W^{S,\mu\nu}$ can be parametrized as

$$W^{S,\mu\nu}(q,P) = -W_1 g^{\mu\nu} + \frac{W_2}{M^2} P^\mu P^\nu + \frac{W_4}{M^2} q^\mu q^\nu + \frac{W_5}{M^2}(P^\mu q^\nu + P^\nu q^\mu) \tag{A.1}$$

with coefficients $W_{1,2,4,5}$ which are called structure functions and depend on q, P or x, Q^2. Notice that we already symmetrized the hadron tensor and made structure functions dimensionless.

From current conservation we have $q_\mu W^{S,\mu\nu} = q_\nu W^{S,\mu\nu} = 0$.

Let us use the first relation $q_\mu W^{S,\mu\nu} = 0$:

$$q_\mu W^{S,\mu\nu} = -W_1 q^\nu + \frac{W_2}{M^2}(p \cdot q) p^\nu + \frac{W_4}{M^2} q^2 q^\nu + \frac{W_5}{M^2}((p \cdot q) q^\nu + q^2 p^\nu) = 0, \tag{A.2}$$

so that

$$W_5 = -\frac{p\cdot q}{q^2}W_2. \tag{A.3}$$

Now we use the second condition $q_\mu W^{S,\mu\nu} = 0$ and use eq. (A.3):

$$q_\nu W^{S,\mu\nu} = -W_1 q^\mu + \frac{W_2}{M^2}(p{\cdot}q)p^\mu + \frac{W_4}{M^2}q^2 q^\mu - \frac{(p\cdot q)}{q^2 M^2}(p^\mu(p{\cdot}q) + q^\mu(p{\cdot}q)q^\mu)W_2 = 0, \tag{A.4}$$

and we obtain

$$W_4 = \frac{M^2}{q^2}W_1 + \frac{(p\cdot q)^2}{q^2 M^2}W_2. \tag{A.5}$$

Now we can rewrite eq. (A.1) as

$$\begin{aligned} W^{S,\mu\nu}(q,P) = {}& -W_1 q^{\mu\nu} + \frac{W_2}{M^2}p^\mu p^\nu + \left(\frac{W_1}{q^2} + (\frac{p\cdot q}{q^2})^2\frac{W_2}{M^2}\right) q^\mu q^\nu \\ & -\frac{(p\cdot q)}{q^2 M^2}(p^\mu q^\nu + p^\nu q^\mu)W_2. \end{aligned} \tag{A.6}$$

We see that we have 2 independent structure functions W_1 and W_2. Let us rewrite eq. (A.6) in standard form. Let us use $x = Q^2/2p\cdot q$, thus $p\cdot q/Q^2 = 1/(2x)$.

$$W^{S,\mu\nu}(q,P) = \left(-g^{\mu\nu} + \frac{q^\mu q^\nu}{q^2}\right) W_1 + \left(P^\mu + \frac{q^\mu}{2x}\right)\left(P^\nu + \frac{q^\nu}{2x}\right) W_2, \tag{A.7}$$

which is the same as eq. (52).

Structure functions F_1 and F_2 are usually defined as

$$F_1(x,Q^2) \equiv W_1(x,Q^2), \tag{A.8}$$

$$F_2(x,Q^2) \equiv W_2(x,Q^2)(P\cdot q) \tag{A.9}$$

and the following explanation is then valid:

$$\begin{aligned} W^{S,\mu\nu}(q,P) = {}& \left(-g^{\mu\nu} + \frac{q^\mu q^\nu}{q^2}\right) F_1(x,Q^2) \\ & + \frac{1}{P\cdot q}\left(P^\mu - q^\mu\frac{P\cdot q}{q^2}\right)\left(P^\nu - q^\nu\frac{P\cdot q}{q^2}\right) F_2(x,Q^2). \end{aligned} \tag{A.10}$$

REFERENCES

[1] Mulders P. J. and Tangerman R. D., *Nucl. Phys. B*, **461** (1996) 197.
[2] Goeke K., Metz A. and Schlegel M., *Phys. Lett. B*, **618** (2005) 90.
[3] Bacchetta A. *et al.*, *JHEP*, **02** (2007) 093.
[4] Bacchetta A., Boglione M., Henneman A. and Mulders P. J., *Phys. Rev. Lett.*, **85** (2000) 712.
[5] Collins J. C., Soper D. E. and Sterman G. F., *Adv. Ser. Direct. High Energy Phys.*, **5** (1988) 1.
[6] Qiu J.-w. and Sterman G., *Phys. Rev. Lett.*, **67** (1991) 2264.
[7] Ji X.-d., Ma J.-p. and Yuan F., *Phys. Rev. D*, **71** (2005) 034005.
[8] Efremov A. V. and Teryaev O. V., *Sov. J. Nucl. Phys.*, **36** (1982) 140.
[9] Efremov A. V. and Teryaev O. V., *Phys. Lett. B*, **150** (1985) 383.
[10] Qiu J.-w. and Sterman G., *Phys. Rev. D*, **59** (1999) 014004.
[11] Ji X., Qiu J.-W., Vogelsang W. and Yuan F., *Phys. Rev. Lett.*, **97** (2006) 082002.
[12] Ji X., Qiu J.-W., Vogelsang W. and Yuan F., *Phys. Rev. D*, **73** (2006) 094017.
[13] Ji X., Qiu J.-W., Vogelsang W. and Yuan F., *Phys. Lett. B*, **638** (2006) 178.
[14] Bacchetta A., Boer D., Diehl M. and Mulders P. J., *JHEP*, **08** (2008) 023.
[15] Boer D., Mulders P. J. and Pijlman F., *Nucl. Phys. B*, **667** (2003) 201.
[16] Anselmino M. *et al.*, *Eur. Phys. J. A*, **39** (2009) 89.
[17] Airapetian A. *et al.*, *Phys. Rev. Lett.*, **94** (2005) 012002.
[18] Alekseev M. *et al.*, *Phys. Lett. B*, **673** (2009) 127.
[19] Taylor J. R., *Scattering Theory. The Quantum Theory of Nonrelativistic Collisions* (John Wiley & Sons) 1972.
[20] Diehl M. and Sapeta S., *Eur. Phys. J. C*, **41** (2005) 515.
[21] Avakian H., Efremov A. V., Schweitzer P. and Yuan F., *Phys. Rev. D*, **81** (2010) 074035.
[22] Boffi S., Efremov A. V., Pasquini B. and Schweitzer P., *Phys. Rev. D*, **79** (2009) 094012.
[23] Pasquini B. and Yuan F., *Phys. Rev. D*, **81** (2010) 114013.
[24] Collins J. C., *Phys. Lett. B*, **536** (2002) 43.
[25] Anselmino M. *et al.*, *Phys. Rev. D*, **72** (2005) 094007.
[26] Anselmino M., Boglione M. and Murgia F., *Phys. Lett. B*, **362** (1995) 164.
[27] Anselmino M. and Murgia F., *Phys. Lett. B*, **442** (1998) 470.
[28] Ji X.-d., Ma J.-P. and Yuan F., *Phys. Lett. B*, **597** (2004) 299.
[29] Collins J. and Qiu J.-W., *Phys. Rev. D*, **75** (2007) 114014.
[30] Efremov A. V., Goeke K., Menzel S., Metz A. and Schweitzer P., *Phys. Lett. B*, **612** (2005) 233.
[31] Vogelsang W. and Yuan F., *Phys. Rev. D*, **72** (2005) 054028.
[32] Collins J. C. *et al.*, *Phys. Rev. D*, **73** (2006) 014021.
[33] Collins J. C. *et al.*, hep-ph/0510342.
[34] Pobylitsa P. V. hep-ph/0301236.
[35] Anselmino M. *et al.* hep-ph/0511017.
[36] de Florian D., Sassot R. and Stratmann M., *Phys. Rev. D*, **75** (2007) 114010.
[37] Diefenthaler M. arXiv: 0706.2242.
[38] Arnold S., Efremov A. V., Goeke K., Schlegel M. and Schweitzer P., (2008).
[39] Martin A., *Czech. J. Phys.*, **56** (2006) F33.
[40] Alekseev M. G. *et al.*, *Phys. Lett. B*, **692** (2010) 240.

[41] Airapetian A. *et al.*, *Phys. Rev. Lett.*, **103** (2009) 152002.
[42] Anselmino M. *et al.*, *J. Phys. Conf. Ser.*, **295** (2011) 012062.
[43] Brodsky S. J., Hwang D. S. and Schmidt I., *Phys. Lett. B*, **530** (2002) 99.
[44] Brodsky S. J., Hwang D. S. and Schmidt I., *Nucl. Phys. B*, **642** (2002) 344.
[45] Bacchetta A., Radici M., Conti F. and Guagnelli M., *Eur. Phys. J. A*, **45** (2010) 373.
[46] Gamberg L. P., Goldstein G. R. and Schlegel M., *Phys. Rev. D*, **77** (2008) 094016.
[47] Yuan F., *Phys. Lett. B*, **575** (2003) 45.
[48] Drago A., *Phys. Rev. D*, **71** (2005) 057501.
[49] Anselmino M. *et al.*, *Phys. Rev. D*, **71** (2005) 074006.
[50] Schweitzer P., Teckentrup T. and Metz A., *Phys. Rev. D*, **81** (2010) 094019.
[51] Gluck M., Reya E. and Vogt A., *Eur. Phys. J. C*, **5** (1998) 461.
[52] Kretzer S., *Phys. Rev. D*, **62** (2000) 054001.
[53] Cherednikov I. O. and Stefanis N. G., *Phys. Rev. D*, **80** (2009) 054008.
[54] Wandzura S. and Wilczek F., *Phys. Lett. B*, **72** (1977) 195.
[55] Abe K. *et al.*, *Phys. Rev. D*, **58** (1998) 112003.
[56] Anthony P. L. *et al.*, *Phys. Lett. B*, **553** (2003) 18.
[57] Accardi A., Bacchetta A., Melnitchouk W. and Schlegel M., *JHEP*, **11** (2009) 093.
[58] Kotzinian A. M. and Mulders P. J., *Phys. Rev. D*, **54** (1996) 1229.
[59] Kotzinian A. M. and Mulders P. J., *Phys. Lett. B*, **406** (1997) 373.
[60] Kotzinian A., Parsamyan B. and Prokudin A., *Phys. Rev. D*, **73** (2006) 114017.
[61] Avakian H. *et al.*, *Phys. Rev. D*, **77** (2008) 014023.
[62] Metz A., Schweitzer P. and Teckentrup T., *Phys. Lett. B*, **680** (2009) 141.
[63] Hagler P., Musch B. U., Negele J. W. and Schafer A., *Europhys. Lett.*, **88** (2009) 61001.
[64] Anselmino M., Efremov A., Kotzinian A. and Parsamyan B., *Phys. Rev. D*, **74** (2006) 074015.
[65] Avakian H. *et al.*, *Phys. Rev. Lett.*, **105** (2010) 262002.
[66] Boer D. and Mulders P. J., *Phys. Rev. D*, **57** (1998) 5780.
[67] Sivers D. W., *Phys. Rev. D*, **41** (1990) 83.
[68] Sivers D. W., *Phys. Rev. D*, **43** (1991) 261.
[69] Gluck M., Reya E., Stratmann M. and Vogelsang W., *Phys. Rev. D*, **63** (2001) 094005.

This page intentionally left blank

Proceedings of the International School of Physics "Enrico Fermi"
Course CLXXX "Three-Dimensional Partonic Structure of the Nucleon"
edited by M. Anselmino, H. Avakian, D. Hasch and P. Schweitzer
(IOS, Amsterdam; SIF, Bologna)
DOI 10.3254/978-1-61499-197-7-197

Models for TMDs and numerical methods

B. Pasquini

Dipartimento di Fisica Nucleare e Teorica, Università degli Studi di Pavia
and INFN, Sezione di Pavia - I-27100 Pavia, Italy

C. Lorcé

IPNO, Université Paris-Sud 11, CNRS/IN2P3 - 91406 Orsay, France
and LPT, Université Paris-Sud 11, CNRS - 91406 Orsay, France

Summary. — We present a systematic study of the transverse-momentum–dependent parton distributions (TMDs) in the framework of quark models. In particular, we review the general formalism for modeling the quark TMDs using the representation in terms of overlap of nucleon light-cone wave functions. Such a formalism can be applied to a large class of quark models. We will discuss the building blocks of these different models, and we will use as explicit example for the calculation of the TMDs a light-cone constituent quark model. Within this model, we also propose a phenomenological study of different observables, trying to learn how model parameters related to particular assumptions on the nucleon structure can be tuned to describe available experimental data.

1. – Introduction

The investigation of how the composite structure of a hadron, consisting of nearly massless constituents, results from the underlying quark-gluon dynamics is a challenging problem, as it is of non-perturbative nature, and displays many facets. What are the longitudinal momentum distributions of partons in a fast-moving unpolarized or polarized

© Società Italiana di Fisica

hadron? What amount of transverse momentum do these partons carry, and how large is the resulting amount of orbital angular momentum? What is the spatial distribution of quarks inside a hadron as seen by a vector probe (coupling to the charge of the system), by an axial vector probe (coupling to the axial charge), or even seen by a more complicated probe?

Two new types of distributions such as the transverse-momentum–dependent parton distributions (TMDs) and the generalized parton distributions (GPDs) allow to address and quantify such questions. At leading-twist, the TMDs are defined as the diagonal matrix elements of the parton density matrix in the longitudinal and transverse-momentum space [1-5]. Taking into account all the independent spin-polarization states of the nucleon and partons, one obtains 8 independent TMDs describing the correlations in the three-dimensional momentum space between the nucleon and quark spin, and between the quark orbital angular momentum and both the nucleon and quark spin. On the other hand, GPDs are probability amplitudes related to the off-diagonal matrix elements of the parton density matrix in the longitudinal momentum space [6-17]. After a Fourier transform to the impact-parameter space, they also provide a three-dimensional picture of the hadron in a mixed momentum-coordinate space [18-20].

The information encoded in the TMDs and the GPDs can be collected in a unified framework through the generalized transverse-momentum–dependent parton distributions (GTMDs); for a classification see refs. [21, 22]. The GTMDs contain the most general one-body information about partons, corresponding to the full one-quark density matrix in momentum space [23]. GTMDs depend on the three-momentum of the quarks as well as on the four-momentum Δ which is transferred by the probe to the nucleon. The Fourier transform of the GTMDs to the impact-parameter space allows to define the Wigner distributions of the parton-hadron system, which represent the quantum-mechanical analogues of the classical phase-space distributions [24-26,16]. Wigner distributions provide 5-dimensional (two-position and three-momentum coordinates) images of the nucleon as seen in the infinite-momentum frame. As such they contain the full correlations between the quark transverse position and three-momentum. In particular limits, they reduce to different parton distributions and form factors as shown in fig. 1. The different arrows in this figure represent particular projections in hadron and quark momentum space, and give the links between the matrix elements of different reduced matrices. In the forward limit $\Delta = 0$, they reduce to the TMDs, while the integration over the quark transverse momentum $\boldsymbol{k}_\perp$ leads to the GPDs. The common limit of TMDs and GPDs is given by the standard parton distribution functions (PDFs). The integration over the longitudinal-momentum fraction x brings to the lower plane of the box in fig. 1, and at each vertex we find the restricted version of the operator defining the distributions in the upper plane. For example, in correspondence of the TMDs we encounter the transverse-momentum–dependent spin densities (TMSD), while from the GPDs we obtain the form factors (FFs). Both FFs and TMSDs have the charges as a common limit. Each of these observables is sensitive to specific properties of the nucleon structure, and contributes from different perspective to form a global and comprehensive view [27]. In these lectures we will concentrate on the model calculation of TMDs, restricting ourselves

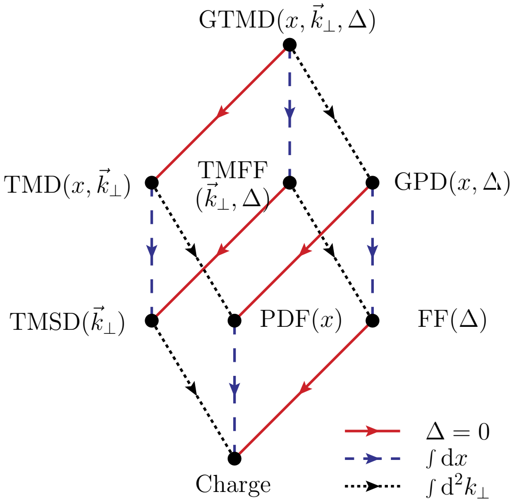

Fig. 1. – (Colour on-line) Representation of the projections of the GTMDs into parton distributions and form factors. The arrows correspond to different reductions in the hadron and quark momentum space: the solid (red) arrows give the forward limit in the hadron momentum, the dotted (black) arrows correspond to integrating over the quark transverse momentum and the dashed (blue) arrows project out the longitudinal momentum of quarks.

to the quark contribution. We will exploit the relations with different observables and parton distributions in the box of fig. 1 to test different model assumptions and their implications for the partonic structure of the nucleon. Various low-energy QCD-inspired models have been employed to model the TMDs [23, 28-55]. Although they all have in common that they strongly oversimplify the complexity of the QCD dynamics in hadrons, studies in different models based on often complementary assumptions, help to unravel non-perturbative aspects of TMDs. Insights into non-perturbative properties are of particular interest when confirmed in various models. The practical value of model results is that they can be used to predict new observables, or to guide educated Ansätze for fits of TMD parametrizations. Especially in the context of TMDs one should not underestimate the conceptual importance of model calculations. Model calculations demonstrated the existence of effects [56], paved the way towards an understanding of universality in the fragmentation process [57], established new TMDs [58, 59], see [60] for a review.

The paper is organized as follows. In sect. **2** we review the definitions of the leading-twist TMDs and introduce a convenient representation of the quark-quark correlator in terms of the net-polarization states of the quark and the hadron. In sect. **3** we discuss model relations among TMDs which hold in a large class of quark models. In particular, we review the derivation given in ref. [61] to explain the physical origin of such relations. There are two linear relations and a quadratic relation which are flavour independent and involve polarized TMDs, while a further linear relation is flavour dependent and involves both polarized and unpolarized TMDs. The relations among polarized TMDs connect the distributions of quarks inside the nucleon for different configurations of the polarization states of the hadron and the parton. As a consequence, it is natural to expect that they can originate from rotational invariance of the polarization states of the system. Rotations are more easily discussed in the basis of canonical spin. Therefore, instead of working in the standard basis of light-cone helicity, we introduce in subsects. **4**˙1 and **4**˙2 the tensor correlator defining the TMDs in the canonical-spin basis. Such a representation is used in subsect. **4**˙3 to discuss the consequences of rotational symmetries of the system. In such a way we will be able to identify the key ingredients for the existence of relations among polarized TMDs in quark models.

In order to complete the discussion, including the flavour-dependent relation among polarized and unpolarized TMDs, we need to introduce specific assumptions about the spin-isospin structure of the nucleon state. Therefore, in sect. **5** we discuss the consequences of rotational invariance using the explicit representation of the TMDs in terms of three-quark (3Q) wave functions. In particular, in subsect. **5**˙1 we derive the overlap representation of the TMDs in terms of light-cone wave functions (LCWFs), while the corresponding representation in terms of wave function in the canonical-spin basis is given in subsect. **5**˙2. In subsect. **5**˙3 we discuss the constraints of rotational symmetry on the nucleon wave function and, as a result, we give an alternative derivation of the flavour-independent relations among TMDs. Finally, in subsect. **5**˙4 we discuss the constraint due to $SU(6)$ symmetry of the spin-flavour dependent part of the nucleon wave function. This additional ingredient allows us to explain the origin of the flavour-dependent relation. The formal derivation of the relations among TMDs is made explicit within different quark models in sect. **6**. There we review different quark models which have been used in the literature for the calculation of TMDs. In particular, we discuss the key ingredients of the models, showing how and to which extent the conditions which lead to relations among TMDs are realized. In sect. **7** we also study the phenomenological implications of the breaking of $SU(6)$ symmetry. We will work in the framework of a light-cone constituent quark model, giving the essential step for the explicit calculation of the TMDs in the model in subsect. **7**˙1. In subsect. **7**˙2 we discuss the model results for T-even TMDs and related spin densities in the transverse-momentum space. In subsect. **7**˙3 we propose a phenomenological study of different observables, fitting the model parameter related to $SU(6)$-symmetry breaking to the double-spin asymmetry in inclusive deep inelastic scattering (DIS). The results from this fit are then exploited to obtain predictions for other observables which are particularly sensitive to $SU(6)$-breaking effects, like the double-spin asymmetry for semi-inclusive deep inelastic scattering (SIDIS) and the neutron electric form factor. A summary of our findings is given in the final section. Technical details and further explanations about the representation in terms of nucleon wave functions are collected in three appendices.

2. – Transverse-momentum–dependent parton distributions

2˙1. *Definitions.* – In this section, we review the formalism for the definition of TMDs, following the conventions of refs. [4, 62-64]. Introducing two lightlike four-vectors $n_\pm$ satisfying $n_+ \cdot n_- = 1$, we write the light-cone components of a generic four-vector a as

$[a^+, a^-, \boldsymbol{a}_\perp]$ with $a^\pm = a \cdot n_\mp$. The density of quarks can be defined from the following quark-quark correlator(^{1}):

$$(1) \qquad \Phi_{ab}(x, \boldsymbol{k}_\perp, S) = \int \frac{\mathrm{d}\xi^- \, \mathrm{d}^2\xi_\perp}{(2\pi)^3} \, e^{i\left(k^+\xi^- - \boldsymbol{k}_\perp \cdot \boldsymbol{\xi}_\perp\right)} \times \Big\langle P, S \Big| \overline{\psi}_b(0) \mathcal{U}^{n_-}_{(0,+\infty)} \mathcal{U}^{n_-}_{(+\infty,\xi)} \psi_a(\xi) \Big| P, S \Big\rangle \Big|_{\xi^+=0},$$

where $k^+ = xP^+$, ψ is the quark field operator with a, b indices in the Dirac space, and $\mathcal{U}$ is the Wilson line which ensures colour gauge invariance [65]. The target state is characterized by its four-momentum P and covariant spin four-vector S satisfying $P^2 = M^2$, $S^2 = -1$, and $P \cdot S = 0$. We choose a frame where the hadron momentum has no transverse components, $P = [P^+, \frac{M^2}{2P^+}, \boldsymbol{0}_\perp]$, and so $S = [S_z \, \frac{P^+}{M}, -S_z \, \frac{M}{2P^+}, \boldsymbol{S}_\perp]$ with $\boldsymbol{S}^2 = 1$. From now on, we replace the dependence on the covariant spin four-vector S by the dependence on the unit three-vector $\boldsymbol{S} = (\boldsymbol{S}_\perp, S_z)$.

TMDs enter the general Lorentz-covariant decomposition of the correlator $\Phi_{ab}(x, \boldsymbol{k}_\perp, \boldsymbol{S})$ which, at twist-two level and for a spin-1/2 target, reads

$$\begin{aligned}(2) \quad \Phi(x, \boldsymbol{k}_\perp, \boldsymbol{S}) = \frac{1}{2}\Bigg\{ & f_1 \, \not{n}_+ - \frac{\epsilon_T^{ij} \, k_\perp^i S_\perp^j}{M} \, f_{1T}^\perp \, \not{n}_+ + S_z \, g_{1L} \, \gamma_5 \not{n}_+ + \frac{\boldsymbol{k}_\perp \cdot \boldsymbol{S}_\perp}{M} \, g_{1T} \, \gamma_5 \not{n}_+ \\ & + h_{1T} \, \frac{[\not{S}_\perp, \not{n}_+]}{2} \, \gamma_5 + S_z \, h_{1L}^\perp \, \frac{[\not{k}_\perp, \not{n}_+]}{2M} \, \gamma_5 \\ & + \frac{\boldsymbol{k}_\perp \cdot \boldsymbol{S}_\perp}{M} \, h_{1T}^\perp \, \frac{[\not{k}_\perp, \not{n}_+]}{2M} \, \gamma_5 + i h_1^\perp \, \frac{[\not{k}_\perp, \not{n}_+]}{2M} \Bigg\},\end{aligned}$$

where $\epsilon_T^{12} = -\epsilon_T^{21} = 1$, and the transverse four-vectors are defined as $a_\perp = [0, 0, \boldsymbol{a}_\perp]$. The nomenclature of the distribution functions follows closely that of ref. [4], sometimes referred to as "Amsterdam notation": f refers to unpolarized quarks; g and h to longitudinally and transversely polarized quark, respectively; a subscript 1 is given to the twist-two functions; subscripts L or T refer to the connection with the hadron spin being longitudinal or transverse; and a symbol $\perp$ signals the explicit presence of transverse momenta with an uncontracted index. Among these eight distributions, the so-called Boer-Mulders function $h_1^\perp$ [62] and Sivers function $f_{1T}^\perp$ [66] are T-odd, *i.e.* they change sign under "naive time-reversal", which is defined as usual time-reversal but without interchange of initial and final states. All the TMDs depend on x and $\boldsymbol{k}_\perp^2$. These functions can be individually isolated by performing traces of the correlator with suitable Dirac

---

(^{1}) In order to simplify the notation, we will omit the colour index, keeping in mind that the quark-quark correlator is diagonal in the colour space.

matrices. Using the abbreviation $\Phi^{[\Gamma]} \equiv \mathrm{Tr}[\Phi\Gamma]/2$, we have

$$\Phi^{[\gamma^+]}(x, \boldsymbol{k}_\perp, \boldsymbol{S}) = f_1 - \frac{\epsilon_T^{ij}\, k_\perp^i S_\perp^j}{M}\, f_{1T}^\perp, \tag{3}$$

$$\Phi^{[\gamma^+\gamma_5]}(x, \boldsymbol{k}_\perp, \boldsymbol{S}) = S_z\, g_{1L} + \frac{\boldsymbol{k}_\perp \cdot \boldsymbol{S}_\perp}{M}\, g_{1T}, \tag{4}$$

$$\Phi^{[i\sigma^{j+}\gamma_5]}(x, \boldsymbol{k}_\perp, \boldsymbol{S}) = S_\perp^j\, h_1 + S_z\, \frac{k_\perp^j}{M}\, h_{1L}^\perp + S_\perp^i\, \frac{2k_\perp^i k_\perp^j - \boldsymbol{k}_\perp^2 \delta^{ij}}{2M^2}\, h_{1T}^\perp + \frac{\epsilon_T^{ji}\, k_\perp^i}{M}\, h_1^\perp, \tag{5}$$

where $j = 1, 2$ is a transverse index, and

$$h_1 = h_{1T} + \frac{\boldsymbol{k}_\perp^2}{2M^2}\, h_{1T}^\perp. \tag{6}$$

The correlation function $\Phi^{[\gamma^+]}(x, \boldsymbol{k}_\perp, \boldsymbol{S})$ is just the unpolarized quark distribution, which integrated over $\boldsymbol{k}_\perp$ gives the familiar light-cone momentum distribution $f_1(x)$. All the other TMDs characterize the strength of different spin-spin and spin-orbit correlations. The precise form of this correlation is given by the prefactors of the TMDs in eqs. (3)–(5). In particular, the TMDs g_{1L} and h_1 describe the strength of a correlation between a longitudinal/transverse target polarization and a longitudinal/transverse parton polarization. After integration over $\boldsymbol{k}_\perp$, they reduce to the helicity and transversity distributions, respectively. By definition, the spin-orbit correlations described by $f_{1T}^\perp$, g_{1T}, $h_1^\perp$, $h_{1L}^\perp$ and $h_{1T}^\perp$ involve the transverse parton momentum and the polarization of both the parton and the target, and vanish upon integration over $\boldsymbol{k}_\perp$.

If one calculates these distributions in the light-cone gauge $A^+ = 0$ using advanced boundary condition for the transverse component of the gauge field, the gauge links in the quark-quark correlator can be ignored [67-69]. However, in this case the wave function amplitudes are not real and, apart from the structural information on the hadron, they also have an imaginary phase mimicking the final state interactions [70, 71].

2·2. *Helicity and four-component bases.*

– The physical meaning of the correlations encoded in TMDs becomes especially transparent when using for the quark field operator the Fourier expansion in momentum space in terms of light-cone Fock operators. To this aim, we first introduce the Fourier expansion in momentum space of the quark field operator ψ^q of flavour q (see *e.g.* [72])

$$\begin{aligned}\psi^q(z^-, \mathbf{z}_\perp) = \int \frac{\mathrm{d}k^+ \mathrm{d}^2\mathbf{k}_\perp}{16\pi^3 k^+} \Theta(k^+) \sum_\lambda \Big\{ & q_\lambda\left(\tilde{k}\right) u_{LC}\left(\tilde{k}, \lambda\right) \exp[-ik^+z^- + i\mathbf{k}_\perp \cdot \mathbf{z}_\perp] \\ & + \bar{q}_\lambda^\dagger\left(\tilde{k}\right) v_{LC}\left(\tilde{k}\right) \exp[+ik^+z^- - i\mathbf{k}_\perp \cdot \mathbf{z}_\perp] \Big\},\end{aligned} \tag{7}$$

where $\tilde{k} = (k^+, \mathbf{k}_\perp)$, λ, represents the parton helicity, and q and $\bar{q}^\dagger$ are the annihilation operator of the quark fields and the creation operators of the antiquark fields, respectively, which fulfill the anticommutations relations

$$\left\{q_{\lambda'}\left(\tilde{k}'\right), q_{\lambda}^{\dagger}\left(\tilde{k}\right)\right\} = \left\{\bar{q}_{\lambda'}\left(\tilde{k}'\right), \bar{q}_{\lambda}^{\dagger}\left(\tilde{k}\right)\right\} \\ = 16\pi^3 k^+ \delta(k'^+ - k^+)\delta^{(2)}(\mathbf{k}'_\perp - \mathbf{k}_\perp)\delta_{q'q}\delta_{\lambda'\lambda}. \tag{8}$$

In eq. (7), the quark LC spinors $u_{LC}(\tilde{k},\lambda)$ and $v_{LC}(\tilde{k},\lambda)$ are the free Dirac light-cone spinor of the quark and antiquark, respectively (see Appendix A).

For simplicity, in this study we will consider only the quark contribution to TMDs, ignoring the contribution from gauge fields and therefore reducing the gauge links in eq. (1) to the identity. As a consequence, we will not be able to discuss the T-odd TMDs, which vanish identically in the absence of gauge-field degrees of freedom. Furthermore, we decompose the correlator (1) into the different quark flavour contributions

$$\Phi = \sum_q \Phi_q. \tag{9}$$

Following the lines of refs. [73-75], we obtain at twist-two level

$$\Phi_q^{[\Gamma]}(x, \boldsymbol{k}_\perp, \boldsymbol{S}) = \frac{1}{\mathcal{N}} \langle P, \boldsymbol{S}| \sum_{\lambda'\lambda} q_{\lambda'}^{\dagger}\left(\tilde{k}\right) q_{\lambda}\left(\tilde{k}\right) M^{[\Gamma]\lambda'\lambda} |P, \boldsymbol{S}\rangle, \tag{10}$$

where $\mathcal{N} = [2x(2\pi)^3]^2\delta^{(3)}(\mathbf{0})$ and $M^{[\Gamma]\lambda'\lambda} = \overline{u}_{LC}(k,\lambda')\Gamma u_{LC}(k,\lambda)/2k^+$. As a result, using (3)–(5), the quark contribution to the T-even TMDs is given by

$$f_1^q(x, \boldsymbol{k}_\perp^2) = \langle P, \Lambda | V^q\left(\tilde{k}\right)|P, \Lambda\rangle, \tag{11}$$

$$\Lambda\, g_{1L}^q(x, \boldsymbol{k}_\perp^2) = \langle P, \Lambda | A^q\left(\tilde{k}\right)|P, \Lambda\rangle, \tag{12}$$

$$\frac{\boldsymbol{k}_\perp \cdot \boldsymbol{S}_\perp}{M}\, g_{1T}^q(x, \boldsymbol{k}_\perp^2) = \langle P, S_\perp | A^q\left(\tilde{k}\right)|P, S_\perp\rangle, \tag{13}$$

$$\Lambda\, \frac{\boldsymbol{k}_\perp}{M}\, h_{1L}^{\perp q}(x, \boldsymbol{k}_\perp^2) = \frac{1}{2}\sum_{\Lambda} \mathrm{sign}\,(\Lambda)\langle P, \Lambda | \boldsymbol{T}_\perp^q\left(\tilde{k}\right)|P, \Lambda\rangle, \tag{14}$$

$$\boldsymbol{S}_\perp h_{1T}^q(x, \boldsymbol{k}_\perp^2) + \frac{\boldsymbol{k}_\perp \cdot \boldsymbol{S}_\perp}{M}\frac{\boldsymbol{k}_\perp}{M} h_{1T}^{\perp q}(x, \boldsymbol{k}_\perp^2) = \frac{1}{2}\sum_{S_\perp} \mathrm{sign}(S_\perp)\langle P, S_\perp | \boldsymbol{T}_\perp^q\left(\tilde{k}\right)|P, S_\perp\rangle, \tag{15}$$

where the quark operators V^q, A^q, and $\boldsymbol{T}_\perp^q$ are defined as

$$V^q\left(\tilde{k}\right) = \sum_\lambda q_\lambda^\dagger\left(\tilde{k}\right) q_\lambda\left(\tilde{k}\right), \tag{16}$$

$$A^q\left(\tilde{k}\right) = \sum_\lambda \mathrm{sgn}(\lambda) q_\lambda^\dagger\left(\tilde{k}\right) q_\lambda\left(\tilde{k}\right), \tag{17}$$

$$T_R^q\left(\tilde{k}\right) = \left[T_L^q\left(\tilde{k}\right)\right]^\dagger = 2q_+^\dagger\left(\tilde{k}\right) q_-\left(\tilde{k}\right), \tag{18}$$

with $T^q_{R,L} = T^q_x \pm i T^q_y$. The quark operators V^q and A^q have a probabilistic interpretation since they are written just in terms of number operators $N^q_\lambda = q^\dagger_\lambda(\tilde{k}) q_\lambda(\tilde{k})$. The operator $\boldsymbol{T}^q_\perp$ has also a probabilistic interpretation but only when written in terms of transversely polarized operators

$$\boldsymbol{s}_\perp \cdot \boldsymbol{T}^q_\perp = \sum_{s_\perp} \mathrm{sgn}(s_\perp) q^\dagger_{s_\perp}(\tilde{k}) q_{s_\perp}(\tilde{k}), \tag{19}$$

where for a generic direction $\boldsymbol{s} = (\sin\theta_s \cos\phi_s, \sin\theta_s \sin\phi_s, \cos\theta_s)$, the creation operators for a polarized quark can be expressed in terms of creation operators for a longitudinally polarized quark as

$$\left(q^\dagger_{+\boldsymbol{s}},\ q^\dagger_{-\boldsymbol{s}}\right) = \left(q^\dagger_+,\ q^\dagger_-\right) u(\theta_s, \phi_s), \tag{20}$$

where the $SU(2)$ rotation matrix $u(\theta, \phi)$ is given by

$$u(\theta, \phi) = \begin{pmatrix} \cos\frac{\theta}{2}\, e^{-i\phi/2} & -\sin\frac{\theta}{2}\, e^{-i\phi/2} \\ \sin\frac{\theta}{2}\, e^{i\phi/2} & \cos\frac{\theta}{2}\, e^{i\phi/2} \end{pmatrix}. \tag{21}$$

The operators $V^q(\tilde{k})$, $A^q(\tilde{k})$, and $\boldsymbol{s}_\perp \cdot \boldsymbol{T}^q_\perp(\tilde{k})$ give the number, the effective longitudinal polarization, and the effective transverse polarization of quarks with flavour q and light-cone momentum $\tilde{k}$, respectively.

We can further disentangle (15) by choosing appropriate target and quark polarizations

$$\begin{aligned} &h^q_1(x, \boldsymbol{k}^2_\perp) = \\ &\frac{1}{4}\left[\sum_{S_x} \mathrm{sign}\,(S_x) \langle P, S_x | T^q_x \left(\tilde{k}\right) | P, S_x\rangle + \sum_{S_y} \mathrm{sign}\,(S_y) \langle P, S_y | T^q_y \left(\tilde{k}\right) | P, S_y\rangle\right], \end{aligned} \tag{22}$$

$$\begin{aligned} &\frac{k^2_x - k^2_y}{M^2}\, h^{\perp q}_{1T}(x, \boldsymbol{k}^2_\perp) = \\ &\frac{1}{2}\left[\sum_{S_x} \mathrm{sign}\,(S_x) \langle P, S_x | T^q_x \left(\tilde{k}\right) | P, S_x\rangle - \sum_{S_y} \mathrm{sign}\,(S_y) \langle P, S_y | T^q_y \left(\tilde{k}\right) | P, S_y\rangle\right], \end{aligned} \tag{23}$$

or

$$\begin{aligned} &\frac{k_x k_y}{M^2}\, h^{\perp q}_{1T}(x, \boldsymbol{k}^2_\perp) = \\ &\frac{1}{2}\sum_{S_x} \mathrm{sign}\,(S_x) \langle P, S_x | T^q_y \left(\tilde{k}\right) | P, S_x\rangle = \frac{1}{2}\sum_{S_y} \mathrm{sign}\,(S_y) \langle P, S_y | T^q_x \left(\tilde{k}\right) | P, S_y\rangle, \end{aligned} \tag{24}$$

Table I. – *Relations between the* 8 *leading-twist TMDs and helicity amplitudes. The table can be used to obtain the TMDs as functions of the helicity amplitudes as well as the inverse relation. The entries in the table give the coefficients in the linear combination which relates the two sets in the first column and in the first row. The helicity amplitudes are also classified in terms of the transfer of orbital angular momentum* Δl_z *between the initial and final state.*

	$\Delta l_z = 0$			$\Delta l_z = +1$				$\Delta l_z = +2$
	$\Phi^q_{++,++}$	$\Phi^q_{+-,+-}$	$\Phi^q_{++,--}$	$\Phi^q_{++,-+}$	$\Phi^q_{+-,--}$	$\Phi^q_{--,-+}$	$\Phi^q_{+-,++}$	$\Phi^q_{+-,-+}$
f_1^q	1	1	·	·	·	·	·	·
g_{1L}^q	1	-1	·	·	·	·	·	·
h_1^q	·	·	1	·	·	·	·	·
$f_{1T}^{\perp q}$	·	·	·	$-i\frac{Mk_R}{\boldsymbol{k}_\perp^2}$	$-i\frac{Mk_R}{\boldsymbol{k}_\perp^2}$	·	·	·
g_{1T}^q	·	·	·	$\frac{Mk_R}{\boldsymbol{k}_\perp^2}$	$-\frac{Mk_R}{\boldsymbol{k}_\perp^2}$	·	·	·
$h_1^{\perp q}$	·	·	·	·	·	$-i\frac{Mk_R}{\boldsymbol{k}_\perp^2}$	$-i\frac{Mk_R}{\boldsymbol{k}_\perp^2}$	·
$h_{1L}^{\perp q}$	·	·	·	·	·	$-\frac{Mk_R}{\boldsymbol{k}_\perp^2}$	$\frac{Mk_R}{\boldsymbol{k}_\perp^2}$	·
$h_{1T}^{\perp q}$	·	·	·	·	·	·	·	$2\left(\frac{Mk_R}{\boldsymbol{k}_\perp^2}\right)^2$

where the nucleon polarization state $|P, \boldsymbol{S}\rangle$ in a generic direction $\boldsymbol{S} = (\sin\theta_S \cos\phi_S, \sin\theta_S \sin\phi_S, \cos\theta_S)$ can be written in terms of longitudinally polarized states $|P, \Lambda\rangle$ as

$$(|P, +\boldsymbol{S}\rangle,\ |P, -\boldsymbol{S}\rangle) = (|P, +\rangle,\ |P, -\rangle) u(\theta_S, \phi_S). \tag{25}$$

In the literature, one often represents correlators in terms of helicity amplitudes which treat in a symmetric way both quark and target polarizations:

$$\Phi^q_{\Lambda'\lambda',\Lambda\lambda}(x, \boldsymbol{k}_\perp) = \frac{1}{\mathcal{N}} \langle P, \Lambda'| q^\dagger_{\lambda'}\left(\tilde{k}\right) q_\lambda\left(\tilde{k}\right) |P, \Lambda\rangle. \tag{26}$$

Thanks to light-cone parity invariance, the helicity amplitudes are not all independent and are constrained by the following relation:

$$\Phi^q_{\Lambda'\lambda',\Lambda\lambda}\left(\tilde{k}\right) = \Phi^q_{-\Lambda'-\lambda',-\Lambda-\lambda}\left(\tilde{k}_P\right), \tag{27}$$

where $\tilde{k}_P = (x, -k_x, k_y)$. From the definitions in eqs. (11)–(15) it follows that it is possible to express each TMD as a linear combination of helicity amplitudes as described in table I. In particular we note that each TMD involves combinations of helicity amplitudes with a definite value of orbital angular momentum transfer Δl_z between the initial and final state. This is a consequence of the conservation of the total angular momentum which gives the constraint $\Delta l_z = (\Delta\Lambda - \Delta\lambda)/2$, with $\Delta\Lambda = \Lambda' - \Lambda$ and analogously $\Delta\lambda = \lambda' - \lambda$.

We can collect the information encoded in table I by introducing the following matrix form:

$$\tag{28} \Phi^q_{\Lambda'\lambda',\Lambda\lambda} = \begin{pmatrix} \frac{1}{2}\left(f_1^q + g_{1L}^q\right) & -\frac{k_R}{2M}\left(ih_1^{\perp q} - h_{1L}^{\perp q}\right) & \frac{k_L}{2M}\left(if_{1T}^{\perp q} + g_{1T}^q\right) & h_1^q \\ \frac{k_L}{2M}\left(ih_1^{\perp q} + h_{1L}^{\perp q}\right) & \frac{1}{2}\left(f_1^q - g_{1L}^q\right) & \frac{k_L^2}{2M^2}h_{1T}^{\perp q} & \frac{k_L}{2M}\left(if_{1T}^{\perp q} - g_{1T}^q\right) \\ -\frac{k_R}{2M}\left(if_{1T}^{\perp q} - g_{1T}^q\right) & \frac{k_R^2}{2M^2}h_{1T}^{\perp q} & \frac{1}{2}\left(f_1^q - g_{1L}^q\right) & -\frac{k_R}{2M}\left(ih_1^{\perp q} + h_{1L}^{\perp q}\right) \\ h_1^q & -\frac{k_R}{2M}\left(if_{1T}^{\perp q} + g_{1T}^q\right) & \frac{k_L}{2M}\left(ih_1^{\perp q} - h_{1L}^{\perp q}\right) & \frac{1}{2}\left(f_1^q + g_{1L}^q\right) \end{pmatrix},$$

where the entries in the rows correspond to $(\Lambda'\lambda') = (++), (+-), (-+), (--)$ and the entries in the column are likewise $(\Lambda\lambda) = (++), (+-), (-+), (--)$.

Alternatively, we can represent the quark correlator (10) in the four-component basis. There are only four twist-two Dirac structures $\Gamma_{\text{twist-2}} = \{\gamma^+, i\sigma^{1+}\gamma_5, i\sigma^{2+}\gamma_5, \gamma^+\gamma_5\}$, corresponding to the four kinds of transition the light-cone helicity of the active quark can undergo (see, *e.g.*, [76-78])

$$\tag{29} M^{[\gamma^+]\lambda'\lambda} = \delta^{\lambda'\lambda}, \qquad M^{[i\sigma^{j+}\gamma_5]\lambda'\lambda} = (\sigma_j)^{\lambda'\lambda}, \qquad M^{[\gamma^+\gamma_5]\lambda'\lambda} = (\sigma_3)^{\lambda'\lambda}$$

with σ_i the three Pauli matrices. For further convenience, we associate a four-component vector(²) to every quantity with superscript Γ

$$\tag{30} a^{[\Gamma]} \mapsto a^\nu = \left(a^0, a^1, a^2, a^3\right) \equiv \left(a^{[\gamma^+]}, a^{[i\sigma^{1+}\gamma_5]}, a^{[i\sigma^{2+}\gamma_5]}, a^{[\gamma^+\gamma_5]}\right).$$

With this notation, the correspondence (29) takes the simple form

$$\tag{31} M^{\nu\lambda'\lambda} = (\bar{\sigma}^\nu)^{\lambda'\lambda},$$

where $\bar{\sigma}^\nu = (\mathbb{1}, \vec{\sigma})$. The symbols $\bar{\sigma}^\mu$ and σ_μ satisfy the relations

$$\tag{32} \frac{1}{2}\,(\bar{\sigma}^\mu)^{\lambda'\lambda}(\sigma_\mu)_{\tau\tau'} = \delta^{\lambda'}_{\tau'}\delta^{\lambda}_{\tau}, \qquad \frac{1}{2}\,\mathrm{Tr}\,[\bar{\sigma}^\mu\sigma_\nu] = \frac{1}{2}\sum_{\lambda'\lambda}(\bar{\sigma}^\mu)^{\lambda'\lambda}(\sigma_\nu)_{\lambda\lambda'} = \delta^\mu_\nu.$$

One can think of $\bar{\sigma}^{\nu\lambda'\lambda} \equiv (\bar{\sigma}^\nu)^{\lambda'\lambda}$ as the matrix of a mere change of basis, the one being labeled by the couple $\lambda\lambda'$ and the other by ν

$$\tag{33} a^\nu = \sum_{\lambda'\lambda} \bar{\sigma}^{\nu\lambda'\lambda}\, a_{\lambda\lambda'}.$$

(²) Note this is *not* a Lorentz four-vector but Einstein's summation convention still applies.

In this basis, we can introduce the tensor correlator $\Phi_q^{\mu\nu}(x,\boldsymbol{k}_\perp)$ which is related to helicity amplitudes as follows:

$$(34)\qquad \Phi_q^{\mu\nu} = \frac{1}{2}\sum_{\Lambda'\Lambda\lambda'\lambda} (\bar{\sigma}^\mu)^{\Lambda\Lambda'}(\bar{\sigma}^\nu)^{\lambda'\lambda}\,\Phi^q_{\Lambda'\lambda',\Lambda\lambda}, \qquad \Phi^q_{\Lambda'\lambda',\Lambda\lambda} = \frac{1}{2}\,\Phi_q^{\mu\nu}(\sigma_\mu)_{\Lambda'\Lambda}(\sigma_\nu)_{\lambda\lambda'}.$$

The tensor correlator is then given by the following combinations of TMDs:

$$(35)\qquad \Phi_q^{\mu\nu} = \begin{pmatrix} f_1^q & \frac{k_y}{M}\,h_1^{\perp q} & -\frac{k_x}{M}\,h_1^{\perp q} & 0 \\ \frac{k_y}{M}\,f_{1T}^{\perp q} & h_1^q + \frac{k_x^2-k_y^2}{2M^2}\,h_{1T}^{\perp q} & \frac{k_xk_y}{M^2}\,h_{1T}^{\perp q} & \frac{k_x}{M}\,g_{1T}^q \\ -\frac{k_x}{M}\,f_{1T}^{\perp q} & \frac{k_xk_y}{M^2}\,h_{1T}^{\perp q} & h_1^q - \frac{k_x^2-k_y^2}{2M^2}\,h_{1T}^{\perp q} & \frac{k_y}{M}\,g_{1T}^q \\ 0 & \frac{k_x}{M}\,h_{1L}^{\perp q} & \frac{k_y}{M}\,h_{1L}^{\perp q} & g_{1L}^q \end{pmatrix}$$

$$= \begin{pmatrix} f_1^q & \frac{k_y}{M}\,h_1^{\perp q} & -\frac{k_x}{M}\,h_1^{\perp q} & 0 \\ \frac{k_y}{M}\,f_{1T}^{\perp q} & h_{1T}^{+q}\,\hat{k}_x^2 + h_{1T}^{-q}\,\hat{k}_y^2 & \left(h_{1T}^{+q} - h_{1T}^{-q}\right)\hat{k}_x\hat{k}_y & \frac{k_x}{M}\,g_{1T}^q \\ -\frac{k_x}{M}\,f_{1T}^{\perp q} & \left(h_{1T}^{+q} - h_{1T}^{-q}\right)\hat{k}_x\hat{k}_y & h_{1T}^{-q}\,\hat{k}_x^2 + h_{1T}^{+q}\,\hat{k}_y^2 & \frac{k_y}{M}\,g_{1T}^q \\ 0 & \frac{k_x}{M}\,h_{1L}^{\perp q} & \frac{k_y}{M}\,h_{1L}^{\perp q} & g_{1L}^q \end{pmatrix},$$

where we introduced the notations $h_{1T}^{\pm q} = h_1^q \pm \frac{\boldsymbol{k}_\perp^2}{2M^2}\,h_{1T}^{\perp q}$ and $\hat{k}_i = k_i/k_\perp$ with $k_\perp = |\boldsymbol{k}_\perp|$. The component Φ_q^{00} gives the density of quarks in the target irrespective of any polarization, *i.e.* the density of unpolarized quarks in the unpolarized target. The components Φ_q^{0j} give the net density of quarks with light-cone polarization in the direction $\boldsymbol{e}_j$ in the unpolarized target, while the components Φ_q^{i0} give the net density of unpolarized quarks in the target with light-cone polarization in the direction $\boldsymbol{e}_i$. Finally, the components Φ_q^{ij} give the net density of quarks with light-cone polarization in the direction $\boldsymbol{e}_j$ in the target with light-cone polarization in the direction $\boldsymbol{e}_i$. The density of quarks with definite light-cone polarization in the direction $\boldsymbol{s}$ inside the target with definite light-cone polarization in the direction $\boldsymbol{S}$ is then obviously given by $\Phi_q(x,\boldsymbol{k}_\perp,\boldsymbol{S},\boldsymbol{s}) = \frac{1}{2}\,\bar{S}_\mu\Phi_q^{\mu\nu}\bar{s}_\nu$, where we have introduced the four-component vectors $\bar{S}_\mu = (1,\boldsymbol{S})$ and $\bar{s}_\nu = (1,\boldsymbol{s})$.

3. – Model relations

In QCD, the eight TMDs are all independent. It appeared however in a large panel of low-energy models that relations among some TMDs exist. At twist-two level, there are three flavour-independent relations(3), two are linear and one is quadratic in the TMDs

$$g_{1L}^q - \left[h_1^q + \frac{\boldsymbol{k}_\perp^2}{2M^2}\, h_{1T}^{\perp q} \right] = 0, \tag{36}$$

$$g_{1T}^q + h_{1L}^{\perp q} = 0, \tag{37}$$

$$\left(g_{1T}^q\right)^2 + 2h_1^q\, h_{1T}^{\perp q} = 0. \tag{38}$$

A further flavour-dependent relation involves both polarized and unpolarized TMDs

$$\mathcal{D}^q f_1^q + g_{1L}^q = 2h_1^q, \tag{39}$$

where, for a proton target, the flavour factors with $q = u, d$ are given by $\mathcal{D}^u = \frac{2}{3}$ and $\mathcal{D}^d = -\frac{1}{3}$. As discussed in ref. [48], at variance with relations (36)–(38), the flavour dependence in relation (39) requires specific assumptions for the spin-isospin structure of the nucleon state, like $SU(6)$ spin-flavour symmetry.

A discussion on how general these relations are can be found in ref. [48]. Let us just mention that they were observed in the bag model [41, 48], light-cone constituent quark models [75], some quark-diquark models [28-39], the covariant parton model [37] and more recently in the light-cone version of the chiral quark-soliton model [23]. Note however that there also exist models where the relations are not satisfied, like in some versions of the spectator model [47] and the quark-target model [51].

As already emphasized, the model relations (36)–(39) are not expected to hold identically in QCD, since the TMDs in these relations follow different evolution patterns. This implies that even if the relations are satisfied at some (low) scale, they would not hold anymore for other (higher) scales. The interest in these relations is therefore purely phenomenological. Experiments provide more and more data on observables related to TMDs, but need inputs from educated models and parametrizations for the extraction of these distributions. It is therefore particularly interesting to see to what extent relations (36)–(39) can be useful as *approximate* relations, which provide simplified and intuitive notions for the interpretation of the data. Note that some preliminary calculations in lattice QCD give indications that relation (37) may indeed be approximately satisfied [79-81].

Using two different approaches, we show in the next sections that the flavour-independent relations (36)–(38) can easily be derived, once the following assumptions are made:

1) the probed quark behaves as if it does not interact directly with the other partons (*i.e.* one works within the standard impulse approximation) and there are no explicit gluons;

---

(3) Other expressions can be found in the literature, but are just combinations of relations (36)–(38).

2) the quark light-cone and canonical polarizations are related by a rotation with axis orthogonal to both light-cone and $\hat{k}_\perp$ directions;

3) the target has spherical symmetry in the canonical-spin basis.

From these assumptions, one realizes that the flavour-independent relations have essentially a geometrical origin, as was already suspected in the context of the bag model almost a decade ago [82]. We note however that the spherical symmetry is a sufficient but not necessary condition for the validity of the individual flavour-independent relations. As discussed in the following section, a subset of relations can be derived using less restrictive conditions, like axial symmetry about a specific direction.

For the flavour-dependent relation (39), we need a further condition for the spin-flavour dependent part of the nucleon wave function. Specifically, we require

4) $SU(6)$ spin-flavour symmetry of the wave function.

As shown in sect. **6**, it is found that all the models satisfying the relations also satisfy the above conditions. We are not aware of any model calculation which satisfies some or all the three flavour-independent relations and at the same time breaks at least one of the conditions 1)-3). However, this is not *a priori* excluded.

4. – Amplitude approach

The first derivation of the TMD relations stays at the level of the amplitudes. As we have seen, the TMDs can be expressed in simple terms using light-cone polarization. On the other hand, rotational symmetry is easier to handle in terms of canonical polarization, which is the natural one in the instant form. We therefore write the TMDs in the canonical-spin basis, and then impose spherical symmetry. But before that, we need to know how to connect light-cone helicity to canonical spin.

4˙1. *Connection between light-cone helicity and canonical spin.* – Relating in general light-cone helicity with canonical spin is usually quite complicated, as the dynamics is involved. Fortunately, the common approach in quark models is to assume that the target can be described by quarks without mutual interactions. In this case the connection simply reduces to a rotation in polarization space with axis orthogonal to both $\hat{k}_\perp$ and $\boldsymbol{e}_z$ directions. The quark creation operator with canonical spin σ can then be written in terms of quark creation operators with light-cone helicity λ as follows:

$$q^\dagger_\sigma = \sum_\lambda D^{(1/2)*}_{\sigma\lambda}\, q^\dagger_\lambda \qquad \text{with} \qquad D^{(1/2)*}_{\sigma\lambda} = \begin{pmatrix} \cos\frac{\theta}{2} & -\hat{k}_R \sin\frac{\theta}{2} \\ \hat{k}_L \sin\frac{\theta}{2} & \cos\frac{\theta}{2} \end{pmatrix}. \tag{40}$$

Note that the rotation does not depend on the quark flavour. The angle θ between light-cone and canonical polarizations is usually a complicated function of the quark momentum k and is specific to each model. It contains part of the model dynamics. The only general property is that $\theta \to 0$ as $k_\perp \to 0$. Due to our choice of reference frame where the target has no transverse momentum, the light-cone helicity and canonical spin of the target can be identified, at variance with the quark polarizations.

4˙2. *TMDs in canonical-spin basis.* – The four-component notation introduced in subsect. **2**˙2 is very convenient for discussing the rotation between canonical spin and light-cone helicity at the amplitude level. Since the light-cone helicity and canonical spin of the target can be identified in our choice of reference frame, we expect the canonical tensor correlator $\Phi^{\mu\nu}_{Cq}$ to be related to the light-cone one in eq. (35) as follows:

$$\Phi^{\mu\nu}_{Cq} = \Phi^{\mu\rho}_{q}\, O_{\rho}^{\ \nu}, \tag{41}$$

with O some orthogonal matrix $O^T O = \mathbb{1}$ representing the rotation at the amplitude level. From eqs. (26), (34), (32) and (40) we find that the orthogonal matrix is given by

$$\begin{aligned} O_{\rho}^{\ \nu} &= \frac{1}{2}\,\mathrm{Tr}\left[D^{(1/2)}\sigma_\rho D^{(1/2)\dagger}\bar{\sigma}^\nu\right] \\ &= \frac{1}{2}\sum_{\sigma'\sigma\lambda'\lambda} D^{(1/2)}_{\sigma\lambda}\,(\sigma_\rho)_{\lambda\lambda'}\,D^{(1/2)*}_{\sigma'\lambda'}\,(\bar{\sigma}^\nu)^{\sigma'\sigma} \\ &= \begin{pmatrix} 1 & 0 & 0 & 0 \\ 0 & \hat{k}_y^2+\hat{k}_x^2\cos\theta & -\hat{k}_x\hat{k}_y\,(1-\cos\theta) & -\hat{k}_x\sin\theta \\ 0 & -\hat{k}_x\hat{k}_y\,(1-\cos\theta) & \hat{k}_x^2+\hat{k}_y^2\cos\theta & -\hat{k}_y\sin\theta \\ 0 & \hat{k}_x\sin\theta & \hat{k}_y\sin\theta & \cos\theta \end{pmatrix}. \end{aligned} \tag{42}$$

The canonical tensor correlator then takes the form

$$\Phi^{\mu\nu}_{Cq} = \begin{pmatrix} f_1^q & \frac{k_y}{M}\,h_1^{\perp q} & -\frac{k_x}{M}h_1^{\perp q} & 0 \\ \frac{k_y}{M}f_{1T}^{\perp q} & \mathfrak{h}_{1T}^{+q}\hat{k}_x^2+h_{1T}^{-q}\hat{k}_y^2 & \left(\mathfrak{h}_{1T}^{+q}-h_{1T}^{-q}\right)\hat{k}_x\hat{k}_y & \frac{k_x}{M}\mathfrak{g}_{1T}^q \\ -\frac{k_x}{M}f_{1T}^{\perp q} & \left(\mathfrak{h}_{1T}^{+q}-h_{1T}^{-q}\right)\hat{k}_x\hat{k}_y & h_{1T}^{-q}\hat{k}_x^2+\mathfrak{h}_{1T}^{+q}\hat{k}_y^2 & \frac{k_y}{M}\mathfrak{g}_{1T}^q \\ 0 & \frac{k_x}{M}\mathfrak{h}_{1L}^{\perp q} & \frac{k_y}{M}\mathfrak{h}_{1L}^{\perp q} & \mathfrak{g}_{1L}^q \end{pmatrix}, \tag{43}$$

where we introduced the notations

$$\begin{pmatrix} \mathfrak{g}_{1L}^q \\ \frac{k_\perp}{M}\,\mathfrak{h}_{1L}^{\perp q} \end{pmatrix} = \begin{pmatrix} \cos\theta & -\sin\theta \\ \sin\theta & \cos\theta \end{pmatrix} \begin{pmatrix} g_{1L}^q \\ \frac{k_\perp}{M}\,h_{1L}^{\perp q} \end{pmatrix}, \tag{44}$$

$$\begin{pmatrix} \frac{k_\perp}{M}\,\mathfrak{g}_{1T}^q \\ \mathfrak{h}_{1T}^{+q} \end{pmatrix} = \begin{pmatrix} \cos\theta & -\sin\theta \\ \sin\theta & \cos\theta \end{pmatrix} \begin{pmatrix} \frac{k_\perp}{M}\,g_{1T}^q \\ h_{1T}^{+q} \end{pmatrix}. \tag{45}$$

Comparing eq. (43) with eq. (35), we observe that the multipole structure is conserved under rotation (41). The rotation from light-cone to canonical polarizations affects only some of the multipole magnitudes, see eqs. (44) and (45).

Note that the orientation of the axes in the transverse plane has been fixed arbitrarily. There is however a privileged direction given by the active quark transverse momentum $\boldsymbol{k}_\perp$. Choosing the orientation of transverse axes so that either $\boldsymbol{k}_\perp = k_\perp\, \boldsymbol{e}_x$ or $\boldsymbol{k}_\perp = k_\perp\, \boldsymbol{e}_y$ simplifies the transformation, as it eliminates the cumbersome factors $\hat{k}_x$ and $\hat{k}_y$ in eqs. (42) and (43). Choosing, *e.g*, the second option, the orthogonal matrix of eq. (42) reduces to

$$O_\rho{}^\nu = \begin{pmatrix} 1 & 0 & 0 & 0 \\ 0 & 1 & 0 & 0 \\ 0 & 0 & \cos\theta & -\sin\theta \\ 0 & 0 & \sin\theta & \cos\theta \end{pmatrix}, \tag{46}$$

and the light-cone and canonical tensor correlators take the following simpler forms:

$$\Phi_q^{\mu\nu} = \begin{pmatrix} f_1^q & \frac{k_\perp}{M}\, h_1^{\perp q} & 0 & 0 \\ \frac{k_\perp}{M}\, f_{1T}^{\perp q} & h_{1T}^{-q} & 0 & 0 \\ 0 & 0 & h_{1T}^{+q} & \frac{k_\perp}{M}\, g_{1T}^q \\ 0 & 0 & \frac{k_\perp}{M}\, h_{1L}^{\perp q} & g_{1L}^q \end{pmatrix}, \tag{47}$$

$$\Phi_{Cq}^{\mu\nu} = \begin{pmatrix} f_1^q & \frac{k_\perp}{M}\, h_1^{\perp q} & 0 & 0 \\ \frac{k_\perp}{M}\, f_{1T}^{\perp q} & h_{1T}^{-q} & 0 & 0 \\ 0 & 0 & \mathfrak{h}_{1T}^{+q} & \frac{k_\perp}{M}\, \mathfrak{g}_{1T}^q \\ 0 & 0 & \frac{k_\perp}{M}\, \mathfrak{h}_{1L}^{\perp q} & \mathfrak{g}_{1L}^q \end{pmatrix}. \tag{48}$$

Playing a little bit with eqs. (44) and (45), we find

$$\begin{pmatrix} \frac{k_\perp}{M}\left(g_{1T}^q + h_{1L}^{\perp q}\right) \\ g_{1L}^q - h_{1T}^{+q} \end{pmatrix} = \begin{pmatrix} \cos\theta & -\sin\theta \\ \sin\theta & \cos\theta \end{pmatrix} \begin{pmatrix} \frac{k_\perp}{M}\left(\mathfrak{g}_{1T}^q + \mathfrak{h}_{1L}^{\perp q}\right) \\ \mathfrak{g}_{1L}^q - \mathfrak{h}_{1T}^{+q} \end{pmatrix}, \tag{49}$$

and three expressions invariant under rotation (41),

$$\left(\frac{k_\perp}{M}\, g_{1T}^q\right)^2 + \left(h_{1T}^{+q}\right)^2 = \left(\frac{k_\perp}{M}\, \mathfrak{g}_{1T}^q\right)^2 + \left(\mathfrak{h}_{1T}^{+q}\right)^2, \tag{50}$$

$$\left(g_{1L}^q\right)^2 + \left(\frac{k_\perp}{M}\, h_{1L}^{\perp q}\right)^2 = \left(\mathfrak{g}_{1L}^q\right)^2 + \left(\frac{k_\perp}{M}\, \mathfrak{h}_{1L}^{\perp q}\right)^2, \tag{51}$$

$$g_{1L}^q\, g_{1T}^q + h_{1L}^{\perp q}\, h_{1T}^{+q} = \mathfrak{g}_{1L}^q\, \mathfrak{g}_{1T}^q + \mathfrak{h}_{1L}^{\perp q}\, \mathfrak{h}_{1T}^{+q}. \tag{52}$$

These three invariant expressions have a simple geometric interpretation. The three-component vector $\sum_i S^i \Phi_q^{ij} \equiv \pi_{\boldsymbol{S}}^{qj}$ represents the net light-cone polarization of a quark with three-momentum $(xP^+, \boldsymbol{k}_\perp)$ and flavour q in a target with net polarization in the

$\boldsymbol{S}$-direction. From eq. (41), we see that the vector $\boldsymbol{\pi}^q_{C\boldsymbol{S}}$ representing the net canonical polarization of the quark is obtained by a rotation of $\boldsymbol{\pi}^q_{\boldsymbol{S}}$

$$\pi^{qj}_{C\boldsymbol{S}} = \sum_k \pi^{qk}_{\boldsymbol{S}}\, O^{kj}. \tag{53}$$

It follows automatically that $\boldsymbol{\pi}^q_{\boldsymbol{S}} \cdot \boldsymbol{\pi}^q_{\boldsymbol{S}'}$ is invariant under rotation (41),

$$\boldsymbol{\pi}^q_{\boldsymbol{S}} \cdot \boldsymbol{\pi}^q_{\boldsymbol{S}'} = \boldsymbol{\pi}^q_{C\boldsymbol{S}} \cdot \boldsymbol{\pi}^q_{C\boldsymbol{S}'}. \tag{54}$$

Expressions (50) and (51) are obtained from (54) for the cases $\boldsymbol{S} = \boldsymbol{S}' = \boldsymbol{e}_\perp$ and $\boldsymbol{S} = \boldsymbol{S}' = \boldsymbol{e}_z$, respectively. They just express the fact that the magnitude of quark net polarization is the same in the light-cone helicity and canonical-spin bases. Expression (52) is obtained for the case $\boldsymbol{S} = \boldsymbol{e}_\perp$ and $\boldsymbol{S}' = \boldsymbol{e}_z$. All the remaining cases do not lead to new independent expressions.

4·3. *Spherical symmetry.* – We are now ready to discuss the implications of spherical symmetry in the canonical-spin basis. Spherical symmetry means that the canonical tensor correlator has to be invariant $O^T_R \Phi_{Cq} O_R = \Phi_{Cq}$ under any spatial rotation $O_R = \left(\begin{smallmatrix} 1 & 0 \\ 0 & R \end{smallmatrix}\right)$ with R the ordinary 3×3 rotation matrix. It is equivalent to the statement that the tensor correlator has to commute with all the elements of the rotation group $\Phi_{Cq} O_R = O_R \Phi_{Cq}$. As a result of Schur's lemma, the canonical tensor correlator must have the following structure:

$$\Phi^{\mu\nu}_{Cq} = \begin{pmatrix} A^q & 0 & 0 & 0 \\ 0 & B^q & 0 & 0 \\ 0 & 0 & B^q & 0 \\ 0 & 0 & 0 & B^q \end{pmatrix}. \tag{55}$$

Comparing this with eqs. (43) or (48), we conclude that spherical symmetry implies

$$f^q_1 = A^q, \tag{56}$$

$$\mathfrak{g}^q_{1L} = \mathfrak{h}^{+q}_{1T} = h^{-q}_{1T} = B^q, \tag{57}$$

$$\mathfrak{g}^q_{1T} = \mathfrak{h}^{\perp q}_{1L} = f^{\perp q}_{1T} = h^{\perp q}_1 = 0. \tag{58}$$

Clearly, only the monopole structures in the canonical-spin basis are allowed to survive. Furthermore, the Sivers and Boer-Mulders functions $f^{\perp q}_{1T}$ and $h^{\perp q}_1$ vanish identically, as expected from the fact that we are neglecting gauge-field degrees of freedom.

Note however that the monopole structures in the canonical-spin basis generate higher multipole structures in the light-cone helicity basis. It follows that spherical symmetry imposes some relations among the multipole structures in the light-cone helicity basis, and therefore among the TMDs. Inserting constraints (57) and (58) into eq. (49), we automatically obtain the linear relations

$$\begin{pmatrix} \frac{k_\perp}{M}\left(g^q_{1T}+h^{\perp q}_{1L}\right) \\ g^q_{1L}-h^{+q}_{1T} \end{pmatrix} = \begin{pmatrix} 0 \\ 0 \end{pmatrix}. \tag{59}$$

Using now the constraints from spherical symmetry in eq. (50), we obtain the quadratic relation (38)

$$0=\left(\frac{k_\perp}{M}\,g^q_{1T}\right)^2+\left(h^{+q}_{1T}\right)^2-\left(h^{-q}_{1T}\right)^2=\frac{\boldsymbol{k}^2_\perp}{M^2}\left[\left(g^q_{1T}\right)^2+2h^q_1\,h^{\perp q}_{1T}\right]. \tag{60}$$

The linear relations (36) and (37) being satisfied, eqs. (51) and (52) do not lead to independent quadratic relations.

We have seen that spherical symmetry is a *sufficient* condition(4) to obtain all three flavour-independent relations. Restricting ourselves to axial symmetries, we find that some of the relations can already be obtained. For example, axial symmetry about $\boldsymbol{e}_z$ alone implies the quadratic relation (38) and

$$g^q_{1L}\,g^q_{1T}+h^{\perp q}_{1L}\,h^{+q}_{1T}=0. \tag{61}$$

Axial symmetry about $\hat{k}_\perp \times \boldsymbol{e}_z$ implies the two linear relations (36) and (37). Relation (61) is naturally also satisfied but is not independent.

5. – Wave function approach

Many quark models are based on a wave function approach. We therefore translate here the derivation of the previous section in the language of 3Q wave functions. The advantage is that we can then also discuss the additional $SU(6)$ spin-flavour symmetry needed for the flavour-dependent relation (39).

5˙1. *Overlap representation of the TMDs on the light cone.* – Restricting ourselves to the 3Q Fock sector, the target state with definite four-momentum $P=[P^+,\frac{M^2}{2P^+},\mathbf{0}_\perp]$

---

(4) From eqs. (49) and (50), one can see that the *minimal* conditions are actually

$$\begin{aligned} \mathfrak{g}^q_{1L}-\mathfrak{h}^{+q}_{1T}&=0,\\ \mathfrak{g}^q_{1T}+\mathfrak{h}^{\perp q}_{1L}&=0,\\ \left(\frac{k_\perp}{M}\,\mathfrak{g}^q_{1T}\right)^2+\left(\mathfrak{h}^{+q}_{1T}\right)^2-\left(h^{-q}_{1T}\right)^2&=0. \end{aligned}$$

They are indeed fulfilled by spherical symmetry, see eqs. (57) and (58).

and light-cone helicity Λ can be written as follows:

$$|P,\Lambda\rangle = \sum_{\lambda_1\lambda_2\lambda_3}\sum_{q_1q_2q_3}\int [\mathrm{d}x]_3\,[\mathrm{d}^2k_\perp]_3\,\psi^{\Lambda;q_1q_2q_3}_{\lambda_1\lambda_2\lambda_3}\left(\tilde{k}_1,\tilde{k}_2,\tilde{k}_3\right)\,\left|\left\{\lambda_i,q_i,\tilde{k}_i\right\}\right\rangle, \tag{62}$$

where $\psi^{\Lambda;q_1q_2q_3}_{\lambda_1\lambda_2\lambda_3}(\tilde{k}_1,\tilde{k}_2,\tilde{k}_3)$ is the three-quark light-cone wave function (3Q LCWF) with λ_i, q_i and $\tilde{k}_i$ referring to the light-cone helicity, flavour and light-cone momentum of quark i, respectively. The total orbital angular momentum of a given component $\psi^{\Lambda}_{\lambda_1\lambda_2\lambda_3}$ is given by the expression $\ell_z = \Lambda-\lambda_1-\lambda_2-\lambda_3$ with $\Lambda,\lambda_i=\pm\frac{1}{2}$. The integration measures in eq. (62) are defined as

$$\begin{aligned}[]
[\mathrm{d}x]_3 &\equiv \left[\prod_{i=1}^{3}\mathrm{d}x_i\right]\delta\left(1-\sum_{i=1}^{3}x_i\right),\\
[\mathrm{d}^2k_\perp]_3 &\equiv \left[\prod_{i=1}^{3}\frac{\mathrm{d}^2k_{i\perp}}{2(2\pi)^3}\right]2(2\pi)^3\,\delta^{(2)}\left(\sum_{i=1}^{3}\boldsymbol{k}_{i\perp}\right).
\end{aligned} \tag{63}$$

Choosing to label the active quark with $i=1$, the TMDs can be obtained by the following overlaps(5) of 3Q LCWFs:

$$f_1^q = \int \mathrm{d}[23]\sum_{\lambda_2\lambda_3}\sum_{q_2q_3}\left[\left|\psi^{+;qq_2q_3}_{+\lambda_2\lambda_3}\right|^2+\left|\psi^{+;qq_2q_3}_{-\lambda_2\lambda_3}\right|^2\right], \tag{64a}$$

$$g_{1L}^q = \int \mathrm{d}[23]\sum_{\lambda_2\lambda_3}\sum_{q_2q_3}\left[\left|\psi^{+;qq_2q_3}_{+\lambda_2\lambda_3}\right|^2-\left|\psi^{+;qq_2q_3}_{-\lambda_2\lambda_3}\right|^2\right], \tag{64b}$$

$$h_1^q = \int \mathrm{d}[23]\sum_{\lambda_2\lambda_3}\sum_{q_2q_3}\left(\psi^{+;qq_2q_3}_{+\lambda_2\lambda_3}\right)^*\psi^{-;qq_2q_3}_{-\lambda_2\lambda_3}, \tag{64c}$$

$$\frac{k_\perp}{M}\,f_{1T}^{\perp q} = \int \mathrm{d}[23]\sum_{\lambda_2\lambda_3}\sum_{q_2q_3}2\,\Im m\left[\hat{k}_R\left(\psi^{+;qq_2q_3}_{+\lambda_2\lambda_3}\right)^*\psi^{-;qq_2q_3}_{+\lambda_2\lambda_3}\right], \tag{64d}$$

$$\frac{k_\perp}{M}\,g_{1T}^{q} = \int \mathrm{d}[23]\sum_{\lambda_2\lambda_3}\sum_{q_2q_3}2\,\Re e\left[\hat{k}_R\left(\psi^{+;qq_2q_3}_{+\lambda_2\lambda_3}\right)^*\psi^{-;qq_2q_3}_{+\lambda_2\lambda_3}\right], \tag{64e}$$

$$\frac{k_\perp}{M}\,h_{1}^{\perp q} = \int \mathrm{d}[23]\sum_{\lambda_2\lambda_3}\sum_{q_2q_3}2\,\Im m\left[\hat{k}_R\left(\psi^{+;qq_2q_3}_{-\lambda_2\lambda_3}\right)^*\psi^{+;qq_2q_3}_{+\lambda_2\lambda_3}\right], \tag{64f}$$

$$\frac{k_\perp}{M}\,h_{1L}^{\perp q} = \int \mathrm{d}[23]\sum_{\lambda_2\lambda_3}\sum_{q_2q_3}2\,\Re e\left[\hat{k}_R\left(\psi^{+;qq_2q_3}_{-\lambda_2\lambda_3}\right)^*\psi^{+;qq_2q_3}_{+\lambda_2\lambda_3}\right], \tag{64g}$$

$$\frac{\boldsymbol{k}_\perp^2}{2M^2}\,h_{1T}^{\perp q} = \int \mathrm{d}[23]\sum_{\lambda_2\lambda_3}\sum_{q_2q_3}\hat{k}_R^2\left(\psi^{+;qq_2q_3}_{-\lambda_2\lambda_3}\right)^*\psi^{-;qq_2q_3}_{+\lambda_2\lambda_3}, \tag{64h}$$

---

(5) In the 3Q approach, the spectator system consists of two quarks. It is straightforward to generalize the expression for helicity amplitudes to any kind of spectator system, as the latter is integrated out.

where we used the notation

$$\text{d}[23] = [\text{d}x]_3\,[\text{d}^2k_\perp]_3\,3\,\delta(x-x_1)\delta^{(2)}(\boldsymbol{k}_\perp - \boldsymbol{k}_{1\perp}). \tag{65}$$

Clearly, the TMDs associated to the monopole structures (f_1^q, g_{1L}^q, h_1^q) are represented by overlaps with no global change of orbital angular momentum $\Delta\ell_z = 0$, the ones associated to the dipole structures $(f_{1T}^{\perp q}, g_{1T}^q, h_1^{\perp q}, h_{1L}^{\perp q})$ involve a change by one unit of orbital angular momentum $|\Delta\ell_z| = 1$ and the one associated to the quadrupole structure $(h_{1T}^{\perp q})$ involves a change by two units of orbital angular momentum $|\Delta\ell_z| = 2$. If one neglects gauge-field degrees of freedom, the brackets in eqs. (64d)–(64g) are real, and one obtains vanishing T-odd TMDs.

5·2. *Overlap representation of the TMDs in the canonical-spin basis.* – Most of the quark models being originally formulated in the instant form, it is more natural to work in the canonical-spin basis instead of the light-cone helicity basis. Since we considered a frame where the target has no transverse momentum, there is no difference between target light-cone and canonical polarizations. Assuming that the quark light-cone helicity and canonical spin are connected by the rotation in eq. (40), the components of the LCWF in the canonical-spin basis $\psi^\Lambda_{\sigma_1\sigma_2\sigma_3}$ (with $\sigma_i = \uparrow,\downarrow$) and in the light-cone helicity basis $\psi^\Lambda_{\lambda_1\lambda_2\lambda_3}$ (with $\lambda_i = \pm$) are related as follows(6):

$$\psi^\Lambda_{\lambda_1\lambda_2\lambda_3} = \sum_{\sigma_1\sigma_2\sigma_3} \psi^\Lambda_{\sigma_1\sigma_2\sigma_3}\, D^{(1/2)*}_{\sigma_1\lambda_1}\, D^{(1/2)*}_{\sigma_2\lambda_2}\, D^{(1/2)*}_{\sigma_3\lambda_3}. \tag{66}$$

The correspondence between the components in the two polarization bases is given in a more explicit form in Appendix B. Since $D^{(1/2)\dagger}D^{(1/2)} = \mathbb{1}$ for the spectator quarks, we find the explicit overlap representations in canonical-spin basis:

$$f_1^q = \int \text{d}[23] \sum_{\sigma_2\sigma_3}\sum_{q_2q_3}\left[\left|\psi^{\uparrow;qq_2q_3}_{\uparrow\sigma_2\sigma_3}\right|^2 + \left|\psi^{\uparrow;qq_2q_3}_{\downarrow\sigma_2\sigma_3}\right|^2\right], \tag{67a}$$

$$\mathfrak{g}_{1L}^q = \int \text{d}[23] \sum_{\sigma_2\sigma_3}\sum_{q_2q_3}\left[\left|\psi^{\uparrow;qq_2q_3}_{\uparrow\sigma_2\sigma_3}\right|^2 - \left|\psi^{\uparrow;qq_2q_3}_{\downarrow\sigma_2\sigma_3}\right|^2\right], \tag{67b}$$

$$\mathfrak{h}_1^q = \int \text{d}[23] \sum_{\sigma_2\sigma_3}\sum_{q_2q_3}\left(\psi^{\uparrow;qq_2q_3}_{\uparrow\sigma_2\sigma_3}\right)^* \psi^{\downarrow;qq_2q_3}_{\downarrow\sigma_2\sigma_3}, \tag{67c}$$

$$\frac{k_\perp}{M}\, f_{1T}^{\perp q} = \int \text{d}[23] \sum_{\sigma_2\sigma_3}\sum_{q_2q_3} 2\,\Im m\left[\hat{k}_R\left(\psi^{\uparrow;qq_2q_3}_{\uparrow\sigma_2\sigma_3}\right)^* \psi^{\downarrow;qq_2q_3}_{\uparrow\sigma_2\sigma_3}\right], \tag{67d}$$

---

(6) Note that $\psi^\Lambda_{\sigma_1\sigma_2\sigma_3}$ cannot be identified in general with the usual rest-frame wave function $\Psi^\Lambda_{\sigma_1\sigma_2\sigma_3}$. They have the same spin structure, but not the same momentum dependence.

$$\frac{k_\perp}{M}\,\mathfrak{g}^q_{1T} = \int \mathrm{d}[23] \sum_{\sigma_2\sigma_3}\sum_{q_2q_3} 2\,\Re e\left[\hat{k}_R \left(\psi^{\uparrow;qq_2q_3}_{\uparrow\sigma_2\sigma_3}\right)^* \psi^{\downarrow;qq_2q_3}_{\uparrow\sigma_2\sigma_3}\right], \tag{67e}$$

$$\frac{k_\perp}{M}\,h^\perp_1 = \int \mathrm{d}[23] \sum_{\sigma_2\sigma_3}\sum_{q_2q_3} 2\,\Im m\left[\hat{k}_R \left(\psi^{\uparrow;qq_2q_3}_{\downarrow\sigma_2\sigma_3}\right)^* \psi^{\uparrow;qq_2q_3}_{\uparrow\sigma_2\sigma_3}\right], \tag{67f}$$

$$\frac{k_\perp}{M}\,\mathfrak{h}^{\perp q}_{1L} = \int \mathrm{d}[23] \sum_{\sigma_2\sigma_3}\sum_{q_2q_3} 2\,\Re e\left[\hat{k}_R \left(\psi^{\uparrow;qq_2q_3}_{\downarrow\sigma_2\sigma_3}\right)^* \psi^{\uparrow;qq_2q_3}_{\uparrow\sigma_2\sigma_3}\right], \tag{67g}$$

$$\frac{\boldsymbol{k}^2_\perp}{2M^2}\,\mathfrak{h}^{\perp q}_{1T} = \int \mathrm{d}[23] \sum_{\sigma_2\sigma_3}\sum_{q_2q_3} \hat{k}^2_R \left(\psi^{\uparrow;qq_2q_3}_{\downarrow\sigma_2\sigma_3}\right)^* \psi^{\downarrow;qq_2q_3}_{\uparrow\sigma_2\sigma_3}, \tag{67h}$$

with $\mathfrak{h}^{+q}_{1T} = \mathfrak{h}^q_1 + \frac{\boldsymbol{k}^2_\perp}{2M^2}\,\mathfrak{h}^{\perp q}_{1T}$ and $h^{-q}_{1T} = \mathfrak{h}^q_1 - \frac{\boldsymbol{k}^2_\perp}{2M^2}\,\mathfrak{h}^{\perp q}_{1T}$. The functions $\mathfrak{g}^q_{1L}, \mathfrak{g}^q_{1T}, \mathfrak{h}^{\perp q}_{1L}, \mathfrak{h}^{+q}_{1T}$ are again related to the TMDs $g^q_{1L}, g^q_{1T}, h^{\perp q}_{1L}, h^{+q}_{1T}$ according to eqs. (44) and (45).

5·3. *Spherical symmetry.* – We now discuss how spherical symmetry restricts the form of the wave function in the canonical-spin basis. Spherical symmetry requires the wave function to be invariant under any rotation, *i.e.*

$$\sum_{\Lambda'\sigma'_1\sigma'_2\sigma'_3} [u(\theta,\phi)]_{\sigma_1\sigma'_1}\,[u(\theta,\phi)]_{\sigma_2\sigma'_2}\,[u(\theta,\phi)]_{\sigma_3\sigma'_3}\,[u(\theta,\phi)]^*_{\Lambda\Lambda'}\,\psi^{\Lambda'}_{\sigma'_1\sigma'_2\sigma'_3} = \psi^{\Lambda}_{\sigma_1\sigma_2\sigma_3}, \tag{68}$$

with the $SU(2)$ rotation matrix $u(\theta,\phi)$ given by eq. (21). In particular, invariance under a $(\pi,0)$-rotation leads to

$$\psi^{-\Lambda}_{-\sigma_1-\sigma_2-\sigma_3} = (-1)^{\Lambda+\sigma_1+\sigma_2+\sigma_3}\,\psi^{\Lambda}_{\sigma_1\sigma_2\sigma_3}, \tag{69}$$

while invariance under $(0,\phi)$-rotations implies that all components with $\ell_z \neq 0$ have to vanish

$$\psi^{\uparrow}_{\uparrow\uparrow\uparrow} = \psi^{\uparrow}_{\downarrow\downarrow\uparrow} = \psi^{\uparrow}_{\downarrow\uparrow\downarrow} = \psi^{\uparrow}_{\uparrow\downarrow\downarrow} = \psi^{\uparrow}_{\downarrow\downarrow\downarrow} = 0. \tag{70}$$

Taking into account constraints (69) and (70) in an arbitrary (θ,ϕ)-rotation, one finally gets(7)

$$\psi^{\uparrow}_{\uparrow\uparrow\downarrow} + \psi^{\uparrow}_{\uparrow\downarrow\uparrow} + \psi^{\uparrow}_{\downarrow\uparrow\uparrow} = 0. \tag{71}$$

---

(7) Note that spherical symmetry neither restricts the number of non-zero components of the wave function in the light-cone helicity basis nor relates them in a simple way, see table II in Appendix B.

Again, spherical symmetry implies that the TMDs are either identically zero or proportional to the unpolarized and polarized amplitudes A^q and B^q,

$$f_1^q = A^q, \tag{72a}$$

$$g_{1L}^q = \cos\theta\, B^q, \tag{72b}$$

$$h_1^q = \frac{\cos\theta + 1}{2}\, B^q, \tag{72c}$$

$$\frac{k_\perp}{M}\, f_{1T}^{\perp q} = 0, \tag{72d}$$

$$\frac{k_\perp}{M}\, g_{1T}^q = \sin\theta\, B^q, \tag{72e}$$

$$\frac{k_\perp}{M}\, h_1^{\perp q} = 0, \tag{72f}$$

$$\frac{k_\perp}{M}\, h_{1L}^{\perp q} = -\sin\theta\, B^q, \tag{72g}$$

$$\frac{\boldsymbol{k}_\perp^2}{2M^2}\, h_{1T}^{\perp q} = \frac{\cos\theta - 1}{2}\, B^q, \tag{72h}$$

with A^q and B^q given by the following overlaps:

$$A^q = \int \mathrm{d}[23] \sum_{q_2 q_3} \left[\left| \psi_{\uparrow\uparrow\downarrow}^{\uparrow;q q_2 q_3} \right|^2 + \left| \psi_{\uparrow\downarrow\uparrow}^{\uparrow;q q_2 q_3} \right|^2 + \left| \psi_{\downarrow\uparrow\uparrow}^{\uparrow;q q_2 q_3} \right|^2 \right], \tag{73}$$

$$\begin{aligned} B^q &= \int \mathrm{d}[23] \sum_{q_2 q_3} \left[\left| \psi_{\uparrow\uparrow\downarrow}^{\uparrow;q q_2 q_3} \right|^2 + \left| \psi_{\uparrow\downarrow\uparrow}^{\uparrow;q q_2 q_3} \right|^2 - \left| \psi_{\downarrow\uparrow\uparrow}^{\uparrow;q q_2 q_3} \right|^2 \right] \\ &= \int \mathrm{d}[23] \sum_{q_2 q_3} \left[\left(\psi_{\uparrow\uparrow\downarrow}^{\uparrow;q q_2 q_3} \right)^* \psi_{\downarrow\uparrow\downarrow}^{\downarrow;q q_2 q_3} + \left(\psi_{\uparrow\downarrow\uparrow}^{\uparrow;q q_2 q_3} \right)^* \psi_{\downarrow\downarrow\uparrow}^{\downarrow;q q_2 q_3} \right]. \end{aligned} \tag{74}$$

The TMD relations (36)–(38) then follow trivially.

5·4. *SU(6) spin-flavour symmetry.* – Many quark models, in addition of being spherically symmetric, assume also the $SU(6)$ spin-flavour symmetry. As a result, the wave function in the canonical spin basis is given by the product of a symmetric momentum wave function ϕ and a spin-isospin component $\Phi_{\sigma_1\sigma_2\sigma_3}^{\Lambda;q_1 q_2 q_3}$:

$$\psi_{\sigma_1\sigma_2\sigma_3}^{\Lambda;q_1 q_2 q_3} = \phi(\tilde{k}_1, \tilde{k}_2, \tilde{k}_3)\Phi_{\sigma_1\sigma_2\sigma_3}^{\Lambda;q_1 q_2 q_3}. \tag{75}$$

The wave function in the spin-flavour space can be written as

$$\Phi_{\sigma_1\sigma_2\sigma_3}^{\Lambda;q_1 q_2 q_3} = \frac{1}{\sqrt{2}} \left[\chi^\alpha \xi^\alpha + \chi^\beta \xi^\beta \right] \tag{76}$$

with

$$\chi^{\alpha} = \frac{1}{\sqrt{2}}\,[\uparrow\uparrow\downarrow - \uparrow\downarrow\uparrow]\,, \qquad \xi^{\alpha} = \frac{1}{\sqrt{2}}\,[uud - udu]\,, \tag{77}$$

$$\chi^{\beta} = \frac{1}{\sqrt{6}}\,[2\downarrow\uparrow\uparrow - \uparrow\downarrow\uparrow - \uparrow\uparrow\downarrow]\,, \qquad \xi^{\beta} = \frac{1}{\sqrt{6}}\,[2duu - udu - uud]\,. \tag{78}$$

As a result, writing explicitly the spin and isospin components of the wave function (75), we find the following results in the canonical spin basis:

(79)

$\psi^{\uparrow;q_1q_2q_3}_{\sigma_1\sigma_2\sigma_3}$	uud	udu	duu
$\uparrow\uparrow\downarrow$	2ϕ	$-\phi$	$-\phi$
$\uparrow\downarrow\uparrow$	$-\phi$	2ϕ	$-\phi$
$\downarrow\uparrow\uparrow$	$-\phi$	$-\phi$	2ϕ

with $\phi = \phi(\{\tilde{k}_i\})$ normalized as $\int [\mathrm{d}x]_3\,[\mathrm{d}^2k_\perp]_3|\phi|^2 = 1/6$. This implies that the unpolarized and polarized amplitudes A^q and B^q are simply proportional

$$A^u = 2A^d = \frac{3}{2}\,B^u = -6\,B^d = 12\int \mathrm{d}[23]|\phi|^2, \tag{80}$$

and so the flavour-dependent relation (39) follows trivially with $\mathcal{D}^q = B^q/A^q$.

6. – Quark models

In this section we review different quark models which have been used for the calculation of TMDs. In particular, we summarize the main ingredients of the models and discuss whether they satisfy the conditions of sect. **3**. In order to facilitate the discussion, we sort the quark models in classes defined as follows:

- The light-cone constituent quark model (LCCQM) of ref. [75] and the light-cone quark-diquark model (LCQDM) of refs. [38,39,83] constitute the class of light-cone models.
- The covariant parton model of ref. [37] constitutes its own class.
- The bag model of refs. [48,49] and the light-cone version of the chiral quark-soliton model (LCχQSM) of refs. [23, 84, 85] constitute the class of mean-field models.
- The quark-diquark models of refs. [28,47,29,31,35] constitute the class of spectator models.

We will not discuss the quark-target model of ref. [51] as it deals with gluons and therefore does already not satisfy the first condition of sect. **3**.

6·1. *Light-cone models.* – The class of light-cone models is characterized by the fact that the target state is expanded in the basis of free parton (Fock) states. One usually truncates the expansion and considers only the state with the lowest number of partons. In the LCCQM, this lowest state consists of three valence quarks, while in the LCQDM it consists of a valence quark and a spectator diquark.

It is well known that light-cone helicity and canonical spin of free partons are simply related by the so-called Melosh rotation [86]. Its $j = 1/2$ and $j = 1$ representations [87] are given by (see Appendix A for the definition of the spinors and polarization four-vectors)

$$(81)\quad D^{(1/2)*}_{\sigma\lambda}\left(\tilde{k}\right) = \frac{\overline{u}_{LC}(k,\lambda)u(k,\sigma)}{2m} = \frac{1}{\sqrt{N}}\begin{pmatrix} \sqrt{2}\,k^+ + m & -k_R \\ k_L & \sqrt{2}\,k^+ + m \end{pmatrix},$$

$$(82)\quad D^{(1)*}_{\sigma\lambda}\left(\tilde{k}\right) = -\varepsilon^*_{LC}(k,\lambda)\cdot\varepsilon(k,\sigma) = \frac{1}{N}\begin{pmatrix} \left(\sqrt{2}k^+ + m\right)^2 & -\sqrt{2}\left(\sqrt{2}k^+ + m\right)k_R & k_R^2 \\ \sqrt{2}\left(\sqrt{2}k^+ + m\right)k_L & \left(\sqrt{2}k^+ + m\right)^2 - \boldsymbol{k}_\perp^2 & -\sqrt{2}\left(\sqrt{2}k^+ + m\right)k_R \\ k_L^2 & \sqrt{2}\left(\sqrt{2}k^+ + m\right)k_L & \left(\sqrt{2}k^+ + m\right)^2 \end{pmatrix},$$

where m is the parton mass and $N = (\sqrt{2}\,k^+ + m)^2 + \boldsymbol{k}_\perp^2$. The LCWF in the canonical-spin basis being identified in these models with the instant-form wave function, it follows that $\sqrt{2}\,k^+ = x\mathcal{M}_0$ with $\mathcal{M}_0 = \sum_i \omega_i$ the mass of the Fock state and ω_i the free energy of parton i. Comparing now eqs. (81) and (83) with eqs. (40) and (C.9), we obtain

$$(83)\qquad \cos\frac{\theta}{2} = \frac{m + x\mathcal{M}_0}{\sqrt{N}} \qquad \text{and} \qquad \sin\frac{\theta}{2} = \frac{k_\perp}{\sqrt{N}}\,.$$

Finally, both the LCCQM and LCQDM consider wave functions with spherical symmetry and $SU(6)$ spin-flavour symmetry. In other words, all the conditions of sect. **3** are satisfied in these models, and so are the TMD relations (36)–(39)(8).

---

(8) In the derivations of sects. **4** and **5**, we tacitly assumed that the rotation connecting light-cone and canonical polarizations depends only on the momentum of the parton under consideration. The Melosh rotation involves the free invariant mass $\mathcal{M}_0$ and therefore the momenta of all partons in the state. We are in fact not allowed to pull the factor due to the rotation of the active quark out of the integral like in eq. (72). Nevertheless, this technical detail does not affect the conclusion about the validity of relations (36)–(39). Our tacit assumption, which does not apply to this specific case, has been introduced to keep the presentation as simple as possible.

6˙2. *Covariant parton model.* – The standard quark-parton model (QPM) refers to the infinite momentum frame (IMF), where the parton mass can be neglected. The covariant parton model is an alternative to the QPM that is not confined to a preferred reference frame. Following the standard assumptions of the QPM, the covariant parton model describes the target system as a gas of quasi-free partons, *i.e.* the partons bound inside the target behave at the interaction with the external probe (at sufficiently high Q^2) as free particles having four-momenta on the mass shell. However, since the covariant parton model does not refer specifically to the IMF, the parton mass(9) m is not neglected. One also assumes explicitly that the parton distributions are spherically symmetric.

The covariant parton model does not refer explicitly to quark canonical spin or light-cone helicity. Instead, it deals with the covariant quark polarization vector. Identifying in the Bjorken limit the Lorentz structures of the hadronic tensor with those of the TMD correlator, the authors of ref. [37] found that the TMDs are given in the covariant parton model by

$$f_1^q = \frac{1}{2}\left[(m+xM)^2 + \boldsymbol{k}_\perp^2\right]\int\{\mathrm{d}\tilde{k}^1\}, \tag{84a}$$

$$g_{1L}^q = \frac{1}{2}\left[(m+xM)^2 - \boldsymbol{k}_\perp^2\right]\int\{\mathrm{d}k^1\}, \tag{84b}$$

$$\frac{k_\perp}{M}\, f_{1T}^{\perp q} = 0, \tag{84c}$$

$$\frac{k_\perp}{M}\, g_{1T}^{q} = (m+xM)k_\perp\int\{\mathrm{d}k^1\}, \tag{84d}$$

$$\frac{k_\perp}{M}\, h_{1}^{\perp q} = 0, \tag{84e}$$

$$\frac{k_\perp}{M}\, h_{1L}^{\perp q} = -(m+xM)k_\perp\int\{\mathrm{d}k^1\}, \tag{84f}$$

$$\frac{\boldsymbol{k}_\perp^2}{2M^2}\, h_{1T}^{\perp q} = -\frac{1}{2}\,\boldsymbol{k}_\perp^2\int\{\mathrm{d}k^1\}, \tag{84g}$$

where M is the target mass, $\{\mathrm{d}\tilde{k}^1\}$ and $\{\mathrm{d}k^1\}$ are the measures associated to the distributions of unpolarized and polarized quarks, respectively. Comparing with eq. (72), we find that

$$\cos\frac{\theta}{2} = \frac{m+xM}{\sqrt{(m+xM)^2+\boldsymbol{k}_\perp^2}} \qquad \text{and} \qquad \sin\frac{\theta}{2} = \frac{k_\perp}{\sqrt{(m+xM)^2+\boldsymbol{k}_\perp^2}}\,, \tag{85}$$

which is nothing else than the Melosh rotation. This is consistent with the fact that the active quark is quasi-free in this model. The difference with light-cone models is that the physical mass of the target M is used in the Melosh rotation instead of the free invariant mass $\mathcal{M}_0$([10]). The conditions 1)–3) of sect. **3** are therefore satisfied in the covariant parton model, and so are the TMD relations (36)–(38). Since this model does not use the language of wave functions, the implementation of $SU(6)$ spin-flavour symmetry is more delicate and one has to assume that the unpolarized and polarized distributions become simply proportional in order to recover the TMD relation (39).

---

(9) Note that the parton mass appearing in the model has to be regarded as an effective mass, in the sense that it corresponds to the mass of the free parton behaving at the interaction like the actual bound parton.

6˙3. *Mean-field models.* – In mean-field models, the target is considered as made of quarks bound by a classical mean field representing the non-perturbative (long-range) contribution of the gluon field. Accordingly, the positive-frequency part of the quark field appearing in the definition of the correlator (1) is expanded in the basis of the bound-state solutions $e^{-iE_nt}\,\varphi_n(k,\sigma)$ instead of the free Dirac light-cone spinors $e^{-ik\cdot x}\,u_{LC}(k,\lambda)$. Moreover, one truncates the expansion to the lowest mode $\varphi\equiv\varphi_1$ with energy $E_{\text{lev}}\equiv E_1$.

In these models, the bound-state solution $\varphi(k,\sigma)$ is called the quark wave function. This object is clearly different from the LCWF introduced in sect. **5**. In particular, the former is a spinor while the latter is an ordinary scalar function. It is however possible to relate them. Since we consider twist-2 Dirac operators Γ, only the good components of the spinors are involved in the quark bilinear $\overline{\varphi}(k,\sigma')\Gamma\varphi(k,\sigma)$. Using $u_G(\lambda)=P_+u_{LC}(k,\lambda)/\sqrt{2^{1/2}k^+}$ (see Appendix A), we find that

$$\begin{aligned}(86)\qquad \overline{\varphi}(k,\sigma')\Gamma\varphi(k,\sigma) &= \varphi^\dagger(k,\sigma')P_+\gamma^0\Gamma P_+\varphi(k,\sigma)\\ &= \sum_{\lambda\lambda'} F^*_{\lambda'\sigma'}(k')\,F_{\lambda\sigma}(k)\,\frac{\overline{u}_{LC}(k,\lambda')\Gamma u_{LC}(k,\lambda)}{\sqrt{2}k^+}\,,\end{aligned}$$

where we have defined $F_{\lambda\sigma}(k)=u^\dagger_G(\lambda)\varphi(k,\sigma)$. In agreement with [88, 89] where one boosts explicitly the system in the mean-field approximation to the IMF, $F_{\lambda\sigma}(k)$ can be interpreted as the quark LCWF with $k_z=xM-E_{\text{lev}}$. The mass M is identified with the nucleon mass M_N in the bag model and with the soliton mass $\mathcal{M}_N$ in the LCχQSM.

The mean field is assumed spherically symmetric in the target rest frame. It follows that the lowest quark-state solution in momentum space takes the form

$$(87)\qquad \varphi(k,\sigma)=\begin{pmatrix} f(|\boldsymbol{k}|)\\ \frac{\boldsymbol{k}\cdot\boldsymbol{\sigma}}{|\boldsymbol{k}|}\,g(|\boldsymbol{k}|)\end{pmatrix}\chi_\sigma,$$

with χ_σ the Pauli spinor. The functions f and g in eq. (87) represent the s ($\ell=0$) and p ($\ell=1$) waves of the bound-state solution. On the other hand, the general 3Q LCWF for a spin-1/2 target involves usually s-, p- and d-waves. There is no contradiction between these two statements since f and g describe a single quark in the target and therefore do not represent partial waves of *total* angular momentum. Note also that in the language

---

(10) In the covariant parton model, only the active parton is considered on-shell. In light-cone models, all the partons are on-shell so that the Fock state itself is off-shell $\mathcal{M}_0\neq M$.

of 3Q LCWF, the s-, p- and d-waves refer to components with $\ell_z = 0$, ± 1 and ± 2, respectively. This is an abuse of language as partial waves should refer to ℓ and not ℓ_z.

The quark LCWF corresponding to (87) is then given by(¹¹)

$$(88)\qquad F_{\lambda\sigma}(k) = \frac{1}{\sqrt{2}}\begin{pmatrix} f(|\boldsymbol{k}|) + \frac{k_z}{|\boldsymbol{k}|}\, g(|\boldsymbol{k}|) & -\frac{k_R}{|\boldsymbol{k}|}\, g(|\boldsymbol{k}|) \\ \frac{k_L}{|\boldsymbol{k}|}\, g(|\boldsymbol{k}|) & f(|\boldsymbol{k}|) + \frac{k_z}{|\boldsymbol{k}|}\, g(|\boldsymbol{k}|) \end{pmatrix}_{\sigma\lambda}.$$

It describes in particular how canonical spin σ and light-cone helicity λ are related. Comparing with eq. (40), we find that

$$(89)\qquad \cos\frac{\theta}{2} = \frac{f(|\boldsymbol{k}|) + \frac{k_z}{|\boldsymbol{k}|}\, g(|\boldsymbol{k}|)}{\sqrt{N}} \qquad \text{and} \qquad \sin\frac{\theta}{2} = \frac{\frac{k_\perp}{|\boldsymbol{k}|}\, g(|\boldsymbol{k}|)}{\sqrt{N}},$$

with $N = f^2(|\boldsymbol{k}|) + 2\,\frac{k_z}{|\boldsymbol{k}|}\, f(|\boldsymbol{k}|)g(|\boldsymbol{k}|) + g^2(|\boldsymbol{k}|)$. The 3Q LCWF written as $\prod_{i=1}^{3} F_{\lambda_i\sigma_i}(k_i)$ times the standard $SU(6)$ spin-flavour wave function with target polarization $\Lambda = \sum_i \sigma_i$, is then consistent with spherical symmetry in the canonical-spin basis. All the conditions of sect. **3** being satisfied in mean-field models, the TMD relations (36)–(39) follow automatically.

6˙4. *Spectator models.* – The basic idea of spectator models is to evaluate the quark-quark correlator Φ of eq. (1) by inserting a complete set of intermediate states and then truncating this set at tree level to a single on-shell spectator diquark state, *i.e.* a state with the quantum numbers of two quarks. The diquark can be either an isospin singlet with spin 0 (scalar diquark) or an isospin triplet with spin 1 (axial-vector diquark). The target is then seen as made of an off-shell quark and an on-shell diquark. Spectator models differ by their specific choice of target-quark-diquark vertices, polarization four-vectors associated with the axial-vector diquark, and form factors which take into account in an effective way the composite nature of the target and the spectator diquark.

As advocated in ref. [90], the parton distributions can conveniently be computed using the language of LCWFs. The scalar quark-diquark LCWF is defined as

$$(90)\qquad \psi^{\Lambda}_{\lambda}\left(\tilde{k}\right) \propto \overline{u}_{LC}(k,\lambda)\mathcal{Y}_s u_{LC}(P,\Lambda)$$

with target momentum $P = [P^+, \frac{M^2}{2P^+}, \boldsymbol{0}_\perp]$. We do not need to specify all the factors in the definition as we are only interested in the structure of the wave function in the light-cone helicity basis. The scalar vertex is of the Yukawa type $\mathcal{Y}_s = g_s(k^2)\,\mathbb{1}$ with $g_s(k^2)$ some form factor. Writing down explicitly the components, one finds

$$(91)\qquad \psi^{\Lambda}_{\lambda}\left(\tilde{k}\right) \propto \frac{g_s(k^2)}{\sqrt{x}}\begin{pmatrix} m + xM & -k_R \\ k_L & m + xM \end{pmatrix}_{\Lambda\lambda}.$$

(¹¹) Replacing $\varphi(k,\sigma)$ by the free Dirac spinor $u(k,\sigma)$, one recovers the Melosh rotation given by eq. (81) $u^\dagger_G(\lambda)u(k,\sigma) = \sqrt{2^{1/2}k^+}\, D^{(1/2)*}_{\sigma\lambda}(\tilde{k})$.

Note the striking resemblance with the Melosh rotation matrix of eq. (81). One can similarly define a rest-frame scalar quark-diquark wave function as

$$\Psi^\Lambda_\sigma \propto \overline{u}(k,\sigma)\mathcal{Y}_s u(P_{\text{rest}},\Lambda) = g_s(k^2)\sqrt{2M(E+m)}\,\delta_{\Lambda\sigma} \tag{92}$$

with target momentum $P_{\text{rest}} = (M,\mathbf{0})$. This wave function is obviously spherically symmetric(^{12}). Furthermore, eq. (91) suggests that the quark light-cone helicity and canonical spin are simply related by a Melosh rotation, as if the quark was free [91]. In other words, the conditions 1)–3) of sect. **3** are satisfied in scalar diquark models with Yukawa-like vertex, and so are the TMD relations (36)–(38).

The axial-vector quark-diquark LCWF is defined as

$$\psi^\Lambda_{\lambda\lambda_D}\left(\tilde{k}\right) \propto \overline{u}_{LC}(k,\lambda)\varepsilon^*_{LC\mu}(K,\lambda_D)\mathcal{Y}^\mu_a u_{LC}(P,\Lambda). \tag{93}$$

The spectator model of Jakob *et al.* [28] assumes the following structure for the axial-vector vertex $\mathcal{Y}^\mu_a = \frac{g_a(k^2)}{\sqrt{3}}\gamma_5(\gamma^\mu + \frac{P^\mu}{M})$ and the following momentum argument for the polarization four-vector $K = P$. The motivation for such a choice is to ensure that, in the target rest frame, the diquark spin-1 states are purely spatial. Indeed, the rest-frame axial-vector quark-diquark wave function reads in this model

$$\Psi^\Lambda_{\sigma\sigma_D} \propto \overline{u}(k,\sigma)\varepsilon^*_\mu(K,\sigma_D)\mathcal{Y}^\mu_a u(P_{\text{rest}},\Lambda) = \frac{g_a(k^2)}{\sqrt{3}}\sqrt{2M(E+m)}\,(\boldsymbol{\epsilon}_{\sigma_D}\cdot\boldsymbol{\sigma})_{\sigma\Lambda}\,. \tag{94}$$

It satisfies constraints (C.13) and is therefore spherically symmetric. Writing down explicitly the components of the corresponding LCWF, one finds

$$\begin{gathered}\psi^+_{+0} \propto \frac{g_a(k^2)}{\sqrt{3x}}(m+xM), \qquad \psi^+_{-0} \propto -\frac{g_a(k^2)}{\sqrt{3x}}\,k_R, \\ \psi^+_{-+} = -\sqrt{2}\,\psi^+_{+0}, \qquad \psi^-_{--} = \sqrt{2}\,\psi^+_{-0}, \qquad \psi^+_{+-} = \psi^+_{--} = 0,\end{gathered} \tag{95}$$

the other components being given by $\psi^{-\Lambda}_{-\lambda-\lambda_D} = (-1)^{\Lambda+\lambda+\lambda_D}\left(\psi^\Lambda_{\lambda\lambda_D}\right)^*$, with $\Lambda,\lambda = \pm\frac{1}{2}$ and $\lambda_D = +1, 0, -1$. Again, one recognizes the characteristic factors of the Melosh rotation [91]. Comparing the structure of the components of the LCWF in eq. (95) with the structure of the components of the LCWF given in table IV after applying the constraints of spherical symmetry in the canonical-spin basis (C.13), one concludes that only the quark polarization is rotated. This is in agreement with the fact that the momentum argument of the polarization four-vector ε_μ does not have any transverse

---

(^{12}) The rest-frame wave function in eq. (92) is expressed in terms of canonical spin and therefore has the same spin structure as the LCWF expressed in the canonical-spin basis. It follows that the constraints due to spherical symmetry discussed in Appendix C˙1 apply also here. Furthermore, the momentum-dependent part of the wave function in the rest frame does not depend on a specific direction.

momentum, and so there is no rotation of the diquark polarization. All the conditions 1)–3) of sect. **3** being satisfied in the axial-vector diquark model of ref. [28], the TMD relations (36)–(38) follow automatically. The flavour-dependent relation (39) can be obtained by further imposing $SU(6)$ spin-flavour symmetry to the wave function(13).

On the contrary, some versions of the spectator model presented by Bacchetta *et al.* in ref. [47] do not support any TMD relation. We therefore expect that at least one of the conditions 1)–3) of sect. **3** is not satisfied. These versions are based on the axial-vector vertex $\mathcal{Y}^\mu_a = \frac{g_a(k^2)}{\sqrt{2}}\gamma^\mu\gamma_5$ and involve the diquark momentum $K = P - k$ in the polarization four-vector. With these choices, it is found that the condition 3) of sect. **3** is not fulfilled since the corresponding rest-frame wave function does not satisfy the requirements of spherical symmetry

$$\Psi^\Lambda_{\sigma\sigma_D} \not\propto (\boldsymbol{\epsilon}_{\sigma_D}\cdot\boldsymbol{\sigma})_{\sigma\Lambda}\,, \tag{96}$$

in accordance with the discussions of refs. [92]- [94] and the comment in ref. [47] that in this approach the partons do not necessarily occupy the lowest-energy available orbital (with quantum numbers $J^P = \frac{1}{2}^+$ and $L_z = 0$.)

7. – $SU(6)$-symmetry breaking in a light-cone constituent quark model

In this section we apply the formalism introduced in the previous sections for the calculation of T-even TMDs from LCWFs to a specific model, namely the light-cone constituent quark model. For recent quark-model calculation of the T-odd TMDs we refer to [47, 35, 44, 42, 43, 95, 33, 32]. First, we specify the LCWF of (66) which assumes $SU(6)$ symmetry for the spin-flavour component of the wave function. Then, we add a component of the LCWF which breaks the $SU(6)$ symmetry.

In a first step the percentage of $SU(6)$-breaking terms in the total LCWF is left as free parameter, and we discuss in general the effects of these terms on the TMD results. This calculation can be reproduced numerically using the Mathematica program which can be downloaded from ref. [96] in both the Windows and Linux versions(14). In particular, this program allows one to reproduce the model calculation for i) the T-even TMDs; ii) the spin densities in the transverse-momentum space as a function of the quark and nucleon polarizations; iii) the $\boldsymbol{k}^2_\perp$ dependence of the x moments of the TMDs, with a comparison of the model results with the Gaussian ansatz.

---

(13) The scalar and axial-vector diquarks represent in principle more than just two quarks. For this reason, they have *a priori* different masses, cutoffs, form factors, ... When we impose $SU(6)$ symmetry, we implicitly consider that the quark-diquark picture originates from a 3Q picture. The scalar and axial-vector diquarks then just differ by their spin and flavour structures which are uniquely determined by the $SU(6)$ symmetry.

(14) In order to run the program, you also need the auxiliary functions available at the same web address with the name "Functions-TMD.zip".

In a second step, we study different observables, which are particularly sensitive to $SU(6)$ breaking and can be used to fix the free parameter of the model corresponding to the percentage of $SU(6)$-breaking terms in the LCWF of the nucleon. Explicit examples of this fitting procedure are given in a second Mathematica file [97]. In particular, in this program we present different strategies for fitting the available experimental data of three observables: i) the inclusive polarized asymmetry A_1; ii) the ratio F_2^n/F_2^p of the neutron to proton unpolarized structure function of DIS; iii) the nucleon electroweak form factors. In these notes we will discuss, as an example, the fit of the double-spin asymmetry A_1 in DIS, leaving for a future work a systematic study to select the best-fitting procedure.

7˙1. *Light-cone constituent quark model.* – The $SU(6)$-symmetric component of the LCWF in the LCCQM has the form in eq. (66), with the $SU(2)$ matrix relating the light-cone helicity and the spin given by the Melosh rotation discussed in subsect. **6˙1** and the wave function in the canonical spin basis given in eq. (75). For the symmetric momentum wave function one assumes the following functional form:

$$\phi\left(\left\{\tilde{k}_i\right\}\right) = 2(2\pi)^3\left[\frac{1}{M_0}\frac{\omega_1\omega_2\omega_3}{x_1x_2x_3}\right]^{1/2}\frac{N'}{(M_0^2+\beta^2)^\gamma}, \tag{97}$$

where N' is a normalization factor, and the scale β, the parameter γ for the power-law behaviour, and the quark mass m are taken from ref. [98], *i.e.* $\beta = 0.607\,\mathrm{GeV}$, $\gamma = 3.4$ and $m = 0.267\,\mathrm{GeV}$. According to Schlumpf's analysis [99] these values lead to a very good description of many baryonic properties.

We now introduce an admixture of mixed-symmetry component in the nucleon wave function given by

$$\Psi^{\Lambda;q_1q_2q_3}_{\sigma_1\sigma_2\sigma_3} = \cos\delta\,\psi^{\Lambda;q_1q_2q_3}_{\sigma_1\sigma_2\sigma_3} + \sin\delta\,\tilde{\psi}^{\Lambda;q_1q_2q_3}_{\sigma_1\sigma_2\sigma_3}, \tag{98}$$

where $\psi^{\Lambda;q_1q_2q_3}_{\sigma_1\sigma_2\sigma_3}$ is the $SU(6)$-symmetric component of eq. (75) and $\tilde{\psi}^{\Lambda;q_1q_2q_3}_{\sigma_1\sigma_2\sigma_3}$ is a mixed-symmetry component. The factor $\cos^2\delta$ and $\sin^2\delta$ give the percentages in the nucleon wave function of $SU(6)$-symmetric and $SU(6)$-breaking terms, respectively. For the $SU(6)$-breaking component we take an appropriate combination of mixed-symmetry spin-isospin wave functions with two-momentum wave function of mixed symmetry

$$\tilde{\psi}^{\Lambda;q_1q_2q_3}_{\sigma_1\sigma_2\sigma_3}\left(\left\{\tilde{k}_i\right\}\right) = \frac{1}{2}\left[\phi^\beta\left(\chi^\alpha\xi^\alpha - \chi^\beta\xi^\beta\right) + \phi^\alpha\left(\chi^\alpha\xi^\beta + \chi^\beta\xi^\alpha\right)\right], \tag{99}$$

where the spin and isospin wave functions are defined as in (77), and the momentum-dependent part is given by

$$\phi^\alpha\left(\left\{\tilde{k}_i\right\}\right) = N^\alpha\frac{\vec{\alpha}\cdot\vec{\beta}}{\vec{\alpha}^2+\vec{\beta}^2}\phi\left(\left\{\tilde{k}_i\right\}\right), \qquad \phi^\beta = N^\beta\frac{\vec{\beta}^2-\vec{\alpha}^2}{\vec{\alpha}^2+\vec{\beta}^2}\phi\left(\left\{\tilde{k}_i\right\}\right). \tag{100}$$

In eq. (100) N^α and N^β are normalization factors and the Jacobi coordinates are defined as

$$\vec{\alpha} = \frac{1}{\sqrt{2}}\left(\vec{k}_2 - \vec{k}_3\right), \qquad \vec{\beta} = \sqrt{\frac{3}{2}}\,\vec{k}_1. \tag{101}$$

As a result, writing explicitly the spin and isospin components of the wave function (100), we find the following results in the canonical spin basis:

(102)

$\tilde{\psi}^{\uparrow;q_1q_2q_3}_{\sigma_1\sigma_2\sigma_3}$	uud	udu	duu
$\uparrow\uparrow\downarrow$	$\phi^\beta - \sqrt{3}\phi^\alpha$	$-2\phi^\beta$	$\phi^\beta + \sqrt{3}\phi^\alpha$
$\uparrow\downarrow\uparrow$	$-2\phi^\beta$	$\phi^\beta + \sqrt{3}\phi^\alpha$	$\phi^\beta - \sqrt{3}\phi^\alpha$
$\downarrow\uparrow\uparrow$	$\phi^\beta + \sqrt{3}\phi^\alpha$	$\phi^\beta - \sqrt{3}\phi^\alpha$	$-2\phi^\beta$

with the normalizations $\int[\mathrm{d}x]_3\,[\mathrm{d}^2k_\perp]_3|\phi^\alpha|^2 = \int[\mathrm{d}x]_3\,[\mathrm{d}^2k_\perp]_3|\phi^\beta|^2 = 1/6$.

We note that the mixed-symmetry components of the nucleon wave function correspond to a state with $l_z = 0$ and satisfy relation (71) derived from rotational invariance. Therefore, the LCWF overlap representation of the TMDs keeps the form given in eqs. (72), with the functions A^q and B^q calculated from the LCWF in eq. (98). In particular, separating the contribution from the $SU(6)$-symmetric component, the $SU(6)$-breaking term and the interference term we can write

$$A^q = \cos^2\delta\, A^q_{\mathrm{sym}} + 2\cos\delta\sin\delta\, A^q_{\mathrm{int}} + \sin^2\delta\, A^q_{\mathrm{br}}, \tag{103}$$

$$B^q = \cos^2\delta\, B^q_{\mathrm{sym}} + 2\cos\delta\sin\delta\, B^q_{\mathrm{int}} + \sin^2\delta\, B^q_{\mathrm{br}}. \tag{104}$$

A^q_{sym} and B^q_{sym} are the contributions calculated in eq. (80), while the contribution from the $SU(6)$-breaking term reads

$$A^u_{\mathrm{br}} = \frac{A^d_{\mathrm{br}}}{2} = 6[(\phi^\beta)^2 + (\phi^\alpha)^2)], \tag{105}$$

$$B^u_{\mathrm{br}} = 4(\phi^\beta)^2, \quad B^d_{\mathrm{br}} = -(\phi^\beta)^2 + 3\,(\phi^\alpha)^2. \tag{106}$$

Furthermore, the contribution from the interference between the two components is given by

$$A^u_{\mathrm{int}} = -A^d_{\mathrm{int}} = \frac{3}{5}B^u_{\mathrm{int}} = 3B^d_{\mathrm{int}} = 6\sqrt{2}\,\phi\,\phi^\beta. \tag{107}$$

We immediately notice that the admixture of mixed-symmetry components leads to the breaking of the flavour-dependent relation (39) between the unpolarized and polarized TMDs, while it does not spoil the remaining relations among polarized TMDs. Furthermore, the up- and down-quark contribution to the TMDs are no longer proportional.

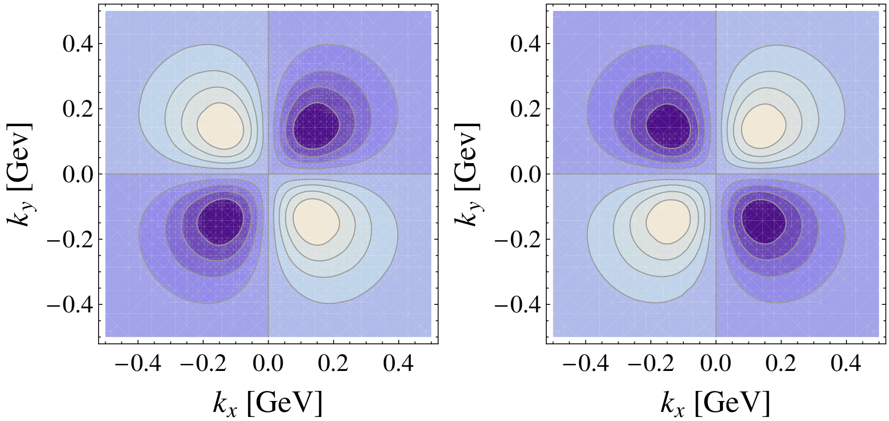

Fig. 2. – Density of quarks in the $\boldsymbol{k}_\perp$ plane for net transverse polarization of quarks and proton in perpendicular directions. The left and right panel show the results for up and down quarks, respectively.

7$\cdot$2. *Results for TMDs.* – In this subsection we report a few results for the TMDs in the LCCQM which can be explicitly calculated from the program of ref. [96]. In particular we discuss the spin densities in the transverse-momentum plane given by

$$\begin{aligned}(108)\quad \rho\Big(k_x, k_y, (\lambda, \vec{s}_\perp), \Big(\Lambda, \vec{S}_\perp\Big)\Big) = \frac{1}{2}\Big[& f_1 + S^i_\perp \epsilon^{ij} k^j \frac{1}{M} f^\perp_{1T} + \lambda\Lambda\, g_{1L} + \lambda\, S^i_\perp k^i \frac{1}{M}\, g_{1T} \\ & + s^i_\perp \epsilon^{ij} k^j \frac{1}{M}\, h^\perp_1 + \Lambda\, s^i_\perp k^i \frac{1}{M}\, h^\perp_{1L} \\ & + s^i_\perp S^i_\perp h_1 + s^i_\perp \left(2k^i k^j - \vec{k}^2_\perp \delta^{ij}\right) S^j_\perp \frac{1}{2M^2}\, h^\perp_{1T}\Big],\end{aligned}$$

where, for a generic TMD j, we introduced the first-x moment defined as

$$(109)\qquad j(\boldsymbol{k}^2_\perp) = \int \mathrm{d}x\, j(x, \boldsymbol{k}^2_\perp).$$

As discussed in sect. **2**, the unpolarized TMD f_1, the helicity TMD g_{1L}, and the transversity TMD h_1 in eq. (108) correspond to monopole distributions in the momentum space for unpolarized, longitudinally and transversely polarized quarks, respectively. They can be obtained from the overlap of LCWFs which are diagonal in the orbital angular momentum, but probe different transverse momentum and helicity correlations of the quarks inside the nucleon.

All the other TMDs require a transfer of orbital angular momentum between the initial and final state. The $h^\perp_{1T}$ TMD describes the distortion due to the transverse polarizations in perpendicular directions of the quark and the nucleon [100]. In this case, the nucleon helicity flips in the direction opposite to the quark helicity, with a mismatch of two units for the orbital angular momentum of the initial and final LCWFs. In fig. 2 we show the results for both up and down quarks in the case of a $SU(6)$-symmetric LCWF.

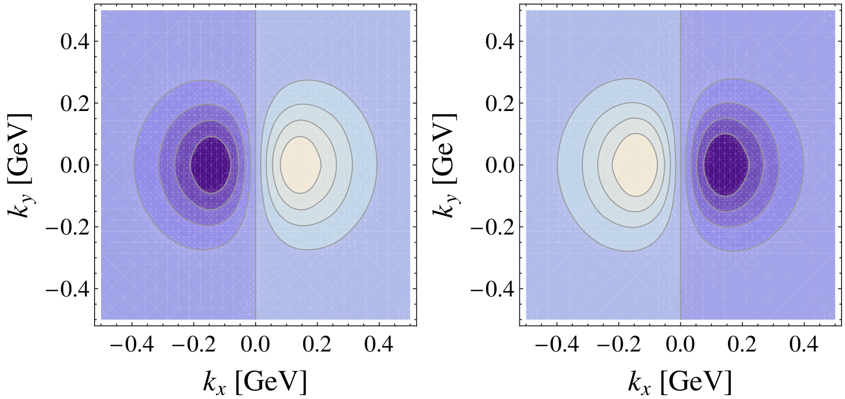

Fig. 3. – Quark densities in the $\boldsymbol{k}_\perp$ plane for net longitudinal polarization of quarks in a transversely polarized proton for up (left panel) and down (right panel) quark.

The results for definite quark and nucleon polarizations in transverse directions are obtained by adding the monopole contributions from f_1 and h_1 in eq. (108). In the case of quark and nucleon transversely polarized in perpendicular directions ($\rho(k_x, k_y, s_x, S_y) = \rho(k_x, k_y, s_y, S_x)$), one has from eq. (108) the sum of the monopole contributions from f_1 and h_1, and of the quadrupole contribution from $h_{1T}^\perp$, ignoring the contributions from the T-odd TMDs which are vanishing in the absence of gluon degrees of freedom. Since the quadrupole distortion induced by $h_{1T}^\perp$ is quite small with respect to f_1 and h_1, the density for definite polarization differs slightly from a monopole distribution.

Among the distributions in eq. (108), the dipole correlations related to g_{1T} and $h_{1L}^\perp$ have characteristic features of intrinsic transverse momentum, since they are the only ones which have no analog in the spin densities related to the GPDs in the impact parameter space [101, 102, 36]. In particular, g_{1T} and $h_{1L}^\perp$ correspond to quark densities with specular configurations for the quark and nucleon spin: g_{1T} describes longitudinally polarized quarks in a transversely polarized nucleon, while $h_{1L}^\perp$ gives the distribution of transversely polarized quarks in longitudinally polarized nucleon. Therefore, g_{1T} requires helicity flip of the nucleon which is not compensated by a change of the quark helicity, and vice versa $h_{1L}^\perp$ involves helicity flip of the quarks but is diagonal in the nucleon helicity. As a result, in both cases, the LCWFs of the initial and final states differ by one unit of orbital angular momentum and the associated distributions have a dipole structure. The results in the $SU(6)$-symmetric version of the LCCQM for the densities with longitudinally polarized quarks in a transversely polarized proton are shown in fig. 3. The results for definite quark and nucleon polarizations are obtained by adding the monopole contribution of f_1 (the contribution from the Sivers function is ignored because we do not include gauge-field degrees of freedom). As shown in fig. 4, the sideways shift in the positive (negative) $\hat{x}$ direction for up (down) quark due to the dipole term $\propto \lambda S^i k^i \frac{1}{M} g_{1T}$ is sizable and corresponds to an average deformation $\langle \vec{k}_x^u \rangle = 55.8\,\text{MeV}$, and $\langle k_x^d \rangle = -27.9\,\text{MeV}$. The dipole distortion $\propto \Lambda\, s^i k^i \frac{1}{m}\, h_{1L}^\perp$ in the case of transversely

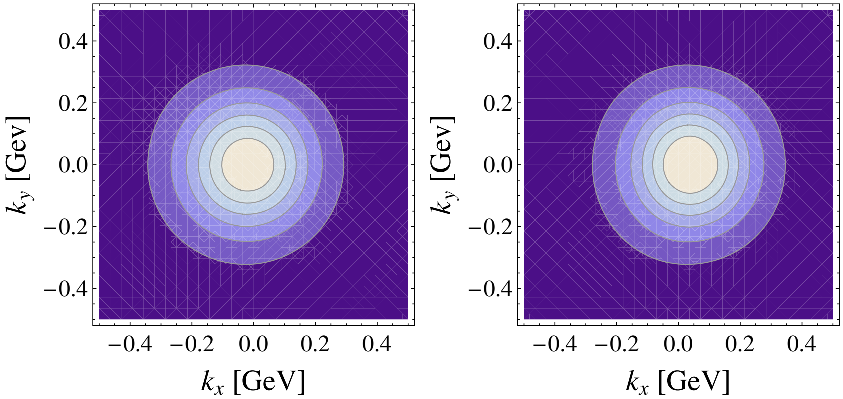

Fig. 4. – Quark densities in the $\boldsymbol{k}_\perp$ plane for longitudinally polarized quarks in a transversely polarized proton for up (left panel) and down (right panel) quark.

polarized quarks in a longitudinally polarized proton is equal but with opposite sign, since in our model $h_{1L}^{\perp} = -g_{1T}$. These model results are supported by a recent lattice calculation [79-81] which gives, for the density related to g_{1T}, $\langle \vec{k}_x^u \rangle = 67(5)\,\text{MeV}$, and $\langle k_x^d \rangle = -30(5)\,\text{MeV}$. For the density related to $h_{1L}^{\perp}$, they also find shifts of similar magnitude but opposite sign: $\langle \vec{k}_x^u \rangle = -60(5)\,\text{MeV}$, and $\langle k_x^d \rangle = 15(5)\,\text{MeV}$.

In the program of ref. [96] one can also calculate and simultaneously visualize the effects of $SU(6)$ breaking for the spin densities, and for the x and $\boldsymbol{k}_\perp^2$ dependence of the TMDs. For example, we summarize a few results which can be easily verified following the calculation in the program: first of all, one finds that the $\boldsymbol{k}_\perp^2$ dependence of the TMDs is not Gaussian. In particular, the $\boldsymbol{k}_\perp^2$ dependence is the same for up and down quark within the $SU(6)$-symmetric version of the model, while the admixture of mixed-symmetry components breaks this flavour independence.

7·3. *Observables.* – One of the observables which is largely sensitive to effects of $SU(6)$ breaking is the inclusive double-spin asymmetry A_1 in DIS with lepton and target nucleon longitudinally polarized. It can be expressed in terms of the unpolarized $f_1^q(x)$ and polarized $g_1^q(x)$ parton distributions as

$$A_1 = \frac{\sum_q e_q^2\, x\, g_1^q(x)}{\sum_q e_q^2\, x\, f_1^q(x)}\,, \tag{110}$$

which becomes, in the case of proton and neutron target,

$$A_1^p = \frac{4g_1^u(x) + g_1^d(x)}{4f_1^u(x) + f_1^d(x)}\,, \qquad A_1^n = \frac{4g_1^d(x) + g_1^u(x)}{4f_1^d(x) + f_1^u(x)}\,, \tag{111}$$

where we used isospin symmetry in such a way that the structure functions of the neutron are related to those of the proton by interchanging u and d flavours.

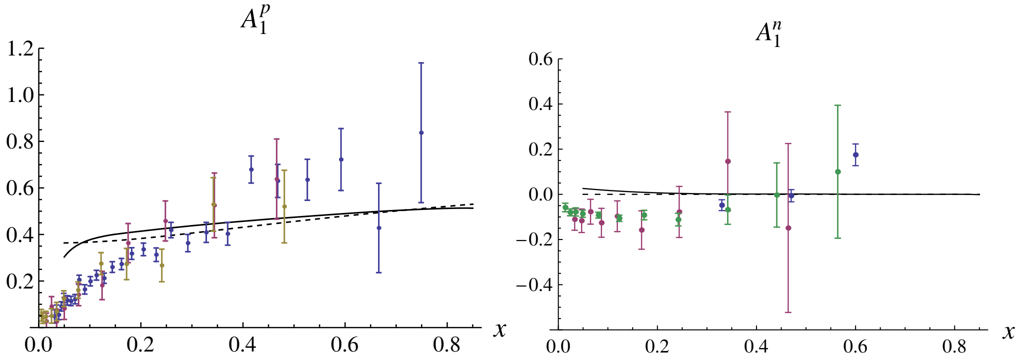

Fig. 5. – The inclusive double-spin asymmetry A_1 in DIS off proton (left panel) and neutron (right panel) as a function of x. The theoretical curves are obtained with $g_1^q(x)$ and $f_1^q(x)$ from the LCCQM with $SU(6)$ symmetry as follows: both function LO to the $\langle Q^2\rangle = 2.5\,\text{GeV}^2$ of the experiments (solid curves) and both at the low scale of the model (dashed curves). The experimental data for A_1^p are from refs. [107-110] and for A_1^n from refs. [111-114].

We notice that in a $SU(6)$-symmetric model, one has $g_1^u(x) = -4g_1^d(x)$, which implies $A_1^n = 0$ at the scale of the model. At higher scale, $A_1^n \neq 0$ due to evolution, but the effects remain small. This is illustrated in fig. 5 where we show the results for the proton and neutron at the initial scale of the model (dashed curves) and after leading order (LO) evolution to $Q^2 = 2.5\,\text{GeV}^2$. We also see that experimentally A_1^n (extracted by subtracting deuteron and proton data, or from ^{3}He data, modulo nuclear corrections) is found clearly non-zero, giving a signature of $SU(6)$-breaking effects. Following the calculation in the Mathematica program of ref. [97], we can use this sensitivity to $SU(6)$ breaking to fit the parameter δ of the model in eqs. (103), (104) to the experimental data for A_1. In [97] we give different examples for the strategies which can be used in the fitting procedure. Here we discuss only one of them which seems the most suitable for the LCCQM. In order to decide the criteria of the fit, we should answer the following questions. First, in which x-range and with what accuracy is the model applicable? Second, how stable are the results under evolution? A related key question emerging not only here but in any nonperturbative calculation concerns the scale at which the model results for the parton distributions hold. From the point of view of QCD where both quark and gluon degrees of freedom contribute, the role of the low-energy quark models is to provide initial conditions for the QCD evolution equations. Therefore, we assume the existence of a low-scale Q_0^2 where glue and sea quark contributions are suppressed, and the dynamics inside the nucleon is described in terms of three valence (constituent) quarks confined by an effective long-range interaction. In fact, glue and sea quark degrees of freedom might be thought of at this low scale to be contained in the structure of the constituent quarks, which are massive objects. The actual value of Q_0^2 is fixed evolving back unpolarized data, until the valence distribution matches the condition that the second moment $\langle x(Q_0^2)\rangle_{\text{val}}$, *i.e.* the momentum fraction carried by

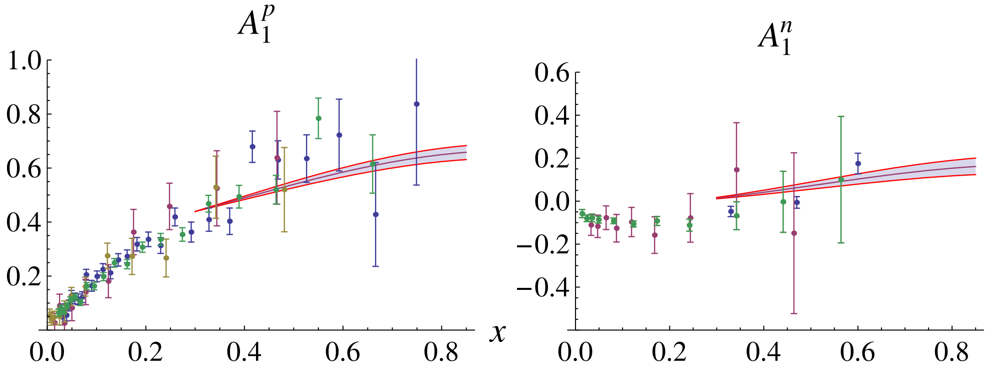

Fig. 6. – The inclusive double-spin asymmetry A_1 in DIS off proton (left panel) and neutron (right panel) as a function of x. The theoretical curves are obtained from LO evolution to $Q^2 = 2.5$ GeV^2 of the PDFs calculated in the LCCQM with admixture of $SU(6)$ components in the nucleon wave function. The parameter describing the percentage of the $SU(6)$-symmetric and $SU(6)$-breaking components is obtained from the fit to the experimental data, with the result $\delta = 7.25$. The experimental data for A_1^p are from refs. [107-110] and for A_1^n from refs. [111-114].

the valence quarks, is equal to one [106]. Following [122], we start with the LO-value of $\langle x(Q^2)\rangle_{\rm val} = 0.35$ at $10\,{\rm GeV}^2$ [123] and using LO evolution equations we find the matching condition $\langle x(Q_0^2)\rangle_{\rm val} = 1$, at $Q_0 = 420\,{\rm MeV}$. Although there is no rigorous relation between the QCD quarks and the constituent quarks, which requires a more fundamental description of the transition from soft to hard regimes, this strategy reflects the present state of the art for quark model calculations [103-105], and has been validated with a fair comparison to experiments [23, 45, 103, 106].

As can be seen in fig. 5, the description of the experimental data is reasonable. For $x \gtrsim 0.15$ the model describes the A_1 data within an accuracy of about 30%. The description improves in the valence-x region of $x \gtrsim 0.25$. Since the model contains no antiquark- and gluon-degrees of freedom, it is not surprising to observe that it does not work at small x. In conclusion, it can be said that the results are weakly scale dependent, and the model well catches the main features of the observable A_1 in its range of applicability, namely in the valence-x region. Therefore, we choose to fit the parameter describing the admixture of $SU(6)$-breaking terms in the nucleon wave function using the LO results for A_1 of proton and neutron evolved at the average $\langle Q^2\rangle = 2.5$ GeV^2 of the available experimental data, and restricting ourselves to the valence region $x \geq 0.3$.

The results of the fit are: $\delta = 7.25$ degrees with $\chi^2 = 52.41$ for a total of $N = 28$ experimental points ($\chi^2_{\rm red} = \chi^2/(N-1) = 1.94$). The fitted value of δ corresponds to a percentage of 98.4% (1.6%) for the $SU(6)$-symmetric (-breaking) component of the nucleon wave function. The results of the fit are shown in fig. 6, with the error band corresponding to the 1σ region. We see that with a small percentage of $SU(6)$ breaking we are able to give an overall good description of the asymmetry for both proton and neutron target in the valence region.

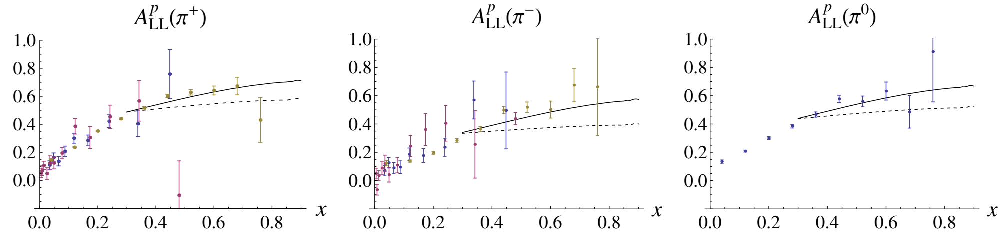

Fig. 7. – The semi-inclusive double-spin asymmetry A_{LL} in DIS of pions off a proton target as function of x. The dashed curves correspond to the LCCQM results in the $SU(6)$-symmetric version, while the solid curves include the contribution from $SU(6)$-breaking terms, with a percentage determined from the fit of the model to the A_1 (see text). For the fragmentation function D_1 we used the parametrization at $Q^2 = 2.5\,\text{GeV}^2$ from ref. [115]. The data are from refs. [116, 117].

The results of the fit can be also tested with other observables. In particular we consider the double spin asymmetrsy A^p_{LL} which can be accessed in SIDIS of hadrons off proton target. For a more extensive discussion about the calculation within the LCCQM of the azimuthal asymmetries in SIDIS related to T-even TMDs we refer to [45], while for comprehensive reviews of recent and planned experiments to access the TMDs we refer to [27, 124, 125]. Assuming the Gaussian ansatz for the $\boldsymbol{k}_\perp^2$ dependence of the f_1 and g_1 TMDs, this asymmetry can be written as

$$A_{LL} = \frac{F_{LL}}{F_{UU}} = \frac{\sum_a e_a^2\, x\, g_1^a(x)\, D_1^a(z)}{\sum_a e_a^2\, x\, f_1^a(x)\, D_1^a(z)}\,, \tag{112}$$

which reduces to A_1 in eq. (110) if no hadrons are observed in the final state. In eq. (112), $D_1(z)$ is the unpolarized fragmentation function describing the hadronization process of the struck quark decaying into the detected hadrons, with z the energy fraction taken out by the detected hadron. In the calculation we used for $D_1(z)$ the LO parametrization [115] at $Q^2 = 2.5\,\text{GeV}^2$. In fig. 7, we show the results for A_{LL} in DIS production of pions off proton target. In particular, the theoretical curves are obtained with the model results of $g_1(x)$ and $f_1(x)$ evolved at LO to $Q^2 = 2.5\,\text{GeV}^2$. The dashed curves show the results from the $SU(6)$-symmetric version of the LCCQM, and the solid curves correspond to the LCCQM predictions with a percentage of $SU(6)$-breaking terms as obtained from the fit of A_1. In both cases, we show the predictions only for $x \geq 0.3$, corresponding to the range where we performed the fit for A_1. We clearly see that the inclusion of $SU(6)$-breaking terms leads to a quite good agreement with the data in the valence region.

Another observable which is particularly sensitive to $SU(6)$ breaking is the electric neutron form factor G_E^n. It is well known that in the non-relativistic $SU(6)$ constituent quark model G_E^n is identically equal to zero. The inclusion of relativistic effects, like in the LCCQM, produces non-zero results. However, the predictions remain small and do not reproduce the behaviour of the experimental data, as shown by the dashed curve

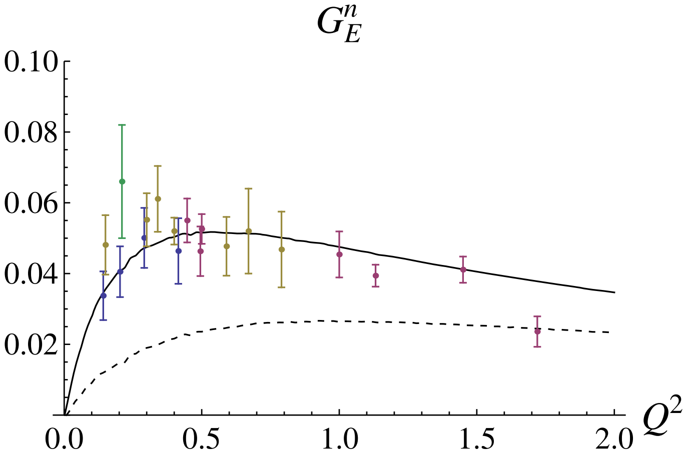

Fig. 8. – The electric form factor of the nucleon. The dashed curve shows the prediction within the $SU(6)$-symmetric version of the LCCQM. The solid curve is the LCCQM results with the inclusion of 1.6% of $SU(6)$-breaking component in the nucleon wave function. The references to the data can be found in [121].

in fig. 8. Corrections can come from the meson-cloud of the nucleon [118-120]. The meson-cloud contribution was recently calculated within the LCCQM in ref. [120] and it was found quite smooth, significant only at $Q^2 \leq 0.5\,\mathrm{GeV}^2$, but not able to reproduce the trend of the data. Only the inclusion of $SU(6)$-breaking terms can give a substantial improvement. This is shown by the solid curve in fig. 8, obtained within the LCCQM with the percentage of $SU(6)$-breaking terms which was obtained from the fit to the asymmetry A_1. Remarkably, the good agreement with the experimental data provides an important consistency check for our estimate of the $SU(6)$-breaking contribution to the nucleon wave function.

8. – Conclusions

In this work we presented a study of the transverse-momentum–dependent parton distributions in the framework of quark models. In particular we discussed several quark models, introducing the different formalisms for the practical calculation of the TMDs and identifying the common building blocks besides the specific assumptions for modeling the quark dynamics. We sorted these models in different classes: the light-cone models, the covariant parton model, the mean-field models and the spectator models. Most of these models predict relations among the leading-twist T-even TMDs. In particular, there are in total four independent relations among the leading-twist T-even TMDs: three of them are flavour independent and connect polarized TMDs, while a fourth flavour-dependent relation involves both polarized and unpolarized TMDs. Since in QCD the eight TMDs are all independent, it is clear that such relations should be traced back to some common simplifying assumptions in the models. First of all, it was noticed that they break down in models with gauge-field degrees of freedom. Furthermore, most quark models are valid at some very low scale and these relations are expected to break under QCD evolution to higher scales. Despite these limitations, such relations are intriguing because they can provide guidelines for building parametrizations of TMDs to be tested with experimental data and can also give useful insights for the understanding of the origin of the different spin-orbit correlations of quarks in the nucleon. We have shown that these model relations have essentially a geometrical origin, and can be traced back to properties of rotational invariance of the system. In particular, we identified the conditions which are sufficient for the existence of the flavour-independent relations. They are:

1) the probed quark behaves as if it does not interact directly with the other partons (*i.e.* one works within the standard impulse approximation) and there are no explicit gluons;

2) the quark light-cone and canonical polarizations are related by a rotation with axis orthogonal to both the light-cone and quark transverse-momentum directions;

3) the target has spherical symmetry in the canonical-spin basis.

For the flavour-dependent relation, one needs a further condition for the spin-flavour dependent part of the nucleon wave function. Specifically, it is required

4) $SU(6)$ spin-flavour symmetry of the wave function.

On the basis of the above assumptions, we were able to derive the model relations among TMDs within two different approaches.

The first approach is based on the representation of the quark correlator entering the definition of TMDs in terms of the polarization amplitudes of the quarks and nucleon. Such amplitudes are usually expressed in the basis of light-cone helicity. However, in order to discuss in a simple way the rotational properties of the system, we introduced the representation in the basis of canonical spin. In this framework, we showed that the conditions 1)–3) are sufficient for the existence of all three flavour-independent relations. We also showed that a subset of these three relations can be derived relaxing the assumption of spherical symmetry and using the less restrictive condition of axial symmetry under a rotation around a specific direction.

The second approach is based on the representation of TMDs in terms of quark wave functions. In particular, we expressed the TMDs as overlap of light-cone wave functions, and we derived the relation with the corresponding representation in terms of overlap of wave functions in the canonical-spin basis. After discussing the consequence of spherical symmetry on the spin structure of the wave function, we were able to obtain an alternative derivation of the relations among polarized T-even TMDs. Finally, for the remaining relation among polarized and unpolarized T-even TMDs, we used the $SU(6)$ symmetry for the spin-isospin dependence of the nucleon wave function.

On the basis of this study, we have shown how and to which extent the conditions 1)-4) are realized in the different classes of quark models. In particular we verified that all the models satisfying the TMD relations also satisfy the above conditions, while models where the TMD relations do not hold fail with at least one of the above conditions.

As specific example we discussed in details a light-cone constituent quark model, giving the necessary ingredients to perform the calculation of the T-even TMDs. The calculation can be reproduced numerically using two Mathematica programs which are available on-line. In particular, the first program allows one to reproduce the model calculation for i) the T-even TMDs; ii) the spin densities in the transverse-momentum space as a function of the quark and nucleon polarizations; iii) the $\boldsymbol{k}_\perp^2$ dependence of the x moments of the TMDs, with a comparison of the model results with the Gaussian ansatz. The calculation can be reproduced using the $SU(6)$-symmetric version of the light-cone constituent quark model as well as introducing the effects of $SU(6)$-symmetry breaking in the light-cone wave function which lead to the violation of the relation between unpolarized and polarized TMDs. The second Mathematica program allows one to obtain predictions for different observables, which are particularly sensitive to $SU(6)$ breaking and can be used to fix the free parameter of the model corresponding to the percentage of $SU(6)$-breaking terms in the LCWF of the nucleon. In particular, in this program we present different strategies for fitting the available experimental data of three observables: i) the inclusive polarized asymmetry A_1; ii) the ratio F_2^n/F_2^p of the neutron to proton unpolarized structure function of DIS; iii) the nucleon electroweak form factors. In these notes we discussed, as an example, the fit of the double-spin asymmetry A_1 in DIS. Using the results from this fit, we also discussed predictions for the semi-inclusive double-spin asymmetry A_{LL} in DIS of pions off proton target and for the electric neutron form factor. The good agreement of these observables with the experimental data provides an important consistency check for our estimate of the $SU(6)$-breaking contribution to the nucleon wave function.

This exercise provides a good example of the practical value of models in phenomenological studies, showing how model parameters related to particular assumptions on the quark dynamics can be tuned to describe available experimental data, and then can be used to learn new information on the partonic structure of the nucleon.

* * *

We are thankful to P. Schweitzer and H. Avakian for invaluable suggestions in the preparation of these lectures and for stimulating discussions. BP would like to express her gratitude to the organizers and participants of the Course "Three-dimensional Partonic Structure of the Nucleon" for creating a very lively and friendly atmosphere. This work was supported in part by the European Community Joint Research Activity "Study of Strongly Interacting Matter" (acronym HadronPhysics3, Grant Agreement n. 283286) under the Seventh Framework Programme of the European Community, and by the Italian MIUR through the PRIN 2008EKLACK "Structure of the nucleon: transverse momentum, transverse spin and orbital angular momentum" and by the P2I ("Physique des deux Infinis") project.

Appendix A.

Spinors and polarization four-vectors

We collect in this Appendix the different types of free spinors and polarization vectors. The free canonical Dirac spinor $u(k,\sigma)$ and polarization four-vector $\varepsilon^\mu(k,\sigma)$ are given by

$$u(k,\sigma) = \begin{pmatrix} \sqrt{E+m}\,\mathbb{1} \\ \sqrt{E-m}\,\frac{\boldsymbol{k}\cdot\boldsymbol{\sigma}}{|\boldsymbol{k}|} \end{pmatrix} \chi_\sigma, \tag{A.1}$$

$$\varepsilon^\mu(k,\sigma) = \left(\frac{\boldsymbol{\epsilon}_\sigma \cdot \boldsymbol{k}}{m}, \boldsymbol{\epsilon}_\sigma + \frac{\boldsymbol{k}\,(\boldsymbol{\epsilon}_\sigma \cdot \boldsymbol{k})}{m(E+m)} \right), \tag{A.2}$$

where $\chi_\uparrow = \left(\begin{smallmatrix}1\\0\end{smallmatrix}\right)$, $\chi_\downarrow = \left(\begin{smallmatrix}0\\1\end{smallmatrix}\right)$, and the polarization three-vectors are $\boldsymbol{\epsilon}_{\Uparrow,\Downarrow} = \frac{1}{\sqrt{2}}(\mp 1, -i, 0)$ for $s_z = \pm 1$, and $\boldsymbol{\epsilon}_\odot = (0,0,1)$ for $s_z = 0$. The free light-cone Dirac spinor $u_{LC}(k,\lambda)$ and polarization four-vector $\varepsilon^\mu_{LC}(k,\lambda)$ are given by

$$u_{LC}(k,+) = \frac{1}{\sqrt{2^{3/2}k^+}} \begin{pmatrix} \sqrt{2}k^+ + m \\ k_R \\ \sqrt{2}k^+ - m \\ k_R \end{pmatrix}, \qquad u_{LC}(k,-) = \frac{1}{\sqrt{2^{3/2}k^+}} \begin{pmatrix} -k_L \\ \sqrt{2}\,k^+ + m \\ k_L \\ -\sqrt{2}\,k^+ + m \end{pmatrix}, \tag{A.3}$$

$$\varepsilon^\mu_{LC}(k,\pm) = \left[0, \frac{\boldsymbol{\epsilon}_{\perp\pm} \cdot \boldsymbol{k}_\perp}{k^+}, \boldsymbol{\epsilon}_{\perp\pm} \right], \qquad \varepsilon^\mu_{LC}(k,0) = \frac{1}{m} \left[k^+, \frac{\boldsymbol{k}_\perp^2 - m^2}{2k^+}, \boldsymbol{k}_\perp \right], \tag{A.4}$$

with $\boldsymbol{\epsilon}_{\perp\pm} = \frac{1}{\sqrt{2}}(\mp 1, -i)$. Both types of spinors and polarization four-vectors coincide in the rest frame $k_{\text{rest}} = (m, \boldsymbol{0})$

$$u(k_{\text{rest}},\sigma) = u_{LC}(k_{\text{rest}},\sigma) = \sqrt{2m} \begin{pmatrix} \chi_\sigma \\ 0 \end{pmatrix}, \tag{A.5}$$

$$\varepsilon^\mu(k_{\text{rest}},\sigma) = \varepsilon^\mu_{LC}(k_{\text{rest}},\sigma) = (0, \boldsymbol{\epsilon}_\sigma)\,. \tag{A.6}$$

The "good" light-cone spinors are the simultaneous eigenstates of the operator γ_5 and the projector $P_+ = \frac{1}{2}\,\gamma^-\gamma^+$

$$P_+ u_G(\lambda) = u_G(\lambda), \qquad \gamma_5 u_G(\lambda) = \lambda\, u_G(\lambda), \qquad u_G(\lambda) \equiv \frac{1}{\sqrt{2}} \begin{pmatrix} \mathbb{1} \\ \sigma_3 \end{pmatrix} \chi_\lambda, \tag{A.7}$$

and one can write

$$P_+ = \sum_\lambda u_G(\lambda) u_G^\dagger(\lambda). \tag{A.8}$$

TABLE II. – *Decomposition in the canonical-spin basis* $\psi^{\uparrow}_{\sigma_1\sigma_2\sigma_3}$ *of the components of the 3Q LCWF in the light-cone helicity basis* $\psi^{+}_{\lambda_1\lambda_2\lambda_3}$. *The components are grouped according to the values of total orbital angular momentum* ℓ_z.

		$\ell_z=-1$		$\ell_z=0$	
		$\psi^{\uparrow}_{\uparrow\uparrow\uparrow}$	$\psi^{\uparrow}_{\uparrow\uparrow\downarrow}$	$\psi^{\uparrow}_{\uparrow\downarrow\uparrow}$	$\psi^{\uparrow}_{\downarrow\uparrow\uparrow}$
$\ell_z=-1$	ψ^{+}_{+++}	$z_1z_2z_3$	$z_1z_2l_3$	$z_1l_2z_3$	$l_1z_2z_3$
$\ell_z=0$	ψ^{+}_{++-}	$-z_1z_2r_3$	$z_1z_2z_3$	$-z_1l_2r_3$	$-l_1z_2r_3$
	ψ^{+}_{+-+}	$-z_1r_2z_3$	$-z_1r_2l_3$	$z_1z_2z_3$	$-l_1r_2z_3$
	ψ^{+}_{-++}	$-r_1z_2z_3$	$-r_1z_2l_3$	$-r_1l_2z_3$	$z_1z_2z_3$
$\ell_z=+1$	ψ^{+}_{--+}	$r_1r_2z_3$	$r_1r_2l_3$	$-r_1z_2z_3$	$-z_1r_2z_3$
	ψ^{+}_{-+-}	$r_1z_2r_3$	$-r_1z_2z_3$	$r_1l_2r_3$	$-z_1z_2r_3$
	ψ^{+}_{+--}	$z_1r_2r_3$	$-z_1r_2z_3$	$-z_1z_2r_3$	$l_1r_2r_3$
$\ell_z=+2$	ψ^{+}_{---}	$-r_1r_2r_3$	$r_1r_2z_3$	$r_1z_2r_3$	$z_1r_2r_3$

			$\ell_z=+1$		$\ell_z=+2$
		$\psi^{\uparrow}_{\downarrow\downarrow\uparrow}$	$\psi^{\uparrow}_{\downarrow\uparrow\downarrow}$	$\psi^{\uparrow}_{\uparrow\downarrow\downarrow}$	$\psi^{\uparrow}_{\downarrow\downarrow\downarrow}$
$\ell_z=-1$	ψ^{+}_{+++}	$l_1l_2z_3$	$l_1z_2l_3$	$z_1l_2l_3$	$l_1l_2l_3$
$\ell_z=0$	ψ^{+}_{++-}	$-l_1l_2r_3$	$l_1z_2z_3$	$z_1l_2z_3$	$l_1l_2z_3$
	ψ^{+}_{+-+}	$l_1z_2z_3$	$-l_1r_2l_3$	$z_1z_2l_3$	$l_1z_2l_3$
	ψ^{+}_{-++}	$z_1l_2z_3$	$z_1z_2l_3$	$-r_1l_2l_3$	$z_1l_2l_3$
$\ell_z=+1$	ψ^{+}_{--+}	$z_1z_2z_3$	$-z_1r_2l_3$	$-r_1z_2l_3$	$z_1z_2l_3$
	ψ^{+}_{-+-}	$-z_1l_2r_3$	$z_1z_2z_3$	$-r_1l_2z_3$	$z_1l_2z_3$
	ψ^{+}_{+--}	$-l_1z_2r_3$	$-l_1r_2z_3$	$z_1z_2z_3$	$l_1z_2z_3$
$\ell_z=+2$	ψ^{+}_{---}	$-z_1z_2r_3$	$-z_1r_2z_3$	$-r_1z_2z_3$	$z_1z_2z_3$

APPENDIX B.

Components of the 3Q LCWF in the light-cone and canonical polarization bases

Based on eq. (66), table II shows explicitly how the components of the 3Q LCWF in light-cone polarization basis are decomposed in the canonical-spin basis. We used for convenience the notations $z_i = \cos\frac{\theta_i}{2}$, $l_i = \hat{k}_{iL}\sin\frac{\theta_i}{2}$ and $r_i = \hat{k}_{iR}\sin\frac{\theta_i}{2}$ for the components of the rotation matrix $D^{(1/2)*}_{\sigma_i\lambda_i}$ of eq. (40). For example, from the first row of table II, we have

$$\begin{aligned}\psi^{+}_{+++} = {} & z_1z_2z_3\,\psi^{\uparrow}_{\uparrow\uparrow\uparrow} + z_1z_2l_3\,\psi^{\uparrow}_{\uparrow\uparrow\downarrow} + z_1l_2z_3\,\psi^{\uparrow}_{\uparrow\downarrow\uparrow} + l_1z_2z_3\,\psi^{\uparrow}_{\downarrow\uparrow\uparrow}\\ & + l_1l_2z_3\,\psi^{\uparrow}_{\downarrow\downarrow\uparrow} + l_1z_2l_3\,\psi^{\uparrow}_{\downarrow\uparrow\downarrow} + z_1l_2l_3\,\psi^{\uparrow}_{\uparrow\downarrow\downarrow} + l_1l_2l_3\,\psi^{\uparrow}_{\downarrow\downarrow\downarrow}.\end{aligned} \tag{B.1}$$

Table III. – *Decomposition in the canonical-spin basis* $\psi^{\Uparrow}_{\sigma}$ *of the components of the scalar quark-diquark LCWF in the light-cone helicity basis* ψ^{+}_{λ}. *The components are grouped according to the values of total orbital angular momentum* ℓ_z.

		$\ell_z = 0$ $\psi^{\Uparrow}_{\uparrow}$	$\ell_z = +1$ $\psi^{\Uparrow}_{\downarrow}$
$\ell_z = 0$	ψ^{+}_{+}	z	l
$\ell_z = +1$	ψ^{+}_{-}	$-r$	z

It is interesting to note that any single component of the 3Q LCWF in the canonical-spin basis contributes to all components in the light-cone helicity basis, and vice versa. So even if one considers that the wave function has only components with $\ell_z = 0$ in the canonical-spin basis, the components of the wave function in the light-cone helicity basis present all the values $\ell_z = -1, 0, +1, +2$, the orbital angular momentum being generated by the rotation matrices $D^{(1/2)*}_{\sigma_i\lambda_i}$.

Appendix C.

Connection to a quark-diquark picture

We show in this Appendix how the 3Q picture can be connected to a quark-diquark picture. In the latter, one considers the whole spectator system as an object with the quantum numbers of two quarks, namely a diquark. One may also assume that this diquark does not contain any internal orbital angular momentum. From a 3Q picture, this amounts to set $\tilde{k}_2 = \tilde{k}_3 = \tilde{k}_D/2$ and $m_D = 2m$ with $\tilde{k}_D$ and m_D the light-cone momentum and mass of the diquark, and m the mass of a valence quark.

C˙1. *Scalar diquark.* – The scalar diquark is obtained by coupling the two spectator quarks so to form a system with total angular momentum $j = 0$. The LCWF of the scalar quark-diquark system can be written in terms of the 3Q LCWF as follows:

$$\psi^{\Lambda}_{\lambda}\left(\tilde{k}, \tilde{k}_D\right) = \frac{1}{\sqrt{2}}\left[\psi^{\Lambda}_{\lambda+-}\left(\tilde{k}, \frac{\tilde{k}_D}{2}, \frac{\tilde{k}_D}{2}\right) - \psi^{\Lambda}_{\lambda-+}\left(\tilde{k}, \frac{\tilde{k}_D}{2}, \frac{\tilde{k}_D}{2}\right)\right]. \tag{C.1}$$

The total orbital angular momentum of a given component ψ^{Λ}_{λ} is given by the expression $\ell_z = \Lambda - \lambda$ with $\Lambda, \lambda = \pm\frac{1}{2}$.

The corresponding LCWF in the canonical-spin basis is defined through

$$\psi^{\Lambda}_{\lambda} = \sum_{\sigma} \psi^{\Lambda}_{\sigma}\, D^{(1/2)*}_{\sigma\lambda}, \tag{C.2}$$

and can consistently be written as

$$\psi^{\Lambda}_{\sigma}\left(\tilde{k}, \tilde{k}_D\right) = \frac{1}{\sqrt{2}}\left[\psi^{\Lambda}_{\sigma\uparrow\downarrow}\left(\tilde{k}, \frac{\tilde{k}_D}{2}, \frac{\tilde{k}_D}{2}\right) - \psi^{\Lambda}_{\sigma\downarrow\uparrow}\left(\tilde{k}, \frac{\tilde{k}_D}{2}, \frac{\tilde{k}_D}{2}\right)\right]. \tag{C.3}$$

The explicit decomposition of eq. (C.2) is displayed in table III.

Spherical symmetry in the canonical-spin basis reads

$$\sum_{\Lambda'\sigma'} [u(\theta,\phi)]_{\sigma\sigma'}\, [u(\theta,\phi)]^*_{\Lambda\Lambda'}\, \psi^{\Lambda'}_{\sigma'} = \psi^{\Lambda}_{\sigma}, \tag{C.4}$$

and in particular implies

$$\psi^{-\Lambda}_{-\sigma} = (-1)^{\Lambda-\sigma}\, \psi^{\Lambda}_{\sigma}, \tag{C.5a}$$

$$\psi^{\uparrow}_{\downarrow} = 0, \tag{C.5b}$$

in agreement with eqs. (69), (70) and (C.3).

C˙2. *Axial-vector diquark.* – The axial-vector diquark is obtained by coupling the two spectator quarks so to form a system with total angular momentum $j = 1$. The LCWF of the axial-vector quark-diquark system can be written in terms of the 3Q LCWF as follows:

$$\begin{aligned} \psi^{\Lambda}_{\lambda +}\left(\tilde{k},\tilde{k}_D\right) &= \psi^{\Lambda}_{\lambda ++}\left(\tilde{k},\frac{\tilde{k}_D}{2},\frac{\tilde{k}_D}{2}\right),\\ \psi^{\Lambda}_{\lambda 0}\left(\tilde{k},\tilde{k}_D\right) &= \frac{1}{\sqrt{2}}\left[\psi^{\Lambda}_{\lambda +-}\left(\tilde{k},\frac{\tilde{k}_D}{2},\frac{\tilde{k}_D}{2}\right) + \psi^{\Lambda}_{\lambda -+}\left(\tilde{k},\frac{\tilde{k}_D}{2},\frac{\tilde{k}_D}{2}\right)\right],\\ \psi^{\Lambda}_{\lambda -}\left(\tilde{k},\tilde{k}_D\right) &= \psi^{\Lambda}_{\lambda --}\left(\tilde{k},\frac{\tilde{k}_D}{2},\frac{\tilde{k}_D}{2}\right). \end{aligned} \tag{C.6}$$

The total orbital angular momentum of a given component $\psi^{\Lambda}_{\lambda\lambda_D}$ is given by the expression $\ell_z = \Lambda - \lambda - \lambda_D$ with $\Lambda, \lambda = \pm\frac{1}{2}$ and $\lambda_D = +1, 0, -1$.

The corresponding LCWF in the canonical-spin basis is defined through

$$\psi^{\Lambda}_{\lambda\lambda_D} = \sum_{\sigma\sigma_D} \psi^{\Lambda}_{\sigma\sigma_D}\, D^{(1/2)*}_{\sigma\lambda}\, D^{(1)*}_{\sigma_D\lambda_D}, \tag{C.7}$$

with the rotation for the axial-vector diquark given by

$$D^{(1)*}_{\sigma_D\lambda_D}\left(\tilde{k}_D\right) = \begin{pmatrix} \frac{1+\cos\theta_D}{2} & -\frac{\hat{k}_R}{\sqrt{2}}\sin\theta_D & \hat{k}_R^2\,\frac{1-\cos\theta_D}{2} \\ \frac{\hat{k}_L}{\sqrt{2}}\sin\theta_D & \cos\theta_D & -\frac{\hat{k}_R}{\sqrt{2}}\sin\theta_D \\ \hat{k}_L^2\,\frac{1-\cos\theta_D}{2} & \frac{\hat{k}_L}{\sqrt{2}}\sin\theta_D & \frac{1+\cos\theta_D}{2} \end{pmatrix}, \tag{C.8}$$

or equivalently,

$$\text{(C.9)}\qquad D^{(1)*}_{\sigma_D\lambda_D}\left(\tilde{k}_D\right) = \begin{pmatrix} \cos^2\frac{\theta_D}{2} & -\sqrt{2}\,\hat{k}_R\,\sin\frac{\theta_D}{2}\cos\frac{\theta_D}{2} & \hat{k}_R^2\,\sin^2\frac{\theta_D}{2} \\ \sqrt{2}\,\hat{k}_L\,\sin\frac{\theta_D}{2}\cos\frac{\theta_D}{2} & \cos^2\frac{\theta_D}{2}-\sin^2\frac{\theta_D}{2} & -\sqrt{2}\,\hat{k}_R\,\sin\frac{\theta_D}{2}\cos\frac{\theta_D}{2} \\ \hat{k}_L^2\,\sin^2\frac{\theta_D}{2} & \sqrt{2}\,\hat{k}_L\,\sin\frac{\theta_D}{2}\cos\frac{\theta_D}{2} & \cos^2\frac{\theta_D}{2} \end{pmatrix}.$$

Provided that $\theta_D(\tilde{k}_D) = \theta(\tilde{k}_D/2)$, we can consistently write the axial-vector quark-diquark LCWF in the canonical-spin basis as

$$\text{(C.10)}\qquad \begin{aligned} \psi^{\Lambda}_{\sigma\Uparrow}\left(\tilde{k},\tilde{k}_D\right) &= \psi^{\Lambda}_{\sigma\uparrow\uparrow}\left(\tilde{k},\frac{\tilde{k}_D}{2},\frac{\tilde{k}_D}{2}\right), \\ \psi^{\Lambda}_{\sigma\odot}\left(\tilde{k},\tilde{k}_D\right) &= \frac{1}{\sqrt{2}}\left[\psi^{\Lambda}_{\sigma\uparrow\downarrow}\left(\tilde{k},\frac{\tilde{k}_D}{2},\frac{\tilde{k}_D}{2}\right)+\psi^{\Lambda}_{\sigma\downarrow\uparrow}\left(\tilde{k},\frac{\tilde{k}_D}{2},\frac{\tilde{k}_D}{2}\right)\right], \\ \psi^{\Lambda}_{\sigma\Downarrow}\left(\tilde{k},\tilde{k}_D\right) &= \psi^{\Lambda}_{\sigma\downarrow\downarrow}\left(\tilde{k},\frac{\tilde{k}_D}{2},\frac{\tilde{k}_D}{2}\right). \end{aligned}$$

The explicit decomposition of eq. (C.7) is displayed in table IV.

Spherical symmetry in the canonical-spin basis reads

$$\text{(C.11)}\qquad \sum_{\Lambda'\sigma'\sigma'_D}\,[u(\theta,\phi)]_{\sigma\sigma'}\,[U(\theta,\phi)]_{\sigma_D\sigma'_D}\,[u(\theta,\phi)]^*_{\Lambda\Lambda'}\,\psi^{\Lambda'}_{\sigma'\sigma'_D} = \psi^{\Lambda}_{\sigma\sigma_D},$$

where

$$\text{(C.12)}\qquad U(\theta,\phi) = \begin{pmatrix} \frac{1+\cos\theta}{2}\,e^{-i\phi} & -\frac{1}{\sqrt{2}}\,\sin\theta\,e^{-i\phi} & \frac{1-\cos\theta}{2}\,e^{-i\phi} \\ \frac{1}{\sqrt{2}}\,\sin\theta & \cos\theta & -\frac{1}{\sqrt{2}}\,\sin\theta \\ \frac{1-\cos\theta}{2}\,e^{i\phi} & \frac{1}{\sqrt{2}}\,\sin\theta\,e^{i\phi} & \frac{1+\cos\theta}{2}\,e^{i\phi} \end{pmatrix},$$

and in particular implies

$$\text{(C.13a)}\qquad \psi^{-\Lambda}_{-\sigma-\sigma_D} = (-1)^{\Lambda+\sigma+\sigma_D}\,\psi^{\Lambda}_{\sigma\sigma_D},$$

$$\text{(C.13b)}\qquad \psi^{\uparrow}_{\uparrow\Uparrow} = \psi^{\uparrow}_{\downarrow\odot} = \psi^{\uparrow}_{\uparrow\Downarrow} = \psi^{\uparrow}_{\downarrow\Downarrow} = 0,$$

$$\text{(C.13c)}\qquad \psi^{\uparrow}_{\downarrow\Uparrow} = -\sqrt{2}\,\psi^{\uparrow}_{\uparrow\odot},$$

in agreement with eqs. (69)–(71) and (C.10).

Table IV. – *Decomposition in the canonical-spin basis* $\psi^{\uparrow}_{\sigma\sigma_D}$ *of the components of the axial-vector quark-diquark LCWF in the light-cone helicity basis* $\psi^{+}_{\lambda\lambda_D}$*. The components are grouped according to the values of total orbital angular momentum* ℓ_z*.*

		$\ell_z=-1$	$\ell_z=0$	
		$\psi^{\uparrow}_{\uparrow\Uparrow}$	$\psi^{\uparrow}_{\uparrow\odot}$	$\psi^{\uparrow}_{\downarrow\Uparrow}$
$\ell_z=-1$	ψ^{+}_{++}	zz_D^2	$\sqrt{2}\,zz_Dl_D$	lz_D^2
$\ell_z=0$	ψ^{+}_{+0}	$-\sqrt{2}\,zz_Dr_D$	$z(z_D^2-r_Dl_D)$	$-\sqrt{2}\,lz_Dr_D$
	ψ^{+}_{-+}	$-rz_D^2$	$-\sqrt{2}\,rz_Dl_D$	zz_D^2
$\ell_z=+1$	ψ^{+}_{-0}	$\sqrt{2}\,rz_Dr_D$	$-r(z_D^2-r_Dl_D)$	$-\sqrt{2}\,zz_Dr_D$
	ψ^{+}_{+-}	zr_D^2	$-\sqrt{2}\,zz_Dr_D$	lr_D^2
$\ell_z=+2$	ψ^{+}_{--}	$-rr_D^2$	$\sqrt{2}\,rz_Dr_D$	zr_D^2

		$\ell_z=+1$		$\ell_z=+2$
		$\psi^{\uparrow}_{\downarrow\odot}$	$\psi^{\uparrow}_{\uparrow\Downarrow}$	$\psi^{\uparrow}_{\downarrow\Downarrow}$
$\ell_z=-1$	ψ^{+}_{++}	$\sqrt{2}\,lz_Dl_D$	zl_D^2	ll_D^2
$\ell_z=0$	ψ^{+}_{+0}	$l(z_D^2-r_Dl_D)$	$\sqrt{2}\,zz_Dl_D$	$\sqrt{2}\,lz_Dl_D$
	ψ^{+}_{-+}	$\sqrt{2}\,zz_Dl_D$	$-rl_D^2$	zl_D^2
$\ell_z=+1$	ψ^{+}_{-0}	$z(z_D^2-r_Dl_D)$	$-\sqrt{2}\,rz_Dl_D$	$\sqrt{2}\,zz_Dl_D$
	ψ^{+}_{+-}	$-\sqrt{2}\,lz_Dr_D$	zz_D^2	lz_D^2
$\ell_z=+2$	ψ^{+}_{--}	$-\sqrt{2}\,zz_Dr_D$	$-rz_D^2$	zz_D^2

REFERENCES

[1] Collins J. C. and Soper D. E., *Nucl. Phys. B*, **193** (1981) 381; **213** (1983) 545(Erratum).

[2] Collins J. C. and Soper D. E., *Nucl. Phys. B*, **194** (1982) 445.

[3] Kotzinian A., *Nucl. Phys. B*, **441** (1995) 234.

[4] Mulders P. J. and Tangerman R. D., *Nucl. Phys. B*, **461** (1996) 197; **484** (1997) 538(Erratum).

[5] Boer D., Jakob R. and Mulders P. J., *Nucl. Phys. B*, **504** (1997) 345.

[6] Dittes F. M., Müller D., Robaschik D., Geyer B. and Hořejši J., *Phys. Lett. B*, **209** (1988) 325.

[7] Müller D., Robaschik D., Geyer B., Dittes F. M. and Hořejši J., *Fortschr. Phys.*, **42** (1994) 101.

[8] Ji X., *Phys. Rev. Lett.*, **78** (1997) 610.

[9] Radyushkin A. V., *Phys. Lett. B*, **380** (1996) 417.

[10] Ji X., *Phys. Rev. D*, **55** (1997) 7114.

[11] Radyushkin A. V., *Phys. Lett. B*, **385** (1996) 333.

[12] Ji X., *J. Phys. G: Nucl. Part. Phys.*, **24** (1998) 1181.

[13] GOEKE K., POLYAKOV M. V. and VANDERHAEGHEN M., *Prog. Part. Nucl. Phys.*, **47** (2001) 401.

[14] DIEHL M., *Phys. Rep.*, **388** (2003) 41.

[15] JI X., *Ann. Rev. Nucl. Part. Sci.*, **54** (2004) 413.

[16] BELITSKY A. V. and RADYUSHKIN A. V., *Phys. Rep.*, **418** (2005) 1.

[17] BOFFI S. and PASQUINI B., *Riv. Nuovo Cimento*, **30** (2007) 387.

[18] SOPER D. E., *Phys. Rev. D*, **15** (1977) 1141.

[19] BURKARDT M., *Phys. Rev. D*, **62** (2000) 071503; **66** (2002) 119903(Erratum).

[20] BURKARDT M., *Int. J. Mod. Phys. A*, **18** (2003) 173.

[21] MEISSNER S., METZ A., SCHLEGEL M. and GOEKE K., *JHEP*, **0808** (2008) 038.

[22] MEISSNER S., METZ A. and SCHLEGEL M., *JHEP*, **0908** (2009) 056.

[23] LORCÉ C., PASQUINI B. and VANDERHAEGHEN M., *JHEP*, **1105** (2011) 041.

[24] JI X., *Phys. Rev. Lett.*, **91** (2003) 062001.

[25] BELITSKY A. V., JI X. D. and YUAN F., *Phys. Rev. D*, **69** (2004) 074014.

[26] LORCÉ C. and PASQUINI B., *Phys. Rev. D*, **84** (2011) 014015.

[27] BOER D., DIEHL M., MILNER R., VENUGOPALAN R., VOGELSANG W., KAPLAN D., MONTGOMERY H., VIGDOR S. *et al.*, arXiv:1108.1713 [nucl-th].

[28] JAKOB R., MULDERS P. J. and RODRIGUES J., *Nucl. Phys. A*, **626** (1997) 937.

[29] GOLDSTEIN G. R. and GAMBERG L. P., arXiv:hep-ph/0209085.

[30] POBYLITSA P. V., arXiv:hep-ph/0212027.

[31] GAMBERG L. P., GOLDSTEIN G. R and OGANESSYAN K. A., *Phys. Rev. D*, **67** (2003) 071504.

[32] LU Z. and MA B. Q., *Nucl. Phys. A*, **741** (2004) 200.

[33] CHEREDNIKOV I. O., D'ALESIO U., KOCHELEV N. I. and MURGIA F., *Phys. Lett. B*, **642** (2006) 39.

[34] LU Z. and SCHMIDT I., *Phys. Rev. D*, **75** (2007) 073008.

[35] GAMBERG L. P., GOLDSTEIN G. R. and SCHLEGEL M., *Phys. Rev. D*, **77** (2008) 094016.

[36] PASQUINI B., BOFFI S. and SCHWEITZER P., *Mod. Phys. Lett. A*, **24** (2009) 2903.

[37] EFREMOV A. V., SCHWEITZER P., TERYAEV O. V. and ZAVADA P., *Phys. Rev. D*, **80** (2009) 014021.

[38] SHE J., ZHU J. and MA B. Q., *Phys. Rev. D*, **79** (2009) 054008.

[39] ZHU J. and MA B. Q., *Phys. Lett. B*, **696** (2011) 246.

[40] LU Z. and SCHMIDT I., *Phys. Rev. D*, **82** (2010) 094005.

[41] AVAKIAN H., EFREMOV A. V., SCHWEITZER P., TERYAEV O. V., YUAN F. and ZAVADA P., *Mod. Phys. Lett. A*, **24** (2009) 2995.

[42] COURTOY A., SCOPETTA S. and VENTO V., *Phys. Rev. D*, **80** (2009) 074032.

[43] COURTOY A., FRATINI F., SCOPETTA S. and VENTO V., *Phys. Rev. D*, **78** (2008) 034002.

[44] PASQUINI B. and YUAN F., *Phys. Rev. D*, **81** (2010) 114013.

[45] BOFFI S., EFREMOV A. V., PASQUINI B. and SCHWEITZER P., *Phys. Rev. D*, **79** (2009) 094012.

[46] PASQUINI B. and LORCÉ C., arXiv:1008.0945 [hep-ph].

[47] BACCHETTA A., CONTI F. and RADICI M., *Phys. Rev. D*, **78** (2008) 074010.

[48] AVAKIAN H., EFREMOV A. V., SCHWEITZER P. and YUAN F., *Phys. Rev. D*, **81** (2010) 074035.

[49] AVAKIAN H., EFREMOV A. V., SCHWEITZER P. and YUAN F., *Phys. Rev. D*, **78** (2008) 114024.

[50] EFREMOV A. V., SCHWEITZER P., TERYAEV O. V. and ZAVADA P., *Phys. Rev. D*, **83** (2011) 054025.

[51] MEISSNER S., METZ A. and GOEKE K., *Phys. Rev. D*, **76** (2007) 034002.

[52] WAKAMATSU M., *Phys. Rev. D*, **79** (2009) 094028.

[53] Schweitzer P., Urbano D., Polyakov M. V., Weiss C., Pobylitsa P. V. and Goeke K., *Phys. Rev. D*, **64** (2001) 034013.

[54] Bourrely C., Buccella F. and Soffer J., *Phys. Rev. D*, **83** (2011) 074008.

[55] Del Dotto A., Pace E., Salmé G. and Scopetta S., arXiv:1110.6757 [nucl-th].

[56] Brodsky S. J., Hwang D. S. and Schmidt I., *Phys. Lett. B*, **530** (2002) 99.

[57] Metz A., *Phys. Lett. B*, **549** (2002) 139.

[58] Afanasev A. and Carlson C. E., arXiv:hep-ph/0308163.

[59] Metz A. and Schlegel M., *Eur. Phys. J. A*, **22** (2004) 489.

[60] Metz A. and Schlegel M., *Annalen Phys.*, **13** (2004) 699.

[61] Lorcé C. and Pasquini B., *Phys. Rev. D*, **84** (2011) 034039.

[62] Boer D. and Mulders P. J., *Phys. Rev. D*, **57** (1998) 5780.

[63] Goeke K., Metz A. and Schlegel M., *Phys. Lett. B*, **618** (2005) 90.

[64] Bacchetta A., Diehl M., Goeke K., Metz A., Mulders P. J. and Schlegel M., *JHEP*, **0702** (2007) 093.

[65] Bomhof C. J., Mulders P. J. and Pijlman F., *Phys. Lett. B*, **596** (2004) 277.

[66] Sivers D. W., *Phys. Rev. D*, **41** (1990) 83.

[67] Ji X. and Yuan F., *Phys. Lett. B*, **543** (2002) 66.

[68] Belitsky A. V., Ji X. and Yuan F., *Nucl. Phys. B*, **656** (2003) 165.

[69] Boer D., Mulders P. J. and Pijlman F., *Nucl. Phys. B*, **667** (2003) 201.

[70] Brodsky S. J., *Nucl. Phys. A*, **827** (2009) 327C.

[71] Brodsky S.J., Pasquini B., Xiao B. W. and Yuan F., *Phys. Lett. B*, **687** (2010) 327.

[72] Brodsky S. J., Pauli H. C. and Pinsky S. S., *Phys. Rept.*, **301** (1998) 299.

[73] Diehl M., Feldmann T., Jakob R. and Kroll P., *Nucl. Phys. B*, **596** (2001) 33; **605** (2001) 647(Erratum).

[74] Brodsky S. J., Diehl M. and Hwang D. S., *Nucl. Phys. B*, **596** (2001) 99.

[75] Pasquini B., Cazzaniga S. and Boffi S., *Phys. Rev. D*, **78** (2008) 034025.

[76] Boffi S., Pasquini B. and Traini M., *Nucl. Phys. B*, **649** (2003) 243.

[77] Boffi S., Pasquini B. and Traini M., *Nucl. Phys. B*, **680** (2004) 147.

[78] Pasquini B., Pincetti M. and Boffi S., *Phys. Rev. D*, **72** (2005) 094029; **76** (2007) 034020

[79] Hägler Ph., Musch B. U., Negele J. W. and Schäfer A., *Europhys. Lett.*, **88** (2009) 61001.

[80] Musch B. U., Hägler Ph., Negele J. W. and Schäfer A., *Phys. Rev. D*, **83** (2011) 094507.

[81] Musch B. U., arXiv:0907.2381 [hep-lat].

[82] Efremov A. V. and Schweitzer P., *JHEP*, **0308** (2003) 006.

[83] Ma B.-Q., *J. Phys. G*, **G17** (1991) L53.

[84] Lorcé C., *Phys. Rev. D*, **74** (2006) 054019.

[85] Lorcé C., *Phys. Rev. D*, **78** (2008) 034001.

[86] Melosh H. J., *Phys. Rev. D*, **9** (1974) 1095.

[87] Ahluwalia D. V. and Sawicki M., *Phys. Rev. D*, **47** (1993) 5161.

[88] Petrov V. Y. and Polyakov M. V., arXiv:hep-ph/0307077.

[89] Diakonov D. and Petrov V. Y., *Phys. Rev. D*, **72** (2005) 074009.

[90] Brodsky S. J., Hwang D. S., Ma B.-Q. and Schmidt I., *Nucl. Phys. B*, **593** (2001) 311.

[91] Ellis J. R., Hwang D. S. and Kotzinian A., *Phys. Rev. D*, **80** (2009) 074033.

[92] Gross F., Ramalho G. and Pena M. T., *Phys. Rev. C*, **77** (2008) 015202.

[93] Ramalho G., Pena M. T. and Gross F., *Eur. Phys. J. A*, **36** (2008) 329.

[94] Gross F., Ramalho G. and Pena M. T., *Phys. Rev. C*, **77** (2008) 035203.

[95] Gamberg L. and Schlegel M., *Phys. Lett. B*, **685** (2010) 95; *Mod. Phys. Lett. A*, **24** (2009) 2960.

[96] Pasquini B., `http:www.pv.infn.it/~pasquini/Varenna/TMDs-calculation-final-WINDOWS.nb` (Windows version); `http:www.pv.infn.it/~pasquini/Varenna/TMDs-calculation-final-LINUX.nb` (Linux version).

[97] Pasquini B., `http:www.pv.infn.it/~pasquini/Varenna/Fit-final.nb`.

[98] Schlumpf F., hep-ph/9211255.

[99] Schlumpf F., *J. Phys. G: Nucl. Part. Phys.*, **20** (1994) 237; *Phys. Rev. D*, **49** (1993) 6246(E); **50** (1994) 6895; **51** (1995) 2262; Brodsky S. J. and Schlumpf F., *Phys. Lett. B*, **329** (1994) 111.

[100] Miller G. A., *Phys. Rev. C*, **76** (2007) 065209.

[101] Diehl M. and Hägler Ph., *Eur. Phys. J. C*, **44** (2005) 87.

[102] Pasquini B. and Boffi S., *Phys. Lett. B*, **653** (2007) 23.

[103] Scopetta S., Vento V. and Traini M., *Phys. Lett. B*, **421** (1998) 64; **442** (1998) 28.

[104] Broniowski W., Arriola E. R., and Golec-Biernat K., *Phys. Rev. D*, **77** (2008) 034023.

[105] Pasquini B., Traini M. and Boffi S., *Phys. Rev. D*, **71** (2005) 034022.

[106] Traini M., Vento V., Mair A. and Zambarda A., *Nucl. Phys. A*, **614** (1997) 472; Mair A. and Traini M., *Nucl. Phys. A*, **624** (1997) 564.

[107] Abe K. *et al.* (E143 Collaboration), *Phys. Rev. D*, **58** (1998) 112003.

[108] Ashman J. *et al.* (European Muon Collaboration), *Phys. Lett. B*, **206** (1998) 364.

[109] Adeva B. *et al.* (Spin Muon Collaboration), *Phys. Rev. D*, **60** (1999) 072004; **62** (2000) 079902(Erratum).

[110] Airapetian A. *et al.* (HERMES Collaboration), *Phys. Lett. B*, **442** (1998) 484.

[111] Zheng X. *et al.* (Jefferson Lab Hall A Collaboration), *Phys. Rev. Lett.*, **92** (2004) 012004. Zheng X. *et al.* (Jefferson Lab Hall A Collaboration), *Phys. Rev. C*, **70** (2004) 065207.

[112] Anthony P. L. *et al.* (E142 Collaboration), *Phys. Rev. D*, **54** (1996) 6620.

[113] Ackerstaff K. *et al.* (HERMES Collaboration), *Phys. Lett. B*, **404** (1997) 383.

[114] Abe K. *et al.* (E154 Collaboration), *Phys. Lett. B*, **405** (1997) 180; *Phys. Rev. Lett.*, **79** (1997) 26.

[115] Kretzer S., *Phys. Rev. D*, **62** (2000) 054001.

[116] Adeva B. *et al.* (Spin Muon Collaboration), *Phys. Lett. B*, **420** (1998) 180.

[117] Airapetian A. *et al.* (HERMES Collaboration), *Phys. Rev. D*, **71** (2005) 012003.

[118] Miller G. A., *Phys. Rev. C*, **66** (2002) 032201.

[119] Rinehimer J. A. and Miller G. A., *Phys. Rev. C*, **80** (2009) 025206.

[120] Pasquini B. and Boffi S., *Phys. Rev. D*, **76** (2007) 074011.

[121] Perdrisat C. F., Punjabi V. and Vanderhaeghen M., *Prog. Part. Nucl. Phys.*, **59** (2007) 694.

[122] Pasquini B. and Schweitzer P., *Phys. Rev. D*, **83** (2011) 114044.

[123] Martin A. D., Stirling W. J., Thorne R. S. and Watt G., *Eur. Phys. J. C*, **63** (2009) 189.

[124] Barone V., Bradamante F. and Martin A., *Prog. Part. Nucl. Phys.*, **65** (2010) 267.

[125] Anselmino M., Avakian H., Boer D., Bradamante F., Burkardt M., Chen J. P., Cisbani E., Contalbrigo M. *et al.*, *Eur. Phys. J. A*, **47** (2011) 35.

Proceedings of the International School of Physics "Enrico Fermi"
Course CLXXX "Three-Dimensional Partonic Structure of the Nucleon"
edited by M. Anselmino, H. Avakian, D. Hasch and P. Schweitzer
(IOS, Amsterdam; SIF, Bologna)
DOI 10.3254/978-1-61499-197-7-245

Deep virtual Compton scattering: From data to generalized parton distributions (or Compton form factors)

M. Guidal

Institut de Physique Nucléaire d'Orsay - Orsay, France

Summary. — We present some of the latest developments in the field of Generalized Parton Distributions (GPD). Experimentally, a lot of data has been recently released from the DESY and Jefferson Lab (JLab) facilities. Theoretically, much progress has been made with the recent emergence of fitting codes and algorithms which provide some first 3-d imaging insights on the quark structure of the nucleon. In this paper, we concentrate our discussions on the deep virtual compton scattering process and to the quark sector.

1. – Introduction

Much of what we have learned on the structure of the nucleon these past 40 years or so has come from the scattering of high energy leptons (from a few 100 MeV to a few 100 GeV).

One of the most elementary lepton scattering experiments is the elastic lepton-nucleon scattering process $eN \to e'N'$. Such experiments were first carried out at Stanford in the 50's by Hofstadter and collaborators. In this process, one accesses the "form factors"

© Società Italiana di Fisica

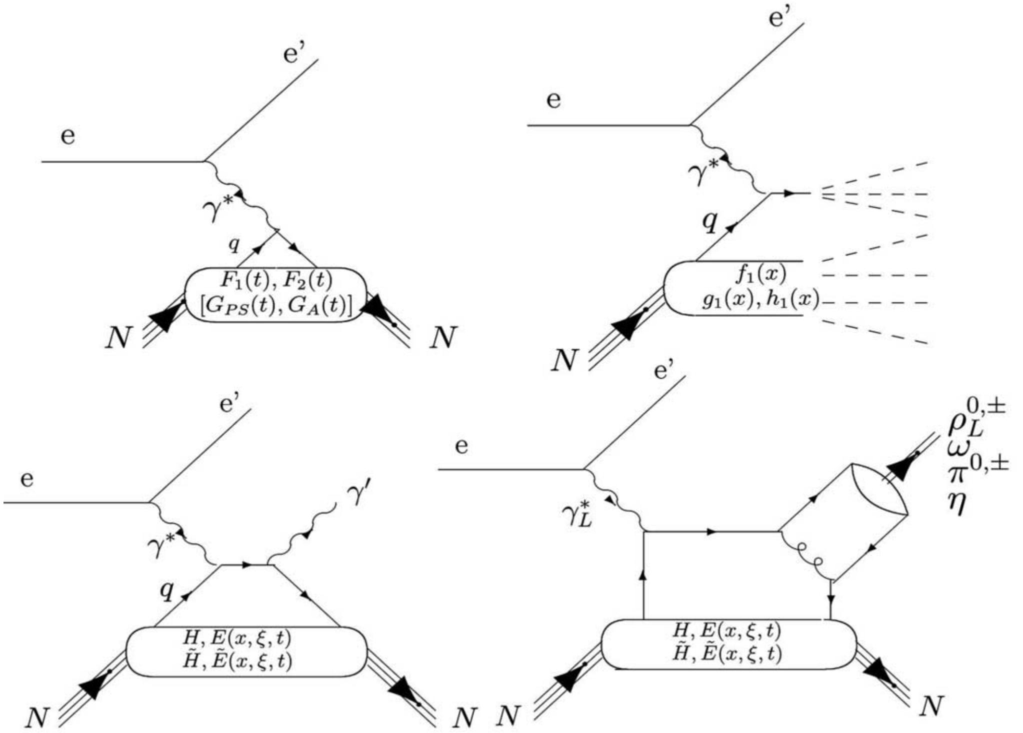

Fig. 1. – Top left: elastic scattering $eN \to e'N'$ where the complex structure of the nucleon is parametrized in terms of FFs. Top right: deep inelastic scattering $eN \to e'X$ where the complex structure of the nucleon is parametrized in terms of PDFs. Bottom left and right: deep exclusive scattering $eN \to e'(M, \gamma)$ where the complex structure of the nucleon is parametrized in terms of GPDs. Bottom left: "handbag diagram" for Deep Virtual Compton Scattering (DVCS); Bottom right: "handbag diagram" for Deep Virtual Meson Production (DVMP).

(FF) of the nucleon. See fig. 1 (top left). The FFs depend only the squared momentum transfer of the lepton to the nucleon $Q^2 = -(e - e')^2$ (or equivalently $t = (N - N')^2$). They reflect the composite nature of the nucleon. With a (vector) virtual photon probe, one can define two FFs $F_1(t)$ and $F_2(t)$. There are two FFs because the nucleon has a spin $\frac{1}{2}$. Its spin can be flipped ($F_2(t)$) or not ($F_1(t)$) in the process. If ones uses an axial or a pseudo-scalar probe, one can define two more FFs: $G_A(t)$ and $G_{PS}(t)$. In a frame where the nucleon goes to the speed of light along a certain direction, the FFs give access, via the equivalent of a Fourier transform on the t variable, to the *transverse spatial* density of electromagnetic (or axial) charges in the nucleon.

Another class of elementary lepton scattering experiments is inclusive electron-nucleon scattering $eN \to e'X$, generically called "Deep Inelastic Scattering" (DIS). Such experiments were started in the late 60's at the Stanford Linear Accelerator Center (SLAC) laboratory. One accesses in such process the "Parton Distribution Functions" (PDF) of the nucleon. See fig. 1 (top right). The PDFs depend, at QCD first order (*i.e.* omitting $\log(Q^2)$ corrections), only on one variable, $x_B = \frac{Q^2}{2m_N(E_e - E_{e'})}$, the so-called Bjorken variable. In the quark sector, at QCD (Quantum Chromo-Dynamics) leading twist, *i.e.* keeping only the leading power terms in a $\frac{1}{Q^2}$ expansion, there are three PDFs which can be accessed in principle: $f_1(x_B)$, $g_1(x_B)$ and $h_1(x_B)$, according to the polarization of the target (respectively, unpolarized, longitudinally and transversely polarized (given a polarized lepton beam)). In a frame where the nucleon goes to the speed of light along a certain direction, the PDFs can be interpreted as the probability to find a parton with the *longitudinal momentum* fraction x_B in a nucleon.

At the end of the last century, a third class of process has come under intensive investigation, theoretically as well as experimentally. It is exclusive electron-nucleon scattering $eN \to e'N'(M,\gamma)$, where M stands for a meson and γ for a photon. This class of processes is generically called "Deep Exclusive Scattering" (DES). See fig. 1 (bottom). The cross-sections of these processes are much smaller than those of the elastic or DIS processes. Only with the recent advent of the high luminosity lepton beam facilities combined with high-resolution detectors to ensure the exclusivity of the reaction, can these processes be accessed in an efficient way. The structure functions of the nucleon which are accessed in DES are the so-called "Generalized Parton Distributions" (GPDs). The theoretical formalism was introduced and first developped in the mid 90's by D. Müller *et al.* [1], X. Ji [2] and A. Radyushkin [3]. There are more particles and kinematic degrees of freedom in DES and therefore GPDs depend on more variables. At leading-order QCD, there are precisely three, which are x, ξ (which is actually equivalent to x_B: $\xi = \frac{x_B}{2-x_B}$) and t. In the quark sector, at QCD leading twist, there are eight GPDs: $H, \tilde{H}, E, \tilde{E}, H_T, \tilde{H}_T, E_T, \tilde{E}_T$. In DVCS and DVMP, only the first four can be accessed at QCD leading twist and they reflect the four independent spin/helicity transitions between the initial and final nucleons/quarks in the "handbag" diagrams of the bottom part of fig. 1. The GPDs give rise to several interpretations: in a frame where the nucleon goes to the speed of light along a certain direction, they represent the probability amplitude of finding a quark in the nucleon with a *longitudinal* momentum fraction $x + \xi$ and of putting it back into the nucleon with a *longitudinal* momentum fraction $x - \xi$ (plus some transverse momentum "kick", which is represented by t). Also, at $\xi = 0$, they can be interpreted as the probability amplitude of finding in a nucleon a parton with *longitudinal* momentum fraction x at a given *transverse* impact parameter $b_\perp$, which is the conjugate variable of t [4-6]. One sees then how the information contained in a traditional PDF, such as the ones measured in DIS, and the information contained in a FF, as measured in elastic lepton-nucleon scattering, are now combined and correlated in the GPD description.

In the forward limit ($\xi, t \to 0$), GPDs actually reduce to PDFs and their first x-moment are equal to FFs. Also, their second x-moment gives access to the quark orbital contribution to the nucleon spin. One shoud finally stress that the factorisation between the hard process of the upper part of the "handbag diagrams" and the lower "blob" which is parametrized by the GPDs in fig. 1 is valid for large Q^2 and small t. We refer the reader to the proceeding of the lecture of M. Diehl or to reviews [7-10] for the detailed

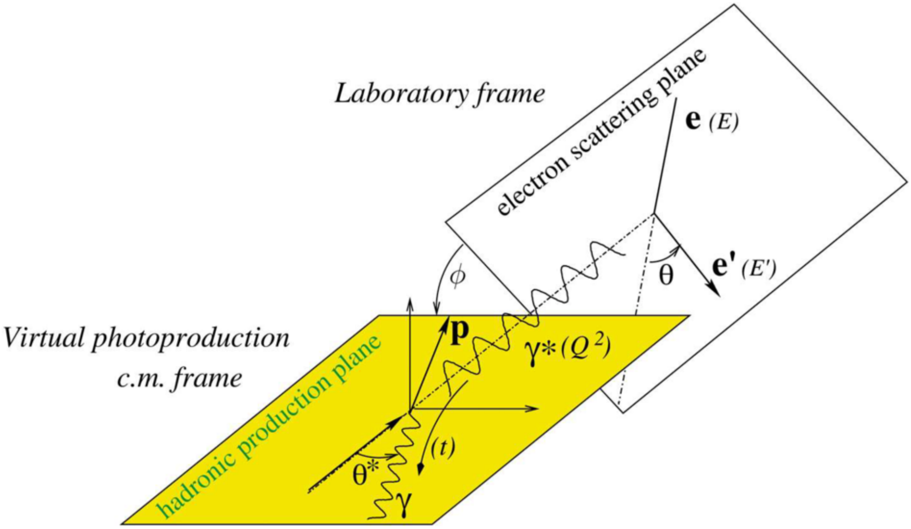

Fig. 2. – Reference frames and relevant variables for the description of the $e^p \to e'p\gamma$ reaction.

theoretical formalism and these general properties of the GPDs.

In the next section, we are going to explain the relation between GPDs and experimental observables. For the rest of the paper, we will actually focus on the DVCS channel. The reason, besides sake of space of these proceedings, is the absence, at QCD leading twist/order, of any strong coupling α_s in the DVCS "hard" amplitude, compared to the DVMP one (see bottom diagrams of fig. 1), which makes the interpretation of DVCS more straightforward. Indeed, α_s is "running" and, in particular, is rising as Q^2 (or more generally, the scale associated to the quark-gluon vertex to which Q^2 is proportional) decreases. The low-scale regime of α_s is not fully under control and therefore it is believed that the corrections to the simple QCD leading twist "handbag" diagram should be much more important in DVMP compared to DVCS. Also, the DVMP diagram involves, besides GPDs, another non-perturbative QCD quantity, the final meson distribution amplitude whose form is still under debate. The DVCS channel is therefore considered, at least theory-wise, as the "cleanest" and the "gloden channel" to access GPDs.

2. – From GPDs to data

In order to fully describe the 3-body final state reaction $ep \to ep\gamma$, there are four independent variables. They are usually chosen as Q^2, x_B, t and ϕ. We have already defined Q^2, x_B and t. The variable ϕ is the azimuthal angle between the electron scattering plane and the hadronic production plane. See fig. 2.

We recall that the GPDs depend on three variables: x, ξ and t with ξ equivalent to x_B. At QCD leading order, GPDs do not depend on Q^2. Like for PDFs, this absence of

Q^2 dependence reflects the fact that the virtual photon interacts with *pointlike* quarks. At QCD higher order, there is a Q^2 dependence but it can be predicted and calculated through the so-called evolution equations. We therefore omit it in the following.

We thus see that if the variables ξ and t can be measured, x is not experimentally accessible. The variable x which, we underline, is different from x_B, is a "mute" variable which is integrated over, due to the loop in the handbag diagrams (see fig. 1). Precisely, the DVCS amplitude is proportional to: $\int_{-1}^{+1} \mathrm{d}x \frac{H(x,\xi,t)}{x-\xi+i\epsilon} + \dots$ (where the ellipsis stand for similar terms in E, $\tilde{H}$ and $\tilde{E}$). The $\frac{1}{x-\xi+i\epsilon}$ term is the propagator of the quark between the incoming virtual photon and the outgoing photon. The previous expression can be decomposed into a real and an imaginary part: $PP(\int_{-1}^{+1} \mathrm{d}x \frac{H(x,\xi,t)}{x-\xi}) - i\pi H(\xi,\xi,t)$. This means that the maximum information that can be extracted from the experimental data at a given (ξ, t) point is $H(\pm\xi,\xi,t)$, when measuring an observable sensitive to the imaginary part of the DVCS amplitude, and $\int_{-1}^{+1} \mathrm{d}x \frac{H(\mp x,\xi,t)}{x\pm\xi}$, when measuring an observable sensitive to the real part of the DVCS amplitude.

If ones reduces the range of x from $\{-1, 1\}$ to $\{0, 1\}$ in the convolutions, there are therefore in principle eight GPD-related quantities that can be extracted:

$$\text{(1)} \qquad \mathrm{Re}\{\mathcal{H}\} = P\int_0^1 \mathrm{d}x\,[H(x,\xi,t) - H(-x,\xi,t)]\,C^+(x,\xi),$$

$$\text{(2)} \qquad \mathrm{Re}\{\mathcal{E}\} = P\int_0^1 \mathrm{d}x\,[E(x,\xi,t) - E(-x,\xi,t)]\,C^+(x,\xi),$$

$$\text{(3)} \qquad \mathrm{Re}\{\tilde{\mathcal{H}}\} = P\int_0^1 \mathrm{d}x\,\left[\tilde{H}(x,\xi,t) + \tilde{H}(-x,\xi,t)\right]C^-(x,\xi),$$

$$\text{(4)} \qquad \mathrm{Re}\{\tilde{\mathcal{E}}\} = P\int_0^1 \mathrm{d}x\,\left[\tilde{E}(x,\xi,t) + \tilde{E}(-x,\xi,t)\right]C^-(x,\xi),$$

$$\text{(5)} \qquad \mathrm{Im}\{\mathcal{H}\} = H(\xi,\xi,t) - H(-\xi,\xi,t),$$

$$\text{(6)} \qquad \mathrm{Im}\{\mathcal{E}\} = E(\xi,\xi,t) - E(-\xi,\xi,t),$$

$$\text{(7)} \qquad \mathrm{Im}\{\tilde{\mathcal{H}}\} = \tilde{H}(\xi,\xi,t) + \tilde{H}(-\xi,\xi,t),$$

$$\text{(8)} \qquad \mathrm{Im}\{\tilde{\mathcal{E}}\} = \tilde{E}(\xi,\xi,t) + \tilde{E}(-\xi,\xi,t)$$

with

$$\text{(9)} \qquad C^{\pm}(x,\xi) = \frac{1}{x-\xi} \pm \frac{1}{x+\xi}\,.$$

These are called the Compton Form Factors (CFFs) (be aware of slightly different notations in the literature ($-\pi$ factors in the definition of the "Im" CFFs, "$-$" signs for the "Re" CFFs,...), for instance with ref. [11]).

GPDs and CFFs, like FFs and PDFs, are defined for each quark flavor. Experimentally, the flavor decomposition can be done by measuring GPDs on the proton and on the neutron (DVMP provides also additional ways to carry out this flavor decomposition). For the proton, the combination of GPDs or CFFs accessed is $H^p(\xi,\xi,t) =$

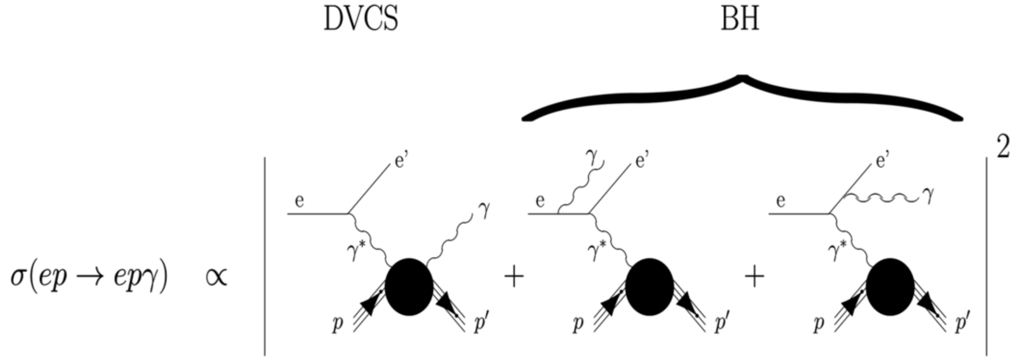

Fig. 3. – The cross-section of the $ep \to ep\gamma$ reaction is proportional to the squared amplitude: $|M_{\mathrm{DVCS}} + M_{\mathrm{BH}}|^2$. The DVCS process is proportional to GPDs while the BH process is proportional to FFs. The two processes interfere.

$\frac{4}{9}H^u(\xi,\xi,t) + \frac{1}{9}H^d(\xi,\xi,t)$ and for the neuton $H^n(\xi,\xi,t) = \frac{4}{9}H^d(\xi,\xi,t) + \frac{1}{9}H^u(\xi,\xi,t)$ (and similarly for E, $\tilde{H}$ and $\tilde{E}$).

Another issue is that the $ep \to ep\gamma$ reaction is not purely made of the DVCS process. The latter is accompanied by the Bethe-Heitler (BH) process, in which the final state photon is radiated by the incoming or scattered electron and not by the nucleon itself. See fig. 3. The BH process, which is not sensitive to GPDs, is experimentally indistinguishable from the DVCS and interferes with it, thus complicating the matter. Considering that the nucleon form factors F_1 and F_2 are well known at small t, the BH process is however precisely calculable theoretically. Depending on the (x_B, Q^2, t, ϕ) phase space regions, it can largely dominate or be negligible compared to DVCS.

Finally, since we have four GPDs, *i.e.* eight CFFs, the question arises of how to access them separately. We recall that the four GPDs reflect the four various spin/helicity nucleon/quark independent combinations in the handbag diagram. Therefore, the way to separate each of the eight CFFs consists in using the spin degrees of freedom of the beam and of the target and measure various polarization observables. In ref. [11], first-order analytical relations between the $ep \to ep\gamma$ observables and the CFFs have been derived. We present here a few of them:

$$\Delta\sigma_{LU} \propto \sin\phi \,\mathrm{Im}\left\{F_1\mathcal{H} + \xi(F_1+F_2)\tilde{\mathcal{H}} - kF_2\mathcal{E} + \ldots\right\}, \tag{10}$$

$$\Delta\sigma_{UL} \propto \sin\phi \,\mathrm{Im}\left\{F_1\tilde{\mathcal{H}} + \xi(F_1+F_2)\left(\mathcal{H} + \frac{x_B}{2}\mathcal{E}\right) - \xi kF_2\tilde{\mathcal{E}} + \ldots\right\}, \tag{11}$$

$$\Delta\sigma_{LL} \propto (A + B\cos\phi) \,\mathrm{Re}\left\{F_1\tilde{\mathcal{H}} + \xi(F_1+F_2)\left(\mathcal{H} + \frac{x_B}{2}\mathcal{E}\right) + \ldots\right\}, \tag{12}$$

$$\Delta\sigma_{UT} \propto \sin\phi \,\mathrm{Im}\left\{k(F_2\mathcal{H} - F_1\mathcal{E}) + \ldots\right\}, \tag{13}$$

where $\Delta\sigma$ stands for a difference of polarized cross-sections, with the first index referring to the polarization of the beam ("U" for unpolarized and "L" for longitudinally polarized) and the second one to the polarization of the target ("U" for unpolarized, "L" for longitudinally polarized and "T" for a transversely polarized target). $k = \frac{-t}{4m_N^2}$ is a kinematical factor. In eqs. (10)–(13), one recognizes the F_1 and F_2 nucleon FF which come from the interference with the BH process.

Neglecting terms multiplied by kinematical factors such as ξ, x_B and k, one can see that, on a proton target, $\Delta\sigma_{LU}$ is dominantly sensitive to $\mathrm{Im}\{\mathcal{H}^p\}$, $\Delta\sigma_{UL}$ to $\mathrm{Im}\{\tilde{\mathcal{H}}^p\}$, $\Delta\sigma_{LL}$ to $\mathrm{Re}\{\tilde{\mathcal{H}}^p\}$ and $\Delta\sigma_{UT}$ to $\mathrm{Im}\{\mathcal{H}^p\}$ and $\mathrm{Im}\{\mathcal{E}^p\}$. In the case of a neutron target, the sensitivity of these spin observables to the CFFs is not the same due to the different values of the FFs ($F_1 \approx 0$ in particular). Thus, on a neutron target, $\Delta\sigma_{LU}$ is dominantly sensitive to $\mathrm{Im}\{\mathcal{E}^n\}$ and $\mathrm{Im}\{\tilde{\mathcal{H}}^n\}$, $\Delta\sigma_{UL}$ to $\mathrm{Im}\{\mathcal{H}^n\}$, $\Delta\sigma_{LL}$ to $\mathrm{Re}\{\mathcal{H}^n\}$ and $\Delta\sigma_{UT}$ to $\mathrm{Im}\{\mathcal{H}^n\}$. Here, we have displayed explicitly the "p" and "n" superscripts to underline that GPDs on the proton and on the neutron are not equal, as mentioned earlier. One also notes in general that single spin observables are sensitive to the "Im" CFFs, while double-spin observables are sensitive to the "Re" CFFs.

In summary, given the deconvolution issue regarding x, the interference of the DVCS and BH processes, the large number (eight at leading twist) of independent quantities to be extracted from the data and the quark flavor separation to carry out, it is clearly a non-trivial task to extract the GPDs from the experimental data and, ultimately to map them in the three variables x, ξ, t. It requires a broad experimental program measuring several DVCS (or DVMP) spin observables on several targets over large ranges in x_B, t and Q^2.

The first stage of any general program of measuring GPDs can *a priori* be to extract the eight CFFs from the data for a given ξ, t point, in a model-independent way as much as possible. This would be only the beginning of the program, since the x dependence would still need to be deconvoluted using in principle a model with adjustable parameters. At this stage, let us mention that there might actually be a couple of ways around this issue: firstly, if the Double-DVCS process, (*i.e.* with a virtual photon in the final state) can be measured, then varying the virtuality of the final state photon provides an extra lever arm and this allows to measure the GPDs at each x, ξ, t values (though with some limitations if the final photon is timelike) [12, 13]. Secondly, dispersion relations could in principle reduce from eight to five the number of GPD quantities to be extracted, by expressing the real part CFFs defined by eqs. (1)–(4) in terms of integrals over ξ of the respective imaginary part CFFs defined by eqs. (5)–(8), plus a real subtraction constant (at fixed ξ and t). This strategy requires one to measure data over a very wide range in ξ (at fixed t) unless one has good reasons to truncate the integral or to extrapolate. We refer the reader to refs. [14-17] for discussions on this subject.

3. – The DVCS data

In this section, we shortly review the existing experimental data related to DVCS. Only these past ten years, experimental data which can lend themselves to GPD interpretation and of sufficient precision have been obtained.

We start by the $ep \to ep\gamma$ cross-sections which have been measured in the Hall A of JLab [18]. Figure 4 shows these 4-fold (beam-polarized and unpolarized) differential

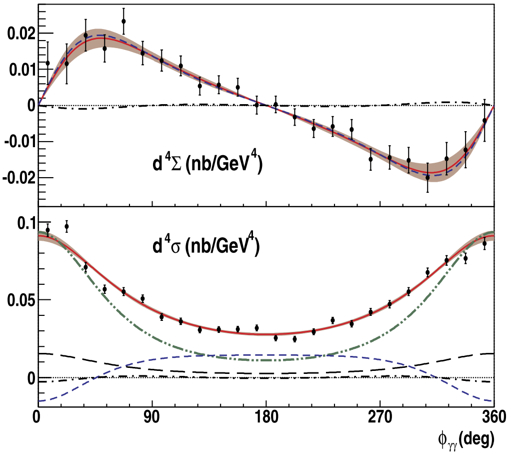

Fig. 4. – (Colour on-line) The figure on the top shows the difference of (beam) polarized cross-sections for DVCS on the proton, as a function of the ϕ angle, measured by the JLab Hall A Collaboration [18]. The average kinematics is $\langle x_B \rangle = 0.36$, $\langle Q^2 \rangle = 2.3\,\text{GeV}^2$ and $\langle -t \rangle = 0.28\,\text{GeV}^2$. The figure on the bottom shows the total (*i.e.* unpolarized) cross-section as a function of ϕ. The red curves show a fit to the data. The BH contribution is represented by the green curve. The difference between the data and the BH is attributed to the DVCS whose twist-3 contribution is estimated by the dot-dashed curve (*i.e.* it is very small).

cross sections $\frac{\mathrm{d}\sigma}{\mathrm{d}x_B \mathrm{d}Q^2 \mathrm{d}t \mathrm{d}\phi}$ (*i.e.* without any integration over an independent variable) at $\langle x_B \rangle = 0.36$, $\langle Q^2 \rangle = 2.3\,\text{GeV}^2$ and $\langle -t \rangle = 0.28\,\text{GeV}^2$.

The particular shape in ϕ of the unpolarized cross section (upper panel of fig. 4) is typical of the BH process. In this case, the final state photon is radiated by the beam or the scattered electron and, more precisely, in a very peaked cone along their direction. This means that this outgoing photon can barely be out of the electron-proton plane. In other words, the BH process is strongly peaked around $\phi = 0°$ where, *a priori*, it completely dominates the cross-section.

The difference of beam-polarized cross-sections, *i.e.* $\Delta\sigma_{LU}$, is displayed in the lower panel of fig. 4. It allows to extract the imaginary part of the DVCS amplitude (see eq. (10)). This observable has been measured for two other Q^2 values and thus has permitted to extract the Q^2 dependence of this imaginary part of the amplitude. At QCD leading order, as we discussed, it is predicted to be Q^2 independent. This Q^2-dependence is presented on fig. 5, where it can be seen that it seems to follow this "scaling" law and, therefore, to confirm that one indeed accesses the leading twist handbag process at the JLab kinematics. Of course, the Q^2 domain covered by the Hall A experiment to study this Q^2 dependence is quite limited and this conclusion, although clearly very encouraging, should be taken with caution.

At this stage, we should also mention that the (unpolarized) $ep \to ep\gamma$ cross-section has also been measured at much higher energy ($30 < W < 120\,\text{GeV}$, $2 < Q^2 < \text{GeV}^2$ where W is the center-of-mass energy of the γ^*-p system), by the H1 and ZEUS Collab-

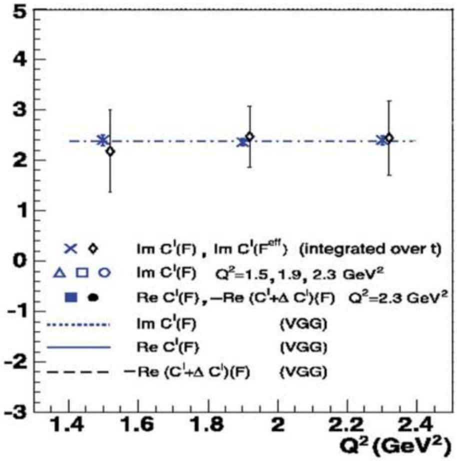

Fig. 5. – The figure shows the Q^2 dependence of the imaginary part of the proton DVCS amplitude extracted from the polarized cross-section shown in fig. 4 which was measured at 3 different Q^2 values.

orations [19, 20]. At such large W (*i.e.* low x_B), the DVCS process is sensitive mostly to "gluon" GPDs which we do not cover in this short paper.

In the Hall B of JLab, the CLAS Collaboration which uses a large acceptance spectrometer, has measured the beam spin asymmetry of the $ep \to ep\gamma$ process. This asymmetry is ratio of the difference of (beam) polarized cross section $\Delta\sigma_{LU}$ to the unpolarized one. Following the notation previously introduced, this asymmetry is denoted A_{LU}. It arises from the interference of the DVCS process (when the outgoing photon is emitted by the nucleon) and the BH process (when the outgoing photon is radiated by the incoming or scattered lepton). It is an observable which is relatively straightforward to extract experimentally since, in a first-order approximation, normalization factors such as the efficiency/acceptance of the detector and, more generally, many sources of systematic errors cancel in the ratio.

For A_{LU}, a shape close to a sinϕ is seen, as was expected from eq. (10). This asymmetry was fitted by a function of the form $\frac{a \sin\phi}{1+c\cos\phi+\mathrm{d}\cos 2\phi}$. Figure 6 shows the fitted the value of this fitted asymmetry at $\phi = 90\,^\circ$ for the $\approx 60(x_B, Q^2, t)$ bins.

The JLab CLAS Collaboration has also measured DVCS asymmetries with a longitudinally polarized target (A_{UL}) [22]. Due to the limited statistics, the $\sin(\phi)$ moment of A_{UL} (see eq. (11)) could be extracted only for 3 (x_B, Q^2, t) bins. The values of these $\sin(\phi)$ moments are shown in fig. 7.

Finally, at higher energies ($W \approx 4.5\,\mathrm{GeV}$), the HERMES Collaboration, which can polarize its target longitudinally as well as transversely, has measured an essentially complete set of DVCS asymmetries: A_{LU}, A_{UL}, A_{LL}, A_{UT}, A_{LT}. In addition, HERMES could use an electron beam as well as a positron beam. This has led to the measurement of a novel asymmetry A_C, *i.e.* the beam charge asymmetry. The combination of the

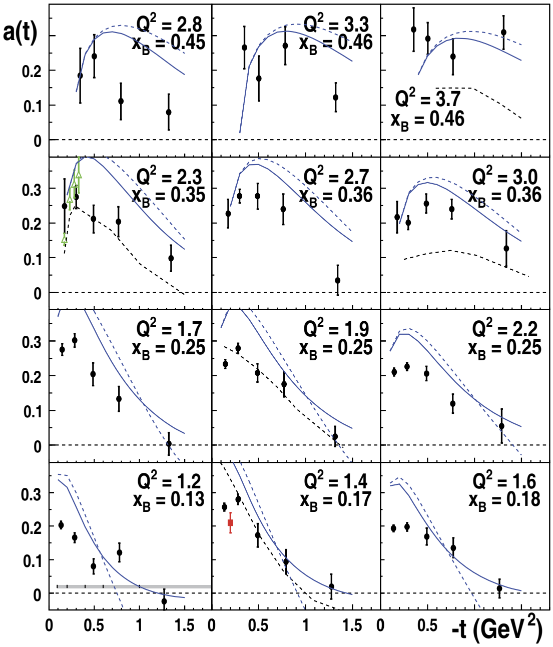

Fig. 6. – Solid circles: DVCS beam spin asymmetry at $\phi = 90^\circ$ as a function of t for different (x_B, Q^2) bins, as measured by the JLab Hall B/CLAS Collaboration [21]. See this latter reference for a description of the curves and references to the few other data points.

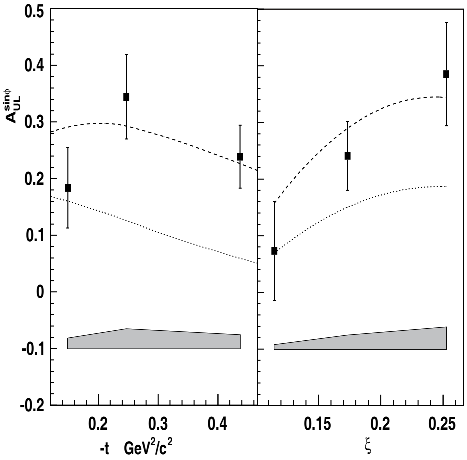

Fig. 7. – The $\sin(\phi)$ moments of the lTSA [22]. Left: three bins $-t$, integrated over ξ; right: three bins in ξ, integrated over t. The curves are described in ref. [7].

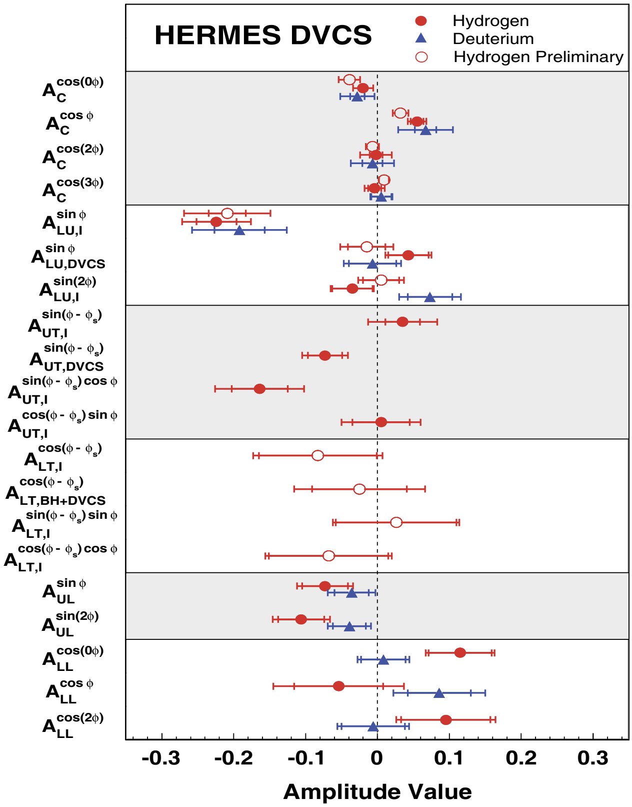

Fig. 8. – Overview of all DVCS azimuthal asymmetry amplitudes measured at HERMES. Figure taken from ref. [23]. See therein for the references to the data.

beam charge, beam and target polarizations degrees of freedom has led to the fit of a impressive series of ϕ moments which are displayed in fig. 8.

4. – From data to GPDs

Now that so many DVCS data have been accumulated, as shown in the previous section, one can ask the question how to extract the GPD information from them. These past two years, three groups (Müeller and Kumericki [24], Moutarde [25] and Guidal [26-29]) have developped fitting codes and algorithms aimed at extracting the GPD information from the DVCS data.

In this paper, due to space and time limits, we limit ourselves to a brief description of the quasi-model–independent fitting procedure of refs. [26-29]. The procedure consists, at a given experimental $(\xi, -t)$ kinematic point, in taking the CFFs as free parameters and in extracting them from DVCS experimental observables using the well established

DVCS and BH theoretical amplitudes [11, 30]. This task is not trivial. One has to fit eight parameters, *i.e.* the eight CFFs of eqs. (1)–(8), out of a limited set of data and observables (especially at JLab kinematics), with limited precision. This leads in general to an underconstrained problem. However, as some observables are in general dominated by a few particular CFFs, as we saw with eqs. (10)–(13), one actually manage to extract a few specific CFFs.

With this fitting algorithm, one managed to determine:

- The $\mathrm{Im}\{\mathcal{H}\}$ and $\mathrm{Re}\{\mathcal{H}\}$ CFFs at $\langle x_B \rangle \approx 0.36$, and for several t values, by fitting simultaneously [26] the JLab Hall A proton DVCS beam-polarized and unpolarized cross sections [18]. This could indeed be expected since $\Delta\sigma_{LU}$ is dominated by $\mathrm{Im}\{\mathcal{H}\}$ (eq. (10)) while the unpolarized cross-section is dominated by $\mathrm{Re}\{\mathcal{H}\}$.

- The $\mathrm{Im}\{\mathcal{H}\}$ and $\mathrm{Im}\{\tilde{\mathcal{H}}\}$ CFFs, at $\langle x_B \rangle \approx 0.35$ and $\langle x_B \rangle \approx 0.25$, and for several t values, by fitting simultaneously [28] the JLab CLAS proton DVCS beam-polarized and longitudinally polarized target spin asymmetries [21, 22]. Again, this could be expected since $\Delta\sigma_{LU}$ (or equivalently A_{LU}) is dominated by $\mathrm{Im}\{\mathcal{H}\}$ (eq. (10)) and $\Delta\sigma_{UL}$ (or equivalently A_{UL}) is dominated by $\mathrm{Im}\{\tilde{\mathcal{H}}\}$ (eq. (11)).

- The $\mathrm{Im}\{\mathcal{H}\}, \mathrm{Re}\{\mathcal{H}\}$ and $\mathrm{Im}\{\tilde{\mathcal{H}}\}$ CFFs, at $\langle x_B \rangle \approx 0.09$, and for several t values, by fitting simultaneously [27, 29] the series of HERMES beam-charge, beam-polarized, transversely and longitudinally polarized target spin asymmetry moments [31-34]. A_C allows to constraint $\mathrm{Re}\{\mathcal{H}\}$, $A_{LU}\,\mathrm{Im}\{\mathcal{H}\}$ and $A_{UL}\,\mathrm{Im}\{\tilde{\mathcal{H}}\}$. Unfortunately, the other asymmetries, due to unsufficient precision in the data, didn't allow in this approach to constrain the other CFFs (while in principle, with "ideal" infinitisemal resolution, they should have).

In fig. 9, the results of these fits are compiled and shown as empty squares. Each panel has the same scales for ease of comparison. The results of the other two approaches are also shown: the stars are the result of the CFF fit of ref. [25] and the curves the result of the model-based fit of ref. [24] (solid: without the Hall A data of ref. [18] and dashed: including the Hall A data in the fit). The solid points show the predictions of the VGG model [7, 30, 35], which is not the result of a fit, but of a model whose parameters have been fixed. Except for $\mathrm{Re}\{\mathcal{H}\}$ where there are marked differences between the different approaches, it seems that all these works show the same trends within error bars.

The results of the quasi-model-independent fit of refs. [26-29] have average uncertainties of the order of 30%. This is due to the limited precision of the data and/or the limited number of experimental observables to be fitted. Obviously, having more observables to fit simultaneously and more precise data (which can be foreseen in the near future) can only reduce these uncertainties. Also, one has to keep in mind that all eight CFFs are kept as free parameters. If, guided by some theoretical considerations, one can remove some of the CFFs from the fit and thus reduce the number of free parameters, error bars on the results will obviously diminish. For instance, in ref. [25] (stars on fig. 9), all GPDs but H have been neglected resulting in smaller uncertainties (an additional error has

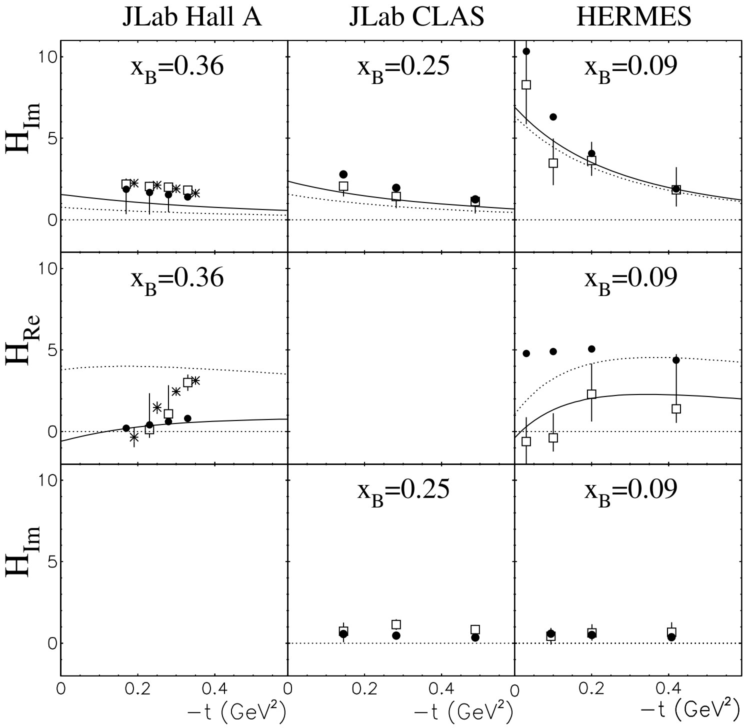

Fig. 9. – The $\mathrm{Im}\{\mathcal{H}\}, \mathrm{Re}\{\mathcal{H}\}$ and $\mathrm{Im}\{\tilde{\mathcal{H}}\}$ CFFs (noted respectively as H_{Im}, H_{Re} and $\tilde{H}_{\mathrm{Im}}$ in the figure), as defined in eqs. (1), (5) and (7), as a function of $-t$. The empty squares show the results of our works, the stars the result of the CFF fit of ref. [25], the curves the results of the model-based fit of ref. [24] and the solid points show the predictions of the VGG model [30,7,35].

then to be introduced in order to take into account the neglect of the other GPDs; an attempt of the estimation of such addditional error has been done in ref. [25]). For the present time, in the approach of refs. [26-29], the uncertainties reflect all the ignorance on all GPDs other than the ones which come out from the fits and their full potential influence. In particular, it is found in ref. [28] that the central value on the fitted $\mathrm{Im}\{\mathcal{H}\}$ CFF would vary by a factor of ≈ 3 whether one would fit the JLab Hall A proton DVCS cross sections [18] by taking into account only the H GPD or by taking into account all four GPDs.

In fig. 9, some general features and trends can be distinguished. We comment them briefly in the following:

– Concerning $\mathrm{Im}\{\mathcal{H}\}$, it seems that, at fixed $-t$, this CFF increases as x_B decreases (*i.e.* going from JLab to HERMES kinematics). This is reminiscent of the x-dependence of the standard proton unpolarized parton distribution as measured in DIS, to which the GPD H reduces in forward kinematics ($\xi = t = 0$). Another feature is that the t-slope of $\mathrm{Im}\{\mathcal{H}\}$ seems to increase with x_B decreasing. This could then suggest that low-x quarks (the "sea") would extend to the periphery of the nucleon while the high-x (the "valence") would tend to remain in the center of the nucleon. Indeed, as was mentioned in the introduction, the t-dependence of GPDs can be interpreted as a reflection of the spatial distribution of some charge in some specific frame.

- $\mathrm{Re}\{\mathcal{H}\}$ has a very different t-dependence than $\mathrm{Im}\{\mathcal{H}\}$ both at JLab and at HERMES energies: while $\mathrm{Im}\{\mathcal{H}\}$ decreases with $-t$ increasing, $\mathrm{Re}\{\mathcal{H}\}$ increases (at least up to $-t \approx 0.3\,\mathrm{GeV}^2$) and may change its sign, starting negative at small $-t$ and reaching positive values at larger $-t$: all four aproaches (empty squares, stars, solid points and solid curves) show this "zero-crossing" at JLab kinematics. We also notice that both VGG and the dashed curve of the model-based fit of ref. [24] overestimate the fitted values for $\mathrm{Re}\{\mathcal{H}\}$ compared to the work of refs. [26-29].

- Concerning $\mathrm{Im}\{\tilde{\mathcal{H}}\}$, we notice that it is in general smaller than $\mathrm{Im}\{\mathcal{H}\}$, which can be expected for a polarized quantity compared to an unpolarized one. There is very little x_B dependence. The t-dependence is also rather flat. The weaker t-dependence of $\mathrm{Im}\{\tilde{\mathcal{H}}\}$ compared to $\mathrm{Im}\{\mathcal{H}\}$ suggests that the axial charge (to which the $\tilde{H}$ GPD is related) has a narrower distribution in the nucleon than the electromagnetic charge.

5. – Conclusion

In this paper, we have given a short introduction to the field of generalized parton distributions and reviewed all the relevant experimental data, focusing on DVCS and on the valence region. We have shown how some new first 3D information on the structure of the nucleon could be extracted from the data, thanks to the recent emergence of DVCS data fitting codes.

Several new experiments are planned and new data expected in the coming years at JLab 6 and 12 GeV, COMPASS and HERMES (where new data analysis are still under progress with a recoil detector) which should provide soon stronger constraints on the extraction of GPDs. A rich harvest of data related to DES and GPDs lies therefore in front of us and with the contiunuation of the development of dedicated fitter codes and advances in theory; all hopes are permitted for the extraction of the GPDs.

REFERENCES

[1] MÜLLER D., ROBASCHIK D., GEYER B., DITTES F.-M. and HOREJSI J., *Fortschr. Phys.*, **42** (1994) 101.
[2] JI X., *Phys. Rev. Lett.*, **78** (1997) 610; *Phys. Rev. D*, **55** (1997) 7114.
[3] RADYUSHKIN A. V., *Phys. Lett. B*, **380** (1996) 417; *Phys. Rev. D*, **56** (1997) 5524.
[4] BURKARDT M., *Phys. Rev. D*, **62** (2000) 071503; **66** (2002) 119903(Erratum); *Int. J. Mod. Phys. A*, **18** (2003) 173.
[5] DIEHL M., *Eur. Phys. J. C*, **25** (2002) 223; **31** (2003) 277(Erratum).

[6] Ralston J. P. and Pire B., *Phys. Rev. D*, **66** (2002) 111501.
[7] Goeke K., Polyakov M. V. and Vanderhaeghen M., *Prog. Part. Nucl. Phys.*, **47** (2001) 401.
[8] Diehl M., *Phys. Rep.*, **388** (2003) 41.
[9] Belitsky A. V. and Radyushkin A. V., *Phys. Rep.*, **418** (2005) 1.
[10] Boffi S. and Pasquini B., *Riv. Nuovo Cimento*, **30** (2007) 387.
[11] Belitsky A., Muller D. and Kirchner A., *Nucl. Phys. B*, **629** (2002) 323.
[12] Guidal M. and Vanderhaeghen M., *Phys. Rev. Lett.*, **90** (2003) 012001.
[13] Belitsky A. V. and Muller D., *Phys. Rev. Lett.*, **90** (2003) 022001.
[14] Teryaev O. V., arXiv/0510031 hep-ph; Anikin I. V. and Teryaev O. V., *Phys. Rev. D*, **76** (2007) 056007.
[15] Diehl M. and Ivanov D. Y., arXiv:0707.0351 hep-ph.
[16] Kumericki K., Muller D. and Passek-Kumericki K., *Nucl. Phys. B*, **794** (2008) 244.
[17] Polyakov M. and Vanderhaeghen M., arXiv:0803.1271 [hep-ph].
[18] Muñoz Camacho C. *et al.*, *Phys. Rev. Lett.*, **97** (2006) 262002.
[19] Chekanov S. *et al.*, *Phys. Lett. B*, **573** (2003) 46.
[20] Aktas A. *et al.*, *Eur. Phys. J*, **44** (2005) 1.
[21] Girod F.-X. *et al.*, *Phys. Rev. Lett.*, **100** (2008) 162002.
[22] Chen S. *et al.*, *Phys. Rev. Lett.*, **97** (2006) 072002.
[23] Yaschenko S., *Proceedings of the 19th Particles & Nuclei International Conference (PANIC 2011), MIT, Cambridge, USA, Jul 24-29, 2011.*
[24] Kumericki K. and Müller D., *Nucl. Phys. B*, **841** (2010) 1.
[25] Moutarde H., *Phys. Rev. D*, **79** (2009) 094021.
[26] Guidal M., *Eur. Phys. J. A*, **37** (2008) 319; **40** (2009) 119(Erratum).
[27] Guidal M. and Moutarde H., *Eur. Phys. J. A*, **42** (2009) 71.
[28] Guidal M., *Phys. Lett. B*, **689** (2010) 156.
[29] Guidal M., *Phys. Lett. B*, **693** (2010) 17.
[30] Vanderhaeghen M., Guichon P. A. M. and Guidal M., *Phys. Rev. D*, **60** (1999) 094017.
[31] Airapetian A. *et al.*, *JHEP*, **0806** (2008) 066.
[32] Airapetian A. *et al.*, *JHEP*, **0911** (2009) 083.
[33] Airapetian A. *et al.*, *JHEP*, **1006** (2010) 019.
[34] Airapetian A. *et al.*, *Phys. Lett. B*, **704** (2011) 15.
[35] Guidal M., Polyakov M. V., Radyushkin A. V. and Vanderhaeghen M., *Phys. Rev. D*, **72** (2005) 054013.

This page intentionally left blank

Proceedings of the International School of Physics "Enrico Fermi"
Course CLXXX "Three-Dimensional Partonic Structure of the Nucleon"
edited by M. Anselmino, H. Avakian, D. Hasch and P. Schweitzer
(IOS, Amsterdam; SIF, Bologna)
DOI 10.3254/978-1-61499-197-7-261

Analysis tools for azimuthal asymmetries

A. A. Rostomyan

DESY - Notkestrasse 85, 22607 Hamburg, Germany

Summary. — The statistical tools discussed during these lectures can be applied in the analysis of the data from real experiments, for example in the extraction of single-spin or double-spin azimuthal asymmetries. The extraction might be relatively easy if there is a reasonable amount of statistics, there are no gaps in the acceptance or significant inefficiencies in the detectors. Otherwise, powerful statistical tools have to be applied. During the lectures, the least-squares, the unbinned (standard and extended) and binned maximum-likelihood methods of asymmetry extraction have been introduced. In this write up, only the method of standard maximum likelihood is discussed. Maximum likelihood is a technique for estimating the values of parameters given a finite sample of data. It is approximately unbiased and efficient.

1. – Definition of azimuthal asymmetries

The complete expression for the polarized lepton-proton cross-section is given in [1] which is basically the same for semi-inclusive deep inelastic scattering, for hadron pair production, for exclusive meson production, and for deeply virtual Compton scattering. The cross-section is presented as a superposition of unpolarized and polarized cross-

© Società Italiana di Fisica

sections σ_{XY} with various polarization states of target (S) and beam (P):

$$\sigma = \sigma_{UU} + P_L\sigma_{LU} + S_L\sigma_{UL} + P_L S_L\sigma_{LL} + S_T\sigma_{UT} + P_L S_T\sigma_{LT} \; . \tag{1}$$

In σ_{XY} the first subscript, X, specifies the lepton beam polarization, and the second one, Y, the target polarization. The lepton beam and the target can be unpolarized (U), longitudinally (L) or transversely (T) polarized.

In accordance with the Trento convention [2], the beam (or the target) azimuthal spin-asymmetry $\mathcal{A}$ is defined as the cross-section asymmetry for two opposite spin states of the beam (or the target),

$$\mathcal{A}(\phi) = \frac{1}{P}\frac{\mathrm{d}\sigma^{\rightarrow}(\phi) - \mathrm{d}\sigma^{\leftarrow}(\phi)}{\mathrm{d}\sigma^{\rightarrow}(\phi) + \mathrm{d}\sigma^{\leftarrow}(\phi)} \; , \tag{2}$$

where P is the beam (or the target) polarization, and the subscript $^{\rightarrow(\leftarrow)}$ stands for a positive (negative) polarization state. The definition of the azimuthal angle ϕ between the lepton and the hadron planes is also given in [2]. The azimuthal modulations associated with beam or target spin asymmetries are defined [2] as, *e.g.*,

$$\langle \sin\phi \rangle = \frac{\int \mathrm{d}\phi \, \sin\phi \, \left(\mathrm{d}\sigma^{\rightarrow}(\phi) - \mathrm{d}\sigma^{\leftarrow}(\phi)\right)}{\int \mathrm{d}\phi \, \left(\mathrm{d}\sigma^{\rightarrow}(\phi) + \mathrm{d}\sigma^{\leftarrow}(\phi)\right)} \; , \tag{3}$$

The integration in eq. (3) results in a denominator that is the ϕ-independent part of the unpolarized cross-section σ_{UU}.

Experimentally, the cross-sections are derived from the number of events or yield $\mathrm{d}N^{\rightarrow(\leftarrow)}$. Neglecting radiative and smearing effects, the yield is related to the cross-section by the acceptance ϵ of the spectrometer $\mathrm{d}N^{\rightarrow(\leftarrow)} \propto \epsilon\mathrm{d}\sigma^{\rightarrow(\leftarrow)}$. The acceptance is a multiplicative factor that does not depend on the polarization state of the target or beam and thus should cancel in the asymmetry definition given by eq. (2). However, if the asymmetries are calculated in bins of one kinematic quantity while integrated over the others, the effect of the acceptance cancellation may not happen. In this case simpler asymmetry extraction methods, like the *moments method* or the *method of least squares (χ^2 method)* are biased. In addition, these methods are not applicable for low statistical samples since they make incorrect error propagation assuming Gaussian distribution of events in a bin. The solution might be the usage of the *unbinned maximum likelihood* method [3, 4] in asymmetry extractions.

2. – Maximum-likelihood method

Consider a random variable x (here x can represent also a multidimensional vector) which is distributed according to a *probability density function* (p.d.f.) $f(\theta;\, x)$, where $\theta\,(\theta_0, \theta_1 \ldots \theta_n)$ is a set of n parameters which values are unknown. If the functional form of the p.d.f. $f(\theta;\, x)$ is known, the method of maximum likelihood is a technique for estimating the values of the parameters.

Suppose a measurement of a random variable x has been repeated N times, yielding the values x_1, $x_2 \ldots x_N$. The probability for the first measurement to be in the interval $[x_1, x_1 + \mathrm{d}x_1]$ is $f(\theta;\, x_1)\mathrm{d}x_1$. Since the measurements are all assumed to be independent, the probability to have the first one in $[x_1, x_1 + \mathrm{d}x_1]$, the second in $[x_2, x_2 + \mathrm{d}x_2]$ and so forth, is given by

$$\prod_i^N f_i(\theta;\, x_i)\mathrm{d}x_i \; . \tag{4}$$

If the hypothesized p.d.f. and parameter values are correct, a high probability is expected for the parameter values close to the true values. In contrast, a parameter value far away from the true value should yield a low probability. Since $\mathrm{d}x_i$ do not depend on the parameters, the same reasoning also applies to the following function L:

$$L(\theta) = \prod_i^N f_i(\theta;\, x_i) \; , \tag{5}$$

which is called *likelihood function.* The parameter values are found as the point in the parameter space where the likelihood function, the joint of N probability densities, is at its maximum. It is usually easier to work with $\log L$,

$$\log L(\theta) = \sum_i^N \log f_i(\theta;\, x_i) \; . \tag{6}$$

Since both are maximized for the same parameter values θ, the parameters are those which maximize the log-likelihood function or, equivalently, minimize the negative log-likelihood function:

$$-\log L(\theta) = -\sum_i^N \log f_i(\theta;\, x_i) \; . \tag{7}$$

Thus, as long as the likelihood function is a differentiable function of the parameters θ, the maximum-likelihood estimators $\widehat{\theta}$, *i.e.* the parameters, are found solving the likelihood equations

$$\frac{\partial \log L}{\partial \theta_i} = 0, \qquad\qquad i = 0, 1, \ldots n \; . \tag{8}$$

Any multiplicative θ-independent factor in the p.d.f. $f(\theta;\, x)$ may be omitted, since the purpose of interest is the maximum (minimum) of the (negative) log-likelihood function $\log L$. If more than one local maximum (minimum) exists, the highest (lowest) one is taken.

It is important to note that the p.d.f. should be normalized to unity:

$$\int f(\theta;\, x)\,\mathrm{d}x = 1\,. \tag{9}$$

If this is not the case,

$$\int f(\theta;\, x)\,\mathrm{d}x = \mathcal{N}(\theta)\,, \tag{10}$$

the normalization of the p.d.f. to unity can be arranged by taking into account the normalization integral $\mathcal{N}(\theta)$:

$$\int \frac{f(\theta;\, x)}{\mathcal{N}(\theta)}\,\mathrm{d}x = 1\,. \tag{11}$$

In evaluating the log-likelihood function, it is important to include all normalization factors that depend on θ:

$$\log L(\theta;\, x) = \sum_{i=1}^{N} \log f(\theta;\, x_i) - N \log \mathcal{N}(\theta)\,. \tag{12}$$

The normalization integral may be omitted if it does not depend on parameters θ.

The *extended maximum-likelihood* method differs from the standard method in that the normalization of the p.d.f. is allowed to vary. This is essential for the measurements where the number of samples obtained is itself a physical quantity [5]. Otherwise the properties of standard and extended maximum-likelihood methods are generally the same.

The uncertainties on the parameters are evaluated from the inverse of the covariance matrix, *i.e.* the matrix of second derivatives:

$$V^{-1}(\theta_i,\theta_j) = \mathrm{cov}^{-1}(\theta_i,\theta_j) = -\left[\frac{\partial^2 \log L}{\partial\theta_i \partial\theta_j}\right]\Bigg|_{\hat{\theta}}\,. \tag{13}$$

2˙1. *Graphical illustration of statistical uncertainties of parameters.* – Let us consider one parameter case: θ_0. If expanding the log-likelihood function in a Taylor series about the maximum-likelihood estimate $\hat{\theta}_0$,

$$\log L(\theta_0) = \log L(\hat{\theta}_0) + \left[\frac{\partial \log L}{\partial \theta_0}\right]_{\theta_0=\hat{\theta}_0} (\theta_0 - \hat{\theta}_0) + \frac{1}{2!}\left[\frac{\partial^2 \log L}{\partial \theta_0^2}\right]_{\theta_0=\hat{\theta}_0} (\theta_0 - \hat{\theta}_0)^2 + \ldots \tag{14}$$

by definition of $\hat{\theta}_0$, $\log L(\hat{\theta}_0) = \log L_{\max}$ and the second term in the expansion is equal to zero. Ignoring higher-order terms in eq. (14):

$$\log L(\hat{\theta}_0 \pm \sigma) = \log L_{\max} - \frac{1}{2}\frac{(\theta_0 - \hat{\theta}_0)^2}{\sigma^2} = \log L_{\max} - \frac{1}{2}\,. \tag{15}$$

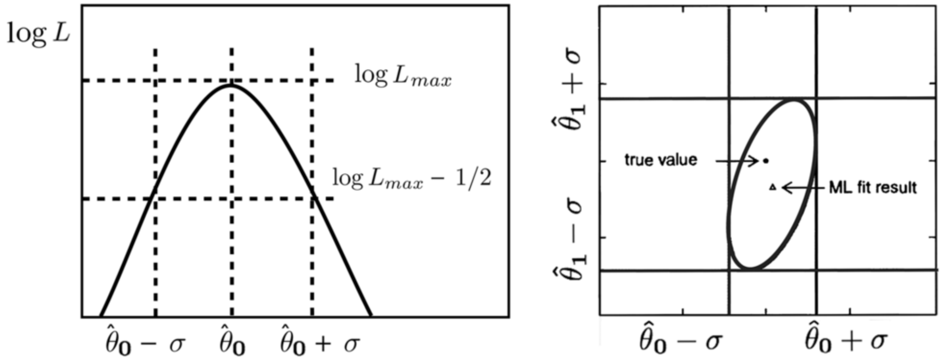

Fig. 1. – A log-likelihood function showing 1σ limits for one (left) and two (right) parameter cases [4].

This is the definition of the statistical uncertainty in the maximum-likelihood method which means that a change in the parameter θ of one standard deviation σ from its maximum likelihood estimate leads to a decrease in the log-likelihood of 1/2 from its maximum value. It has been shown that the likelihood function becomes a Gaussian curve and the log-likelihood function becomes a parabola in the large sample limit [3,4].

The graphical illustration of the interpretation of the statistical uncertainty is given in fig. 1. The log-likelihood function $\log L$ as a function of θ_0 is a parabola. The standard deviation of $\hat{\theta}_0$ is estimated by changing the value of $\hat{\theta}_0$ until $\log L(\hat{\theta}_0)$ decreases by 1/2. The horizontal lines indicate the $\log L_{\mathrm{max}}$ and $\log L_{\mathrm{max}} - 1/2$ and the vertical lines correspond to the maximum-likelihood estimate of $\hat{\theta}_0$ and $\hat{\theta}_0 \pm \sigma$.

In the case of more than one parameter, in the large sample limit, the likelihood is a multidimensional Gaussian. The log-likelihood function is harder to illustrate graphically, though for the two-parameter case it can still be shown as a contour. The case when the two parameters are correlated, is illustrated on the right side of fig. 1. The positions of the true values and the maximum-likelihood estimates in the parameter space are shown along with a contour corresponding to $\log L = \log L_{\mathrm{max}} - 1/2$. The fact that the parameters are correlated is seen from the fact that the contour is tilted. In the large sample limit the tangents to the curve correspond to $\hat{\theta}_0 \pm \sigma_0$ and $\hat{\theta}_1 \pm \sigma_1$. Since the two parameters θ_0 and θ_1 are correlated, the covariance or the correlation coefficient should be included in the reporting fit results. For small samples, the likelihood function can take complicated shapes, and there might be more than one local maximum. For a given log-likelihood function, a scan through parameter values can verify whether the maximum is a local or a global one. The uncertainties on parameters are still determined by findings the points in the parameter space where the log-likelihood function $\log L$ changes by 1/2.

2˙2. *Advantages and disadvantages. – The reliability of the result using this or that method has to be proved by Monte Carlo studies.* For large statistical samples, most of the estimators are unbiased ($\propto 1/N$) and efficient. For low statistics, the unbinned maximum-likelihood method is preferred. It provides the best estimation of uncertainties, since propagating the uncertainties no assumption of Gaussian distribution of events is needed (in contrast to the least-squares method). If there are correlations between the parameters, these correlations can be taken into account propagating the uncertainties.

In the cases when the bin size is large and the desired information is smaller than the bin size, there is no loss of information due to the binning in the unbinned maximum-likelihood method. Instead all the events enter the fit with their characteristic behaviors.

For most the cases in the data analysis, the maximization cannot be performed analytically, especially when working in more than one dimension (more than one variable or more than one fit parameter). The differentiation of $\log L$ may end up with an equation that cannot be solved analytically, instead numeric computation methods should be used. This implies reliance on the existing software packages. Usually the supplied programs do not maximize, but minimize the *negative* log-likelihood function (see eq. (7)).

3. – MINUIT

One of the function minimization softwares in HEP is MINUIT [6]. This package was originally written in Fortran [6]. It has been converted to a C^{++} class [7] which is a straightforward conversion of the original Fortran version. MINUIT is integrated in PAW (Fortran) and ROOT (C^{++}) packages. It does multi-parameter function minimization, analyzes the shape of the function around the minimum and performs parameter uncertainty evaluation. The function to be minimized might be the χ^2 or the negative log-likelihood.

The minimization algorithm requires the calculation of derivatives of the function with respect to the parameters and this is normally done numerically by the fitting routine. To find the minimum of the function, it is recommended to use the MINUIT function MIGRAD [6,8]. As discussed in sect. **2**, in the case of maximum-likelihood method, the p.d.f. should be properly normalized. The consequence of not normalizing is usually that the fit simply does not converge, some parameters running away to infinity. On its way to the minimum, MIGRAD may have traversed a region which has unphysical behavior, *e.g.*, the p.d.f. gets negative values. In order to leave that region, penalties have to be assigned to these parameter values (*i.e.* low probabilities to these parameter values, or large negative values to $\log L$) or a smoothening of the p.d.f. has to be performed (transform the p.d.f. with a function which is always positive and goes asymptotically to zero for p.d.f. going to minus infinity). In order to insure good and fast convergence, the analyzer can supply starting values for the parameters. Limits on variable parameters should be used only when needed in order to prevent the parameter from taking an unphysical value. When a satisfactory minimum has been found using limits, the limits should then be removed if possible, in order to perform the uncertainty analysis without limits.

The calculation or interpretation of the resulting parameter uncertainties is considerably more complicated. Whatever method (χ^2 or maximum likelihood) is used, in order to calculate the parameter uncertainties, the analyzer should define (with ErrorDef command) what is meant by one "error" (one or two standard deviations). In MINUIT the uncertainty on a parameter is defined as the change of the parameter which would produce a change of the function value equal to 1. If the function is a negative log-likelihood function, then the one standard deviation is chosen by setting ErrorDef = 0.5(1) or, alternatively, the log-likelihood function should be multiplied by 2. In the simplest case when the function is exactly parabolic at the minimum, this is equivalent to defining the uncertainty as the inverse of the second derivative at the minimum. To calculate the uncertainties of the parameters, it is recommended to use the Minuit function HESSE [6,8]. It does calculate the full matrix of second derivatives of the function with respect to the current values of parameters, and inverts it, printing out the resulting error matrix. Hence the error matrix produced by HESSE contains the parameter correlations which is a very important property of HESSE. Although a parameter may be either positively or negatively correlated with another, the effect of correlations is always going to increase the uncertainties on the parameters. After HESSE, the uncertainties are usually quite accurate, unless there has been a problem, *e.g.*, highly correlated parameters, etc.

MINUIT, when it prints out the parameter and uncertainty values, also gives some indication of how reliable it thinks they are. It is important always to check the outputs of MINUIT (what exactly to check was discussed on the slide 53 of ref. [9]). The resulting estimate of $\hat{\theta}$ will be close to the true value of θ but it is unlikely to coincide exactly. How good is the estimate? This has to be tested by Monte Carlo studies.

4. – Implementation of the maximum-likelihood method

Let us consider the case of an unpolarized target and a longitudinally polarized beam(2). In this case the cross-section given by eq. (3) reduces to

$$\sigma = \sigma_{UU} + P_L \sigma_{LU} \, . \tag{16}$$

The p.d.f. that describes the yield of the experimental data (see sect. **1**) reads

$$\begin{aligned} \mathrm{d}N\big(\theta;\, x, y, z, P_{h\perp}, \phi, P_L\big) &= \epsilon\big(x, y, z, P_{h\perp}, \phi\big) \\ &\times \Big[\sigma_{UU}\big(\theta; x, y, z, P_{h\perp}, \phi\big) + P_L \sigma_{LU}\big(\theta; x, y, z, P_{h\perp}, \phi, P_L\big)\Big] \\ &= \epsilon\big(x, y, z, P_{h\perp}, \phi\big) \bar{\sigma}_{UU}\big(x, y, z, P_{h\perp}\big) \\ &\times \Big[1 + A_{UU}^{\cos\phi}\big(x, y, z, P_{h\perp}\big)\cos\phi + A_{UU}^{\cos 2\phi}\big(x, y, z, P_{h\perp}\big)\cos 2\phi \\ &\quad + P_L A_{LU}^{\sin\phi}\big(x, y, z, P_{h\perp}\big)\sin\phi\Big] \\ &\equiv f\big(\theta; x, y, z, P_{h\perp}, \phi, P_L\big) \, , \end{aligned} \tag{17}$$

---

(1) This is due to the fact that $-\log L = \chi^2/2$. The default value of ErrorDef = 1 corresponds to one standard deviation for χ^2 function.

(2) The case of longitudinally polarized target is similar and for a transversely polarized target there is an additional dependence on the angle ϕ_s (the definition of this angle is given in [1]).

where x, y, z and $P_{h\perp}$ are the well-known kinematic variables, ϵ is the acceptance function that may depend on the same kinematic variables as the cross-section, $\bar{\sigma}_{UU}$ is the ϕ-independent unpolarized cross-section. In the maximum-likelihood method, the polarization is treated as any other kinematic variable. The azimuthal modulations of the cross-section given in [1] result in the corresponding asymmetry modulations: $A_{UU}^{\cos\phi}$, $A_{UU}^{\cos 2\phi}$ and $A_{LU}^{\sin\phi}$. While maximizing the likelihood function,

$$L(\theta) = \prod_{i}^{N} \frac{f\big(\theta;\, x_i, y_i, z_i, P_{h\perp_i}, \phi_i, P_{L_i}\big)}{\mathcal{N}(\theta)} , \tag{18}$$

the various azimuthal amplitudes of the asymmetry are considered as free parameters θ. In fitting the parameters θ, the acceptance efficiency ϵ and the azimuthal averaged cross-section $\bar{\sigma}_{UU}$ in the numerator can be omitted since they do not depend on the fit parameters. However, they have to be taken into account in evaluating the normalization integral $\mathcal{N}$:

$$\begin{aligned}\mathcal{N}(\theta) = \int & \mathrm{d}x\mathrm{d}y\mathrm{d}z\mathrm{d}P_{h\perp}\mathrm{d}\phi\mathrm{d}P_L \epsilon\big(x,y,z,P_{h\perp},\phi\big)\bar{\sigma}_{UU}\big(x,y,z,P_{h\perp}\big) \\ & \times\Big[1 + A_{UU}^{\cos\phi}\big(x,y,z,P_{h\perp}\big)\cos\phi + A_{UU}^{\cos 2\phi}\big(x,y,z,P_{h\perp}\big)\cos 2\phi \\ & \quad + P_L A_{LU}^{\sin\phi}\big(x,y,z,P_{h\perp}\big)\sin\phi\Big] .\end{aligned} \tag{19}$$

The polarized part of the normalization integral can be ignored if the unpolarized and the polarized cross-sections are factorized and, in addition, if the net polarization of the whole data set is equal to zero [10],

$$P^{\rightarrow}L^{\rightarrow} = P^{\leftarrow}L^{\leftarrow} , \tag{20}$$

with $L^{\rightarrow}$ and $L^{\leftarrow}$ being the corresponding luminosities. If necessary, this condition can be reached by weighting events recorded with one polarization state [10]:

$$\begin{aligned}\log L = & \sum_{i=1}^{N^{\rightarrow}} \omega_i \log\Big[1 + A_{UU}^{\cos\phi}\cos\phi + A_{UU}^{\cos 2\phi}\cos 2\phi + P_L^{\rightarrow} A_{LU}^{\sin\phi}\sin\phi\Big] \\ & + \sum_{i=1}^{N^{\leftarrow}} \log\Big[1 + A_{UU}^{\cos\phi}\cos\phi + A_{UU}^{\cos 2\phi}\cos 2\phi + P_L^{\leftarrow} A_{LU}^{\sin\phi}\sin\phi\Big] \\ & + N\log\mathcal{N}_{UU}(\theta) ,\end{aligned} \tag{21}$$

where $\omega = (P^{\leftarrow}L^{\leftarrow})/(P^{\rightarrow}L^{\rightarrow})$ is the weight that is chosen in such a way that scales down the sample with higher net polarization. If the zero net polarization of the data sample is achieved, then the unpolarized part of the normalization integral $\mathcal{N}_{UU}(\theta)$ can be computed numerically,

$$\mathcal{N}_{UU}(\theta) = \sum_{i}^{N_{MC}} \left[1 + A_{UU}^{\cos\phi}\big(x,y,z,P_{h\perp}\big)\cos\phi + A_{UU}^{\cos 2\phi}\big(x,y,z,P_{h\perp}\big)\cos 2\phi\right], \tag{22}$$

using a Monte Carlo simulation that generates the unpolarized part of the cross-section with isotropic azimuthal distribution. After the reconstruction of this simulated data in the experimental acceptance, the events will be distributed according to $\epsilon(x,y,z,P_{h\perp},\phi) \times \bar{\sigma}_{UU}\big(x,y,z,P_{h\perp}\big)$. It is important that all the kinematic distributions apart from the azimuthal one are well reproduced by the Monte Carlo simulation. In that case, all distortions of the angular distribution (including the gaps) are purely due to the spectrometer acceptance since the angular distribution itself was generated flat.

The normalization integral can be omitted at all if it does not depend on the fit parameters θ. This can be arranged by fixing the unpolarized azimuthal modulations of the asymmetry by already measured values. In this case (the net polarization still should be equal to zero) the denominator of eq. (18) would not depend on the fit parameters and can be omitted.

4·1. *Beam/target polarization balancing.* – Introducing weights in the likelihood function is quite useful not only for beam/target polarization balancing but also for other purposes, *e.g.*, background subtraction, hadron identification, etc. In this case, a bit more is needed in order to evaluate the statistical uncertainties properly. According to ref. [11], the covariance matrix has to be corrected,

$$\widehat{V}^{-1} = \mathcal{F}\left(\mathcal{F}'^{-1}\mathcal{F}\right), \tag{23}$$

where the matrices $\mathcal{F}$ and $\mathcal{F}'$ are the covariance matrices

$$\mathcal{F}_{ij} = \left.\frac{\partial^2 \log L}{\partial\theta_i\partial\theta_j}\right|_{\widehat{\theta}}, \qquad \mathcal{F}'_{ij} = \left.\frac{\partial^2 \log L'}{\partial\theta_i\partial\theta_j}\right|_{\widehat{\theta}} \tag{24}$$

with $\log L$ given by eq. (21) and $\log L'$ given as

$$\begin{aligned}\log L = &\sum_{i=1}^{N^{\rightarrow}} \omega_i^2 \log\left[1 + A_{UU}^{\cos\phi}\cos\phi + A_{UU}^{\cos 2\phi}\cos 2\phi + P_L^{\rightarrow} A_{LU}^{\sin\phi}\sin\phi\right] \\ &+\sum_{i=1}^{N^{\leftarrow}} \log\left[1 + A_{UU}^{\cos\phi}\cos\phi + A_{UU}^{\cos 2\phi}\cos 2\phi + P_L^{\leftarrow} A_{LU}^{\sin\phi}\sin\phi\right].\end{aligned} \tag{25}$$

It is important to note that if the MINUIT package is used for minimization of the negative log-likelihood function, then for proper error propagation, both covariance matrices have to be evaluated by the MINUIT function HESSE.

Conclusions

Several asymmetry extraction methods have been discussed during the lecture. The unbinned maximum-likelihood method has been pointed out as the preferred method in case of low statistics and large acceptance effects. It is important to note that there are no perfect estimators though in practice one usually assumes perfect efficiency and zero bias. In case of doubts, one should check the reliability of the estimation of the parameter values with Monte Carlo tests.

The second part of the lecture was dedicated to exercises testing the goodness of the fit methods using a toy Monte Carlo. The aim was to generate data according to a given distribution and extract the corresponding asymmetries with this or that method, increasing and decreasing the statistics, generating acceptance effects, etc. The full list of exercises is given on slides 33 and 47 of ref. [9]. Some of the codes performing the simulation and the extraction of asymmetries can be found in [12].

* * *

I would like to thank the organizers for invitation to this very interesting school. Also I would like to thank E. Avetisyan and A. Movsisyan for their help in preparation of the exercises.

REFERENCES

[1] Diehl M. and Sapeta S., *Eur. Phys. J. C*, **41** (2005) 515.
[2] Bacchetta A., D'Alesio U., Diehl M. and Miller C. A., *Phys. Rev. D*, **70** (2004) 117504.
[3] Barlow R. J., *Statistics: A Guide to the Use of Statistical Methods in the Physical Sciences* (John Wiley and Sons) 1999.
[4] Cowan G., *Statistical Data Analysis* (Oxford University Press, Oxford) 1998.
[5] Barlow R. J., *Nucl. Instrum. Methods Phys. Res. A*, **297** (1990) 496.
[6] James F., *MINUIT - Function Minimization and Error Analysis - Reference Manual* (CERN Program Library Long Writeup D506) 1994.
[7] Brun R., *Implementation of MINUIT package in ROOT*, `http://root.cern.ch/root/html/TMinuit.html`.
[8] James F., *The Implementation of Errors* (CERN, Geneva) 2004.
[9] Rostomyan A., `http://www.sif.it/SIF/resources/public/files/va2011/rostomyan_0706.pdf`.
[10] Miller C. A., *Extracting azimuthal fourier moments from sparse data*, in *HERMES Transversity Week* (Gent) 2006, `http://hermes.desy.de/notes/pub/TALK/Andy.HERMESTransWeek06.pdf`.
[11] Solmitz F. T., *Annu. Rev. Nucl. Part. Sci.*, **14** (1964) 375.
[12] Rostomyan A., exercises for this lecture, `http://www.desy.de/~ami/Varenna_SummerSchool_2011/Exercises`

Proceedings of the International School of Physics "Enrico Fermi"
Course CLXXX "Three-Dimensional Partonic Structure of the Nucleon"
edited by M. Anselmino, H. Avakian, D. Hasch and P. Schweitzer
(IOS, Amsterdam; SIF, Bologna)
DOI 10.3254/978-1-61499-197-7-271

Spin physics at COMPASS: Present and future

G. K. Mallot

European Organization for Nuclear Research, CERN - 1211 Genève 23, Switzerland

Summary. — This lecture discusses the COMPASS experiment at Cern performing deep inelastic scattering of polarised muons off polarised targets. The main results from the measurements performed since 2002 with longitudinal and transverse target polarisation are presented. The second part of the lecture discusses the plans and preparations for future measurements related to generalised parton distributions and transverse-momentum–dependent distribution functions. These experiments comprise deeply virtual Compton scattering as well as hard exclusive meson production in muon scattering off a liquid-hydrogen target on the one hand and Drell-Yan dimuon production using a negative pion beam and a transversely polarised proton target on the other hand. During the GPD muon experiment, precise data will also be taken on hadron production and transverse-momentum–dependent distributions with the unpolarised proton target.

1. – Introduction

Partons were discovered at Slac in the 1960's when scattering electrons from nuclei at large momentum transfers Q^2. The observed Q^2 independence of the hadronic part of the cross-section, the structure functions, revealed point-like constituents in the nucleon. Later these partons were identified with the quarks. The eventually observed weak Q^2 dependence of the structure functions could be attributed to the splitting of partons, *i.e.* quarks and gluons, into partons with a smaller momentum fraction in the infinite momentum frame. At the electron-proton collider Hera at Desy the spin-independent

© Società Italiana di Fisica

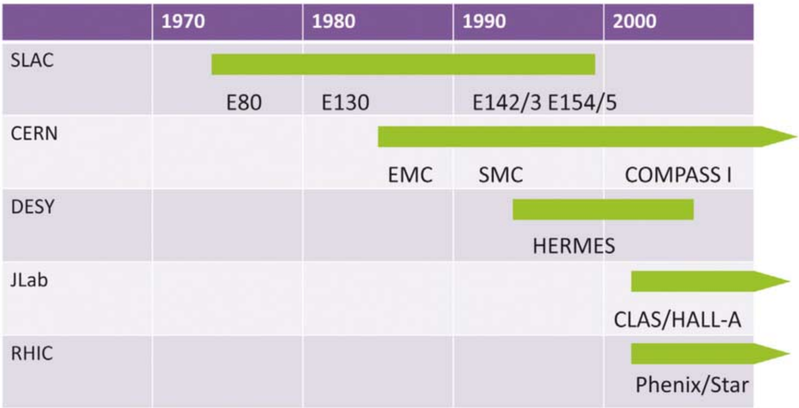

Fig. 1. – Laboratories and experiments studying spin-dependent structure functions of the nucleon.

quark and gluon distributions were then finally studied with high precision at very large momentum transfer and down to tiny momentum fractions.

A detailed understanding of the nucleon structure must include spin degrees of freedom and ultimately should explain the nucleon spin of $1/2\hbar$. The first attempt to study the spin-dependent structure functions of the nucleon was made at Slac followed by the Emc experiment at Cern which showed in 1988 that the quark spins contribute little to the nucleon spin. Triggered by this entirely unexpected result, experiments were subsequently launched at Cern (Smc, Compass), Slac (E142/3, E154/5), Desy (Hermes), and Rhic (Star, Phenix) in order to check the Smc result and to measure the structure functions of the neutron/deuteron (fig. 1). The results confirmed the findings by Emc for the proton and revealed a similar situation for the neutron. The effects in the proton and neutron cancel in the fundamental Bjorken sum rule, which links the difference of proton and neutron spin-dependent structure functions to the neutron weak decay constant g_V/g_A.

After the small quark spin contribution to the nucleon spin was established unambiguously, the focus turned on the gluon polarisation. In this situation the Compass Collaboration was founded in 1996 and the experiment was approved in 1998 with first data taking in 2002. Contrary to the previous Smc experiment, which focused on inclusive scattering, the COMPASS spectrometer is optimised for large hadron acceptance and hadron identification in semi-inclusive deep inelastic scattering (SIDIS). The primary goals of the first phase of Compass until 2012 are measurements of the spin-dependent quark distributions or the light flavours g_1^q (or Δq), the size of the gluon polarisation g_1^g or (or Δg), and the Collins and Sivers asymmetries and thus transversity h_1 (or $\Delta_T q$) and the Sivers function $f_{1T}^{\perp}$. After a description of the Compass spectrometer in sect. **2**, these results will be discussed in sects. **3** and **4**. Another large part of the programme not presented here concerns hadron spectroscopy and tests of chiral perturbation theory including a dedicated measurement of the pion polarisability.

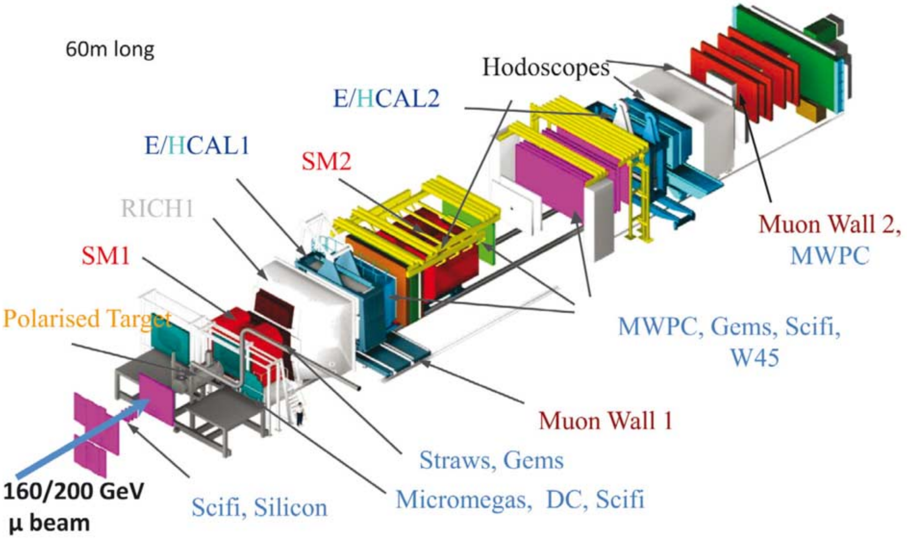

Fig. 2. – The Compass spectrometer, for a description see text.

Section **5** covers the approved Compass plans for the nearer future 2014–2016/7. Here the Collaboration will focus on generalised parton distribution functions (GPDs) and transverse-momentum–dependent (TMD) parton distribution functions. The former will be studied in deeply virtual Compton scattering off a liquid-hydrogen target and the latter by Drell-Yan (DY) reactions of a negative pion beam impinging on a transversely polarised proton target.

2. – The COMPASS experiment at CERN

A schematic view of the Compass spectrometer [1] is presented in fig. 2. A polarised muon beam of energy 160–200 GeV and with a polarisation of about 80% impinges from the left on a solid-state polarised target consisting of two or three cells with proton or deuteron target material polarised in opposite directions. The usable beam intensity is typically 2×10^7/s during a 9.6 s long spill. The repetition rate varies and was typically about 1/40 s. The momentum of each beam particle is measured in the beam momentum station. Downstream of the target, the scattered muon and produced hadrons are detected in a two-stage magnetic spectrometer with the two dipole magnets, SM1 and SM2.

Charged particles are tracked in the beam regions by scintillating fibre stations (Scifi) and by silicon detectors. In the inner region close to the beam, gaseous detectors of the micromegas and GEM types are deployed. Both are based on very small multiplication gaps with high field strength where the electron avalanche develops. The positive charges produced in these gaps can be evacuated rapidly which leads to high rate capabilities. The backbone of tracking in the intermediate region are multiwire proportional chambers

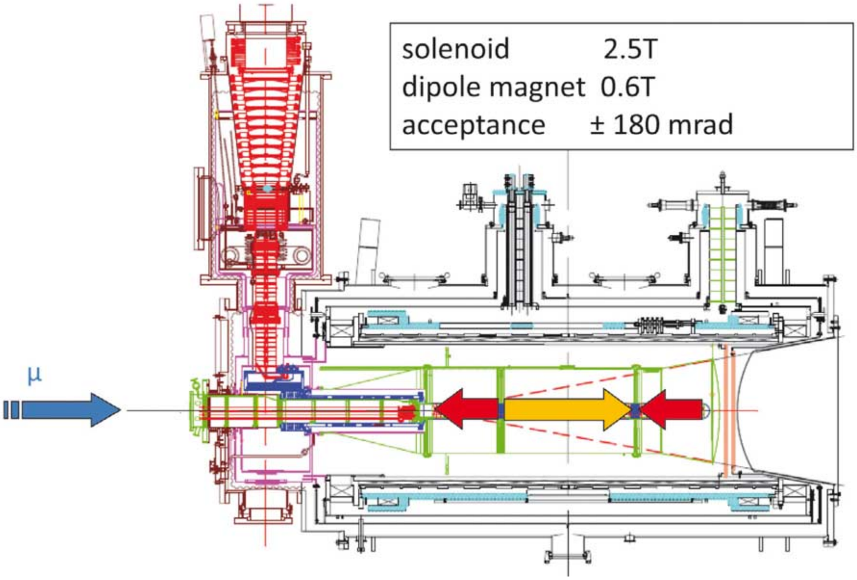

Fig. 3. – The Compass polarised target system.

(MWPC). Finally, the large area tracking away from the beam region is covered by drift chambers (DC, W45) and drift tubes (Straws, Muon Wall 1 and 2, Rich Wall (not shown)).

The velocity of charged particles is measured in a ring-imaging Cherenkov detector (RICH), which can separate pions and kaons from 9 GeV up to 50 GeV. The Cherenkov photons are emitted along the 3 m long path in the radiator volume filled with the heavy C_4F_{10} gas. In total 116 mirrors reflect light from ultraviolet to visible to the photon detectors with about 80 k analog read-out channels. The inner quarter of the photon detector is made by multianode-photomultiplier tubes, while the outer part relies on MWPCs with a photosensitive CsI cathode.

The energy of charged particles is measured in sampling hadron calorimeters (HCAL 1 and 2), while neutral particles, in particular high-energy photons, are detected in electromagnetic calorimeters (ECAL1 and 2). They comprise lead glass modules as well as scintillator/lead "shashlik" modules in the inner high-radiation region.

Event recording is triggered by the scattered muon, which is "identified" by its ability to traverse thick hadron absorbers, located just upstream of the Muon Wall detectors. The event selection is based on various systems of scintillator hodoscopes and logic modules applying selections criteria like target pointing and energy loss in the scattering. The patterns causing a trigger were optimised by Monte Carlo simulations. The spectrometer has about 250 k read-out channels, which can be recorded with a frequency of 20 kHz for an event length in the order of 40 kByte.

The heart of the experiment is the polarised target system (fig. 3). While the muon beam comes naturally polarised due to the parity violation in the decay of the parent

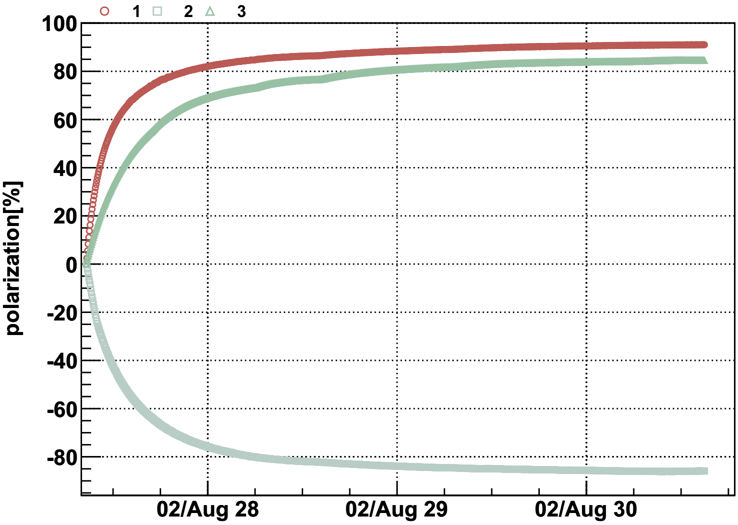

Fig. 4. – Polarisation build-up for the 3-cell ammonia target in 2007 for the outer cells (upper curves) and central cell (lower curve).

pions, polarising protons and deuteron is very difficult. Gas targets cannot be used with the muon beam due to the low beam intensity compared to electron beams. An advantage of muon beams is the high muon energy, which presently cannot be reached by electron beams. The polarised target system comprises a 2.5 T solenoid magnet, a 0.6 T dipole magnet, a ^{3}He/^{4}He dilution refrigerator, a 70 GHz microwave system and an NMR system to measure the target polarisation. The target material is cooled down to about 60 mK in frozen spin mode. In the presence of the 2.5 T field all free electrons are polarised. Their polarisation is transferred to the protons and deuterons by microwave irradiation. This process of dynamic nuclear polarisation can only be used with few materials. In Compass irradiated ammonia (NH_3) and lithium-6 deuteride (^{6}LiD) were selected as proton and deuteron targets, respectively. Lithium-6 is very close to a system of a free deuteron and a helium-4 core and has essentially the same magnetic moment as the deuteron. Thus ^{6}LiD corresponds to two deuterons plus a helium nucleus. Typically, polarisations of 85% for protons and 50% for deuterons were reached (fig. 4). A key feature of Compass is that both target polarisations are present simultaneously in separate target cells along the beam, *e.g.* "→, ←" for the two-cell configuration till 2004 and "→, ←, →" for the three-cell configuration from 2006 onwards. Thus in an asymmetry measurement most systematic uncertainties cancel. Using the dipole and solenoid magnet, the magnetic field can be rotated from, *e.g.*, pointing downstream to transverse to upstream. The spin follows the magnetic field adiabatically and thus the spin orientations can be changed within 30 min. Such a field rotation is performed typically once per day for the longitudinal polarisation in order to cancel potentially

Table I. – *Data taking of COMPASS.*

Period	Beam	Target	Polarisation
2002–2004	muon	“deuteron”	long. & transv.
2005	Cern accelerator shutdown		
2006	muon	“deuteron”	long.
2007	muon	“proton”	long. & transv.
2008–2009	hadron	hydrogen, nuclear	–
2010	muon	“proton”	transv.
2011	muon	“proton”	long.
2012	hadron	Ni	–
2013	Cern accelerator shutdown		

remaining systematic effects. The field can also be kept transverse for measurements with transverse target polarisation. Here the polarisation is inverted by repolarising typically once per week. In the shutdown year 2005 the superconducting target magnet was replaced by a new one, increasing the angular acceptance from ±70 mrad to ±180 mrad.

The experiment has been taking data since 2002 (table I). The years 2008–2009 were dedicated to the hadron spectroscopy programme of Compass with pion, kaon and proton beams. In 2012 the pion polarisability will be measured using a negative pion beam and a thin nickel target. Later in this year a pilot run for deeply virtual Compton scattering and hard exclusive meson production will take place.

3. – Longitudinal spin structure results

3·1. *Quarks.* – Studies of the longitudinal spin structure of the nucleon in deep inelastic scattering (DIS) proceed via the determination of cross-section asymmetries. Such measurements require a longitudinal polarisation of both the incoming lepton and the target nucleon. The process is sketched in fig. 5. Measured is the event number asymmetry $A_{\mathrm{exp}} = (N^{\overset{\rightarrow}{\Leftarrow}} - N^{\overset{\rightarrow}{\Rightarrow}})/(N^{\overset{\rightarrow}{\Leftarrow}} + N^{\overset{\rightarrow}{\Rightarrow}})$, where the single and double arrows indicate the beam and target polarisations, respectively. As in Compass the two target polarisations are measured simultaneously with the same beam, flux and acceptance cancel to first order and A_{exp} is proportional to the virtual-photon nucleon cross-section asymmetry

$$A_1 = \frac{1}{f P_\mu P_T D} A_{\mathrm{exp}}. \tag{1}$$

Here P_μ and P_T denote the beam and target polarisations, and D is the depolarisation factor, which describes the polarisation transfer from the lepton to the virtual photon. The ratio of the spin-averaged cross-section due to all polarisable nucleons in the target to that of all nucleons in the target is the dilution factor f. The factors D and f lie

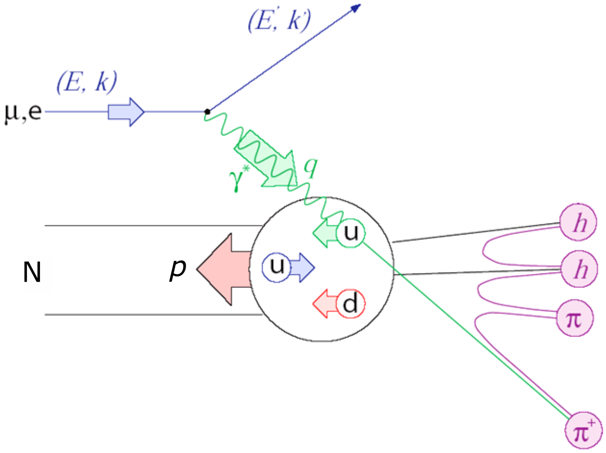

Fig. 5. – Sketch of semi-inclusive deep inelastic scattering off a nucleon.

between 0 and 1. For the targets used, the dilution factor varies from about 0.15 for NH_3 to 0.4 for ^{6}LiD.

In terms of the parton distribution functions (PDF) g_1 and f_1, the asymmetry A_1 is given in leading order (LO) by

$$A_1 = \frac{\sum_q e_q^2 g_1(x, Q^2)}{\sum_q e_q^2 f_1(x, Q^2)} \tag{2}$$

and for semi-inclusive DIS by

$$A_1^h = \frac{\sum_q e_q^2 g_1(x, Q^2) D_{1q}^h(z, Q^2)}{\sum_q e_q^2 f_1(x, Q^2) D_{1q}^h(z, Q^2)} \,. \tag{3}$$

Here, $Q^2 = -(k - k')^2$ is the negative square of the 4-momentum transfer and $x = Q^2/(2Pq)$ is the Bjorken scaling variable, indicating the momentum fraction of the nucleon carried by the struck quark in the infinite momentum frame. For SIDIS, the fragmentation functions (FF) D_{1q}^h describe the fragmentation of a quark q into a hadron h. In addition to Q^2 they depend on the the laboratory energy fraction $z = E_h/\nu$, which the observed hadron carries with respect to the total energy transfer ν from the lepton to the nucleon.

The proton [2] and deuteron [3] asymmetries measured by COMPASS are presented as a function of x in figs. 6 and 7, respectively. Only asymmetries for $Q^2 > 1\,\mathrm{GeV}^2$ are shown. The inclusive asymmetries, *i.e.* not requiring an additional hadron, are shown on the left, followed by the asymmetries for identified pions and kaons. Note that kaon measurements for the proton only exist from COMPASS. The spin-dependent structure functions g_1^p and g_1^d corresponding to the inclusive asymmetries are shown in figs. 8 and 9.

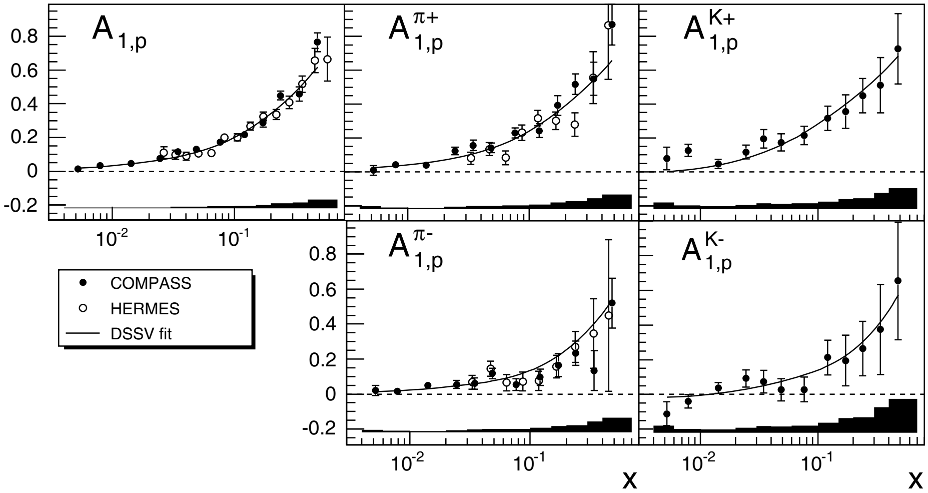

Fig. 6. – Proton asymmetries [2] compared to Hermes results [4] and the DSSV fit [5].

The fundamental Bjorken sum rule links the first moment Γ_1^{NS} of the non-singlet structure function $g_1^{NS}(x,Q^2) = g_1^p(x,Q^2) - g_1^n(x,Q^2)$ to the ratio of the axial to vector coupling constants in the neutron beta decay g_A and g_V

$$\Gamma_1^{NS}(Q^2) = \frac{1}{6}\left|\frac{g_A}{g_V}\right| C_1^{NS}(Q^2). \tag{4}$$

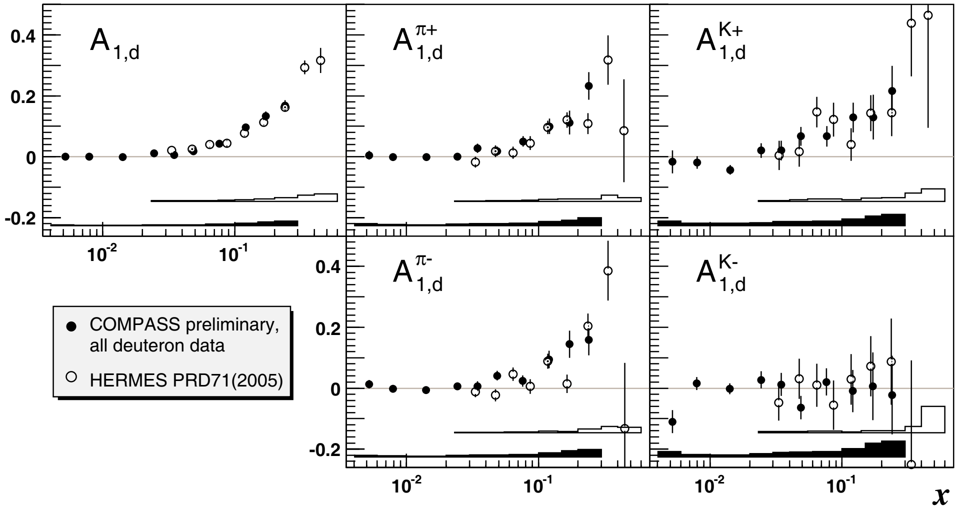

Fig. 7. – Deuteron asymmetries [3] compared to Hermes results [6].

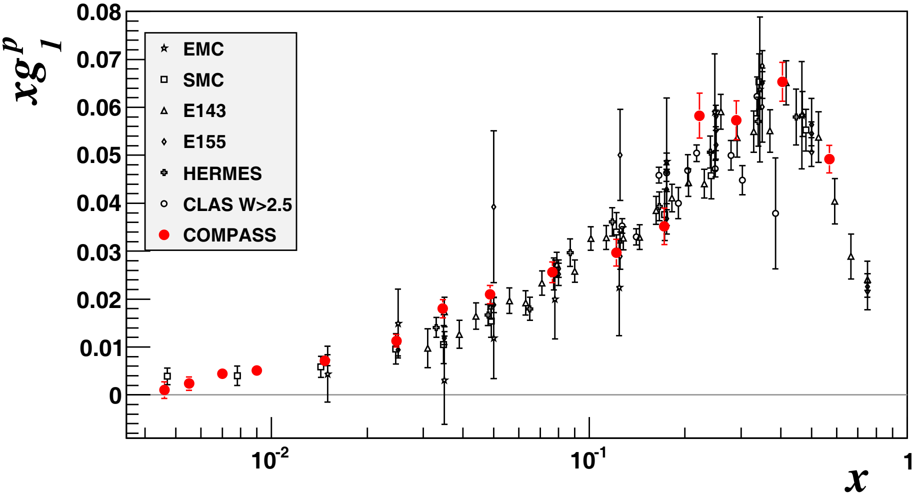

Fig. 8. – Proton structure function xg_1 as a function of x at the Q^2 of the measurement.

The neutron structure function g_1^n can be obtained from the proton and deuteron structure functions and the coefficient function C_1^{NS} describing higher-order corrections is known from theory to third order in α_s.

From the COMPASS proton and deuteron data this sum rule can be tested very accurately. We obtain $|g_A/g_V| = 1.28 \pm 0.07$ (stat.) ± 0.10 (syst.) compared to 1.2694 ± 0.0028 from neutron β decay. The values are in excellent agreement and thus the Bjorken sum rule is confirmed at the 10% level (fig. 10).

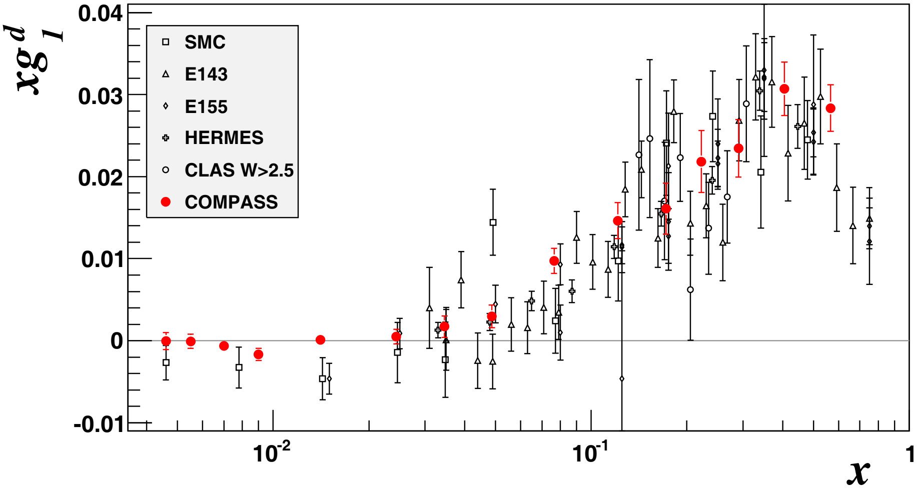

Fig. 9. – Deuteron structure function xg_1 as a function of x at the Q^2 of the measurement.

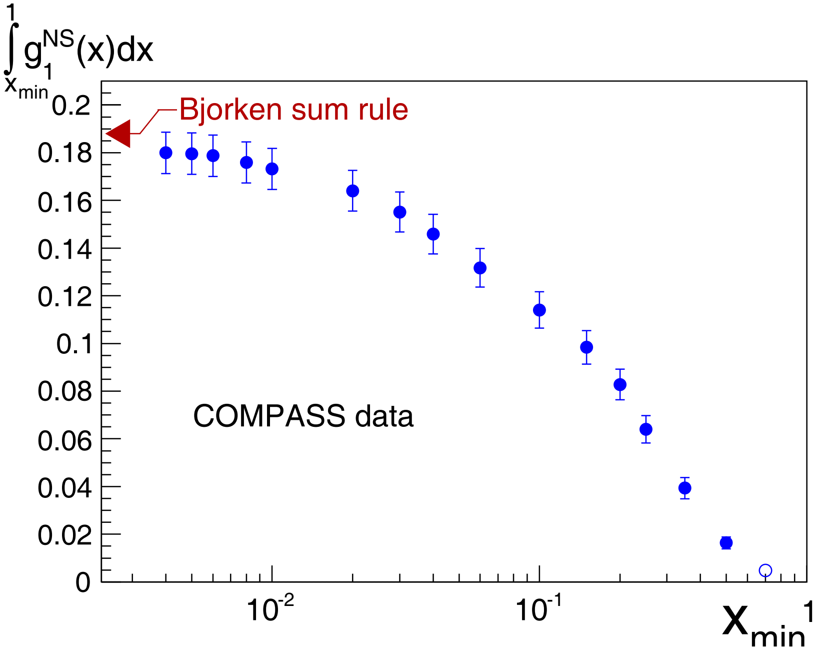

Fig. 10. – Integral $\int_{x_{\rm min}}^1 g_1^{NS}(x)\,{\rm d}x$ of the non-singlet structure function g_1^{NS} as a function of the lower integration limit $x_{\rm min}$.

From the semi-inclusive asymmetries, the quark distributions can be determined for the various flavours starting from eq. (3). The information on the initially struck quark is partly preserved in the fragmentation process and parametrised by the FFs. An up quark prefers to fragment into a positive pion while a down quark prefers fragmenting into a negative pion. Using isospin symmetry and the rather well-known fragmentation functions of up and down quarks as well as the poorly known fragmentation functions of strange quarks, one can build a system of equations containing the measured inclusive asymmetries, the asymmetries for identified hadrons as well as the wanted PDFs of the individual flavours. A fit with six flavours (u, d, s and antiquarks) did not show any significant difference for strange quarks and antiquarks. Therefore a five-flavour fit with $\Delta s = \Delta\bar{s}$ was used for the result shown in fig. 11 as a function of x [2]. The up-quark polarisation is strongly positive at $x > 0.1$, *i.e.* the spins of the up (down) quark point predominantly in the same direction as that of the proton (neutron). The down-quark polarisation is negative and the combined strange and antistrange quark polarisation is slightly negative. The latter comes from the region $x < 2 \times 10^{-2}$, while for larger x the distribution Δs rather vanishes.

Of particular interest are the first moments of the spin-dependent quark distributions $\Delta q = \int \Delta q(x)\,{\rm d}x$. They are given for $Q^2 = 3\,{\rm GeV}^2$ in table II. The regions unmeasured by Compass, $0 < x < 0.004$ and $0.7 < x$, were extrapolated using the PDFs from the

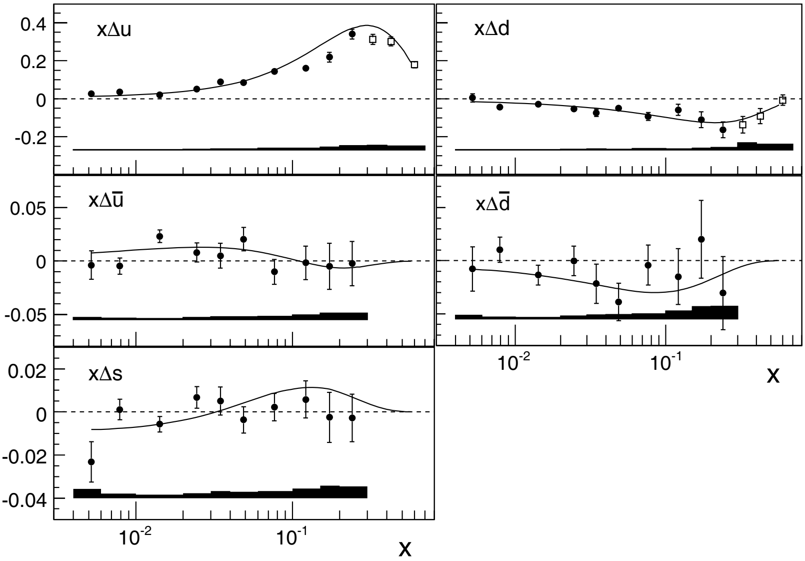

Fig. 11. – The quark helicity distributions $x\Delta u$, $x\Delta d$, $x\Delta u$, $x\Delta d$ and $x\Delta s$ at $Q_0^2 = 3\,\mathrm{GeV}^2$ as a function of x. The values for $x < 0.3$ (black dots) are derived at LO from the COMPASS spin asymmetries using the DSS fragmentation functions [7]. Those at $x > 0.3$ (open squares) are derived from the values of the polarised structure function $g_1(x)$ quoted in [8, 9] assuming $\Delta q = 0$. The bands at the bottom of each plot show the systematic errors. The curves show the predictions of the DSSV fit calculated at NLO [5].

DSSV fit [5]. The range $0.3 < x < 0.7$ was taken from the inclusive data assuming that the sea quark distributions vanish in this region. The result is summarised in table II and compared to the DSSV fit. The sum of all quark contributions $\Delta\Sigma = \sum_q \Delta q$

TABLE II. – *Full first moments of the quark helicity distributions at $Q_0^2 = 3\,\mathrm{GeV}^2$. The unmeasured contributions at low and high x were estimated by extrapolating the data towards $x = 0$ and $x = 1$ and by using the DSSV parametrisation* [5].

	Extrapol. full moment	DSSV
Δu	$0.71 \pm 0.02 \pm 0.03$	$0.71 \pm 0.02 \pm 0.03$
Δd	$-0.34 \pm 0.04 \pm 0.03$	$-0.35 \pm 0.04 \pm 0.03$
$\Delta\overline{u}$	$0.02 \pm 0.02 \pm 0.01$	$0.03 \pm 0.02 \pm 0.01$
$\Delta\overline{d}$	$-0.05 \pm 0.03 \pm 0.02$	$-0.07 \pm 0.03 \pm 0.02$
$\Delta s(\Delta\overline{s})$	$-0.01 \pm 0.01 \pm 0.01$	$-0.05 \pm 0.01 \pm 0.01$
Δu_v	$0.68 \pm 0.03 \pm 0.03$	$0.68 \pm 0.03 \pm 0.03$
Δd_v	$-0.29 \pm 0.06 \pm 0.03$	$-0.28 \pm 0.06 \pm 0.03$
$\Delta\Sigma$	$0.32 \pm 0.03 \pm 0.03$	$0.22 \pm 0.03 \pm 0.03$

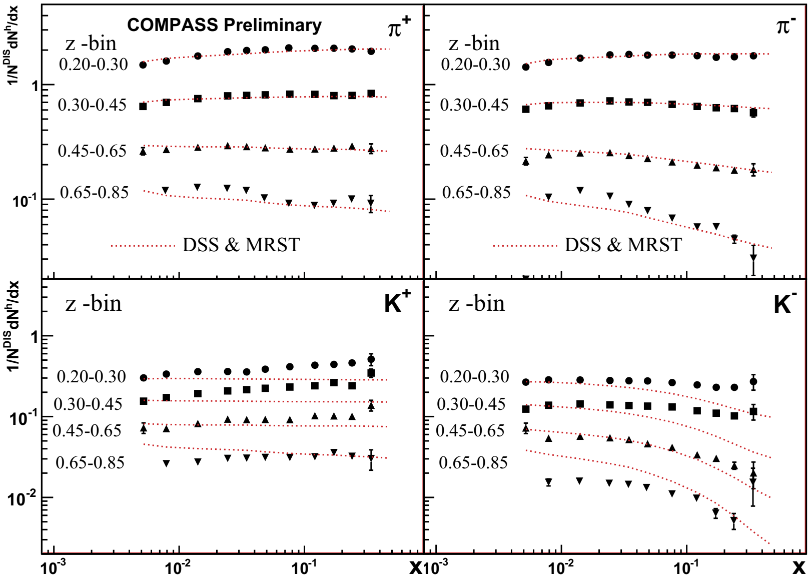

Fig. 12. – Preliminary hadron multiplicities from Compass for π^+, π^-, K^+ and K^- as a function of x in various z bins. The curves are obtained with the DSS fragmentation functions and MRST04 PDFs.

obtained from the semi-inclusive Compass data as $0.32 \pm 0.03 \pm 0.03$ agrees very well with the inclusive Compass result from g_1^d of $a_0 = 0.33 \pm 0.03$ [8]. The DSSV fit yields a considerably smaller value of $0.22 \pm 0.03 \pm 0.03$. The observed difference comes mainly from the negative behaviour of $\Delta s(x)$ assumed at small x. It should be noted that the results for $\Delta s(x)$ crucially depend on the used fragmentation functions as illustrated in ref. [2]. From the new, preliminary hadron multiplicities for an isoscalar target (fig. 12) it is obvious that fragmentation into (negative) kaons is not described well by the DSS [7] fragmentation functions, which were used both in the Compass analysis and in the DSSV fit. This casts some doubt on the reliability of the present determinations of the strange quark polarisation from semi-inclusive data. More data and further work on the fragmentation functions is required.

3˙2. *Gluons.* – Following the discovery of the small quark spin contribution to the nucleon spin, a scenario was put forward, where the gluon spin masks the contribution of the quark spins via the axial anomaly. Even values of $6\hbar$ for $\Delta g = \int_0^1 g(x)\,\mathrm{d}x$ were proposed [10]. With more data and slightly increasing quark spin contribution, the value for Δg dropped to about $2\hbar$, still four times the nucleon spin. A large negative orbital angular momentum L_z is required in this scenario to restore the nucleon spin of $1/2(\hbar)$

$$\frac{1}{2} = \frac{1}{2}\Delta\Sigma + \Delta g + L_z. \tag{5}$$

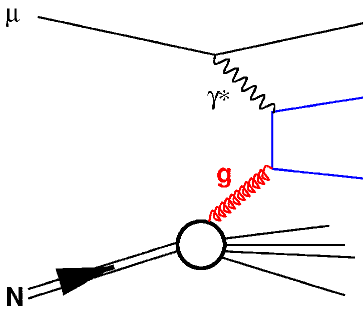

Fig. 13. – Sketch of the photon-gluon fusion process.

The gluon polarisation can be determined from scaling violations in the spin-dependent structure function g_1. However, the present range in Q^2 is insufficient to obtain $\Delta g(x)$ or its first moment with a sufficient precision. In SIDIS one has a direct handle on the gluon polarisation via the photon-gluon fusion (PGF) process (fig. 13). The measured cross-section asymmetry for PGF events is directly proportional to the gluon polarisation

$$A_1^{PGF} \propto \langle \hat{a}_{PGF} \rangle R_{PGF} \langle \Delta g / g \rangle \qquad (6)$$

averaged over the covered range in the gluon momentum fraction x_g. However, there are competing processes yielding the same final state as PGF. Therefore Monte Carlo simulations are required in order to determine the fraction of PGF events R_{PGF} in the sample as well as the average analysing power $\langle \hat{a}_{\mathrm{PGF}} \rangle$ of the hard process. At Compass the following final states were studied:

- pairs of light hadrons with high transverse momentum p_T with respect to the virtual photon in events with $Q^2 > 1\,\mathrm{GeV}^2$ (LO) ([11] and preliminary results),
- pairs of light hadrons with high-p_T in events with $Q^2 < 1\,\mathrm{GeV}^2$ (LO) [12],
- single charmed mesons (D^0, D^*) (LO) ([13] and preliminary LO, NLO results),
- single hadrons in events with $Q^2 < 1\,\mathrm{GeV}^2$ (NLO, in preparation).

The cleanest of these processes is open-charm production via PGF because there is basically no physics background. The D^0 meson is identified via its decay $D^0 \to K^+\pi^- + c.c.$ The cross-section is small and combinatorial $K\pi$ background is large. Looking however at D^0 from $D^{*+} \to D^0\pi_s^+ + \mathrm{c.c.}$, the situation improves drastically due to the additional detection of the slow π_s (fig. 14).

In light-hadron production contributions from leading-order scattering and QCD-Compton processes are much larger and thus R_{PGF} is smaller. The stronger dependence on Monte Carlo simulations introduces a larger model dependence, which can however be controlled. All Compass LO results for the gluon polarisation are in agreement and shown in fig. 15 together with results from Smc and Hermes. A preliminary NLO analysis

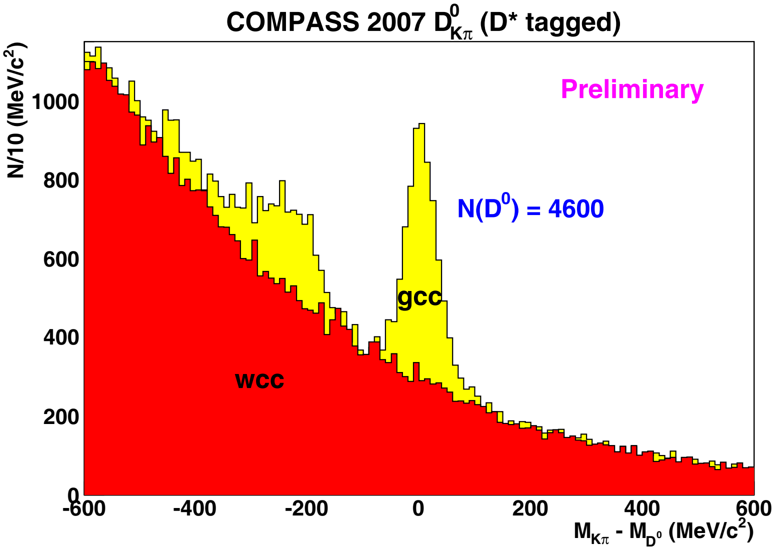

Fig. 14. – (Colour on-line) Mass spectrum of reconstructed D^0 mesons from D^* decay. Also shown is the combinatorial background of $K\pi$ pairs with wrong charge combination ("wcc", red). The structure left of the D^0 peak is a reflection of the D^0 peak is a reflection of the $D^0 \to K\pi\pi^0$ decay, which can also be used in the determination of the gluon polarisation (preliminary 2007 data).

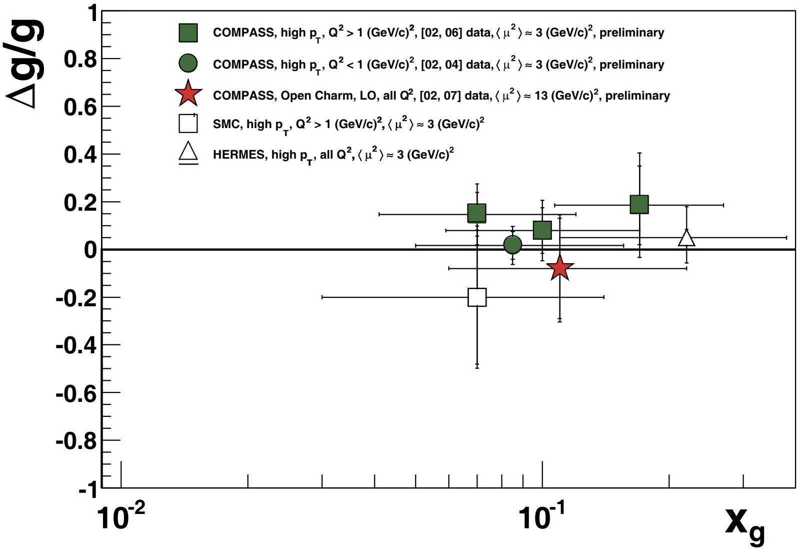

Fig. 15. – LO results for $\Delta g/g$ from analyses of hadron production via PGF as a function of the gluon momentum fraction x_g.

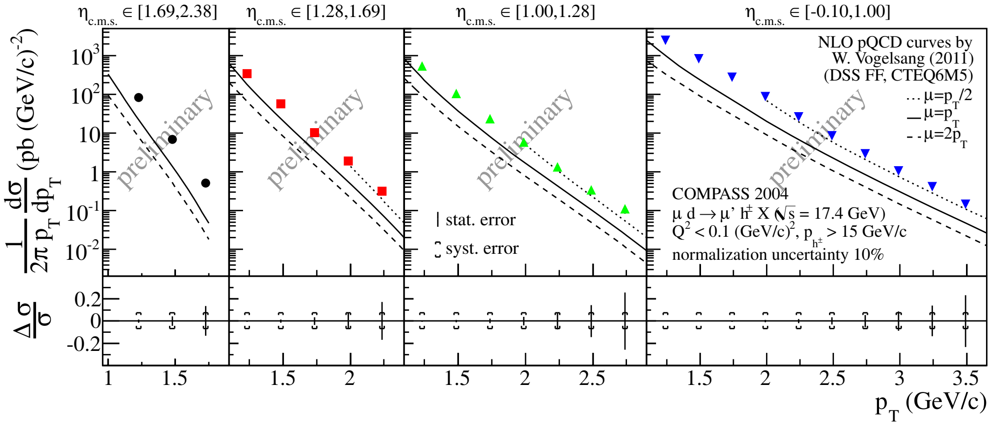

Fig. 16. – Cross-section as a function of the transverse momentum of the produced hadron in three bins of the centre-of-mass pseudo-rapidity η. The curves show preliminary results of NLO resummed calculations by the W. Vogelsang, Tübingen.

of the open-charm data yields $\Delta g/g|_{\mathrm{NLO}} = -0.20 \pm 0.21\ (\mathrm{stat.}) \pm 0.08\ (\mathrm{syst.})$. The main effect in going from LO to NLO is a shift of the average probed gluon momentum fraction x_g to larger values $\langle x_g \rangle = 0.28^{+0.19}_{-0.10}$. All results for the gluon polarisation are small, but nevertheless a significant contribution to the nucleon spin of $1/2\hbar$ cannot be excluded. However, scenarios with gluon polarisations in the order of several $\hbar$ are ruled out, a finding also confirmed by the Rhic experiments in polarised pp collisions.

Finally, Compass is working in collaboration with theorists on an analysis of single-hadron production in analogy to the Rhic π^0 analysis at much higher energies. A first result indicates that this method is applicable at Compass energies as well. In fig. 16 the agreement of the preliminary analysis and calculations is shown for three scales $\mu = p_T/2$, $\mu = p_T$ and $\mu = 2p_T$. For the smallest scale excellent agreement between data and theory is observed over almost five orders of magnitude. However, the small-scale and the rather large-scale dependence ask for further improvements on the theory side. Nevertheless, it is likely that from these data a precise and reliable determination of $\Delta g/g$ in NLO can be obtained in the future.

4. – Transverse spin structure results

Apart from the spin-averaged PDFs f_1 and the spin-dependent PDFs g_1, a third structure function, h_1 or transversity, is needed to describe the nucleon at the twist-2 level. Like g_1 for the longitudinal case, h_1 describes the polarisation of quarks in the transverse case. Since h_1 is chiral odd, it needs to be coupled to a chiral-odd fragmentation function in order to appear in the photon-nucleon cross-section. There two such functions presently being used, the Collins function $H_1^{\perp}$ for single hadrons and the interference fragmentation function (IFF) $H_1^{\sphericalangle}$ for hadron pairs. Both lead to azimuthal

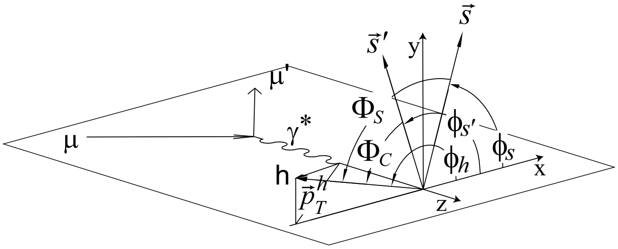

Fig. 17. – Definition of the Collins and Sivers angles. The vectors $\vec{p}_T^{\,h}$, $\vec{s}$ and $\vec{s}\,'$ are the hadron transverse momentum and the spin of the initial and struck quark, respectively.

cross-section asymmetries for scattering off transversely polarised targets.

The three PDFs mentioned above exhaust the information on nucleon structure at twist-2 if intrinsic transverse momenta k_T of quarks are integrated over. In total there are eight intrinsic-transverse-momentum (k_T)-dependent PDFs at leading twist, all of which vanish upon integration apart of $f_1(x, k_T)$, $g_1(x, k_T)$ and $h_1(x, k_T)$ which reduce to the above mentioned PDFs. Of the TMD distributions the Sivers function $f_{1T}^{\perp}$ and the Boer-Mulders function $h_1^{\perp}$ are of particular interest. The former describes unpolarised partons in a transversely polarised nucleon, the latter transversely polarised partons in an unpolarised nucleon.

4.1. *Transversity*. – The azimuthal cross-section asymmetry $A_{UT} \propto A_C \sin\Phi_C$ generated by transversity and the Collins effect shows a $\sin\Phi_C$ dependence with an amplitude of

$$A_C^h \propto \frac{\sum_q e_q^2 h_1^q(x) H_1^{\perp,h/q}(z, p_T)}{\sum_q e_q^2 f_1^q(x) D_1^{h/q}(z)}\,, \tag{7}$$

where z is the energy fraction carried the hadron, p_T the hadron's transverse momentum and $D_1(z)$ the standard FF. The angle $\Phi_C = \phi_h - \phi_s - \pi$ is given by the azimuthal angles ϕ_h and ϕ_S of the hadron and the nucleon spin as defined in fig. 17.

A similar expression is obtained for the 2-hadron case with the IFF for the azimuthal cross-section asymmetry proportional to $A_{RS} \sin\phi_{RS} \sin\theta$

$$A_{RS}^h \propto \frac{\sum_q e_q^2 h_1^q(x) H_1^{\sphericalangle,hh/q}(z, M_{hh}^2)}{\sum_q e_q^2 f_1^q(x) D_1^{hh/q}(z, M_{hh}^2)}\,. \tag{8}$$

Here $H_1^{\sphericalangle}(z, M^2)$ and $D_1(z, M^2)$ denote the 2-hadron spin-dependent and spin-independent fragmentation functions, respectively. The angles are defined in fig. 18.

The preliminary results of the 2010 proton data for the Collins asymmetry are shown in fig. 19 (top). Large asymmetries of opposite sign are observed for positive and negative hadrons. Their magnitudes increase with x_B and exceed 5% at large x. The preliminary

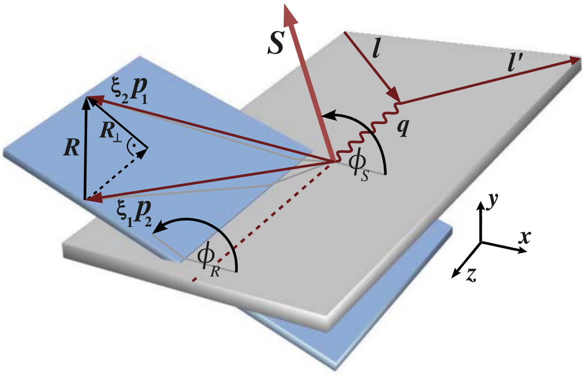

Fig. 18. – Definition of the azimuthal angles ϕ_R and ϕ_S for two-hadron production in deep inelastic scattering, where $\boldsymbol{l}$, $\boldsymbol{l}'$, $\boldsymbol{q}$ and $\boldsymbol{p_i}$ are the 3-momenta of beam, scattered muon, virtual photon and hadrons. Note that the azimuthal plane is defined by the directions of the relative hadron momentum and the virtual photon [14].

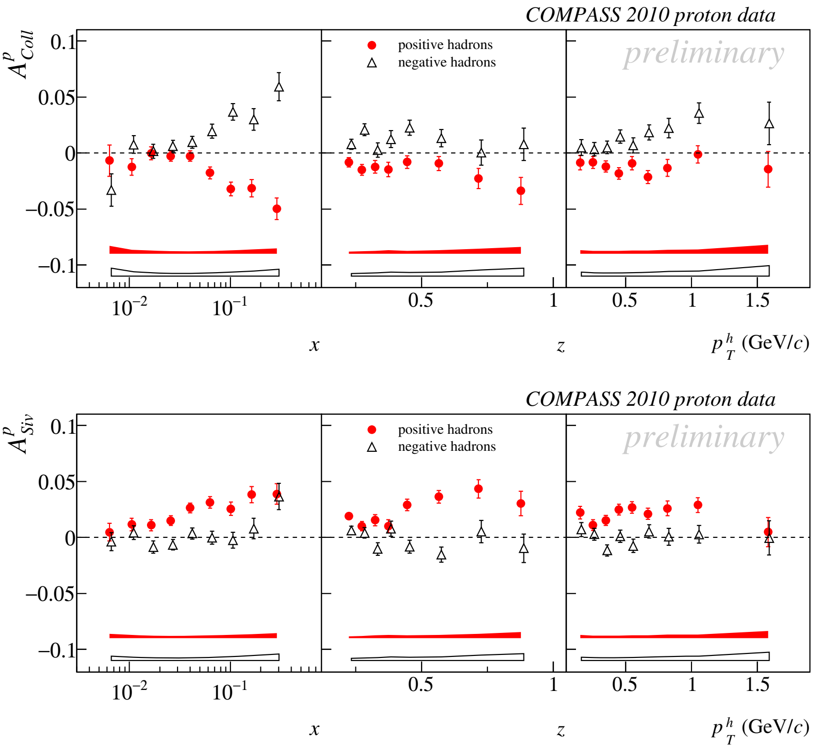

Fig. 19. – Preliminary Collins (top) and Sivers (bottom) asymmetries for the proton as a function of x, z and p_T from the 2010 data.

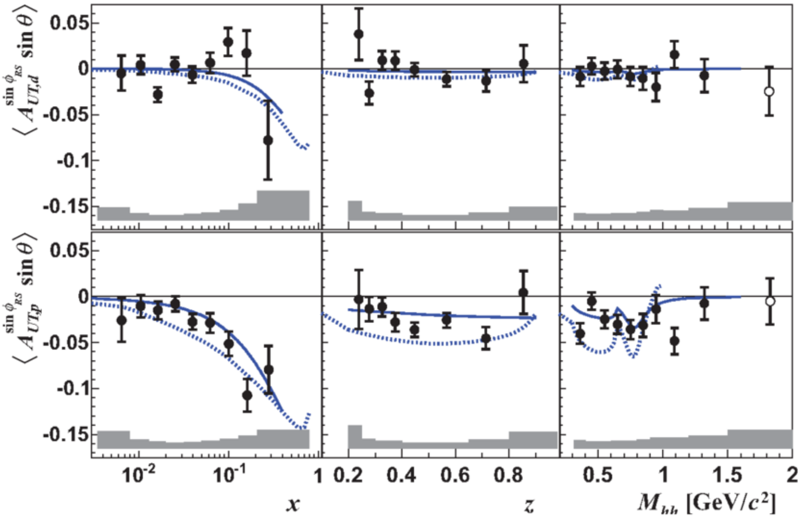

Fig. 20. – Deuteron (top) and proton (bottom) 2-hadron asymmetries, integrated over θ as a function of x, z, and M_{hh}. For details and the curves showing predictions see ref. [14].

2-hadron proton (2007) and deuteron (2002–2004) results are displayed in fig. 20 both for the deuteron (top) and the proton (bottom) [14]. As for the 2-hadron asymmetries, also the Collins asymmetries for the deuteron are compatible with zero (not shown here). This is an important result indicating that up and down quark transversity distributions have opposite sign.

4·2. *Transverse-momentum dependent distributions.* – The transverse-momentum (k_T)–dependent Sivers function $f_{1T}^{\perp,q}(x,k_T)$ causes an azimuthal asymmetry

$$A_S^h \propto \frac{\sum_q e_q^2 f_{1T}^{\perp,q}(x,p_T/z) D_1^{h/q}(z)}{\sum_q e_q^2 f_1^q(x,p_T/z) D_1^{h/q}(z)}\,, \tag{9}$$

which arises from a final state interaction. The cross-section asymmetry is proportional to $A_S \sin\Phi_S$, where the Sivers angle $\Phi_S = \phi_h - \phi_S$ is given by the difference of the azimuthal angles of the hadron and the spin vector as shown in fig. 17.

The latest Compass results for the proton are shown in fig. 19. A rather strong positive asymmetry is observed for positive hadrons increasing with x and reaching asymmetries of up to 4%. For negative hadrons the asymmetry is compatible with zero for $x < 0.1$ with an indication of an increasing asymmetry at the largest x values. There is a hint of decreasing Sivers asymmetry with increasing mass of the hadronic final state W. This trend first observed in the 2007 data [15] persists in the new 2010 data and might explain the somewhat larger asymmetries observed by Hermes [16].

For the deuteron the asymmetries appear to vanish over the full kinematic range

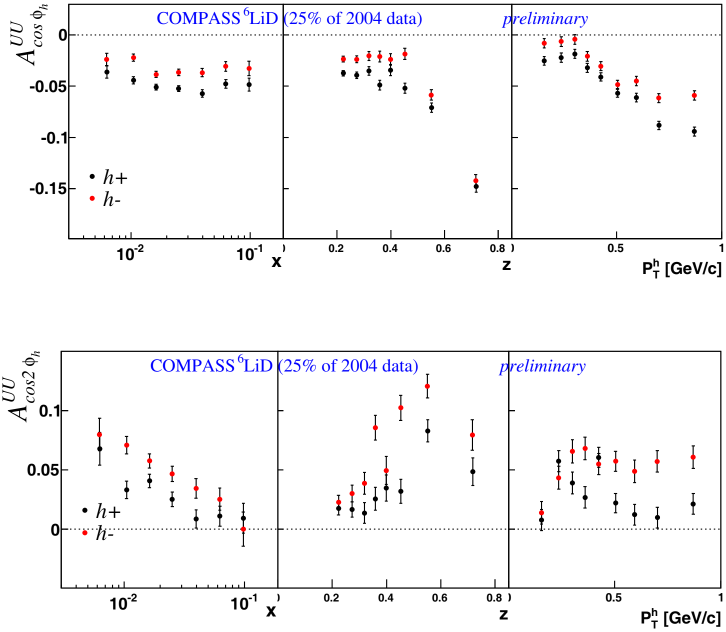

Fig. 21. – Cahn (top) and Boer-Mulders asymmetries for ^{6}LiD target and positive and negative hadrons as a function of x, z, and p^h_T. The kinematic factors are divided out.

accessible to COMPASS [17, 18] both for the Sivers and the Collins asymmetries. This important result points to a cancellation of the up and down quarks asymmetries. All Collins and Sivers asymmetries were—or will be—also evaluated for identified pions and kaons.

Two preliminary spin-averaged asymmetries obtained for an unpolarised isoscalar target (^{6}LiD) are shown in fig. 21. The upper $\cos\phi$ asymmetry is due to the Cahn effect and reaches almost 10% at large p_T. The lower $\cos 2\phi$ asymmetry originates from the Boer-Mulders TMD distribution describing transversely polarised partons in an unpolarised nucleon. Large asymmetries are observed—this time at small x_B—despite the fact that it is a deuteron-like target, where most of the other asymmetries are suppressed. The $\sin\phi$ asymmetry (not shown), however, is small.

5. – COMPASS plans for the future

The COMPASS Collaboration submitted in 2010 a proposal for new measurements to the CERN programme committee (SPSC) [19]. The proposal was approved in December 2010 and experiments will start in 2012 with a pion/kaon polarisability measurement (not discussed here). The future programme starting 2014 after the accelerator shutdown focuses on TMD distributions and GPDs. A polarised Drell-Yan experiment will take

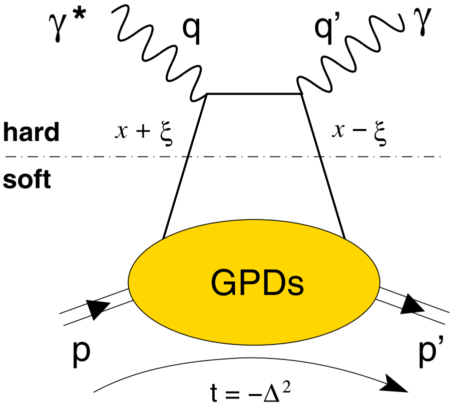

Fig. 22. – Handbag diagram for the DVCS process at leading twist.

place in 2014 and in 2015/2016 deeply virtual Compton scattering (DVCS) and hard exclusive meson production (HEMP) will be studied with an unpolarised target. A pilot run for the latter experiment is planned already for late 2012. In parallel with the GPD programme high statistics SIDIS data will be taken.

5˙1. *GPD programme.* – The novel concept of generalised parton distributions is by now well established and widely considered as the tool to get a more detailed understanding of how quark and gluons build up the nucleon. GPDs are universal distributions which contain as limiting cases nucleon form factors on the one hand and PDFs on the other. The distributions H^f and $\widetilde{H}^f$ $(f = u, d, s, g)$ describe processes where the nucleon helicity is preserved and contain as limiting cases the PDFs f_1 and g_1, respectively. Processes where the nucleon helicity is flipped are described by the GPDs E^f and $\widetilde{E}^f$ for which no such limiting case exists. GPDs correlate transverse spatial and longitudinal momentum and thus provide a kind of "nucleon tomography". They depend on four variables x, ξ, t, and Q^2. The cleanest process to assess GPDs is DVCS shown in fig. 22, which also defines the relevant momentum fractions, x (not the Bjorken scaling variable) and ξ, and the momentum transfers, t and Q^2. The former two variables represent respectively average and half the difference between the initial and final longitudinal momentum fractions of the nucleon, carried by the parton throughout the process. The Bjorken scaling variable x_B is in this kinematics related to the skewness as $\xi \simeq x_B/(2-x_B)$ in the Bjorken limit.

The interest in these distributions was boosted, when X.-D. Ji showed that there is a sum rule for the total angular momentum J^f of a quark or a gluon and the corresponding GPDs [20]

$$J^f(Q^2) = \frac{1}{2}\lim_{t\to 0}\int_{-1}^{1} \mathrm{d}x\, x\left[H^f(x,\xi,t,Q^2) + E^f(x,\xi,t,Q^2)\right], \tag{10}$$

which holds for any value of ξ. Knowing the quark spin contribution to the nucleon spin, one can—in principle—determine the orbital angular-momentum contribution. This is

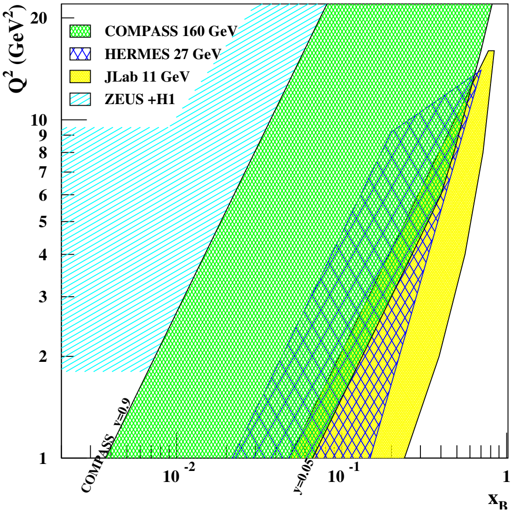

Fig. 23. – (Colour on-line) Kinematic domains for measurements of hard exclusive processes shown for the COMPASS (green area enclosed by the lines $y = 0.9$ and $y = 0.05$), HERMES and JLab fixed-target experiments and the HERA collider experiments H1 and Zeus.

presently the only unambiguous method to assess the angular orbital momentum and to solve the nucleon spin puzzle. However, an actual measurement will require a world-wide effort of various experiments. The kinematic domains of some experiments are displayed in fig. 23. COMPASS will explore the uncharted territory in between the collider region and that of the lower-energy fixed-target HERMES and JLab experiments.

The DVCS process interferes with the Bethe-Heitler (BH) process due to identical final states (fig. 24). The cross-section then contains five terms

$$\mathrm{d}\sigma^{\mu p\to\mu p\gamma} = \mathrm{d}\sigma^{\mathrm{BH}} + \mathrm{d}\sigma_0^{\mathrm{DVCS}} + P_\mu \mathrm{d}\Delta\sigma^{\mathrm{DVCS}} + e_\mu \Re\mathrm{e}\, I + P_\mu e_\mu \Im\mathrm{m}\, I, \tag{11}$$

where I denotes the DVCS-BH interference term. A characteristic feature of this cross-section is its ϕ dependence, the azimuthal angle between lepton scattering plane and real-photon production plane (fig. 25).

In 2009 COMPASS performed a preparatorial measurement with a 40 cm long liquid-hydrogen target to validate the Monte Carlo simulations and to demonstrate the feasibility of the measurement. The result is shown in fig. 26. An important feature is that the normalisation can be fixed at small x_B, where the well-known BH process dominates. The observed ϕ distributions nicely match the MC prediction, although statistics is poor. In the largest x_B bin a clear contribution from DVCS is visible.

From eq. (11) one can build the sum $\mathcal{S}$ and difference $\mathcal{D}$ of the $\mu p \to \mu p\gamma$ cross-section for simultaneous change of lepton charge e_μ and polarisation P_μ of the incoming lepton

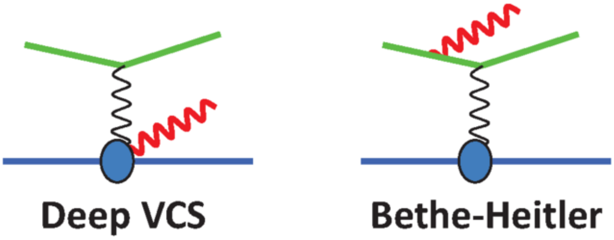

Fig. 24. – DVCS and Bethe-Heitler processes.

beam (+ to − and ← to →)

$$\mathcal{D} = \mathrm{d}\sigma^{\overset{+}{\leftarrow}} - \mathrm{d}\sigma^{\overset{-}{\rightarrow}} = 2(\mathrm{d}\sigma_0^{\mathrm{DVCS}} + \Re\mathrm{e}\, I) \tag{12}$$
$$\mathcal{S} = \mathrm{d}\sigma^{\overset{+}{\leftarrow}} + \mathrm{d}\sigma^{\overset{-}{\rightarrow}} = 2(\mathrm{d}\sigma_0^{\mathrm{BH}} + \mathrm{d}\sigma_0^{\mathrm{DVCS}} + \Im\mathrm{m}\, I).$$

The muon beam used at COMPASS has exactly this behaviour that negative muons have opposite polarisation than positive muons due to the weak pion decay. Upon integration over the azimuthal angle ϕ (fig. 25) the interference contribution to $\mathcal{S}$ vanishes [21] and after subtraction of the BH cross-section, one obtains the DVCS cross-section. This cross-section depends on the squared momentum transfer t from the initial to final nucleon (fig. 22). At small x_B one has the relation $\langle r_\perp^2(x_B)\rangle \approx 2B(x_B)$ if the exclusive cross-section is parametrised as $\mathrm{d}\sigma/\mathrm{d}t \propto \exp[-B(x_B]|t|$. The transverse distance $r_\perp$ is measured between the struck quark and the centre of mass of the spectator system. Thus, independent of any GPD parametrisation, one obtains a measure of the transverse nucleon size as a function of x_B. Using a parametrisation of the type $B(x_B) = B_0 + 2\alpha' \log(x_0/x_B)$, one can characterise the t slope of the cross-section by the parameter α' shown in fig. 27. The projected precision of a t-slope measurement is presented in fig. 27. A new electromagnetic calorimeter, ECAL0, will improve the precision of the measurement and enlarge the accessible range towards larger x_B. Combined

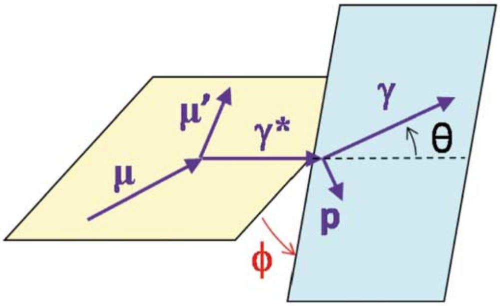

Fig. 25. – Definition of angles for the DVCS process.

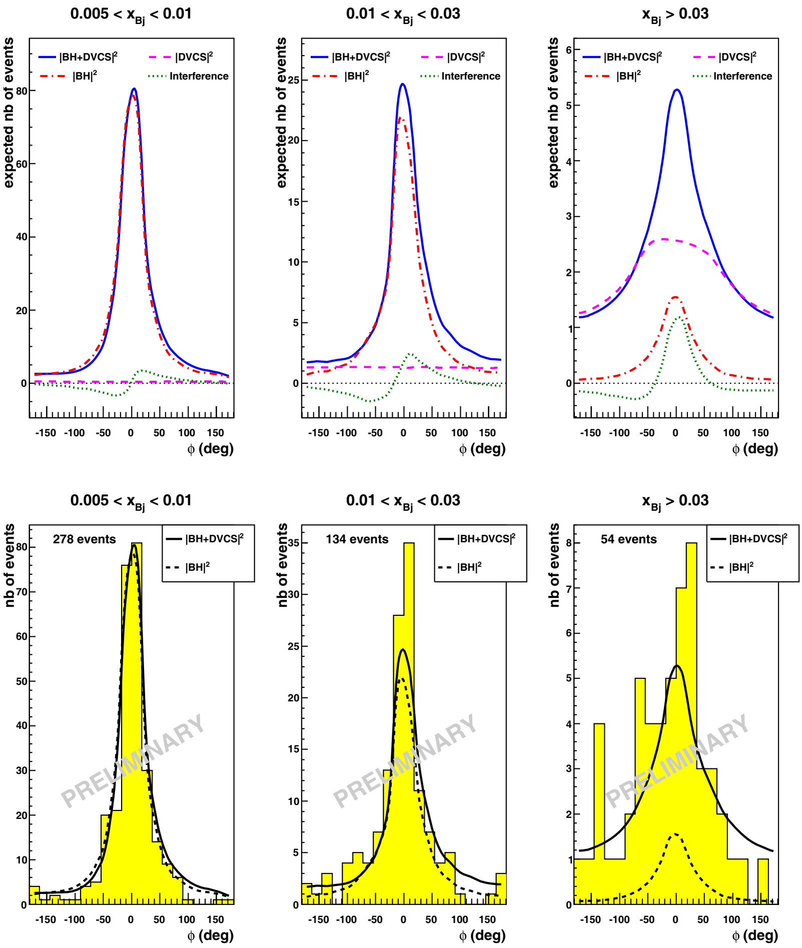

Fig. 26. – Event numbers as a function of ϕ for three bins in x_B obtained from a Monte Carlo simulation (top) and data from a test run in 2009 (bottom). The Monte Carlo simulation is normalised to the lower x_B bin where BH dominates. The curves in the lower plot are the same as the solid (total) and dash-dotted (BH) curves in the upper plot.

with the Hera data and future JLab data a comprehensive picture of the evolution of the nucleon's transverse size with x_B will be achieved in a model-independent way. For the 2012 pilot DVCS run we project already a significant measurement combining the three central x_B bins of fig. 27 into one large x_B.

For DVCS with $\xi = 0$ there is only a pure transverse momentum transfer $t = -\Delta_\perp^2$. The Fourier transform of the $\Delta_\perp^2$ dependence of the GPD $H^f(x, 0, -\Delta_\perp^2)$ for fixed x describes the spatial distribution of partons of species f carrying the momentum fraction x. This is sketched in fig. 28. Here the impact parameter b is the transverse distance

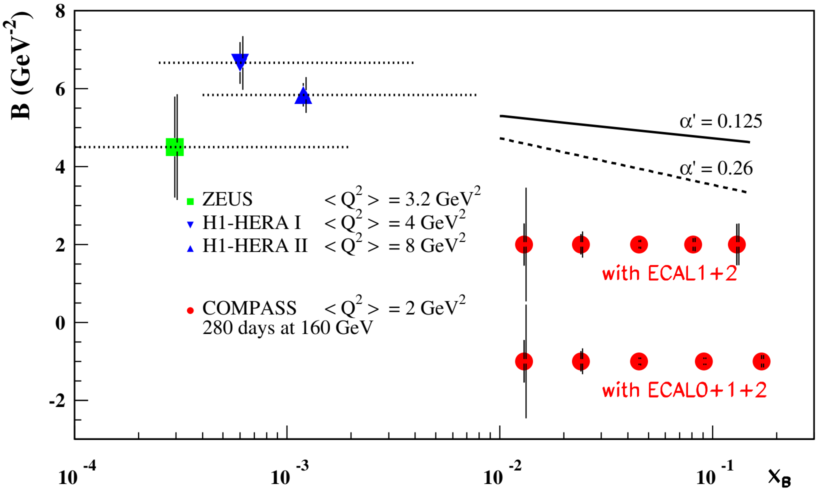

Fig. 27. – (Colour on-line) Projections for the measurement of the x_B dependence of the t-slope parameter $B(x_B)$ of the DVCS cross-section calculated for $1\,\text{GeV}^2 < Q^2 < 8\,\text{GeV}^2$ (red filled dots, right). The left vertical bar on the points indicates the statistical error only while the right one includes also the quadratically added systematic uncertainty, using only ECAL1 and ECAL2 (upper row) and also an additional ECAL0 calorimeter (lower row). For comparison some Hera results with similar $\langle Q^2\rangle$ are also shown [22,23]. Dashed horizontal lines indicate the x_B range of these measurements. Two different slopes are indicated for $\alpha' = 0.125\,\text{GeV}^2$ and $0.26\,\text{GeV}^2$.

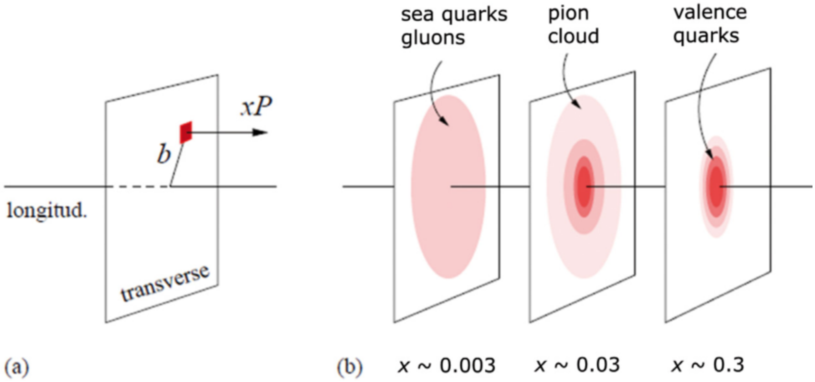

Fig. 28. – Nucleon tomography. a) The Fourier transform of the $-\Delta_\perp^2$ dependence of the GPD $H^f(x, 0, -\Delta_\perp^2)$ for fixed x describes the distribution of the transverse distance $b \equiv |\boldsymbol{b}_\perp|$ of partons, carrying the fraction x of the nucleon's longitudinal momentum P, from the centre of momentum of the nucleon. b) Sketch of tomographic views of the transverse spatial parton distribution in the nucleon at certain parton longitudinal momentum fractions x. Figure adapted from ref. [24].

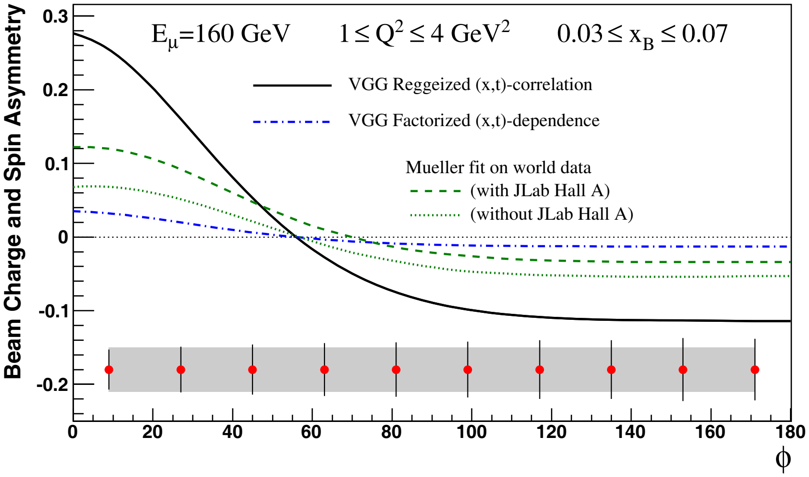

Fig. 29. – (Colour on-line) Projected statistical accuracy for a measurement of the dependence of the beam charge-and-spin asymmetry on ϕ. As an example the 2-dimensional bin $0.03 < x_B < 0.07$ and $1\,\mathrm{GeV}^2 < Q^2 < 4\,\mathrm{GeV}^2$ is shown. Predictions are calculated using the VGG model [25]. The black (solid) and blue (dash-dotted) curves correspond to two different variants of this model. The green curves show predictions based on the first fit of world data [26] including JLab Hall A (dashed line) or not (dotted line).

between the struck quark and the centre of mass of the whole nucleon. Thus for $x \to 1$ the distribution must shrink towards zero.

The ϕ dependence of the difference $\mathcal{D}$, the sum $\mathcal{S}$ and the asymmetry $\mathcal{A} = \mathcal{D}/\mathcal{S}$ of the DVCS cross-sections defined in eq. (12) allow for the extraction of quantities related to Compton form factors (CFF) which in turn depend on the GPDs. With an unpolarised target, COMPASS DVCS results will mainly provide information on the CFF $\mathcal{H}$ and thus constrain the GPD H. For details of the ϕ dependence see ref. [19] and references therein. Results will be obtained in (x_B, Q^2) bins. An example for the projected precision in such a bin is shown in fig. 29 for the beam charge-and-spin asymmetry $\mathcal{A}$.

Some handle on the flavour separation of GPDs may be obtained from measurements of hard exclusive meson production, where the meson replaces the real photon of DVCS. Contrary to the DVCS case, gluon GPDs contribute in leading order in HEMP and BH interference does not exist. It is foreseen to measure cross-sections for a large set of mesons (π, η, ρ, ω, ϕ, J/ψ, …), which are all sensitive to different combinations of quark and gluon GPDs. The GPD E can in principle be assessed using a transversely polarised target. Such measurements are under consideration for a later stage of the programme.

Another physics topic, which will be pursued in parallel with DVCS, is the study of spin-independent TMD distributions like the Boer-Mulders distribution and of fragmentation functions, in particular for strange quarks. Also the spin-averaged strange quark PDF needs further studies. Up to now COMPASS used polarised NH_3 and ^{6}LiD. With

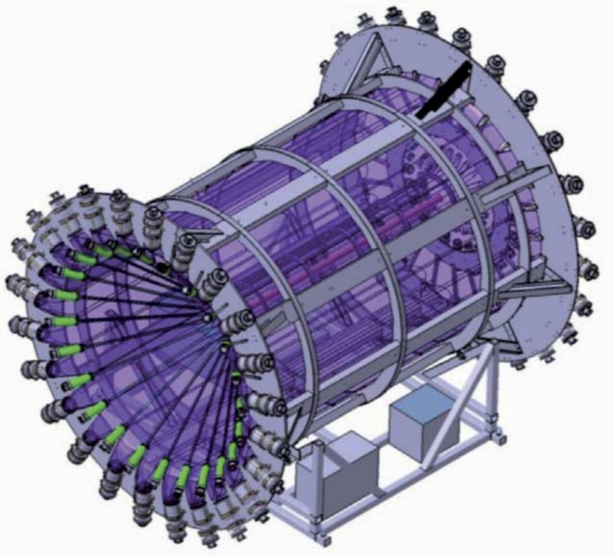

Fig. 30. – The Camera recoil detector.

the liquid-hydrogen target a clean unpolarised proton measurement will be possible for the first time in Compass.

A major rearrangement of the spectrometer target region will be necessary for the GPD measurements. The polarised target has to be removed and a recoil proton detector, the Camera detector, will be installed. It consists of two concentric scintillator barrels of 3.6 m length and 2.2 m diameter for the outer barrel (fig. 30). The photomultiplier signals will be digitised with 1 GHz to cope with the high rate and pile-up. Camera is essential to ensure the exclusivity of the observed reactions. It houses on the central axis a 2.5 m long liquid-hydrogen target. In order to improve the acceptance of real photons, a third electromagnetic calorimeter, ECAL0, will be constructed and placed just downstream of the Camera detector. Multipixel avalanche photodiodes were chosen for the readout to avoid problems due the magnetic field of the close spectrometer magnet SM1. For the pilot run in 2012 the Camera detector and part of ECAL0 will be available. It is also planned to replace the MWPCs photodetectors of the RICH by a new system based on thick GEMs with CsI coating. This is in particular important for the HEMP and FF measurements.

5˙2. *Drell-Yan programme.* – The second approach to the transverse nucleon structure in the future Compass programme is via the Drell-Yan process shown in fig. 31. The advantage in DY processes is that fragmentation functions are not involved. However, this has to be paid by a convolution of two distribution functions. A completely symmetric situation is the scattering of a polarised antiproton off a polarised proton. A more accessible option which in addition guarantees high luminosity is pion-proton scattering.

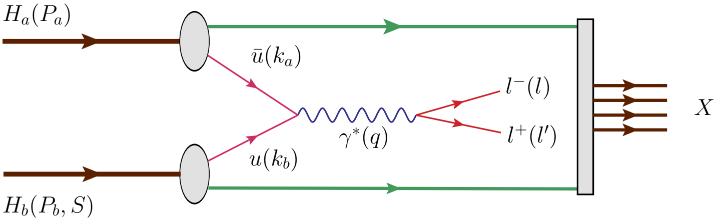

Fig. 31. – Sketch of the Drell-Yan process. A quark and antiquark from target and projectile fuse into a virtual photon decaying into a $\mu^+\mu^-$ pair.

A negative pion contains an anti-up-quark as valence quark, just like an antiproton. The DY process then proceeds via the fusion of an anti-up-quark from the pion and a up quark from the proton and the cross-section is given by $\sigma^{\mathrm{DY}} \propto \sum_f f_{\bar{u}|\pi^-} \otimes f'_{u|p}$, where f and f' are generic place holders of PDFs. The process is strongly dominated by the up-quark distributions.

Using a transversely polarised proton target, one can study TMD distributions like the Sivers and Boer-Mulders distributions. Theory predicts that these naive T-odd TMD distributions obey only a restricted universality. Contrary to normal PDFs they should change sign when observed in SIDIS and DY, respectively.

$$f_{1T}^{\perp}\big|_{\mathrm{DY}} = -f_{1T}^{\perp}\big|_{\mathrm{DIS}} \qquad \text{and} \qquad h_1^{\perp}\big|_{\mathrm{DY}} = -h_1^{\perp}\big|_{\mathrm{DIS}}\,. \tag{13}$$

This sign change is due to going from a final-state interaction in SIDIS to an initial-state interaction in DY (fig. 32) [27]. A violation of this prediction would imply drastic consequences on how cross-sections are calculated in QCD. Therefore it has generated widespread interest in a direct comparison of TMD distributions obtained from SIDIS and DY, respectively. Plans for future polarised DY experiments exist at various laboratories (table III). The COMPASS DY experiment is planned and approved for 2014. It will use a 190 GeV negative pion beam and a transversely polarised proton (NH_3) target. The measurement will primarily assess transversity h_1 and the T-odd Sivers and Boer-Mulders TMD distributions, $f_{1T}^{\perp}$ and $h_1^{\perp}$ for up quarks. For all of these COMPASS SIDIS measurements exist, showing non-vanishing asymmetries for the proton.

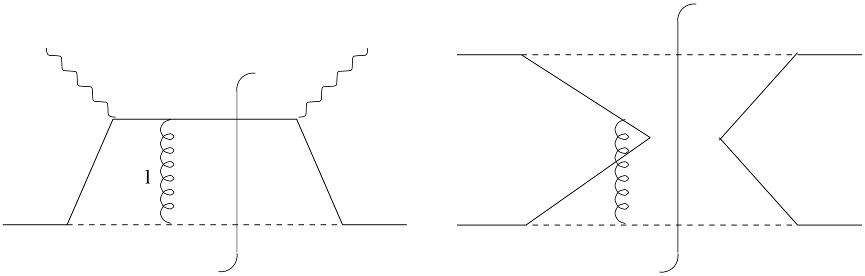

Fig. 32. – Graph for single-spin asymmetries for SIDIS (left) and DY (right) from ref. [27].

Table III. – *Future Drell-Yan experiments.*

Facility	Type		s (GeV^2)	Time-line
Rhic (Star, Phenix)	collider,	$p^{\Uparrow}p^{\Uparrow}$	200^2, 500^2	> 2015
Rhic(internal target)	fixed target,	$p^{\Uparrow}p^{\Uparrow}$	500	> 2016
Rhic(AnDY)	collider,	$p^{\Uparrow}p^{\Uparrow}$	500^2	> 2013
Jparc	fixed target,	$pp^{\Uparrow}$	$60 \div 100$	> 2017
Gsi(Pax)	collider,	$\bar{p}^{\Uparrow}p^{\Uparrow}$	200	> 2020
Gsi (Panda)	fixed target,	$\bar{p}p$	30	> 2017
Nica	collider,	$p^{\Uparrow}p^{\Uparrow}$, $d^{\Uparrow}d^{\Uparrow}$	676	> 2017
Compass	fixed target,	$\pi^-p^{\Uparrow}$	$300 \div 400$	2014

To avoid the J/ψ region and the region of background from charm decays, the experiments will focus on dimuon masses $4\,\text{GeV} < M_{\mu\mu} < 9\,\text{GeV}$. The region below the J/ψ mass, $2\,\text{GeV} < M_{\mu\mu} < 2.5\,\text{GeV}$, will also be studied but analysis will be more involved. Here the signal-to-background ratio will be unfavourable, in the order of unity. A first dimuon mass spectrum taken in a short test run in 2009 is shown fig. 33.

The measurable azimuthal asymmetries depend on the angles ϕ_S and ϕ defined in fig. 34 and on the Feynman variable $x_F = x_\pi - x_p$, where x_π and x_p are the momentum

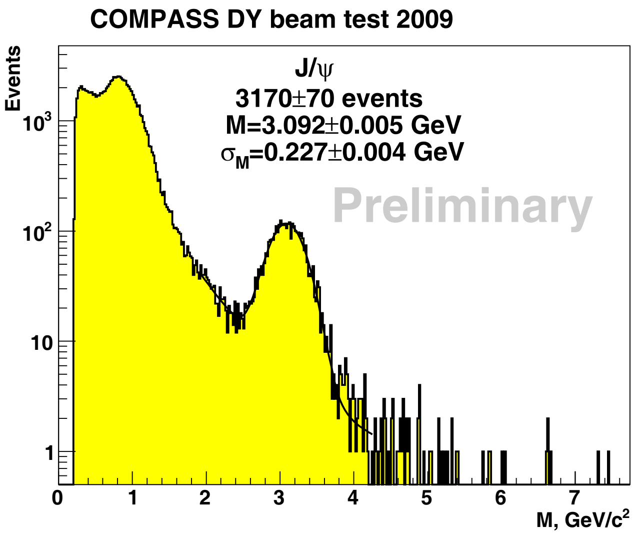

Fig. 33. – Event numbers *vs.* the dimuon mass from a short beam test in 2009. The save region is above 4 GeV, away from the prominent J/ψ peak.

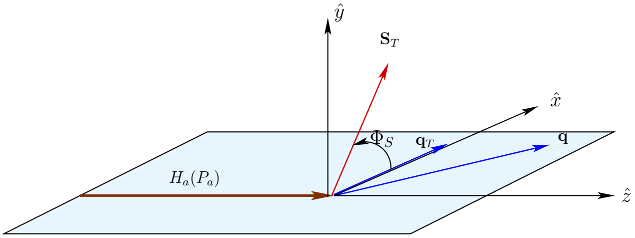

Fig. 34. – Definition of the azimuthal angle ϕ_S of transverse target spin $\boldsymbol{S}_T$ in the target rest frame.

fractions carried by the involved quarks in the pion and proton, respectively. The COMPASS acceptance in the (x_π, x_p)-plane is shown in fig. 35. It is large for $x_F > 0$ and reaches about 50% at $x_F \approx 0.4$. The projected $A_T^{\sin\phi_S}$ asymmetry measurement in the high-mass region $4\,\text{GeV} < M_{\mu\mu} < 9\,\text{GeV}$ is compared to predictions in fig. 36. The planned measurement will certainly be able to answer the sign question of T-odd TMD distributions and allow for a comparison of the absolute size of the effects in SIDIS and DY. However, a determination of the shape of the Sivers TMD distribution in DY will only be possible in the less clean low-mass range (fig. 37 left) or with further measurements. The shaded grey area and the central line in figs. 36 and 37 correspond to a calculation based on a TMD PDF fit to data [28]. For the other curves see ref. [19]. The Boer-Mulders related asymmetry $A_T \cos 2\phi$ will be determined with high precision in both the low- and high-mass regions.

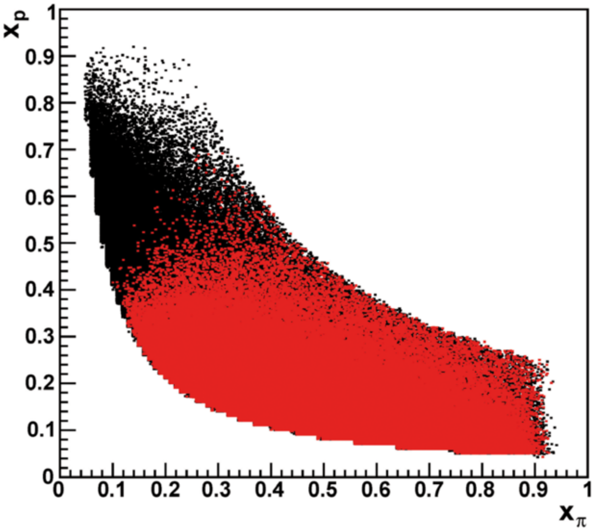

Fig. 35. – Covered kinematic region in x_π *vs.* x_p for a dimuon mass $4\,\text{GeV} < M_{\mu\mu} < 9\,\text{GeV}$.

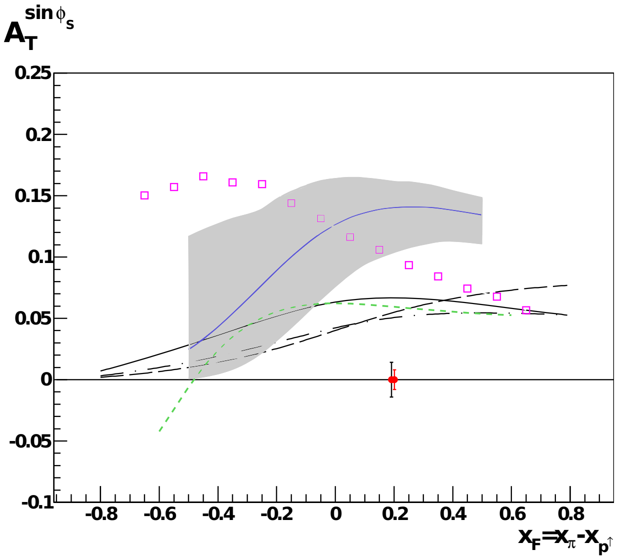

Fig. 36. – Theoretical predictions and expected statistical (left) and systematic (right) error for a measurement of the Sivers asymmetry in the high-mass region.

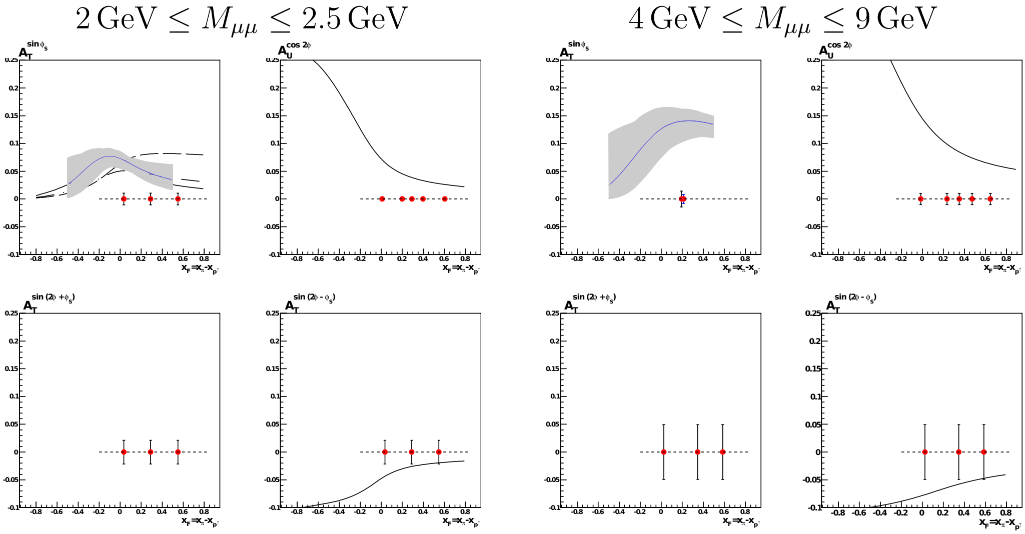

Fig. 37. – Projections for measurements of the $A_T^{\sin\phi_S}$ (Sivers), $A_U^{2\cos\phi_S}$ (Boer-Mulders), $A_T^{\sin(2\phi+\phi_S)}$ and $A_T^{\sin(2\phi-\phi_S)}$ asymmetries for the low-mass region (left) and the high-mass region (right) as a function of the variable $x_F = x_\pi - x_p$.

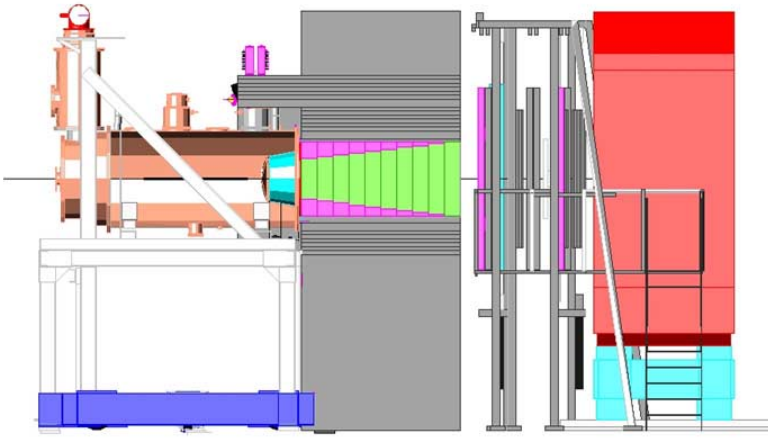

Fig. 38. – (Colour on-line) Layout of the target region for the DY measurement. The polarised target left is followed by massive hadron absorber. To the right the tracking stations and the first spectrometer (red) are shown.

Major modifications will be required to the Compass spectrometer for the DY measurements. As the measurement is statistics limited optimising the luminosity is mandatory. This in turn brings up serious radiation and detector occupancy issues, which can be solved using a massive hadron absorber downstream of the target. The polarised target has to be moved upstream with all attached services by about 3 m to create space for the absorber as shown in fig. 38. The absorber itself will consist of a tungsten core surrounded by alumina (Al_2O_3) and concrete blocks. Alumina was chosen to minimise multiple scattering. This is an essential element to disentangle the oppositely polarised target cells in the track reconstruction. On the downstream side a stainless-steel section will replace the alumina part.

6. – Conclusions

After the measurement of the pion polarisability in 2012 and the accelerator shutdown in 2013, Compass will focus on the 3-dimensional and transverse structure of the nucleon. In a pilot GPD run at the end of 2012 first data will be collected and a result for the t slope of the ϕ-integrated deeply-virtual-Compton-scattering cross-section be obtained.

The year 2014 will be dedicated to the Drell-Yan measurement with a negative pion beam and a transversely polarised proton target. This will bring the first result for the size and the sign of the T-odd TMD distributions in Drell-Yan reactions. In 2015 and 2016 the production runs for the GPD measurement with a pure liquid-hydrogen target will take place, comprising deeply virtual Compton scattering and hard exclusive meson production. Simultaneously, data on the spin-independent TMD distributions and on fragmentation functions will be taken. With this programme Compass will continue to make major contributions to the field of nucleon structure.

* * *

I acknowledge the precious help of many Compass colleagues in preparing this lecture and thank the organisers for the inspiring school.

REFERENCES

[1] Abbon P. *et al.* (COMPASS Collaboration), *Nucl. Instrum. Methods A*, **577** (2007) 455.
[2] Alekseev M. G. *et al.* (COMPASS Collaboration), *Phys. Lett. B*, **693** (2010) 227.
[3] Alekseev M. *et al.* (COMPASS Collaboration), *Phys. Lett. B*, **680** (2009) 1.
[4] Airapetian A. *et al.* (HERMES Collaboration), *Phys. Rev. D*, **75** (2007) 012007.
[5] de Florian D., Sassot R., Stratmann M. and Vogelsang W., *Phys. Rev. Lett.*, **101** (2008) 072001; *Phys. Rev. D*, **80** (2009) 034030.
[6] Airapetian A. *et al.* (HERMES Collaboration), *Phys. Rev. D*, **71** (2005) 012003.
[7] de Florian D. *et al.*, *Phys. Rev. D*, **75** (2007) 114010.
[8] Alexakhin V. Yu. *et al.* (COMPASS Collaboration), *Phys. Lett. B*, **647** (2007) 8.
[9] Alekseev M. G. *et al.* (COMPASS Collaboration), *Phys. Lett. B*, **690** (2010) 466.
[10] Ross G. G., Univ. of Oxford preprint OUTP-89-39P, Aug. 1989.
[11] Adolph Ch. *et al.* (COMPASS Collaboration), [hep-ex/1202.4064], submitted to *Phys. Lett. B*.
[12] Ageev E. S. *et al.* (COMPASS Collaboration), *Phys. Lett. B*, **633** (2006) 25.
[13] Alekseev M. *et al.* (COMPASS Collaboration), *Phys. Lett. B*, **676** (2009) 31.
[14] Adolph C. *et al.* (COMPASS Collaboration), *Phys. Lett. B.*, **713** (2012) 10.
[15] Alekseev M. *et al.* (COMPASS Collaboration), *Phys. Lett. B*, **692** (2010) 240.
[16] Airapetian A. *et al.* (HERMES Collaboration), *Phys. Rev. Lett.*, **103** (2009) 152002.
[17] Ageev E. S. *et al.* (COMPASS Collaboration), *Nucl. Phys. B*, **765** (2007) 31.
[18] Alekseev M. *et al.* (COMPASS Collaboration), *Phys. Lett. B*, **673** (2009) 127.
[19] Gautheron F. *et al.* (COMPASS Collaboration), CERN-SPSC-2010-014, SPSC-P-340, 17 May 2010.
[20] Ji X.-D., *Phys. Rev. Lett.*, **78** (1997) 610.
[21] Belitsky A. V. *et al.*, *Nucl. Phys. B*, **629** (2002) 323.
[22] Aaron F. D. *et al.* (H1 Collaboration), *Phys. Lett. B*, **659** (2008) 796.
[23] Chekanov S. *et al.* (Zeus Collaboration), *JHEP*, **05** (2009) 108.
[24] Arrington J. *et al.*, Conceptual Design Report (CDR) for The Science and Experimental Equipment for The 12 GeV Upgrade of CEBAF (Prepared for the DOE Science Review, April 6–8, 2005), Jeffson Lab (2005). `http://www.jlab.org/div_dept/physics_division/GeV/doe_review/CDR_for_Science_Review.pdf`.
[25] Vanderhaeghen M. *et al.*, *Phys. Rev. D*, **60** (1999) 094017.
[26] Kumerički K. and Müller D., *Nucl. Phys. B*, **841** (2010) 1.
[27] Collins J. C., *Phys. Lett. B*, **536** (2002) 43.
[28] Anselmino M. *et al.*, in *Proceedings of Transversity 2008: II International Workshop on Transverse Polarization Phenomena in Hard Scattering Processes, 27–31 May 2008, Ferrara, Italy*, edited by Ciullo G. *et al.* (World Scientific) 2009, ISBN:978-981-4277-77-8, p. 138.

Proceedings of the International School of Physics "Enrico Fermi"
Course CLXXX "Three-Dimensional Partonic Structure of the Nucleon"
edited by M. Anselmino, H. Avakian, D. Hasch and P. Schweitzer
(IOS, Amsterdam; SIF, Bologna)
DOI 10.3254/978-1-61499-197-7-303

The JLab 12 GeV upgrade and the initial science program

Selected topics

V. D. Burkert

Jefferson Lab - Newport News, VA 23606, USA

Summary. — An overview is presented of the upgrade of JLab's cw electron accelerator from the current maximum beam energy of 6 GeV to the upgraded maximum energy of 12 GeV. Construction of the 12 GeV upgrade project has started in 2008. A broad experimental program has been developed to map the nucleon's intrinsic correlated spin and momentum distribution through measurements of deeply exclusive and semi-inclusive processes, and to probe the quark and gluon confinement by studying the spectrum of mesons with exotic quantum numbers. Other programs include the forward parton distribution function at large x_B, the quark and gluon polarized distribution functions, measurements of electromagnetic form factors of the nucleon ground state and of nucleon resonance transitions at high Q^2, and the exploration of physics beyond the Standard Model in high-precision parity-violating processes. The higher beam energy is also well suited to explore quark hadronization properties using the nucleus as a laboratory.

1. – Introduction

The challenge of understanding nucleon electromagnetic structure still continues after more than five decades of experimental scrutiny. From the initial measurements of elastic

© Società Italiana di Fisica

form factors to the accurate determination of parton distributions through deep inelastic scattering (DIS), the experiments have increased in statistical and systematic accuracy. It was realized in recent years that the parton distribution functions represent special cases of a more general, and much more powerful way of characterizing the structure of the nucleon, the generalized parton distributions (GPDs) [1-5]. The GPDs describe the simultaneous distribution of particles with respect to both position and momentum. In addition to the information about the spatial density (form factors) and momentum density (parton distribution), these functions reveal the correlation of the spatial and momentum distributions, *i.e.* how the spatial shape of the nucleon changes when probing quarks of different wavelengths.

The concept of GPDs has led to completely new methods of "spatial imaging" of the nucleon, either in the form of two-dimensional tomographic images, or in the form of genuine three-dimensional images in two-dimensional transverse space and longitudinal momentum space. GPDs also allow us to quantify how the orbital motion of quarks in the nucleon contributes to the nucleon spin—a question of crucial importance for our understanding of the dynamics underlying nucleon structure. The spatial view of the nucleon enabled by the GPDs provides us with new ways to test dynamical models of nucleon structure. The mapping of the nucleon GPDs, and a detailed understanding of the spatial quark and gluon structure of the nucleon, have been widely recognized as the key objectives of nuclear physics of the next decade. This requires a comprehensive program, combining results of measurements of a variety of processes in electron–nucleon scattering with structural information obtained from theoretical studies, as well as with expected results from future lattice QCD simulations.

While GPDs, and also the more recently introduced transverse-momentum–dependent distribution functions (TMDs), open up new avenues of research, the traditional means of studying the nucleon structure through electromagnetic elastic and transition form factors, and through flavor- and spin-dependent parton distributions must also be employed with high precision to extract physics on the nucleon structure in the transition from the regime of quark confinement to the domain of asymptotic freedom. These avenues of research can be explored using the 12 GeV cw beam of the JLab upgrade with much higher precision than has been possible before, and can help reveal some of the remaining secrets of QCD. Also, the high luminosity available will allow us to explore the regime of extreme quark momentum, where a single quark carries 80% or more of the proton's total momentum.

The strong force is mediated by the exchange of gluons between quarks as well as between gluons. The presence of gluons has been observed in high energy e^+e^- collisions where they generate a third jet of particles in addition to the two jets coming from the fragmentation of the produced $q\bar{q}$ pair. A clear understanding of the role of gluons in interactions at the lower energies is still missing. Models that describe the interaction through gluon flux tubes predict that the glue plays an active role and can be excited and lead to novel states of mesons and baryons (hybrid states). The search for some of these hybrid states is the focus of the photo-production experiments in the new Hall D, and are also studied with CLAS12.

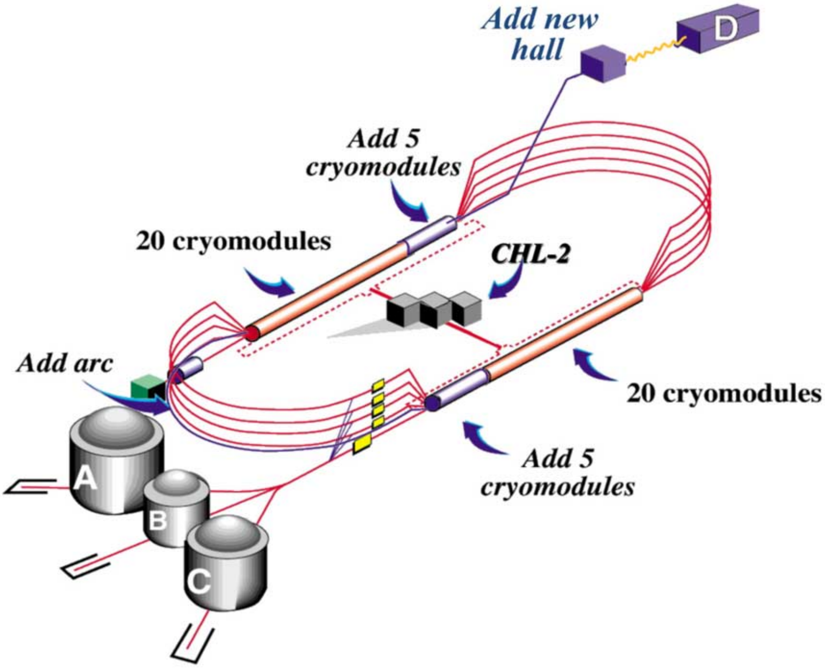

Fig. 1. – The Jefferson Lab continuous electron beam accelerator facility showing the components needed for the 12 GeV upgrade.

The plan for this report is to give a brief overview in sect. **2** of the upgrade of the JLab accelerator to 12 GeV and discuss the experimental equipment that is currently under construction to carry out the science program during the first 5 years of operation. In sect. **3** and sect. **4** I discuss the program to study the generalized parton distribution function (GPDs) and the transverse momentum-dependent functions (TMDs) using polarization degrees of freedom, which covers a major portion of this contribution. They are the main ingredients to develop the multi-dimensional representation of quarks in the nucleon in coordinate and momentum space. In sects. **5** through **9**, I discuss some of the other programs: structure functions and form factors at high Q^2, gluonic excitations, quark and hadrons in the nuclear medium, and physics beyond the Standard Model. This is an overview and covers a broad future physics program, I will not be able to go into depth of any of the topics discussed. The phenomenological underpinnings of much of the material, especially the part related to GPDs and TMDs, has been presented in lectures and seminars in the earlier part of the school by experts, and I refer the reader to these contributions for details.

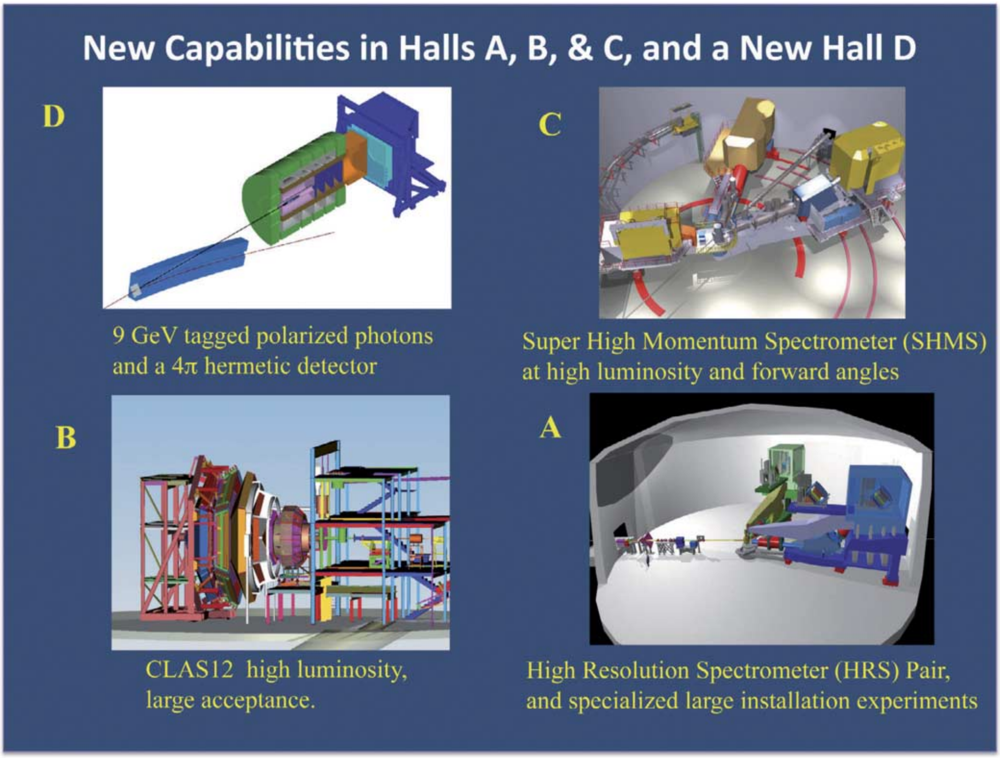

New Capabilities in Halls A, B, & C, and a New Hall D

D

9 GeV tagged polarized photons
and a 4π hermetic detector

C

Super High Momentum Spectrometer (SHMS)
at high luminosity and forward angles

B

CLAS12 high luminosity,
large acceptance.

A

High Resolution Spectrometer (HRS) Pair,
and specialized large installation experiments

Fig. 2. – Baseline experimental equipment to support the scientific program for the JLab 12 GeV energy upgrade. Description in the text.

2. – The electron accelerator and the 12 GeV experimental equipment

The Jefferson Lab electron accelerator is shown schematically in fig. 1. The two linear accelerators are based on superconducting radio frequency technology. Spin-polarized electrons are generated in the gun and pre-accelerated to 50 MeV in the injector shown at the upper left end of the racetrack. Electrons are injected into the north linac and boosted to about 600 MeV. They are then bent in the arcs by 180 degrees and injected into the south linac to be accelerated up to 1200 MeV. This is repeated four more times when the final maximum energy of 6000 MeV is reached. For the energy upgrade five accelerating cryo-modules with four times higher gradients per unit length are added to both linacs to reach a maximum energy at the existing end stations of nearly 11 GeV. One arc and one more path through the north linac are added to accelerate the beam to 12 GeV and transport it to the new Hall D. Major equipment upgrades are planned to support a broad program in nuclear physics. The experimental base equipment is part of the 12 GeV upgrade scope, and is shown in fig. 2. In Hall D, a large hermetic detector is under construction with a solenoid magnet at its core. It has tracking capabilities and photon detection over nearly the full 4π solid angle. The bottom left panel shows the new CLAS12 spectrometer, with large solid angle coverage and increased luminosity for electron scattering experiments. The top panel on the right shows the pair of focusing magnetic spectrometers in Hall C including the new super-high momentum spectrometer SHMS on the left. In Hall A, the existing high-resolution spectrometer pair HRS^2 will be retained. The Hall will also house large installation equipment for specialized experiments. The solenoid detector in Hall D, CLAS12, and the SHMS in Hall C are part of the base equipment, and are projected to be available for physics by the end of 2014. There are additional pieces of equipment proposed that are outside the scope of the 12 GeV project and require separate funding. In Hall A several proposals are under consideration, a super bite spectrometer (SBS) with large solid angle, a spectrometer toroidal magnet spectrometer for a parity violation experiment in electron-electron scattering, and a solenoid detector for parity violation experiments in DIS and for SIDIS experiments (SOLID). There are also plans to incorporate a large acceptance RICH detector into CLAS12 for improved charged particle identification capabilities, and various ancillary detectors for neutron detection and quasi-real photon tagging. Complementing the new equipment that is under construction, are the highly polarized electron gun, high power cryogenic targets, and several polarized targets using NH_3, ND_3, HD, butanol, and ^3He to support a broad range of polarization measurements.

3. – Generalized parton distributions and deeply virtual Compton scattering

It is now well recognized [2, 6-8] that deeply virtual Compton scattering and deeply virtual meson production are most suitable for accessing the twist-2 vector GPDs H, E and the axial GPDs $\tilde{H}$, $\tilde{E}$ in x, ξ, t, where x is the momentum fraction of the struck quark, ξ the longitudinal momentum transfer to the quark, and t the transverse momentum transfer to the nucleon. Having access to a 3-dimensional image of the nucleon (two dimensions in transverse space, one dimension in longitudinal momentum) opens up completely new insights into the complex internal structure and dynamics of the nucleon. In addition, GPDs carry information of more global nature. For example, the nucleon matrix element of the energy-momentum tensor contains 3 form factors that encode information on the angular momentum distribution $J^q(t)$ of the quarks with flavor q in transverse space, their mass-energy distribution $M_2^q(t)$, and their pressure and force distribution $d_1^q(t)$. How can we access these form factors? The only known process to directly measure them is elastic graviton scattering off the nucleon, which is all but impossible in practice. However, these form factors also appear as moments of the two vector GPDs [9], thus offering prospects of accessing gravitational form factors through the detailed mapping of GPDs. The quark angular momentum form factor in the nucleon is given by

$$J^q(t) = \int_{-1}^{+1} \mathrm{d}x x [H^q(x,\xi,t) + E^q(x,\xi,t)],$$

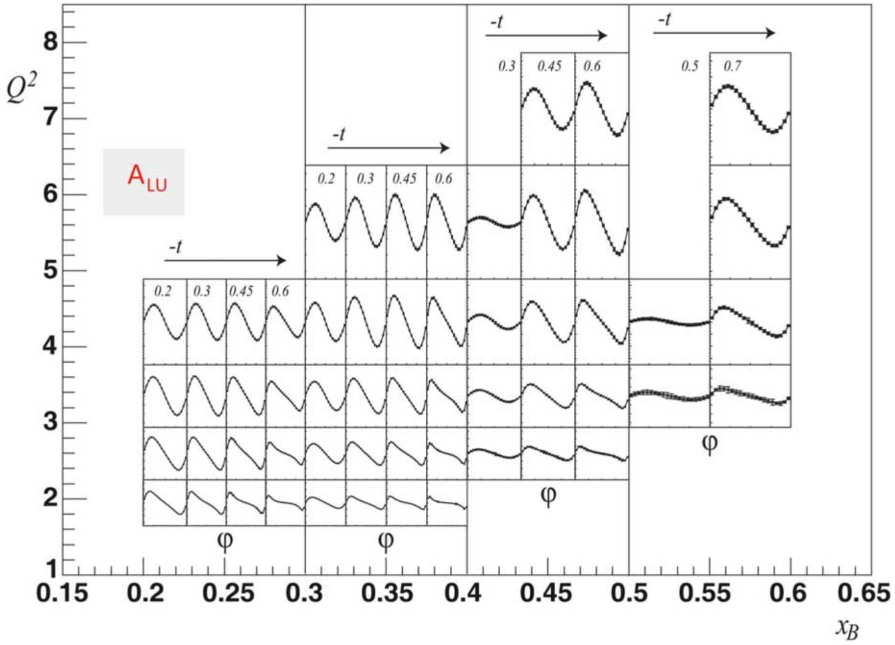

Fig. 3. – Projected data for the azimuthal dependence of the beam spin asymmetry A_{LU}.

and the mass-energy and force-pressure distribution

$$M_2^q(t) + 4/5 d_1^q(t)\xi^2 = \int_{-1}^{+1} \mathrm{d}x x H^q(x, \xi, t).$$

The mass-energy and force-pressure distribution of the quarks are given by the second moment of GPD H, and their relative contribution is controlled by ξ. A separation of $M_2^q(t)$ and $d_1^q(t)$ requires measurement of these moments in a large range of ξ. The beam helicity-dependent cross-section asymmetry is given in leading twist as

$$A_{LU} \approx \sin\phi[F_1(t)H + \xi(F_1 + F_2)\tilde{H}]\mathrm{d}\phi,$$

where ϕ is the azimuthal angle between the electron scattering plane and the hadronic production plane. The kinematically suppressed term with GPD E is omitted. The asymmetry is mostly sensitive to the GPD $H(x = \xi, \xi, t)$. In a wide kinematics [10,11] the beam asymmetry A_{LU} was measured at Jefferson Lab at modestly high Q^2, ξ, and t, and in a more limited kinematics [12] the cross section difference $\Delta\sigma_{LU}$ was measured with high statistics. Moreover, a first measurement of the target asymmetry $A_{UL} = \Delta\sigma_{UL}/2\sigma$ was carried out [13], where

$$A_{UL} \approx \sin\phi[F_1\tilde{H} + \xi(F_1 + F_2)H].$$

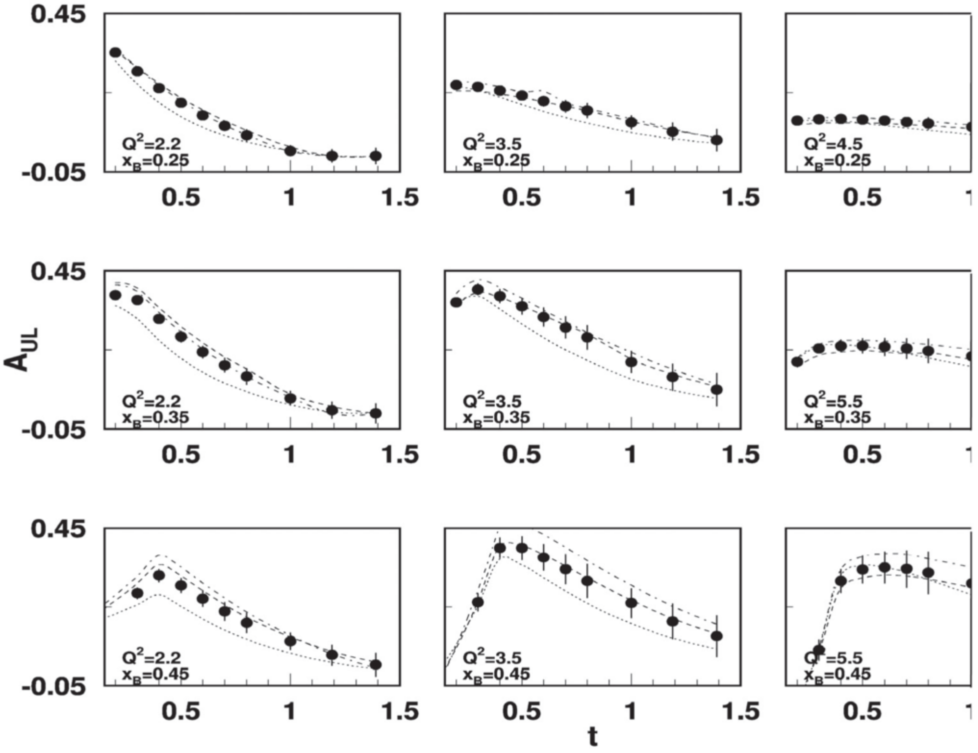

Fig. 4. – Projected data for the t-dependence of the longitudinal target spin asymmetry A_{UL}.

The combination of A_{LU} and A_{UL} allows the separation of GPD $H(x = \xi, \xi, t)$ and $\tilde{H}(x = \xi, \xi, t)$. Using a transversely polarized target the asymmetry

$$A_{UT} \approx \cos\phi \sin(\phi - \phi_s)[t/4M^2(F_2 H - F_1 E)]$$

can be measured, where ϕ_s is the azimuthal angle of the target polarization vector relative to the electron scattering plane. A_{UT} depends in leading order on GPD E. Measurement of A_{UT} can thus be the most efficient way of determining GPD E.

First DVCS experiments carried out at JLab [10-13] and DESY [14] showed promising results in terms of the applicability of the handbag mechanism to probe GPDs. The 12 GeV upgrade offers much improved possibilities for accessing GPDs. Figure 3 shows the expected statistical precision of the electron beam asymmetry A_{LU} for $\vec{e}p \to ep\gamma$ for some sample kinematics. Using a longitudinally polarized target one can also measure the target spin asymmetry in $e\vec{p} \to ep\gamma$ with high precision. Figure 4 shows the expected statistical accuracy for the moment $A_{UL}^{\sin\phi}$. Using a transversely polarized target, the transverse target spin asymmetry A_{UT} can be measured. The t-dependence of A_{UT} is shown in fig. 5 for a single bin in Q^2 and x.

Measurements of all 3 asymmetries and the unpolarized cross section will enable the

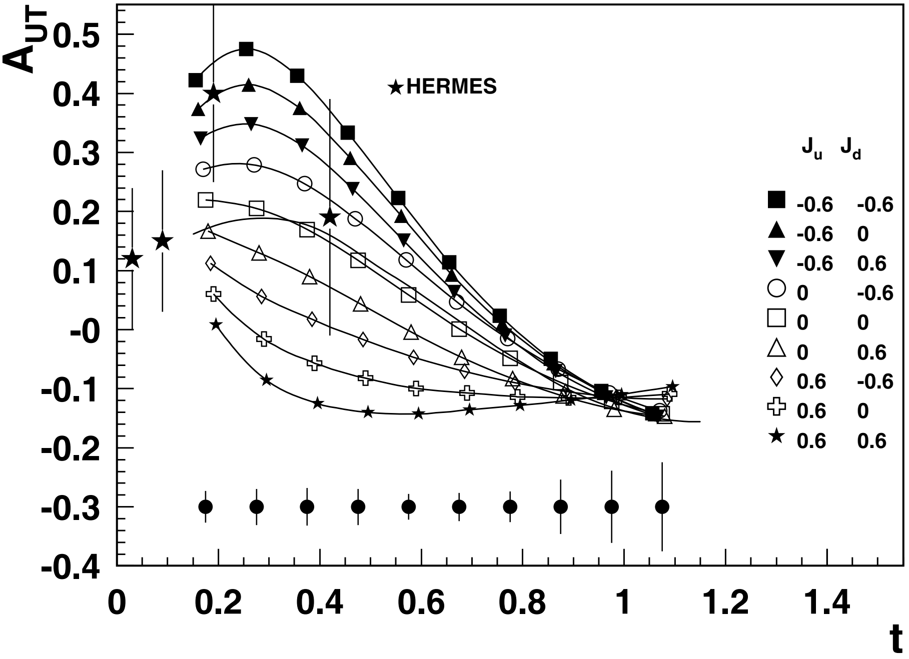

Fig. 5. – Projected data for the t-dependence of the transverse target spin asymmetry $A_{UT}^{\sin\phi\cos\phi-\phi_s}$. The t-dependence of A_{UT} is shown for a single bin at $Q^2 = 2\,\mathrm{GeV}^2$ and $x = 0.25$.

separation of GPDs H, $\tilde{H}$ and E at some specified kinematics. To obtain a complete picture of the quark distribution in the nucleon, the GPDs need to be measured for both flavors u-quarks and d-quarks. This requires measurement of DVCS not only on the proton but also on the neutron. Figure 6 shows projections of the DVCS experiment to measure the beam-spin asymmetry for the neutron $en(p_s) \to e\gamma n(p_s)$ If the t-dependences are known, a Fourier transformation of, *e.g.*, GPD $H^u(x = \xi, t)$ gives information about the u-quark distribution in impact parameter space. Similarly for GPD $\tilde{H}^q$ and GPD E^q. Figure 7 shows examples of simulated images of the polarized u and d quark distributions in transverse space using a model parameterization of GPDs [7]. Detailed spatial information is obtained, quite equivalent to X-ray imaging in CAT scan of the human body.

At sufficiently high energies, deeply virtual meson production (pseudo-scalar mesons or vector mesons) will play an important role in disentangling the flavor- and spin-dependence of GPDs (see table I). In exclusive mesons only the longitudinal photon coupling in $\gamma^* p \to Nm$ enables direct access to GPDs through the handbag mechanism and must be isolated from the transverse coupling. There is evidence that transverse contribution cannot be neglected at currently available energies of 6 GeV [15], and the

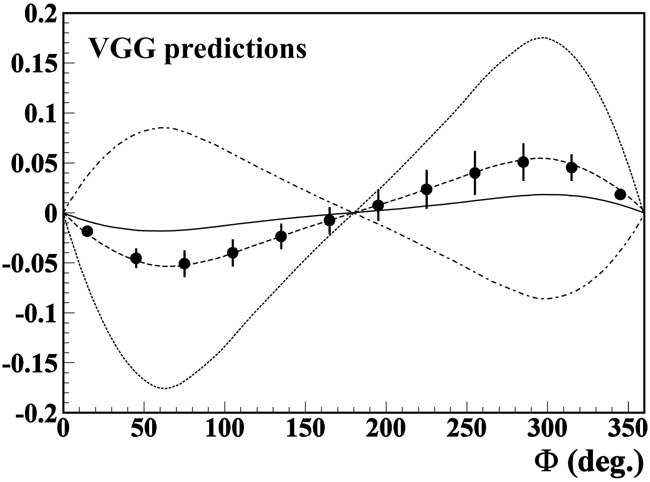

Fig. 6. – Projections of the DVCS experiment for beam-spin asymmetry A_{LU} on the neutron for one bin in Q^2, x_B, t. The different lines indicate asymmetries for different values of the nucleon spin carried by u and d quarks as predicted by the VGG model [16]. The magnitude of A_{LU} on the neutron is predicted much smaller than what has been measured on the proton.

dominance of the handbag mechanism in the longitudinal cross section must first be established at the upgrade energy before meson production can be incorporated in global fits that include exclusive meson production data aiming at the extraction of GPDs from these data.

4. – Semi-inclusive deeply inelastic scattering and TMDs

Semi-inclusive deeply inelastic scattering (SIDIS) processes, where the leading, high momentum hadron is detected in coincidence with the scattered lepton, are used for "flavor tagging" of quarks to select contributions from different quark species. Currently, the emphasis is to study SIDIS processes that encode information on the transverse momentum distributions of quarks, information that is not otherwise accessible. For example, azimuthal distributions of final state particles in SIDIS provide access to the orbital motion of quarks and play an important role in the study of transverse-momentum–dependent distributions (TMDs) of quarks in the nucleon.

TMD distributions describe transitions of a nucleon with one polarization in the initial state to a quark with another polarization in the final state. The diagonal elements in table II are the momentum, longitudinal and transverse spin distributions of partons, and represent well-known parton distribution functions related to the square of the leading-twist, light-cone wave functions. Off-diagonal elements require non-zero orbital angular momentum and are related to the wave function overlap of $L = 0$ and $L = 1$ Fock states of the nucleon. The chiral-even distributions $f_{1T}^{\perp}$ and g_{1T} are the imaginary parts of the corresponding interference terms, and the chiral-odd $h_1^{\perp}$ and h_{1L} are

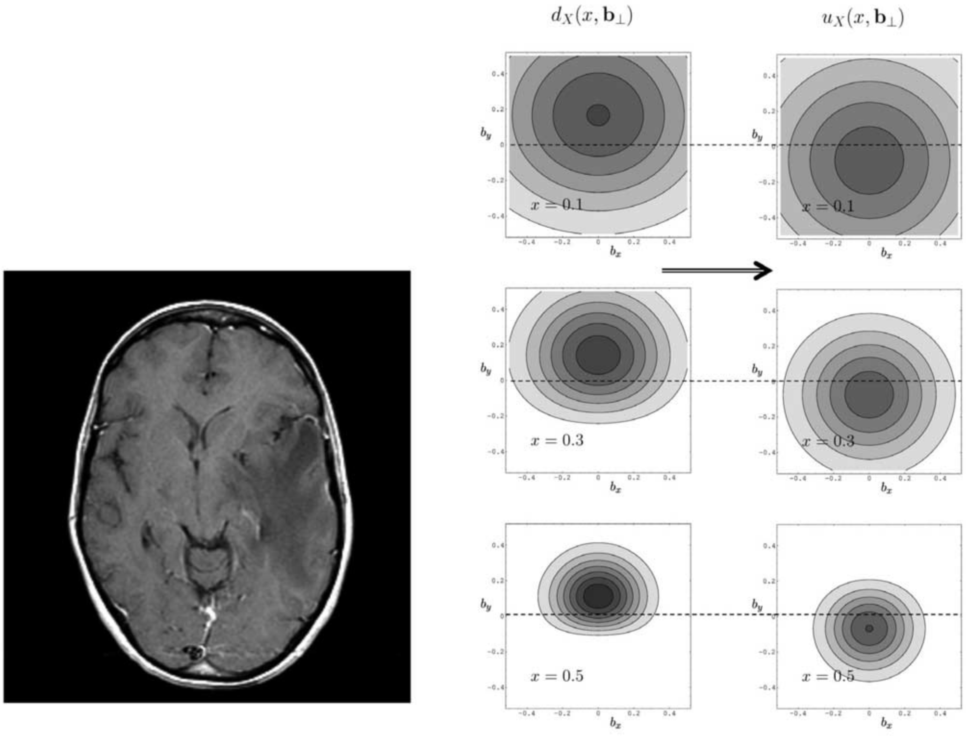

Fig. 7. – Left panel: slice of a 3-D tomographic image of a human brain from a CAT scan. Right panel: simulated quark distributions in a transversely polarized proton [7]. The arrow indicates the direction of the proton polarization. The centroids of the d-quarks (left column) appear shifted upwards and the distributions appear deformed from the symmetric distribution in unpolarized protons; the centroids of the u-quark distributions are shifted in the opposite direction, generating a u-d quark flavor dipole.

the real parts. The TMDs $f_{1T}^{\perp}$ and $h_1^{\perp}$ are related to the imaginary part of the interference of wave functions for different orbital momentum states and are known as the Sivers [17] and Boer-Mulders [18, 19] functions. They describe unpolarized quarks in the transversely polarized nucleon and transversely polarized quarks in the unpolarized nucleon, respectively. The most simple mechanism that can lead to a Boer-Mulders function is a correlation between the spin of the quarks and their orbital angular momentum. In combination with a final state interaction that is on average attractive, already a measurement of the sign of the Boer-Mulders function, would thus reveal the correlation between orbital angular momentum and spin of the quarks.

Similar to the extraction of GPDs, TMD studies will greatly benefit from the higher energy and luminosity available at 12 GeV. A comprehensive program is in preparation at JLab to study these new quark distribution functions. The aim is to measure all relevant

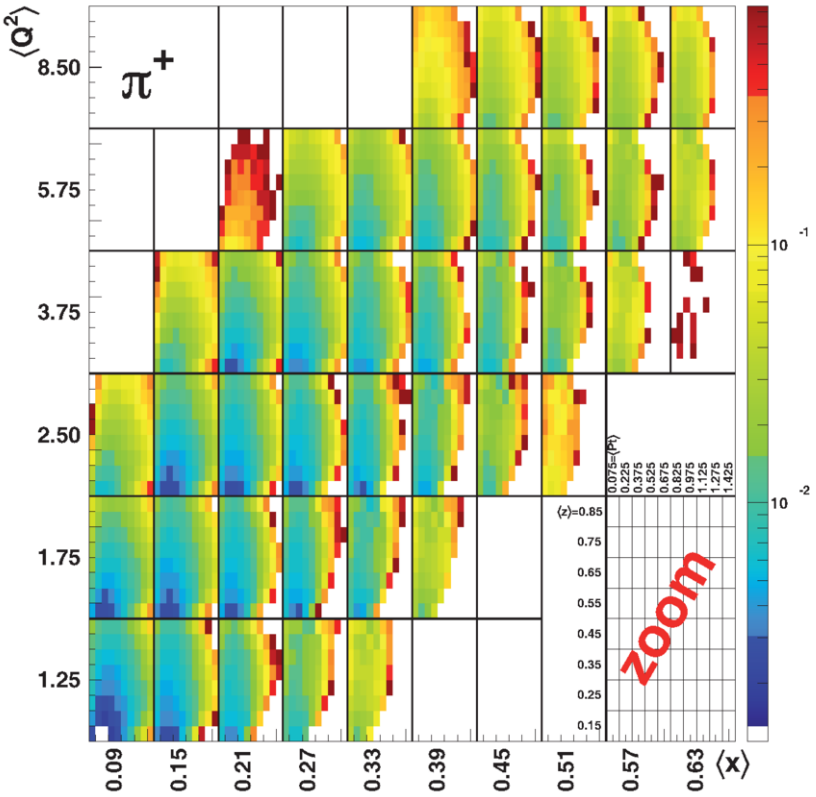

Fig. 8. – (Colour on-line) Kinematic coverage and projected uncertainties of the 4-dimensional π^+ yield in Q^2, x, z, and p_T. The color code shows the relative errors in each bin.

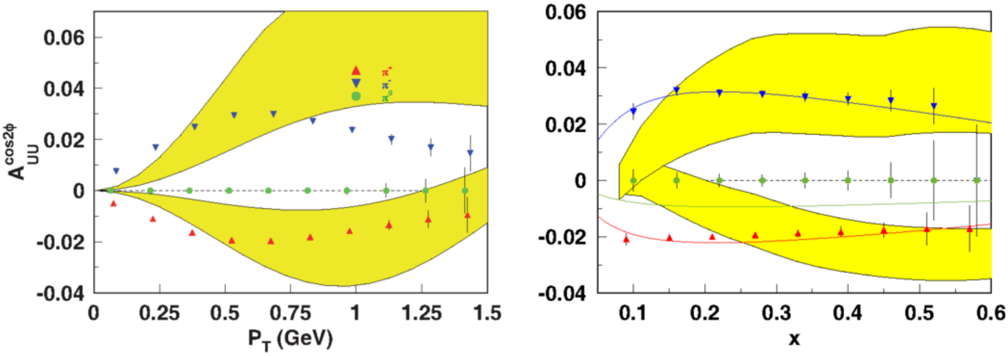

Fig. 9. – (Colour on-line) The $\cos 2\phi$ moment (Boer-Mulders asymmetry) for pions as a function of Q^2 and P_T for $Q^2 > 2\,\mathrm{GeV}^2$ with CLAS12 at 11 GeV from 2000 hours of running. Values are calculated assuming $H_1^{\perp u\to\pi^+} = -H_1^{\perp u\to\pi^-}$. Only statistical uncertainties are shown. The yellow band between the two curves indicates the range of two model predictions.

Table I. – *Sensitivity of deeply virtual Compton scattering and deeply virtual meson production processes to the leading twist GPDs for different quark flavors.*

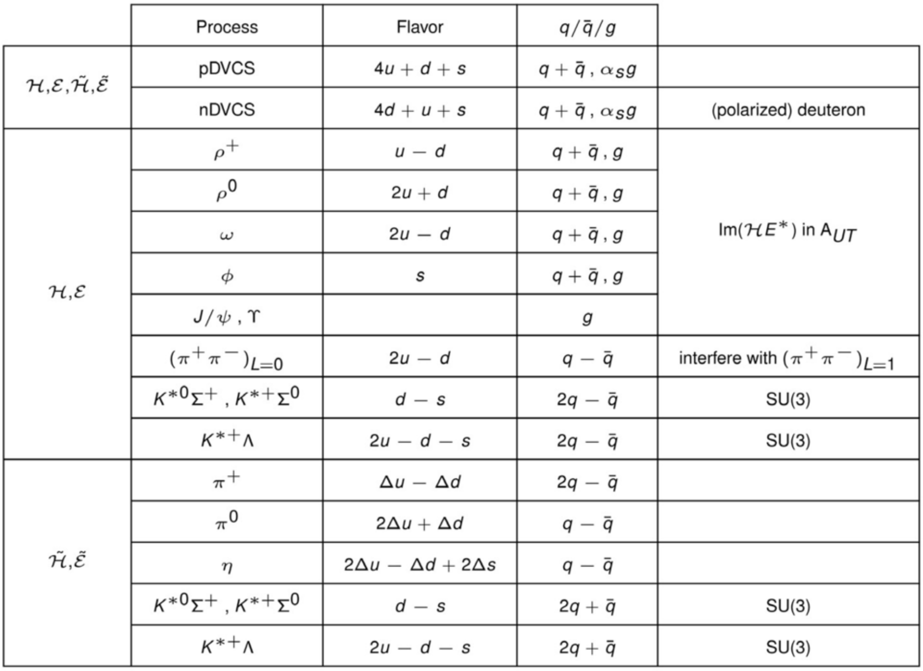

	Process	Flavor	$q/\bar{q}/g$	
$\mathcal{H}$,$\mathcal{E}$,$\tilde{\mathcal{H}}$,$\tilde{\mathcal{E}}$	pDVCS	$4u+d+s$	$q+\bar{q}$, $\alpha_s g$	
	nDVCS	$4d+u+s$	$q+\bar{q}$, $\alpha_s g$	(polarized) deuteron
$\mathcal{H}$,$\mathcal{E}$	ρ^+	$u-d$	$q+\bar{q}$, g	Im($\mathcal{H}E^*$) in A_{UT}
	ρ^0	$2u+d$	$q+\bar{q}$, g	
	ω	$2u-d$	$q+\bar{q}$, g	
	ϕ	s	$q+\bar{q}$, g	
	J/ψ , Υ		g	
	$(\pi^+\pi^-)_{L=0}$	$2u-d$	$q-\bar{q}$	interfere with $(\pi^+\pi^-)_{L=1}$
	$K^{*0}\Sigma^+$, $K^{*+}\Sigma^0$	$d-s$	$2q-\bar{q}$	SU(3)
	$K^{*+}\Lambda$	$2u-d-s$	$2q-\bar{q}$	SU(3)
$\tilde{\mathcal{H}}$,$\tilde{\mathcal{E}}$	π^+	$\Delta u-\Delta d$	$2q-\bar{q}$	
	π^0	$2\Delta u+\Delta d$	$q-\bar{q}$	
	η	$2\Delta u-\Delta d+2\Delta s$	$q-\bar{q}$	
	$K^{*0}\Sigma^+$, $K^{*+}\Sigma^0$	$d-s$	$2q+\bar{q}$	SU(3)
	$K^{*+}\Lambda$	$2u-d-s$	$2q+\bar{q}$	SU(3)

SIDIS processes in the full 4-D phase space available in Q^2, x, z and p_T. Figure 8 shows the phase space coverage and statistical precision expected for semi-inclusive π^+ production. Some examples of kinematics coverage and statistical precision in the Boer-Mulders asymmetry for pions are presented in fig. 9.

Several experiments will measure the Mulders-Kotzinian asymmetry on longitudinally polarized proton target and on ^{3}He target. Figure 10 shows an example of the expected

Table II. – *Leading-twist transverse momentum-dependent distribution functions. U, L, and T stand for transitions of unpolarized, longitudinally polarized, and transversely polarized nucleons (rows) to corresponding quarks (columns).*

N/q	U	L	T
U	$\mathbf{f_1}$		$h_1^{\perp}$
L		$\mathbf{g_1}$	$h_{1L}^{\perp}$
T	$f_{1T}^{\perp}$	g_{1T}	$\mathbf{h_1}\, h_{1T}^{\perp}$

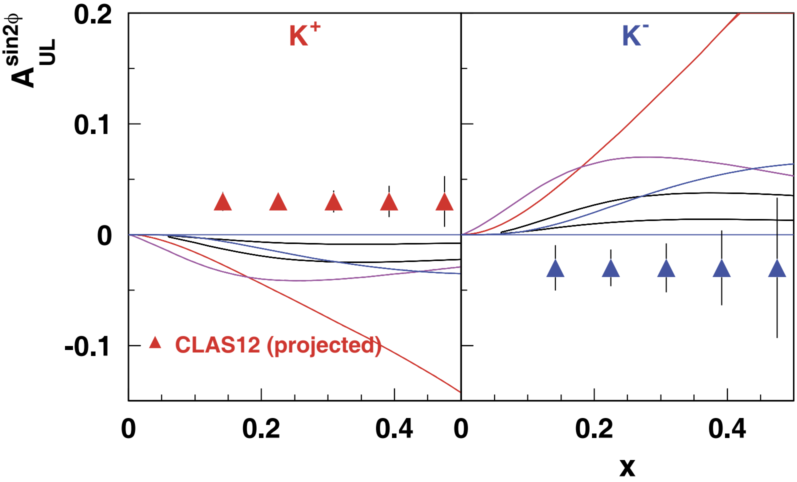

Fig. 10. – Projected x-dependence of the polarized spin target asymmetry at 11 GeV with CLAS12 for kaons for one bin in Q^2, z, p_T.

asymmetry and statistical precision for charged kaon production. Several experiments have been proposed to study the Sivers asymmetries on polarized ^{3}He and on polarized hydrogen. Examples of kinematic dependences are shown in fig. 11. Although pions have been the main focus of SIDIS experiment in the past, the K$^+$ and K$^-$ channels have recently emerged as of high interest as well. Results from the HERMES experiment show unexpectedly large Boer-Mulders asymmetries for kaons compared to pions, and the opposite signs for K$^-$ and π^-. Several experiments will measure semi-inclusive processes for kaon productions. With the excellent particle identification and high luminosity expected for CLAS12, these puzzling issues can be addressed efficiently. Figure 10 shows the statistical precision for K$^+$ and K$^-$ production on longitudinally polarized hydrogen in one kinematic bin in Q^2, z, and p_T.

The experimental effort will produce high-quality asymmetry data in a large range of the 4-dimensional space in Q^2, x, z, p_T. The challenge will be to extract from these large amounts of data the TMDs that encode the quark's intrinsic spin-momentum correlations.

5. – Inclusive structure functions and moments

Polarized and unpolarized structure functions of the nucleon provide a window into the internal quark longitudinal momentum and helicity densities of nucleons. The study of these structure functions provides insight into the two defining features of QCD—asymptotic freedom at small distances, and confinement and non-perturbative effects at large distance scales. After more than three decades of measurements at many accelerator facilities worldwide, a truly impressive amount of data has been collected, covering several orders of magnitude in both kinematic variables x and Q^2. However, there are still

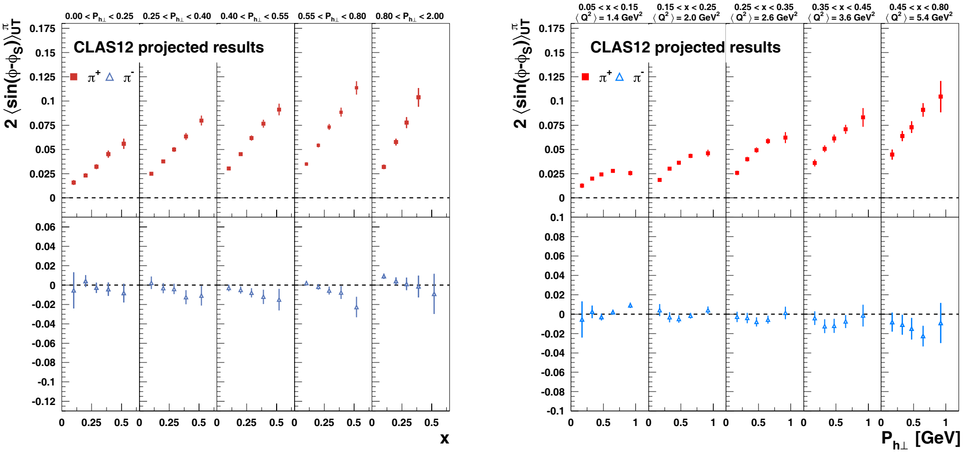

Fig. 11. – Projected data for the Sivers function *vs.* x for different transverse momentum bins (left panel) and *vs.* p_T for different x bins.

important regions of the accessible phase space where data are not available or have large uncertainties, and where significant improvements are possible through high-luminosity experiments at 12 GeV.

One of the open questions is the behavior of the structure functions in the extreme kinematic limit $x \to 1$.

In this region effects from the virtual sea of quark-antiquark pairs are suppressed, making this region simpler to model than the small-x region. This is also the region where pQCD can make absolute predictions. However, the large-x domain is difficult to reach as cross-sections are kinematically suppressed, the parton distributions are small and final states interactions (partonic or hadronic) are large. First steps into the large-x domain became possible at energies of 5–6 GeV [24, 26]. The interest triggered by these first results and the clear necessity to extend the program to larger x (for recent reviews see [27,28]) provided one of the cornerstones of the JLab 12 GeV upgrade physics program.

5·1. *Valence quark structure and flavor dependence at large x.* – The unpolarized proton structure function $F_2^p(x)$ has been mapped out in a large range of x leading to precise knowledge of the quark distribution $u(x)$. The corresponding structure function $F_2^n(x)$ is well measured only for $x < 0.5$ as nuclear corrections, using deuterium as a target, are large and very uncertain at $x > 0.5$. Corrections for Fermi motion are clearly insufficient. A new technique, tested recently at JLab [29], proved very effective in reducing the nuclear corrections. The experiment uses a novel radial time-projection-chamber (rTPC) with gas-electron-multiplier (GEM) readout as detector for the low-energy spectator proton in the reaction $en(p_s) \to ep_sX$. Measurement of the spectator

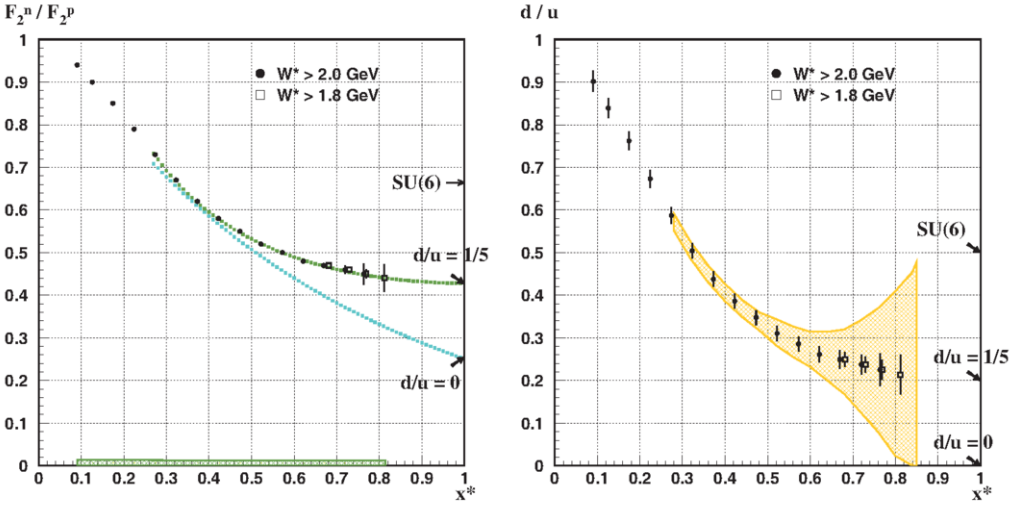

Fig. 12. – (Colour on-line) Projected data for the ratio F_2^n/F_2^p (left) and d/u (right) for 11 GeV beam energy. The error bars in the right panel contain both statistical and systematic uncertainties. The yellow area shows the uncertainty of current data due to poorly known nuclear corrections.

proton for momenta as low as 70 MeV/c and at large angles minimizes the poorly known nuclear corrections at large x. The techniques will be used with CLAS12 to accurately determine the ratio $d(x)/u(x)$ to much larger x values. Figure 12 shows the projected data for $F_2^n(x)/F_2^p(x)$ and $d(x)/u(x)$. A dramatic improvement is projected at large x. Another experiment in Hall A measures inclusive scattering on two mirror nuclei ^{3}He and ^{3}H for which the nuclear wave functions are very similar. The cross-section ratio $\sigma(e\ ^3\mathrm{He} \rightarrow e\ X)/\sigma(e\ ^3\mathrm{H} \rightarrow e\ X)$ is then largely free of nuclear corrections and the ratio of structure functions F_2^n/F_2^p and $u(x)/d(x)$ can be extracted.

5·2. *Spin structure functions and parton distributions.* – The lack of precise data in the valence quark region and especially at very large x values is even more obvious for the spin structure function $g_1(x, Q^2)$, both on the proton and neutron. New experiments at 12 GeV will significantly improve our knowledge of the basic spin structure function. Two experiments will study polarized parton distributions at $x \leq 0.9$ on polarized protons and polarized neutrons. Using standard detection equipment, a redesigned polarized target adapted to CLAS12 and 30 (50) days of running on a longitudinally polarized NH_3 (ND_3) target, high-precision results can be achieved as shown in fig. 13. Similar coverage is projected using a polarized ^{3}He as a quasi-neutron target in Hall A. These data will discriminate among models in the large-x region. The projected results shown in fig. 13 are with a $W > 2$ GeV constraint. Studies of hadron-parton duality will tell us if this constraint can be relaxed so that spin structure functions may be used for $x \leq 0.9$ in the extraction of parton spin densities from global fits including these data. Results

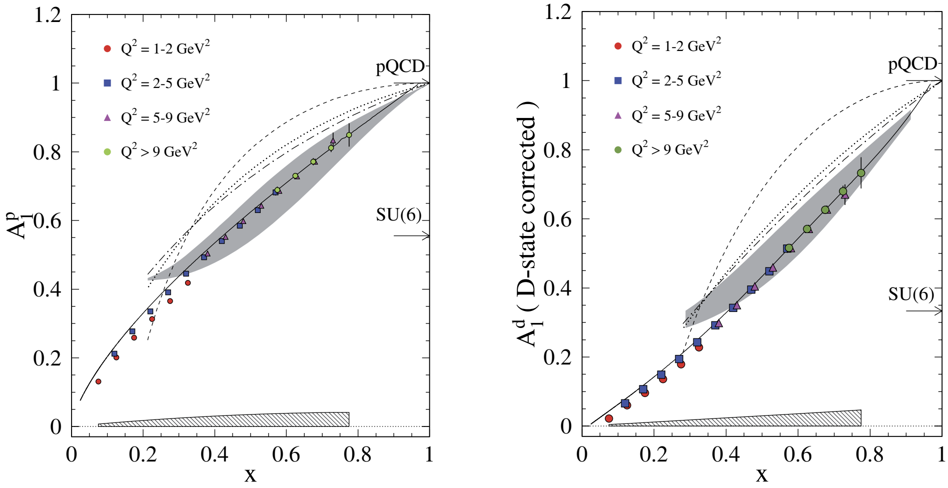

Fig. 13. – Anticipated results on A_1^p.The four different symbols represent four different Q^2 ranges. The statistical uncertainty is given by the error bars while the systematic uncertainty is given by the shaded band.

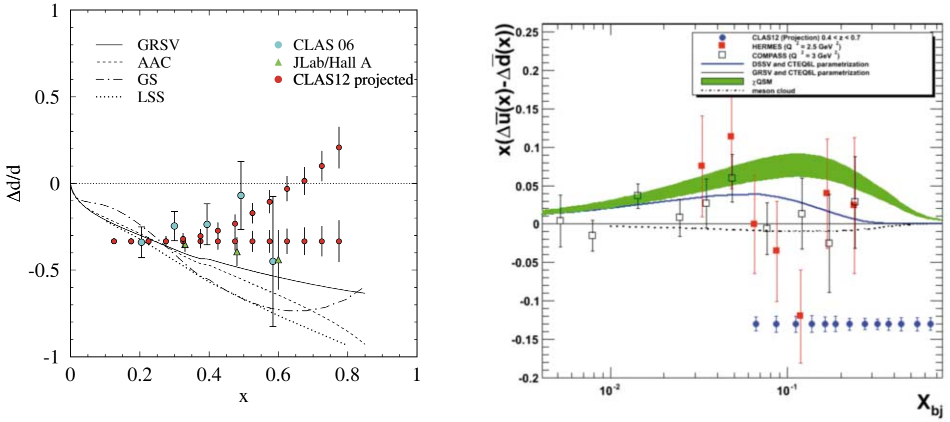

Fig. 14. – Left panel: expected results for $(\Delta d+\Delta\bar{d})/(d+\bar{d})$. The central values of the data are following two arbitrary curves to demonstrate how the two categories of predictions, namely the ones that predict $\Delta d/d$ stays negative (LO and NLO analyses of polarized DIS data: GRSV, LSS, AAC, GS, statistical model, and a quark-hadron duality scenario) and the ones predicting $\Delta d/d \to 1$ when $x \to 1$ (leading order pQCD and a quark-hadron duality scenario). The right panel shows the expected uncertainties for the asymmetry of the polarized sea quarks.

on protons and neutrons targets will allow for the extraction of the d-quark polarization $(\Delta d+\Delta\bar{d})/(d+\bar{d})$, and the asymmetry of the polarized sea $x[\Delta\bar{u}(x)-\Delta\bar{d}(x)]$. The precision expected from these measurements is shown in fig. 14.

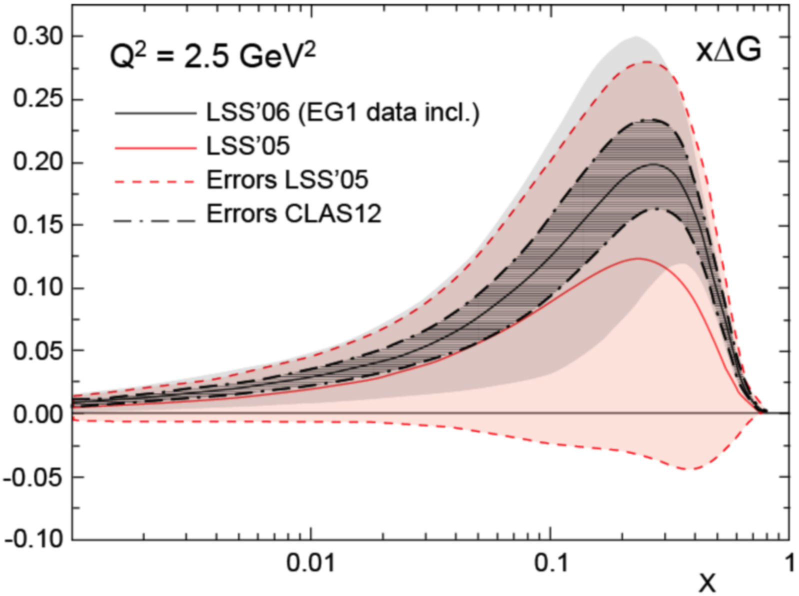

Fig. 15. – Expected uncertainties for $x\Delta G(x)$. The black solid curve shows the central value of the present analysis that includes CLAS EG1 data. The dash-dotted lines give the error band when the expected CLAS12 data are included in the LSS QCD analysis.

5·3. *Global analysis of polarized parton densities.* – The larger window that will open up over the DIS domain with the 12 GeV upgrade will permit to place more stringent constraints on the parton distributions in global fits to polarized structure function data. JLab data at lower energies had already unique impact at large x. The improvement from the 12 GeV upgrade is also significant at low and moderate x, noticeably for the polarized gluon distribution $\Delta G(x)$. To demonstrate the precision achievable with the expected CLAS12 data, we have plotted in fig. 15 the expected impact of future JLab data at 12 GeV on the next-to-leading order QCD analyses of the polarized gluon distribution [30]. A dramatic improvement can be achieved with the expected data from experiment. The data will not only reduce the error band on $\Delta G(x)$, but will likely allow a more detailed modeling of its x-dependence. Significant improvements are expected for the quark distributions as well, especially for the polarized s-quark density.

5·4. *Moments of spin structure functions.* – Moments of structure functions are related to the nucleon static properties by sum rules. Inclusive deep inelastic scattering data at JLab have permitted evaluation of the moments at low and intermediate Q^2 [20-25]. With a maximum beam energy of 6 GeV, however, the measured fractional strength of the moments becomes rather limited for Q^2 greater than a few GeV^2. The 12 GeV upgrade extends this range to much higher Q^2.

At sufficiently large Q^2, the Bjorken sum rule relates the integral $\Gamma_1^{p-n}(Q^2) =$

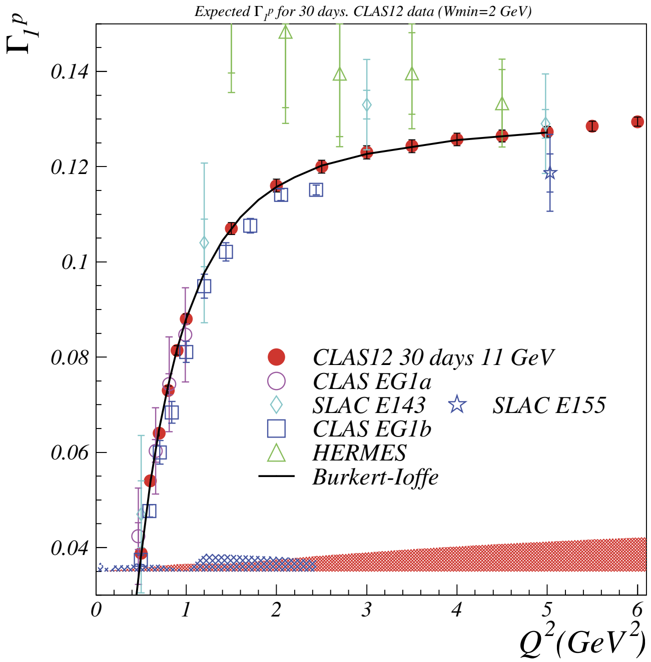

Fig. 16. – (Colour on-line) Expected precision on Γ_1^p for CLAS12 and 30 days of running. CLAS EG1a [20,21] data and preliminary results from EG1b are shown for comparison. The data and systematic uncertainties include estimates of the unmeasured DIS contribution. HERMES [34] data, and E143 [35] and E155 data [36] from SLAC are also shown (including DIS contribution estimates). The solid line is a model from [37,38].

$\Gamma_1^p(Q^2) - \Gamma_1^n(Q^2) = \int[g_1^p(x,Q^2) - g_1^n(x,Q^2)]\mathrm{d}x$ to the nucleon axial charge [31]. Figure 16 shows the expected precision on Γ_1^p. Published results and preliminary results from CLAS are also displayed for comparison. The hatched blue band corresponds to the systematic uncertainty on the CLAS EG1b data points. The red band indicates the estimated systematic uncertainty from CLAS12. The systematic uncertainties for EG1 and CLAS12 include the uncertainty on the unmeasured DIS part estimated using a frequently used model [32]. As can be seen, moments can be measured up to $Q^2 = 6\,\mathrm{GeV}^2$ with a statistical accuracy improved several fold over that of the existing world data.

Finally, moments in the low ($\simeq 0.5\,\mathrm{GeV}^2$) to moderate ($\simeq 4\,\mathrm{GeV}^2$) Q^2 range enable us to extract higher-twist parameters, which represent correlations between quarks in the nucleon. This extraction can be done by studying the Q^2 evolution of the first moments [33,39]. Higher twists have been consistently found to have, overall, a surprisingly smaller effect than expected. Going to lower Q^2 enhances the higher-twist effects but makes it harder to disentangle a high twist from the yet higher ones. Furthermore, the uncertainty on α_s becomes prohibitive at low Q^2. Hence, higher twists turn out to be hard to measure, even at the present JLab energies. Adding data at higher Q^2 to the

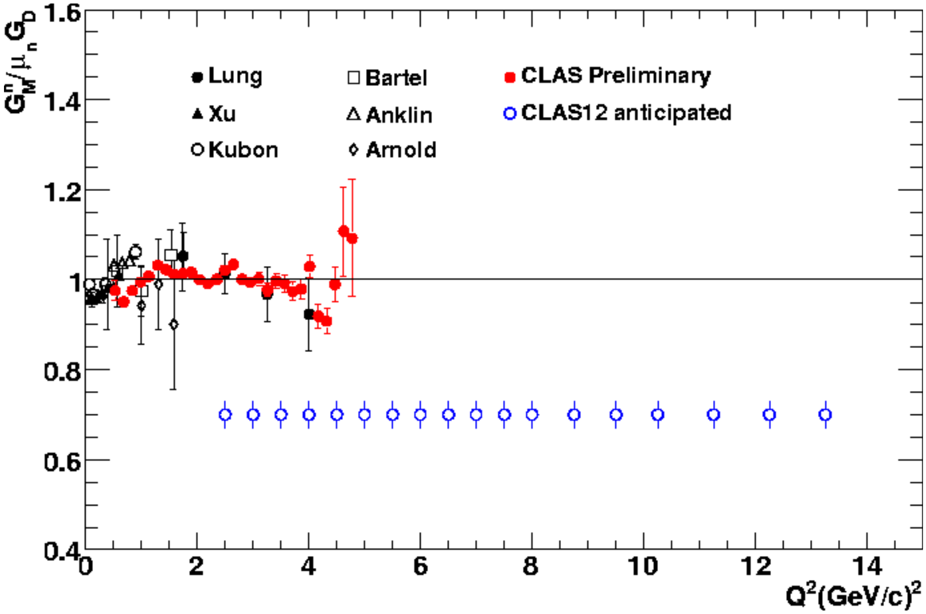

Fig. 17. – (Colour on-line) The magnetic form factor for the neutron. The recent JLab data, and projected uncertainties at 12 GeV with CLAS12 (blue open circles) are shown.

present JLab data set removes the issues of disentangling higher twists from each other and of the α_s uncertainty. The smallness of higher twists, however, requires statistically precise measurements with small point-to-point correlated systematic uncertainties. Such precision at moderate Q^2 has not been achieved by the experiments done at high energy accelerators, while JLab at 12 GeV presents the opportunity to reach it considering the expected statistical and systematic uncertainties of the new experiments. The total point-to-point uncorrelated uncertainty on the twist-4 term for the Bjorken sum, f_2^{p-n}, decreases by a factor of 5-6 compared to results obtained in ref. [40].

6. – Electromagnetic form factors at short distances

6˙1. *Nucleon elastic form factors.* – The most basic observables that reflect the composite nature of the nucleon are its electromagnetic form factors. The electric and magnetic form factors characterize the distributions of charge and magnetization in the nucleon as a function of the spatial resolving power. Further, these quantities can be described and related to other observables through the generalized parton distributions discussed in sect. **3**.

Measurements of the elastic form factors continues will remain an important aspect of the physics program at 12 GeV, and will be part of the program in several experiments at JLab. The magnetic form factor of the neutron requires special experimental setups for neutron detection and the *in situ* neutron efficiency calibration measurement, for which CLAS12 is well suited. Figure 17 shows the existing JLab data [41] as well as the extension in Q^2 projected for the 12 GeV program.

Nucleon ground and excited states represent different eigenstates of the Hamiltonian, therefore to understand the interactions underlying nucleon formation from fundamental constituents, the structure of both the ground state and the excited states must be studied.

6˙2. *Nucleon resonance transition form factors.* – The nucleon resonance transition form factors reveal the nature of the excited states and encode the transition charge and current densities on the light cone. The N^* program at JLab (for recent overviews see: [42, 43]) has already generated results for the transition form factors at Q^2 up to 6 GeV^2 for the $\Delta(1232)$, and up to 7.5 GeV^2 for the $N(1535)S_{11}$. The latest results [44,45] on the transition form factors of the Roper resonance $N(1440)P_{11}$ for Q^2 up to 4.5 GeV^2, have demonstrated the sensitivity to the degrees of freedom that are effective in the excitation of particular states. The JLab energy upgrade will allow us to probe resonance excitations at much higher Q^2, where the elementary quarks degrees of freedom may become evident in the resonance formation through the approach to scaling as constituents quarks approach their asymptotic mass values. Figure 18 shows the projected Q^2 dependence of the $A_{1/2}$ transition amplitude for the $N(1440)P_{11}$ resonance obtained from single pion electro-production. Resonances at higher mass tend to decouple from the single pion channel. The transition form factors of those excited states can be efficiently measured in double-pion processes [46] such as $ep \to ep\pi^+\pi^-$.

7. – Gluonic excitations of hadrons.

The presence of gluons has been established in high energy e^+e^- collisions where the reaction $e^+e^- \to 3$ jets was observed. This process is predicted in perturbative QCD and is quantitatively described as the result of hard gluon bremsstrahlung from one of the high energy quarks in the annihilation process $e^+e^- \to q\bar{q}g$. One of the open problems in hadron physics is if gluons (or the "glue") actively participate in processes at low energy, such as the excitations of hadrons. The most promising way of establishing the effect of the "glue" in spectroscopy is the study of the meson spectrum.

7˙1. *Hybrid mesons.* – Our understanding of how quarks form mesons has evolved within QCD and we expect a rich spectrum of mesons that takes into account not only the quark degrees of freedom, but also the gluonic degrees of freedom. Excitations of the gluonic field binding the quarks can give rise to excitations of the glue (hybrid mesons). A picture of these hybrid mesons is one where these particles are excitations of a gluonic flux tube that forms between the quark and antiquark. Particularly interesting is that many of these hybrid mesons are expected to have exotic quantum numbers $J^{PC} = 0^{+-}$, 1^{-+}, 2^{+-} that cannot be achieved in simple $q\bar{q}$ systems. In the flux tube model these states do not mix with conventional meson states which simplifies dramatically the search for hybrid mesons. A simple mechanism to produce mesons with

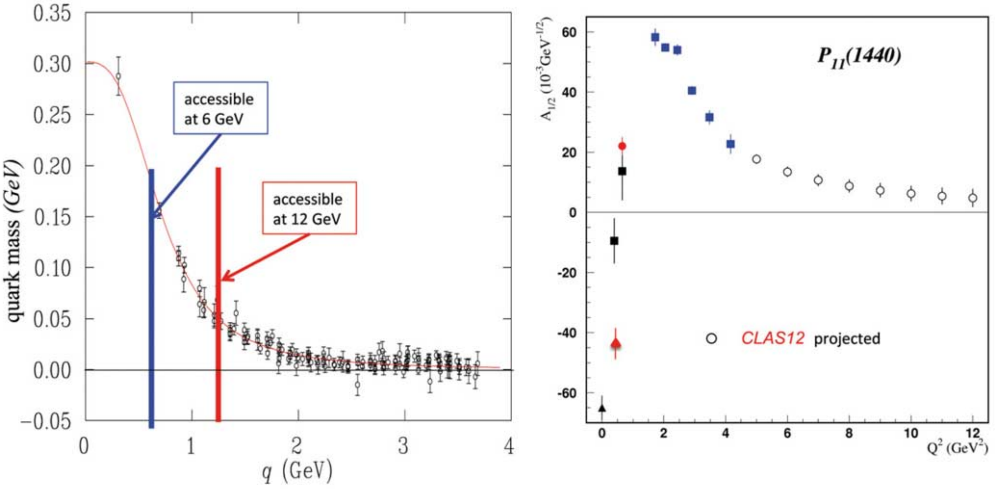

Fig. 18. – (Colour on-line) Left panel: evolution of the quark mass with momentum transfer. The region left of the blue line is accessible at 6 GeV beam energy, the region left of the red line can be accessed at 12 GeV in N^* excitations with $Q^2 \leq 12\,\text{GeV}^2$. Right panel: published and projected electro-coupling amplitudes for the Roper resonance with a 12 GeV electron beam.

exotic quantum numbers using photon beams is illustrated in fig. 19. The isolation of mesons with exotic quantum numbers provides strong evidence for gluonic excitations, however they do not uniquely identify hybrid mesons. Complex configurations, such as 4-quark states ($q\bar{q}q\bar{q}$) may have same quantum numbers as gluonic states ($q\bar{q}G$). For this reason it is essential to establish not only the existence of one or two states, but as many states as possible to characterize the systematics underlying the measured spectrum. The level splitting between the ground-state flux tube and the first excited transverse modes is expected to be about $1\,\text{GeV}/c^2$, and lattice QCD calculations indicate the lightest exotic hybrid (the $J^{PC} = 1^{-+}$) has a mass of about $1.9 \pm 0.2\,\text{GeV}$.

There are tantalizing suggestions, mainly from experiments using beams of π mesons, that exotic hybrid mesons do exist. The evidence is by no means clear cut, owing in part, to the apparently small production rates for these states in the decay channels examined. It is safe to conclude that the extensive data collected to date with pion probes have not uncovered the hybrid meson spectrum. Based on models, such as the flux-tube model, we expect the production of hybrid mesons in photon-induced reactions to be comparable to the production of normal mesons. Photoproduction of mesons using a $\approx 9\,\text{GeV}$, linearly polarized photon beam provides a unique opportunity to search for exotic hybrids. Existing data are extremely limited for charged final states, and no data exist for multi-neutral final states. To carry out such a search, the GlueX program in Hall D will look at many different final states involving both charged particles and photons, but particular emphasis will be placed on those reactions that have 3 or more

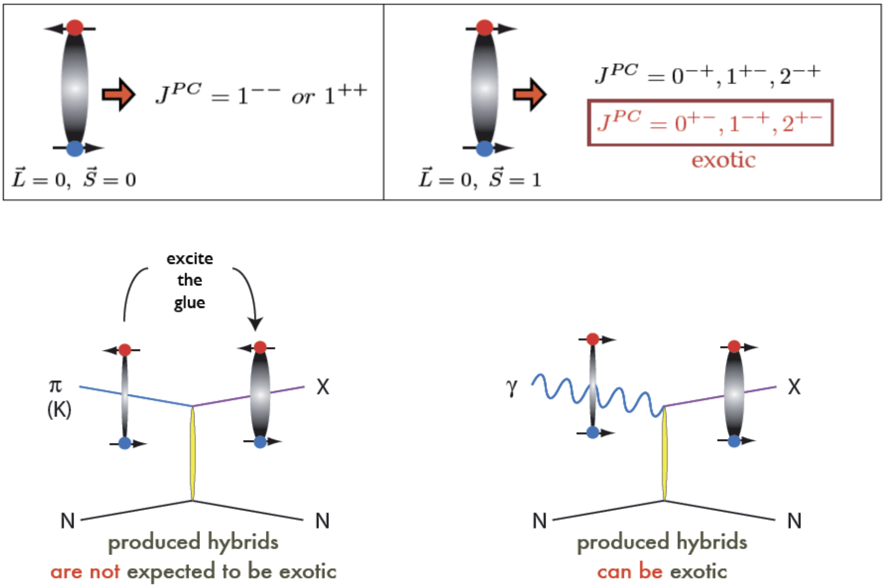
$J^{PC} = 1^{--}$ or 1^{++}
$\vec{L} = 0,\ \vec{S} = 0$
$J^{PC} = 0^{-+}, 1^{+-}, 2^{-+}$
$J^{PC} = 0^{+-}, 1^{-+}, 2^{+-}$
exotic
$\vec{L} = 0,\ \vec{S} = 1$
excite the glue
π (K)
X
N
N
produced hybrids
are not expected to be exotic
γ
X
N
N
produced hybrids
can be exotic

Fig. 19. – Possible production mechanisms of mesons with exotic quantum numbers with photon beams. In this picture mesons with exotic quantum numbers are preferentially produced in reactions with real photons.

pions in the final state. The discovery potential for GlueX comes first from the very high statistics based on 10^7 tagged photons per second on target, which will exceed existing photoproduction data by several orders of magnitude. The GlueX experimental search in Hall D has a mass reach up to about 2.8 GeV to observe mesons with masses up to $2.5\,\text{GeV}/c^2$.

An alternative approach has been taken in Hall B with CLAS12. This experiment will use a quasi-real photon beam whose energy is measured by detecting the electrons scattered from the hydrogen production target at very forward electron scattering angles. The forward tagger makes use of a high-granularity, high-resolution crystal calorimeter to detect the small angle electrons in the energy range of up to 4 GeV. The difference to photon energy tagging of real photons is that real photon tagging requires two independent interactions—the real photon being generated in an electromagnetic interaction with the atomic electrons of the radiator, and the real photon interacting hadronically with the proton in the production target. The latter process has a typical probability of about $\ll 1\%$. In virtual photon tagging there is only one interaction involved as the virtual photon is produced in the hadronic interaction in the production target, potentially allowing much higher production rates than what can be achieved in real photo-production. The experimental challenge is to separate the hadronic interaction

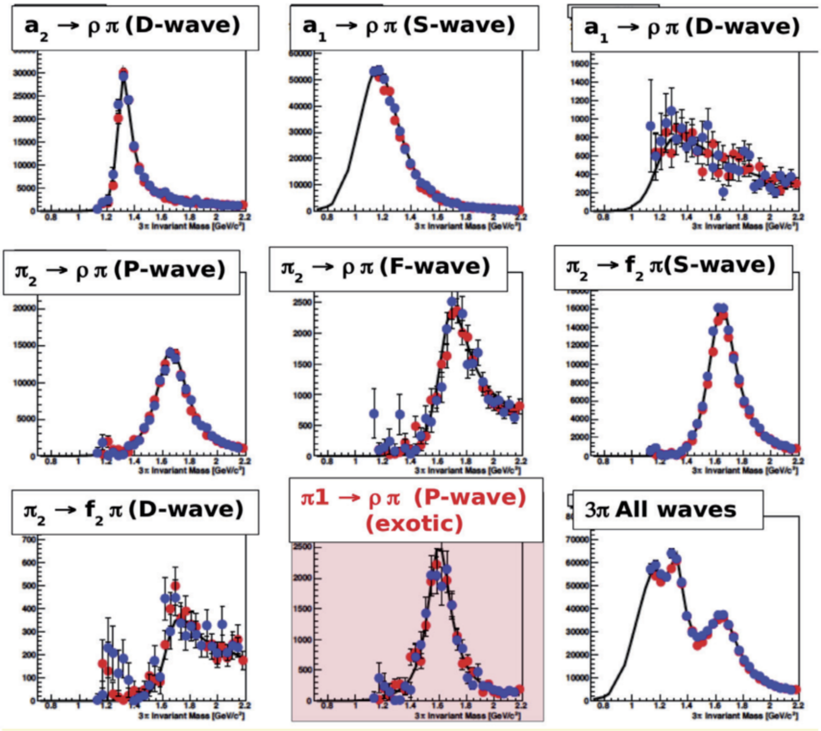

Fig. 20. – Events with 3-pions in the final state are generated in specific partial waves (solid lines) including one with exotic J^{PC} quantum numbers, and then tracked through the CLAS12 detector system and then reconstructed (points with error bars). They reconstructed events retain their initial partial wave contents.

in the target from the electromagnetic ones that occur at much higher rates. Another benefit is that virtual photons are linearly polarized providing an important degree of freedom that can be utilized in the partial wave analysis of multi-particle final states to reduce ambiguities. Figure 20 shows the results of a partial wave analysis. The events are simulated with different partial wave content, then tracked through the CLAS12 acceptance and then subjected to a partial wave analysis. The results of the analysis show that the initial partial wave content is preserved.

7·2. *Hybrid baryons.* – The search for gluonic excitations has so far been limited to mesons, although baryons may also be excited through gluonic degrees of freedom. Studies of hybrid baryons are equally important to hybrid mesons in the quest to better understand the complex confinement mechanisms in hadrons. However, gluonic baryons $|qqqG\rangle$ and ordinary 3-quark baryons $|qqq\rangle$ have the same quantum number, making it impossible to uniquely identify them. One possibility is to look for an overpopulation of states with specific spin-parity J^P assignments compared to the number of such states predicted in the constituent quark model. The excited glue adds ≈ 1 GeV to the mass of hybrid baryons, putting the lowest mass hybrid baryons with strangeness $S = 0$ into the range from 1.8 to 2 GeV.

8. – Quarks and hadrons in the nuclear medium

8·1. *Color transparency.* – Color transparency (CT) is a unique prediction of QCD, and implies that under certain conditions, the nuclear medium will allow the transmission of hadrons with reduced absorption. The phenomenon of CT is predicted in the quark-gluon basis and is totally unexpected in a hadronic interaction picture. The following conditions must be present to observe CT: the interactions must create a small-size object (point-like configuration, PLC) that has a small cross-section when traveling in a hadronic medium, and the distance over which it expands to its full hadronic size must be larger than the nucleus size. Such conditions require high enough energy transfer to the target where the photon couples to PLCs, and the full hadronization occurs outside the nucleus. Color transparency effects have been observed at very high energies at hadron machines, but at what momentum transfer CT sets in is still a not fully settled question. Small increases in nuclear transparency consistent with theoretical predictions have been observed at JLab with 5-6 GeV electron beams in pion production. The energy doubling of the JLab electron accelerator to 12 GeV will provide much better conditions where a significantly increased transparency should be observable with high sensitivity, as is shown, *e.g.*, in fig. 21.

8·2. *Quark propagation and hadron formation.* – The use of electron beams at 12 GeV allows us to address fundamental questions of how colored quarks struck in the interaction with high energy photons transform into colorless hadrons. Questions that we want to have answered are, how long can a light colored quark remain de-confined? The production time T_p measures this quantity. Because de-confined quarks emit gluons, T_p can be measured via medium-stimulated gluon emission resulting in a broadening of the transverse momentum distribution of the final hadrons. Another important question to address is: How long does it take to form the color field of a hadron? This can be measured by the formation time T_f^h. Since hadrons interact strongly with the nuclear medium, T_f^h can be determined by measuring the attenuation of hadrons in the nuclear medium by using nuclei of different sizes.

These questions can be addressed by measuring the hadronic multiplicity ratio

$$R_M^h(z,\nu,p_T^2,Q^2,\phi) = \frac{\left\{\frac{N_h^{DIS}(z,\nu,p_T^2,Q^2,\phi)}{N_e^{DIS}(\nu,Q^2)}\right\}_A}{\left\{\frac{N_h^{DIS}(z,\nu,p_T^2,Q^2,\phi)}{N_e^{DIS}(\nu,Q^2)}\right\}_D}$$

versus all kinematical quantities. In this expression, N_h is the number of hadrons produced in DIS events and N_e^{DIS} is the number of associated DIS electrons. The numerator corresponds to target nucleus A, and the denominator corresponds to deuterium. ν is the energy transferred by the electron, and z is the hadron energy divided by ν. In the QCD-improved parton model, R_M^h is given by the ratios of sums over products of the

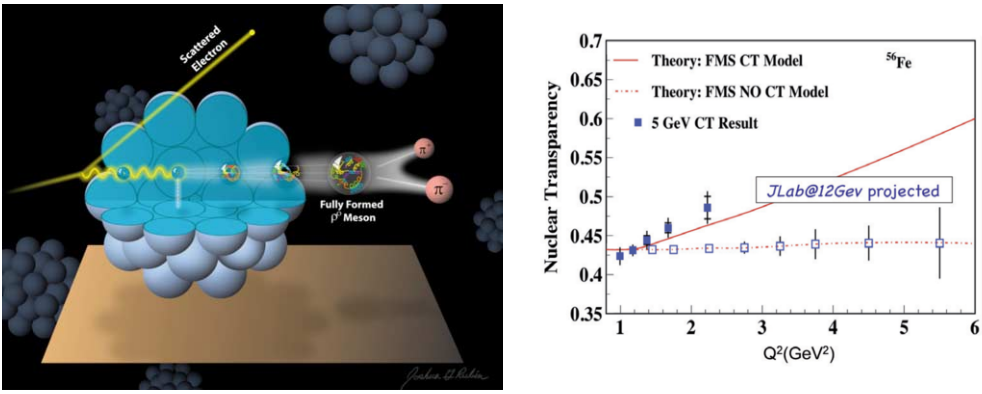

Fig. 21. – Projected color transparency effects in Fe. The open circles represent projected results with CLAS12 at 12 GeV.

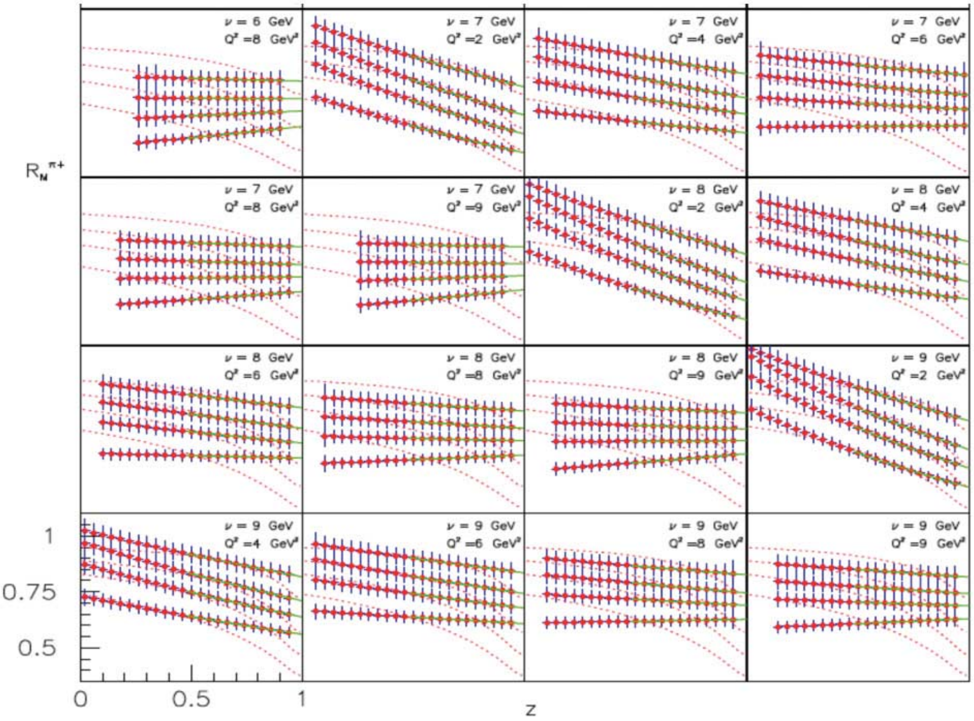

Fig. 22. – Z dependence of the hadronic multiplicity ration (top to bottom in each plot) for ^{14}N, ^{40}Ar, ^{197}Au for 16 bins in Q^2, ν. The solid line is a gluon bremsstrahlung model calculation [47] for $z > 0.5$ for pions. The dotted lines are parameterizations of HERMES 27 GeV data.

Table III. – *Expected hadron production rates for* 1,000 *DIS events at* 11 *GeV beam energy.*

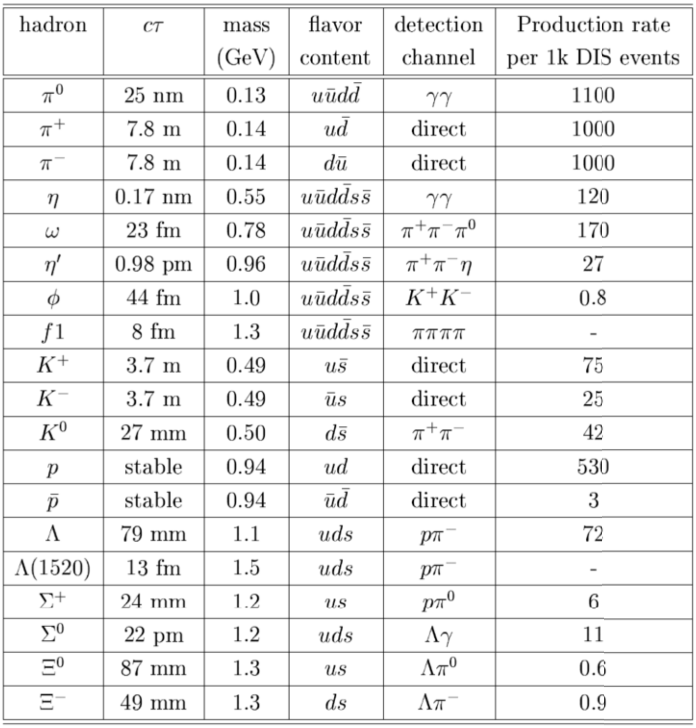

hadron	$c\tau$	mass (GeV)	flavor content	detection channel	Production rate per 1k DIS events
π^0	25 nm	0.13	$u\bar{u}d\bar{d}$	$\gamma\gamma$	1100
π^+	7.8 m	0.14	$u\bar{d}$	direct	1000
π^-	7.8 m	0.14	$d\bar{u}$	direct	1000
η	0.17 nm	0.55	$u\bar{u}d\bar{d}s\bar{s}$	$\gamma\gamma$	120
ω	23 fm	0.78	$u\bar{u}d\bar{d}s\bar{s}$	$\pi^+\pi^-\pi^0$	170
η'	0.98 pm	0.96	$u\bar{u}d\bar{d}s\bar{s}$	$\pi^+\pi^-\eta$	27
ϕ	44 fm	1.0	$u\bar{u}d\bar{d}s\bar{s}$	K^+K^-	0.8
$f1$	8 fm	1.3	$u\bar{u}d\bar{d}s\bar{s}$	$\pi\pi\pi\pi$	-
K^+	3.7 m	0.49	$u\bar{s}$	direct	75
K^-	3.7 m	0.49	$\bar{u}s$	direct	25
K^0	27 mm	0.50	$d\bar{s}$	$\pi^+\pi^-$	42
p	stable	0.94	ud	direct	530
$\bar{p}$	stable	0.94	$\bar{u}\bar{d}$	direct	3
Λ	79 mm	1.1	uds	$p\pi^-$	72
$\Lambda(1520)$	13 fm	1.5	uds	$p\pi^-$	-
Σ^+	24 mm	1.2	us	$p\pi^0$	6
Σ^0	22 pm	1.2	uds	$\Lambda\gamma$	11
Ξ^0	87 mm	1.3	us	$\Lambda\pi^0$	0.6
Ξ^-	49 mm	1.3	ds	$\Lambda\pi^-$	0.9

quark distribution functions with fragmentation functions. The proposed measurement will provide two to three orders of magnitude more data than any previous experiment in this energy range and will include a much larger collection of hadron species. Table III shows the expected rates for the production of a large number of hadron species. Examples of projected data for the multiplicity ratio $R^h_M(z, \nu, p^2_T, Q^2, \phi)$ are shown in fig. 22.

9. – Search for new physics

9·1. *Search for physics beyond the Standard Model.* – The Standard Model (SM) of High Energy Physics has been highly successful in accurately predicting a large number of experimental observations. Its predictions have been probed at the highest energy accelerators at HERA, the Tevatron at Fermilab, and now at the LHC at CERN. So far, no clear deviations from the SM have been identified. While most of the searches for physics beyond the SM involve very high-energy accelerators where new particle types may be produced in high-energy collisions, deviations from the SM may also be observed in high-precision experiments at lower energies. Parity-violating electron scattering may be the best tool to study possible SM-violating effects in precision measurements of the

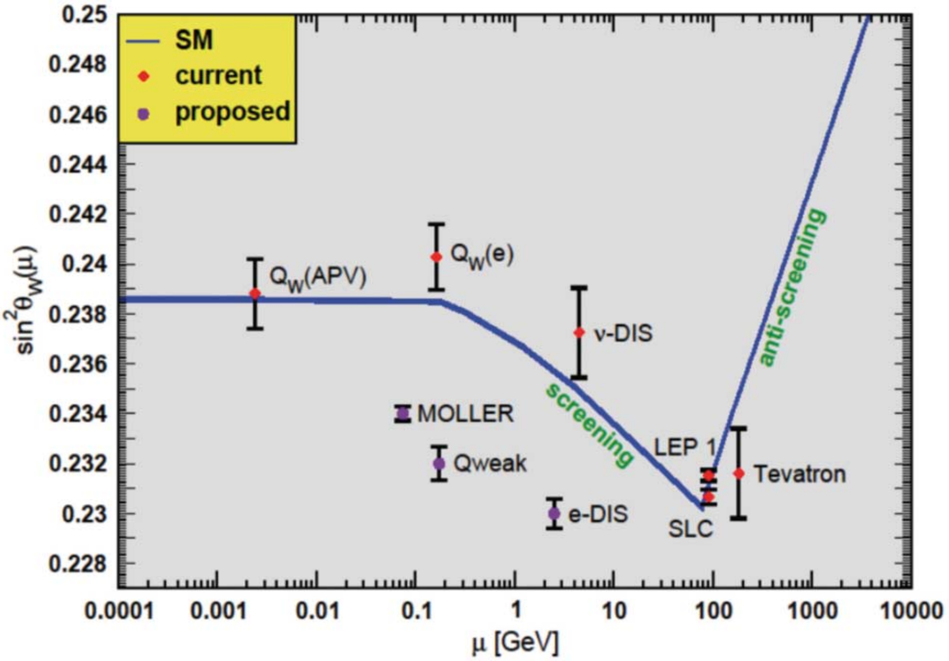

Fig. 23. – Current knowledge of the weak mixing angle in comparison to the SM predictions.

electro-quark couplings that relate to the weak mixing angle $\sin^2\Theta_W$. New physics such as quark compositeness, or new gauge bosons beyond the Z^0, may cause small deviations from the SM predictions at relatively low energies that can be revealed in very-high-precision experiments. With the high luminosity available at JLab such effects maybe be detectable. Two experiments have been proposed to measure with high precision the weak mixing angle $\sin^2\Theta_W$ in parity-violating electron-electron scattering (Moller scattering), and in deep inelastic electron scattering. Figure 23 shows the Standard Model prediction for the energy dependence of the weak mixing angle in comparison with measurements. Previous measurements indicate a possible discrepancy for several of the data points each one at the $\geq 1\sigma$ level. The new measurements will significantly improve the precision of the experimental data base.

9·2. *Heavy photon search.* – Recent satellite measurements have shown a dramatic excess of positrons ranging in energy from 10 GeV to several hundred 100 GeV. One of the leading interpretations for this anomaly involves the existence of a new gauge vector boson that couples very weakly to e^+e^- pairs and can be produced through interaction with the dark matter in the universe, see fig. 24. New light vector particles and their associated interactions are ubiquitous in extensions of the Standard Model. However, the symmetries of the Standard Model restrict the interaction of ordinary matter with such new states. Indeed, most interactions consistent with Standard Model

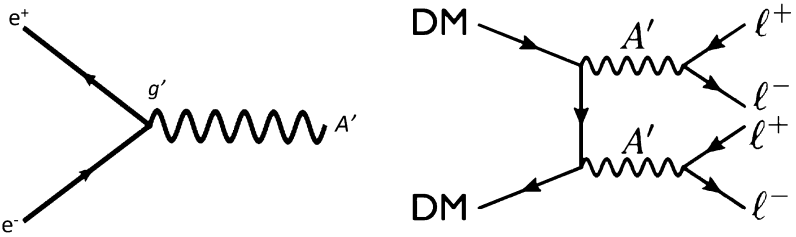

Fig. 24. – Possible graphs contributing to the excess of positrons (left) and the coupling of the purported A' vector-boson to dark matter (right).

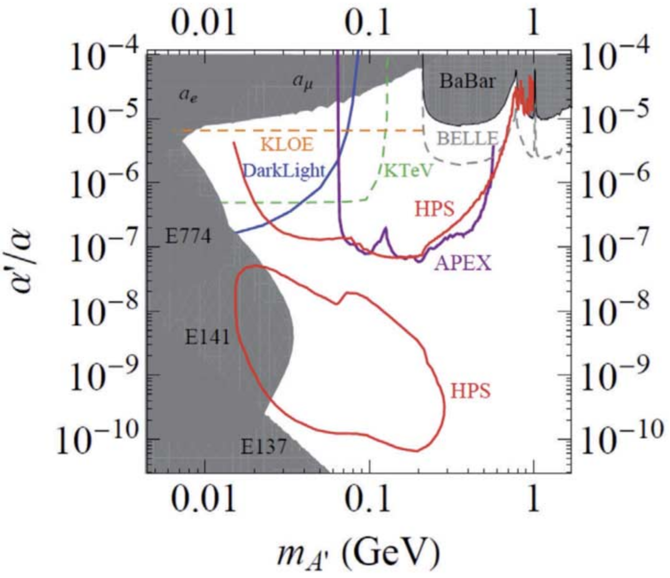

Fig. 25. – Exclusion zones for the ratio of heavy photon to electromagnetic coupling strengths to e^+e^- pairs *vs.* the heavy photon mass. The various lines show the exclusion zones from previous and planned measurements.The proposed and planned measurements at JLab are shown by the lines marked HPS and APEX. The two zones in the upper part are for the HPS and APEX experiment to search for narrow peaks in the mass spectrum of the e^+e^- pair. The zone marked HPS in the lower part includes the search for detached vertices that would indicate the presence of a long-lived A' with weak coupling.

gauge symmetries and Lorentz invariance have couplings suppressed by a high mass scale. One of the few unsuppressed interactions is the coupling of charged Standard Model particles to a new gauge boson A', which is quite poorly constrained for small coupling constants as shown in fig. 25.

Heavy photons mix with the ordinary photon through kinetic mixing, which induces their weak coupling to electrons, $\epsilon \approx 10^{-3}$. Since they couple to electrons, heavy photons are radiated in electron scattering and can subsequently decay into narrow e^+e^- resonances which can be observed above the copious QED background. For suitably small couplings, heavy photons travel detectable distances before decaying, providing a second signature. Two experiments have been proposed at JLab to extend considerably the kinematic zone covered by experiment in the search for the A'. The APEX experiment in Hall A uses high-resolution magnetic spectrometers to search for narrow peaks in the e^+e^- mass spectrum. The HPS experiment in Hall B, in addition to searching for peaks in the mass spectrum also searches for detached vertices from the decay of a long-lived A'. The latter probes a region with much weaker coupling of the A' to e^+e^- pairs as seen in the bottom part of fig. 25.

10. – Conclusions

The JLab energy upgrade and the planned new experimental equipment are well matched to an exciting scientific program aimed at studies of the complex hadron structure in terms of the generalized parton distributions and the transverse-momentum–dependent distributions, GPDs and TMDs. They both provide fundamentally new insights into the complex multi-dimensional quark structure of the nucleon. The exploration of the gluonic excitations of hadrons is a complementary effort to study the active role that gluons play in the excitation spectrum. The high precision afforded by the high luminosity and the large acceptance detectors, and the development of novel techniques to measure scattering off nearly free neutrons, will enable the exploration of phase space domains with extreme conditions that could not be studied before. High-luminosity measurements will also probe part of the phase space where deviations from the Standard Model of particle physics might be observed, potentially leading to new discoveries.

* * *

I like to thank my colleagues at Jefferson Lab for many discussions on the exciting science with the JLab 12 GeV upgrade and for providing me with many of the graphs that I included in this contribution. This work was carried out under DOE contract No. DE-AC05-06OR23177.

REFERENCES

[1] MUELLER D. *et al.*, *Fortsch. Phys.*, **42** (1994) 101, hep-ph/9812448.
[2] JI X., *Phys. Rev. D*, **55** (1997) 7114.
[3] JI X., *Phys. Rev. Lett.*, **8** (1997) 610.
[4] RADYUSHKIN A., *Phys. Lett. B*, **380** (1996) 417.
[5] RADYUSHKIN A., *Phys. Rev. D*, **56** (1997) 5524.
[6] BELITSKY A. V., MUELLER D. and KIRCHNER A., *Nucl. Phys. B*, **629** (2002) 323.
[7] BURKARDT M., *Int. J. Mod. Phys. A*, **18** (2003) 173.
[8] BELITSKY A. V., JI X. and YUAN F., *Phys. Rev. D*, **69** (2004) 074014.
[9] GOEKE K. *et al.*, *Phys. Rev. D*, **75** (2007) 094021.

[10] Stepanyan S. *et al.*, *Phys. Rev. Lett.*, **87** (2001) 182002.

[11] Girod F. X. *et al.*, *Phys. Rev. Lett.*, **100** (2008) 162002.

[12] Munoz-Camacho C. *et al.*, *Phys. Rev. Lett.*, **97** (2006) 262002.

[13] Chen S. *et al.*, *Phys. Rev. Lett.*, **97** (2006) 072002.

[14] Airapetian A. *et al.*, *Phys. Rev. Lett.*, **87** (2001) 182001.

[15] De Masi R. *et al.*, *Phys. Rev. C*, **77** (2008) 042201.

[16] Vanderhaeghen M., Guichon M. and Guidal M., *Phys. Rev. D*, **60** (1999) 094017.

[17] Sivers W. D., *Phys. Rev. D*, **41** (1990) 83.

[18] Boer D. and Mulders P. J., *Phys. Rev. D*, **57** (1998) 5780.

[19] Mulders P. J. and Tangerman R. D., *Nucl. Phys. B*, **461** (1996) 197.

[20] Fatemi R. *et al.*, *Phys. Rev. Lett.*, **91** (2003) 222002.

[21] Yun J. *et al.*, *Phys. Rev. C*, **67** (2003) 055204.

[22] Zheng X. *et al.*, *Phys. Rev. C*, **70** (2004) 065207.

[23] Amarian M. *et al.*, *Phys. Rev. Lett.* , **92** (2004) 022301.

[24] Dharmawardane V. *et al.*, *Phys. Lett. B*, **641** (2006) 11.

[25] Prok Y. *et al.*, *Phys.Lett. B*, **672** (2009) 12.

[26] Bosted P. *et al.*, *Phys. Rev. C*, **75** (2007) 035203.

[27] Christy M. E. and Melnitchouk W., *J. Phys.: Conf. Ser*, **299** (2011) 01200.

[28] Chen J. P., Deur A., Kuhn S. and Meziani Z. E., *J. Phys.: Conf. Ser.*, **299** (2011) 012005.

[29] Baillie N. *et al.*, arXiv:1110.2770(2011).

[30] Leader E., Sidorov S. and Stamenov D., *Phys. Rev. D*, **75** (2007) 074027.

[31] Bjorken J. D., *Phys. Rev.*, **148** (1966) 1467.

[32] Thomas E. and Bianchi N., *Nucl. Phys. Proc. Suppl.*, **82** (2000) 26.

[33] Osipenko M. *et al.*, *Phys. Rev. D*, **71** (2005) 054007.

[34] Airapetian A. *et al.*, *Eur. Phys. J. C*, **26** (2003) 527.

[35] Abe K. *et al.*, *Phys. Rev. D*, **58** (1998) 112003.

[36] Anthony P. L. *et al.*, *Phys. Lett. B*, **493** (2000) 19.

[37] Burkert V. D. and Ioffe B. L., *Phys. Lett. B*, **296** (1992) 223.

[38] Burkert V. D. and Ioffe B. L., *J. Exp. Theor. Phys.*, **78** (1994) 619

[39] Chen J. P., Deur A. and Meziani Z.-E., *Mod. Phys. Lett. A*, **20** (2005) 2745.

[40] Deur A. *et al.*, *Phys. Rev. Lett.*, **93** (2004) 212001.

[41] Lachniet J. *et al.*, *Phys. Rev. Lett.*, **102** (2009) 192001.

[42] Aznauryan I. G. and Burkert V. D., *Prog. Part. Nucl. Phys*, **67** (2012) 1-54.

[43] Aznauryan I. G., Burkert V. D., Lee T.-S. H. and Mokeev V., *J. Phys. Conf. Ser.*, **299** (2011) 012008.

[44] Aznauryan I. *et al.*, *Phys. Rev. C*, **78** (2008) 045209.

[45] Aznauryan I. *et al.*, *Phys. Rev. C*, **80** (2009) 055203.

[46] Ripani M. *et al.*, *Phys. Rev. Lett.*, **91** (2003) 022002.

[47] Kopeliovich B. Z., Nemchick J., Predazzi E. and Hayashigaki A., *Nucl. Phys. A*, **740** (2004) 211.

Proceedings of the International School of Physics “Enrico Fermi”
Course CLXXX “Three-Dimensional Partonic Structure of the Nucleon”
edited by M. Anselmino, H. Avakian, D. Hasch and P. Schweitzer
(IOS, Amsterdam; SIF, Bologna)
DOI 10.3254/978-1-61499-197-7-333

The structure of the nucleon at an EIC

D. Hasch

INFN, Laboratori Nazionali di Frascati - 00044 Frascati (RM), Italy

Summary. — The project of a polarised Electron Ion Collider (EIC) is currently discussed intensively in the high energy nuclear physics community. With such a facility, a real breakthrough in “spin physics” and the study of the three-dimensional structure of the nucleon is expected. This lecture reviews the physics case for an EIC, concentrating on the topics discussed at this school, as well as the technical challenges and envisaged realisations.

1. – Preface

There is a common agreement within the high-energy and nuclear physics community that a real breakthrough in the study of the spin and three-dimensional structure of the nucleon can only be achieved with a new polarised facility that allows for high-precision measurements over a wide kinematic range. The *golden* option for the spin physics community would be a polarised Electron-Ion Collider (EIC), a facility that will be able to collide polarised electrons with polarised protons and light to heavy nuclei at high, variable energies.

This lecture note provides a brief overview about realisation ideas for an EIC. We will first briefly review the science case for an EIC thereby concentrating on the topics discussed at this school. A very exhaustive discussion of the open physics questions which can be addressed by an EIC can be found in a recent review [1].

© Società Italiana di Fisica

Among the projects for realisation we will discuss the two solutions under study in the US, concentrating on the more general aspects and the technical challenges. The continuous efforts for these projects are documented at the laboratories web pages [2, 3]. Wherever possible we will give more specific references for the reader interested in further details.

2. – Introduction: The physics case of an EIC

Among the four pillars for the science case of an EIC, as identified in [1], we discussed in detail at this school the first two:

- The spin and flavor structure of the proton.
- Three-dimensional structure of nucleons and nuclei in momentum and configuration space.
- QCD matter in nuclei.
- Electroweak physics and the search for physics beyond the Standard Model.

The description of the three-dimensional structure of the nucleon, from which the observable physical world is formed, goes directly to the heart of exploring and understanding the QCD dynamics of matter. High energy lepton-nucleon scattering experiments with the observation of inclusive Deep-Inelastic Scattering (DIS) processes ($lN \to l'X$) have been performed for decades and have been interpreted as the most common way to investigate the internal structure of nucleons. Within the standard framework of pertubative QCD, the cross-section for this inclusive process, at large momentum transfer Q^2, can be expressed as a convolution of parton distributions with the calculable elementary hard interactions [4]. These parton distributions, $f_{a/h}(x, Q^2)$, give the number density of a parton a with a certain fraction x of the momentum of the parent hadron h. For the proton, unprecedented wide energy scales were reached with the HERA collider at DESY (operating till 2007), the only electron-proton collider built so far, and impressive progress was made over the last two decades in extracting parton distributions. The successful prediction of the scale (Q^2) dependence of these parton distributions has been one of the great triumphs of pertubative QCD. The protons at HERA, however, were not polarised and most of the topics discussed at this school could be studied so far only at fixed-target experiments [5], and hence, over a rather limited energy range.

The EIC would be the brightest femtoscope scale lepton-collider ever, exceeding the intensity of the HERA collider a thousand fold. In addition to being the first electron collider exploring the structure of *polarised* protons, an EIC will also be the first electron-nucleus collider, probing the gluon and sea quark structure of nuclei for the first time. This knowledge about the three-dimensional nucleon structure is also of essential importance for other fields in high energy physics. Giving just one example, the information about the initial spatial distribution of quarks and gluons in the nucleon is indispensable for the interpretation of heavy-ion collision data and the quest for the Quark-Gluon-Plasma.

Along the way for a realisation of such a new, challenging facility, more polarised lepton-nucleon scattering data will become available from COMPASS-II at CERN [6] and the Jefferson Laboratory experiments operating at the high luminosity CEBAF upgraded to an electron energy of 12 GeV (JLab12) [7].

Why do we wish to get more?

While with the JLab12 facility, the structure of hadrons will be studied in the valence quark region (at relatively high values of $x > 0.1$) with unprecedented accuracy, COMPASS covers the kinematics of intermediate x values exploring the transition from the valence to sea quark region with marginal overlap with JLab12 kinematics. However, none of the experiments will provide data over a wide range in Q^2 for studying the evolution properties of polarised and the novel parton distributions we discussed at this school. Neither they will provide data at low x where the gluon contributions dominate.

For the physics topics discussed at this school, an EIC would be a unique facility in providing:

- a wide kinematic range in x and Q^2, allowing to fully explore the scaling properties of parton distributions and hence derive detailed flavour-dependent information and access to gluon distributions;
- access to low x region, which is so far (and will remain) completely unexplored;
- high enough Q^2 over nearly full kinematic range for a clean interpretation of the data within the framework of pertubative QCD;
- high luminosity for fully differential analysis of data, which is essential especially for the observables related to the three-dimensional nucleon structure;
- pure nuclear polarized targets without dilution (see [5] for the complications caused by using solid-state targets).

In addition, collider kinematics have many advantages over fixed-target experiment kinematics in being, for instance, largely uncorrelated and providing clean separation between so-called current (struck quark) and target remnant fragmentation region.

We will then be able to address questions like: Why is the quark spin content so small and which role do the gluons play? How are partons spatially distributed inside the nucleon and how do they move in the transverse plane? Do they orbit and carry orbital angular momentum? Is there a correlation between orbital motion of partons, their spin and the spin of the nucleon? How gets all this modified in a nuclear environment?

The following two sections provide some more details about the topics discussed at this school and the anticipated knowledge we might gain with an EIC.

2·1. *Spin and flavour structure of the proton.* – Polarised deep-inelastic scattering experiments, in course since the late eighties, have established the surprising finding by the EMC experiment [8] that the quark's intrinsic spin contributes only little to the proton spin, just about 30%.

The challenge to understand the spin structure of the proton has inspired vast theoretical and experimental activities [4-6]. Significant progress can be expected from the unique capability of an EIC to reach small momentum fractions x down to about 10^{-4} and large momentum resolution scales Q, with high precision. This vastly extended kinematic reach will enable the determination of the gluon and quark/anti-quark spin contributions to the proton spin to about 10% accuracy or better from global analyses of the spin structure function $g_1^p(x, Q^2)$ and its scaling violations [4]. The latter is strongly correlated with the x dependence of the polarised gluon distribution. The anticipated accuracy in the determination of the gluon polarisation is especially exciting in view of the sparse experimental information available from other clean processes like the photon-gluon fusion process tagged via charm production [6].

An EIC will further provide unprecedented insight into the flavor structure of the nucleon, a key element in mapping the "landscape" of hadron structure. This could be achieved by *semi-inclusive* deep-inelastic scattering (SIDIS) as pioneered by the fixed-target lepton scattering experiments HERMES and COMPASS. Here, at least one hadron is observed in addition to the scattered lepton providing a means of "flavour tagging" [4-6]. At an EIC, semi-inclusive measurements would extend to much higher Q^2 than in fixed-target scattering, where the reaction becomes significantly cleaner and therefore more tractable theoretically. With the high luminosity of an EIC, the kinematic coverage for SIDIS in x and Q^2 will be similar to what can be achieved in inclusive DIS and extractions of the light-flavor helicity distributions and their anti-quark distributions will be possible with exquisite precision. With dedicated studies of kaon production, the elusive strange and anti-strange distributions will also be accessible. Such a detailed flavour decomposition will likely give insights into the question why the combined quark and anti-quark spin contribution to the proton spin turns out to be so small.

A key to unravel the spin structure of the nucleon will be the determination of the contributions from quark and gluon orbital angular momenta. This quest has motivated new theoretical and experimental investigations.

2'2. *Three-dimensional nucleon structure.* – The challenge to understand the role of orbital angular momentum has inspired new studies of the transverse structure of the proton and the correlation between spin and transverse-momentum effects in QCD via TMDs [9-12]. A possible three-dimensional imaging of the nucleon has been put forward by introducing novel *generalised* parton distributions (GPDs) [13-15].

These new functions offer opportunities to study a uniquely new aspect of the nucleon substructure: the localisation of partons in the plane transverse to the motion of the nucleon. As such they provide a nucleon *tomography.* The ability to describe longitudinal momentum distributions at a fixed transverse localisation is a prerequisite for studying the so-called Ji-relation [16], which links a certain combination of GPDs to the total angular momentum of a parton in the nucleon. From this quantity, the still hunted orbital angular momentum of partons in the nucleon could possibly be extracted, a question of crucial importance for the understanding of the nucleon structure.

GPDs can be studied in hard exclusive reactions, where the nucleon stays intact and the final state is fully observed. Such exclusive processes are much more challenging to be measured than traditional inclusive and semi-inclusive scattering processes as they require a difficult full reconstruction of final state particles and their cross-sections are usually small, demanding high-luminosity machines.

Today, our knowledge about GPDs is very sparse and mostly limited to first guesses of valence quark GPDs extracted from pioneering measurements at Hermes and JLab [14]. Additional information is provided by the HERA collider experiments, however, with very low precision. A high-energy high-luminosity EIC will be an ideal machine for the studies of hard exclusive reactions and the extraction of quark and gluon GPDs, allowing uniquely to study the evolution properties of GPDs and obtaining a transverse image of quarks and gluons in the nucleon (or nucleus) [13].

A large variety of different exclusive processes will be studied at an EIC. While the exclusive production of real photons (deeply virtual Compton scattering) is sensitive to singlet quark and gluon GPDs, exclusive electroproduction of mesons (ρ, J/ψ, ϕ, π, K, etc.) will allow one to disentangle the spin and flavor dependences of GPDs. The technical challenges for a full event reconstruction will be tracked from the very first step of planning interaction regions and spectrometers (see sects. **6** and **7**).

Exclusive processes with nuclei in a collider and, subsequently, the spatial image of sea quarks and gluons in nuclei will be studied for the first time, providing indispensable knowledge for the interpretation of heavy-ion collision data from RHIC and the LHC.

The transverse structure of the proton and the correlation between spin and transverse-momentum effects in QCD can be described by so-called transverse-momentum–dependent distributions (short TMDs), $f_{a/h}(x, k_\perp, Q^2)$. Here, $k_\perp$ is the intrinsic parton momentum component transverse to that of the nucleon.

Historically, TMDs have first been suggested to explain the surprisingly large and otherwise puzzling single-spin asymmetries observed in hadronic reactions with transversely polarised protons. More recently, these functions have received much attention because of the intriguing aspect of certain TMDs being nonzero only in the presence of nucleon wave function components with different orbital angular momentum.

Two TMDs, the so-called Sivers and the Boer-Mulders distributions, are rather exotic in being naive-time-reversal-odd (short: T-odd(1)). For a long time T-odd effects were believed to vanish due to time reversal invariance [17]. Recently it was shown that initial- and finale-state interactions can produce T-odd effects without violating T-invariance [18-20]. These T-odd distributions play a crucial role in our understanding of nucleon structure. Their observation, already confirmed for the Sivers distribution, is a clear indication of parton orbital motion and the presence of non-trivial phases from initial- or final-state interaction, that survive in the Bjorken limit. The origin and expected process dependence of these functions, challenging the traditional concept of factorisation and universality of PDFs, are related to fundamental QCD effects. In fact, the symmetry properties of QCD require the Sivers and Boer-Mulders distributions to appear with opposite sign in the expressions for DIS and Drell-Yan cross-sections [19], the latter describing the lepton-pair production due to quark annihilation in high-energy hadron collisions. The experimental verification of this peculiar breaking of universality for T-odd TMD distributions, exhibits an important test for the description of single-spin asymmetries within the framework of QCD. Its invalidation would have profound consequences for our understanding of high-energy reactions involving hadrons. The chiral-even Sivers distribution describes the correlation of the parton intrinsic motion with the nucleon spin, while the chiral-odd Boer-Mulders distribution relates this intrinsic parton motion with its own spin in an *un*polarised nucleon. Hence, the latter distribution has the striking peculiarity that it might give unexpected spin effects even in unpolarised processes.

---

(1) Naive time reversal involves the time reversal of three momenta and angular momenta without interchange of initial and final states.

TMD distributions are most successfully measured in SIDIS involving the spin and/or azimuthal angular dependence of the cross-section. As for the previous topics, the wide kinematic range and high luminosity achievable with an EIC will provide unique access to the flavour structure of TMDs and the gluon distributions. The especially interesting dependence on the transverse hadron momentum will be explored over a wide range for the first time. This will allow to test uniquely the proposed unified description of TMD observables at low and high transverse momenta (see chapter 2.2.5 in [1] and [10]).

2·3. *Some more exciting topics for an EIC.* – A fundamental feature of QCD is gluon saturation, which arises as a consequence of the fact that gluon distributions at a fixed Q^2 cannot grow rapidly indefinitely with decreasing x. The properties of matter in this novel saturation regime of strong colour fields in QCD is described by a saturation scale which grows both with decreasing x and with increasing nuclear size. Model estimates of this nuclear "oomph" give a saturation scale in a large nucleus at EIC energies to be of the same magnitude as the saturation scale in a proton at a TeV scale electron-proton collider; electron-nucleus collisions therefore provide an efficient method to explore saturation in QCD.

While the physics of an EIC is primarily motivated by the study of strong interactions, its physics case is strengthened by its potential to contribute to electroweak studies as well. Experience has shown that a new accelerator that pushes the frontiers either in energy, and/or luminosity and intensity, is of high interest for studies of electroweak physics. An EIC of high energy and luminosity, would provide excellent prospects for extractions of electroweak parameters—like, for example, the Weinberg angle—and their evolution with Q^2. Such measurements would complement the precise measurements at the Z-pole, and could be used in particular to search for new physics effects. The interested reader is referred to chapter 5 and 6 of [1].

3. – EIC realisations: Introduction

Worldwide there are four designs for an electron-ion collider under discussion, two in the US and two in Europe. In this lecture we will concentrate on the two options under consideration in the US as they are the by far most developed designs, which are also most suitable for making breakthroughs in the physics topics discussed at this school. Nevertheless, we will briefly outline the two EIC options under consideration in Europe at the end of this section. Obviously, if an EIC will be realised, only one of the options will be chosen.

The two designs for an EIC in the US base on existing accelerators at Brookhaven National Laboratory (BNL) and Jefferson Laboratory (JLab). At BNL, the addition of a new linear electron accelerator to the existing polarised proton and ion beams of the operating Relativistic Heavy Ion Collider (RHIC) is under design for the eRHIC solution [2]. At JLab, the MEIC/ELIC design employs new electron and ion storage rings together with the 12 GeV upgraded existing Continuous Electron Beams Accelerator Facility (CEBAF) [3].

The characteristics of these two designs are very similar as they aim at the same science objectives. The most important include:

- highly polarised ($> 70\%$) electron and nucleon beams,
- ion beams from deuterium to the heaviest nuclei—uranium or lead,
- centre-of-mass energies from about 20 GeV to about 150 GeV,
- maximum collision luminosity in the order of $\sim 10^{34}\,\mathrm{cm}^{-2}\,\mathrm{s}^{-1}$.

This anticipated high polarisation, wide kinematic range and high luminosity will allow for a precision imaging of the nucleon and for ground breaking new experiments to probe our understanding of QCD. Reaching this luminosity frontier for colliders requires novel concepts and significant R&D for cooling the proton and ion beams, for highly efficient electron linacs and high-intensity polarised electron sources. The development of a new technique, *coherent electron cooling*, is underway at BNL while conventional electron cooling is being pushed to high RF power at JLab. Energy recovery linear accelerators at high energy and intensity are a key technology for an EIC. Further, the eRHIC design demands an increase in the intensity produced by polarised electron sources of over an order of magnitude beyond what is available at present. Most of these challenges will be discussed in more detail below (see sect. **5**).

For the two designs, the possibility for having multiple interaction regions is foreseen and both plan staged realisations till reaching the highest centre-of-mass energies.

In Europe, two EIC options are under consideration. At CERN, the addition of an electron beam to the existing proton and heavy-ion beams of the LHC is under discussion for an EIC of very high energy. With an electron beam (either a linac or ring) of about 70 GeV, centre-of-mass energies of 1.4 TeV could be reached and a luminosity of about $10^{33}\,\mathrm{cm}^{-2}\,\mathrm{s}^{-1}$ is anticipated. This LHeC will not provide polarised beams and will therefore not address most of the topics discussed at this school.

Feasibility studies for an EIC at the *planned* Facility for Antiproton and Ion Research (FAIR) at GSI in Germany started recently. Under discussion is an Electron-Nucleon Collider (ENC), which could be realised by colliding electrons in a 3 GeV storage ring with the 15 GeV protons in the High Energy Storage Ring of FAIR. The centre-of-mass energy at an ENC would be of about 14 GeV with an expected luminosity of about

$10^{32}\,\mathrm{cm}^{-2}\,\mathrm{s}^{-1}$ [21]. This solution does not (yet) envisage variable beam energies and would hence be quite limited in its kinematic range. Also the luminosity would lay about an order of magnitude below the values expected for the designs at RHIC or JLab. However, the studies for an ENC at FAIR just started and the performance parameters are still very preliminary.

4. – EIC realisations: Baseline designs at BNL and JLab

We first describe the general layouts for the EIC designs at BNL and JLab. As novel high-luminosity colliders they face many technical challenges. In the subsequent sections we will give some more details about specific technical innovations and required R&D for the accelerator part, which might already be mentioned in the layout description. The general concept of detector design is outlined in sect. **7**.

4˙1. *eRHIC at BNL.* – The eRHIC design is based on one of RHICs existing hadron rings and a new multi-pass Energy-Recovery Linac (ERL) located inside the RHIC tunnel, as schematically shown in fig. 1. Using the ERL as the electron accelerator assures high luminosity in the 10^{33}–$10^{34}\,\mathrm{cm}^{-2}\,\mathrm{s}^{-1}$ range, and provides a natural staging of eRHIC.

Electrons from the polarised pre-injector will be accelerated to their top energy by passing six times through two superconducting radio frequency cavity (SRF) linacs. After colliding with the hadron beam, the electrons will be decelerated by the same linacs and dumped (see **5**˙2 for more details). The six-pass magnetic system with small-gap magnets will be installed from the start, while the electron energy will be staged from 5 GeV to 30 GeV stepwise by increasing the lengths of the SRF linacs.

The eRHIC design foresees electron-hadron collisions in up to three interaction regions, considering upgrades for the existing PHENIX and STAR detectors as well as a new dedicated eRHIC detector. The interaction region design involves a 10 mrad crab-crossing scheme (see subsect. **5**˙3), where the hadrons traverse the detector at a 10 mrad horizontal angle, while electrons go straight through. This configuration guaranties the absence of harmful high-energy X-rays from synchrotron radiation. The quadrupole needed for obtaining the high beam quality at the interaction region (like a small amplitude function of $\beta^* = 5\,\mathrm{cm}$, see subsect. **5**˙1) are at the limits of current accelerator technology. They require very high gradients and can be built only with modern superconducting technology.

eRHIC is designed to collide electron beams with energies from 5 GeV to 30 GeV with hadrons, *viz.*, either with polarised protons of energy between 100 GeV and 325 GeV or heavy ions with energies from 50 GeV to 130 GeV per nucleon. Accordingly, eRHIC will cover the centre-of-mass energy range from about 45 GeV to 200 GeV for polarised electron-proton collisions, and from about 32 GeV to 125 GeV for electron-heavy-ion collisions.

The projected luminosity for the various hadron beams at top energy is given in table I. Table II shows the projected luminosity for polarised electron-proton collisions for various different beam energies. The limitations on luminosity resulting from various

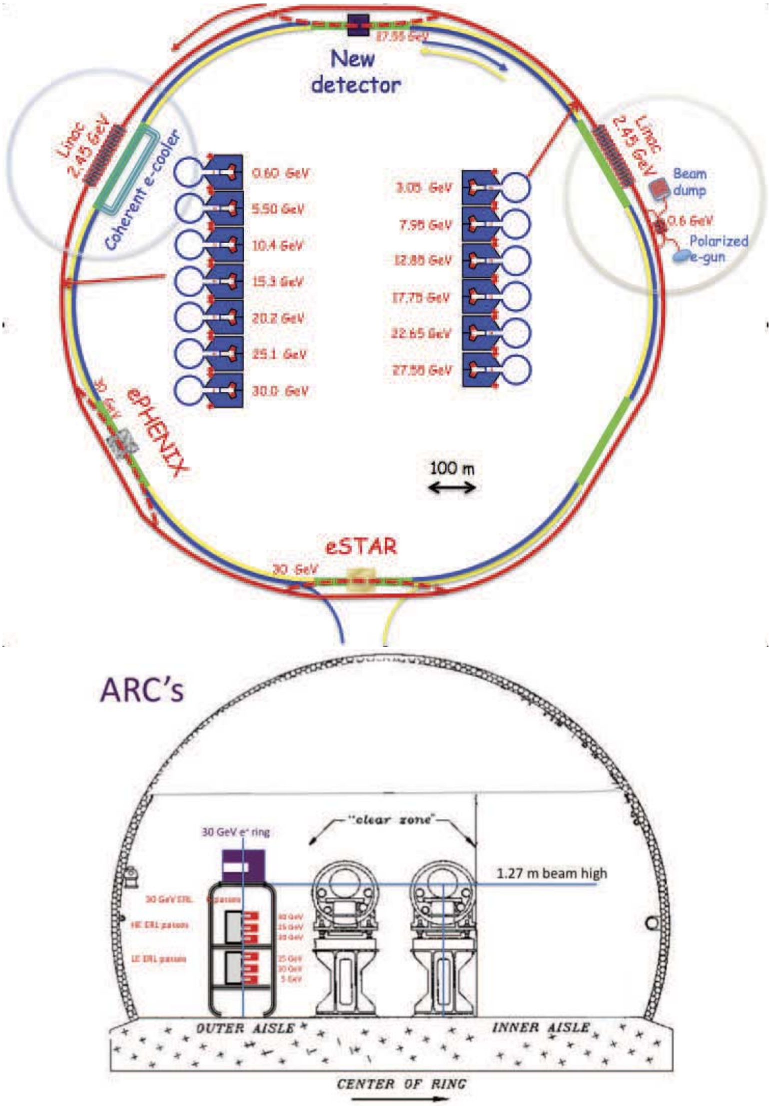

Fig. 1. – Layout of eRHIC (top) and location of the recirculation arcs in the RHIC tunnel (bottom). See text for details. The figure is taken from [1].

considerations are involved in these projections. The main trend is that eRHIC's luminosity does not depend on the energy of the electron beam (below 20 GeV) and reaches its maximum at the hadron beam's highest energy.

An additional major parameter describing eRHIC's overall performance is its expected *average* luminosity. Since the ERL provides fresh electron bunches for each circulation, the electron beam can be strongly abused, *i.e.* it can be heavily distorted during a

Table I. – *Projected eRHIC luminosity for various hadron beams at top energy. The table is taken from* [1].

Quantity (unit)	e	p	^{3}He	^{197}Au	^{238}U
Energy (GeV)	5–20	325	215	130	130
Centre-of-mass energy (GeV)		80–161	131	102	102
Number of bunches or distance between bunches	74 ns	166	166	166	166
Bunch intensity (nucleons) (10^{11})	0.24	2	3	3	3.15
Bunch charge (nC)	3.8	32	30	19	20
Beam current (mA)	50	420	390	250	260
Normalised emittance of hadrons 95% (mm · mrad)		1.2	1.2	1.2	1.2
Normalised emittance of electrons, rms (mm · mrad)		5.8–23	7–35	12–57	12–57
Polarisation (%)	80	70	70	none	none
RMS bunch length (cm)	0.2	4.9	8.3	8.3	8.3
Amplitude function β^* (cm)	5	5	5	5	5
Luminosity per nucleon ($10^{34}\,\mathrm{cm}^{-2}\,\mathrm{s}^{-1}$)		1.46	1.39	0.86	0.92

collision. Beam-beam effects, which play an important role for the beam performance, are then controlled on the hadron beam. The plan is to use coherent electron cooling for controlling the parameters of the hadron beam. Its lifetime will then be affected only by scattering on residual gas, and by burn-off in collisions with electrons. Hence, the hadron beam's luminosity lifetime could be as long as a few days, and, in the most likely

Table II. – *Projected eRHIC luminosity (in* $\mathrm{cm}^{-2}\,\mathrm{s}^{-1}$*) for polarised electron-proton collisions. The table is taken from* [1].

	Protons			
Electrons	100 GeV	130 GeV	250 GeV	325 GeV
5 GeV	$0.62 \cdot 10^{33}$	$1.4 \cdot 10^{33}$	$9.7 \cdot 10^{33}$	$15 \cdot 10^{33}$
10 GeV	$0.62 \cdot 10^{33}$	$1.4 \cdot 10^{33}$	$9.7 \cdot 10^{33}$	$15 \cdot 10^{33}$
20 GeV	$0.62 \cdot 10^{33}$	$1.4 \cdot 10^{33}$	$9.7 \cdot 10^{33}$	$1.5 \cdot 10^{33}$
30 GeV	$0.12 \cdot 10^{33}$	$0.3 \cdot 10^{33}$	$1.9 \cdot 10^{33}$	$3 \cdot 10^{33}$

scenario, the average delivered luminosity will be determined by the reliability of RHIC systems. An average luminosity of about 70% of the peak luminosity listed in table II can then be anticipated.

Many technical challenges have to be faced for the realisation of eRHIC, such as generating 50 mA of polarised electron current and accelerating the electrons using an energy-recovering linac, coherent electron cooling of the hadron beam and a crab-crossing scheme at the interaction point. We will discuss them in more detail in sect. **5**.

4˙2. *MEIC at JLab.* – The MEIC ("medium" EIC) design is based on a compact figure-8 shaped ring-ring concept using the existing high-luminosity Continuous Electron Beam Accelerator Facility (CEBAF) [5]. The novel *figure-8* ring design, shown schematically in fig. 2, is optimised for delivering and preserving high polarisation of ion beams for collisions at multiple interaction points.

The current design accommodates 3 GeV to 11 GeV electrons and up to 96 GeV protons or 48 (38) GeV/nucleus for light (heavy) ions, covering a medium centre-of-mass energy range of up to 65 GeV and reaching a luminosity of above $10^{34}\,\text{cm}^{-2}\,\text{s}^{-1}$. The design is upgradable (then called ELIC) to accommodate 20 GeV electrons and about 250 GeV proton energies at a late stage, with luminosities up to $10^{35}\,\text{cm}^{-2}\,\text{s}^{-1}$.

As a design concept, the high luminosity of MEIC is attained by utilising high bunch repetition rate, crab crossing colliding electron and ion beams with short bunch length and small transverse emittances, and strong final focusing at collision points (for details see **5**). To support such a conceptual design, extensive R&D programs have been established at Jefferson Lab, supplemented by several external collaborations.

The MEIC design calls for the construction of a green-field ion accelerator complex and two collider rings, one for electrons and the other for medium energy ions, as shown in fig. 2. There are four crossing points of these figure-8 collider rings foreseen. The two collider rings of identical circumferences are vertically stacked and the ion beams are transported into the plane of the electron ring via a vertical chicane, where horizontal crab crossings will be used to collide the two beams.

A large figure-8 ring, also drawn in fig. 2 (in grey), accommodates high-energy ion beams in a future energy upgrade. In that case, the compact medium-energy collider ring will act as another large booster. On the electron side, the 12 GeV upgraded CEBAF SRF linac will serve as a full-energy injector into the electron collider ring. It will be possible to continue the fixed-target program for the CEBAF whenever there is a need, since each filling of the electron ring is very short.

Two different types of interaction region (IR) designs are considered, one for a full-acceptance detector the other for a high-luminosity detector. The key difference of the IR designs is the space between the collision point and the location of the first final focusing quadrupole magnet.

The MEIC main parameters are summarised in table III for collisions of 60 GeV protons and 5 GeV electrons and two different detector designs: a full-acceptance (or high-luminosity) detector.

An essential component of the design is an electron cooling facility, which is required

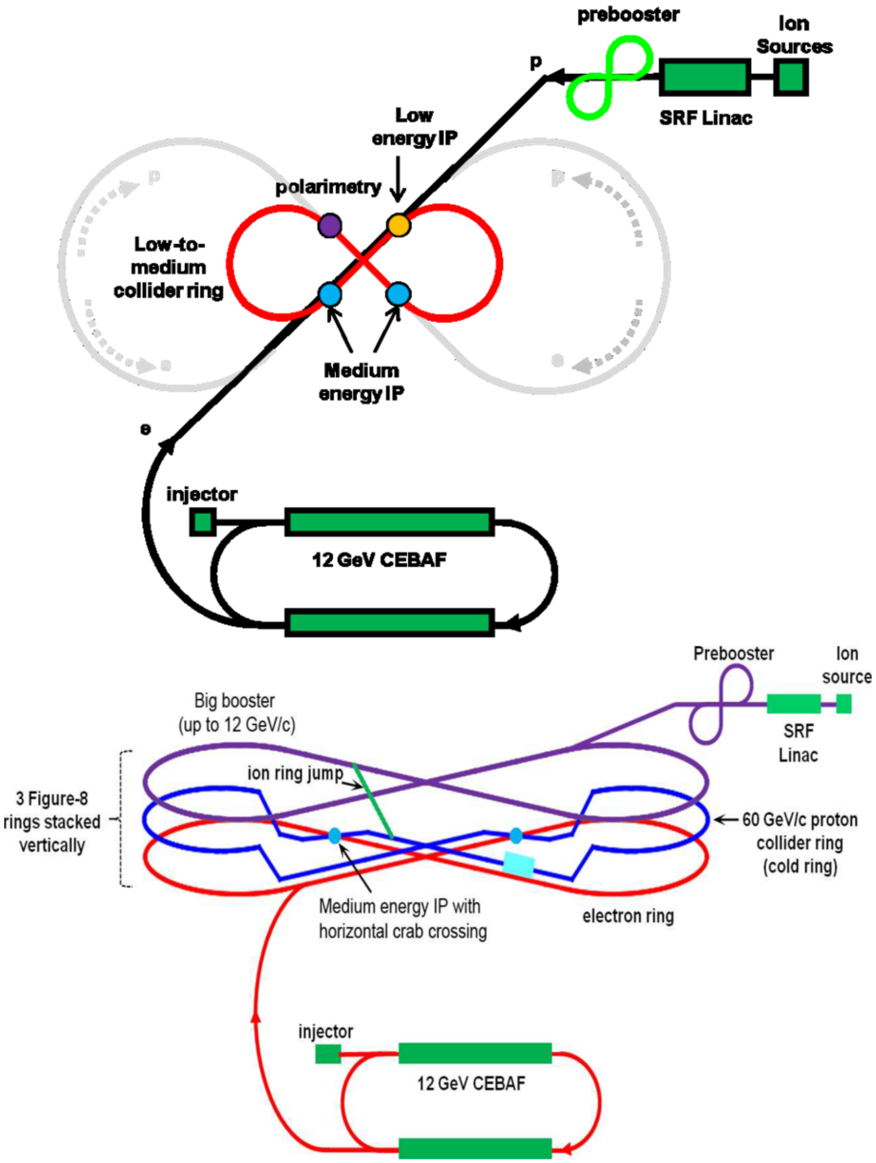
prebooster
Ion Sources
p
SRF Linac
Low energy IP
polarimetry
Low-to-medium collider ring
p
p
Medium energy IP
e
injector
12 GeV CEBAF
Prebooster
Ion source
Big booster (up to 12 GeV/c)
SRF Linac
ion ring jump
3 Figure-8 rings stacked vertically
60 GeV/c proton collider ring (cold ring)
Medium energy IP with horizontal crab crossing
electron ring
injector
12 GeV CEBAF

Fig. 2. – Layout and side view of the MEIC. See text for details. Figures taken from [1].

for reducing ion beam transverse emittance and along with strong radio-frequency bunching. This requirement will push standard electron-cooling technologies (see subsect. **5**˙4 for more details) to its limits. Most importantly, electron cooling will be continued during the collision mode to suppress the intra-beam scattering induced beam heating and emittance growth.

TABLE III. – *MEIC design parameters for the full-acceptance detector. Values for the high-luminosity detector are given in parentheses. The table is taken from* [1].

Quantity	Unit	p^- beam	e beam
Beam energy	GeV	60	5
Collision frequency	MHz	749	
Particles per bunch	10^{10}	0.416	2.5
Beam current	A	0.5	3
Polarisation	%	> 70	~ 80
Energy spread	10^{-3}	0.3	0.71
RMS bunch length	mm	10	7.5
Horizontal emittance (norm.)	μm	0.35	53.5
Vertical emittance (norm.)	μm	0.07	10.7
Horizontal amplitude function β^*	cm	10 (4)	10 (4)
Vertical amplitude function β^*	cm	2 (0.8)	2 (0.8)
Vertical beam-beam tuneshift		0.015	0.03
Laslett tuneshift		0.06	small
Distance from IP to 1^{st} final focusing quad	m	7 (4.5)	3.5
Luminosity per IP	$10^{33}\,\mathrm{cm}^{-2}\,\mathrm{s}^{-1}$	0.56 (1.42)	

The main design goal of MEIC ion complex is to create and accelerate polarised or unpolarised ion beams with appropriate time, spatial and phase space structure matching the electron beam in order to implement the high-luminosity concept. It is important to note that, while, on the one hand, the MEIC design requires bunch length and transverse emittances order of magnitude smaller than that of the conventional ion beams, on the other hand, due to a high bunch repetition rate, the MEIC ion bunch intensity is unusually low (at 4×10^9), approximately 50 times smaller than RHIC ion beam, thereby drastically easing the process of forming such ion beams and intensity-dependent collective beam instabilities.

For the MEIC as well, many technical challenges have to be faced for its realisation, such as for example electron cooling of the ion beams, crab crossing scheme at the interaction point and polarisation life time and spin tracking. We will discuss them in more detail in sect. **5**.

5. – EIC realisations: Challenges and R&D

Being at the frontier of accelerator design, innovative techniques will be employed for EIC realisations:

- – Energy Recovering Linacs (ERL).
- – Crab crossing of the colliding beams.
- – Coherent electron Cooling (CeC) of the hadron beam at RHIC.
- – Figure-8 shaped collider rings at JLab for polarisation preservation.

In the following we will briefly describe the basic features of these new techniques, which will be employed to reach unprecedented high luminosities at a collider. For a more exhaustive discussion the interested reader is referred to the literature.

5·1. *Luminosity at a collider.* – Here, we just want to give a brief overview about the main parameters which determine the luminosity achievable at a collider. More details can be found for example in [22].

The event rate R at a collider is proportional to the interaction cross-section and a factor of proportionality named *luminosity.* For a given interaction cross-section, high event rates can hence be achieved by maximising the luminosity. If two bunches containing n_1 and n_2 particles collide with frequency f, the luminosity is

$$L = f \frac{n_1 n_2}{4\pi\sigma_x\sigma_y}\,, \tag{1}$$

where σ_x and σ_y characterise the Gaussian transverse beam profiles in horizontal (bend) and vertical directions. The beam size is described by two quantities, the transverse emittance ϵ and the amplitude function β. While the transverse emittance is a beam quality parameter reflecting the process of bunch preparation, the amplitude function depends on the beam optics and is determined by the accelerator magnet configuration. Expressed in terms of the beam profile and amplitude function, the transverse emittance reads

$$\epsilon = \pi\sigma^2/\beta\,. \tag{2}$$

Of particular importance is the value of the amplitude function at the interaction point, β^*, which should be as small as possible. With these quantities, eq. (1) becomes

$$L = f \frac{n_1 n_2}{4\sqrt{\epsilon_x\beta_x^*\epsilon_y\beta_y^*}}\,. \tag{3}$$

Thus, in order to achieve high luminosity one has to prepare high population bunches of low emittance, collide them with high frequency at locations where the beam optics provides as low values of the amplitude functions as possible.

Typical values of the amplitude function β^* for the hadron beam are [22] Tevatron: 0.28 m, HERA: 0.18 m and RHIC: 0.8 m, while for the EIC the eRHIC design aims for $\beta^* = 0.05$ m and MEIC for $\beta^* = 0.02$ m.

5·2. *Energy recovering linacs.* – Energy recovering linacs (ERL) hold the promise of becoming the future backbone of the modern accelerator facilities. They combine the efficiency advantage of storage rings with the improved beam quality achievable in a linac.

ERLs were first developed and studied as a new type of synchrotron radiation machine, based on a superconducting linac and a one-turn return arc (like a storage ring), at Cornell University and at JLab [23, 24] for producing brilliant X-ray beams.

We describe here just the basic principle of an ERL. A bright electron source injects electrons into a superconducting radio frequency (RF) cavity that accelerates electrons to full energy. They circulate around a magnetic return arc to the point of their end use, which might be an undulator to produce brilliant X-ray beams or the interaction region with protons or ions. The circumference of the arc is adjusted such that the path length of the electrons returning to the linac is 180 degrees out of accelerating phase. Thus these electrons, passing again through the RF cavity, are now decelerated, giving up their energy to the cavity, and are then directed to a beam dump. Subsequently this energy is available for the acceleration of another bunch of electrons. Each electron makes one trip around the arc and its energy is recycled in the main linac, hence the name, Energy Recovery Linac.

Because the energy of the electrons is periodically taken from and then put back into the electro-magnetic fields in microwave cavities, these cavities must constantly be operated. The ERL will hence employ novel superconducting microwave cavities to produce hardly any heat when operated continuously at high fields. The energy of the linac can be increased by increasing the length (the number of cavities) of the ERL.

ERLs combine the efficiency advantage of storage rings with the improved beam quality achievable in a linac. In a storage ring, electrons are stored for hours in an equilibrium state, while in an ERL the energy of the electrons is stored and the electrons themselves are used only once. The space parameters of the electron beam are hence determined by the quality of its source and can reach a very high brilliance and intensity. These characteristics offer also a credible concept for electron cooling of high energy, colliding ion beams as considered for the eRHIC design.

Most interesting for the subject discussed here, ERLs might also provide polarised electron beams for collisions with protons and ions in an EIC. High polarization at about 80% is expected to be delivered by a high-current polarised electron source. As the electron beam is dumped after each collision, it can be disrupted much more during collision and potentially higher luminosities might be reached as a result of the higher allowed beam-beam tuneshift parameters (which limits the "allowed" distortion of the beams due to collision).

Before realisation for an EIC, substantial R&D is required. The challenges centre around three major topics: source brightness and intensity, emittance preservation, and high peak and average current effects in a superconducting RF environment. Several test facilities are under construction or commissioning to address these science and technology challenges, one of them at the BNL to test the specific needs for application at an EIC [25].

5·3. *Crab crossing.* – Colliding beams under a certain angle provides a simple and efficient way to quickly separate the two beams near an interaction point and to avoid undesired parasitic collisions, which induce emittance growth and beam life time deterioration. Such a scheme is especially important for beams with a high repetition rate, *i.e.* a small bunch spacing. In order to restore head-on collisions and hence to avoid luminosity loss, a so-called crab crossing scheme was suggested [26]. The basic idea is to deflect front and back of bunches in opposite ways, such yielding head-on collisions even with angle-crossed beams. The bunches are rotated through transverse deflections using crab cavities, an electromagnetic cavity providing a time varying magnetic field.

Crab crossing was successfully demonstrated at KEK-B e^+e^- collider in Japan [27], but still needs to be tested with highest luminosity. The application of crab crossing to hadron beams is a new challenging field [28].

One however needs to keep in mind that synchrotron radiation generated by bending the electron beam close to the interaction region can produce challenging backgrounds for detectors. This needs to be studied carefully.

5˙4. *Electron cooling.* – Electron cooling is a process to shrink the size, divergence, and energy spread of ion beams *without* removing particles from the beam. Since the number of particles remains unchanged and the space coordinates and their derivatives (angles) are reduced, the phase space occupied by the stored particles is compressed, which is equivalent to reducing the temperature of the beam.

Electron cooling, first proposed by Gersh Budker (INP, Novosibirsk) in 1966, is a proven method for relatively low hadron beam energies. It has been successfully applied at Fermilab also to very high energetic proton (and antiproton) beams [29].

Basically, electron cooling works as follows: the velocity of the electrons is made equal to the average velocity of the ions. The ions undergo Coulomb scattering in the electron gas and lose energy, which is transferred from the ions to the co-streaming electrons until some thermal equilibrium is attained. To be efficient, the electron beam must contain many more particles than the ion beam, requiring the development of a high-current electron system. This scheme is schematically shown in fig. 3 for application planned at the MEIC. It is based on an ERL and and an circulator ring. A high-charge electron bunch from a photo-cathode is accelerated in a SRF ERL to required energy of 10 to 50 MeV and then sent to a specially designed circulator cooler ring, with optics matching the cooling channel for cooling of a proton or ion bunch. An individual bunch circulates a large number of revolutions (up to a few hundred) in the ring before its quality is degraded by intra- and inter-beam scatterings, after which it returns to the same SRF linac for energy recovery.

Coherent Electron Cooling is an exciting concept towards cooling ion beams through amplification of charge distributions in electron beams making use of the free-electron laser (FEL) amplification mechanism [30]. Basically it works as schematically shown in fig. 4: the hadron beam passes a *modulator* where it is co-streaming with an electron beam of same velocity. Each ion induces a density modulation in the electron beam that is amplified in a high-gain FEL. In the *kicker* the hadrons interact with the electric field of the electron beam that they have induced, and receive energy kicks toward their central energy, such reducing their energy spread.

This method promises extremely fast cooling virtually independent of energy of the ions. Recently, the performance of ERLs promises the use of the FEL amplification mechanism to realise Coherent Electron Cooling at high ion energies.

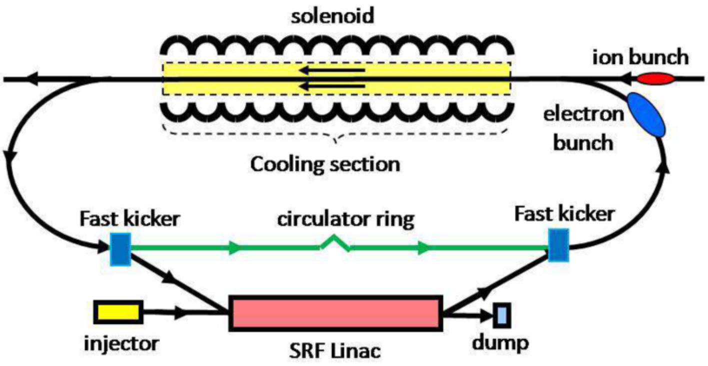

Fig. 3. – Schematic of electron cooling for the MEIC. See text for details. The figure is taken from [1].

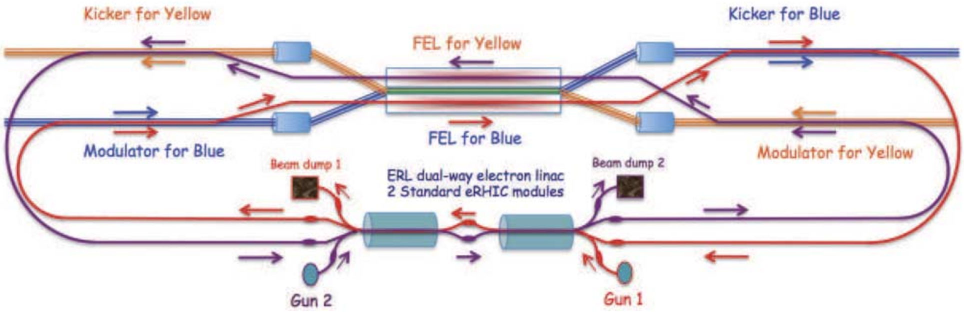

Fig. 4. – Schematic of *coherent* electron cooling for eRHIC. See text for details. The figure is taken from [1].

5·5. *Ring design.* – The MEIC's figure-8 shape in all rings is an optimal solution to preserve full polarisation of light ion beams by avoiding spin resonances during acceleration in multiple booster and collider rings.

It is also the only practical way to accelerate polarised deuterons and to arrange for longitudinal spin polarisation at the interaction point, which is impossible with conventional methods like siberian snakes and spin rotators (see [31]) due to the deuterons small $g-2$ value. The figure-8 layout allows for energy independence of the spin tune, as well as the transverse polarisation of deuterons.

6. – EIC realisations: Kinematics and requirements

The physics program of an EIC is very broad and covers several different physics processes, as outlined in the introduction. In particular, it spans over a wide range in centre-of-mass energy provided by different combinations of both beam energy and particle species. This imposes several challenges on the design of a detector and the interaction region.

The physics processes that define the cornerstones for the requirements due to the involved kinematics are

- inclusive measurements ($ep/A \to e{+}X$) requiring detection of the scattered electron and/or the full scattered hadronic debris with high precision;
- semi-inclusive processes ($ep/A \to e + h + X$) requiring the detection and identification of at least one hadron in coincidence with the scattered electron;
- exclusive processes ($ep/A \to e + N/A + \gamma/h$) requiring the detection of all particles in the reaction.

Generally, for all electron-hadron beam energy combinations, the scattered electron goes into the direction of the original electron beam for low Q^2 and more and more into a central detector acceptance for higher Q^2. For a fixed hadron beam energy the electron scattering angle becomes smaller at a fixed Q^2 with increasing electron energy.

We define here the beam directions along z with the hadron beam in the positive z direction (forward region) and the electron beam in negative z direction (backward region).

6˙1. *Kinematic range in x and Q^2.* – Figure 5 shows the x-Q^2 range for two different centre-of-mass energies, demonstrating that a wide kinematic range can be accessed by varying the beam energies.

The correlation between x and Q^2 for a collider environment is generally weaker than for fixed-target experiments. Nonetheless, it becomes stronger for small scattering angles or corresponding small inelasticity y, and momentum and scattering angle resolution for the scattered electron become an issue. At the HERA collider the degradation in resolution started at about $y = 0.1$. To circumvent this problem, HERA reconstructed the electron kinematics from the hadronic final state and has reached successful measurements down to y of 0.005.

In general, one would like to access as large a range in Q^2 at fixed x as possible for a given beam energy combination, and reach as low y as possible. This requirement directly implies two important considerations for the detector design:

- good hadronic coverage in the forward direction,
- low noise and/or good noise suppression algorithms in the hadronic calorimeter to allow for hadron detection at low momenta.

For polarisation observables, however, one should keep in mind that low values of y translate into a low so-called depolarisation factor. The depolarisation factor corrects for the polarisation transfer from the electron to the virtual photon, and is small at low y. Observables involving electron polarisation are inverse proportional to this factor, which reduces the effective polarised luminosity and increases the uncertainties of the measured quantities at low y. For fixed centre-of-mass energy, the x-Q^2 range for precision measurements of observables involving electron polarisation will hence be reduced as compared to single-hadron polarisation observables or unpolarised ones.

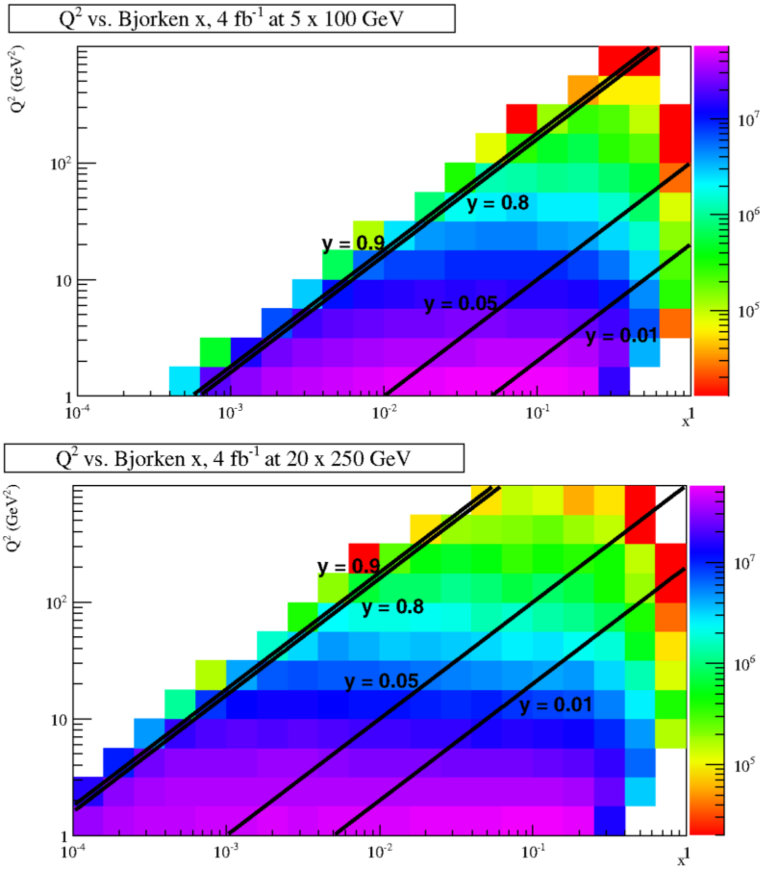

Fig. 5. – The x-Q^2 range for centre-of-mass energies of 45 GeV (top) and 140 GeV (bottom). The black lines indicate different y cuts placed on the electron kinematics (see text). The figures are taken from [1].

6˙2. *Particle identification.* – Kinematic variables like x, Q^2 or y are usually calculated involving the measured momentum and polar angle of the scattered electron. Typically, electron rates are a factor 10–100 smaller than photon and charged hadron rates, which places the requirement for good electron identification capabilities.

Hadron identification over the full kinematic range is also indispensable for the physics program of an EIC. For lower electron beam energies, hadrons originating from semi-inclusive processes are scattered predominantly in the forward (ion) direction. With increasing electron beam energy, the hadrons increasingly populate the central region of the detector, and at the highest electron energies, hadrons are even largely produced going backward (*i.e.* in the lepton beam direction). Hence, to be able to distinguish electrons and hadrons, and to identify the different hadron types over a wide momentum and angular range an EIC detector needs to have detectors capable of good particle identification in the forward, central and backward direction, *i.e.* everywhere.

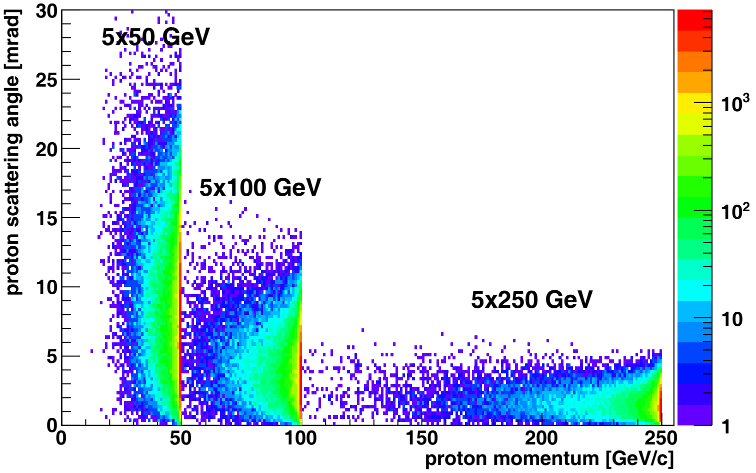

Fig. 6. – Scattered proton momentum *vs.* scattering angle in the laboratory frame for DVCS events with different beam energy combinations. The figures are taken from [1].

6˙3. *Vertex detectors.* – There is specific interest in detecting events with heavy quarks (charm or bottom). For many observables it is sufficient to tag the charm and the bottom quark content via the detection of additional leptons (electron, positron, muons) to the scattered electron. The leptons from charmed mesons can be identified via a displaced vertex. This can be achieved by integrating a high-resolution vertex detector into the detector design. For measurements of the charmed (bottom) fragmentation functions, or to study medium modifications of heavy quarks in the nuclear environment, at least one of the charmed (bottom) mesons must be completely reconstructed to have access to the kinematics of the parton. This requires, in addition to measuring the displaced vertex, good particle identification in order to reconstruct the meson via its hadronic decay products.

6˙4. *The very forward (backward) region.* – The most challenging constraints on the detector design for the very small angle region comes from exclusive processes and the need to detect the remaining hadronic state in addition to the exclusively produced photon or meson (pair). For the interpretation of the observables it is extremely important that the scattered nucleon (or nucleus) remains intact during the reaction.

Figure 6 illustrates exemplary the kinematic requirements using deeply virtual compton scattering ($ep \to e\gamma p$), showing the scattered proton momentum *versus* its scattering angle for three different beam energy combinations. In all cases, one obtains small to extremely small scattering angles, extending to or completely within the 0.5° angular detector cutoff often used to ensure clearance of any detector element from the beam. Because of this, the detection of these protons, or more general recoil baryons, is intimately connected with the exact interaction region design.

Detection of the intact nucleus following an exclusive reaction in eA collisions is even more complicated and the strategy to ensure exclusive production on a nucleus is to veto nuclear breakup, by detecting the neutrons from incoherent events.

7. – EIC realisations: Detector concepts

We give here only the general detector concept based on the discussion of key physics processes and their kinematic conditions (see sect. **6**). More details can be found in chapter 6 and 7 of [1]. Optimised detectors are essential to carry out the broad physics program planned at an EIC. Their design is intimately connected to both the envisaged physics program and the layout of the accelerator interaction regions through the location of magnets, configuration of crossing angles, and available space. A particular challenge is to detect forward-going scattered protons from exclusive reactions.

An EIC detector will certainly include a large central detector likely containing a solenoidal magnetic field (of order of 4 T); tracking devices for momentum and angular resolution; electromagnetic and hadronic calorimetry; particle identification involving Cherenkov detectors, and vertex detectors. Furthermore, detectors in the (very) forward and backward directions will be required to augment a large central detector. They should comprise particle identification, calorimetry (both electron and hadron) and possibly magnetic field.

With multiple interaction regions, it may be more advantageous to consider different, more specialised detectors at the various interaction regions, like for example: forward/backward *vs.* central or high luminosity *vs.* full coverage.

Figure 7 presents a global outline of a possible EIC detector layout and its integration in the interaction region, here exemplary chosen for the MEIC solution. The general components would be very similar for a detector at eRHIC (see chapter 7.3.3 in [1]). The detector concepts include a central solenoid and forward dipole, extensive low mass tracking for low x and good particle ID in the central and forward/backward regions. In fig. 7, the central detector comprises the components operating within the solenoid. Detection of low-Q^2 electrons and the solution to measure forward and ultra-forward (in the ion direction) going hadronic or nuclear fragments (including neutron detection) is indicated in the upper part of fig. 7, too. This concept presents an essentially 100% full acceptance detector.

Due to the asymmetric beam energies, the interaction point will be offset towards the electron side to allow for more distance for tracking of high-momentum hadrons produced at small angles and for efficient detection of the scattered electron.

The central detector should have an equal angular coverage for tracking and electromagnetic calorimetry. The details of particle identification will develop with time, but should provide excellent electron/hadron separation and hadron identification over the full momentum range.

For both concepts (eRHIC and MEIC), the electron beam traverses the centre region without any bending, while the proton/ion beam traverses at the crab crossing angle. This configuration minimises harmful background from synchrotron radiation.

Minimising the effects of systematic uncertainties is an important aspect of detector

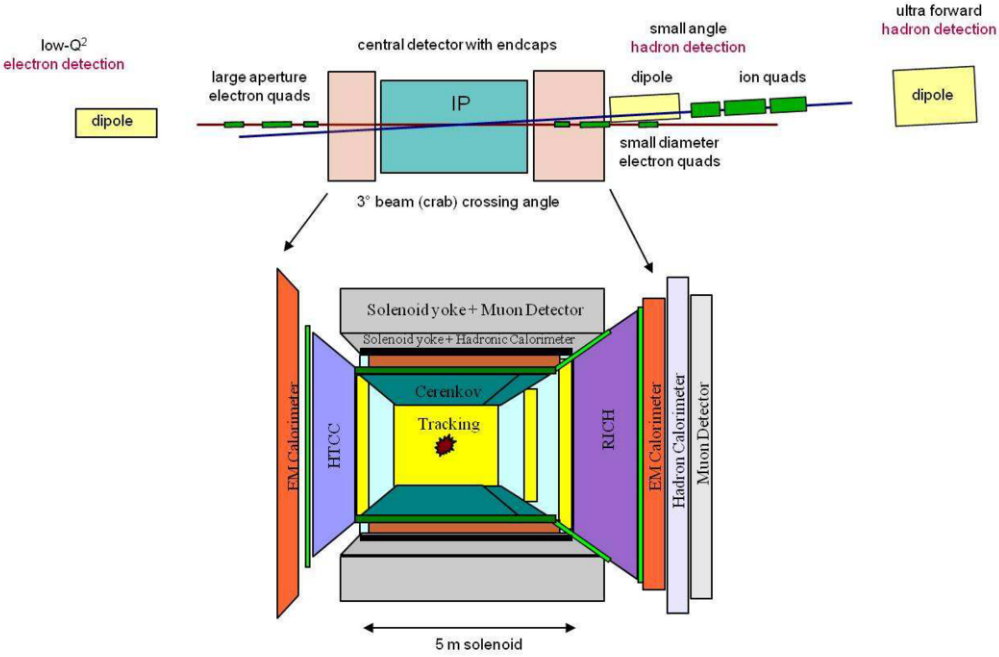

Fig. 7. – Interaction region and central detector layout, and its placement in the general integrated detector and interaction region for MEIC. The hadron beam comes from the left and the lepton beam from the right. Forward direction is defined in the ion beam direction. The figures are taken from [1].

design. Absolute and relative luminosity determination is a key to extracting important observables, for instance small polarisation asymmetries. Measurement of the polarisation of electron and hadron beams has a high priority. As with the accelerator, R&D for EIC detectors will be essential.

8. – Conclusions

A polarised Electron-Ion Collider is an exciting new projected which has attracted many enthusiastic colleagues and is currently under intense conceptual preparation in the US and Europe. Such a new facility, if being built, will deliver first data most likely from the mid twenties on. In the meantime, we will gain new insides into the questions discussed at this school mainly for the valence quark kinematic region. This leaves a vast field of *terra incognita* for this new project and a stimulating atmosphere for preparation of this new era in “spin physics”.

It would be a great success of this school if somebody of you feels invited to join our activities towards the realisation of an EIC!

* * *

I like to acknowledge all colleagues, who contributed to the review about the "science case of an EIC" [1], which was the main source of information for preparing these lecture notes. It is a pleasure to thank all participants and the organisers for this inspiring school and good time in Varenna.

REFERENCES

[1] Boer D., Diehl M., Milner R., Venugopalan R., Vogelsang W. *et al.*, *Gluons and the quark sea at high energies: Distributions, polarization, tomography*, INT-PUB-11-034, BNL-96164-2011, JLAB-THY-11-1373; arXiv:1108.1713 (2011).
[2] The Electron Ion Collider at BNL, `https://wiki.bnl.gov/eic/index.php/`.
[3] The Electron Ion Collider at JLab, `http://www.jlab.org/meic`.
[4] Stratman M., Pertubative QCD: parton distributions, factorization and all that; lecture at this school.
[5] Kuhn S., this volume, p. 1.
[6] Mallot G., this volume, p. 271.
[7] Burkert V., this volume, p. 303.
[8] Ashman J. *et al.*, *Phys. Lett. B*, **206** (1988) 364.
[9] Mulders P., this volume, p. 33.
[10] Bacchetta A., this volume, p. 107.
[11] Prokudin A., this volume, p. 157.
[12] Pasquini B. and Lorcè C., this volume, p. 197.
[13] Diehl M., this volume, p. 81.
[14] Guidal M., this volume, p. 245.
[15] Vanderhaegen M., Form factors and GPDs; lecture at this school.
[16] Ji X.-D., *Phys. Rev. Lett.*, **78** (1997) 610.
[17] Collins J. C., *Nucl. Phys. B*, **396** (1993) 161.
[18] Brodsky S. J., Hwang D. S. and Schmidt I., *Phys. Lett. B*, **530** (2002) 99.
[19] Collins J. C., *Phys. Lett. B*, **536** (2002) 43.
[20] Belitsky A. V., Ji X. and Yuan F., *Nucl. Phys. B*, **656** (2003) 165.
[21] Lehrach A., Aulenbacher K., Boldt O., Heine R., Hillert W. *et al.*, *J. Phys. Conf. Ser.*, **295** (2011) 012156.
[22] Accelerator physics of colliders, `http://pdg.lbl.gov/2006/reviews/accelrpp.ps`.
[23] Energy Recovery Linac, `http://erl.chess.cornell.edu/`.
[24] Merminga N. L., *Conf. Proc. C*, **070625** (2007) 22.
[25] Litvinenko V., Beavis D. R., Ben-Zvi I., Blaskiewicz M., Burrill A. *et al.*, *Conf. Proc. C*, **0806233** (2008) MOPC057.
[26] Palmer R., *eConfC*, **8806271** (1988) 613.
[27] Funakoshi Y., Abe T., Akai K., Akemoto M., Akiyama A. *et al.*, *Conf. Proc. C*, **0806233** (2008) WEXG01.
[28] Kim H. and Sen T., *Conf. Proc. C*, **100523** (2010) 4740, *1st International Particle Accelerator Conference: IPAC'10, 23-28 May 2010, Kyoto, Japan* p. 3.
[29] The electron cooling mission, `http://www-ecool.fnal.gov`.
[30] Litvinenko V. N. and Derbenev Y. S., *Phys. Rev. Lett.*, **102** (2009) 114801.
[31] Aschenauer E., Spin physics at RHIC; lecture at this school.

This page intentionally left blank

Proceedings of the International School of Physics "Enrico Fermi"
Course CLXXX "Three-Dimensional Partonic Structure of the Nucleon"
edited by M. Anselmino, H. Avakian, D. Hasch and P. Schweitzer
(IOS, Amsterdam; SIF, Bologna)
DOI 10.3254/978-1-61499-197-7-357

Fermi problem

P. Schweitzer

Departement of Physics, University of Connecticut - Storrs, CT 06269, USA

Summary. — The participants of the School were assigned a "Fermi problem". An analysis of the results is presented, and future developments are outlined.

1. – Introduction

Enrico Fermi was not only one of the greatest physicists of the 20th century [1]. He was also a brilliant and inspiring teacher. His lectures were notable for their clarity, and their focus on the essential. Several of his lecture notes became popular text books some of which are still in print.

"Fermi possessed a sure way of starting off in the right direction, of setting aside the irrelevancies, of seizing all the essentials and proceeding to the core of the matter" [2]. He once said about himself: "I can calculate anything in physics within a factor 2 on a few sheets: to get the numerical factor in front of the formula right might well take a physicist a year to calculate, but I am not interested in that" [3]. In fact, an often told story is how Fermi dropped small pieces of paper when the air blast of the first atomic bomb explosion (Trinity test in New Mexico on July 16, 1945) arrived. From the distance the paper pieces traveled he estimated the power of the explosion. His quick estimate was confirmed within factor 2 after days of complex data analysis [4].

Perhaps this skill is what Fermi wanted to teach his students, when he assigned the problems that are nowadays known as "Fermi problems", where he would ask to estimate

© Società Italiana di Fisica

TABLE I. – *The estimated time for the Italian population to drink the water of the Como lake.*

time	# estimates	time	# estimates	time	# estimates
100 days	1	341 years	1	960 years	2
100 years	1	350 years	1	1000 years	4
150 years	1	400 years	1	1250 years	1
158 years	1	460 years	1	1300 years	1
180 years	1	500 years	3	1379 years	1
300 years	1	910 years	1	6850 years	1

the answer, often on the basis of scarce or no data. A famous Fermi problem is to estimate the number of piano tuners in Chicago. The solution involves a chain of educated guesses. The assumption is that, although in each step one may overestimate or underestimate, it is unlikely to overestimate (or underestimate) each time. There is a good chance that the errors cancel, if the estimates are made without bias. To tackle physics problems in this way requires a deep understanding of the laws of nature, which Fermi certainly had. An insightful biography about Fermi was written by Emilio Segré [5].

The participants of the School (students, teachers, organizers, guests) were assigned the problem described in sect. **2**. The author is not aware whether Enrico Fermi ever assigned a problem of this type to his students. Maybe he would have liked this one.

2. – The problem

The Fermi problem assigned to the participants of the school was the following.

> *Let us assume that all Italians would drink water only from the Como Lake. After how much time would the lake be empty?*

The participants were also provided a small map (copied from a local tourist guide) of the Como lake with, among others, the following information about the lake:

surface:	$145.91\,\mathrm{km}^2$
minimal width:	$650\,\mathrm{m}$
maximal width:	$4.3\,\mathrm{km}$
maximal length:	$46\,\mathrm{km}$
maximal depth:	$414\,\mathrm{m}$

TABLE II. – *Binning of the raw data from table I.*

time interval	# estimates	time interval	# estimates	time interval	# estimates
0–1 years	1	300–500 years	8	1200–1400 years	3
100–200 years	4	900–1100 years	7	6800–7000 years	1

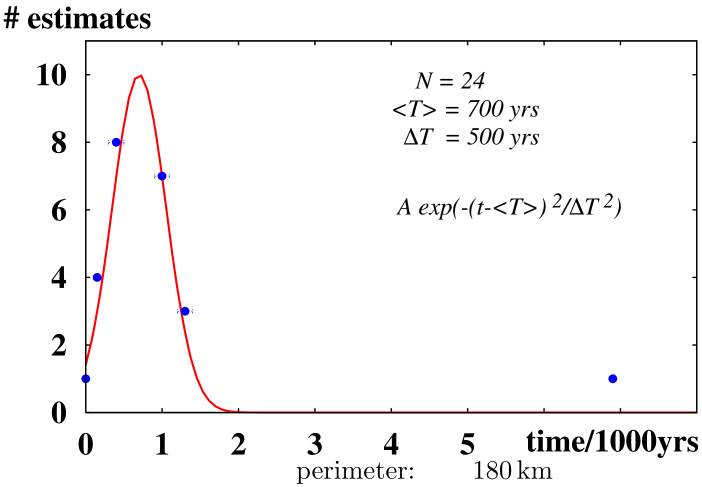

Fig. 1. – The description of the binned data from table II by a Gaussian.

3. – Analysis of the results

24 solutions were returned, which was considered satisfactory in view of the fact that the homework was assigned over the weekend. The raw data are shown in table I. The participants estimated times between 100 days and 6850 years. The most frequent estimates were the round numbers 500 and 1000 years.

The raw data was binned as shown in table II. Binning is not always recommended by experts, since it may introduce a bias [6]. The binned data is shown in fig. 1. The

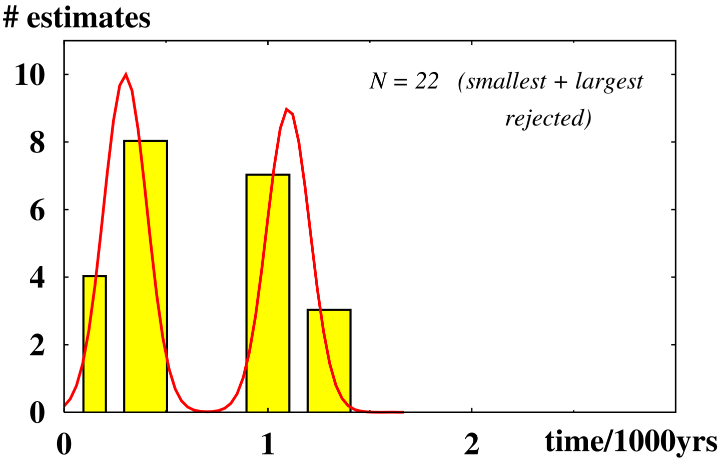

Fig. 2. – The description of the binned data from table II by two Gaussians.

binned data can be well described by a broad Gaussian around $\langle T\rangle \approx 700$ years with a width of $\Delta T \approx 500$ years. This result was confirmed by a precise analysis of unbinned data with the best fit $\langle T\rangle = 668.09$ years and 1σ deviation $\Delta T = 401.48$ years [6].

At this point one could conclude as follows. The participants of the School estimated that the Italian population would need about (700 ± 500) years to drink the water of the Como lake at a 1σ confidence level. However, one may also refine the analysis and look for possible substructures.

This was done in fig. 2, where the shortest and the longest estimated times were rejected in order to focus on the region between 100–1500 years. From this perspective the data hint at two possible signals of comparable strengths, which can be well described by Gaussians, one centered around $\langle T\rangle = 300$ years, the other around $\langle T\rangle = 1100$ years, each with a width of about $\Delta T = 150$ years. This may indicate possible social self-interactions within different subgroups of the participants. Several hypotheses were subsequently discussed at the School, although a general consensus was not achieved.

Summary

To summarize, the participants of the School estimated that the Italian population would drink the water of the Como lake in about (700 ± 500) years. However, the data indicate substructures within the participants, with one subgroup estimating a shorter time (300 ± 150) years, and the other subgroup a longer time (1100 ± 150) years. More data are needed in order to resolve the (social) substructures among the school participants. It is also vital to look for new observables, in order to go beyond the one-dimensional picture presented here. Future Fermi Schools in Varenna will help to resolve the situation.

* * *

It is a pleasure to thank the participants of the School for taking the time to solve the Fermi problem, and the many fruitful discussions in this and many other contexts.

REFERENCES

[1] The Nobel Prize in Physics 1938, Enrico Fermi, `http://www.nobelprize.org/nobel_prizes/physics/laureates/1938/`.
[2] ANDERSON H. L., Fermi's collaborator in the Manhattan Project, about Fermi in [3].
[3] BRETSCHER E. and COCKCROFT J. D., *Enrico Fermi. 1901-1954*, *Biogr. Mems Fell. R. Soc.*, **1** (1955) 68, doi: 10.1098/rsbm.1955.0006.
[4] Enrico Fermi's own narrative, quoted on the "History Pages" of the Los Alamos National Lab, `http://www.lanl.gov/history/story.php?story_id=13`.
[5] SEGRÈ E., *Enrico Fermi, Physicist* (University of Chicago Press) 1995.
[6] JOOSTEN S., private communication.

International School of Physics "Enrico Fermi"

Villa Monastero, Varenna

Course CLXXX

28 June – 8 July 2011

"Three-Dimensional Partonic Structure of the Nucleon"

Directors

Mauro ANSELMINO
Dipartimento di Fisica Teorica
Università di Torino
Via P. Giuria 1
10125 Torino
Italy
tel: +39 011 6707227
fax: +39 011 6707214
`mauro.anselmino@to.infn.it`

Harut AVAKIAN
Jefferson Lab
12000 Jefferson Avenue
Newport News VA 23606
USA
tel: +1 757 2697764
fax: +1 757 269-5800
`avakian@jlab.org`

Scientific Secretaries

Delia HASCH
INFN
Laboratori Nazionali di Frascati
Via E. Fermi 40
00044 Frascati (RM)
Italy
tel: +39 06 94032310
fax: +39 06 94032559
`delia.hasch@lnf.infn.it`

Peter SCHWEITZER
Department of Physics
University of Connecticut
U-3046
2152 Hillside Road
Storrs CT 06269
USA
tel: +1-860 486 0443
fax: +1 860 486 3346
`peter.schweitzer@phys.uconn.edu`

© Società Italiana di Fisica

Lecturers

Elke ASCHENAUER
Physics Department
Brookhaven National Laboratory
20 Pennsylvania Avenue
Upton NY 11973
USA
tel: +1 631 344 4769 +1
fax: +1 631 344 1334
`elke@bnl.gov`

Alessandro BACCHETTA
Dipartimento di Fisica Nucleare e Teorica
Università di Pavia
Via Bassi 6
27100 Pavia
Italy
tel: +39 0382 987449
fax: +39 0382 526938
`alessandro.bacchetta@pv.infn.it`

Markus DIEHL
Deutsches Elektronen-Synchroton DESY
Notkestraße 85
22603 Hamburg
Germany
tel: +49 40 8998 3447
fax: +49 40 8998 2777
`markus.diehl@desy.de`

Piet MULDERS
Department of Physics and Astronomy
Faculty of Sciences
Vrije Universiteit Amsterdam
De Boelelaan 1081
1081 HV Amsterdam
The Netherlands
tel: +31 20 598 7863
fax: +31 20 5987992
`mulders@few.vu.nl`

Barbara PASQUINI
Dipartimento di Fisica Nucleare e Teorica
Università di Pavia
Via Bassi 6
27100 Pavia
Italy
tel: +39 0382 987450
fax: +39 0382 526938
`Barbara.Pasquini@pv.infn.it`

Armine ROSTOMYAN
Deutsches Elektronen-Synchroton DESY
Notkestraße 85
22603 Hamburg
Germany
tel: +49 40 8998 3445
fax: +49 40 8998 4034
`Armine.Rostomyan@desy.de`

Marco STRATMANN
Physics Department
Brookhaven National Laboratory
Upton NY 11973
USA
tel: +1 631 344 8157
fax: +1 631 344 7561
`marco@ribf.riken.jp`
`marco@bnl.gov`

Seminar Speakers

Volker BURKERT
Jefferson Lab
12000 Jefferson Avenue
Newport News VA 23606
USA
`burkert@jlab.org`

Michel GUIDAL
Institut de Physique Nucléaire d'Orsay
Université Paris-Sud
15 rue Georges Clémenceau
F-91406 Orsay
France
`guidal@ipno.in2p3.fr`

Philip HAEGLER
Physik Department der TU München
James-Franck-Str. 1
D-85747 Garching
Germany
tel: +49 89 289 14403
`haegler@p2h.de`

Sebastian KUHN
Old Dominion University
5115 Hampton Boulevard
Norfolk VA 23529
USA
`skuhn@odu.edu`

Gerhard MALLOT
CERN
CH-1211
Geneva 23
Switzerland
tel: +41 22 767 6423
fax: +41 22 766 8591
`gerhard.mallot@cern.ch`

Alexei PROKUDIN
Jefferson Lab
12000 Jefferson Avenue
Newport News
VA 23606
USA
tel: +1 757 269 5385
fax: +1 757 269 7002
`prokudin@jlab.org`

Marc VANDERHAEGEN
Institut für Kernphysik
Johannes Gutenberg-Universität
Johann-Joachim-Becher-Weg 45
D-55099 Mainz
Germany
tel: +49 6131 39 23695
fax: +49 6131 39-25474
`marcvdh@kph.uni-mainz.de`

Students

Mher AGHASYAN
INFN
Laboratori Nazionali di Frascati
Via E. Fermi 40
00044 Frascati (RM)
Italy
tel: +39 06 9403
fax: +39 06 9403 2559
`Mher.Aghasyan@lnf.infn.it`

Tobias BERANEK
University Mainz
Institute of Nuclear Physics
J.-J.-Becher Weg 45
55128 Mainz
Germany
tel: +49 6131 3927133
`beranek@kph.uni-mainz.de`

Susanna BERTELLI
INFN, Sezione di Ferrara
Via Saragat 1, ed. C
44122 Ferrara
Italy
tel: +39 3484742051
`bertelli@fe.infn.it`

Jennifer BOWLES
University of Glasgow
Nuclear Physics
University Ave G12 8QQ
Glasgow G12 8QQ
UK
tel: +44 141 330 6398
`j.bowles@physics.gla.ac.uk`

Irina BRODSKI
University Giessen
II Physics Institute
H.-Buff-Ring 16
35392 Giessen
Germany
tel: +49-641-9719316
`Irina.Brodski@math.uni-giessen.de`

Martinus BUFFING
VU University
Department of Physics
De Boelelaan 1081
1081 Hv Amsterdam
The Netherlands
tel: +312 05987892
`m.g.a.buffing@vu.nl`

Jan CEPILA
FNSPE CTU
Prague, Brehova, 7
11519 Praha 1
Czech
tel: +42 0608233105
`jan.cepila@fjfi.cvut.cz`

Nicolas DU FRESNE VON HOHENESCHE
University Mainz
Institute of Nuclear Physics
J.-J.-Becher Weg 45
55128 Mainz
Germany
tel: +41 22 7676538
`dufresne@cern.ch`

Carmine ELIA
INFN, Sezione di Trieste
Via Valerio 1
34126 Trieste
Italy
tel: +39 040 5583385
`carmine.elia@ts.infn.it`

Ilnur GABDRAKHMANOV
JINR
Sector 6, Cab.014
Joliot Curie 6
Dubna
Russia
tel: +7 49621 63461
`ilnur@theor.jinr.ru`

Eranuhi GHANDILYAN
Laboratory of Experimental Physics
Yerevan Physics Institute
Alikhanyan brothers street
Yerevan
Armenia
tel: +374 10 355340
`gh_eranuhi@yahoo.com`

Wes GOHN
University of Connecticut
Department of Physics
2152 Hillside Rd.
Storrs CT 06269
USA
tel: +1 860 486 5539
`gohn@jlab.org`

Mayya GOLEMBIOVSKAYA
DESY
Notkestr. 85
22607 Hamburg
Germany
tel: +49 17638525251
`mayya@mail.desy.de`

Baptiste GUEGAN
IPNO
Bat 100
91406 Orsay, Cedex
France
tel: +33 0169155091
guegan@ipno.in2p3.fr

Julia GUTTMANN
University Mainz
Institute of Nuclear Physics
J.-J.-Becher Weg 45
55128 Mainz
Germany
guttmann@kph.uni-mainz.de

Sylvester JOOSTEN
University of Illinois
Loomis Lab of Physics
1110 West green street
Urbana IL 61801
USA
tel: +1 217 333 3190
sylvester@physics.illinois.edu

Hoyoung KANG
Seoul National University
Department of Physics and Astronomy
599 Gwanak-ro
Seoul 151-747
Korea
tel: +82 2 880 6587
hykang@jlab.org

James KEY
University of New Mexico
Albuquerque 87131
USA
tel: +1 205 401 1340
keyaaron@unm.edu

Vardan KHACHATRYAN
ANSL
Alkhanyan Brothers St. 2
0036 Yerevan
Armenia
vardan.khachatryan@cern.ch

Viachaslau KHANDRAMAI
ICAS
Gomel State technical University
October Ave 48
246746 Gomel
Belarus
tel: +375 232 483349
v.khandramai@gmail.com

Suman KOIRALA
Old Dominion University
Physics Department
Elkhorn Ave 4600
23529 Norfolk VA
USA
tel: +1 757 683 5810
skoirala@jlab.org

Nicholas KVALTINE
University of Virginia
Physics Department
382 McCormick Rd
PO Box 400714
Cherlottesville 22904-4714
USA
tel: +1 434 924 3357
kvaltine@jlab.org

Aram MOVSISYAN
ANSL
Alkhanyan Brothers St. 2
0036 Yerevan
Armenia
tel: +374 1034 4736
aram.movsisyan@desy.de

Miroslav MYSKA
Institute of Physics
Academy of Science
Unina Slovance 2
18221 Prague
Czech
`myskam@fzu.cz`

Emanuele NOCERA
INFN, Sezione di Milano
Via Celoria 16
20133 Milano
Italy
tel: +39 347 2336588
`emanuele.nocera@mi.infn.it`

Vladislav PAUK
University Mainz
Institute of Nuclear Physics
J.-J.-Becher Weg 45
55128 Mainz
Germany
tel: +49 6131 3927164
`paukvp@gmail.com`

Anush PETROSYAN
ANSL
Alkhanyan Brothers St. 2
Yerevan 375036
Armenia
tel: +374 10 344 736
`ankanuclear@mail.yerphi.am`

Alexandr PIMIKOV
JiNR
Sector 6, Cab.014
Joliot Curie 6
141980 Dubna
Russia
tel: +7 915 3514933
`pimikov@theor.jinr.ru`

Silvia PISANO
INFN
Laboratori Nazionali di Frascati
Via E. Fermi 40
00044 Frascati (RM)
Italy
tel: +39 06 9403 2941
`silvia.pisano@lnf.infn.it`

Daniel PITONYAK
Temple University
Department of Physics
Barton hall
19122-6082 Philadelphia, PA
USA
tel: +1 215 204 7634
`daniel.pitonyak@temple.edu`

Matteo RINALDI
INFN, Sezione di Perugia
Via A. Pascoli
06100 Perugia
Italy
tel: +39 338 8648255
fax: +39 075 44666
`ghizmor@hotmail.it`

Giovanni ROMANELLI
Dipartimento di Fisica
Università di Roma Tor Vergata
Via della Ricerca Scientifica 1
00133 Roma
Italy
tel: +39 06 7259 4297
`giova_rom@libero.it`

Park SANGHWA
Seoul National University
599 Gwanak-ro
Seoul 151-742
Korea
tel: +82 2 875 4611
`sanghwa@snu.ac.kr`

Katharina SCHMIDT
University Mainz
Institute of Nuclear Physics
J.-J.-Becher Weg 45
55128 Mainz
Germany
tel: +49 761 203 5804
`katharina.schmidt@cern.ch`

Gary SMITH
University of Glasgow
Kelvin Building Room 415
University Ave G12 8QQ
Glasgow
UK
tel: +44 141 330 2971
`gary.smith@physics.gla.ac.uk`

Daria SOKHAN
IPNO
Bat.1000-M053
91406 Orsay
France
`daria@ipno.in2p3.fr`

Frederik VAN DER VEKEN
University of Antwerp
CGB U238
Groenenborgerlaan 171
2020 Antwerpen
Belgium
tel: +3232653590
`federik.vanderveken@ua.ac.be`

Grant WEBB
University of Kentucky
Department of Physics
Lexington KY 40506-0055
USA
tel: +1 606 356 1744
`grant.webb@uky.edu`

Xiaonu XIONG
LBNL
Nuclear Theory Group
One Cyldson Road
W70R0319
Berkley 94720
USA
tel: +1 510 486 5466
`xxiong@lbl.gov`

Vitaly ZAGREBELNY
DESY
Notkestr. 85
22607 Hamburg
Germany
tel: +49 176 38527021
`vitalzag@mail.desy.de`

Observers

Tord JOHANSSON
Uppsala University
Department of Physics
Box 516
75120 Uppsala
Sweden
tel: +46 184713886
`tord.johansson@physics.uu.se`

Misha OSIPENKO
INFN, Sezione di Genova
Via Dodecaneso 33
16146 Genova
Italy
tel: +39 010 3536276
`osipenko@ge.infn.it`

Sergio PEREIRA ANEFALOS
INFN
Laboratori Nazionali di Frascati
Via E. Fermi 40
00044 Frascati (RM)
Italy
tel: +39 06 94032569
`sergio.pereira@lnf.infn.it`

PROCEEDINGS OF THE INTERNATIONAL SCHOOL OF PHYSICS "ENRICO FERMI"

Course I (1953)
Questioni relative alla rivelazione delle particelle elementari, con particolare riguardo alla radiazione cosmica
edited by G. Puppi

Course II (1954)
Questioni relative alla rivelazione delle particelle elementari, e alle loro interazioni con particolare riguardo alle particelle artificialmente prodotte ed accelerate
edited by G. Puppi

Course III (1955)
Questioni di struttura nucleare e dei processi nucleari alle basse energie
edited by C. Salvetti

Course IV (1956)
Proprietà magnetiche della materia
edited by L. Giulotto

Course V (1957)
Fisica dello stato solido
edited by F. Fumi

Course VI (1958)
Fisica del plasma e relative applicazioni astrofisiche
edited by G. Righini

Course VII (1958)
Teoria della informazione
edited by E. R. Caianiello

Course VIII (1958)
Problemi matematici della teoria quantistica delle particelle e dei campi
edited by A. Borsellino

Course IX (1958)
Fisica dei pioni
edited by B. Touschek

Course X (1959)
Thermodynamics of Irreversible Processes
edited by S. R. de Groot

Course XI (1959)
Weak Interactions
edited by L. A. Radicati

Course XII (1959)
Solar Radioastronomy
edited by G. Righini

Course XIII (1959)
Physics of Plasma: Experiments and Techniques
edited by H. Alfvén

Course XIV (1960)
Ergodic Theories
edited by P. Caldirola

Course XV (1960)
Nuclear Spectroscopy
edited by G. Racah

Course XVI (1960)
Physicomathematical Aspects of Biology
edited by N. Rashevsky

Course XVII (1960)
Topics of Radiofrequency Spectroscopy
edited by A. Gozzini

Course XVIII (1960)
Physics of Solids (Radiation Damage in Solids)
edited by D. S. Billington

Course XIX (1961)
Cosmic Rays, Solar Particles and Space Research
edited by B. Peters

Course XX (1961)
Evidence for Gravitational Theories
edited by C. Møller

Course XXI (1961)
Liquid Helium
edited by G. Careri

Course XXII (1961)
Semiconductors
edited by R. A. Smith

Course XXIII (1961)
Nuclear Physics
edited by V. F. Weisskopf

Course XXIV (1962)
Space Exploration and the Solar System
edited by B. Rossi

Course XXV (1962)
Advanced Plasma Theory
edited by M. N. Rosenbluth

Course XXVI (1962)
Selected Topics on Elementary Particle Physics
edited by M. Conversi

Course XXVII (1962)
Dispersion and Absorption of Sound by Molecular Processes
edited by D. Sette

Course XXVIII (1962)
Star Evolution
edited by L. Gratton

Course XXIX (1963)
Dispersion Relations and their Connection with Casuality
edited by E. P. Wigner

Course XXX (1963)
Radiation Dosimetry
edited by F. W. Spiers and G. W. Reed

Course XXXI (1963)
Quantum Electronics and Coherent Light
edited by C. H. Townes and P. A. Miles

Course XXXII (1964)
Weak Interactions and High-Energy Neutrino Physics
edited by T. D. Lee

Course XXXIII (1964)
Strong Interactions
edited by L. W. Alvarez

Course XXXIV (1965)
The Optical Properties of Solids
edited by J. Tauc

Course XXXV (1965)
High-Energy Astrophysics
edited by L. Gratton

Course XXXVI (1965)
Many-body Description of Nuclear Structure and Reactions
edited by C. L. Bloch

Course XXXVII (1966)
Theory of Magnetism in Transition Metals
edited by W. Marshall

Course XXXVIII (1966)
Interaction of High-Energy Particles with Nuclei
edited by T. E. O. Ericson

Course XXXIX (1966)
Plasma Astrophysics
edited by P. A. Sturrock

Course XL (1967)
Nuclear Structure and Nuclear Reactions
edited by M. Jean and R. A. Ricci

Course XLI (1967)
Selected Topics in Particle Physics
edited by J. Steinberger

Course XLII (1967)
Quantum Optics
edited by R. J. Glauber

Course XLIII (1968)
Processing of Optical Data by Organisms and by Machines
edited by W. Reichardt

Course XLIV (1968)
Molecular Beams and Reaction Kinetics
edited by Ch. Schlier

Course XLV (1968)
Local Quantum Theory
edited by R. Jost

Course XLVI (1969)
Physics with Intersecting Storage Rings
edited by B. Touschek

Course XLVII (1969)
General Relativity and Cosmology
edited by R. K. Sachs

Course XLVIII (1969)
Physics of High Energy Density
edited by P. Caldirola and H. Knoepfel

Course IL (1970)
Foundations of Quantum Mechanics
edited by B. d'Espagnat

Course L (1970)
Mantle and Core in Planetary Physics
edited by J. Coulomb and M. Caputo

Course LI (1970)
Critical Phenomena
edited by M. S. Green

Course LII (1971)
Atomic Structure and Properties of Solids
edited by E. Burstein

Course LIII (1971)
Developments and Borderlines of Nuclear Physics
edited by H. Morinaga

Course LIV (1971)
Developments in High-Energy Physics
edited by R. R. Gatto

Course LV (1972)
Lattice Dynamics and Intermolecular Forces
edited by S. Califano

Course LVI (1972)
Experimental Gravitation
edited by B. Bertotti

Course LVII (1972)
History of 20th Century Physics
edited by C. Weiner

Course LVIII (1973)
Dynamics Aspects of Surface Physics
edited by F. O. Goodman

Course LIX (1973)
Local Properties at Phase Transitions
edited by K. A. Müller and A. Rigamonti

Course LX (1973)
C*-Algebras and their Applications to Statistical Mechanics and Quantum Field Theory
edited by D. Kastler

Course LXI (1974)
Atomic Structure and Mechanical Properties of Metals
edited by G. Caglioti

Course LXII (1974)
Nuclear Spectroscopy and Nuclear Reactions with Heavy Ions
edited by H. Faraggi and R. A. Ricci

Course LXIII (1974)
New Directions in Physical Acoustics
edited by D. Sette

Course LXIV (1975)
Nonlinear Spectroscopy
edited by N. Bloembergen

Course LXV (1975)
Physics and Astrophysics of Neutron Stars and Black Hole
edited by R. Giacconi and R. Ruffini

Course LXVI (1975)
Health and Medical Physics
edited by J. Baarli

Course LXVII (1976)
Isolated Gravitating Systems in General Relativity
edited by J. Ehlers

Course LXVIII (1976)
Metrology and Fundamental Constants
edited by A. Ferro Milone, P. Giacomo and S. Leschiutta

Course LXIX (1976)
Elementary Modes of Excitation in Nuclei
edited by A. Bohr and R. A. Broglia

Course LXX (1977)
Physics of Magnetic Garnets
edited by A. Paoletti

Course LXXI (1977)
Weak Interactions
edited by M. Baldo Ceolin

Course LXXII (1977)
Problems in the Foundations of Physics
edited by G. Toraldo di Francia

Course LXXIII (1978)
Early Solar System Processes and the Present Solar System
edited by D. Lal

Course LXXIV (1978)
Development of High-Power Lasers and their Applications
edited by C. Pellegrini

Course LXXV (1978)
Intermolecular Spectroscopy and Dynamical Properties of Dense Systems
edited by J. Van Kranendonk

Course LXXVI (1979)
Medical Physics
edited by J. R. Greening

Course LXXVII (1979)
Nuclear Structure and Heavy-Ion Collisions
edited by R. A. Broglia, R. A. Ricci and C. H. Dasso

Course LXXVIII (1979)
Physics of the Earth's Interior
edited by A. M. Dziewonski and E. Boschi

Course LXXIX (1980)
From Nuclei to Particles
edited by A. Molinari

Course LXXX (1980)
Topics in Ocean Physics
edited by A. R. Osborne and P. Malanotte Rizzoli

Course LXXXI (1980)
Theory of Fundamental Interactions
edited by G. Costa and R. R. Gatto

Course LXXXII (1981)
Mechanical and Thermal Behaviour of Metallic Materials
edited by G. Caglioti and A. Ferro Milone

Course LXXXIII (1981)
Positrons in Solid-State Physics
edited by W. Brandt and A. Dupasquier

Course LXXXIV (1981)
Data Acquisition in High-Energy Physics
edited by G. Bologna and M. Vincelli

Course LXXXV (1982)
Earthquakes: Observation, Theory and Interpretation
edited by H. Kanamori and E. Boschi

Course LXXXVI (1982)
Gamow Cosmology
edited by F. Melchiorri and R. Ruffini

Course LXXXVII (1982)
Nuclear Structure and Heavy-Ion Dynamics
edited by L. Moretto and R. A. Ricci

Course LXXXVIII (1983)
Turbulence and Predictability in Geophysical Fluid Dynamics and Climate Dynamics
edited by M. Ghil, R. Benzi and G. Parisi

Course LXXXIX (1983)
Highlights of Condensed Matter Theory
edited by F. Bassani, F. Fumi and M. P. Tosi

Course XC (1983)
Physics of Amphiphiles: Micelles, Vesicles and Microemulsions
edited by V. Degiorgio and M. Corti

Course XCI (1984)
From Nuclei to Stars
edited by A. Molinari and R. A. Ricci

Course XCII (1984)
Elementary Particles
edited by N. Cabibbo

Course XCIII (1984)
Frontiers in Physical Acoustics
edited by D. Sette

Course XCIV (1984)
Theory of Reliability
edited by A. Serra and R. E. Barlow

Course XCV (1985)
Solar-Terrestrial Relationship and the Earth Environment in the Last Millennia
edited by G. Cini Castagnoli

Course XCVI (1985)
Excited-State Spectroscopy in Solids
edited by U. M. Grassano and N. Terzi

Course XCVII (1985)
Molecular-Dynamics Simulations of Statistical-Mechanical Systems
edited by G. Ciccotti and W. G. Hoover

Course XCVIII (1985)
The Evolution of Small Bodies in the Solar System
edited by M. Fulchignoni and Ľ. Kresàk

Course XCIX (1986)
Synergetics and Dynamic Instabilities
edited by G. Caglioti and H. Haken

Course C (1986)
The Physics of NMR Spectroscopy in Biology and Medicine
edited by B. Maraviglia

Course CI (1986)
Evolution of Interstellar Dust and Related Topics
edited by A. Bonetti and J. M. Greenberg

Course CII (1986)
Accelerated Life Testing and Experts' Opinions in Reliability
edited by C. A. Clarotti and D. V. Lindley

Course CIII (1987)
Trends in Nuclear Physics
edited by P. Kienle, R. A. Ricci and A. Rubbino

Course CIV (1987)
Frontiers and Borderlines in Many-Particle Physics
edited by R. A. Broglia and J. R. Schrieffer

Course CV (1987)
Confrontation between Theories and Observations in Cosmology: Present Status and Future Programmes
edited by J. Audouze and F. Melchiorri

Course CVI (1988)
Current Trends in the Physics of Materials
edited by G. F. Chiarotti, F. Fumi and M. Tosi

Course CVII (1988)
The Chemical Physics of Atomic and Molecular Clusters
edited by G. Scoles

Course CVIII (1988)
Photoemission and Absorption Spectroscopy of Solids and Interfaces with Synchrotron Radiation
edited by M. Campagna and R. Rosei

Course CIX (1988)
Nonlinear Topics in Ocean Physics
edited by A. R. Osborne

Course CX (1989)
Metrology at the Frontiers of Physics and Technology
edited by L. Crovini and T. J. Quinn

Course CXI (1989)
Solid-State Astrophysics
edited by E. Bussoletti and G. Strazzulla

Course CXII (1989)
Nuclear Collisions from the Mean-Field into the Fragmentation Regime
edited by C. Detraz and P. Kienle

Course CXIII (1989)
High-Pressure Equation of State: Theory and Applications
edited by S. Eliezer and R. A. Ricci

Course CXIV (1990)
Industrial and Technological Applications of Neutrons
edited by M. Fontana and F. Rustichelli

Course CXV (1990)
The Use of EOS for Studies of Atmospheric Physics
edited by J. C. Gille and G. Visconti

Course CXVI (1990)
Status and Perspectives of Nuclear Energy: Fission and Fusion
edited by R. A. Ricci, C. Salvetti and E. Sindoni

Course CXVII (1991)
Semiconductor Superlattices and Interfaces
edited by A. Stella

Course CXVIII (1991)
Laser Manipulation of Atoms and Ions
edited by E. Arimondo, W. D. Phillips and F. Strumia

Course CXIX (1991)
Quantum Chaos
edited by G. Casati, I. Guarneri and U. Smilansky

Course CXX (1992)
Frontiers in Laser Spectroscopy
edited by T. W. Hänsch and M. Inguscio

Course CXXI (1992)
Perspectives in Many-Particle Physics
edited by R. A. Broglia, J. R. Schrieffer and P. F. Bortignon

Course CXXII (1992)
Galaxy Formation
edited by J. Silk and N. Vittorio

Course CXXIII (1992)
Nuclear Magnetic Double Resonsonance
edited by B. Maraviglia

Course CXXIV (1993)
Diagnostic Tools in Atmospheric Physics
edited by G. Fiocco and G. Visconti

Course CXXV (1993)
Positron Spectroscopy of Solids
edited by A. Dupasquier and A. P. Mills jr.

Course CXXVI (1993)
Nonlinear Optical Materials: Principles and Applications
edited by V. Degiorgio and C. Flytzanis

Course CXXVII (1994)
Quantum Groups and their Applications in Physics
edited by L. Castellani and J. Wess

Course CXXVIII (1994)
Biomedical Applications of Synchrotron Radiation
edited by E. Burattini and A. Balerna

Course CXXIX[1] (1994)
Observation, Prediction and Simulation of Phase Transitions in Complex Fluids
edited by M. Baus, L. F. Rull and J. P. Ryckaert

Course CXXX (1995)
Selected Topics in Nonperturbative QCD
edited by A. Di Giacomo and D. Diakonov

Course CXXXI (1995)
Coherent and Collective Interactions of Particles and Radiation Beams
edited by A. Aspect, W. Barletta and R. Bonifacio

---

[1] This course belongs to the NATO ASI Series C, Vol. 460 (Kluwer Academic Publishers).

Course CXXXII (1995)
Dark Matter in the Universe
edited by S. Bonometto and J. Primack

Course CXXXIII (1996)
Past and Present Variability of the Solar-Terrestrial System: Measurement, Data Analysis and Theoretical Models
edited by G. Cini Castagnoli
and A. Provenzale

Course CXXXIV (1996)
The Physics of Complex Systems
edited by F. Mallamace and H. E. Stanley

Course CXXXV (1996)
The Physics of Diamond
edited by A. Paoletti and A. Tucciarone

Course CXXXVI (1997)
Models and Phenomenology for Conventional and High-Temperature Superconductivity
edited by G. Iadonisi, J. R. Schrieffer
and M. L. Chiofalo

Course CXXXVII (1997)
Heavy Flavour Physics: a Probe of Nature's Grand Design
edited by I. Bigi and L. Moroni

Course CXXXVIII (1997)
Unfolding the Matter of Nuclei
edited by A. Molinari and R. A. Ricci

Course CXXXIX (1998)
Magnetic Resonance and Brain Function: Approaches from Physics
edited by B. Maraviglia

Course CXL (1998)
Bose-Einstein Condensation in Atomic Gases
edited by M. Inguscio, S. Stringari
and C. E. Wieman

Course CXLI (1998)
Silicon-Based Microphotonics: from Basics to Applications
edited by O. Bisi, S. U. Campisano, L. Pavesi
and F. Priolo

Course CXLII (1999)
Plasmas in the Universe
edited by B. Coppi, A. Ferrari
and E. Sindoni

Course CXLIII (1999)
New Directions in Quantum Chaos
edited by G. Casati, I. Guarneri
and U. Smilansky

Course CXLIV (2000)
Nanometer Scale Science and Technology
edited by M. Allegrini, N. García
and O. Marti

Course CXLV (2000)
Protein Folding, Evolution and Design
edited by R. A. Broglia, E. I. Shakhnovich
and G. Tiana

Course CXLVI (2000)
Recent Advances in Metrology and Fundamental Constants
edited by T. J. Quinn, S. Leschiutta
and P. Tavella

Course CXLVII (2001)
High Pressure Phenomena
edited by R. J. Hemley, G. L. Chiarotti,
M. Bernasconi and L. Ulivi

Course CXLVIII (2001)
Experimental Quantum Computation and Information
edited by F. De Martini and C. Monroe

Course CXLIX (2001)
Organic Nanostructures: Science and Applications
edited by V. M. Agranovich
and G. C. La Rocca

Course CL (2002)
Electron and Photon Confinement in Semiconductor Nanostructures
edited by B. Deveaud-Plédran,
A. Quattropani and P. Schwendimann

Course CLI (2002)
Quantum Phenomena in Mesoscopic Systems
edited by B. Altshuler, A. Tagliacozzo
and V. Tognetti

Course CLII (2002)
Neutrino Physics
edited by E. Bellotti, Y. Declais
and P. Strolin

Course CLIII (2002)
From Nuclei and their Constituents to Stars
edited by A. Molinari, L. Riccati,
W. M. Alberico and M. Morando

Course CLIV (2003)
Physics Methods in Archaeometry
edited by M. Martini, M. Milazzo
and M. Piacentini

Course CLV (2003)
The Physics of Complex Systems (New Advances and Perspectives)
edited by F. Mallamace and H. E. Stanley

Course CLVI (2003)
Research on Physics Education
edited by E.F. Redish and M. Vicentini

Course CLVII (2003)
The Electron Liquid Model in Condensed Matter Physics
edited by G. F. Giuliani and G. Vignale

Course CLVIII (2004)
Hadron Physics
edited by T. Bressani, U. Wiedner and A. Filippi

Course CLIX (2004)
Background Microwave Radiation and Intracluster Cosmology
edited by F. Melchiorri and Y. Rephaeli

Course CLX (2004)
From Nanostructures to Nanosensing Applications
edited by A. D'Amico, G. Balestrino and A. Paoletti

Course CLXI (2005)
Polarons in Bulk Materials and Systems with Reduced Dimensionality
edited by G. Iadonisi, J. Ranninger and G. De Filippis

Course CLXII (2005)
Quantum Computers, Algorithms and Chaos
edited by G. Casati, D. L. Shepelyansky, P. Zoller and G. Benenti

Course CLXIII (2005)
CP Violation: From Quarks to Leptons
edited by M. Giorgi, I. Mannelli, A. I. Sanda, F. Costantini and M. S. Sozzi

Course CLXIV (2006)
Ultra-Cold Fermi Gases
edited by M. Inguscio, W. Ketterle and C. Salomon

Course CLXV (2006)
Protein Folding and Drug Design
edited by R. A. Broglia, L. Serrano and G. Tiana

Course CLXVI (2006)
Metrology and Fundamental Constants
edited by T. W. Hänsch, S. Leschiutta, A. J. Wallard and M. L. Rastello

Course CLXVII (2007)
Strangeness and Spin in Fundamental Physics
edited by M. Anselmino, T. Bressani, A. Feliciello and Ph. G. Ratcliffe

Course CLXVIII (2007)
Atom Optics and Space Physics
edited by E. Arimondo, W. Ertmer, W. P. Schleich and E. M. Rasel

Course CLXIX (2007)
Nuclear Structure far from Stability: New Physics and New Technology
edited by A. Covello, F. Iachello, R. A. Ricci and G. Maino

Course CLXX (2008)
Measurements of Neutrino Mass
edited by F. Ferroni, F. Vissani and C. Brofferio

Course CLXXI (2008)
Quantum Coherence in Solid State Physics
edited by B. Deveaud-Plédran, A. Quattropani and P. Schwendimann

Course CLXXII (2008)
Astrophysics of Galaxy Clusters
edited by A. Cavaliere and Y. Rephaeli

Course CLXXIII (2009)
Nano Optics and Atomics: Transport of Light and Matter Waves
edited by R. Kaiser, D. S. Wiersma and L. Fallani

Course CLXXIV (2009)
Physics with Many Positrons
edited by R. S. Brusa, A. Dupasquier and A. P. Mills jr.

Course CLXXV (2009)
Radiation and Particle Detectors
edited by S. Bertolucci, U. Bottigli and P. Oliva

Course CLXXVI (2010)
Complex Materials in Physics and Biology
edited by F. Mallamace and H. E. Stanley

Course CLXXVIII (2010)
From the Big Bang to the Nucleosynthesis
edited by A. Bracco and E. Nappi

Course CLXXIX (2011)
Laser-Plasma Acceleration
edited by F. Ferroni, L. A. Gizzi
and R. Faccini

Course CLXXXII (2011)
Neutrino Physics and Astrophysics
edited by G. Bellini and L. Ludhova